

LAMINAR SLOT JET AND SLOT JET IMPINGEMENT HEAT TRANSFER

Thesis Submitted in Partial Fulfilment of the Requirements
for the Award of the Degree of

DOCTOR OF PHILOSOPHY
IN
ENGINEERING

by
KHANDKAR AFTAB HOSSAIN

Under the supervision of
Prof. R.C. ARORA



DEPARTMENT OF MECHANICAL ENGINEERING
INDIAN INSTITUTE OF TECHNOLOGY
Kharagpur-721 302, INDIA
1996

DEDICATED TO MY

DEAR PARENTS

CERTIFICATE

This is to certify that the thesis entitled "Laminar Slot Jet and Slot Jet Impingement Heat Transfer" submitted by **Khandkar Aftab Hossain**, a Research Scholar in the Department of Mechanical Engineering of Indian Institute of Technology, Kharagpur is a record of bonafide research work carried out by him under my supervision and guidance. The thesis, in my opinion, is worthy of consideration for the award of the degree of Doctor of Philosophy in Mechanical Engineering in accordance with the rules and regulations of I.I.T., Kharagpur. The results presented in this thesis have not been submitted elsewhere for the award of any other degree.

Date: 27.5.96.



(Prof. R. C. Arora)
Supervisor
Professor
Mechanical Engineering Department
I.I.T., Kharagpur

BIODATA

Name : **Khandkar Aftab Hossain**

Nationality : Bangladeshi

Qualification : B.Sc.Engg. (Mechanical), 1982
Khulna Engineering College, Khulna
at present Bangladesh Institute of
Technology (BIT), Khulna-9203
Bangladesh.

M.Sc. Engg. (Mechanical), 1990
Bangladesh University of Engineering
and Technology, Dhaka-1000, Bangladesh.

Present Occupation : Assistant Professor
Department of Mechanical Engineering
Bangladesh Institute of Technology (BIT)
Khulna-9203, Bangladesh.

Permanent address : 62, Gagon Babu Road
Khulna-9100, Bangladesh.

ACKNOWLEDGEMENTS

The author expresses his deep and sincere sense of gratitude to Prof. R. C. Arora, for suggesting the problems, guidance and encouragement throughout the period of this investigation.

The advice and help received from Prof. R. K. Brahma in the Department of Mechanical Engineering is gratefully acknowledged.

I would like to express my sense of gratitude to Prof. B. C. Majumdar, former Head of Mechanical Engineering Department for his help and encouragement.

The author expresses his indebtedness to Prof. M. A. Faruqi, Head of Mechanical Engineering Department for providing the computation facility in the CAD/CAM centre of the Mechanical Engineering Department.

I would like to express my indebtedness to Indian Council for Cultural Relations (I.C.C.R.) for providing the Scholarship during the whole period of this investigation.

Date: 27.5.96



Khandkar Aftab Hossain

PREFACE

Jet impingement has a very wide range of applications in industry. Jet impingement is used in drying of paper, veneer and textiles; manufacture of plastics, ceramic products and film materials; cooling of V.L.S.I. chips and steel strips in high speed and extra wide rolling mills. The applications of free jets including the effects of buoyancy are : the discharge of pollutants into atmosphere and distribution of supply air in airconditioned spaces. The offset type of jet occurs in the flows entering heat exchangers, discharge of effluents from power plants and flow into combustion chamber. Impinging jets are used for localized, controlled cooling and to achieve high heat transfer rates.

In the present investigation, the numerical results are presented for, (i) free slot jet, (ii) free axisymmetric jet, (iii) jet impingement on a circular cylinder and (iv) vertically downward slot jet impinging on a flat plate with and without buoyancy in the laminar range of Reynolds numbers for all the cases. The offset slot jet in the range of low Reynolds numbers, has been investigated, for the first time.

Literature search indicates that the solutions of Navier-Stokes equations near the slot-exit plane the for free slot jet and the free axisymmetric jet are not available in detail. The temperature distribution is not available in detail for the laminar free slot jet and free axisymmetric jet. The numerical iv

solutions of Navier-Stokes equations and energy equation have been obtained for these two jets by SIMPLE algorithm for different Reynolds numbers and Prandtl numbers with the uniform and the parabolic velocity and temperature profiles at the nozzle-exit.

The information at low Reynolds numbers is not available for the jet impingement on a circular cylinder. The Navier-Stokes equations have been numerically solved by SIMPLER algorithm and results are presented for the skin friction coefficient, pressure distribution on the cylinder surface and velocity profiles at different Reynolds numbers, nozzle-to-plate spacings, and nozzle widths.

Vertically downward buoyant slot jet impinging on a flat surface has been investigated by many authors, however results are not available for the parabolic slot exit velocity and temperature profiles. In the present investigation, numerical solutions of laminar vertically downward slot jet impinging on a flat surface with and without buoyancy have been obtained for different Reynolds numbers, nozzle-to-surface spacings, Richardson numbers, Prandtl numbers and for both, the parabolic and uniform slot-exit velocity and temperature profiles. Empirical correlations have been developed for the average Nusselt number, maximum Nusselt number and the stagnation point Nusselt number in absence of buoyancy for the laminar flow.

In the literature, there is lack of information on the offset slot jet in the range of low Reynolds numbers. In this investigation, numerical solutions have been obtained for the laminar offset slot jet with the uniform and the parabolic slot

exit velocity and temperature profiles for different Reynolds numbers, offset ratios and Prandtl numbers. Empirical correlations have been developed for the reattachment length, maximum Nusselt number and the average Nusselt number in the separated region.

In general, it has been obtained that SIMPLE and SIMPLEC algorithms for the solutions of Navier-Stokes equations and energy equation, are quite robust. However, convergence problems were faced at higher Reynolds numbers, particularly for uniform nozzle-exit velocity and temperature profiles.

ABSTRACT

In this investigation, the numerical solutions of Navier-Stokes equations and energy equation are presented for (i) laminar free slot jet, (ii) laminar free axisymmetric jet, (iii) laminar jet impingement on a circular cylinder, (iv) vertically downward laminar slot jet impinging on a flat surface with and without buoyancy, and (v) offset slot jet in the range of low Reynolds numbers for both, the uniform and the parabolic slot-exit velocity and temperature profiles. SIMPLE and SIMPLEC algorithm have been used for the numerical solutions.

The velocity and temperature profiles are presented near the nozzle-exit and far away from the nozzle-exit plane for free slot jet and free axisymmetric jet. The centreline velocity and temperature become coincident for all Reynolds numbers when plotted against $\bar{X} = X/Re$. The velocity profiles become coincident for all Reynolds numbers far away from nozzle-exit in Schlichting's variable η and with half jet width as characteristic length. The results are in good agreement with the available experimental results. The jet diffuses at a fast rate at lower Reynolds numbers and the jet spread decreases at higher Reynolds numbers.

Jet impingement over a cylinder has been investigated for low Reynolds numbers. The results for skin friction, pressure distribution and velocity profiles on cylinder surface, are presented. The results do not depend strongly on slot width. The effect of decrease in slot-to-cylinder spacing is equivalent to increase in Reynolds number. The flow separation occurs earlier at

higher Reynolds numbers.

In case of vertically downward slot jet impinging on a flat surface, the buoyancy force significantly affects the flow field, the local Nusselt number, local friction factor and the pressure distribution along the impingement surface. The jet behaves almost like a non-buoyant jet for values of Richardson numbers less than 0.014 with uniform slot-exit profiles and Richardson number less than 0.007 with parabolic slot-exit profiles. The jet detaches from the surface and rises up like a plume for $Ri \geq 0.014$ with uniform slot-exit profiles and for $Ri \geq 0.007$ with parabolic slot-exit profiles. The jet does not come into contact with the surface at all for $Ri \geq 1.25$ for both, the uniform and parabolic slot-exit profiles. Empirical correlations have been developed for determining the average Nusselt number, maximum Nusselt number and the stagnation point Nusselt number for both the types of velocity and temperature profiles in absence of buoyancy for laminar flow. The maximum Nusselt number occurs at the stagnation point for parabolic slot-exit profiles, whereas for uniform slot-exit profiles, it occurs slightly away from the stagnation point.

The offset ratio significantly influences the local Nusselt number, local friction factor and the pressure along the impingement surface for offset slot jet in the range of low Reynolds numbers. Secondary recirculation is observed at an offset ratio of 7 and Reynolds number of 80. The reattachment length is observed to be approximately constant at higher values of Reynolds numbers. Empirical correlations have been developed for the reattachment length, maximum Nusselt number and the average Nusselt number in the separated region.



Key word: slot jet, axisymmetric jet, reattachment length, separated region, wall jet, laminar, buoyant jet, offset jet, stagnation point, reattachment point, free jet, circular cylinder, recirculation.

CONTENTS

	Page No.
Certificate	i
Bio-data	ii
Acknowledgement	iii
Preface	iv
Abstract	vii
Contents	x
Nomenclature	xii
CHAPTER-I :	1
Introduction	1
1.1 Free Jet	3
1.2 Jet Impingement	5
1.3 Offset Jet	7
1.4 Scope of Present Investigation	9
CHAPTER-II :	12
Review	12
2.1 Wall Jet	13
2.2 Free Slot Jet	16
2.3 Free Axisymmetric Jet	21
2.4 Slot Jet Impingement on a Circular Cylinder	27
2.5 Jet Impingement on Normal Surface	32
2.6 Offset Slot Jet	59
CHAPTER-III :	67
Problem Formulation and Numerical Modelling	67
3.1 Free Slot Jet	69
3.1.1 Governing Equations	70
3.1.2 Numerical Solution Procedure	73
3.1.2.1 Pressure Correction Equations	87
3.1.3 Sequence of Operation in SIMPLE	91
3.1.4 Similarity Solution	92
3.1.5 Boundary Conditions Specified in the Computer Programme	95
3.2 Free Axisymmetric Jet	103
3.2.1 Governing Equations	104

3.2.2	Numerical Solution Procedure	107
3.2.3	Similarity Solution	108
3.3	Slot Jet Impingement on a Circular Cylinder	113
3.3.1	Governing Equations	114
3.3.2	Numerical Solution Procedure	116
3.4	Vertically downward Slot Jet Impinging upon a Flat Surface	134
3.4.1	Governing Equations	135
3.4.2	Numerical Solution Procedure	138
3.5	Offset Slot Jet	141
3.5.1	Governing Equations	142
3.5.2	Numerical Solution Procedure	145
CHAPTER-IV :		153
Results and discussion		153
4.1	Free Slot Jet	153
4.2	Free Axisymmetric Jet	208
4.3	Slot Jet Impingement on a Circular Cylinder	244
4.3	Vertically downward Slot Jet Impinging upon a Flat Surface	261
4.5	Offset Slot Jet	309
CHAPTER-V :		363
Conclusions		363
5.1	Free Slot Jet	365
5.2	Free Axisymmetric Jet	366
5.3	Slot Jet Impingement on a Circular Cylinder	367
3.4	Vertically downward Slot Jet Impinging upon a Flat Surface	368
5.5	Offset Slot Jet	369
5.6	Scope of Future Work	370
REFERENCES :		373

NOMENCLATURE

a	Coefficient of the discretized equations
b	Constant of the discretized equations
B	Nozzle half width, $W/2$
C_f	Skin friction coefficient, $\tau/\rho V_j^2$, $\tau/\rho U_j^2$
C_f^*	C_f/\sqrt{Re}
d	Diameter of the nozzle
h_x	Heat transfer coefficient,
h	Height of the domain in y-direction
h_1	Height from the impingement surface to the nozzle exit plane for vertically downward jet or height of lower lip of nozzle for offset jet
H	h/W
H_1	h_1/W
Gr	Grashof number = $g\beta(T_j - T_w)W^3/\nu^2$
g	Acceleration due to gravity
J_e	Momentum of the jet in the axial direction at jet exit
K_e	Enthalpy of jet at jet exit
k	Thermal conductivity of fluid
l	Length of the domain in the x-direction or nozzle-to-cylinder spacing
L_A	Reattachment length
n,s,e,w	Mid points of control volumes faces.
N,S,E,W,P	Locations of grid points, P and its four neighbors
Nu	Local Nusselt number, $h_x W/k$
Nu_0	Stagnation point Nusselt number

- Nu_{avg} Average Nusselt number
 Nu_{max} Maximum Nusselt number
 O.R. Offset ratio, $H_1 + \frac{1}{2}$
 p Pressure
 p_∞ Reference pressure
 P Dimensionless pressure, $(P-P_\infty)/\rho_o U_j^2$, $(P-P_\infty)/\rho_o V_j^2$
 Pr Fluid Prandtl number, $C_p \mu/k$
 Re Reynolds number at jet exit, $\frac{U_j W}{\nu}$, $V_j R_o/\nu$, $V_j W/\nu$, $\frac{U_j r_o}{\nu}$
 R_o Cylinder radius
 r Coordinate in radial direction
 R Dimensionless radial distance, $\frac{r}{R_o}$
 r_o Nozzle radius
 r_1 Radial distance from the cylinder centre to the nozzle exit plane
 $R_{0.5U_{max}}$ Radial distance from the cylinder surface to the point where, $U=U_{max}/2$
 $R_{0.5T_{max}^*}$ Radial distance from the cylinder surface to the point where, $T^*=T_{max}^*/2$
 $R_{0.5U}$ Half jet radius, that is, the radial distance from the jet axis to the point where, $U=U_c/2$
 $R_{0.5T^*}$ Half jet radius, that is, the radial distance from the jet axis to the point where, $T^*=T_c^*/2$
 Ri Richardson number, Gr/Re^2
 S Source term
 T Temperature
 T^* Dimensionless temperature, $\frac{(T - T_\infty)}{(T_j - T_\infty)}$, $\frac{(T - T_w)}{(T_j - T_w)}$
 T_c Centre line temperature along the axis of symmetry

u Velocity component in x or azimuthal direction
 U Dimensionless velocity component in x or azimuthal direction
 U_{\max} Maximum jet exit velocity in x or azimuthal direction
 U_c Centre line velocity along the axis of symmetry
 v Velocity component in y or radial direction
 V Dimensionless velocity component in y or radial direction
 W Nozzle width
 x Coordinate along the axis of symmetry
 X Dimensionless coordinate, x/W
 \bar{X} $x/(W Re)$, $x/(d Re)$
 XCV(I) The x-direction widths of main control volumes
 XCVI(I) The part of XCV(I) that overlaps on the control volume for U(I,J)
 XCVIP(I) The part of XCV(I) that overlaps on the control volume for U(I+1,J)
 XDIF(I) Width of u-control volume in x or azimuthal direction
 y Coordinate normal to the axis of symmetry
 Y Dimensionless coordinate, y/W
 $Y_{0.5U}$ Half jet width, that is, height from the line of symmetry to the point where, $U = U_c/2$.
 $Y_{0.5T^*}$ Half jet width, that is, height from the line of symmetry to the point where, $T^* = T_c^*/2$.
 YCV(J) The widths of main control volumes in y or radial direction
 YDIF(J) Width of u-control volume in y or radial direction
 ARX(J) The area of the main control volume face normal to the x-direction

ARXJ(J) The part of ARX(J) that overlaps on the main control volume for V(I,J)

ARXJP(J) The part of ARX(J) that overlaps on the main control volume for V(I,J+1)

RMN(J) The value of radius r for the location to which V(I,J) refers

R(J) The radius r for a main grid point (I,J)

I Index denoting the position in x direction

IM Index of right nozzle lip in x or azimuthal direction

IM1 IM-1

IM2 IM+1

L1 The value of I for the last grid location in the x-direction

L2 L1- 1

L3 L2- 1

J Index denoting the position in y direction

JM Index of the nozzle exit plane in y or radial direction

JM1 JM-1

M1 The value of J for the last grid location in the y direction

M2 M1- 1

M3 M2- 1

f Scaling factor for determining $U_{L1,J}$

Greek letters

α Thermal diffusivity, relaxation factor

ϕ General dependent variable

Γ Dimensionless diffusion coefficient



- η Similarity variable $\eta = Y/3X^{2/3}$ or R/X
 ν Kinematic viscosity
 μ Viscosity
 ρ' Density
 ρ_0 Reference density
 ρ Nondimensional density, $\rho = \frac{\rho'}{\rho_0}$
 θ Azimuthal angle in radians
 θ_1 Nozzle half width in azimuthal direction
 θ_E Dividing line between entrainment boundary and outflow boundary
 β Coefficient of thermal expansion
 τ Wall shear stress

Subscripts

- c Centre line
 j Jet exit
 max, m Maximum
 o Jet exit plane
 s.r. Separated region
 ∞ Ambient condition
 ϕ General dependent variable
 w Cylinder surface, wall

CHAPTER-1

INTRODUCTION

Jet impingement has become an accepted technique for cooling wherever high heat transfer rates are required. The attractive features of the jet impingement are the low cost, simplicity of equipment, the flexibility of a fine degree of control through mass flow rate and attainment of high heat transfer rates with small temperature differences. Impinging gas and liquid jets are extensively used in a wide variety of industrial processes for cooling and heating applications.

Adcock [1], and Morgan et al. [2] have described the impinging circular water jets which were used for cooling hot moving steel strips in hot strip mills. It was observed that the grain size can be controlled by the cooling rate and the grain size contributes to strength and toughness of the steel. Kohring [3], has described the application of water wall (slot jet) in the cooling of steel strips in high speed and extra wide steel rolling mills.

Cooling of gas turbine components has motivated most of the research related to jet impingement on flat and curved surfaces with jet exit velocities upto near sonic velocities using single and array of jets. In recent years, jet impingement has found applications in cooling of V.L.S.I. chips as described by Hollworth et al. [4]. Heated air jets are used in aircraft for

deicing of wings and wind shield surfaces. Air jets are also used for cooling and toughening or tempering of glass, drying of textiles, veneer, paper, plastics, ceramic products and film materials. Impingement jets are also used for annealing of non-ferrous metals, the main advantages being the enhanced and controlled localized cooling or heating.

Some of the other applications include mixing process of plastic molds as reported in Akaike and Nemoto [5], vertical take-off and landing (VTOL), surgery, cryo-surgery, fuel injection into furnaces, discharge of pollutants into atmosphere and distribution of supply air in airconditioned spaces. The flow phenomena associated with the offset jet occurs in flows entering into heat exchangers, discharge of effluents from power plants and flows into combustion chambers, as reported in Pelfrey and Liburdy [6].

Fluid discharged from a small opening into the surroundings is called a jet. Jets in incompressible flow are usually produced by converging nozzles in which the pressure decreases and velocity increases in the flow direction. The pressure at the nozzle exit plane reduces to ambient pressure and velocity attains a maximum value. The velocity profile at the nozzle exit depends upon nozzle geometry. Jet may be slot or rectangular jet, square jet, circular jet, round jet, or elliptic jet depending upon the shape of nozzle at the exit plane.

The nozzle exit velocity profile may be fully developed or uniform or in general, of an arbitrary shape depending upon the inside nozzle geometry in the flow direction. A jet which does not

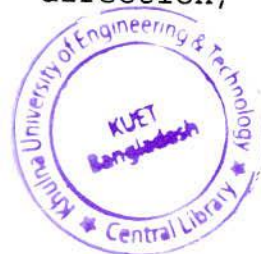
come into contact with any solid surface after its exit, is called a free jet. A jet of a liquid in gas has free surface and does not entrain surrounding fluid. A liquid jet in same liquid or a gas jet in same gas, does not have a free surface. The latter is referred to as a submerged jet which entrains the surrounding fluid. A jet issuing from an orifice in a plane wall is different from a jet issuing from a nozzle. In the former, the entrainment is perpendicular to jet axis and parallel to wall near jet exit. In the latter, there is entrainment around the outer surface of nozzle also. A round jet is a jet issuing from the end of a circular tube. This is different from a jet issuing from a small circular hole in a wall which is usually referred to as an axisymmetric jet.

The above classification is essentially that of isothermal jets which are driven solely by momentum. Natural convection flow above a point heat source, generated solely by buoyancy is called a plume. Buoyant jet is driven by momentum in the initial region. As it moves downstream it becomes buoyancy dominated and ultimately exhibits the characteristics of a plume.

1.1 FREE JET

A brief description of free jet and jet impingement is given here for clarification of the discussions to follow.

The jet emanates from a nozzle with a velocity greater than that of the surrounding fluid which may be stagnant also. The jet at its outer periphery comes into contact with surrounding fluid and tries to drag it along in the streaming direction, that is,



imparts momentum to it. This sets the surrounding fluid in motion, since by continuity the fluid which has been dragged must be replaced by fluid coming towards the jet from outer boundaries. It is called entrainment. In this process, the jet fluid loses its momentum and energy. The centreline velocity of the jet upto some axial distance is not affected by mixing and diffusion occurring at its periphery. This unaffected region of jet is called potential core. The flow in potential core is unaffected by viscosity and its length depends upon Reynolds number.

The centreline velocity decreases beyond the potential core in the axial direction. The rate of decay of centre line velocity away from the potential core region for laminar slot jet is proportional to $(x/W)^{-1/3}$ and for laminar axisymmetric jet, it is proportional to $(x/d)^{-1}$. The pressure and the total momentum of the jet remain constant along the main flow direction. The jet spreads in the transverse direction by diffusion of momentum and entrainment. The temperature of the warm jet injected into cold surrounding fluid, decreases due to the diffusion and due to the entrainment of surrounding cold fluid. The decay of non-dimensional centreline temperature is also proportional to $(x/W)^{-1/3}$ for laminar slot jet and $(x/d)^{-1}$ for laminar axisymmetric jet just like the decay of centreline velocity. The potential core for temperature depends upon the Reynolds number and Prandtl's number. Laminar jet at low Reynolds number is essentially a dissipated jet in which large viscous forces cause rapid diffusion of the jet into surrounding fluid.

1.2 JET IMPINGEMENT

According to Hrycak et al. [7], impinging turbulent jets exhibit four distinct flow regions namely, (i) potential core region, (ii) free jet region (iii) impinging or stagnation flow region, and (iv) wall jet region. These four regions are observed for laminar flow also. In turbulent flow, the mixing of entrained flow with the jet, generates turbulence at the outer periphery of the jet, which penetrates towards the jet centre line. The region of the cross section of jet where the velocity remains unchanged, that is, unaffected by viscosity, is called the potential core. This mixing induced turbulence may be intense for initially laminar jets also. Otherwise, laminar jets are diffusive in nature.

Impinging jet behaves essentially like a free jet ahead of stagnation point. The pressure however, does not remain constant. It increases as the flow approaches the stagnation region. The mixing induced turbulence penetrates towards the centre of the jet. The potential core extends upto 6 to 7 times the nozzle diameter for a circular jet and upto 4.7 to 7.7 times the slot width for a slot jet. The turbulence intensity has two peaks on either side of the jet axis. As the width of potential core decreases, the peaks move closer to the axis. A turbulent jet has fully developed turbulence at the end of potential core region and the turbulence intensity reaches a peak value. The centreline velocity beyond this point in turbulent jet, decreases like $(x/W)^{-1/2}$ for a slot jet and $(x/d)^{-1}$ for an axisymmetric jet. In the stagnation region, the centreline velocity decreases to a zero



value and pressure approaches the stagnation pressure.

Consequent upon the impingement, the jet spreads over the impingement surface and flows along it. In case of slot jet, the flow is divided into two parts and in case of circular jet it spreads axisymmetrically over the surface. The velocity along the surface is constrained to become zero because of no-slip condition and velocity at the edge of jet is small. Hence, velocity profile over the surface has a maxima. There develops a boundary layer along the surface starting from the stagnation point. The velocity increases in this region and pressure decreases from its stagnation point value. For analysis purpose, this region is divided into two parts, namely a boundary layer near the impingement surface and an outer layer. The boundary layer grows from the stagnation point. If the impingement surface is a flat surface, the pressure decreases to the ambient pressure value downstream of stagnation point and this region is called the wall jet region.

In wall jet region the velocity rises from zero value at the wall to a maximum value and then decreases to the value of the ambient fluid. The boundary layer grows at a faster rate than that in the stagnation region. In case of impingement on a cylinder, the flow separates from the cylinder surface due to adverse pressure gradient. There is a recirculation region at the rear end of the cylinder

If buoyancy is considered, the flow phenomenon is modified significantly depending upon the relative magnitude of buoyancy which is indicated by Richardson number, $Ri = Gr/Re^2$. It

is possible to have buoyancy aided and buoyancy retarded flows. A jet of relatively hot fluid flowing downwards will have a tendency to rise up due to buoyancy. Yuan et al. [8], have shown that a slot jet behaves like a non-buoyant jet at $Re=50$ and $Ri=0.1$, if the slot exit velocity and temperature profiles are uniform.

The fluid separates from the impingement surface at a certain distance from the stagnation point, if Richardson number is greater than 0.013 for uniform slot exit velocity and temperature profiles. The distance at which fluid is lifted off from the surface depends on the mixed convection parameter $Ri=Gr/Re^2$. Subsequently, the heated jet turns by 180° and moves towards the top boundary. Cold fluid is entrained from top left boundary as well as from right boundary and gets mixed with the main jet flow. At the point of separation from the surface, reverse flow occurs, the pressure gradient is positive and friction factor coefficient is zero. At still higher values of Ri , the fluid does not impinge on the surface at all, but turns upwards by 180° at a short distance from the jet exit plane and goes toward the top boundary along the wall of the nozzle. A small recirculation region is observed just near the lip of the nozzle. As the Richardson number increases, the potential core length of jet decreases, that is, the depth of penetration of the jet fluid decreases. Buoyancy reduces the heat transfer rate significantly from the impingement surface.

1.3 OFFSET JET

An altogether different flow phenomenon is observed if the

impingement surface is parallel to jet axis but offset from it. The reduced entrainment from the surface side, results in a low pressure between the jet and the surface, causing the jet to curve towards the surface and eventually attach to it. Subsequently, it flows like a wall jet along the surface towards the outflow region. The point where it strikes the surface is referred to as the point of reattachment.

One or two recirculating regions may occur between the jet exit and the point of reattachment depending upon offset ratio. The line joining the lower lip of the nozzle and the point of reattachment is called the separating streamline. In the primary recirculation region, the fluid rotates in clockwise direction if the jet flows from left to right. Beyond a particular offset ratio the secondary recirculation is observed very close to the corner of the jet exit plane and the offset surface. The fluid in the secondary recirculation region rotates in counter-clockwise direction. In both the recirculation regions, the pressure remains uniform and below the ambient value.

As the jet approaches the impingement surface, the pressure increases and velocity decreases. At the stagnation point, referred to as the reattachment point, the pressure is maximum, but the jet velocity decreases along the separating stream line and tends to zero at this point. Subsequently, the boundary layer develops again resulting in a wall jet. The ratio of height from the offset surface to jet axis and the jet width is known as the offset ratio and the distance from the nozzle exit wall to reattachment point is known as the reattachment length.

1.4 SCOPE OF PRESENT INVESTIGATION

A search of the literature indicates that most of the studies related to jets have been carried out for turbulent flows. Laminar jets, in general, have received less attention. Laminar jets find limited applications like in cooling of steel strips in rolling mills, mixing of liquid plastics and in air pollution studies. The study of laminar flow always helps in the understanding of related turbulent flow. Also the laminar flow results are useful in understanding the impact of buoyancy on the flow structure. In this investigation, the laminar free jet, the jet impingement with and without buoyancy and the offset jet impingement along with their heat transfer characteristics are discussed for the two jet exit velocity and temperature profiles.

There is lack of precise information near the exit plane of free jet since most of the earlier investigations deal only with boundary layer equations and similarity solutions away from the jet exit. In this investigation, solutions of Navier-Stokes equations and the energy equation have been obtained for a slot jet and an axisymmetric circular jet with uniform and parabolic jet exit velocity and temperature profiles for various values of Reynolds number and Prandtl numbers. The results are compared with existing boundary layer and other available solutions and similarity parameters are explored and discussed in various regions. The complete details of temperature profiles for free jets were not available in open literature. The solution of energy equation in the boundary layer form, based on Schlichting's similarity solution has been reported by Cebeci and Bradshaw [9].

In the present investigation, the free slot jet and the free axisymmetric jet problem has been solved by *SIMPLE* algorithm due to Patankar [10].

The information at low Reynolds numbers is not available for the jet impingement on a circular cylinder. The Navier-Stokes equations have been numerically solved by *SIMPLEC* algorithm and results are presented for the skin friction coefficient, pressure distribution on the cylinder surface and velocity profiles at different Reynolds numbers, nozzle-to-plate spacings, and nozzle widths.

Yuan et al. [8], investigated a buoyant jet impinging on a surface vertically downwards, with uniform velocity and temperature profiles at the jet exit. The boundary conditions used along the outer wall of the nozzle were interpolative. Fumizawa [11], has carried out a similar study for a round axisymmetric jet where he has considered no-slip and impermeability boundary conditions along the outer wall of nozzle but entrainment has not been considered properly. Further, it has been pointed out by Sparrow and Lee [12], that parabolic jet exit velocity profile gives double the heat transfer coefficient at stagnation point compared to the uniform jet exit velocity profile. This flow phenomenon has been studied in this investigation with proper boundary conditions along the nozzle wall and the entrainment at top and at right outlet boundaries for uniform and parabolic jet exit velocity and temperature profiles. The local Nusselt number distribution along the plate, friction factor coefficient and pressure distribution have been obtained for various Reynolds

numbers, Richardson numbers, and nozzle-to-plate spacings with and without buoyancy for both the types of velocity and temperature profiles. Correlations have been developed in order to predict the maximum, average and the stagnation point Nusselt numbers in absence of buoyancy. The *SIMPLEC* algorithm due to Doormaal and Raithby [13] is used for numerical simulation, in this investigation.

Literature survey indicates that the laminar offset jet has probably not been investigated in great details. References are available for uniform and boundary layer type flow over a backward facing step and the turbulent offset jet. Laminar offset jet has been investigated for various Reynolds numbers, Prandtl numbers and offset ratios in the present investigation. The distribution of local Nusselt number, friction factor coefficient and pressure distribution on the offset surface have been presented. The correlations have been developed for predicting the maximum and the average Nusselt number in the separated region and for the reattachment length in terms of the parameters investigated herein. In the present investigation, the *SIMPLEC* algorithm due to Doormaal and Raithby [13] is used for the computation.



CHAPTER-II

REVIEW

The wide ranging applications of jets and jet impingement have motivated the research in this area for more than forty years and a multitude of experimental data have been obtained by different methods. The jet impingement problem has been investigated for different nozzle orientations and geometries like, single round nozzle, array of round nozzles, single slot nozzle, array of slot nozzles and elliptical nozzles on either flat or curved surfaces and cylinders of various cross sections. The investigations have been experimental, analytical as well as numerical. Laminar as well as turbulent flows have been considered with uniform or parabolic velocity and temperature profiles at the nozzle exit plane. The aim of these investigations has been to establish the dependence of local and average Nusselt numbers on Reynolds number and geometrical parameters like diameter and width of nozzle, the spacing of jets in array, distance between nozzle and impingement surface, geometry of impingement surface etc.

The literature regarding experimental, analytical and numerical investigations related to jet impingement may be classified under the following categories.

1. Wall jet
2. Free slot jet
3. Free axisymmetric jet
4. Slot jet impingement on a circular cylinder

5. Jet impingement on a normal surface.
6. Offset jet.

2.1 WALL JET

When a jet spreads over a surface into surroundings of similar composition as the jet, it is called a wall jet. If it spreads in one direction on a plane surface, it is called plane wall jet and if it spreads radially in wall direction, it is called radial wall jet. Wall jets also constitute part of more complex flows as in impinging jets. When a jet of fluid impinges on a solid surface at an angle, four regions are observed, namely, free jet regime, stagnation regime, transition regime and the wall jet regime. Wall jet region is a fully developed boundary layer region in which the velocity is zero at the solid surface and at the outer edge of the jet with a maximum value in the interior. The jet momentum does not remain constant as in free jets. Laminar plane wall jet was first examined theoretically by Tetervin [14]. Tetervin [14] predicted that wall jet thickness increases as $3/4$ th. power of the downstream distance and that the velocity decreases inversely as $\frac{1}{2}$ power of the downstream distance. The name wall jet seems to have been ascribed by Glauert [15]. The similarity solution has been theoretically investigated for laminar as well as turbulent plane, axisymmetric and radial wall jets. Glauert has given the similarity solutions for the laminar plane wall jet and the laminar radial wall jet. Glauert [15] has further shown that the similarity solution of plane wall jet is valid when the virtual origin is shifted. A similarity

solution was found for turbulent flow by introducing eddy viscosity and assuming that the reverse flow did not occur in the wall jet region. Boundary layer equations were used in both the cases. According to Glauert, the wall jet has the flow characteristics which are composite of free jet flow and boundary layer type of flow. It was observed that for turbulent flow, the similarity solution obtained by Glauert, is not valid for the whole region because in the inner part of the jet, that is, near the wall, the velocity profile follows $\frac{1}{7}$ th. power law due to Blasius, whereas in the outer part of the jet, away from the jet centreline, the velocity profile is similar to free turbulent jet.

The velocity distributions for the incompressible, turbulent, plane wall jet and the variation of the velocity and length scales in the downstream direction have been measured by Schwarz and Cosart [16]. It has been reported that all mean velocity data can be reduced to a single universal curve with the length scale, δ and the velocity scale u_m . It has been observed that the velocity scale varies as a power of x with an exponent -0.555 and the length scale with 1 . Empirical expressions have been developed to correlate the length and velocity scales with nozzle exit velocity, nozzle width and the physical properties of the fluid. The $\overline{u'v'}$ correlation has been given as a function of the distance from the wall. This is computed from the mean velocity data assuming self-preserving characteristics.

Myers et al. [17] have investigated analytically as well as experimentally the heat transfer characteristics of turbulent wall jet with step a temperature distribution on the surface. It was

observed that the velocity and temperature profiles were not similar to the velocity and temperature profiles for the flow over the flat surface. A correlation has been given for local Nusselt number in the region of $x/W > 45$. An analytical expression has been obtained for Stanton number by solving momentum and energy integral equations using $\frac{1}{7}$ th. power law velocity and temperature profiles.

Bajura and Szewczyk [18] have investigated analytically as well as experimentally the laminar two-dimensional wall jet for Reynolds number in the range of 270 to 770. They have observed that the wall jet may be divided into two regions, namely, an inner region near the wall and an outer region near the free surface. In the inner region the pressure gradient is zero like the flow over a flat surface. In the outer region the flow is like a free jet. The similarity was observed when the velocity and the distance were nondimensionalized with respect to maximum velocity u_m and the jet half width δ respectively. The maximum velocity and the jet half width varied as $x^{-0.48}$ and $x^{0.74}$ respectively. The experimental and theoretical values of y/δ at which maximum velocity occurred, were 0.57 and 0.548 respectively. A correlation between virtual origin and Reynolds number has also been proposed. Bajura and Szewczyk [18], observed that when jet exit Reynolds number was less than 300, the disturbances died away while transition to turbulent flow occurred for Reynolds numbers greater than 855. The amplification of disturbances in the outer layer was 30 % more than that in the inner layer.

In a further visual study of wall jet by Bajura and Catalano [19], it was pointed out that flow interaction between neighboring vortices plays an important role in the transition process. They proposed five stages of transition based on interactions between vortices in the inner and outer layers.

Rajaratnam [20] has reviewed the developments in turbulent wall jets. Hammond [21] has obtained an analytical expression for complete velocity profile of a plane turbulent wall jet and has reviewed the earlier work.

Tsuji et al. [22] visually observed double row vortical transition structure, comprising of the primary vortices in the outer layer region and the corresponding secondary vortices in the inner layer. Similar structure during transition was also observed by Hsiao and Sheu [23]. Hsiao and Sheu [24], have further studied the details of double row vortical structure and the phenomenon of vortex lift off from the wall surface.

2.2 FREE SLOT JET

In most of the practical applications except a few, the jets are turbulent, since the jets are inherently unstable. The jets in absence of rigid boundaries are called free jets. A liquid jet in air, away from a wall is also a free jet, but it has a free surface and there is no entrainment. A free liquid jet in liquid and a free air jet in air are also referred to as submerged jets. These jets entrain the surrounding fluid.

The classical method of analysis proposed by Schlichting in 1933 and reported in Schlichting [25] assumes that the plane jet

originating with a specified momentum from a line source — an infinitesimal slot in a plane vertical wall has self preserving velocity profile away from the slot exit. The jet, being exposed to surrounding fluid from all the sides, has constant ambient pressure and the jet momentum remains constant in the streaming direction. Schlichting obtained a similarity solution of the boundary layer equations which is not valid near the jet exit plane. The closed form solution for the two-dimensional case was given by Bickley [26] although Schlichting had also found the solution. It is not possible to simulate an infinitesimal slot experimentally. Experimental results are available for slots of finite width with a finite exit velocity and these do not agree with Schlichting's similarity solution. To show a good agreement between theory and experiment the position of infinitesimal line source of theoretical jet is shifted to a new origin referred to as virtual origin. This gives good agreement between the slot jet and Schlichting's solution away from the jet exit. Near the slot exit, Schlichting's similarity solution does not agree with the experimental results, indicating a lack of similarity.

Andrade [27] measured the velocity distribution for a water slot jet injected into a water reservoir and compared the results with theoretical results. It was observed that the plane jet is more difficult to maintain in a steady state than a circular jet. The slightest convection current tends to twist the jet and makes it non-two-dimensional. The nozzle width and length were 0.3 mm and 20.3 mm respectively. The jet was quite stable at $Re=10$ as compared to that at $Re=20$. The jet became quite unstable with the

turbulence setting in at $Re=30$. A good agreement was observed at low Reynolds numbers between the theoretical results and experimental results interpreted from a virtual origin. The virtual origin was selected inside the nozzle and an expression was derived for its location.

Chanaud and Powell [28] conducted experiments with laminar air and water jets issuing from two dimensional slits with an aim to determine the condition of neutral stability. The investigations on the instability of jets based on solutions of Rayleigh's equation and Orr-Sommerfeld equation have been reviewed. Neutral stability has been discussed with reference to a plot of Strouhal number Vs. Reynolds number. The critical Reynolds number was observed to be dependent upon the disturbance amplitude. It has been observed that the Bickley's velocity profile is not valid near the slit exit, which may lead to errors in the calculation of conditions for instability. The measured velocity profiles near slit exit did not agree with Bickley's velocity profile with the virtual origin proposed by Andrade. However, at far downstream locations, the velocity profile was in agreement with Bickley's velocity profile.

Sato and Sakao [29] investigated the instability of a two-dimensional air jet in the Reynolds numbers range of 10 to 1200. Two slits 0.2 mm by 30 mm and 1.1 mm by 100 mm were used. The slits however were not located on the wall. The flow was entrained around the nozzle containing the slit. The velocity profiles were measured by hot-wire anemometer. They have concluded that the jet becomes turbulent if the Reynolds number exceeds 30,

while it definitely remains laminar for $Re < 10$. The mean velocity distribution was found to be in good agreement with Bickley's solution with the location of origin approximately shifted. The location of virtual origin did not agree with those of Andrade [27] and Chanaud and Powell [28]. The discrepancy was attributed to the difference in the nozzle geometry used by various investigators. A significant loss in momentum was also observed.

Pai and Hsieh [30] have numerically solved the boundary layer equations to study the flow development near the jet exit for laminar slot jet and axisymmetric jet with uniform, parabolic and tri-angular velocity profiles at the nozzle exit plane. The solutions have been obtained in the presence of free stream also. The results have been compared with the experimental result of Chanaud and Powell [28] and Sato and Sakao [29]. It has been found that the agreement of the experimental results at $Re = 68$ for the parabolic jet exit velocity profile, is fairly good.

Peyret [31] investigated the unsteady evolution of horizontal jet in a stratified fluid and observed a recirculating flow pattern at $Re = 100$.

Lai and Simmons [32] have found numerical solution with local similarity in the vicinity of jet exit for uniform and parabolic jet exit profiles by Keller Box method which is described in detail by Cebeci and Bradshaw [9]. They have used Bickley's [26] similarity variables with virtual origin and retained the non-similar terms obtained from the boundary layer equations. They have found that the centre line velocity agrees with Schlichting's similarity solution beyond $X > 0.3$ with virtual

origin at $X = -0.222$ for uniform jet exit velocity profile. The agreement with similarity solution for parabolic jet exit velocity profile was observed beyond $X > 0.07$ with virtual origin at -0.088 . Their results are in good agreement with those of Pai and Hsieh [30] also. The similarity solution for the energy equation, based upon Schlichting's similarity velocity profile, is reported by Cebeci and Bradshaw [9]. This is obtained by solving the energy equation in the boundary layer form.

The laminar plane jet and slot jet velocity profiles are of the form $u = u_m \text{Sech}^2 y/b$. This profile has inflection point on both the sides of line of symmetry. Hence, according to Rayleigh's theory of linear inviscid stability, the jets are unstable. Stability of the profile has been investigated analytically by Curle [33], Tatsumi and Kakutani [34], Howard [35], Clenshaw and Elliot [36] and Kaplan [37]. The solutions of Orr-Sommerfeld equations were found to be both even and odd functions of y , but Andrade observed only even symmetric modes in his experiments. Numerical calculations of Kaplan indicate a critical Reynolds number of 4 which is in agreement with the results of Tatsumi and Kakutani.

Fox and Lessen [38] pointed out that at such a low Reynolds numbers, the jet flow can not be considered to be parallel flow. Recent calculations show that nonparallel jets have a critical Reynolds number of 12 which is in agreement with Andrade's experimental findings. On the other hand Schlichling [25] quotes a experimental value of $Re = 30$ due to Andrade. The velocity profile $u = u_m \text{Sech}^2 y/b$ ignores the spread of the jet and is applicable far

away from the jet exit. It seems likely that the neglect of the jet spread is probably responsible for the difference between calculated and observed values of critical Reynolds number [39].

Impinging jet unlike free jet, is under the influence of a pressure gradient. The pressure decreases away from the stagnation point. This gives rise to a favorable pressure gradient, which increases the stability of the jet.

Gardon and Akfirat [40] measured the local heat transfer coefficients in the stagnation region of a jet impinging on a flat plate and concluded that the jet remains laminar upto some distance at Reynolds numbers of 650 to 950. In a jet with $Re = 450$, the Nusselt number was constant upto $L/W < 5$ (region of potential core) and beyond that, it diminished in proportion to $(L/W)^{-1/2}$, indicating that the jet is laminar throughout its length.

Similarly, the data of Sparrow and Wong [41] also indicate that the jet with parabolic exit velocity profile remains laminar upto $Re = 450$ for $L/W < 16$ and upto $Re = 950$ for $L/W = 10$.

Accordingly, Van Heiningen et al. [42] have carried out numerical calculation of jet impingement upto $Re = 950$. However, Yuan et al. [8] have carried out numerical calculations for buoyancy effects on laminar impinging jets upto $Re = 500$ and actually presented the results upto $Re = 50$. According to them upper limit of laminar flow is $Re = 500$ as suggested by Guantner et al. [43].

2.3 FREE AXISYMMETRIC JET

Schlichting [25] gave a closed form solution of the boundary

layer equations for axisymmetric, incompressible, steady, laminar jet under the assumptions of constant static pressure and constant axial momentum. This solution is valid only at large distances downstream of jet exit plane. The jet is assumed to be discharged from an infinitesimal circular orifice in a plane vertical wall with very high velocity and finite momentum which is assumed to be constant in the streaming direction. Schlichting's solution indicates that the axial velocity decreases as X^{-1} and mass flow rate increases as X in the streaming direction.

Andrade and Tsien [44] experimentally determined the velocity distribution of an axisymmetric water jet discharged from a 0.91 mm diameter orifice into a tank containing water. Very fine suspended aluminum particles of 0.05 to 0.08 mm diameter with a strong illumination system were used to determine the velocity distribution. A good agreement with Schlichting's analytical solution was observed at large distances from the jet exit. The position of the point source of Schlichting's theoretical jet was shifted inside the nozzle to a new location referred to as virtual origin, to obtain good agreement. An expression has been given for the location of virtual origin as a function of Reynolds number. Investigations were carried out in the Reynolds number range of 55 - 300. They were unable to obtain results near the jet exit. The jet exit velocity profile was not measured but inferred from momentum considerations.

Landau [45] has proposed a point source model for a round laminar jet which is an exact solution of Navier-Stokes equations. This solution does not rely upon boundary layer



simplifications. A spherical-polar coordinate system is used and a similarity solution is found that results in a closed form expression for the velocity field. This solution becomes equivalent to the solution obtained from boundary layer equations for $Re > 8$. This equivalence is obtained by expanding Landau's solution in a series involving the angle of spread.

Squire [46] also presented the solution for temperature field in a heated non-buoyant jet by considering a heat source at the same point from where the jet originates. This solution also reduces to the boundary layer solution at sufficiently large Reynolds numbers. Temperature distribution in the form of temperature contours is presented. It is observed that the radial velocity distribution and the temperature distribution are the same at Prandtl number of unity. The details regarding round jets are also available in Rosenhead [39].

Reynolds [47] has experimentally investigated the axisymmetric liquid jet injected into liquid surroundings. The water jet was strained with a dye to observe the flow pattern. It was observed that the jet remains laminar in the Reynolds numbers range of approximately $30 \leq Re \leq 300$ and becomes unstable near the nozzle exit plane for $Re > 300$.

Pai and Hsieh [30] have solved boundary layer equations numerically by an explicit finite difference method with and without a free stream superimposed on the axisymmetric jet. The results have been compared with the experimental results of Andrade and Tsien [44], corrected with appropriate virtual origin for uniform and parabolic jet exit velocity profiles. The

agreement for the case of parabolic jet exit profile was better than that for the uniform profile. However at low Reynolds numbers the agreement was not good in both the cases.

Gauntner et al. [43] have suggested $Re = 500$ as the upper limit of laminar flow. McNaughton and Sinclair [48] define this flow as a dissipated laminar jet below $Re = 150$, in which the large viscous forces cause rapid diffusion of the jet into the surrounding fluid.

Morton [49] has proposed a point source model for axisymmetric jet as well as for plumes and wakes.

Kent [50] has investigated the unsteady laminar axisymmetric jet by an integral method and found a numerical solution.

Hatta & Nozaki [51] have considered turbulent jets, and in the appendix of their paper, a method of treating the laminar case is also described.

Rankin and Sridhar [52] have considered an integral form of boundary layer equations and obtained a numerical solution in the developing region of laminar jet with uniform jet exit velocity profile. They solved only the velocity field and have described a graphical method for determining the potential core radius and the parameters of the Schlichting's velocity profile.

Rankin et al. [53] have used Laser-Doppler anemometer to study the laminar axisymmetric submerged jet of water with parabolic jet exit velocity profile. The jet centreline velocity, jet half width and velocity profiles have been presented at various Reynolds numbers in the developing region as well as in the developed region. The results have been compared with those of

Arulraja [54], Schlichting [25], and Pai and Hsieh [30]. It was observed that the jet momentum does not remain constant, but decreases near the jet exit and then gradually increases and finally attains a constant value at a large distance downstream. It has been shown that $(x/d) Re^{-1}$ is the proper non-dimensional axial coordinate to characterize the jet development. The jet half width and centreline velocity are the characteristics length and velocity respectively required for collapse of data into single curve. Rankin et al. [53] have given an exhaustive review of experimental and analytical work done on axisymmetric jets upto 1983.

Tucker and Islam [55] have experimentally investigated the transition from laminar to turbulent flow of axisymmetric free jet with initially parabolic velocity profile in the Reynolds number range of 2,342 to 11,000. They have also given a numerical solution of the boundary layer equations by explicit finite difference method for the laminar portion of the jet in absence of pressure gradients. Experiments were carried out with air jets, and turbulence intensities and mean velocities were measured using a DISA constant temperature hot-wire anemometer. It has been observed that the jet was initially laminar for the range of Reynolds numbers investigated and the jet became turbulent as it moved downstream. The centreline velocity near nozzle exit, decreases very slightly and in linear manner with distance. Further downstream, a location is reached where the centreline velocity decreases rapidly with x/d and this location decreases with the increasing nozzle exit Reynolds numbers. It has been

observed that the transition from laminar to turbulent flow depends on the Reynolds numbers and small disturbances at the nozzle exit plane. The location of sudden change of slope in centreline velocity indicates the existence of transition from laminar to turbulent flow. A correlation, $L/d = 22.33 + 0.00185 Re$ has been presented to determine the location of transition from the nozzle exit.

Hrycak et al. [56] have given similar results based upon theoretical considerations and verified it experimentally. The length of potential core in turbulent jet has been shown to be independent of Reynolds number. They observed the critical Reynolds number to be around 1000 by observation of smoke patterns. The potential core length was observed to increase with increasing Reynolds number upto 1000 and then decrease as the Reynolds number increased further, and finally for very large Reynolds numbers in turbulent range, the core length varied between 6.0 to 6.7 nozzle diameters.

Akaike and Nemoto [5] have carried out experimental investigation in the developing region of an axisymmetric laminar water jet issuing into the surrounding calm water. They have considered a fully developed parabolic velocity profile and a velocity profile with a potential core at the nozzle exit. Navier-Stokes equations in vorticity-stream function form were also solved for jet exit velocity profile with a potential core. Schlichting's solution for the radial and axial velocities was used to model the entrainment and outflow velocity at radial and axial boundaries respectively. Experiments were conducted in the

Reynolds number range of 100 to 600. Flow visualization was done by hydrogen bubble method and velocity profiles were measured by a miniature cone type hot film probe. It was observed that velocity profile agrees with Schlichting's profile at $(x/d) Re^{-1} = 0.034$ which is very close to the value of 0.036 given by Rankin et al. [53] for parabolic jet exit velocity profile. The agreement with Schlichting's velocity profile was not so good for the jet exit velocity profile which had a potential core. It was observed that the potential core in the flow developing region depends upon Reynolds number apart from the nondimensional distance x/d . For turbulent flows, it has been shown by Hatta and Nozaki [51] that potential core radius vanishes at $x/d \approx 11$ and is independent of Re . The variation of the potential core radius depends on the nondimensional distance \bar{X} and it was observed that the potential core vanishes at $\bar{X} \approx 0.04$.

2.4 SLOT JET IMPINGEMENT ON A CIRCULAR CYLINDER

Jet impingement heat transfer from a cylinder is of relevance to vapor deposition process at outer surface of cylinder, manufacture of paper and of glass. Despite its practical relevance this configuration has only sparsely been investigated. The exhaustive 1977 survey article of Martin [57] on jet impingement did not include any reference on this topic.

Slot jet impingement over a heated cylindrical surface is a typical problem in the field of external flow.

Schuh and Persson [58] have experimentally investigated the average heat transfer coefficient on a circular cylinder placed

symmetrically in a two-dimensional turbulent slot jet of finite width. The wall temperature of the cylinder was maintained at constant value and the Reynolds number based on the cylinder diameter and initial jet velocity varied between 20,000 and 50,000. The maximum heat transfer rate was obtained for a jet with slot width equal to one-eighth of the cylinder diameter and the cylinder placed at a distance of eight times the slot width from slot exit. It has been found that the heat transfer coefficient in case of jet impingement is about 20% higher than that for a cylinder in unlimited parallel flow with negligible turbulence in the main stream and with an undisturbed speed equal to that at the nozzle exit. Heat transfer coefficients and pressure distribution have been reported for various nozzle widths ranging from 0.06 to 2.5 times of the cylinder diameter.

Kumada et al. [59] have employed the naphthalene sublimation method to measure the mass transfer rate instead of heat transfer rate. The local and mean mass transfer coefficients have been measured for diameter to nozzle width ratios of 3 to 25, nozzle to cylinder distances of 2 to 40 times the nozzle width, and Reynolds numbers of 3×10^3 to 5.3×10^4 . The velocity distributions in the boundary layer have been presented for a few cases.

Sparrow et al. [60] have measured local heat transfer coefficients on a circular cylinder due to impingement by a circular jet. The jet diameters used were 0.189, 0.313 and 0.424 times the cylinder diameter, while cylinder spacing varied from 5 to 15 cylinder diameters from slot exit. The Reynolds numbers varied between 4,000 to 25,000. The heat transfer coefficients

were obtained from mass transfer experiments involving naphthalene sublimation technique. Results for Sherwood numbers have been presented for various values of parameters. Nusselt number has been related to Sherwood number. Naphthalene sublimation technique gives the equivalent of isothermal boundary condition. The heat transfer coefficient has been observed to be maximum at the impingement point and for a fixed jet diameter and Reynolds number, the peak heat transfer coefficient increases as the distance between the initiation of the jet and the cylinder surface decreases. It was further observed that peak heat transfer coefficient increases with the decrease of the jet diameter at fixed values of the jet initiation distance and the Reynolds number. Correlations of the peak Nusselt number with the geometrical parameters and Reynolds number have been derived. The drop-off in the peak heat transfer coefficient with increasing axial distance from the impingement point was observed to be more rapid for smaller jet initiation distances (at a fixed nozzle diameter and Reynolds number). The impingement pattern was also examined by flow visualization.

Sparrow and Alhomoud [61] have measured heat transfer coefficients by slot jet impingement on a circular cylinder by using naphthalene sublimation technique. The slot length was kept parallel to the cylinder axis. In one set of experiments, the plane of symmetry of the jet was aligned with the axis of the cylinder, while in other experiments the cylinder was offset from the plane of symmetry of the jet. Offset ratio ϵ / D of 0.0, 0.5 and 1.0 were used and two slots of slot width 0.25 D and 0.5 D

were used, D being the cylinder diameter. The distance between slot exit and the cylinder varied from $3.25 D$ to $7.25 D$ while Reynolds number varied from $4,000$ to $40,000$. The flow visualization studies indicated, that even in case of offset, the jet impinged on the cylinder, though not at the apex of the cylinder as in the aligned case. It was found that the heat transfer coefficient increased with the increase in slot width and Reynolds number, but decreased with increase in slot-to-cylinder separation distance and offset. For $\epsilon/D = 1.0$, the reduction in the heat transfer coefficient in their experiment was slightly in excess of 50% .

Faruque, et al. [62] have experimentally investigated the local and average heat transfer coefficients for slot jet impingement on an isothermal circular cylinder. The results are reported in the Reynolds number range of $6,000$ to $45,000$ for diameter to slot width ratios of 7.5 , 10 , 12 and 15 , and for nozzle to cylinder spacings varying between 2 to 24 times the slot width. Results are also presented for eccentricity ratio ϵ/D of 0.1 , 0.2 , 0.3 , 0.4 and 0.5 . Smaller nozzle widths gave higher heat transfer rates at same Reynolds number. In all the cases, the maximum heat transfer rates occurred when the cylinder was placed at distance of 8 nozzle widths from jet exit. Correlations for Nusselt number have been presented for stagnation point heat transfer and average heat transfer rates.

Arora et al. [63] have numerically solved the Navier-Stokes equations and energy equation by *SIMPLER* algorithm for laminar slot jet impingement over a heated cylinder. The nozzle walls were

considered to be along the radius of the cylinder, so that cylindrical polar coordinate system with origin at cylinder axis can describe the whole of flow domain. The flow domain consisted of the cylinder and the semi-circle passing through the nozzle exit plane as the outer boundary. The radial entrainment velocity at the outer boundary was determined by equating the pressure to ambient pressure in the outer boundary control volumes. The flow characteristics and Nusselt numbers have been given for various slot widths, ratios of impingement distance to slot width and for $Re = 10$ to 30 . Nusselt number was found to be independent of slot width as predicted by Gardon and Akfirat [40] for the laminar cases. The numerical scheme used by them did not converge for Reynolds number greater than 30 .

Recently, Kang and Greif [64] have numerically investigated the fluid flow and heat transfer characteristics for a laminar, heated, buoyant slot jet impinging on a circular cylinder. Numerical solutions using SIMPLE algorithm have been obtained by utilizing a non-orthogonal curvilinear coordinate grid. The effects of Reynolds number and Grashof number, the jet width, the distance between the nozzle and cylinder, on the flow and heat transfer have been investigated and correlation curves have been presented. It is observed that the point of separation moves downstream for smaller Reynolds numbers, higher wall temperature and greater buoyancy. It is reported that the average Nusselt number increases with increase of Grashof numbers and Reynolds numbers. The width of jet and the distance between nozzle and the cylinder have a strong effect on the heat transfer.

2.5 JET IMPINGEMENT ON A NORMAL SURFACE

Friedman and Mueller [65] were the first to measure the average cooling effect by arrays of jets, using a large area calorimeter. They used arrays of nozzles and slots. They also used jets issuing from perforated plates. The results were not presented in terms of nondimensional numbers. The results were given in terms of empirical coefficients applicable to various arrangements.

Perry [66] studied single circular jet impingement. He measured the average heat transfer rates, although he was interested in local heat transfer rates. The results were averaged over the size of test section used. The results were obtained by calorimetric technique which does not allow great reduction in the size, hence the spatial resolution was limited.

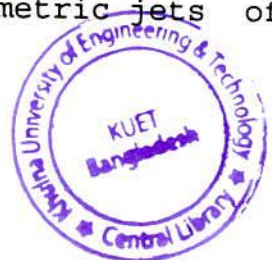
Ehrich [67] gave the potential flow solution for impinging jet on a flat plate. This solution is in terms of the ratio H_1 of nozzle height from the flat plate to the half width of the nozzle. Expressions have been given for the free surface velocity and mean stream velocity. The solution for $H_1 = 3$ agrees substantially well with that for $H_1 = \infty$.

Vickers [68] measured the local heat transfer coefficients from a single laminar jet impinging on a flat plate in the low Reynolds number range.

Daane and Han [69] studied heat transfer coefficients for impinging two dimensional jets over a limited range of Reynolds numbers and nozzle-to-plate spacings. Schrader [70] has also investigated impingement of round jets normal to surfaces.

An experimental study of the heat transfer characteristics of the slot jet impinging on a flat target has been performed by Metzger [71]. Nozzles with a breadth of 19 mm and widths of 0.25, 0.51, 1.02, 1.5 and 2.04 mm were used. The jet impinged on two heated copper targets of half length 12.7 and 6.35 mm which were mounted in blocks of balsa wood. Influence of Reynolds number has also been studied. The average heat transfer coefficient has been found to be maximum at nozzle to target distance of $L/W = 8$ for all Reynolds numbers and for all values of other geometrical parameters. Therefore, experiments have been conducted to investigate the effect of other variables, for fixed value of L/W at 8. Experiments were also conducted with a circular nozzle in order to compare its performance with the slot jet. The heat transfer characteristics have been investigated for nozzle-to-target spacings of 1, 5, and 10 times the nozzle diameters. However, in contrast to the slot jet, no maxima was observed for heat transfer in this region. It has been concluded that the shape of the area to be cooled is of primary importance in deciding the type of the jet to be used. Results of the slot jet have been compared with those for circular jet. A correlation has been given for the average heat transfer coefficient.

Gardon and Cobonpue [72] have experimentally measured the local heat transfer coefficients by impingement of single circular jet and an array of circular jets, impinging on a electrically heated aluminum plate. Heat flux was measured by a heat flux sensor of 0.9 mm diameter designed by Gardon [73]. The stagnation point Nusselt numbers have been reported for axisymmetric jets of



diameters 2.26 mm, 3.18 mm, 4.4 mm, 6.35 mm and 8.1 mm in the Reynolds number range of 7,000 to 1,12,000. A correlation has been given for the stagnation point Nusselt number and it has been observed to be maximum between nozzle-to-plate spacings of 6 to 7 diameters. The local Nusselt number was found to have two more peaks in radial direction. One peak is attributed to high radial velocities and other peak to transition from laminar flow in stagnation region to turbulent flow. The results for a square array of 5x5 nozzles at 50.8 mm centres and 7x7 array at 30.4 mm centres, are also reported. An approach velocity of the jets at the plate location is defined and Nusselt number has been correlated with the Reynolds number based on this approach velocity.

Huang [74] has experimentally measured the average and the local heat transfer coefficients for vertical turbulent round jet of air impinging on a plane surface. The results have been presented in the Reynolds numbers range of 1,000 to 10,000 with nozzle diameters of 3.18 mm and 6.35 mm for a single jet and multiple jets. Empirical correlations have been developed for the local and the average heat transfer coefficients in terms of nozzle exit Reynolds numbers and the Prandtl numbers for a single jet.

Watson [75] investigated the impingement of water jet with a free surface on flat plate experimentally and analytically. The jet strikes on the plate and spreads radially outwards. The boundary layer starts to develop from the stagnation point and gradually engulfs the whole flow field. He sought a similarity

solution at a large radial distance from the stagnation point, where the influence of jet impact completely diminishes. The whole flow field from the stagnation point onwards is divided into following four regions,

(i) The stagnation region : This region near the stagnation point, extends upto a distance of approximately one jet radius. In this region, the velocity of fluid rapidly rises from zero value at the stagnation point to the maximum velocity and boundary layer starts to develop. In this region, the boundary layer thickness is of the order of $(\nu R_0/U_j)^{1/2}$. The region very close to the stagnation point may be approximated by stagnation flow in infinite fluid, wherein the main stream velocity increases linearly with x .

(ii) A flat plate region : This is the region at radial distance greater than the one radius of the jet. The magnitude of the maximum velocity in this region remains unchanged and there is practically no pressure gradient in the flow direction. The velocity profile follows Blasius velocity profile for a flat plate.

(iii) The transition region : The boundary layer reaches the free surface and the viscous stresses become important for the whole flow field. In this region, the flow is transitional, that is, velocity profile changes from Blasius type velocity profile to Watson's similarity profile.

(iv) Similarity region : In this region, the dimensionless velocity profile remains unchanged. The flow becomes independent of the way in which it originated, that is, the influence of jet

geometry and initial condition completely vanishes. Watson's similarity solution is valid in this region for large Reynolds numbers. A hydraulic jump in which the film thickness on the plate increases abruptly will ultimately occur.

Watson has given expressions for the radius of hydraulic jump for laminar as well as turbulent flows. Analogous problems of two dimensional flow have also been treated.

Chaudhury [76] has given analytical solution of energy equation inclusive of viscous dissipation for axisymmetric laminar liquid jet impinging on a flat plate. He has considered the plate to be insulated upto the fourth regime as described by Watson and considered the plate to be isothermal in the fourth regime. A similarity solution of energy equation has been obtained in this regime by using Watson's similarity solution for velocity components. In a second problem, the whole of the plate was assumed to be isothermal and the energy integral equation has been solved in second and fourth regime by using fourth order polynomials for velocity and temperature profiles. The correlations for Nusselt numbers have been given for various Prandtl numbers. The stagnation region has been neglected for both the cases.

Heat transfer characteristics of air jets issuing from slots of 1.59, 3.17 and 6.35 mm widths, 152.4 mm breadth and impinging normally on a 152.4x152.4 mm square aluminum plate, have been reported by Gardon and Akfirat [77]. Both the average and the local heat transfer coefficients were measured by a 0.9 mm diameter heat flux sensor. It has been reported that the

stagnation point heat transfer is maximum for values of L/W between 7 to 10 and that the maximum heat transfer is a function of Reynolds number. For turbulent jets with nozzle-to-plate spacing greater than 14 times the slot width, a correlation has been proposed for the stagnation point heat transfer coefficient. The local heat transfer coefficients have been reported for different L/W ratios. The variation of local heat transfer coefficient has been obtained only for fully developed turbulent jets with their characteristic bell-shaped velocity distribution. It has been found that the normalized local heat transfer coefficient, h/h_0 , depends on the Reynolds number and the dimensionless distance from the stagnation point. Correlations have been given for the average heat transfer coefficients in terms of Reynolds number for the three slot widths and for two values of distance between nozzle and the target.

Korger and Krizek [78] have determined the local mass transfer coefficient for the slot jet of air impinging on naphthalene plates, using the technique of sublimation. The experiments have been carried out in two regions, which have different local mass transfer coefficients. These two regions are: L/W ratio less than 8.5 and L/W greater than 8.5 respectively. The relationships for maximum and mean values of mass transfer coefficients have been established in both the regions, and a criterion equation is derived for mean mass transfer coefficients in the region of $L/W > 8.5$. The results have also been verified for a group of parallel slot nozzles.

Heat transfer results have been reported by Schuh and

Pettersson [79] for impingement of air through arrays of slots. Jets of widths 1 and 5 mm with jet spacings of 25, 40 and 100 mm and with slot-to-plate spacings of 2, 4, and 8 times the slot width, have been considered. Experiments have been carried out for slot exit velocities of 4 to 100 m/sec. Results have been compared with those of single slot jet by Metzger [71] and a good agreement is observed for large values of x/W namely, 50 and 100. For lower values of x/W , the difference between the results for the array of slot jets and the single slot jet indicate the detrimental effect due to the interference of the jets at closer spacings.

The heat transfer characteristics of a slot jet impinging on a flat copper surface for slot of widths of 6.25, 12.5 and 18.75 mm, nozzle-to-plate spacing of 2 to 16 times the slot width, and Reynolds numbers of 4,600 to 1,02,000 have been studied by Cadek [80]. The local heat transfer coefficients were measured by a circular foil heat flux sensor of a 0.91 mm diameter sensing area. Experiments have been carried out in the range of x/W ratio from 0 to 36. Good agreement has been observed between the theory and the experiment in both the stagnation and the wall jet regions for $2 \leq L/W \leq 4$. For $L/W > 8$. The agreement is found to be better in the wall jet region, but in the stagnation region, the measured values exceed the theoretical values. The correlations of Gardon and Akfirat [77] have been recommended for design calculations.

Cartwright and Russell [81] have presented experimental heat transfer results for jet impingement with nozzle-to-plate spacings of 8 to 47 times the slot width, nozzle exit Reynolds number of 25,000 to 1,10,000, and the distance along the wall upto 132 times

the slot width. It has been observed that, at low Reynolds numbers, the heat transfer coefficient is maximum at the stagnation point and decreases monotonically with increasing distance from the stagnation point. At large Reynolds numbers, the heat transfer coefficient exhibits a maximum at some distance away from the stagnation point. An analytical attempt has been made to predict the heat transfer rate in the wall jet region beyond $x/W > 36$. The failure of predictions in the impingement region have been attributed to the high level of turbulence that exists in the free jet before the impingement.

Runchal et al. [82] have solved Navier-Stokes equations with constant eddy viscosity to model a turbulent plane jet impinging normally on a solid wall. The studies deal more with flow pattern predictions and effects of finite mesh size than with transport of turbulence. This work has been extended by Wolfshtein [84].

Kumada and Mabuchi [83] have investigated the mass transfer coefficient for two-dimensional jet impinging normally on a flat plate. It has been reported that Sherwood numbers at the stagnation point obtained experimentally are about twice of those predicted by the theory. The jet turbulence is cited as the cause for this. The theoretical predictions for local Sherwood numbers have been obtained, which agree well with the experimental data. Gardon's [77] correlation for Nusselt number has also been checked experimentally.

Wolfshtein [84] has solved the impinging turbulent jet problem by an iterative finite-difference technique in vorticity-stream function formulation. Navier-Stokes equations

were solved in the axisymmetric, stagnation and near-stagnation region with assumed free jet velocity profiles. The numerical technique has been described in his Ph. D. dissertation and is essentially the one due to Gosman [85]. Reynolds stresses are assumed to be related to the mean strain rate by a scalar eddy viscosity. The eddy viscosity is assumed to depend on the level of kinetic energy fluctuations and a length scale. The level of energy has been obtained from a second-order differential equation, while the length scale of turbulence is prescribed on the basis of experimental information.

Hrycak et al. [7] have experimentally investigated the turbulent axisymmetric jet of air impinging on flat plate in the Reynolds numbers range of 300 to 5×10^4 based on nozzle radius. Nozzle diameters of 6.35 mm, 12.7 mm and 19.05 mm and nozzle-to-plate spacings of 2 to 30 nozzle diameters have been considered. It has been observed that the flow remain laminar upto $Re = 500$. The potential core length was observed to become maximum at $Re = 500$; it decreased sharply as Reynolds number was increased further until $Re = 1,750$ to $2,750$, beyond which it increased slightly upto $Re = 5,000$. Beyond $Re = 5000$, the potential core length remained nearly constant. Static pressures along the impingement plate were observed to be dependent on nozzle-to-plate spacing and less dependent on the nozzle diameter and Reynolds number. An expression for the decay of maximum velocity in the wall jet region has been developed, which predicts that the rate of decay of maximum velocity in the wall jet region is faster than the decay of maximum velocity in the free jet. This was

substantiated by experimental data. A correlation for the spread of the jet in the radial wall jet region in terms of the nozzle-to-plate spacing and radial distance has been developed.

Scholtz and Trass [86], have measured the local mass transfer coefficient for laminar circular jet of air impinging on a flat surface with parabolic velocity profile at the nozzle exit plane. They have used the naphthalene sublimation technique. The solution for inviscid round jet in spherical polar coordinates has been obtained in part-I of the paper. The theoretical results for velocity and pressure distribution compare well with the experimentally measured values. In part-II of the paper, boundary layer equations have been solved by Blasius series method to determine the local mass transfer coefficient. The inviscid flow results and the experimentally measured pressure distribution were used as the boundary condition to solve the boundary layer equations. They found that at lower nozzle-to-plate spacings, that is, $0.1 \leq H/R \leq 0.5$, the rate of mass transfer coefficient increased as the nozzle-to-plate spacing decreased. The mass transfer coefficient for $H/R = 0.1$ was maximum at a radial distance of one nozzle radius and was twice the stagnation point value. At higher nozzle-to-plate spacings, that is, $0.5 \leq H/R \leq 12$, the mass transfer rate from the surface becomes independent of the nozzle-to-plate spacings. Reynolds numbers considered varied from 500 to 1,960, nozzle-to-plate spacings from 0.1 to 12 nozzle radius and nozzle diameters from 19 mm to 50.4 mm.

An analytical method has been developed by Andreyev [87] for predicting the local Nusselt number in the stagnation region of a

slot jet. The model has been compared with the experimental results and an empirical correlation has been given. A modification has also been given to account for the effect of jet turbulence.

Miyazaki and Silberman [88] have solved the boundary layer equations and energy equation by a finite difference method to evaluate the skin friction coefficient and the heat transfer coefficient for slot jet impinging on a flat surface for different nozzle-to-plate spacings. They have used the inviscid solution given by Ehrich [68] for free stream velocity and then Görtler's transformation to obtain local similarity. The skin friction coefficient and the local Nusselt number both are observed to decrease with increase in the nozzle-to-plate spacings. The Nusselt number was observed to be maximum at a distance of half nozzle width from the stagnation point.

Livingood and Hrycak [89] have presented an exhaustive literature survey for the heat transfer by turbulent air jets impinging on flat surfaces. They have considered circular as well as slot jets including the effects of cross-flow on impingement heat transfer. The experimental and the theoretical results from various investigations have been compared and some correlations have been suggested.

Sparrow and Wong [41] have experimentally measured the local mass transfer coefficients for slot jet of air impinging on a naphthalene coated surface normal to the jet axis. The velocity profiles used in experiments were laminar, fully developed parabolic velocity profiles at nozzle exit. The results have been

reported for the Reynolds number range of 150 to 950 based on nozzle width and nozzle-to-plate spacings ranging from 2 to 20 times of the nozzle width. It has been observed that the local mass transfer coefficient at a particular Reynolds number and a fixed nozzle-to-plate separation distance, has a maximum value at the stagnation point and decreases with the increase of axial distance. Again, at a fixed Reynolds number, the stagnation point mass transfer coefficient decreases with the increase of nozzle-to-plate separation distance. Stagnation point values are correlated with 0.6 power of Reynolds number.

Sparrow and Lee [12] have made an analysis of the fluid flow and the heat transfer characteristics associated with impingement of a slot jet with a nonuniform velocity profile at the slot exit. Consideration is given to velocity profiles similar to that for a fully developed laminar channel flow. The velocity field within the impinging jet is determined by an inviscid flow model. The inviscid velocity profiles are used for the analysis of the boundary layer equations for heat and mass transfer on the impingement surface. It has been observed that the stagnation point heat transfer coefficient, corresponding to the initially nonuniform velocity profile is almost twice as large as that for an initially flat velocity profile. Furthermore, it has been observed that within the range of investigation, the heat transfer coefficients are insensitive to the separation distance between the jet exit and the impingement surface. The analytical results have been compared with experimentally determined mass transfer coefficients.

Van Heiningen et al. [40] have numerically solved the Navier-Stokes equations and the energy equation for semi-confined laminar slot jet impingement on a permeable surface by a finite difference method. Following Gosman et al. [85], the Navier-Stokes equations were transformed into vorticity-stream function form and solved by a hybrid or upwind formulation. A fully developed and a flat velocity profiles at jet exit have been considered along with the suction at the impingement surface. Results have been obtained for Reynolds numbers of 100, 450 and 950 with nozzle-to-plate spacings of 4 times nozzle width. The temperature profile was uniform in all the cases. It has been observed that for parabolic velocity profile the jet contracts slightly just after the nozzle exit plane whereas for uniform velocity profile jet expands continuously from the nozzle exit plane. The results have been compared with the results of Miyazaki et al. [88], Sparrow and Lee [12] and Gardon and Akfirat [40].

Martin [57] has published an extensive literature survey emphasizing the engineering applications of impinging jets. The empirical equations have been presented for the prediction of heat and mass transfer coefficients within a large and technological important range of variables based on experimental data for single round nozzle, array of round nozzles, single slot nozzle and array of slot nozzles.

Ero [90] has numerically solved the Navier-Stokes equations, energy and mass transport equations for jet impingement on a flat surface by a finite difference method. The Navier-Stokes equations were transformed into vorticity stream function form. The domain

of solution did not include the nozzle exit plane. Heat and mass transfer coefficients were found to be higher for the Gaussian velocity profile than for the parabolic velocity profile, since the Gaussian velocity profile attains higher centreline velocity compared to the parabolic velocity profile. The heat and mass transfer coefficients have been presented for a Reynolds number of 1000 based on nozzle width and average velocity at the nozzle exit plane.

Masliyah & Nguyen [91] have measured the local mass transfer coefficients resulting from impingement of a two-dimensional laminar slot jet on flat surface by using holographic technique. A regression equation has been suggested in terms of local Sherwood number for a Schmidt number of 2.85. The characteristic length for Sherwood number and Reynolds number has been taken as twice the slot width.

Obot et al. [92] have carried out an extensive study to determine the effects of nozzle inlet shape (contoured and sharp-edged) and nozzle length/diameter ratio on impingement heat transfer. It has been reported that the effect of nozzle inlet shape on stagnation point heat transfer coefficient was most pronounced for the short nozzle, and moderate for nozzles which were 10 and 20 diameters long, but the effect was negligible for nozzles which were 40 or more diameters long. Beyond nozzle to plate dimensionless spacings of 12, the stagnation point and the average heat transfer coefficients have been found to be essentially independent of nozzle inlet shape and nozzle length.

Obot et al. [93] have presented an extensive critical review

of heat and mass transfer correlations for turbulent impinging jets of various configurations. A table consisting of the recommended form of selected correlations has been given. It has been observed that most of the correlations have been obtained for impingement on stationary surfaces. The case of the coupled heat and the mass transfer and the case of temperature-dependent fluid properties have not been investigated. The effect of nozzle geometry have been shown to be very important in determining the performance of jet impingement systems.

Inada et al. [94] have considered a two-dimensional water jet with finite nozzle width, impinging normally on a flat surface. Local heat transfer coefficients have been estimated and the effect of distance between the jet exit and the flat plate has been investigated. The calculated results have been compared with the experimental results of the local heat transfer coefficients along the flat surface with constant heat flux.

Deshpande and Vaishnav [95] have numerically solved the Navier-Stokes equations for laminar axisymmetric jet impinging on a flat surface with the uniform and the parabolic velocity profiles at the jet exit plane. The vorticity-stream function formulation was used along with the coordinate transformation, so that a uniform grid spacing could be used in regions of rapid change of velocities. Gosman's [85] method has been used for numerical solution. It appears that entrainment boundary condition has not been applied properly. Solutions have been presented for Reynolds number in the range of 0 to 2,000 and nozzle-to-plate spacings of 3 and 4 times the nozzle radius. It was observed that

the flow became turbulent at $Re = 1,600$ with the parabolic velocity profile at the nozzle exit and a nondimensional impingement distance of 4. The stream line pattern shows recirculating cells which appear to be physically unrealistic. At the outflow boundary, Glauert's wall jet similarity has been used.

Hin-Sum Law and Masliyah [96] have studied both experimentally and theoretically, the local mass transfer due to impingement of a two-dimensional laminar confined slot jet on a flat surface for jet Reynolds numbers upto 400, and for two different nozzle-to-plate spacings. The experimental results were obtained by holography. Navier-Stokes equations and mass transport equations were solved in vorticity-stream function formulation using hybrid differencing scheme.

Striegl and Diller [97] have experimentally studied the effects of entrainment temperature on local heat transfer rate to single and multiple, turbulent impinging slot jets. In order to determine the effect of entrainment of the surrounding fluid, single jet was issued into an environment at a temperature which was varied between the temperature of the air and the temperature of the heated impingement plate. The single jet correlations have been applied to multiple jets by using the measured temperature in the recirculation region to include the effect of entrainment.

Downs and James [98] have presented an exhaustive literature survey of impingement heat transfer by a single slot jet and array of slot and round jets. Their work summarizes the findings of forty-seven papers dealing with experimental investigations and theoretical analysis. Most of the papers are related to turbulent

flows, with a very few papers on laminar flow. The correlations developed by various authors along with the range and limitations of parameters, have been presented.

Elbanna and Sabbagh [99] have experimentally studied the flow characteristics of the interaction of two slot jets impinging against a normal plane. Measurements of pressure, turbulent intensities and average velocities in the flow field have been performed. Flow visualization studies were also carried out. Parameters included in this investigation are the distance between jet exit and normal plane and the strengths of the jets. The response of the flow field to the variation in these parameters has been characterized. The rate of jet decay for two jets was found to be greater than that for a single impinging jet. The weaker of the two jets was found to spread and decay faster than the stronger of the two jets.

Wang et al. [100] have made an analytical study of the heat transfer between an axisymmetric free impinging jet and a solid flat plate with non-uniform wall temperature or wall heat flux. The results show that the non-uniformity of wall temperature or the wall heat flux have considerable effect on the stagnation point Nusselt number. Increasing the wall temperature or wall heat flux with the radial distance, reduces the stagnation point Nusselt number while, decreasing the wall temperature or the wall heat flux with the radial distance, enhances the heat transfer at the stagnation point.

Zumbrunnen et al. [101] have experimentally measured the local heat transfer coefficients for transitional liquid slot jet

for cooling of the micro-electronic circuits. Two nozzles were used for the study. Two separate nozzle widths were used and the effects of the change of nozzle widths were observed. The effects of Reynolds numbers on the heat transfer coefficient were also observed.

Goldstein et al. [102] have carried out an experimental investigation that characterizes the convective heat transfer of a heated circular air jet impinging on a flat surface. The radial distributions of the recovery factor, the effectiveness and the local heat transfer coefficients have been presented. It has been observed that the recovery factor and the effectiveness depend on the spacing from jet exit to the impingement plate but, do not depend on the jet Reynolds number. The effectiveness does not depend on the temperature difference between the jet and the ambient. A correlation has been given for the effectiveness. It is observed that the heat transfer coefficient is independent of the temperature difference between the jet and the ambient, if it is defined with respect to the difference between the heated wall temperature and the adiabatic wall temperature.

Wolf et al. [103] have experimentally investigated the effects of the nonuniform water jet velocity profile on impingement cooling. The static and stagnation pressure measurements have been carried out along the impingement surface and within the jet respectively. The surface heat flux and local wall temperatures were inferred from a two-dimensional, finite difference solution of the energy equation within the heater. Heat transfer coefficient distributions have been presented for heat

fluxes ranging from 0.24 to 1.47 MW/ m² and for Reynolds numbers (based on the average nozzle exit velocity and nozzle width) ranging from 15,000 to 54,000. The nonuniform profile was found to enhance the heat transfer significantly as compared to uniform velocity profile. However, enhancement is attributed primarily to the increased levels of free-stream turbulence and only secondarily to the change in the velocity profile.

Goldstein et al. [104] have conducted an experimental investigation to characterize the convective heat transfer from a flat surface to a row of impinging, circular, submerged air jets formed by square-edged orifices having a length/diameter ratio of unity. The distribution of recovery factor, effectiveness and the local heat transfer coefficients are presented. Spanwise-average and surface-average heat transfer coefficients are also presented. It is observed that the heat transfer coefficient is independent of the temperature difference between the jet and the ambient. In the range of the study, the effectiveness is found to be independent of the jet Reynolds number and the temperature difference between the jet and the ambient. It has been found that the spanwise-average and the surface-average heat transfer coefficients have the largest values on the impingement line and decrease with increasing distance away from it.

Sami-Al-Sanea [105] has numerically solved the Navier-Stokes equations for laminar jet of air impinging on isothermal flat surface for three cases namely, (i) the free slot jet impinging on a heated flat plate, (ii) the semi-confined slot jet issuing from top wall and impinging on a parallel bottom heated wall and (iii)

the same geometry as case (ii) with cross flow. *SIMPLE* method with modifications following Pun and Spalding [106], has been used to solve the Navier-Stokes equations. In contrast to *SIMPLE* method, all the momentum and energy equations are simultaneously solved line by line. Uniform and parabolic velocity profiles have been used at the nozzle exit plane, but the mean value of the profiles are unity at the nozzle exit. Reynolds numbers ranging from 50 to 450, Prandtl number from 0.1 to 100, impingement surface length varying from 6.5 to 20 and the nozzle-to-plate spacings of 1 to 16, have been considered in the investigation. It has been observed that the Nusselt number at the stagnation point is 45% higher for parabolic velocity profile than for the uniform velocity profile at slot exit. The variation of Nusselt number with axial distance along the surface was observed to be significantly different upto $X = 1$ for the two initial velocity profiles but it becomes coincident beyond $X > 1$. The variations in Nusselt numbers have been found to be the same for free impinging jet and semi-confined jet at the stagnation region but slightly differ far away from the stagnation point.

Brahma [107] has analytically solved the boundary layer form of momentum and energy equations for impingement of a jet over a flat surface for different nozzle-to-plate spacings. The boundary layer equations were solved by Blasius-Frossling series solution method using the available potential flow solution of Ehrlich [68]. A correlation has been developed to predict the stagnation point Stanton number in terms of velocity gradient at the stagnation point and Reynolds numbers at the nozzle exit plane based on

nozzle exit velocity and nozzle half-width.

Womac et al. [108] have experimentally investigated the circular, free surface liquid jet impingement and submerged jet impingement of water and fluoro-carbon liquid over square heat sources, resembling electronic integrated circuit chips, with uniform jet-exit velocity profile. An excellent review of the earlier investigations has been presented for both the types of jet impingement. Experiments were conducted with four different nozzle diameters, nozzle-to-heat source spacings upto 10 diameters and Reynolds numbers in the range of 670 - 1,28,000. The limitations of the existing correlations have been discussed and two correlations have been presented, one for free-surface jet impingement and another for submerged jet impingement. These are based on area weighted combination of the separate correlations for impingement region and wall jet region. Heat transfer coefficient, for a submerged jet was found to be weakly dependent upon L/d for $L/d < 4$, while for $L/d > 4$ it varied significantly with L/d . For $Re \geq 4,000$, the heat transfer coefficient is greater under submerged conditions than under free surface jet conditions.

Stevens et al. [109] have experimentally measured the flow structure in the stagnation zone of impinging circular free surface liquid jets. Laser Doppler velocimeter was used for the measurements. The jet was formed from fully developed pipe flow. Nozzles of diameters ranging from 2.1 mm to 14 mm with nozzle-to-plate spacings of 1 to 4 times the nozzle diameters were considered. The results have been presented for nozzle-to-plate spacings of one diameter and for Reynolds numbers in the range of

2,600 to 62,000. It was observed that radial velocities in the stagnation region of pipe type nozzles, vary linearly with the radial co-ordinate at a given axial location for axial and radial distances less than one diameter. The radial gradient of nondimensional radial velocity was found to be linearly dependent on axial co-ordinate. An estimate has been made for the point where the jet deceleration begins due to the presence of the plate. This distance was found to be half a diameter above the plate for nozzle-to-plate spacings in the range of 1 to 4 diameters. A gravity induced contraction was observed at low Reynolds number.

Stevens et al. [110] have experimentally measured the flow structure of impinging axisymmetric, turbulent, free surface liquid jets of nozzle diameters in the range of 7.6 - 23 mm and nozzle-to-plate spacings of 1 and 0.75 times of the nozzle diameter. The Reynolds numbers were in the range of 2,600 - 53,100. A laser Doppler velocimeter was used for the measurements. The maximum radial velocity was found to occur very near the surface for radial location less than 2.5 nozzle diameters. This is contrary to the assumption common to analytical treatments that the velocity outside the boundary layer is everywhere equal to the pre-impingement jet velocity. Analytical predictions of the layer velocity profile, the layer depth and the free surface velocity, have been compared with experimental measurements. The turbulence measurements in the layer have been reported. The turbulence was found to be maximum near the impingement surface and gradually increased with radial distance.

Elison et al. [111], have experimentally measured the local heat transfer coefficients for impinging circular liquid jets in the initially laminar, transitional and turbulent regions with Reynolds number in the range of 300 - 7,000 and with nozzle diameters of 0.25, 0.32 and 0.58 mm. The impingement was on the constant heat flux surface and the local heat transfer coefficients were determined from the measured values of surface temperatures. The free-surface jet and the submerged jet both, were considered with fully developed velocity profiles at the nozzle exit. The stagnation point Nusselt number was observed to be independent of the nozzle-to-plate spacing for free surface jets whereas, for initially turbulent submerged jets, the stagnation point Nusselt number was observed to decrease rapidly beyond the nozzle-to-plate spacing of 8. For initially laminar submerged jets the local Nusselt number was observed to decay rapidly in the radial direction at lower Reynolds numbers. It has been observed that the stagnation point Nusselt numbers correlate approximately with $Re^{0.5}$ and $Re^{0.8}$ for initially turbulent and laminar jets respectively. It is rather puzzling and reasons have been given for this trend.

Lytle et al. [112] have experimentally measured the local heat transfer coefficients for the impingement by an axisymmetric jet of air at low nozzle-to-plate spacings by infrared thermal imaging technique. The flow structure was investigated by Laser Doppler velocimeter and wall pressure measurements. Nozzle-to-plate spacings of less than one nozzle diameter and Reynolds numbers ranging from 3,600 to 27,600 were considered. At

nozzle-to-plate spacing of less than 0.25 and high Reynolds numbers, secondary peak was observed in the mean velocity profiles and local Nusselt numbers. The magnitude of the Nusselt numbers at the secondary peak was greater than the stagnation point Nusselt numbers. In the mean velocity profiles, primary peak was observed around a radial location of 0.5 diameter and a secondary peak was also observed. The heat transfer enhancement was observed due to the global-continuity-forced acceleration of the impinging fluid as it escapes from the nozzle-to-plate gap, as well as transition from laminar to turbulent boundary layer.

Huang et al. [113] have experimentally measured the local and the average Nusselt numbers for axisymmetric turbulent jet of air impinging on a heated surface at Reynolds numbers in the range of 6,000-60,000 and at the different nozzle-to-surface spacings. They have developed a correlation for the average Nusselt numbers with Reynolds number Re , Prandtl numbers Pr , nozzle-to-surface spacing H_1 and radial distance R from the stagnation point. The maximum Nusselt number was observed at a nondimensional nozzle-to-surface spacing of $H_1=4.7$. It was observed that the average Nusselt number and the maximum Nusselt number depend on H_1 and R significantly. Correlations have been proposed to predict the average and the maximum Nusselt numbers at small H_1 .

Mollendorf and Gebhart [114] have solved the boundary layer equations to study the effect of buoyancy on round, laminar, vertical jet. A perturbation analysis has been carried out to study the effect of small amount of buoyancy since the similarity solution is not possible, if the effect of buoyancy is included.

The resulting perturbation equations have been numerically solved for various Prandtl numbers. It has been shown that the predominant effect of positive buoyancy is to increase the axial velocity of the jet. The magnitude of the effect is shown to increase for decreasing Prandtl numbers.

Seban et al. [115] have measured the temperature distribution of a heated, turbulent, axisymmetric air jet discharged vertically downwards into ambient air. The velocity and temperature profiles at jet exit plane were uniform. The centre line temperature distribution and depth of penetration of jet with buoyancy, has been predicted. The depth of penetration decreases with the increase of buoyancy. The negative buoyancy decelerates the jet flow and this ultimately reverses the jet to produce an upward flow surrounding the central, downward flow. Solutions of momentum integral and energy equations with Gaussian distribution for velocity and temperature are available, but these neglect the upward flow. Seban et al. have compared their experimental results with these results and have found a good agreement.

Ogino et al. [116] have investigated experimentally and theoretically, the heated, turbulent, round, vertically upward buoyant jet discharged into a linearly stratified ambient. Uniform velocity and temperature profiles were used at the nozzle exit. They have derived a 'scaling law' for correlating the centreline velocity and temperature from the dimensional analysis of mass conservation, momentum and energy equations, and have compared these with experimental results. Similar results have been derived and experimentally confirmed for linearly stratified ambient. The

zero momentum height and zero buoyancy height have been correlated with the product of discharge Froude number and the temperature gradient of ambient fluid, based on the experiments on water jet.

Satyanarayana and Jaluria [117] have experimentally investigated the thermal characteristics of a laminar, circular, heated jet of water injected into a tank of water, at various inclinations with the horizontal axis. A nozzle of 0.6 cm diameter located on the wall of the tank has been used in all the experiments. Two locations of the nozzle, namely, 1.5 cm above the bottom and at the middle of the tank wall have been considered. The temperature distributions, the jet trajectories and the depth of penetration for inclined jet have been presented. It has been observed that the downward penetration of the jet before it turns upward, increases with the increase of jet inclination, decrease of jet temperature (Ri) and increase of flow rate. The mixed convection parameter, $Ri = Gr/Re^2$ influenced the results significantly. An analytical model based on integral method approach is developed on the basis of experimental data and a good agreement is observed between the experimental results and the theoretical results.

Yuan et al. [8] have numerically investigated the Navier-Stokes equations by SIMPLEC method for laminar, heated, two dimensional jet impinging on an isothermal surface to determine the effects of buoyancy on the flow, and thermal structure of the region near impingement. Uniform velocity profile has been used at the slot exit. Reynolds numbers in the range of 10 - 500, Grashof numbers in the range of 10 - 1,25,000, Richardson numbers in the

range of -3 to 1.5 and nozzle-to-plate spacings of 2 to 8 have been considered. Both, the downward facing and the upward facing jets have been considered for the investigation. At lower values of Richardson numbers, the fluid flow characteristics and temperature distribution behave like a non-buoyant jet. When the absolute value of Ri is sufficiently small, both the skin friction coefficient and the Nusselt number are slightly enhanced for the upward facing jets and slightly reduced for downward facing jets. But with an increase in Richardson number the buoyancy dominates the flow. For a downward facing jet, at large positive Ri the buoyancy retards the flow and the flow in the wall jet region separates from the surface. For very large positive Richardson numbers, the jet does not impinge on the surface and, the wall friction factor and the heat transfer rate decrease. But for upward facing jet, the large positive values of Ri strengthen the jet, therefore the wall friction factor and the heat transfer rate increase. It has been observed that the local Nusselt number experiences a peak away from the axis of the jet which is enhanced for highly buoyant flows.

Potthast et al. [118] have given numerical solutions for the semi-confined axisymmetric axial and the radial buoyant air jets impinging vertically downwards on an isothermal flat plate. Both, the uniform and the parabolic velocity profiles have been used at the nozzle exit, but the mean value for both the profiles is taken as unity. It was observed that the steady non-buoyant jet with a parabolic jet exit velocity profile gives maximum Nusselt number at the stagnation point which decreases at a faster rate than that

for the uniform jet exit velocity profile and unsteady buoyant jets. Friction factor coefficients are also presented for axial and radial axisymmetric jets. The flow becomes chaotic at higher values of Re and Gr . Steady radial jet with 60° inclination gives 5% more heat transfer rate than the steady axial jet.

2.6 OFFSET SLOT JET

Bourque and Newman [119] have investigated theoretically, the fluid flow characteristics of two-dimensional, incompressible, turbulent jet over an offset and inclined plate and have compared the results with the experimental results. The pressure inside the recirculation region was assumed to be uniform and the jet centre line was assumed to be a circular arc of radius r . The jet separates from the boundaries at the slot lips and reattaches to the plate downstream, giving rise to a recirculation region. It was assumed that the presence of the boundary has no effect on the velocity distribution of the jet. Thus, the velocity field is taken from the solution of the two-dimensional free turbulent jet. The radius of curvature was determined by applying momentum theorem locally for the horizontal component at the point of reattachment. This model does not account for the rise in pressure and deceleration of the jet as it approaches the point of reattachment. An expression is derived to calculate the reattachment length as a function of offset ratio. The flow becomes independent of offset ratio, offset surface length and nozzle exit Reynolds number when those are sufficiently large. This model gives reasonable predictions of the reattachment point.

Bourque [120] in a later paper relaxed the constant radius of curvature restriction but the other assumptions were retained.

Ayukawa et al. [121] have investigated the oscillations due to small pressure fluctuation in the recirculating region for turbulent offset slot jet both theoretically and experimentally. It was observed that the amplitude of the oscillating jet increases along the jet axis and decreases with the increasing frequency of pressure fluctuation within the bubble. In the theoretical analysis, the viscous terms were neglected and linearized equations were solved using Görtler's velocity profile for the jet. The theoretical results have been found to be in good agreement with the experimental results.

Akiharu et al. [122] have numerically investigated the Coanda effect in laminar region for discontinues diffusing flow. They considered a conduit whose width is abruptly expanded by a ratio of 1:3. They have considered unsteady vorticity transport equation and solved it by marching in time for the assumed initial flow patterns. An initially symmetrical flow pattern resulted in a symmetrical flow pattern as solution of Navier-Stokes equations at large times. An initially unsymmetrical flow pattern resulted in an unsymmetrical steady state solution of Navier-Stokes equations at large times. They observed Coanda effect in the laminar region. But Navier-Stokes equations failed to give an unique solution in the laminar region when Coanda effect occurred. An initially symmetrical flow pattern remains symmetrical upto a particular Reynolds number and beyond this Reynolds number, the flow becomes unsymmetrical. But at low Reynolds numbers, the flow remains

symmetrical and recovers its symmetry in spite of small disturbances.

Nozaki et al. [123] have experimentally studied the effects of initial turbulence intensity on turbulent offset jet for offset ratios ranging from 1 to 20, but not at very small offset ratios. The authors had observed in their earlier investigation, that the behavior of the reattachment flow is independent of Reynolds numbers if it is larger than 1.0×10^4 hence, the experiments were conducted in the Reynolds number range 3.0×10^4 to 5.0×10^4 . It has been observed that the jet reattachment point shifts towards the upstream with the increase of turbulence intensity. For initial turbulence intensity greater than 0.6, the flow becomes self-preserving very rapidly and the parameters downstream, do not depend upon the initial turbulence intensity. The empirical constants of eddy viscosity have been related to the turbulence intensity. The calculated results agree with experimental results for a wide range of offset ratios.

Hoch et al. [124] have theoretically and experimentally investigated the flow characteristics of submerged turbulent offset slot jet with the uniform velocity profile at slot exit and with and without a secondary free stream. The entire flow field is divided into three regions namely, (i) Pre-attachment region, (ii) Impingement region and (iii) Wall jet region. Unlike Bourque and Newman [119], they have not assumed the pressure in the recirculation region and radius of curvature of jet centre line both to be constant. The velocity field of free jet, had variable jet spread and entrainment has been considered. Solutions have

been obtained by momentum integral method in the three regions. A polynomial profile has been assumed for the jet trajectory. It was observed that the jet reattachment length increases with the increase of the offset ratios and the secondary free stream velocity. Pressure inside the pre-attachment region remains below the ambient level. The jet trajectory, axial velocity distribution and the reattachment pressure compared very well with the experimental data in the range of offset ratios greater than 12 and free stream velocity greater than 0.3 times the jet-exit velocity.

Hoch et al. [125] in a parallel paper, have theoretically and experimentally investigated the temperature distribution in a submerged, heated, turbulent, offset slot jet in the presence of secondary free stream velocity over an adiabatic offset surface. The energy integral equation with variable half width has been solved using the velocity profiles derived earlier by Hoch et al. [124]. It has been observed that the Gaussian nature of temperature profiles in the reattachment region of jet and the uniformity of temperature in the recirculation region were substantiated experimentally. The secondary free stream velocity had only a minor influence on the maximum axial temperature, whereas offset ratio had significant effect on maximum axial temperature in the pre-attachment region and this effect diminished progressively downstream.

Aung [126] has reported on the experimental study of the fluid flow and the heat transfer characteristics downstream of heated back step, using a laminar boundary layer type of flow

approaching the step. Temperature distributions were measured using a Mach-Zehnder interferometer. It has been observed that the maximum heat transfer occurred downstream of the reattachment point, the increase being proportionately larger for smaller steps. The reattachment length was found to increase with the increase of Reynolds number in the laminar region. The local heat transfer coefficient increased monotonically across the reattachment point and quantitatively, it is less than the flat plate value. A correlation for the average heat transfer coefficient has, been proposed in terms of Reynolds number and the step height.

Aung et al. [127] have numerically solved the Navier-Stokes equations and the energy equation in the vorticity-stream function form for a back step using a boundary layer type of flow approaching the step. Results have been presented for step heights of 3.8 mm, 6.35 mm and 12.7 mm and the Reynolds number based on step height ranging from 63 to 420. An upwind scheme has been used for convective terms and central difference scheme for the diffusion terms. It has been shown that the size of initial boundary layer thickness can have opposing effects on the reattachment distance. The reattachment distance was found to increase with an increase in Reynolds number. However, no correlation could be obtained in terms of step height and Reynolds number. It has been observed that the local Stanton number grows rapidly from the corner of the step, eventually levels off and then decreases slightly. At smaller step height, the local Stanton number was observed to be less than the flat plate value all along

the length, but at higher step height, the local Stanton number eventually merges with the flat plate value, downstream.

Pelfrey et al. [6] have experimentally measured the mean flow characteristics of submerged turbulent offset slot jet by Laser-Doppler anemometer. All the results have been presented for a Reynolds number of 15,000, offset ratio 7 and the uniform velocity profile at the slot exit. The location of dividing streamline was determined by numerical integration of velocity profiles along a vertical plane from the wall at each downstream locations until the mass flux becomes zero. A fourth order polynomial was fitted to construct the dividing streamline. There was evidence of a secondary recirculation region near the corner of jet exit wall and the offset surface. The reattachment point was identified as the point, where the velocity gradient became zero along the wall. The position of maximum velocity was determined by interpolation of velocity vectors at downstream locations and then a fifth order polynomial was used to curve fit the points. It has been observed that, in streamline co-ordinates defined by the jet maximum velocity locus, the velocity decay and upper jet spread rates are similar to plane jets.

Holland et al. [128] have experimentally measured the thermal characteristics of submerged, heated, turbulent, offset slot jet over an adiabatic surface. The results have been reported for a single Reynolds number of 15,000 and three values of offset ratios. The investigation has been carried out in the three flow regions namely, the recirculation region, the impingement region and the wall jet region. The surface temperature was observed to



be maximum within the recirculation region for all the offset ratios. It occurred closer to jet exit for larger offset ratios. The temperature within the recirculation region, was observed to be close to the impingement location temperature, however the thermal distribution was observed to be dependent on the offset ratios, specially near the wall. The thermal energy content within the recirculation region was observed to remain relatively uniform for both low and high offset ratios. It has been summarized that high offset ratios create greater flow curvature and entrain more of ambient fluid. It has further been pointed out that, just downstream of impingement, the temperature profile becomes locally similar based on the wall temperature and jet temperature half width scaled with the impingement distance. This is similar to the profile given by Hoch and JiJi [124] except that they have used velocity half length.

There is lack of precise information near the slot exit plane of free jet, since most of the earlier investigations deal only with the solutions of boundary layer equations and similarity solutions away from the slot-exit. The complete details of temperature profiles for free slot-jets and free axisymmetric jets were not available in open literature. The solution of energy equation in the boundary layer form, based on Schlichting's similarity solution has been reported by Cebeci and Bradshaw [9] for plane jet.

The information at low Reynolds numbers is not available for the jet impingement on a circular cylinder. Kang and Greif [64] have given the solutions for $Re \geq 100$.

Yuan et al. [8] have investigated the buoyant slot jet impinging on a surface vertically downwards, with uniform velocity and temperature profiles at the slot-exit. The boundary conditions used along the outer wall of the nozzle were interpolative. Fumizawa [11] has carried out a similar study for a round axisymmetric jet, with no-slip and impermeability boundary conditions along the outer wall of nozzle but entrainment has not been considered properly. Further, it has been pointed out by Sparrow and Lee [12] that solution of boundary layer equation for parabolic slot-exit velocity profile gives double the heat transfer coefficient at stagnation point compared to the uniform slot-exit velocity profile. Solutions of Navier-Stokes equations and energy equation for parabolic slot-exit velocity and temperature profiles are not available for buoyant jet.

Literature survey indicates that the laminar offset jet has not been investigated in great details. References are available for boundary layer type flow over a backward facing step and the turbulent offset jet with uniform jet-exit velocity and temperature profiles.

CHAPTER-III

PROBLEM FORMULATION AND NUMERICAL MODELLING

Jet impingement heat transfer has been, for a number of years, an accepted technique for cooling of hot components in gas turbine engines. Impinging jets are of great practical interest in many industrial applications requiring localized controlled cooling apart from electronic component cooling, annealing of non-ferrous sheet metals, tempering of glass, drying of textiles, wood and paper. In recent years, concern over thermal pollution has motivated numerous theoretical and experimental investigations on heated jets. The studies have mainly been concerned with slot and circular jets which are turbulent at the slot exit. The case of jet impingement heat transfer by laminar jets has received relatively less attention. Laminar jets have limited applications but the results are useful in understanding the impact of buoyancy on the flow structure and transport process and also in understanding of turbulent jets.

Bickley [26] and Schlichting [25], gave classical similarity solution of boundary layer equations for the free plane jet and axisymmetric jet. Landau [45], gave an exact solution of Navier-Stokes equations for a round laminar jet and Squire [46], also gave a solution of temperature field. Ehrlich [67], gave potential flow solution for impinging slot jet which was extended by Sparrow and Lee [12].

A number of investigators have given similarity and local

similarity solutions for various regions of jet impingement. Jet impingement has been investigated in great details experimentally also for single and array of jets on flat and curved surfaces. Numerical solutions of boundary layer equations were given by various authors. With the increase in computation power and development of robust algorithms, numerical solutions of Navier-Stokes equations and energy equation have also been obtained by various authors for different jet impingement problems. This investigation is also an attempt in that direction. SIMPLE algorithm due to Patankar [10] and its extension SIMPLEC by Doormaal and Raithby [13] have proved to be very reliable and robust algorithms for solution of Navier-Stokes equations and energy equation. These have been used in this investigation for the study of jets and jet impingements. Five problems, all for laminar flow, have been addressed to in this investigation, namely, free slot jet, free axisymmetric jet, jet impingement over a circular cylinder, vertically downward buoyant slot jet impinging on a flat surface and an offset slot jet. In the following sections these problems are formulated and the solution techniques are outlined.

The laminar submerged slot jet and laminar submerged axisymmetric jet into still surroundings have been investigated by using SIMPLE (Semi-Implicit Method for Pressure Linked Equations) algorithm. The computational domain is divided into a number of small control volumes of variable mesh sizes, finer mesh being chosen where better accuracy is required. The governing differential equations are then integrated over these control

volumes to obtain a set of discretized linear algebraic equations. These discretized equations are then solved by Tri-Diagonal Matrix Algorithm (TDMA) with under-relaxation as suggested by Patankar [10]. In SIMPLE algorithm, the pressure field is guessed and the discretized momentum equations are solved to obtain the estimate for velocity components. The pressure and velocity components in all the control volumes are corrected so as to satisfy the continuity equation. The corrected velocity and pressure fields with under relaxation, are used to find a better estimate for the velocity and the pressure. The iterations are continued until convergence to a required accuracy is obtained. Briefly, this is the procedure adopted in SIMPLE algorithm.

The laminar jet impingement on a circular cylinder, the laminar vertically downward heated jet impinging over a flat surface with and without buoyancy and the laminar offset slot jet impinging over a flat plate have been investigated by SIMPLEC (SIMPLE Consistent), the modification of SIMPLE algorithm following Doormaal and Raithby [13].

3.1 FREE SLOT JET

The jet emanates from a rectangular slot or nozzle of width 'W' in a wall and is discharged into still surroundings consisting of same fluid as that of the jet. A jet which does not interact with any solid surface is called a free jet.

A rectangular Cartesian coordinate system with the origin at the centre of the nozzle exit, is chosen for analysis. The x-axis is chosen along the axis of the jet and the y-axis is along the

wall from which the jet emanates. The flow field is symmetric about the jet centre line. Therefore, only the upper half of the flow field is considered as computational domain, which is shown in the Figure 3.1.1.

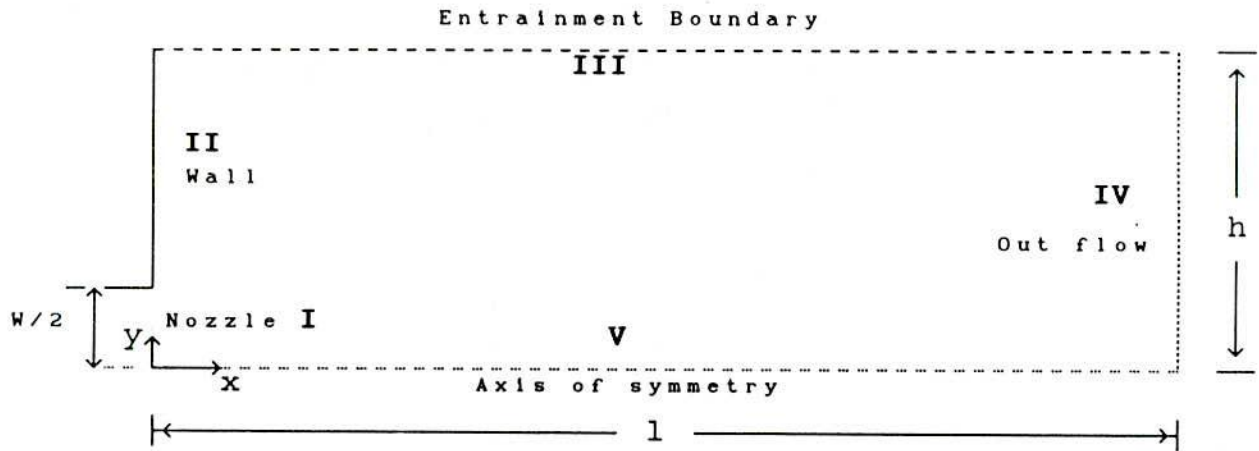


Figure 3.1.1. Computational Domain of Free Slot Jet.

The velocity components along x and y directions are u and v respectively. The jet is considered to have either uniform or parabolic velocity and temperature profiles at the slot exit plane with the jet temperature being higher than that of the ambient temperature.

3.1.1 Governing Equations

The flow is considered to be steady, laminar, incompressible and two-dimensional. The fluid properties are assumed to be constant. The viscous dissipation is neglected. The Navier-Stokes equations and the energy equation in conservative form are as follows,

CONTINUITY EQUATION,

$$\frac{\partial(\rho' u)}{\partial x} + \frac{\partial(\rho' v)}{\partial y} = 0 \quad (3.1.1)$$

X-MOMENTUM EQUATION,

$$\frac{\partial}{\partial x}(\rho' uu) + \frac{\partial}{\partial y}(\rho' uv) = - \frac{\partial P}{\partial x} + \frac{\partial}{\partial x} \left[\mu \frac{\partial u}{\partial x} \right] + \frac{\partial}{\partial y} \left[\mu \frac{\partial u}{\partial y} \right] \quad (3.1.2)$$

Y-MOMENTUM EQUATION,

$$\frac{\partial}{\partial x}(\rho' uv) + \frac{\partial}{\partial y}(\rho' vv) = - \frac{\partial P}{\partial y} + \frac{\partial}{\partial x} \left[\mu \frac{\partial v}{\partial x} \right] + \frac{\partial}{\partial y} \left[\mu \frac{\partial v}{\partial y} \right] \quad (3.1.3)$$

ENERGY EQUATION,

$$\frac{\partial}{\partial x}(\rho' uT) + \frac{\partial}{\partial y}(\rho' vT) = \alpha \frac{\partial}{\partial x} \left[\frac{\partial T}{\partial x} \right] + \alpha \frac{\partial}{\partial y} \left[\frac{\partial T}{\partial y} \right] \quad (3.1.4)$$

The slot exit velocity U_j and slot width W are chosen as the characteristic velocity and length respectively. The pressure is non-dimensionalized by $\rho_0 U_j^2$ and temperature is non-dimensionalized by the difference of jet exit temperature T_j and ambient fluid temperature T_∞ , that is, $(T_j - T_\infty)$. For parabolic profiles, U_j and T_j are the maximum velocity and temperatures at the nozzle exit respectively. According to the above considerations, the non-dimensionalization scheme is as follows,

$$U = \frac{u}{U_j}, \quad V = \frac{v}{U_j}, \quad P = \frac{(P - P_\infty)}{\rho_0 U_j^2}, \quad L = \frac{x}{W}, \quad H = \frac{y}{W}$$

$$T^* = \frac{(T - T_\infty)}{(T_j - T_\infty)}, \quad X = \frac{x}{W}, \quad Y = \frac{y}{W} \quad \text{and} \quad \text{Re} = \frac{U_j W}{\nu}, \quad \rho = \rho' / \rho_0$$

where, ρ_0 is a reference density.

These variables are substituted in Navier-Stokes equations and the energy equation in rectangular cartesian co-ordinate system. The nondimensional form of Navier-Stokes equations and energy equation are as follows,

CONTINUITY EQUATION,

$$\frac{\partial}{\partial X}(\rho U) + \frac{\partial}{\partial Y}(\rho V) = 0 \quad (3.1.5)$$

X-MOMENTUM EQUATION,

$$\frac{\partial}{\partial X}(\rho U^2) + \frac{\partial}{\partial Y}(\rho UV) = -\frac{\partial P}{\partial X} + \frac{1}{Re} \frac{\partial}{\partial X} \left[\frac{\partial U}{\partial X} \right] + \frac{1}{Re} \frac{\partial}{\partial Y} \left[\frac{\partial U}{\partial Y} \right] \quad (3.1.6)$$

Y-MOMENTUM EQUATION,

$$\frac{\partial}{\partial X}(\rho UV) + \frac{\partial}{\partial Y}(\rho V^2) = -\frac{\partial P}{\partial Y} + \frac{1}{Re} \frac{\partial}{\partial X} \left[\frac{\partial V}{\partial X} \right] + \frac{1}{Re} \frac{\partial}{\partial Y} \left[\frac{\partial V}{\partial Y} \right] \quad (3.1.7)$$

ENERGY EQUATION,

$$\frac{\partial}{\partial X}(\rho UT^*) + \frac{\partial}{\partial Y}(\rho VT^*) = \frac{1}{Re \cdot Pr} \frac{\partial}{\partial X} \left[\frac{\partial T^*}{\partial X} \right] + \frac{1}{Re \cdot Pr} \frac{\partial}{\partial Y} \left[\frac{\partial T^*}{\partial Y} \right] \quad (3.1.8)$$

where, Re is the slot exit Reynolds number based on the maximum slot exit velocity U_j and the width of the nozzle W , and Pr is the fluid Prandtl number. The density has been retained in the above equations for the sake of making the scheme general, otherwise the flow is incompressible.

Boundary Conditions

The boundary conditions at the boundaries marked I, II, III, IV and V in the Figure 3.1.1, are as follows,

I. Nozzle Exit :

For uniform velocity and temperature profiles,

$$\text{At } X = 0, 0 \leq Y \leq \frac{1}{2} : U = 1 \text{ and } T^* = 1, V=0 \quad (3.1.9a)$$

For parabolic velocity and temperature profiles,

$$\text{At } X = 0, 0 \leq Y \leq \frac{1}{2} : U = (1 - 4Y^2) \text{ and } T^* = (1 - 4Y^2), V=0 \quad (3.1.9b)$$

$$\text{II Wall : At } X=0, \frac{1}{2} < Y \leq H : U = 0, V = 0, T^* = 0, \quad (3.1.9c)$$

no-slip and impermeability boundary conditions

$$\text{III Entrainment : At } Y= H, 0 < X \leq L : U = 0, \quad \frac{\partial V}{\partial Y} = 0, \quad T^* = 0 \quad (3.1.9d)$$

$$\text{IV Out Flow Boundary : At } X= L, 0 < Y \leq H : \frac{\partial T^*}{\partial X} = 0, \quad \frac{\partial V}{\partial X} = 0$$

$$\int_{X=L}^H U dY = \int_{X=0}^{1/2} U dY + \int_{Y=H}^L V dX \quad (3.1.9e)$$

that is, inflow through the slot exit and entrainment is equated to the out flow from the boundary IV.

$$\text{V Line of Symmetry : At } Y= 0, 0 < X \leq L, : V = 0 \quad \frac{\partial U}{\partial Y} = 0, \quad \frac{\partial T^*}{\partial Y} = 0. \quad (3.1.9f)$$

3.1.2 Numerical Solution Procedure

The flow is symmetric about the jet axis hence, only the upper half of the flow region is considered for computations, to save computational effort. The domain is divided into small non-overlapping control volumes of non-uniform mesh sizes. A fine mesh is chosen where ever the gradients of the variables are expected to be steep, for example, near the wall, the axis of symmetry and the nozzle exit. A grid point is located at the centre of each control volume. The control volumes on the boundaries of the domain, have an additional grid point at the middle of their faces at the boundary. These are called boundary grid points and these are used for specifying the boundary conditions. In conventional finite difference methods, the properties and all the velocity components are specified at the grid points.

In SIMPLE, the x-component of velocity is specified at the middle of the left face of each control volume and the y-component of velocity is specified at the middle of the bottom face of each control volume as shown in Figure 3.1.2. The properties of the fluid like, pressure, density, temperature, viscosity, mass concentration and turbulence intensity etc. are specified at the grid points located at the centre of each control volume and at the boundary grid points. These control volumes are called main control volumes and are used for mass conservation equation, energy equation and pressure equation. A typical main control volume is shown in Figure 3.1.3.

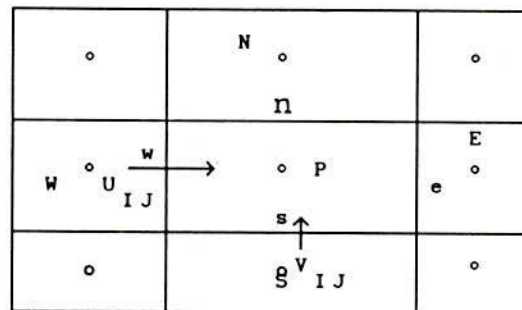


Figure 3.1.2. Typical grid

The control volumes for x and y momentum equations will have $U_{I,J}$ and $V_{I,J}$ at their centres respectively. These are different from each other and from the main control volumes. These are called staggered control volumes.

The properties are assumed to be constant in the control volumes, and vary abruptly from one control volume to the next control volume. The viscosity and thermal conductivity at the control volume faces are obtained by taking the Harmonic mean

between the neighboring grid points. The mass conservation, momentum and energy equations are integrated over their respective control volumes. The integrated continuity equation is then multiplied by the respective velocity or temperature and subtracted from the integrated momentum or energy equations to obtain the discretized equations. Patankar [10], suggests that for the convection diffusion problem, Power-law scheme predicts a result which is very close to the exact solution, is easy to use for calculation of the coefficients and requires less computational time. In this scheme, the flux F and the diffusion D through the control volume faces are required to calculate the cell Peclet number, $Pe = \frac{F}{D}$. Power-law scheme is then used to calculate the coefficients of the discretized equations depending on the cell Peclet number. The set of discretized equations are then solved by assuming pressure field. The pressure is then corrected to satisfy the continuity equation. Under-relaxation and iteration are used for the computation to take care of non-linearity.

The conservative form of mass conservation equation, momentum equations and energy equation (3.1.5 - 3.1.8) may be clubbed into the following single equation for the convenience of numerical scheme,

$$\frac{\partial}{\partial x}(\rho U \phi) + \frac{\partial}{\partial y}(\rho V \phi) = \frac{\partial}{\partial x} \left[\Gamma_{\phi} \frac{\partial \phi}{\partial x} \right] + \frac{\partial}{\partial y} \left[\Gamma_{\phi} \frac{\partial \phi}{\partial y} \right] + S_{\phi} \quad (3.1.9g)$$

where, ϕ is the common dependent variable. The values of ϕ , Γ_{ϕ} , S_{ϕ} for various equations are given in table 3.1.1.

Table 3.1.1

Equations	ϕ	Γ_ϕ	S_ϕ
Continuity	1	0	0
X-Momentum	U	1/Re	$-\frac{\partial P}{\partial X}$
Y-Momentum	V	1/Re	$-\frac{\partial P}{\partial Y}$
Energy	T^*	1/(Re.Pr)	0

The density, ρ will not appear in these equations for incompressible flow and Γ_ϕ in this case will be $\frac{1}{Re}$ and $\frac{1}{Re.Pr}$ in nondimensional momentum equations and energy equation respectively. However, the density term has been retained in the formulation of numerical scheme for the sake of keeping it general. In non-dimensional form of equations, it has been assumed that the density is nondimensionalized with respect to some reference density, so as to obtain the above form of equations.

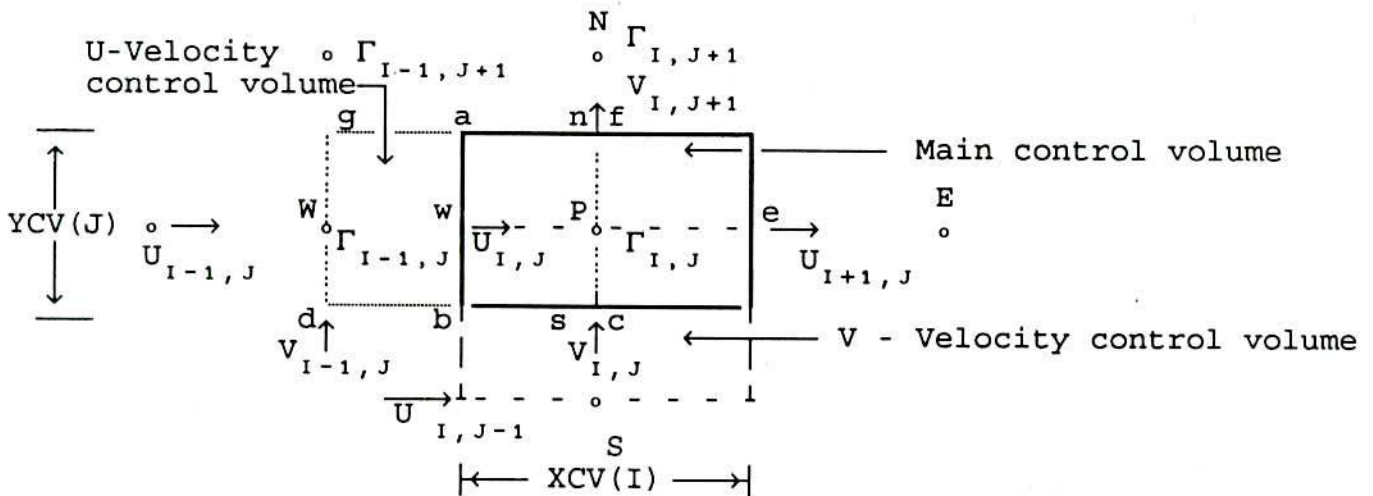


Figure 3.1.3 : The main control volume and the control volumes of U and V component of velocities.

CONTINUITY EQUATION ($\phi = 1$):

Substituting $\phi = 1$, $\Gamma_\phi = 0$ and $S_\phi = 0$ in equation (3.1.9) we

have the continuity equation,

$$\frac{\partial (U\rho)}{\partial X} + \frac{\partial (V\rho)}{\partial Y} = 0$$

The integral of $\frac{\partial (U\rho)}{\partial X}$ over the main control volume shown in Figure 3.1.3 is as follows,

$$\iint \frac{\partial}{\partial X} (\rho U) dXdY = YCV(J) [(\rho U)_e - (\rho U)_w] \quad (3.1.10)$$

where 'e' and 'w' refer to east and west faces of the main control volume respectively. The velocities U_e and U_w are assumed to remain constant over the east and west faces of the control volume. Following Patankar [10], the mass fluxes across the east and west faces can be written as,

$$\begin{aligned} F_e &= (\rho U)_e YCV(J) \\ \text{and } F_w &= (\rho U)_w YCV(J) \end{aligned} \quad (3.1.11)$$

The integral of $\frac{\partial (V\rho)}{\partial Y}$, over the main control volume shown in Figure 3.1.3 is as follows,

$$\iint \frac{\partial}{\partial Y} (\rho V) dXdY = XCV(I) [(\rho V)_n - (\rho V)_s] \quad (3.1.12)$$

According to Patankar [10], the fluxes across the north and south faces may be written as,

$$\begin{aligned} F_n &= XCV(I) (\rho V)_n \\ \text{and } F_s &= XCV(I) (\rho V)_s \end{aligned} \quad (3.1.13)$$

Hence, the discretized form of continuity equation may be written as follows,

$$F_e - F_w + F_n - F_s = 0 \quad (3.1.14)$$

X-MOMENTUM EQUATION ($\phi = U$):

The control volume for X-momentum equation is shown in Figure 3.1.3a. The points P, E, W, N, S are not grid points in this case, but are the locations, where the velocity component $U_{I,J}$ and its immediate neighbors are specified. Substituting $\phi = U$, $\Gamma_\phi = \frac{1}{Re}$ and $S_\phi = -\frac{\partial P}{\partial X}$ in Equation (3.1.9) the x-momentum equation is,

$$\frac{\partial}{\partial X}(\rho U U) + \frac{\partial}{\partial Y}(\rho U V) = -\frac{\partial P}{\partial X} + \frac{\partial}{\partial X}\left[\Gamma \frac{\partial U}{\partial X}\right] + \frac{\partial}{\partial Y}\left[\Gamma \frac{\partial U}{\partial Y}\right] \quad (3.1.15)$$

The density variation is kept for the sake of making the scheme general. It will not appear in incompressible flow. It may be assumed here that the density has been nondimensionalized with respect to reference density. Actually, $\frac{1}{Re}$ will appear on right hand side in non-dimensional form of the equation but Γ has been used here for brevity. Integrating the first term on the left hand side of Equation (3.1.15) over the U-control volume of Figure 3.1.3a, we have,

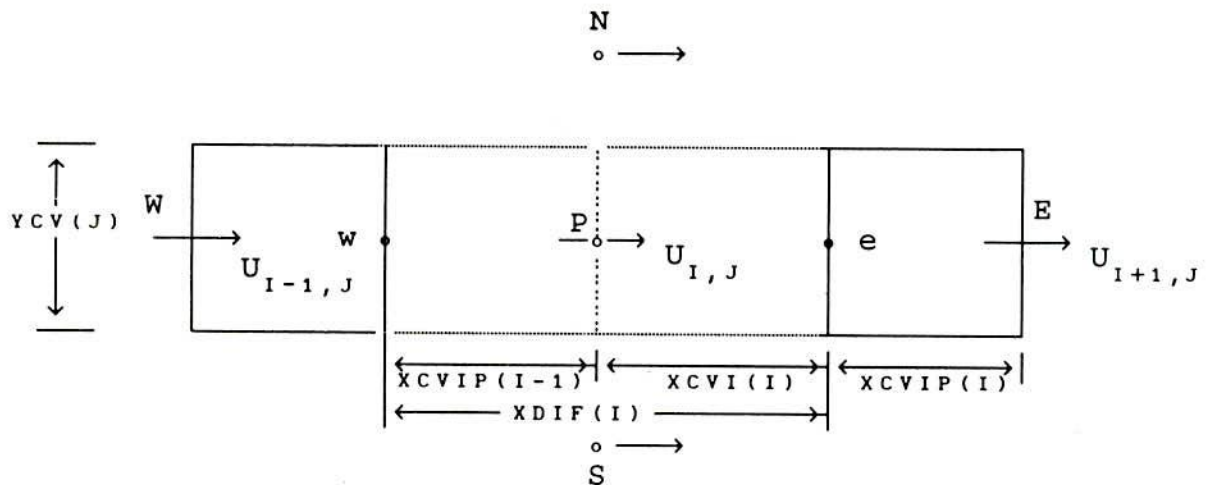


Figure 3.1.3a :The U-Velocity control volume

$$\iint \frac{\partial}{\partial X} (\rho U U) dX dY = YCV(J) [(\rho U)_e U_e - (\rho U)_w U_w] \quad (3.1.16)$$

The fluxes are written as F_e and F_w while the convected quantities U_e and U_w depend on the scheme chosen for discretization. The mass flux F_e is written as the average of mass flux at point 'E' and 'P' since, the point 'e' is midway between point 'P' and 'E', that is,

$$F_e = YCV(J) (\rho U)_e = YCV(J) \frac{\rho_P U_P + \rho_E U_E}{2}$$

The densities at points 'E' and 'P' are obtained by linear interpolation between the densities $\rho_{I,J}$, $\rho_{I+1,J}$ and $\rho_{I-1,J}$, $\rho_{I,J}$

$$\rho_E = FX(I+1) \rho_{I+1,J} + FXM(I+1) \rho_{I,J} \quad (3.1.17)$$

$$\rho_P = FX(I) \rho_{I,J} + FXM(I) \rho_{I-1,J}$$

where, $FX(I+1) = \frac{XCV(I)}{2XDIF(I+1)}$ and $FXM(I+1) = 1 - FX(I+1)$

$$FX(I) = \frac{XCV(I-1)}{2XDIF(I)} \text{ and } FXM(I) = 1 - FX(I)$$

To maintain consistency, the mass flux leaving control volume (I,J) in x-direction must enter the control volume (I+1,J). Hence, the flux across west face of control volume, (I+1,J) is considered to be the same as F_e . The integral of convection term in y-direction, is as follows,

$$\iint \frac{\partial}{\partial Y} (\rho UV) dXdY = [(\rho V)_n U_n - (\rho V)_s U_s] X DIF(I) = F_n U_n - F_s U_s \quad (3.1.18)$$

The density ρ_f is determined by linear interpolation between the densities $\rho_{I,J}$ and $\rho_{I,J+1}$ while ρ_g is determined by linear interpolation between the densities $\rho_{I-1,J+1}$ and $\rho_{I-1,J}$

$$\rho_f = FY(J+1)\rho_{I,J+1} + FYM(J+1)\rho_{I,J}$$

$$\rho_g = FY(J+1)\rho_{I-1,J+1} + FYM(J+1)\rho_{I-1,J}$$

Flux through the north face fg is,

$$F_n = F_{ag} + F_{af} = \rho_g V_{I-1,J+1} + \rho_f V_{I,J+1}$$

The velocities $V_{I,J+1}$ and $V_{I-1,J+1}$ are assumed to be constant over the north faces of control volumes (I,J) and $(I-1,J)$ respectively. Hence, mass flux F_n consists of mass flux due to velocity $V_{I,J+1}$ through area 'af' and due to velocity $V_{I-1,J+1}$ through area 'ag'. The densities at point 'f' and 'g' are used with these two parts respectively. This flux will be treated as the inflow to the next control volume, $(I,J+1)$. In this way the consistency of flux is maintained. The integral of X-diffusion term over the control volume is as follows,

$$\iint \frac{\partial}{\partial X} \left[\Gamma \frac{\partial U}{\partial X} \right] dXdY = YCV(J) \left[\left(\Gamma \frac{\partial U}{\partial X} \right)_e - \left(\Gamma \frac{\partial U}{\partial X} \right)_w \right] \quad (3.1.19)$$

$$\text{where, } \Gamma = \frac{1}{Re}$$

For Central difference scheme, the first term on the right hand side of Equation (3.1.19) is,

$$\begin{aligned} YCV(J) \left[\Gamma \frac{\partial U}{\partial X} \right]_e &= YCV(J) \Gamma_e \left[\frac{U_{I+1,J} - U_{I,J}}{XCV(I)} \right] \\ &= D_e (U_{I+1,J} - U_{I,J}) \end{aligned} \quad (3.1.20)$$

Where, $D_e = \Gamma_e YCV(J) / XCV(I)$

The integral of the second diffusion term $\frac{\partial}{\partial Y} \left[\Gamma \frac{\partial U}{\partial Y} \right]$ is,

$$\iint \frac{\partial}{\partial Y} \left[\Gamma \frac{\partial U}{\partial Y} \right] dx dy = XDIF(I) \left[\left(\Gamma \frac{\partial U}{\partial Y} \right)_n - \left(\Gamma \frac{\partial U}{\partial Y} \right)_s \right] \quad (3.1.21)$$

For Central difference scheme,

$$XDIF(I) \Gamma_n \left(\frac{\partial U}{\partial Y} \right)_n = XDIF(I) \Gamma_n \left[\frac{U_{I,J+1} - U_{I,J}}{YDIF(J+1)} \right] = D_n (U_{I,J+1} - U_{I,J}) \quad (3.1.22)$$

$$\text{Where, } D_n = \frac{\Gamma_n XDIF(I)}{YDIF(J+1)}$$

If the viscosity varies with temperature or in general, varies in space, then Reynolds number or Γ will also vary in space. For a general scheme, this variation is also included. The viscosity is specified at the grid points. The viscosity at the interfaces is calculated by taking the Harmonic mean of viscosities on the opposite sides of interface and is assumed to be uniform over the interface of the control volume. Hence,

$$\Gamma_n = \frac{(af \Gamma_f + ag \Gamma_g)}{fg}$$

$$\Gamma_n = (XCVI(I) \Gamma_f + XCVIP(I-1) \Gamma_g) / XDIF(I) \quad (3.1.23)$$

$$\text{where } \Gamma_f = \frac{2 YDIF(J+1) \Gamma_{I,J} \Gamma_{I,J+1}}{YCV(J+1) \Gamma_{I,J} + YCV(J) \Gamma_{I,J+1}} \quad (3.1.24)$$

$$\text{and } \Gamma_g = \frac{2 \text{ YDIF}(J + 1) \Gamma_{I-1, J+1} \Gamma_{I-1, J+1}}{\text{YCV}(J + 1) \Gamma_{I-1, J} + \text{YCV}(J) \Gamma_{I-1, J+1}} \quad (3.1.25)$$

The integral of the pressure gradient term is as follows,

$$- \iint \frac{\partial P}{\partial X} dx dy = (P_w - P_e) \text{YCV}(J) = (P_{I-1, J} - P_{I, J}) \text{YCV}(J) \quad (3.1.26)$$

Patankar [10], has considered one dimensional convection-diffusion problem to discuss the merits of Central difference, Upwind, Exponential and Power law schemes. This is equivalent to considering the convection and diffusion terms, say in x-direction, that is

$$\frac{\partial}{\partial X} (\rho U U) = \frac{\partial}{\partial X} \left[\Gamma \frac{\partial U}{\partial X} \right]$$

If Central difference scheme is used, then U_e and U_w in Equation (3.1.16) will be $\frac{1}{2} (U_E + U_P)$ and $\frac{1}{2} (U_W + U_P)$ respectively. Combining this with Equation (3.1.20), the discretized one dimensional equation will be,

$$F_e \cdot \frac{1}{2} (U_E + U_P) - F_w \cdot \frac{1}{2} (U_W + U_P) = D_e (U_E - U_P) - D_w (U_P - U_W)$$

$$\text{or} \quad a_p U_P = a_E U_E + a_W U_W$$

$$\text{where,} \quad a_E = D_E - F_e / 2$$

$$a_W = D_W + F_w / 2$$

$$a_p = a_E + a_W + (F_e - F_w) = a_E + a_W$$

since $F_e - F_w = 0$ from the continuity equation. Cell Peclet

Number is defined as,

$$P_e = \rho U \delta x / \Gamma = F/D$$

It is observed that for cell Peclet number, $|P_e| > 2$, either a_E or a_W becomes negative which leads to a unrealistic solution. Central difference scheme gives convergent solutions for low Reynolds numbers with expensive mesh size, but for higher Reynolds numbers, it gives unrealistic oscillatory solutions. Some authors resort to introducing artificial viscosity to damp out these Oscillations. The Upwind differencing also does the same thing.

In Upwind scheme, the convected property at the interface 'e' is taken as the value on the "Upwind" side instead of taking the average value.

If the flow is from left to right, that is, U is positive, $F_e > 0$, the Upwind side of face 'e' is P, hence

$$U_e = U_P \quad \text{if } F_e > 0$$

$$U_e = U_E \quad \text{if } F_e < 0$$

Hence,

$$a_E = D_e + \max(-F_e, 0) \quad \text{and} \quad a_W = D_w + \max(F_w, 0)$$

$$a_P = a_E + a_W + F_e - F_w = a_E + a_W$$

where, the symbol \max implies larger of its arguments.

This scheme gives good results for highly convective situations, that is, for large values of Peclet number and it is not suitable for intermediate values of Peclet numbers.

The one dimensional convection-diffusion equation has a solution in terms of exponentials if F_e and Γ are assumed to be constant and solution is sought between the points 'P' and 'E'. The solution is,

$$\frac{U - U_p}{U_E - U_p} = \frac{\exp((P_e x / XCV(I)) - 1)}{\exp(P_e) - 1}$$

The best results will be obtained if this solution is used to determine the values of U_e . The calculation of exponentials is computationally very expensive. Hence, looking at the trends of the exponential solution, Patankar has suggested a Power law scheme for all values of P_e .

It was observed that U varies linearly with x only for $P_e = 0$, indicating that the Central difference scheme is good only for small Reynolds numbers. Further, it was observed that at the interface, $U = U_{Upwind}$ only for very large values of P_e , whereas Upwind scheme uses it for all values of P_e . For very large values of P_e it was observed that $\frac{dU}{dx} = 0$ at the interface, thus the Central difference scheme over estimates the diffusion terms. Patankar [10] has fitted a fifth order polynomial in P_e which matches reasonably well with the exact solution at all values of P_e . In the Power-law scheme the coefficient a_E is expressed as,

$$\begin{aligned} a_E &= -F_e && : Pe < -10 \\ a_E &= D_e(1 + 0.1Pe)^5 - F_e && : -10 \leq Pe \leq 0 \\ a_E &= D_e(1 - 0.1Pe)^5 - F_e && : 0 \leq Pe \leq 10 \\ a_E &= 0 && : Pe > 10 \end{aligned} \tag{3.1.26a}$$

where, $Pe = F_e/D_e$, is the cell Peclet number.

Following the above procedure, a set of discretized equations may be derived from Equation (3.1.15) for each control volume. These equations will be as follows,

$$a_p U_{I,J} = a_E U_{I+1,J} + a_W U_{I-1,J} + a_N U_{I,J+1} + a_S U_{I,J-1} + b + A_U (P_{I-1,J} - P_{I,J}) \quad (3.1.27)$$

where, $A_U = YCV(J)$. The coefficients a_E , a_W , a_N , a_S , a_U and a_p all have subscripts (I,J) , which have been dropped for brevity.

$$\text{or, } U_{I,J} = \frac{[\sum a_{nb} U_{nb} + b]}{a_p} + \frac{A_U}{a_p} (P_{I-1,J} - P_{I,J}) \quad (3.3.28)$$

where, $\sum a_{nb} U_{nb} = a_E U_{I+1,J} + a_W U_{I-1,J} + a_N U_{I,J+1} + a_S U_{I,J-1}$

All the coefficients are dependent upon velocities which makes these equations non-linear. The solvers used for the solution are for linear equations only, hence the equations are linearized. The velocity field is guessed and coefficients are calculated based upon available U and V values. The new solution is used to update the coefficients and a new still solution is obtained. Therefore, the non-linearity is resolved through iteration. To ensure convergence, an under-relaxation is used which is explained below.

Equation (3.3.28) may be written as

$$\text{or, } U_{I,J} = U_{I,J}^* + \left[\frac{\sum U_{nb} a_{nb} + b}{a_p} - U_{I,J}^* + \frac{A_U}{a_p} (P_{I-1,J} - P_{I,J}) \right] \quad (3.3.29)$$

Where $U_{I,J}^*$ is obtained from the previous iteration and the bracketed term represents the change introduced by the current iteration. The change produced by the current iteration is under-relaxed by a relaxation factor α that is,

$$U_{I,J} = U_{I,J}^* + \alpha \left[\frac{\sum U_{nb} a_{nb} + b}{a_p} - U_{I,J}^* + \frac{A_0}{a_p} (P_{I-1,J} - P_{I,J}) \right] \quad (3.3.30)$$

$$\text{or, } \frac{a_p}{\alpha} U_{I,J} = \sum a_{nb} U_{nb} + b + (1-\alpha) \frac{a_p}{\alpha} U_{I,J}^* + A_0 (P_{I-1,J} - P_{I,J}) \quad (3.3.31)$$

Hence, instead of finding the solution and then under-relaxing it, the under-relaxation is built into the numerical scheme by treating,

$\frac{a_p}{\alpha}$ as a_p and adding $(1 - \alpha) \frac{a_p}{\alpha} U_{I,J}^*$ to the constant term b .

Other coefficients a_w , a_n and a_s are also calculated in a similar manner. The continuity equation must be satisfied for each control volume, which requires that a_p be equal to the sum of its four neighbors, that is,

$$a_p = a_e + a_w + a_n + a_s \quad (3.1.32)$$

It is observed from Equations (3.1.26a) that the coefficient depend upon F and D only. Hence, one has to calculate only F and D to determine the coefficients. Further, the consistency of the scheme requires that the flux and diffusion across the east face of a control volume must be equal to the flux and diffusion across the west face of the control volume on the right side of given control volume. Therefore, $a_w(I+1,J) = a_e(I,J)$ and $a_s(I,J+1) = a_n(I,J)$. As a result, only a_n and a_e have to be calculated for each control volume. The boundary control volumes require special care which will be discussed later.

Y-MOMENTUM EQUATION ($\phi = V$):

Substituting $\phi = V$, $\Gamma_\phi = \frac{1}{Re}$ and $S_\phi = -\frac{\partial P}{\partial Y}$ in equation (3.1.9g) the y-momentum equation is obtained,

$$\frac{\partial}{\partial X}(\rho UV) + \frac{\partial}{\partial Y}(\rho VV) = -\frac{\partial P}{\partial Y} + \frac{\partial}{\partial X}\left[\Gamma \frac{\partial V}{\partial X}\right] + \frac{\partial}{\partial Y}\left[\Gamma \frac{\partial V}{\partial Y}\right] \quad (3.1.33)$$

Following the above mentioned procedure this equation is integrated over V-control volume and the coefficients are obtained by the Power law scheme. The general form of discretized equation for each control volume is as follows,

$$a_P V_{I,J} = a_E V_{I+1,J} + a_W V_{I-1,J} + a_N V_{I,J+1} + a_S V_{I,J-1} + b + A_V (P_{I,J-1} - P_{I,J}) \quad (3.1.34)$$

where, $A_V = XCV(I)$. The coefficients a_E , a_W , a_N , a_S , a_V and a_P all have subscripts (I,J), which have been dropped for brevity. Also, these coefficients are different from those for the x-momentum equation.

3.1.2.1 Pressure Correction Equations

The discretized X and Y-momentum Equations (3.1.27) and (3.1.34) contain pressure terms. The pressure distribution is not known apriori. If the pressures are known, only then the solution of discretized equations is possible by the TDMA in SIMPLE method. So, a pressure field P^* is assumed and the velocity field $U_{I,J}^*$ and $V_{I,J}^*$ is found from the equations

$$a_P U_{I,J}^* = \sum a_{nb} U_{nb}^* + b + A_U (P_{I-1,J}^* - P_{I,J}^*) \quad (3.1.35)$$

$$\text{and } a_p V_{I,J}^* = \sum a_{nb} V_{nb}^* + b + A_v (P_{I,J-1}^* - P_{I,J}^*) \quad (3.1.36)$$

This velocity field, in general, will not satisfy the continuity equation. Our aim is to correct the pressure field by writing $p = p^* + p'$ and find p' , so that the continuity equation is satisfied in each control volume. Let us say, in response to pressure field $P^* + p'$, the velocities change to $U^* + U'$ and $V^* + V'$. It is implied that the corrections U' , V' and p' are such that the continuity equation is satisfied, that is, the following is a solution of discretized equations.

$$\begin{aligned} P &= P^* + P' \\ U &= U^* + U' \\ \text{and } V &= V^* + V' \end{aligned} \quad (3.1.37)$$

$$a_p U_{I,J} = \sum a_{nb} U_{nb} + A_u (P_{I-1,J} - P_{I,J}) \quad (3.1.38)$$

$$\text{and } a_p V_{I,J} = \sum a_{nb} V_{nb} + A_v (P_{I,J-1} - P_{I,J}) \quad (3.1.39)$$

Subtracting Equations (3.1.35) and (3.1.36) from Equations (3.1.38) and (3.1.39), we obtain the equations for velocities correction as follows,

$$a_p U'_{I,J} = \sum a_{nb} U'_{nb} + A_u (P'_{I-1,J} - P'_{I,J}) \quad (3.1.40A)$$

$$\text{and } a_p V'_{I,J} = \sum a_{nb} V'_{nb} + A_v (P'_{I,J-1} - P'_{I,J}) \quad (3.1.40B)$$

Actually, the coefficients are also functions of $U_{I,J}$, $U_{I+1,J}$, $U_{I-1,J}$, $U_{I,J+1}$ etc. But, in the linearized form it is assumed that the coefficients are not affected by $U^* + U'$. The constant 'b' is also assumed to remain unaffected.

If the terms $\sum a_{nb} U'_{nb}$ in Equation (3.1.40A) and $\sum a_{nb} V'_{nb}$ in Equation (3.1.40B) are retained, then every neighbor U'_{nb} and V'_{nb} will have to be expressed in terms of its neighboring pressure corrections and the velocity corrections, that is, every neighbor will bring their neighbors and so on into the Equations. As a result, the velocity correction equation would involve the pressure correction at all grid points in the computational domain and the pressure-correction equations would have to be solved simultaneously for the whole of domain. Since, a direct solution of the whole set of momentum and continuity equations is desired, the omission of the terms $\sum a_{nb} U'_{nb}$ and $\sum a_{nb} V'_{nb}$ in Equations (3.1.40A) and (3.1.40B) enables us to cast the P' equation in a form identical to the other equations, and to adopt a sequential, one-variable-at-a-time, solution procedure. Neglecting the $\sum a_{nb} U'_{nb}$ term in Equation (3.1.40A) and $\sum a_{nb} V'_{nb}$ term in Equation (3.1.40B) yields,

$$U'_{I,J} = \frac{A_u}{a_p} (P'_{I-1,J} - P'_{I,J}) \quad (3.1.41A)$$

$$\text{and } V'_{I,J} = \frac{A_v}{a_p} (P'_{I,J-1} - P'_{I,J}) \quad (3.1.41B)$$

Substituting Equation (3.1.41A and 3.1.41B) in (3.1.37) yields,

$$U_{I,J} = U^*_{I,J} + DU_{I,J} (P'_{I-1,J} - P'_{I,J})$$

$$\text{and } V_{I,J} = V_{I,J}^* + DV_{I,J} (P'_{I,J-1} - P'_{I,J}) \quad (3.1.42)$$

$$\text{Where, } DU_{I,J} = \frac{A_U}{\left[a_P \right]_{I,J}} \quad \text{and } DV_{I,J} = \frac{A_V}{\left[a_P \right]_{I,J}}$$

Similar equations can be written for $U_{I+1,J}$ and $V_{I,J+1}$ as follows,

$$U_{I+1,J} = U_{I+1,J}^* + DU_{I+1,J} (P'_{I,J} - P'_{I+1,J})$$

$$\text{and } V_{I,J+1} = V_{I,J+1}^* + DV_{I,J+1} (P'_{I,J} - P'_{I,J+1}) \quad (3.1.43)$$

Integrating the continuity equation over the main control volume yields,

$$[(\rho_e U_{I+1,J}) - (\rho_w U_{I,J})] YCV(J) + [(\rho_n V_{I,J+1}) - (\rho_s V_{I,J})] XCV(I) = 0 \quad (3.1.44)$$

Substituting, $U_{I,J}$, $U_{I+1,J}$, $V_{I,J}$ and $V_{I,J+1}$ from Equations (3.1.42 - 3.1.43) in Equation (3.1.44) yields,

$$a_P P'_{I,J} = a_E P'_{I+1,J} + a_W P'_{I-1,J} + a_N P'_{I,J+1} + a_S P'_{I,J-1} + b \quad (3.1.45)$$

$$\text{Where } a_E = \rho_e DU_{I+1,J} YCV(J)$$

$$a_W = \rho_w DU_{I,J} YCV(J)$$

$$a_N = \rho_n DV_{I,J+1} XCV(I)$$

$$a_S = \rho_s DV_{I,J} XCV(I)$$

$$a_P = a_E + a_W + a_N + a_S \quad (3.1.46)$$

$$\text{and } b = [\rho_w U_{I,J}^* - \rho_e U_{I+1,J}^*] YCV(J) + [\rho_s V_{I,J}^* - \rho_n V_{I,J+1}^*] XCV(I)$$

$$(3.1.47)$$

The constant term 'b' in Equation (3.1.45) is not expected. It is expected that the term 'b' should be equal to zero to satisfy the continuity equation. The Equation (3.1.47) contains the guessed velocities U^* and V^* from the previous iterations and represents the defect in mass conservation. If the starred velocities are equal to actual velocities in the flow field then 'b' will be equal to zero.

3.1.3 SEQUENCE OF OPERATION IN SIMPLE

In SIMPLE algorithm, the operations are carried out according to the following order,

1. Guess the pressure field P^* .
2. Solve the momentum Equations (3.1.35) and (3.1.36) to obtain U^* and V^* .
3. Solve the pressure correction Equation (3.1.45) to determine pressure correction P' in all the control volumes.
4. Calculate the pressure P from $P = P^* + P'$, that is, equation (3.1.37).
5. Calculate the velocity corrections U' and V' from Equations (3.1.41A and 3.1.41B) and correct the velocities according to Equations (3.1.37) by adding the corrections to the velocities U^* and V^* of step 2.
6. Solve the discretized equations for other variables for example, temperatures, concentration, turbulence intensity etc.
7. Treat the corrected velocities and pressures as new guessed velocities and pressures, return to step 2 and repeat the whole

procedure until a converged solution is obtained.

3.1.4 SIMILARITY SOLUTION

Assuming the pressure to be uniform, transverse velocity to be one order of magnitude smaller than the streamwise velocity and neglecting streamwise diffusion compared to transverse diffusion and neglecting viscous dissipation, we get the following form of boundary layer equations,

$$\frac{\partial U}{\partial X} + \frac{\partial V}{\partial Y} = 0 \quad (3.1.48)$$

$$U \frac{\partial U}{\partial X} + V \frac{\partial U}{\partial Y} = \frac{1}{Re} \frac{\partial^2 U}{\partial Y^2} \quad (3.1.49)$$

$$U \frac{\partial T^*}{\partial X} + V \frac{\partial T^*}{\partial Y} = \frac{1}{Re \cdot Pr} \frac{\partial^2 T^*}{\partial Y^2} \quad (3.1.50)$$

Defining $\bar{X} = \frac{X}{Re}$ and $\bar{V} = V \cdot Re$, Equation (3.1.48 - 3.1.50) reduce to

$$\frac{\partial U}{\partial \bar{X}} + \frac{\partial \bar{V}}{\partial Y} = 0 \quad (3.1.51)$$

$$U \frac{\partial U}{\partial \bar{X}} + \bar{V} \frac{\partial U}{\partial Y} = \frac{\partial^2 U}{\partial Y^2} \quad (3.1.52)$$

$$U \frac{\partial T^*}{\partial \bar{X}} + \bar{V} \frac{\partial T^*}{\partial Y} = \frac{1}{Pr} \frac{\partial^2 T^*}{\partial Y^2} \quad (3.1.53)$$

Schlichting's similarity solution is obtained by the following transformation :

$$\eta = aY / (3\bar{X}^{2/3}), \quad \psi = 2a\bar{X}^{1/3} f(\bar{X}, \eta), \quad T^* = A\bar{X}^{-1/3} g(\eta)$$

$$U = \frac{2a^2}{3} \bar{X}^{-1/3} f'(\eta) \quad \text{and} \quad \bar{V} = \frac{2a}{3} \bar{X}^{-2/3} (2\eta f' - f) \quad (3.1.54)$$

This transformation reduces Equations (3.1.52 and 3.1.53) to the following ordinary differential equations

$$f'''' + 2ff'' + 2f'^2 = 0 \quad (3.1.55)$$

$$g'' + 2Pr (fg)' = 0 \quad (3.1.56)$$

The boundary conditions are :

$$\text{At } \eta=0 ; \quad f=f''=0, \quad g'=0 \quad (3.1.57a)$$

$$\text{As } \eta \rightarrow \infty ; \quad f' \rightarrow 0 \quad g \rightarrow 0 \quad (3.1.57b)$$

The total momentum and enthalpy of jet remain constant at any cross section in the streaming direction, that is,

$$J = 2\rho \int_0^{\infty} u^2 dy = \frac{8}{3} a^3 \rho U_{max}^2 W \int_0^{\infty} f'^2 d\eta = J_e \quad (3.1.57c)$$

$$K = 2\rho C_p \int_0^{\infty} u (T - T_{\infty}) dy = 4aA \rho C_p U_{max} W (T_j - T_{\infty}) \int_0^{\infty} f' g d\eta = K_e \quad (3.1.57d)$$

where, J_e and K_e are the momentum and enthalpy respectively of jet at the slot exit. The solution of Equations (3.1.55 and 3.1.56) subject to boundary conditions (3.1.57a and 3.1.57b) as given by Schlichting for the stream function and by Cebeci and Bradshaw for temperature is as follows,

$$f(\eta) = \tanh(\eta) \quad (3.1.54)$$

$$g(\eta) = \text{sech}^{2Pr}(\eta) \quad (3.1.59)$$

The constants 'a' and 'A' are determined by satisfying conditions (3.1.57c) and 3.1.57d). Substitution of these in Equations (3.1.57c and 3.1.57d) yields,

$$J = \frac{8}{3} a^3 \rho U_{max}^2 W \int_0^{\infty} \text{Sech}^4 \eta d\eta = \frac{16}{9} a^3 \rho U_{max}^2 W = J_e \quad (3.1.60a)$$

$$\begin{aligned} K &= 4aA \rho C_p U_{max} W (T_j - T_{\infty}) \int_0^{\infty} \text{Sech} \eta^{2+2Pr} d\eta \\ &= \frac{2Pr}{2Pr+1} 4aA C_p U_{max} W (T_j - T_{\infty}) \int_0^{\infty} \text{Sech} \eta^{2Pr} d\eta \end{aligned} \quad (3.1.60b)$$

The integral in Equation (3.1.60b) can be evaluated in closed

form only when the Prandtl number has integer values like, 1,2 etc. For integer values of Prandtl number we have,

$$K = 4\rho C_p U_{max} W (T_j - T_\infty) a A \left(\frac{2Pr}{2Pr+1} \right) \left(\frac{2Pr-2}{2Pr-1} \right) \left(\frac{2Pr-4}{2Pr-3} \right) \dots \frac{2}{3} = K_e \quad (3.1.61)$$

The momentum and enthalpy at slot exit depend upon the exit velocity and temperature profiles. The constants a and A are determined from the jet-exit velocity and temperature profiles. For uniform jet-exit velocity and temperature profiles $J_e = \rho U_{max}^2 W$ and $K_e = \rho C_p U_{max} W (T_j - T_\infty)$. While, for parabolic jet exit velocity and temperature profiles,

$$J_e = \frac{8}{15} \rho U_{max}^2 W \quad \text{and} \quad K_e = \frac{8}{15} \rho C_p U_{max} W (T_j - T_\infty).$$

Substitution of these, for uniform jet-exit velocity and temperature profiles, yields,

$$\begin{aligned} a &= \left(\frac{9}{16} \right)^{1/3} = 0.825482 \\ A &= \left(\frac{3}{32} \right)^{1/3} \quad \text{for Pr=1} \\ U &= 0.45428 \bar{X}^{-1/3} f'(\eta) \\ \bar{V} &= 0.55032 \bar{X}^{-2/3} (2\eta f' - f) \\ \eta &= 0.27516 \bar{X}^{-2/3} Y \\ T^* &= \left(\frac{3}{32} \right)^{1/3} \bar{X}^{-1/3} g(\eta) \end{aligned} \quad (3.1.62)$$

For parabolic velocity and temperature profiles

$$\begin{aligned} a &= \left(\frac{3}{10} \right)^{1/3} = \left(\frac{9}{16} \right)^{1/3} \cdot \left(\frac{8}{15} \right)^{1/3} \\ A &= \left(\frac{3}{32} \right)^{1/3} \cdot \left(\frac{8}{15} \right)^{2/3} \quad \text{for Pr=1} \\ U &= 0.45428 \left(\frac{8}{15} \right)^{2/3} \bar{X}^{-1/3} f'(\eta) \\ \bar{V} &= 0.55032 \left(\frac{8}{15} \right)^{1/3} \bar{X}^{-2/3} (2\eta f' - f) \end{aligned} \quad (3.1.63)$$

$$\eta = 0.2231 \bar{X}^{-2/3} \quad Y = 0.27516 \left(\frac{8}{15}\right)^{1/3} \bar{X}^{-2/3} Y$$

$$T^* = \left(\frac{3}{32}\right)^{1/3} \left(\frac{8}{15}\right)^{2/3} \bar{X}^{-1/3} g(\eta)$$

The centre line velocities at $\eta = 0$ may be obtained from these equations. Lai and Simmons [32] have used half the nozzle width as a characteristic length. If we denote \tilde{X} , \tilde{Y} and \tilde{Re} as their variables then,

$$\tilde{Y} = \frac{2Y}{W} = 2Y, \quad \tilde{X} = \frac{2x}{W} \frac{2}{Re} = 4\bar{X}$$

The centre line velocities and temperatures for uniform jet-exit velocity and temperature profiles are as follows

$$U_c = 0.45428 \bar{X}^{-1/3} = 0.45428 (4)^{1/3} \tilde{X}^{-1/3} \quad (3.1.64)$$

$$T_c^* = \left(\frac{3}{32}\right)^{1/3} \bar{X}^{-1/3} = \left(\frac{3}{8}\right)^{1/3} \tilde{X}^{-1/3}$$

For parabolic jet exit velocity and temperature profiles we get,

$$U_c = 0.29876 \bar{X}^{-1/3} = 0.29876 (4)^{1/3} \tilde{X}^{-1/3} \quad (3.1.65)$$

$$T_c^* = \left(\frac{3}{32}\right)^{1/3} \left(\frac{8}{15}\right)^{2/3} \bar{X}^{-1/3} = \left(\frac{3}{32}\right)^{1/3} \left(\frac{16}{15}\right)^{2/3} \tilde{X}^{-1/3}$$

The centreline velocities and temperatures obtained from these expressions with and without virtual origin have been used for comparison with the results of the numerical scheme.

3.1.5 Boundary conditions specified in the computer program.

The domain has been divided into L2 columns and M2 rows of control volumes. The first row of control volume starts with index (2,2) and ends up with the index (2,L2). The index of the last

control volume in first column is (2,M2). The indices of velocities and temperature are shown in Figure 3.1.4 to 3.1.7. The boundary conditions specified in the computer program are as follows,

I. Nozzle exit: The nozzle extends from the control volume $J=2$ to $J=JM$ where $YV(JM+1) = 1/2$

For uniform velocity and temperature profiles,

$$V_{1,J} = 0 : J = 2 \text{ to } JM+1, U_{2,J} = 1 \text{ and } T_{1,J}^* = 1, \text{ For } J = 1 \text{ to } JM$$

For parabolic velocity and temperature profiles,

$$V_{1,J} = 0 : J = 2 \text{ to } JM+1, U_{2,J} = 1 - 4Y^2(J) \text{ and } T_{1,J}^* = 1 - 4Y^2(J),$$

For $J = 1$ to JM .

II. Wall: $U_{2,J} = 0$

$$V_{1,J} = 0$$

For $J = JM + 1$ to $M1$

and $T_{1,J} = 0$

III. Entrainment Boundary:

$$U_{I,M1} = 0$$

$$V_{I,M1} = V_{I,M2}$$

For $I = 2$ to $L2$

$$T_{I,M1} = 0.0$$

$$\Gamma_{I,M1} = 0,$$

For V-velocity

Γ is used in the computer program for viscosity, $(\frac{1}{Re})$ in the momentum equations and thermal diffusivity $(\frac{1}{Re Pr})$ in the energy equation. $\Gamma = 0$, implies that the gradients $\frac{\partial V}{\partial Y} = 0$, at this boundary.

IV. Outflow Boundary:

The U-component of velocity at the outflow boundary is determined by the over all mass balance, that is, the inflow

through the half nozzle width $W/2$ plus the entrainment through the upper boundary III is equated to the flow through the out flow boundary IV. Mathematically,

$$\int_{X=L}^H U dY = \int_{X=0}^{1/2} U dY + \int_{Y=H}^L v dx$$

$$\text{FLOW IN} = \sum_{J=2}^{JM} U_{2,J} YCV(J) + \sum_{I=2}^{L2} V_{I,M1} XCV(I) \quad (3.1.66)$$

It is assumed that the velocity distribution at the boundary $(L1, J)$ cells is similar to the velocity distribution in the $(L2, J)$ cells.

Therefore,

$$U_{L1,J} = f(U_{L2,J} + C) \quad (3.1.67)$$

Where, f is a scaling factor and C is a constant which is included to smoothen the back flow through the outflow boundary. The magnitude of C , is the minimum negative value of $U_{L2,J}$ distribution. Hence the outflow is calculated from

$$\text{FLOW OUT} = f \sum_{J=2}^{M2} U_{L2,J} YCV(J) + C \sum_{J=2}^{M2} YCV(J) \quad (3.1.68A)$$

$$\text{Equating FLOWOUT to FLOWIN, } f = \frac{\text{FLOWIN}}{\sum_{J=2}^{M2} U_{L2,J} YCV(J) + C \sum_{J=2}^{M2} YCV(J)} \quad (3.1.68B)$$

Velocity $U_{L1,J}$ is calculated from Equations (3.1.67) by making use of scaling factor 'f' given by (3.1.68B). The other boundary

conditions are as follows,

$$V_{L1,J} = V_{L2,J}$$

$$T_{L1,J}^* = T_{L2,J}^* \quad \text{For } J = 2 \text{ to } M1$$

$$\Gamma_{L1,J} = 0, \quad \text{For U-component, V-component of velocity and temperature.}$$

V. Line of symmetry:

$$U_{I,1} = U_{I,2}$$

$$V_{I,2} = 0$$

$$T_{I,1}^* = T_{I,2}^*$$

$$\Gamma_{I,1} = 0, \quad \text{For U-component of velocity and temperature}$$

As discussed earlier, $\Gamma_{I,J}$ equal to zero, implies that the gradients $\frac{\partial U}{\partial Y} = 0$ and $\frac{\partial T^*}{\partial Y} = 0$ along the line of symmetry.

The boundary control volumes require special treatment so as to apply the boundary conditions. For instance, the first unknown V-components of velocity at bottom are $V_{I,3}$. If the control volumes are centered around $V_{I,3}$ in the y-direction, then the area between the grid points (I,2) and bottom boundary will be left out. A remedy for this is to extend the first V-control volume upto the bottom boundary making the height of boundary control volume as 1.5 times the height of the usual control volumes. This control volume is shown in Figure 3.1.4.

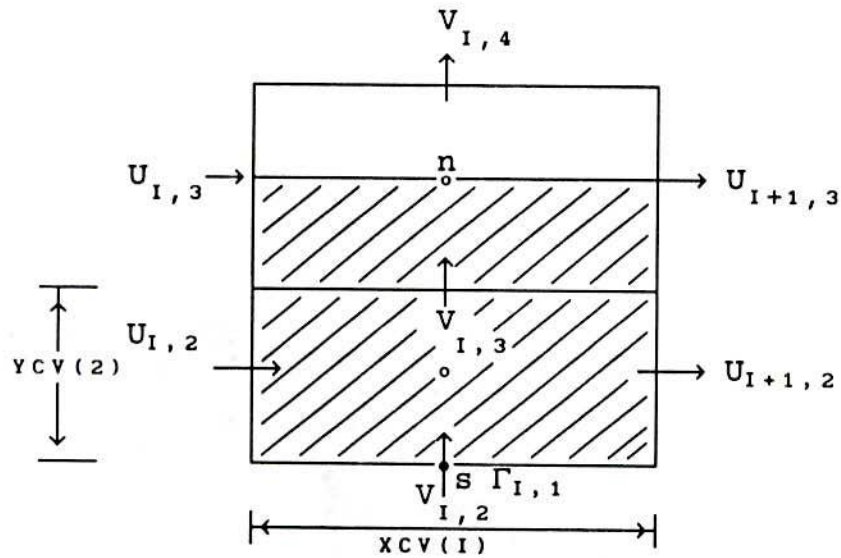


Figure 3.1.4: Bottom boundary V-velocity control volume

The flux, F_n and diffusion coefficient, D_n from the north face are calculated in the usual manner while F_s and D_s are as follows,

$$F_s = XCV(I) V_{I,2} \rho_{I,1} \quad (3.1.69)$$

$$D_s = XCV(I) \Gamma_{I,1} / YCV(2) \quad (3.1.70)$$

The coefficient a_s is determined from Power law scheme, as F_s and D_s are available. The flux from the east face will involve both the velocities $U_{I+1,2}$ and $U_{I+1,3}$.

The last control volume in Y- direction for $J = M2$ will also be 1.5 times the usual control volumes. It is shown in Figure 3.1.5.

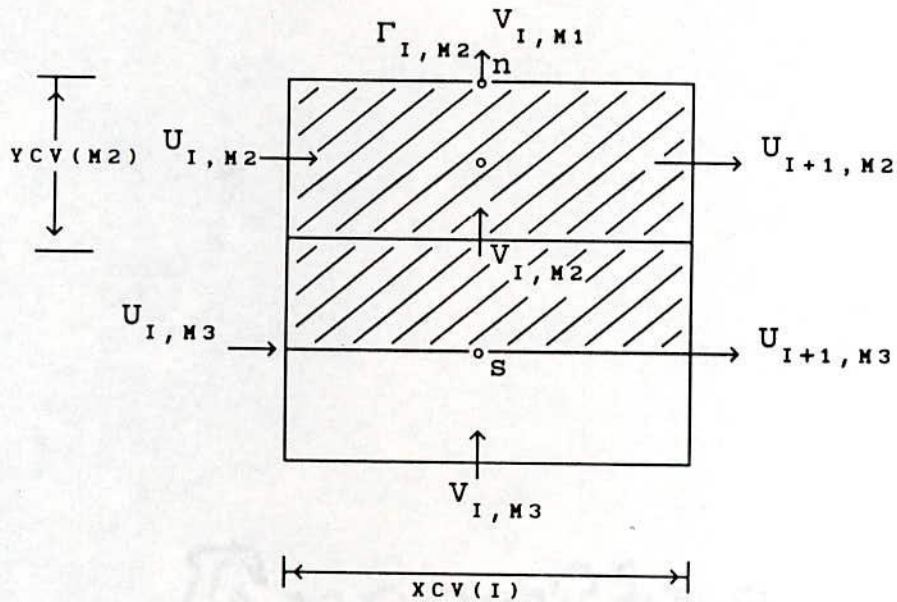


Figure 3.1.5: Top boundary V-velocity control volume

The flux F_n and D_n for this control volume are as follows

$$F_n = XCV(I) \rho_{I,M1} V_{I,M1} \quad (3.1.71)$$

$$D_n = XCV(I) \Gamma_{I,M1} / YCV(M2) \quad (3.1.72)$$

The coefficient a_n is determined from Power law scheme as F_n and D_n are available. The flux from the east face will involve both the velocities $U_{I+1,M2}$ and $U_{I+1,M3}$

First control volume for the X-momentum equation, that is, for $I = 2$ will also be 1.5 times the usual control volumes so that the area right upto left boundary is covered during integration over the control volumes. The first control volume for U-momentum equation is shown in Figure 3.1.6.

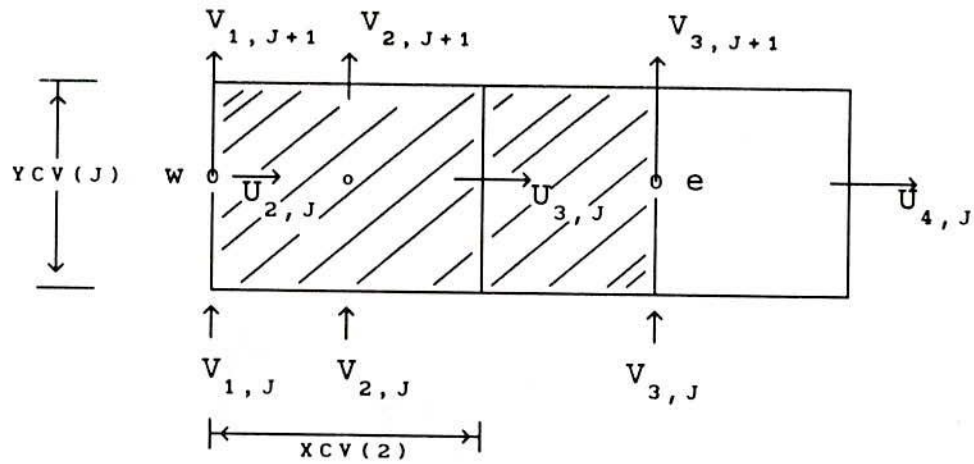


Figure 3.1.6: Left boundary U-velocity control volume

The flux and diffusion from the west face are as follows,

$$F_w = YCV(J) U_{2,J} \rho_{1,J} \quad (3.1.73)$$

$$D_w = YCV(J) \Gamma_{1,J} / XCV(2) \quad (3.1.74)$$

The coefficient a_w is determined from Power law scheme.

Similarly, the last control volume in the x- direction, $I = L2$ will be as shown in Figure 3.1.7.

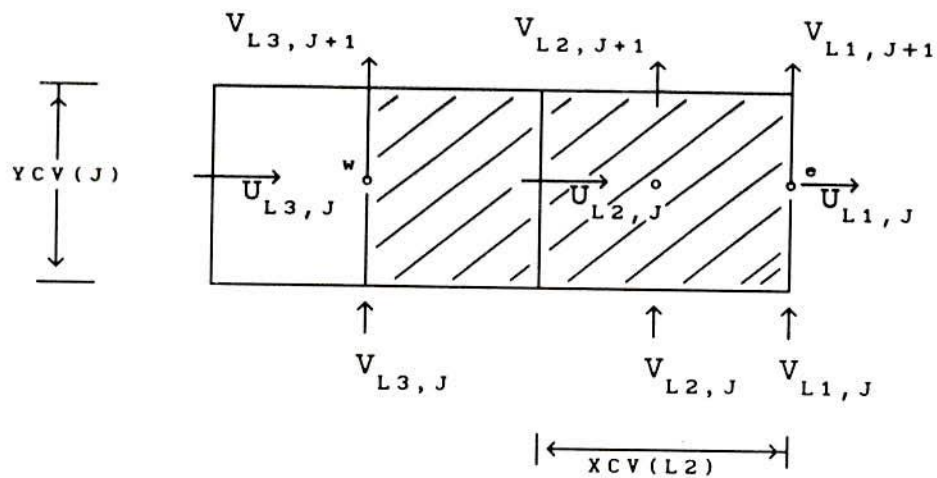


Figure 3.1.7: Right boundary U-velocity control volume

$$F_e = YCV(J) U_{L1,J} \rho_{L1,J} \quad (3.1.75)$$

$$D_e = YCV(J) \Gamma_{L1,J} / XCV(L2)$$

In the x-direction fine grids are specified near the nozzle exit, these are gradually increased and then decreased towards the end of the domain. In the y-direction, an uniform grid is specified from the line of symmetry upto half nozzle width and thereafter, smoothly expanding grids are specified. Several trials were made to select the domain size. The height of the domain is chosen far away from the line of symmetry, so that the gradients of all the variables vanish there and the boundary conditions are satisfied. First estimate of the domain size was obtained from the boundary layer thickness at $X = L$ from Schlichting's solution for free laminar jet. The value of H depends on the chosen value of L . It was observed that for small values of H , the solution did not converge. Once the convergence was obtained the value of H was systematically increased until the converged solution becomes independent of the choice of H . It has been reported by Yuan et al. [8], that the use of overall mass balance requires shorter domain, whereas, continuative boundary conditions at boundary IV requires longer domain. Finally, height $h = 28W$ and $l = 80W$ and Mesh size of 120×88 have been used for the computation. The convergence is checked by monitoring the residues of all the variables while solving the equations of momentum, pressure and energy. The residues of pressure equation reduced to a value around 10^{-5} while the overall mass conservation residue reduced to a value of 10^{-16} . The results have been obtained for Reynolds numbers in the range of 60 to 150 and for Prandtl numbers in the range of 0.01 to 10.

3.2 Axisymmetric free jet

The jet emanates from a circular hole of radius r_0 in a wall and is discharged into still surroundings of same fluid as that of the jet. The jet does not interact with any solid surface. The jet is assumed to be symmetric about its axis. Such a jet is known as axisymmetric free jet or circular jet.

In order to formulate the problem, cylindrical polar coordinate system with the origin at the centre of the circular hole, is considered. The jet is considered to be axisymmetric, hence velocities do not depend upon azimuthal angle and azimuthal component of velocity is also zero. Hence, only the x - r coordinates are required for the analysis. The x -axis is chosen along the axis of the jet and the radial coordinate is perpendicular to the jet axis. The computational domain is shown in the Figure 3.2.1. The velocity component along x and r directions are u and v respectively. The velocity and temperature profiles at the nozzle exit are considered to be either uniform or parabolic.

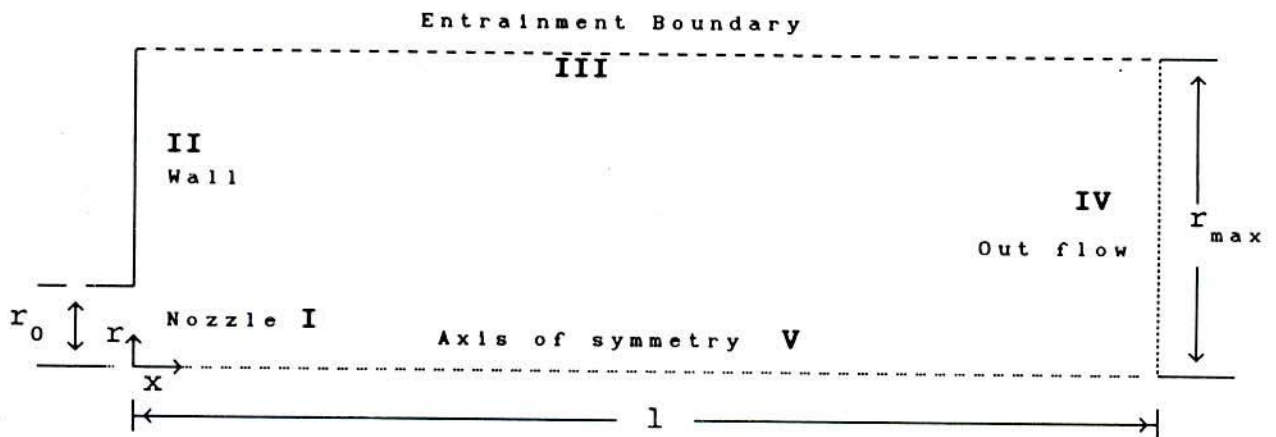


Figure 3.2.1. Computational Domain for Axisymmetric Free Jet

3.2.1 Governing Equations

The flow is considered to be laminar, steady, incompressible and axisymmetric. The properties of the fluid are assumed to be constant and the viscous dissipation is neglected. The continuity, momentum and the energy equation in x-r coordinate are as follows,

CONTINUITY EQUATION,

$$\frac{1}{r} \frac{\partial (vr)}{\partial r} + \frac{\partial (\rho u)}{\partial x} = 0 \quad (3.2.1)$$

AXIAL MOMENTUM EQUATION,

$$\rho \left[v \frac{\partial u}{\partial r} + u \frac{\partial u}{\partial x} \right] = - \frac{\partial P}{\partial x} + \mu \left[\frac{\partial^2 u}{\partial r^2} + \frac{1}{r} \frac{\partial u}{\partial r} + \frac{\partial^2 u}{\partial x^2} \right] \quad (3.2.2)$$

RADIAL MOMENTUM EQUATION,

$$\rho \left[v \frac{\partial v}{\partial r} + u \frac{\partial v}{\partial x} \right] = - \frac{\partial P}{\partial r} + \mu \left[\frac{\partial^2 v}{\partial r^2} + \frac{1}{r} \frac{\partial v}{\partial r} - \frac{v}{r^2} + \frac{\partial^2 v}{\partial x^2} \right] \quad (3.2.3)$$

ENERGY EQUATION,

$$\rho \left[v \frac{\partial T}{\partial r} + u \frac{\partial T}{\partial x} \right] = \alpha \left[\frac{\partial^2 T}{\partial r^2} + \frac{1}{r} \frac{\partial T}{\partial r} + \frac{\partial^2 T}{\partial x^2} \right] \quad (3.2.4)$$

The maximum nozzle exit velocity U_j and the nozzle radius r_0 are chosen as the characteristic velocity and length respectively. In this case, u and v are axial and radial components of velocity respectively. The temperature and pressure are non-dimensionalized by the $(T_j - T_\infty)$ and $\rho_0 U_j^2$ respectively. Non-dimensionalization scheme is as follows,

$$U = \frac{u}{U_j}, \quad V = \frac{v}{U_j}, \quad P = \frac{(P - P_\infty)}{\rho_0 U_j^2}$$

$$T^* = \frac{(T - T_\infty)}{(T_j - T_\infty)}, \quad X = \frac{x}{r_0}, \quad R = \frac{r}{r_0}, \quad R_{\max} = \frac{r_{\max}}{r_0}$$

$$L = \frac{1}{r_0} \quad \text{and} \quad Re = \frac{U_j r_0}{\nu}$$

The continuity, axial momentum, radial momentum and energy equations in non-dimensional conservative form are as follows :

CONTINUITY EQUATION,

$$\frac{1}{R} \frac{\partial (VR)}{\partial R} + \frac{\partial U}{\partial X} = 0 \quad (3.2.5)$$

AXIAL MOMENTUM EQUATION,

$$\frac{1}{R} \frac{\partial (RUV)}{\partial R} + \frac{\partial (UU)}{\partial X} = - \frac{\partial P}{\partial X} + \frac{1}{Re} \frac{1}{R} \frac{\partial}{\partial R} \left[R \frac{\partial U}{\partial R} \right] + \frac{1}{Re} \frac{\partial}{\partial X} \left[\frac{\partial U}{\partial X} \right] \quad (3.2.6)$$

RADIAL MOMENTUM EQUATION,

$$\frac{1}{R} \frac{\partial (VVR)}{\partial R} + \frac{\partial (UV)}{\partial X} = - \frac{\partial P}{\partial R} + \frac{1}{Re} \frac{1}{R} \frac{\partial}{\partial R} \left[R \frac{\partial V}{\partial R} \right] + \frac{1}{Re} \frac{\partial}{\partial X} \left[\frac{\partial V}{\partial X} \right] + S_r \quad (3.2.7)$$

$$\text{Where, } S_r = - \frac{V}{Re R^2}$$

ENERGY EQUATION,

$$\frac{1}{R} \frac{\partial (RVT^*)}{\partial R} + \frac{\partial (UT^*)}{\partial X} = \frac{1}{Re Pr} \frac{1}{R} \frac{\partial}{\partial R} \left[R \frac{\partial T^*}{\partial R} \right] + \frac{1}{Re Pr} \frac{\partial}{\partial X} \left[\frac{\partial T^*}{\partial X} \right] \quad (3.2.8)$$

where, Re and Pr are the nozzle-exit Reynolds number and fluid Prandtl number respectively. Equations (3.2.5 - 3.2.8) may be clubbed into a single equation as follows,

$$\frac{1}{R} \frac{\partial (RV\phi)}{\partial R} + \frac{\partial (U\phi)}{\partial X} = \frac{1}{R} \frac{\partial}{\partial R} \left[R\Gamma_\phi \frac{\partial \phi}{\partial R} \right] + \frac{1}{R} \frac{\partial}{\partial X} \left[R\Gamma_\phi \frac{\partial \phi}{\partial X} \right] + S_\phi \quad (3.2.9)$$

Where ϕ , Γ_ϕ and S_ϕ for continuity, momentum and energy equation are given in table 3.2.1.

Table 3.2.1

Equations	ϕ	Γ_ϕ	S_ϕ
Continuity	1	0	0
X-Momentum	U	1/Re	$-\frac{\partial P}{\partial X}$
Y-Momentum	V	1/Re	$-\frac{\partial P}{\partial R} + S_r$
Energy	T^*	1/(Re.Pr)	0

Boundary conditions

The boundary conditions at the boundaries marked I, II, III, IV and V in the Figure 3.2.1, are specified as follows,

I. Nozzle Exit: At $X=0$, $0 \leq R \leq 1$: $V = 0$

For uniform velocity and temperature profiles,

$$\text{At } X = 0, 0 \leq R \leq 1 : U = 1 \text{ and } T^* = 1 \quad (3.2.10a)$$

For parabolic velocity and temperature profiles,

$$\text{At } X = 0 \text{ and } 0 \leq R \leq 1 : U = (1 - R^2), \quad T^* = (1 - R^2) \quad (3.2.10b)$$

$$\text{II. Wall: At } X=0, 1 < R \leq R_{max} : U = 0, V = 0, T^* = 0, \quad (3.2.10c)$$

no-slip and impermeability boundary conditions

$$\text{III. Entrainment: At } R=R_{max}, 0 < X \leq L : U = 0, \frac{\partial V}{\partial R} = 0, T^* = 0 \quad (3.2.10d)$$

IV. Out flow boundary : At $X= L$, $0 \leq R \leq R_{max}$:

$$2\pi \int_0^{R_{max}} UR dR \Big|_{X=L} = 2\pi \int_0^1 RU dR \Big|_{X=0} + 2\pi R_{max} \int_0^L V dX \Big|_{R=R_{max}} \quad (3.2.10e)$$

$$\frac{\partial V}{\partial X} = 0, \quad \frac{\partial T^*}{\partial X} = 0$$

The $U_{L1,J}$ is determined by a procedure similar to that described in section 3.1.7 for the free slot jet.

V. Line of Symmetry : At $R=0$, $0 < X \leq L$:

$$V = 0, \quad \frac{\partial U}{\partial R} = 0, \quad \frac{\partial T^*}{\partial R} = 0 \quad (3.2.10f)$$

3.2.2 Numerical Solution Procedure

The SIMPLE algorithm suggested by Patankar [10], and described in section 3.1.2 has been used for the numerical solution of the non-dimensional governing equations (3.2.5 - 3.2.8) subject to boundary conditions (3.2.10a - 3.2.10f). The domain is divided into non-overlapping, non-uniform control volumes. Grid points are located at the centre of each control volume. Grid points are also located at the boundaries of the domain for each control volume at its boundary. The axial component of velocity 'U' is specified at the middle of the left face of each control volume and radial component of velocity 'V' is specified at the middle of the bottom face of each control volume. Other variables such as, density, temperature, pressure and other fluid properties are specified at the grid points as shown in Figure 3.1.2. The governing equations are then integrated over the control volumes to obtain a set of discretized equations. Actually, only the flux and diffusion terms are evaluated for each control volume and the coefficients of discretization equation are determined by Power law scheme. The discretized equations can be expressed in the following form,

$$a_P \phi_P = a_E \phi_E + a_W \phi_W + a_N \phi_N + a_S \phi_S + b \quad (3.2.11)$$

For Radial momentum equation, source term contains

$$S = S_c = - \Gamma_{I,J} \frac{V_{(I,J)}}{RMN(J)^2}$$

In the axial direction, fine grids are provided near $X=0$ and $X=L$, with the grids smoothly expanding to coarse grids towards the interior. In the radial direction uniform grids are specified within the nozzle radius r_0 and subsequently smoothly expanding grids are specified. The domain radius, R_{max} and the domain length L are chosen sufficiently far away, so that the gradients of velocities and temperatures vanish on these boundaries. The value of R_{max} depends upon the chosen value of L . It was observed that the solution did not converge for small value of R_{max} . Hence, the value of R_{max} was systematically increased until converged solutions independent of the choice of R_{max} were obtained. Finally, non-dimensional axial length $L = 23$, domain radius $R_{max} = 21$ and 72×62 grids have been used for computation.

The results have been obtained for Reynolds numbers in the range of 60 to 650 for the parabolic jet-exit velocity and temperature profile and 60 to 300 for the uniform jet exit velocity and temperature profile and for Prandtl numbers in the range of 0.01 to 10.

3.2.3 SIMILARITY SOLUTION

The boundary layer equations under the assumption of uniform pressure and negligible, viscous dissipation, are as follows,

$$\frac{\partial U}{\partial X} + \frac{1}{R} \frac{\partial}{\partial R}(VR) = 0 \quad (3.2.12a)$$

$$U \frac{\partial U}{\partial X} + V \frac{\partial U}{\partial R} = \frac{1}{\text{Re}} \frac{\partial}{\partial R} \left(R \frac{\partial U}{\partial R} \right) \quad (3.2.12b)$$

$$U \frac{\partial T^*}{\partial X} + V \frac{\partial T^*}{\partial R} = \frac{1}{\text{Re} \cdot \text{Pr}} \frac{\partial}{\partial R} \left(R \frac{\partial T^*}{\partial R} \right) \quad (3.2.12c)$$

Defining $\bar{X} = \frac{X}{\text{Re}}$ and $\bar{V} = V \cdot \text{Re}$, Equations (3.2.11a - 3.1.11c) reduce to

$$\frac{\partial U}{\partial \bar{X}} + \frac{1}{\bar{R}} \frac{\partial}{\partial \bar{R}} (\bar{V} \bar{R}) = 0 \quad (3.2.13)$$

$$U \frac{\partial U}{\partial \bar{X}} + \bar{V} \frac{\partial U}{\partial \bar{R}} = \frac{1}{\bar{R}} \frac{\partial}{\partial \bar{R}} \left(\bar{R} \frac{\partial U}{\partial \bar{R}} \right) \quad (3.2.14)$$

$$U \frac{\partial T^*}{\partial \bar{X}} + \bar{V} \frac{\partial T^*}{\partial \bar{R}} = \frac{1}{\text{Pr} \bar{R}} \frac{\partial}{\partial \bar{R}} \left(\bar{R} \frac{\partial T^*}{\partial \bar{R}} \right) \quad (3.2.15)$$

Schlichting's similarity solution is obtained by the following transformation :

$$\xi = a R / \bar{X}, \quad \psi = \bar{X} f(\xi), \quad T^* = A g(\xi) / \bar{X}$$

$$U = \frac{a^2 f'(\xi)}{\bar{X} \xi} \quad \text{and} \quad \bar{V} = \frac{a}{\bar{X}} \left(f' - \frac{f}{\xi} \right) \quad (3.1.16)$$

This transformation reduces Equations (3.2.15 and 3.2.16) to followi ordinary differential equations,

$$\frac{d}{d\xi} \left(- \frac{ff'}{\xi} \right) = \frac{d}{d\xi} \left[\xi \frac{d}{d\xi} \left(\frac{f'}{\xi} \right) \right] \quad (3.2.17)$$

$$\text{Pr} \frac{d}{d\xi} (fg) + \frac{d}{d\xi} (\xi g') = 0 \quad (3.2.18)$$

The boundary conditions are :

$$\xi=0 ; \quad f = f' = f'' = 0, \quad g'=0 \quad (3.2.19a)$$

$$\xi=\infty ; \quad f' \rightarrow 0 \quad g \rightarrow 0 \quad (3.2.19b)$$

The total momentum and enthalpy of jet remain constant at every

cross section in the streaming direction, that is,

$$J = 2 \pi \rho \int_0^{\infty} u^2 r dr = 2 \pi \rho r_0^2 U_{max}^2 a^2 \int_0^{\infty} \frac{1}{\xi} f'^2 d\xi = J_e \quad (3.2.20a)$$

$$K = 2\pi\rho C_p \int_0^{\infty} u(T_j - T_{\infty}) r dr = 2\pi\rho r_0^2 U_{max} (T_j - T_{\infty}) A \int_0^{\infty} f' g d\xi = K_e \quad (3.2.20b)$$

where, J_e and K_e are the momentum and enthalpy respectively of jet at slot exit. Solution of Equations (3.2.17 and 3.2.18) subject to boundary conditions (3.2.19a and 3.2.19b) is

$$f(\xi) = \frac{\xi^2}{(1 + \xi^2/4)} \quad (3.2.21)$$

$$g(\xi) = \frac{1}{(1 + \xi^2/4)^{2Pr}} \quad (3.2.22)$$

Substituting these in Equations (3.2.20a and 3.2.20b) yields

$$J = 8\pi\rho r_0^2 U_{max}^2 a^2 \int_0^{\infty} \frac{\xi d\xi}{(1 + \xi^2/4)^2} = \frac{16}{3} \pi\rho r_0^2 U_{max}^2 a^2 = J_e \quad (3.2.23)$$

$$K = 4\pi\rho r_0^2 C_p U_{max} a^2 (T_j - T_{\infty}) A \int_0^{\infty} \frac{\xi d\xi}{(1 + \xi^2/4)^{2+2Pr}}$$

$$K_e = \left(\frac{8}{2Pr+1} \right) \pi\rho r_0^2 C_p U_{max} A (T_j - T_{\infty}) \quad (3.2.24)$$

The constants, a and A are determined from jet exit velocity and temperature profiles. For uniform jet exit velocity and temperature profiles,

$$J_e = \pi\rho r_0^2 U_{max}^2 \text{ and } K_e = \pi\rho r_0^2 C_p U_{max} (T_j - T_{\infty}). \quad (3.2.25)$$

Substitution of J_e and K_e in equations (3.2.23) and (3.2.24)

yields,

$$a = \sqrt{3/16}, \quad A = \frac{(2Pr+1)}{8} \quad (3.2.26)$$

Substituting the values of a and A in Equations (3.1.16) we get,

$$U = \frac{3}{8} \frac{1}{\bar{X}} \frac{1}{(1 + \xi^2/4)^2}$$

$$\bar{V} = \frac{\sqrt{3}}{4} \frac{1}{\bar{X}} \frac{(\xi - \xi^3/4)}{(1 + \xi^2/4)^2} \quad (3.2.27)$$

$$\xi = \frac{\sqrt{3}}{4} \frac{R}{\bar{X}}$$

$$T^* = \frac{(2Pr+1)}{8} \frac{1}{\bar{X}} \frac{1}{(1 + \xi^2/4)^{2Pr}}$$

The momentum and enthalpy at jet-exit for the parabolic jet exit velocity and temperature profiles are as follows,

$$J_e = \frac{\pi}{3} \rho U_{max}^2 r_0^2 \quad \text{and} \quad K_e = \frac{\pi}{3} \rho C_p U_{max} r_0^2 (T_j - T_\infty). \quad (3.2.28)$$

Substitution of J_e and K_e in equations (3.2.23) and (3.2.24) yields,

$$a = 1/4 \quad \text{and} \quad A = \frac{(2Pr+1)}{24} \quad (3.2.29)$$

Substitution of these in Equations (3.1.16), for parabolic jet-exit velocity and temperature profiles, yields,

$$U = \frac{1}{8} \frac{1}{\bar{X}} \frac{1}{(1 + \xi^2/4)^2}$$

$$\bar{V} = \frac{1}{4} \frac{1}{\bar{X}} \frac{(\xi - \xi^3/4)}{(1 + \xi^2/4)^2} \quad (3.2.30)$$

$$\xi = \frac{R}{4 \bar{X}}$$

$$T^* = \frac{(2Pr+1)}{24} \frac{1}{\bar{X}} \frac{1}{(1 + \xi^2/4)^{2Pr}}$$

The centreline velocities and temperature obtained from these equations are as follows,

For uniform jet exit velocity and temperature profiles,

$$U_c = 3/8\bar{X} \quad \text{and} \quad T_c^* = \frac{(2Pr + 1)}{8\bar{X}} \quad (3.2.31)$$

For parabolic jet exit velocity and temperature profile,

$$U_c = 1/8\bar{X} \quad \text{and} \quad T_c^* = \frac{(2Pr + 1)}{24\bar{X}} \quad (3.2.32)$$

3.3 Slot jet impingement on a circular cylinder

The flow and heat transfer from a circular cylinder is conveniently analyzed in cylindrical polar coordinates, while a slot jet is conveniently analyzed in rectangular cartesian coordinates. To analyse the slot jet impingement over a cylinder, one must consider the rectangular cartesian coordinate system near the slot exit and smoothly changeover to cylindrical polar coordinate system as the cylinder is approached. The other alternative is to transform the domain into a rectangular domain and solve the transformed equations, as has been done by Kang and Greif [64]. In this investigation, the problem has been idealized so that it can be treated in cylindrical polar coordinate system alone. The origin of the $(r-\theta)$ coordinate system is chosen at the center of the cylinder. The jet is located at distance r_1 from the center of the cylinder. The axis of the jet is assumed to be aligned to a diameter of the cylinder. The walls of the slot-jet nozzle are considered to be radial lines. The jet is assumed to emanate from the nozzle with radial velocity only, that is, the jet exit velocity is directed towards the center of the cylinder. The outer boundary of the domain is considered to be a circle of radius r_{max} which is very large compared to r_1 , the location of the nozzle. The entrainment at this outer boundary is considered to be in radial direction only. The domain is shown in Figure 3.3.1. The flow is symmetric about the jet axis, that is, about $\theta=0$ and $\theta=\pi$, hence only the upper half of the flow regime has been considered to save the computational effort.

3.3.1 Governing Equations

The fluid properties are assumed to be constant. The flow is considered to be steady, laminar, incompressible and two-dimensional, and the viscous dissipation is neglected. The continuity and the momentum equations in cylindrical polar coordinate under these assumptions are as follows,

CONTINUITY EQUATION,

$$\frac{1}{r} \frac{\partial}{\partial r}(\rho'rv) + \frac{1}{r} \frac{\partial}{\partial \theta}(\rho'u) = 0 \quad (3.3.1)$$

AZIMUTHAL MOMENTUM EQUATION,

$$\frac{1}{r} \frac{\partial}{\partial r}(\rho'ruv) + \frac{1}{r} \frac{\partial}{\partial \theta}(\rho'u^2) + \frac{\rho'uv}{r} = -\frac{1}{r} \frac{\partial P}{\partial \theta} + \mu \left[\nabla^2 u - \frac{u}{r^2} + \frac{2}{r^2} \frac{\partial v}{\partial \theta} \right] \quad (3.3.2)$$

RADIAL MOMENTUM EQUATION,

$$\frac{1}{r} \frac{\partial}{\partial r}(\rho'rvv) + \frac{1}{r} \frac{\partial}{\partial \theta}(\rho'uv) - \frac{\rho'u^2}{r} = -\frac{\partial P}{\partial r} + \mu \left[\nabla^2 v - \frac{v}{r^2} + \frac{2}{r^2} \frac{\partial u}{\partial \theta} \right] \quad (3.3.3)$$

$$\text{where, } \nabla^2 = \frac{\partial^2}{\partial r^2} + \frac{1}{r} \frac{\partial}{\partial r} + \frac{1}{r} \frac{\partial^2}{\partial \theta^2} \quad (3.3.4)$$

The nozzle exit velocity V_j and the cylinder radius R_0 are chosen as the characteristic velocity and length respectively. In this case u and v are the azimuthal and radial components of velocity respectively. The pressure is non-dimensionalized with respect to $\rho_0 V_j^2$. Hence, the non-dimensionalization scheme is as follows,

$$R = \frac{r}{R_0}, \quad U = \frac{u}{V_j}, \quad V = \frac{v}{V_j}, \quad R_1 = \frac{r_1}{R_0}, \quad R_{max} = \frac{r_{max}}{R_0}$$

$$P = (p - p_\infty) / \rho_0 V_j^2, \quad Re = \frac{V_j R_0 \rho_0}{\mu}, \quad \rho = \frac{\rho'}{\rho_0}$$

The numerical scheme used in this investigation is capable of treating the density variation and variation of other properties, hence density variation has been included in the problem formulation. The density is non-dimensionalized with respect to some reference density ρ_0 , that is, $\rho = \rho' / \rho_0$. The non-dimensionalized continuity and momentum equations in cylindrical polar coordinates written in the conservative form are as follows,

CONTINUITY EQUATION,

$$\frac{1}{R} \frac{\partial}{\partial R} (RV) + \frac{1}{R} \frac{\partial}{\partial \theta} (U) = 0 \quad (3.3.5)$$

AZIMUTHAL MOMENTUM EQUATION,

$$\frac{1}{R} \frac{\partial}{\partial R} (RUV) + \frac{1}{R} \frac{\partial}{\partial \theta} (UU) = - \frac{1}{R} \frac{\partial P}{\partial \theta} + \frac{1}{Re} \left[\frac{1}{R} \frac{\partial}{\partial R} (R \frac{\partial U}{\partial R}) + \frac{1}{R} \frac{\partial}{\partial \theta} (\frac{1}{R} \frac{\partial U}{\partial \theta}) \right] + S_\theta \quad (3.3.6)$$

$$\text{where, } S_\theta = - \frac{UV}{R} - \frac{1}{Re R^2} \left[U - 2 \frac{\partial V}{\partial \theta} \right]$$

RADIAL MOMENTUM EQUATION,

$$\frac{1}{R} \frac{\partial}{\partial R} (RVV) + \frac{1}{R} \frac{\partial}{\partial \theta} (UV) = - \frac{\partial P}{\partial R} + \frac{1}{Re} \left[\frac{1}{R} \frac{\partial}{\partial R} (R \frac{\partial V}{\partial R}) + \frac{1}{R} \frac{\partial}{\partial \theta} (\frac{1}{R} \frac{\partial V}{\partial \theta}) \right] + S_r \quad (3.3.7)$$

$$\text{where, } S_r = \frac{U^2}{R} - \frac{1}{Re R^2} \left[V + 2 \frac{\partial U}{\partial \theta} \right] \quad (3.3.8)$$

Where, Re is the slot exit Reynolds number based on the maximum slot exit velocity V_j and cylinder radius R_0 . The continuity and the momentum and energy equations (3.3.5 - 3.3.7) may be expressed by a single equation for numerical formulation as follows,

$$\frac{1}{R} \frac{\partial}{\partial \theta} (U\phi) + \frac{1}{R} \frac{\partial}{\partial R} (RV\phi) = \frac{1}{R} \frac{\partial}{\partial R} \left(\Gamma_\phi R \frac{\partial \phi}{\partial R} \right) + \frac{1}{R} \frac{\partial}{\partial \theta} \left(\frac{\Gamma_\phi}{R} \frac{\partial \phi}{\partial \theta} \right) + S_\phi \quad (3.3.9)$$

Boundary Conditions

The boundary conditions at the boundaries marked I, II, III, IV, V, VI and VII in the Figure 3.3.1, are as follows,

- I Nozzle Exit:** At $R=R_1$, $0 \leq \theta \leq \theta_1$: $U=0$ $V=-1$
- II Entrainment Boundary:** At $R= R_{max}$, $\theta_1 < \theta \leq \theta_E$:
 $U=0$, $\frac{\partial V}{\partial R} = 0$
- III Outflow Boundary:** At $R= R_{max}$, $\theta_E < \theta \leq \pi$:
 $U=0$, and outflow velocity is determined by satisfying the mass flux.
- IV & VI Line of Symmetry:** At $\theta= 0$, $1 \leq R \leq R_1$ and $\theta= \pi$, $1 \leq R \leq R_{max}$:
 $U=0$, $\frac{\partial V}{\partial R} = 0$
- V Cylinder Surface:** At $R=1$, $0 \leq \theta \leq \pi$: $U=0$, $V=0$
- VII Nozzle Surface:** At $\theta=\theta_1$, $R_1 \leq R \leq R_{max}$: $U=0$, $V=0$

3.3.2 Numerical Solution procedure

The computational domain is divided into a number of

non-overlapping non-uniform control volumes. A grid point is located at the center of each control volume. Grid points are also located on the boundaries. The boundary grid points have no volumes. Boundary grid points are used only to specify the boundary conditions and boundary grid points have no other role in the computational scheme. Fine grids are specified near the slot exit and near the cylinder surface. The grids are smoothly expanded to coarse grids from these two locations. Fine grids are also specified near the line of symmetry ($\theta=0$ and $\theta=\pi$) and the grids are smoothly expanded towards the interior in the azimuthal direction.

The governing differential equations are integrated over the control volumes to obtain a set of discretized equations at each of the main grid points. The non-dimensional governing Equations set (3.3.9) has been solved by SIMPLEC algorithm due to Doormaal and Raithby [13]. The SIMPLEC algorithm is similar to SIMPLE algorithm as described in Section 3.1.2.

The two terms on the left hand side of Equation (3.3.9) are the convective terms and first two terms on the right hand side are the diffusion terms. The third term on the right hand side of Equation (3.3.9) represents the source term. The convective terms when integrated over the control volume can be expressed as the product of convected quantity ϕ at the interface and the mass flux at the interface of control volume. The Centrifugal and Coriolis terms, can not be expressed as flux through the control volume faces since these act over the whole of control volume. Hence, these terms are included as source terms in the respective

momentum equations. Similarly, the diffusion terms when integrated over the control volumes can be expressed as gradients over the control volume faces. But the viscous terms $\frac{V}{R^2} + \frac{2}{R^2} \frac{\partial U}{\partial \theta}$ are included as source term in r-momentum equation since, these cannot be expressed as gradients over the control volume faces after integration. The values of ϕ , Γ_ϕ and S_ϕ in the general differential Equation (3.3.9), are given in the following table for the respective equations,

Table: 3.3.1

Equations	ϕ	Γ_ϕ	S_ϕ
Continuity	1	0	0
R-momentum	V	1/Re	$-\frac{\partial P}{\partial R} + S_r$
θ -momentum	U	1/Re	$-\frac{1}{R} \frac{\partial P}{\partial \theta} + S_\theta$

The equations are then integrated over the respective control volumes to obtain the discretized equations.

RADIAL MOMENTUM EQUATION ($\phi = V$)

The control volume for radial momentum equation is shown in Figure 3.3.2. Integrating the first term of radial momentum equation yields,

$$\iint \frac{1}{R} \frac{\partial}{\partial \theta} (\rho UV) R dR d\theta = \text{YDIF}(J) \left[(\rho U)_e V_e - (\rho U)_w V_w \right] \quad (3.3.10)$$

In the numerical scheme, the velocities $U_{I,J}$ and $V_{I,J}$ are

assumed constant over the control volume faces. The velocity over 'aw' part of the east interface is $U_{I+1, J-1}$ and over the 'wb' part of the interface is $U_{I+1, J}$. The mass flux through 'aw' part of the interface is $\rho_a U_{I+1, J-1}$ where ρ_a is the density at point 'a'. Similarly the mass flux through 'wb' part of the interface is $\rho_b U_{I+1, J}$. The densities ρ_a and ρ_b are calculated by linear interpolation between neighboring main grid points. The mass flux ρU is such that densities and velocities are specified at the same location.

$$F_e = (\rho U)_e YDIF(J) = \rho_a ARXJP(J-1)U_{I+1, J-1} + \rho_b ARXJ(J)U_{I+1, J} \quad (3.3.11)$$

The density at location 'a' is determined by linear interpolation between the neighboring densities $\rho_{I+1, J-1}$ and $\rho_{I, J-1}$, that is,

$$\rho_a = FX(I + 1)\rho_{I+1, J-1} + FXM(I + 1)\rho_{I, J-1} \quad (3.3.12)$$

similarly,

$$\rho_b = FX(I + 1)\rho_{I+1, J} + FXM(I + 1)\rho_{I, J} \quad (3.3.13)$$

Where, $FX(I + 1) = XCV(I)/2 XDIF(I + 1)$

$$FXM(I + 1) = 1 - FX(I + 1)$$

The radial component of velocity V_e at the 'e' interface is given by the average of $V_{I, J}$ and $V_{I+1, J}$ for the central difference scheme. It will be equal to $V_{I, J}$ if $F_e > 0$ and $V_{I+1, J}$ if $F_e < 0$, in the upwind scheme. For power-law scheme, it is sufficient to

define the flux and diffusion terms at the east face. Integration of the second term of radial momentum equation over the control volume yields,

$$\iint \frac{1}{R} \frac{\partial}{\partial R} (\rho R V) R dR d\theta = XCV(I) \left[(\rho R V)_n V_n - (\rho R V)_s V_s \right] \quad (3.3.14)$$

The point 'n' is midway between points 'N' and 'P', hence

$$(\rho R V)_n = \left(\rho_P R_P V_{I,J} + \rho_N R_N V_{I,J+1} \right) / 2 \quad (3.3.15)$$

Where, $R_P = RMN(J)$ and $R_N = RMN(J + 1)$

By linear interpolation between two neighboring points, density is determined.

$$\rho_P = FY(J) \rho_{I,J} + FYM(J) \rho_{I,J-1} \quad (3.3.16)$$

$$\rho_N = FY(J + 1) \rho_{I,J+1} + FYM(J + 1) \rho_{I,J} \quad (3.3.17)$$

Therefore,

$$F_n = XCV(I) \left[\rho_P RMN(J) V_{I,J} + \rho_N RMN(J + 1) V_{I,J+1} \right] / 2 \quad (3.3.18)$$

The first diffusion term when integrated over the control volume yields,

$$\iint \frac{1}{R} \frac{\partial}{\partial \theta} \left(\frac{\Gamma}{R} \frac{\partial V}{\partial \theta} \right) R dR d\theta = YDIF(J) \left[\left(\frac{\Gamma}{R} \frac{\partial V}{\partial \theta} \right)_e - \left(\frac{\Gamma}{R} \frac{\partial V}{\partial \theta} \right)_w \right] \quad (3.3.19)$$

where, $YDIF(J) \Gamma_e = ARXJP(J - 1) \Gamma_a + ARXJ(J) \Gamma_b$

The viscosity, Γ_a is determined by the Harmonic mean of

$\Gamma_{I, J-1}$ and $\Gamma_{I+1, J-1}$.

$$\Gamma_a = \frac{2XDIF(I+1)\Gamma_{I, J-1}\Gamma_{I+1, J-1}}{XCV(I)\Gamma_{I+1, J-1} + XCV(I+1)\Gamma_{I, J-1}} \quad (3.3.20)$$

Similarly, Γ_b is obtained by the Harmonic mean of $\Gamma_{I, J}$ and $\Gamma_{I+1, J}$,

$$\Gamma_b = \frac{2XDIF(I+1)\Gamma_{I, J}\Gamma_{I+1, J}}{XCV(I)\Gamma_{I+1, J} + XCV(I+1)\Gamma_{I, J}} \quad (3.3.21)$$

$$\text{and } \left(\frac{dV}{d\theta}\right)_e = \left[V_{I+1, J} - V_{I, J}\right] / XDIF(I+1) \quad (3.3.22)$$

In Power-law scheme the coefficient of diffusion term is required, that is, coefficient of $V_{I+1, J}$, which may be written as,

$$D_e = YDIF(J)\Gamma_e / [RMN(J) XDIF(I+1)] \quad (3.3.23)$$

Similarly, the integration of the second diffusion term of the radial momentum equation over the control volume gives,

$$\iint \frac{1}{R} \frac{\partial}{\partial R} \left(\Gamma R \frac{\partial V}{\partial R} \right) R dR d\theta = XCV(I) \left[\Gamma_n R_n \left(\frac{\partial V}{\partial R} \right)_n - \Gamma_s R_s \left(\frac{\partial V}{\partial R} \right)_s \right] \quad (3.3.24)$$

$$\Gamma_n = \Gamma_{I, J} \quad \text{and} \quad R_n = R(J)$$

Hence, the coefficient of diffusion term D_n is given by,

$$D_n = R(J)XCV(I)\Gamma_{I, J}/YCV(J) \quad (3.3.25)$$

The source term is linearized as follows,

$$S = S_c + S_p V_{I, J} \quad (3.3.26)$$

For convergence, Patankar [10] recommends that S_p should be negative, so that the coefficient a_p remains positive, since S_p is added to a_p term on left hand side of the equation. Following this recommendation, S_c and S_p may be written as follows,

$$S_c = \rho \frac{U^2}{R} - \frac{2\Gamma}{R^2} \frac{\partial U}{\partial \theta} \quad (3.3.27)$$

Where,

$$\frac{U^2}{R} = \frac{\left[\left(U_{I,J} + U_{I+1,J} + U_{I,J-1} + U_{I+1,J-1} \right) / 4 \right]^2}{RMN(J)}$$

$$- \frac{2\Gamma}{R^2} \frac{\partial U}{\partial \theta} = - \frac{\Gamma_{I,J}}{RMN(J)^2} \left[\frac{U_{I+1,J} - U_{I,J}}{XCV(I) R(J)} + \frac{U_{I+1,J-1} - U_{I,J-1}}{XCV(I) R(J-1)} \right]$$

and $S_p = - \frac{\Gamma}{R^2} = - \frac{\Gamma_{I,J}}{RMN(J)^2} \quad (3.3.28)$

The boundary control volumes require special treatment so as to apply the boundary conditions. The first unknown velocity component in radial direction for fixed 'I' is $V_{I,3}$. The control volume for this is extended upto the left boundary, that is, this control volume is 1.5 times the usual control volumes. This makes it convenient to specify the boundary conditions. The first control volume in radial direction is shown in the Figure 3.3.3.

$$F_s = R(1)XCV(I)V_{I,2} \rho_{I,1} \quad (3.3.29)$$

$$D_s = R(1)XCV(I)\Gamma_{I,1}/YCV(2) \quad (3.3.30)$$

The last control volume in radial direction is shown in Figure 3.3.4.

$$F_n = R(M1)XCV(I)\rho_{I,M1}V_{I,M1} \quad (3.3.31)$$

$$D_n = R(M1)XCV(I)\Gamma_{I,M1}/YCV(M2) \quad (3.3.32)$$

The nozzle is located at $r=r_1$, that is, $R=R_1$ or in the notation of algorithm, at $RMN(JM)=R_1$. That is, $J=JM$ is the first main control volume in radial direction which is inside the nozzle. In the azimuthal direction, main control volumes with $I=2$ to $I=IM1$ are within the nozzle. $V_{I,JM}$ is the nozzle exit velocity which is specified. Hence, the control volumes $J=JM1=JM-1$, $2 \leq I \leq IM1$ are also treated like boundary control volumes, that is, these are 1.5 times the usual control volumes. This control volume is shown in Figure 3.3.7. For these control volumes,

$$F_n = RMN(J + 1)XCV(I)V_{I,JM} \rho_{I,JM} \quad J= JM-1 \quad (3.3.33)$$

$$D_n = RMN(J + 1)XCV(I)\Gamma_{I,JM}/YCV(JM1) \quad (3.3.34)$$

$$J=JM1, \quad 2 \leq I \leq IM1,$$

$IM1$ represents the index of last main control volume in azimuthal direction

First control volume in the azimuthal direction, that is, along the line of symmetry for $J= 2$ and $I = 2$, also uses the specified boundary. For this control volume shown in Figure 3.3.5, on the west face, the flux and the diffusion coefficients are as follows:

$$F_w = ARX(J)U_{2,J} \rho_{1,J} + ARXJP(J - 1)U_{2,J-1} \rho_{1,J-1} \quad (3.3.35)$$

$$D_w = \frac{ARX(J)\Gamma_{1,J} + ARXJP(J - 1)\Gamma_{1,J-1}}{XDIF(2) RMN(J)} \quad (3.3.36)$$

Similarly, the last control volume in the azimuthal direction, for $J=2$ and $I=L2$, that is, along the line of symmetry, also uses the specified boundary values. For this control volume shown in Figure 3.3.6, on the east face, the flux and diffusion coefficients are as follows:

$$F_e = ARX(J)U_{L1,J} \rho_{L1,J} + ARXJP(J-1)U_{L1,J-1} \rho_{L1,J-1} \quad (3.3.37)$$

$$D_e = \frac{ARX(J)\Gamma_{L1,J} + ARXJP(J-1)\Gamma_{L1,J-1}}{XDIF(L1) RMN(J)} \quad (3.3.38)$$

The first control volume at the nozzle exit plane $J=JM1$ uses the boundary values of specified velocity and properties. The flux and diffusion for this is calculated as follows,

$$F_w = YCV(JM1)U_{2,JM1} \rho_{1,JM1} + ARXJP(JM1-1)U_{2,JM1-1} \rho_{1,JM1-1} \quad (3.3.39)$$

$$D_w = \left[YCV(JM1)\Gamma_{1,JM1} + ARXJP(JM1-1)\Gamma_{1,JM1-1} \right] / XDIF(2)RMN(JM1) \quad (3.3.40)$$

where, $JM1 = JM - 1$

No slip and impermeability conditions are used along the nozzle surface. Impermeability boundary condition can be satisfied by putting flux from nozzle surface

$$F_w = 0.0$$

These control volumes are also boundary control volumes hence for diffusion, the distance between $V_{I,JM}$ and nozzle exit wall, that is, $XCV(IM)/2$ is used, hence

$$D_w = \frac{ARXJ(J)\Gamma_{IM1,J} + ARXJP(J-1)\Gamma_{IM1,J-1}}{0.5 [XCV(IM) RMN(J)]}, \quad J > JM \quad (3.3.41)$$

where, $\Gamma_{IM1,J}$ and $\Gamma_{IM1,J-1}$ are the values of viscosity at nozzle wall,

The control volume for $V_{IM,JM}$ is partly on the nozzle wall and partly in the flow regime. The flux F_w is taken to be from that part which is in flow regime, the contribution from the nozzle wall being zero. Therefore,

$$F_w = ARXJP(J-1)U_{IM,J-1} \left[FX(IM)\rho_{IM,J-1} + FXM(IM)\rho_{IM-1,J-1} \right] \quad (3.3.42)$$

$$D_w = \frac{ARXJ(J)\Gamma_{IM1,J}}{0.5XCV(IM)RMN(J)} + \frac{ARXJP(J-1)\Gamma_{IM1,J-1}}{XCV(IM)}$$

The control volume for $V_{IM1,JM1}$ is 1.5 times the usual control volume. To maintain consistency under normal circumstances, $a_E(IM1,JM1) = a_w(IM,JM1)$. However, as seen in the Figure 3.3.7, the control volumes for $V_{IM1,JM}$ and $V_{IM,JM1}$ have different lengths in radial direction, hence the coefficient $a_w(IM,JM1)$ is recalculated rather than being put equal to $a_E(IM1,JM1)$. The flux and diffusion coefficient for the west face of $(IM,JM1)$ are as follows,

$$F_w = ARXJ(J)U_{IM,J} \left[FX(IM)\rho_{IM,J} + FXM(IM)\rho_{IM-1,J-1} \right] + ARXJP(J-1)U_{IM,J-1} \left[FX(IM)\rho_{IM,J-1} + FXM(IM)\rho_{IM-1,J-1} \right] \quad (3.3.43)$$

$$D_w = \frac{2}{RMN(J)} \left[\frac{\Gamma_{IM-1,J} \Gamma_{IM,J}}{\left[XCV(IM-1)\Gamma_{IM,J} + XCV(IM)\Gamma_{IM-1,J} \right] ARX(J)} + \frac{\Gamma_{IM-1,J-1} \Gamma_{IM,J-1}}{\left[XCV(IM-1)\Gamma_{IM,J-1} + XCV(IM)\Gamma_{IM-1,J-1} \right] ARXJP(J-1)} \right] \quad (3.3.44)$$

Following the above processes, the discretized equations are obtained for all control volumes and, in general, these may be written as,

$$a_P V_{I,J} = a_E V_{I+1,J} + a_W V_{I-1,J} + a_N V_{I,J+1} + a_S V_{I,J-1} + b \quad (3.3.45)$$

AZIMUTHAL MOMENTUM EQUATION ($\phi = U$)

The control volume for azimuthal momentum equation is shown in Figure 3.3.8. Following a procedure similar to that used for the radial momentum equation, the flux and diffusion coefficients through control volume faces may be written as follows,

$$F_n = RMN(J+1) \left[\rho_c V_{I,J+1} XCV(I) + \rho_d V_{I-1,J+1} XCVIP(I-1) \right] \quad (3.3.46)$$

Where,

$$\begin{aligned} \rho_c &= FY(J+1)\rho_{I,J+1} + FYM(J+1)\rho_{I,J} \\ \text{and } \rho_d &= FY(J+1)\rho_{I-1,I+1} + FYM(J+1)\rho_{I-1,J} \end{aligned} \quad (3.3.47)$$

$$D_n = RMN(J+1) \left[XCV(I)\Gamma_c + XCVIP(i-1)\Gamma_d \right] / YDIF(J+1) \quad (3.3.48)$$

$$\text{Where, } \Gamma_c = \frac{2YDIF(J+1)\Gamma_{I,J}\Gamma_{I,J+1}}{YCV(J)\Gamma_{I,J+1} + YCV(J+1)\Gamma_{I,J}}$$

$$\text{and } \Gamma_d = \frac{2YDIF(J+1)\Gamma_{I-1,J}\Gamma_{I-1,J+1}}{YCV(J)\Gamma_{I-1,J+1} + YCV(J+1)\Gamma_{I-1,J}} \quad (3.3.49)$$

$$F_e = ARX(J)(\rho U)_e = ARX(J) \left[\rho_P U_{I,J} + \rho_E U_{I-1,J} \right] / 2 \quad (3.3.50)$$

$$\text{Where, } \rho_P = FX(I)\rho_{I,J} + FXM(I)\rho_{I-1,J}$$

$$\text{and } \rho_E = FX(I+1)\rho_{I+1,J} + FXM(I+1)\rho_{I,J} \quad (3.3.51)$$

$$D_w = ARX(J) \Gamma_{I,J} / XCV(I) \quad (3.3.52)$$

The coefficients for the control volumes at the boundaries are as follows,

In azimuthal direction at $\theta=0$, the control volume is boundary control volume which is 1.5 times the usual control volumes in θ direction

$$I = 2 \text{ \& } J = 2 \text{ to } JM1: F_w = \rho_{1,J} U_{2,J} ARX(J) \quad (3.3.53)$$

$$D_w = ARX(J) \Gamma_{1,J} / [XCV(2) R(J)] \quad (3.3.54)$$

The region beyond $J > JM1$ is within the nozzle

The control volumes next to the nozzle wall are considered to be boundary control volumes as shown in the Figure 3.3.6. The azimuthal velocity at the nozzle wall is zero, hence the flux is taken as zero, that is, at the nozzle wall,

$$I = IM+1= IM2 \text{ and } J = JM \text{ to } M1$$

$$F_w = 0.0$$

$$D_w = ARX(J) \Gamma_{IM,J} / [XCV(IM) R(J)] \quad (3.3.55)$$

In azimuthal direction at $\theta=\pi$: $I = L1, J = 2$ to $M1$, the control volumes are boundary control volumes which are 1.5 times the usual control volumes in θ direction.

$$F_e = ARX(J) U_{L1,J} \rho_{L1,J} \quad (3.3.56)$$

$$D_e = ARX(J) \Gamma_{L1,J} / [XCV(L2) R(J)] \quad (3.3.57)$$

On the cylinder surface : $J = 2, I = 3$ to $L2$

$$F_s = R(1) \left[XCVI(I) V_{I,2} \rho_{I,1} + XCVIP(I-1) V_{I-1,2} \rho_{I-1,1} \right] \quad (3.3.58)$$

$$D_s = \frac{R(1)}{YDIF(2)} \left[XCVI(I)\Gamma_{I,1} + XCVIP(I-1)\Gamma_{I-1,1} \right] \quad (3.3.59)$$

The control volumes for $U_{IM2,J}$ ($J=JM$ to $M2$) are considered to be boundary control volumes since the boundary condition at the nozzle wall $U_{IM1,J}$ is specified to be zero. The first control volume of this lot, that is, $(IM2, JM)$ does not satisfy consistency condition since it has one full neighbor and a half neighbor $(IM, JM1)$. Hence, F_s and D_s are calculated separately for this control volume, shown in Figure 3.3.7, as follows:

$$J = JM, I = IM2$$

$$F_s = RMN(J) \left[XCVI(I)V_{I,J}\rho_a + XCV(I-1)V_{I-1,J}\rho_b \right] \quad (3.3.60)$$

$$\text{where, } \rho_a = FY(J)\rho_{I,J} + FYM(J)\rho_{I,J-1}$$

$$\rho_b = FY(J)\rho_{I-1,J} + FYM(J)\rho_{I-1,J-1}$$

$$D_s = 2 RMN(J) \left[\frac{XCVI(I) \Gamma_{I,J-1} \Gamma_{I,J}}{\left[YCV(J-1)\Gamma_{I,J} + YCV(J)\Gamma_{I,J-1} \right]} + \frac{XCV(I-1) \Gamma_{I-1,J-1} \Gamma_{I-1,J}}{\left[YCV(J-1)\Gamma_{I-1,J} + YCV(J)\Gamma_{I-1,J-1} \right]} \right] \quad (3.3.61)$$

For the other boundary control volumes shown in Figure 3.3.7, starting with $I = IM2, J= JM$ to $M3$, at nozzle surface, the flux and the diffusion coefficients are as follows:

$$F_n = RMN(J+1) \left[XCVI(I)V_{I,J+1}\rho_c + XCV(I-1)V_{I-1,J+1}\rho_d \right] \quad (3.3.62)$$

$$\text{where, } \rho_c = FY(J+1)\rho_{I,J+1} + FYM(J+1)\rho_{I,J}$$

$$\rho_d = FY(J+1)\rho_{I-1,J+1} + FYM(J+1)\rho_{I-1,J}$$

$$D_n = 2RMN(J+1) \left[\frac{XCVI(I) \Gamma_{I,J} \Gamma_{I,J+1}}{YCV(J)\Gamma_{I,J+1} + YCV(J+1)\Gamma_{I,J}} + \frac{XCV(I-1) \Gamma_{I-1,J} \Gamma_{I-1,J+1}}{YCV(J)\Gamma_{I-1,J+1} + YCV(J+1)\Gamma_{I-1,J}} \right] \quad (3.3.63)$$

In the last control volume along this line, the azimuthal velocity at the boundary is specified to be zero, and density and viscosity are specified at the boundary. The derivative for diffusion will be across a distance of YDIF(M1). As a result F_n and D_n are as follows:

$$F_n = RMN(J+1) \left[XCVI(I) V_{I,M2} \rho_{I,M1} + XCV(I-1) V_{I-1,M2} \rho_{I-1,M1} \right] \quad (3.3.64)$$

$$D_n = \frac{R(M1)}{YDIF(M1)} \left[XCVI(I) \Gamma_{I,M1} + XCV(I-1) \Gamma_{I-1,M1} \right] \quad (3.3.65)$$

The control volumes at the nozzle exit have the nozzle-exit azimuthal velocity component specified to be zero. Hence, the derivative in radial direction for diffusion will be over half of the control volume. As a result F_n and D_n are as follows,

$J = JM1$ and $I = 3, IM$

$$F_n = RMN(J+1) \left[XCVI(I) V_{I,J+1} \rho_m + XCVIP(I-1) V_{I-1,J+1} \rho_n \right] \quad (3.3.66)$$

$$D_n = 4 RMN(J+1) \left[\frac{XCVI(I) \Gamma_{I,J} \Gamma_{I,J+1}}{YCV(J)\Gamma_{I,J+1} + YCV(J+1)\Gamma_{I,J}} + \frac{XCVIP(I-1) \Gamma_{I-1,J} \Gamma_{I-1,J+1}}{YCV(J)\Gamma_{I-1,J+1} + YCV(J+1)\Gamma_{I-1,J}} \right] \quad (3.3.67)$$

Along the last row of control volumes, the azimuthal component of velocities are specified to be zero, hence, the

derivative for the diffusion term is taken across a distance of YDIF(M1). The density and viscosity are also specified at this boundary, hence the flux F_n and diffusion coefficient D_n are as follows,

At $J = M2$ and $I = IM2 + 1$ to $L2$

$$F_n = RMN(J + 1) \left[XCVI(I) V_{I, M1} \rho_{I, M1} + XCVIP(I - 1) V_{I-1, M1} \rho_{I-1, M1} \right] \quad (3.3.68)$$

$$D_n = \frac{R(M1)}{YDIF(M1)} \left[XCVI(I) \Gamma_{I, M1} + XCVIP(I - 1) \Gamma_{I-1, M1} \right] \quad (3.3.69)$$

The source terms are divided into S_c and $S_p U$,

$$S_c = - \frac{UV}{R} + \frac{2\Gamma}{R^2} \frac{\partial V}{\partial \theta} \quad (3.3.70)$$

$$\text{and } S_p U = - \frac{\Gamma}{R^2} U \quad (3.3.71)$$

Where,

$$\frac{2\Gamma}{R^2} \frac{\partial V}{\partial \theta} = \frac{\Gamma_{I, J}}{R(J)^2} \left[\frac{V_{I, J+1} - V_{I-1, J+1}}{XDIF(I) RMN(J + 1)} + \frac{V_{I, J} - V_{I-1, J}}{XDIF(I) RMN(J)} \right] \quad (3.3.72)$$

$$- \frac{UV}{R} = \frac{-1}{R(J)} \left[U_{I, J} \left(V_{I, J} + V_{I, J+1} + V_{I-1, J} + V_{I-1, J+1} \right) \right] / 4 \quad (3.3.73)$$

$$\text{and } S_p = - \frac{\Gamma_{I, J}}{R(J)^2}$$

The coefficients a_E , a_W , a_N and a_S are calculated by the Power-law scheme with under-relaxation. The general discretized equation is as follows:

$$a_P U_{I, J} = a_E U_{I+1, J} + a_W U_{I-1, J} + a_N U_{I, J+1} + a_S U_{I, J-1} + b \quad (3.3.74)$$

The modifications to obtain SIMPLEC algorithm have been done

according to Doormaal and Raithby [13] in x-momentum and y-momentum equations. The equations for velocity correction obtained in Section 3.1.2, namely, Equations (3.1.40A and 3.1.40B) which are as follows:

$$a_p U'_{I,J} = \sum a_{nb} U'_{nb} + A_u (P'_{I-1,J} - P'_{I,J}) \quad (3.1.35)$$

and

$$a_p V'_{I,J} = \sum a_{nb} V'_{nb} + A_v (P'_{I,J-1} - P'_{I,J}) \quad (3.1.36)$$

In SIMPLE algorithm, $\sum a_{nb} U'_{nb}$ and $\sum a_{nb} V'_{nb}$ were neglected. In SIMPLEC, only their deviation from $U'_{I,J}$ and $V'_{I,J}$ are neglected. Subtracting $\sum a_{nb} U'_{nb}$ from both sides of equations (3.1.40A) and $\sum a_{nb} V'_{nb}$ from both sides of Equation (3.1.40B) we have,

$$(a_{p_u} - \sum a_{nb}) U'_{I,J} = \underline{\sum a_{nb} (U'_{nb} - U'_{I,J})} + A_u (P'_{I-1,J} - P'_{I,J}) \quad (3.3.75)$$

and

$$(a_{p_v} - \sum a_{nb}) V'_{I,J} = \underline{\sum a_{nb} (V'_{nb} - V'_{I,J})} + A_v (P'_{I,J-1} - P'_{I,J}) \quad (3.4.76)$$

Neglecting the underlined term and replacing U' by $U - U^*$ in Equations (3.3.75) and (3.3.76) gives,

$$U_{I,J} = U^*_{I,J} + \frac{A_u}{(a_{p_u} - \sum a_{nb})} (P'_{I-1,J} - P'_{I,J})$$

$$\text{or, } U_{I,J} = U^*_{I,J} + DU_{I,J} (P'_{I-1,J} - P'_{I,J}) \quad (3.3.77)$$

$$\text{and } V_{I,J} = V^*_{I,J} + \frac{A_v}{(a_{p_v} - \sum a_{nb})} (P'_{I,J-1} - P'_{I,J})$$

$$\text{or, } V_{I,J} = V_{I,J}^* + DV_{I,J} (P'_{I,J-1} - P'_{I,J}) \quad (3.3.78)$$

where in SIMPLEC algorithm

$$DU_{I,J} = \frac{A_U}{(a_{P_U} - \sum a_{nb})}$$

$$DV_{I,J} = \frac{A_V}{(a_{P_V} - \sum a_{nb})}$$

whereas in SIMPLE algorithm,

$$DU_{I,J} = \frac{A_U}{a_{P_U}} \quad DV_{I,J} = \frac{A_V}{a_{P_V}}$$

and a_{nb} are the coefficients of the neighboring points. U_{nb} and V_{nb} are the velocities of the neighboring points.

It is observed that the presence of nozzle within the flow regime, introduces a large number of changes so as to apply the boundary conditions at the nozzle exit and along the nozzle wall. All the subroutines of the program were modified to accommodate these changes. The logic and structure of the SIMPLEC was retained while introducing the changes, so that problems involving variable properties can also be treated if desired. The width of the nozzle, $r_1 \sin \theta_1$ and the location of the nozzle, r_1 apart from Reynolds numbers are the parameters for which the solutions have been found.

There are two geometrical parameters, namely r_{max} and θ_E which are not known. These were chosen by trial and error, so that the iterations during the solution converge and the converged solution is independent of their choice. The angle θ_E is the

dividing line between the entrainment flow and the out flow. This was chosen to be $\pi/2$. Values of θ_E greater than $\pi/2$ posed convergence problems. The maximum radius r_{max} was chosen by trial and error so as to obtain converged solutions. It was systematically increased from $r_{max}=2r_1$ to higher values and finally, $r_{max}=6r_1$ has been chosen.

The entrainment velocity at the boundary is unknown. As r_{max} is increased, the entrainment velocity at the outer boundary decreases and convergence supposed to occur earlier. However, with the increase in r_{max} , the total number of control volumes also increases, which increases the computational time. The entrainment boundary condition is continuative type, that is, the gradients of velocities vanish at the entrainment boundary. The outflow boundary condition could also have been taken as continuative. The continuative boundary conditions demand a larger r_{max} . The entrainment and outflow may demand different r_{max} for convergence and the larger of the two would have to be chosen. Hence, as a compromise, on the outflow boundary, the overall mass balance has been satisfied to determine the outflow velocity. The residuals of the velocities, pressure and temperature were all monitored during the iterations. The overall mass conservation was also monitored during the iterations. The residual of pressure was observed to reduce to 10^{-11} and over all mass conservation in the control volumes was satisfied to an accuracy of 10^{-16} .

The solutions have been obtained for Reynolds numbers of 30 to 230, nozzle-to-cylinder spacings of 4 to 10 and for nozzle widths of 0.266 to 0.666.

3.4 Vertically downward slot jet impinging upon a flat surface

Jet impingement normal to a surface has become a classical problem which has drawn the attention of many investigators, since it has very wide range of applications, involving enhanced heat transfer rates. The jet strikes the surface and after impingement, flows along the surface like a wall jet in the absence of buoyancy. Therefore, almost uniform rate of heat transfer is maintained in the wall jet region. If buoyancy is included in the flow, the flow phenomenon changes significantly. Beyond a certain value of mixed-convection parameter, Richardson number Ri , the jet detaches from the impingement surface and flows upwards where it mixes with the entrainment fluid and rises like a plume. At higher of value Ri , the jet turns by 180° near the nozzle exit and flows along the nozzle surface.

The rectangular cartesian coordinate system is chosen with the origin at the point of inter section of jet axis with the plate. The x-axis is along the plate and y-axis is perpendicular to it. The velocity components along x and y directions are u and v respectively. The heated jet emanates from a nozzle located at a height h_1 above the flat surface. The flow is symmetric about the jet axis, hence only the right half of the domain has been considered for computations. Uniform as well as fully developed parabolic velocity and temperature profiles have been considered at the nozzle exit. The computational domain of the vertically downwards slot jet impinging upon a flat surface is shown in Figure 3.4.1.

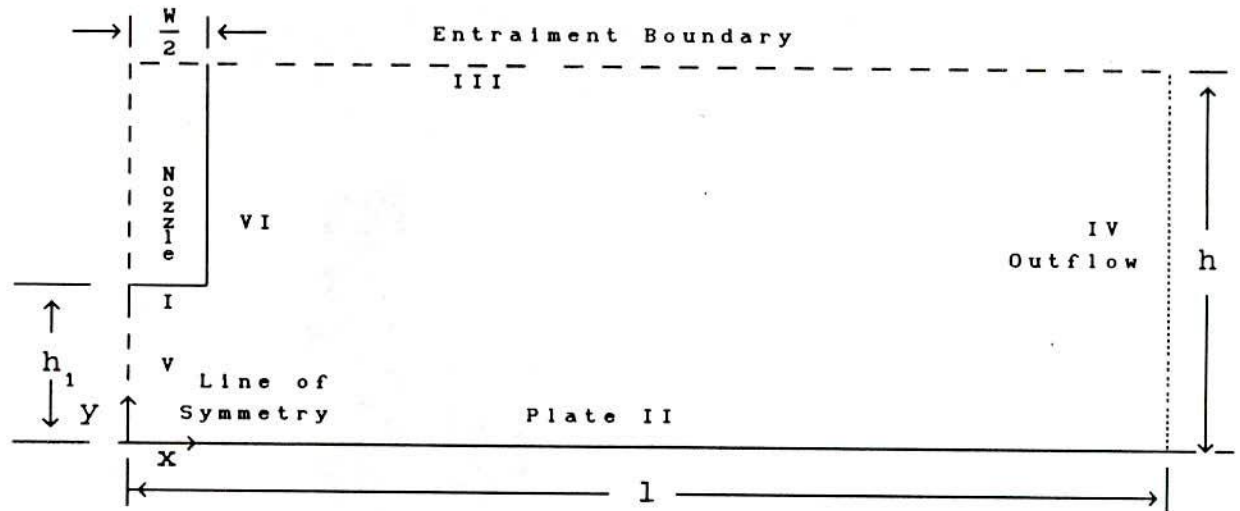


Figure 3.4.1. Computational Domain for Vertically Downward Slot Jet Impinging upon a Flat Surface.

3.4.1 Governing Equations

The flow is considered to be laminar, steady, two-dimensional and incompressible. The fluid properties are assumed to be constant. The change of density with temperatures is considered to the extent that it gives rise to buoyancy force. Boussinesq's approximation has been made to simplify the buoyancy term in the momentum equation. The density and viscosity variation have been included in problem formulation to keep the numerical algorithm in general form, actually these were taken as constants. The mass conservation, momentum and energy equations are follows,

CONTINUITY EQUATION,

$$\frac{\partial(\rho'u)}{\partial x} + \frac{\partial(\rho'v)}{\partial y} = 0 \quad (3.4.1)$$

X-MOMENTUM EQUATION,

$$\frac{\partial}{\partial x} (\rho'u^2) + \frac{\partial}{\partial y} (\rho'uv) = - \frac{\partial P}{\partial x} + \frac{\partial}{\partial x} \left[\mu \frac{\partial u}{\partial x} \right] + \frac{\partial}{\partial y} \left[\mu \frac{\partial u}{\partial y} \right] \quad (3.4.2)$$

Y-MOMENTUM EQUATION,

$$\frac{\partial}{\partial x} (\rho'uv) + \frac{\partial}{\partial y} (\rho'vv) = - \frac{\partial P}{\partial y} + \frac{\partial}{\partial x} \left[\mu \frac{\partial v}{\partial x} \right] + \frac{\partial}{\partial y} \left[\mu \frac{\partial v}{\partial y} \right] + \rho'g \quad (3.4.3)$$

ENERGY EQUATION,

$$\frac{\partial}{\partial x} (\rho'uT) + \frac{\partial}{\partial y} (\rho'vT) = \frac{\partial}{\partial x} \left[\Gamma \frac{\partial T}{\partial x} \right] + \frac{\partial}{\partial y} \left[\Gamma \frac{\partial T}{\partial y} \right] \quad (3.4.4)$$

The nozzle exit velocity, V_j and the nozzle width W are chosen as the characteristic velocity and length respectively. The pressure and the temperature are non-dimensionalized with respect to $\rho_o V_j^2$ and $(T_j - T_w)$ respectively. Accordingly, the non-dimensionalization scheme is as follows,

$$X = \frac{x}{W}, \quad Y = \frac{y}{W}, \quad L = \frac{l}{W}, \quad H_1 = \frac{h_1}{W}, \quad H = \frac{h}{W}, \quad U = \frac{u}{V_j}, \quad V = \frac{v}{V_j}$$

$$P = \frac{(p - p_\infty)}{\rho_o V_j^2}, \quad T^* = \frac{(T - T_w)}{(T_j - T_w)}, \quad Re = \frac{V_j W}{\nu}$$

$$Ri = \frac{Gr}{Re^2}, \quad Gr = \frac{g\beta(T_j - T_w)W^3}{\nu^2}, \quad \rho = \frac{\rho'}{\rho_o}$$

where ρ_o is the reference density

The Navier-Stokes equations and the energy equation in conservative form reduce to,

CONTINUITY EQUATION,

$$\frac{\partial U}{\partial X} + \frac{\partial V}{\partial Y} = 0 \quad (3.4.5)$$

X-MOMENTUM EQUATION,

$$\frac{\partial}{\partial X} (UU) + \frac{\partial}{\partial Y} (UV) = - \frac{\partial P}{\partial X} + \frac{1}{Re} \frac{\partial}{\partial X} \left[\frac{\partial U}{\partial X} \right] + \frac{1}{Re} \frac{\partial}{\partial Y} \left[\frac{\partial U}{\partial Y} \right] \quad (3.4.6)$$

Y-MOMENTUM EQUATION,

$$\frac{\partial}{\partial X} (UV) + \frac{\partial}{\partial Y} (VV) = - \frac{\partial P}{\partial Y} + \frac{1}{Re} \frac{\partial}{\partial X} \left[\frac{\partial V}{\partial X} \right] + \frac{1}{Re} \frac{\partial}{\partial Y} \left[\frac{\partial V}{\partial Y} \right] + Ri T^* \quad (3.4.7)$$

ENERGY EQUATION,

$$\frac{\partial}{\partial X} (UT^*) + \frac{\partial}{\partial Y} (VT^*) = \frac{1}{Re Pr} \frac{\partial}{\partial X} \left[\frac{\partial T^*}{\partial X} \right] + \frac{1}{Re Pr} \frac{\partial}{\partial Y} \left[\frac{\partial T^*}{\partial Y} \right] \quad (3.4.8)$$

Where, Re is the slot exit Reynolds number based on maximum slot exit velocity V , and width of the nozzle W . Pr is the fluid Prandtl number and Ri is Richardson number. Equations (3.4.5 - 3.4.8) may be expressed by a single equation, convenient for discretization as follows,

$$\frac{\partial}{\partial X} (U\phi) + \frac{\partial}{\partial Y} (V\phi) = \frac{\partial}{\partial X} \left[\Gamma_{\phi} \frac{\partial \phi}{\partial X} \right] + \frac{\partial}{\partial Y} \left[\Gamma_{\phi} \frac{\partial \phi}{\partial Y} \right] + S_{\phi} \quad (3.4.9)$$

The values of ϕ , Γ_{ϕ} and S_{ϕ} for the above four equations are given in table 3.4.1

Table 3.4.1

Equations	ϕ	Γ_{ϕ}	S_{ϕ}
Continuity	1	0	0
X-Momentum	U	1/Re	$-\frac{\partial P}{\partial X}$
Y-Momentum	V	1/Re	$-\frac{\partial P}{\partial Y} + Ri T^*$
Energy	T^*	1/(Re.Pr)	0

The boundary conditions at the boundaries marked I, II, III,

IV, V and VI in the Figure 3.4.1, are specified as follows,

I. Nozzle Exit:

For uniform velocity and temperature profiles

$$\text{At } Y = H_1, 0 \leq X \leq \frac{1}{2} : T^* = 1 \text{ and } V_j = -1, U = 0$$

For parabolic velocity and temperature profiles

$$\text{At } Y = H_1, 0 \leq X \leq \frac{1}{2} : V_j = (4X^2 - 1) \text{ and } T^* = (1 - 4X^2), U = 0$$

II. Impingement Surface: At $Y = 0, 0 \leq X \leq L$

$$U = 0, V = 0, T^* = 0 : \text{No-slip and impermeability.}$$

III. Entrainment Boundary: At $Y = H, \frac{1}{2} < X \leq L$

$$\frac{\partial U}{\partial Y} = 0, \frac{\partial V}{\partial Y} = 0 \text{ and } \frac{\partial T^*}{\partial Y} = 0.$$

IV. Outflow Boundary: At $X = L, 0 \leq Y \leq H$

$$\frac{\partial U}{\partial X} = 0, \frac{\partial V}{\partial X} = 0 \text{ and } \frac{\partial T^*}{\partial X} = 0$$

V. Line of symmetry: At $X = 0, 0 \leq Y \leq H_1$

$$U = 0, \frac{\partial V}{\partial X} = 0 \text{ and } \frac{\partial T^*}{\partial X} = 0$$

VI. Nozzle Wall : At $X = \frac{1}{2}, H_1 \leq Y \leq H$

$$U = 0, V = 0, \text{ and } T^* = 0$$

3.4.2 Numerical Solution Procedure

The domain is divided into control volumes of variable mesh sizes. Fine mesh is chosen near the wall and at the nozzle exit and mesh is gradually expanded to coarse grid between the nozzle exit and the wall. In the x direction, a fine grid is chosen near the nozzle wall and is smoothly expanded to coarse grid in the x

direction. A typical grid is shown in the Figure 3.1.2. The non-dimensionalized governing Equations set (3.4.9) has been solved by SIMPLEC algorithm due to Doormaal and Raithby [13]. The SIMPLEC algorithm has been described in Section 3.3.2.

The flux and diffusion coefficients are calculated by a procedure similar to that described in Section 3.1.2 for momentum equations. At the boundaries, nozzle exit and at the nozzle surface the flux and the diffusion coefficients have been calculated by a procedure similar to that described in Section 3.3.2, in cylindrical polar coordinates. The effect of buoyancy is included as a source term in the Y-momentum equation. This term is,

$$S_c = 0.5Ri (T_{I,J}^* + T_{I,J-1}^*)$$

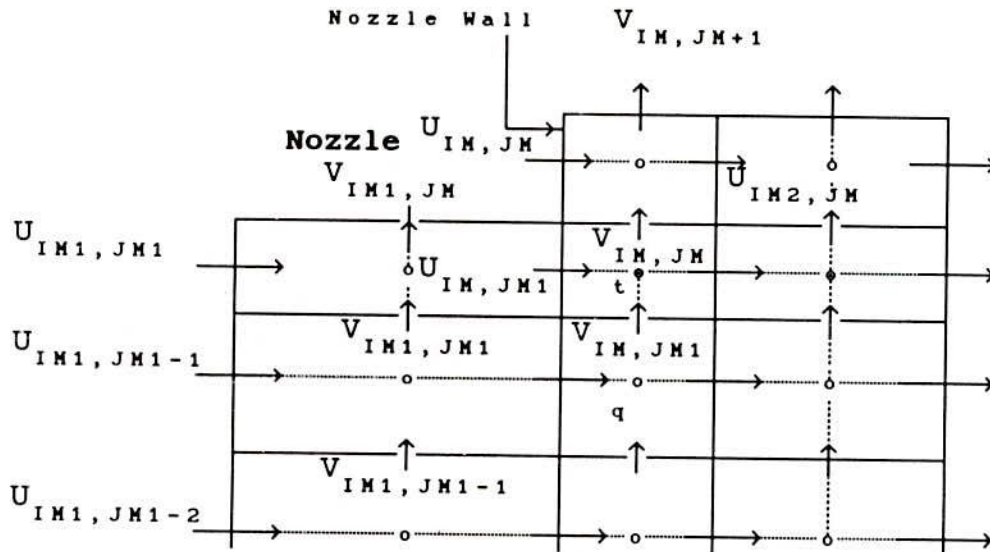


Figure 3.4.2: Control volumes at nozzle exit and nozzle surface

The control volumes next to the nozzle wall for X-momentum equation, are the one and a half boundary control volumes.

Similarly, the control volumes next to nozzle exit for Y-momentum equation, are also one and a half boundary control volumes. These control volumes are shown in Figure 3.4.2. The flux and the diffusion coefficients calculation for these control volumes, require special care, as outlined in Section 3.3.2. All the subroutines of the Computer program were modified to take into account the changes introduced because of the nozzle geometry.

Several trials were made to select the domain size. The height of the domain is chosen far away from the line of symmetry, so that the gradients of all the variables vanish there and the boundary conditions are satisfied. The value of H depends on the chosen value of L. It was observed that for small values of H, the solution did not converge. Once the convergence was obtained the value of H was systematically increased until the converged solution becomes independent of the choice of H.

Finally, the height $h = 24W$ and $l = 48W$ and mesh size of 52×42 have been used for the computation. The convergence is checked by monitoring the residues of all the variables while solving the equations of momentum, pressure and energy. The residues of the pressure equation reduced to a value around 10^{-9} while the overall mass conservation residue reduced to a value of 10^{-16} .

The results have been obtained for Reynolds numbers of 10 to 160 for the uniform slot exit velocity profile and 20 to 210 for the parabolic slot exit velocity profile, Prandtl numbers of 0.05 to 120, Richardson numbers of 0.0 to 1.5 for both, the uniform and the parabolic slot exit velocity and temperature profiles, and for nozzle-to-plate spacings of 0.5 to 4.5.

3.5 Offset Slot Jet

If the impingement surface is parallel to the axis of the jet but offset from the jet exit plane a different fluid flow phenomenon is observed. The jet strikes the surface (or reattaches to the surface) at a finite distance downstream from the slot exit wall. In between the slot exit wall and the reattachment point, one or two recirculation regions may exist. Offset jet type of flow phenomenon is observed, in entrance region of heat exchangers, discharge of effluents from power plants and flows into the combustion chamber,

The rectangular cartesian coordinate system is chosen with the origin at the point of inter section of jet-exit wall and the offset surface. The x-axis is along the offset surface and y-axis is perpendicular to it. The velocity components along x and y directions are u and v respectively. The heated jet emanates from a nozzle located at a height h_1 above the offset surface. The whole domain has been considered for computations since the flow is not symmetrical about the jet axis. Uniform as well as fully developed parabolic velocity and temperature profiles have been considered at the nozzle exit. The computational domain of the offset slot jet impinging upon a flat surface is shown in Figure 3.5.1.

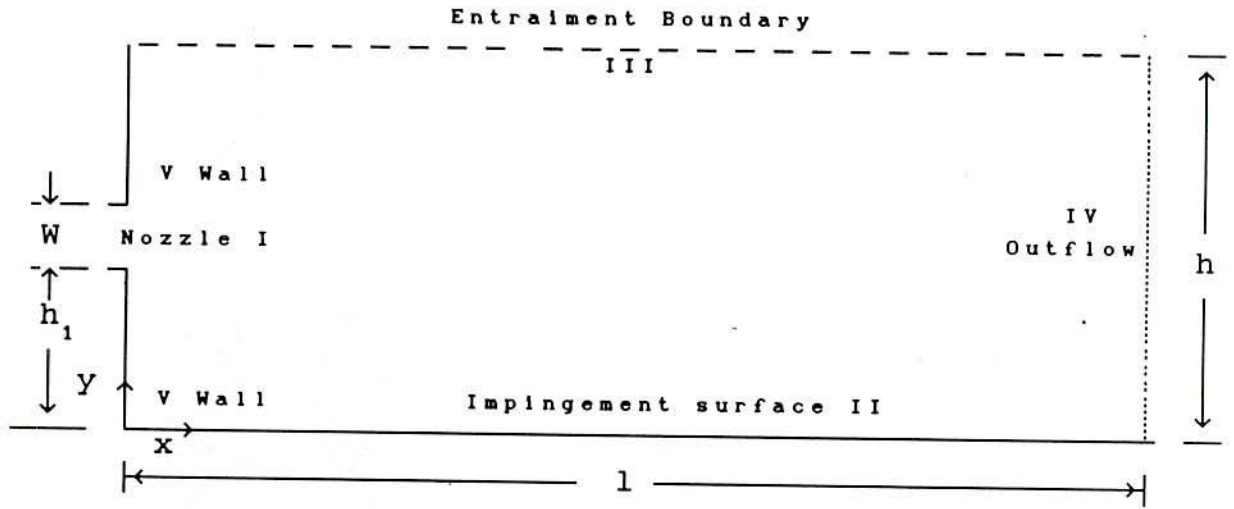


Figure 3.5.1: Computational Domain for Offset Slot Jet

3.5.1 Governing Equations

The steady, laminar, incompressible and two-dimensional flow is considered for the present investigation. The fluid properties are assumed to be constant and viscous dissipation is neglected. Following the above assumptions, the continuity, x-momentum, y-momentum and the energy equation are as follows,

CONTINUITY EQUATION,

$$\frac{\partial(\rho'u)}{\partial x} + \frac{\partial(\rho'v)}{\partial y} = 0 \quad (3.5.1)$$

X-MOMENTUM EQUATION,

$$\frac{\partial}{\partial x} (\rho'u^2) + \frac{\partial}{\partial y} (\rho'uv) = - \frac{\partial P}{\partial x} + \frac{\partial}{\partial x} \left[\mu \frac{\partial u}{\partial x} \right] + \frac{\partial}{\partial y} \left[\mu \frac{\partial u}{\partial y} \right] \quad (3.5.2)$$

Y-MOMENTUM EQUATION,

$$\frac{\partial}{\partial x} (\rho'uv) + \frac{\partial}{\partial y} (\rho'v^2) = - \frac{\partial P}{\partial y} + \frac{\partial}{\partial x} \left[\mu \frac{\partial v}{\partial x} \right] + \frac{\partial}{\partial y} \left[\mu \frac{\partial v}{\partial y} \right] \quad (3.5.3)$$

ENERGY EQUATION,

$$\frac{\partial}{\partial X} (\rho' u T) + \frac{\partial}{\partial Y} (\rho' v T) = \frac{\partial}{\partial X} \left[\alpha \frac{\partial T}{\partial X} \right] + \frac{\partial}{\partial Y} \left[\alpha \frac{\partial T}{\partial Y} \right] \quad (3.5.4)$$

The maximum nozzle exit velocity, U_j and the nozzle width W , are chosen as the characteristic velocity and length respectively. The non-dimensionalization scheme and the governing equations are the same as those for the free slot jet except that offset ratio is introduced here. Offset ratio = $\frac{h_1}{W} + \frac{1}{2} = H_1 + \frac{1}{2}$. The continuity, momentum and energy equation in non-dimensional conservative form are as follows,

CONTINUITY EQUATION,

$$\frac{\partial U}{\partial X} + \frac{\partial V}{\partial Y} = 0 \quad (3.5.5)$$

X-MOMENTUM EQUATION,

$$\frac{\partial}{\partial X} (UU) + \frac{\partial}{\partial Y} (UV) = - \frac{\partial P}{\partial X} + \frac{1}{Re} \frac{\partial}{\partial X} \left[\frac{\partial U}{\partial X} \right] + \frac{1}{Re} \frac{\partial}{\partial Y} \left[\frac{\partial U}{\partial Y} \right] \quad (3.5.6)$$

Y-MOMENTUM EQUATION,

$$\frac{\partial}{\partial X} (UV) + \frac{\partial}{\partial Y} (VV) = - \frac{\partial P}{\partial Y} + \frac{1}{Re} \frac{\partial}{\partial X} \left[\frac{\partial V}{\partial X} \right] + \frac{1}{Re} \frac{\partial}{\partial Y} \left[\frac{\partial V}{\partial Y} \right] \quad (3.5.7)$$

ENERGY EQUATION,

$$\frac{\partial}{\partial X} (UT^*) + \frac{\partial}{\partial Y} (VT^*) = \frac{1}{Re Pr} \frac{\partial}{\partial X} \left[\frac{\partial T^*}{\partial X} \right] + \frac{1}{Re Pr} \frac{\partial}{\partial Y} \left[\frac{\partial T^*}{\partial Y} \right] \quad (3.5.8)$$

Where, Re is the slot exit Reynolds number based on maximum slot exit velocity U_j and width of the nozzle W . Pr is the fluid

Prandtl number. Equations (3.5.5 - 3.5.8) may be expressed by a single equation convenient for discretization as follows:

$$\frac{\partial}{\partial X} (U\phi) + \frac{\partial}{\partial Y} (V\phi) = \frac{\partial}{\partial X} \left[\Gamma_{\phi} \frac{\partial \phi}{\partial X} \right] + \frac{\partial}{\partial Y} \left[\Gamma_{\phi} \frac{\partial \phi}{\partial Y} \right] + S_{\phi} \quad (3.5.9)$$

The values of ϕ , Γ_{ϕ} and S_{ϕ} for the above four equations are given table 5.1.1.

Table :5.1.1

Equations	ϕ	Γ_{ϕ}	S_{ϕ}
Continuity	1	0	0
X-Momentum	U	1/Re	$-\frac{\partial P}{\partial X}$
Y-Momentum	V	1/Re	$-\frac{\partial P}{\partial Y}$
Energy	T^*	1/(Re.Pr)	0

The boundary conditions at the boundaries marked I, II, III, IV and V in the Figure 3.5.1, are specified as follows,

I. Nozzle Exit:

For uniform velocity and temperature profiles

At $H_1 \leq Y \leq H_1 + 1$ and $X = 0$: $U_j = 1$, $T^* = 1$ and $V = 0$,

For parabolic velocity and temperature profiles

At $H_1 \leq Y \leq H_1 + 1$ and $X=0$:

$U_j = 4(Y - H_1)(1 - Y + H_1)$, $T^* = 4(Y - H_1)(1 - Y + H_1)$, $V = 0$.

II. Impingement Surface: At $Y= 0$, $0 \leq X \leq L$,

$U = 0$, $V = 0$, $T^* = 0$: no-slip and impermeability

III. Entrainment Boundary: At $Y= H$, $0 \leq X \leq L$,

$U = 0$, $\frac{\partial V}{\partial Y} = 0$, $T^* = 0$

IV. **Outflow Boundary:** At $X = L$, $0 \leq Y \leq H$,

$$\frac{\partial U}{\partial X} = 0, \quad \frac{\partial V}{\partial X} = 0, \quad \frac{\partial T^*}{\partial X} = 0$$

V. **Wall:** At $X = 0$, $0 \leq Y \leq H_1$ and $H_1 + 1 \leq Y \leq H$

$$U = 0, \quad V = 0 \quad \text{and} \quad T^* = 0.$$

3.5.2 Numerical Solution Procedure

The whole flow field is considered for numerical simulation. Jet emanates from a slot of width W located at a finite height, H_1 above the impingement surface. The domain and the boundaries are shown in the Figure 3.5.1 and a typical grid is shown in Figure 3.1.2.

In Figure 3.1.2, it is shown that the velocities are specified at the middle of the control volume faces and other properties such as pressure, density and temperatures are defined at the centres of the control volumes. Fine grid have been specified near the jet exit wall and have been smoothly expanded upto $X = 3.5$. Fine grids have been chosen near $X = 7$ also and smoothly expanded towards the nozzle exit wall upto $X = 3.5$. Fine grids specified near $X = 7$ have been gradually expanded to coarse grids upto the outflow boundary. The reattachment point was observed in the region of $3.5 < X < 7.0$, for offset ratio of 3, hence fine grids have been used in this region. Fine grids have been chosen near the impingement surface and the lower lip of nozzle. These have been smoothly expanded towards the interior. Fine grids have also been specified near the upper lip of the nozzle and gradually expanded towards the upper boundary. The

discretized equations are obtained by integrating the governing equations over the control volumes. The discretized equations may be expressed in the following general form as,

$$a_P \phi_P = a_E \phi_E + a_W \phi_W + a_N \phi_N + a_S \phi_S + b \quad (3.5.10)$$

Several trials were made to select the domain size. The height of the domain is chosen far away from the impingement surface, so that the gradients of all the variables vanish there and the boundary conditions are satisfied. The value of H depends on the chosen value of L. It was observed that for small values of H, the solution did not converge. Once the convergence was obtained the value of H was systematically increased until the converged solution becomes independent of the choice of H.

Finally, the height $h = 24W$ and $l = 42W$ and mesh of 100×62 have been used for the computation. The convergence is checked by monitoring the residues of all the variables while solving the equations of momentum, pressure and energy. The residues of pressure equation reduced to a value around 10^{-7} while the overall mass conservation residue reduced to a value of 10^{-12} .

In this case also, the set of discretized equations are same as the linear set of equations (3.5.10). These have been solved by SIMPLEC technique.

The results have been presented for Reynolds numbers of 30 to 80 for the uniform slot exit velocity and temperature profiles and 50 to 100 for the parabolic slot exit velocity and temperature profiles, Prandtl numbers of 0.7 to 10, Offset ratios of 3 to 9.

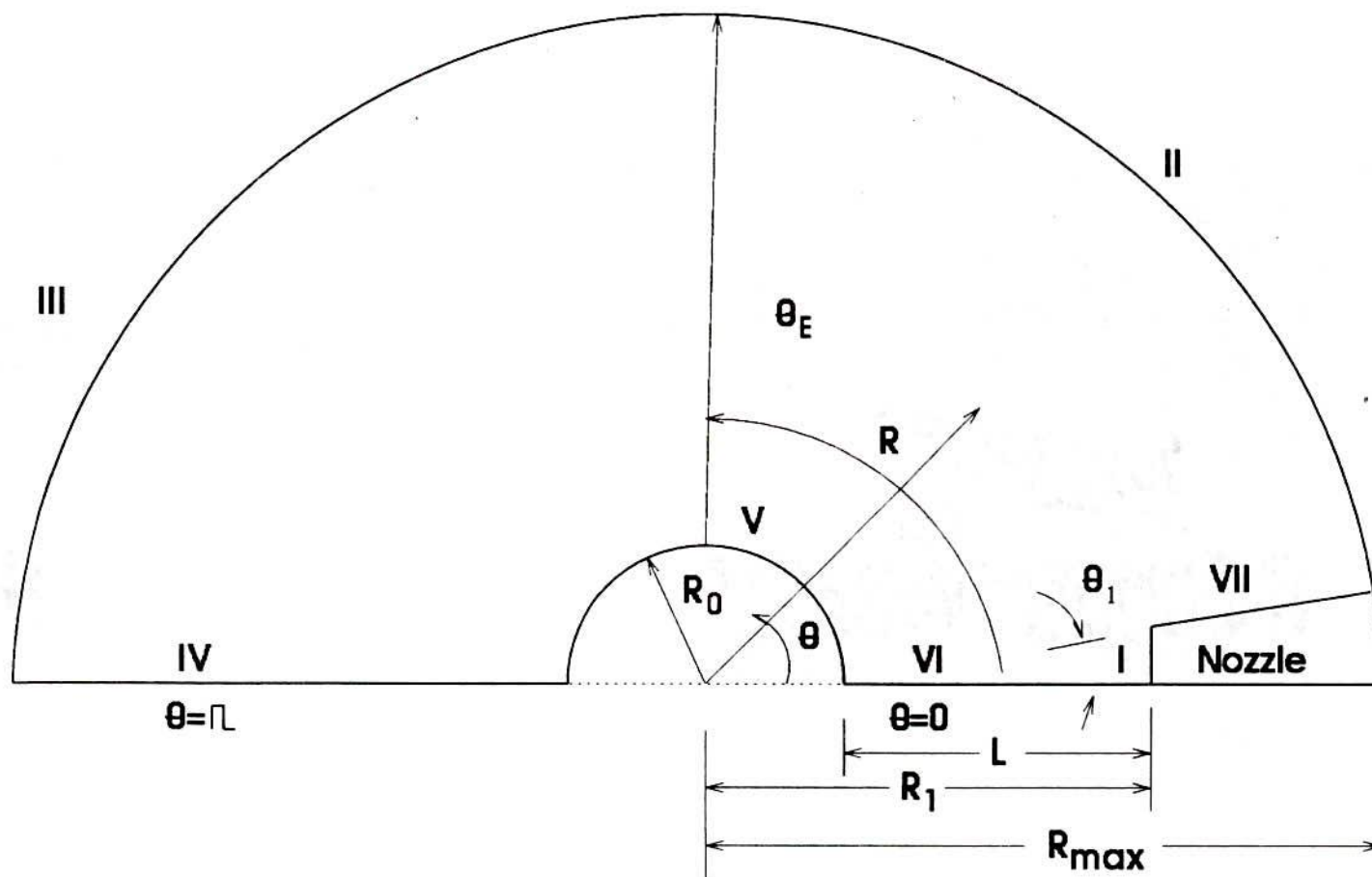


Fig.3.3.1 : Computational Domain for Slot Jet Impingement on a Circular Cylinder.



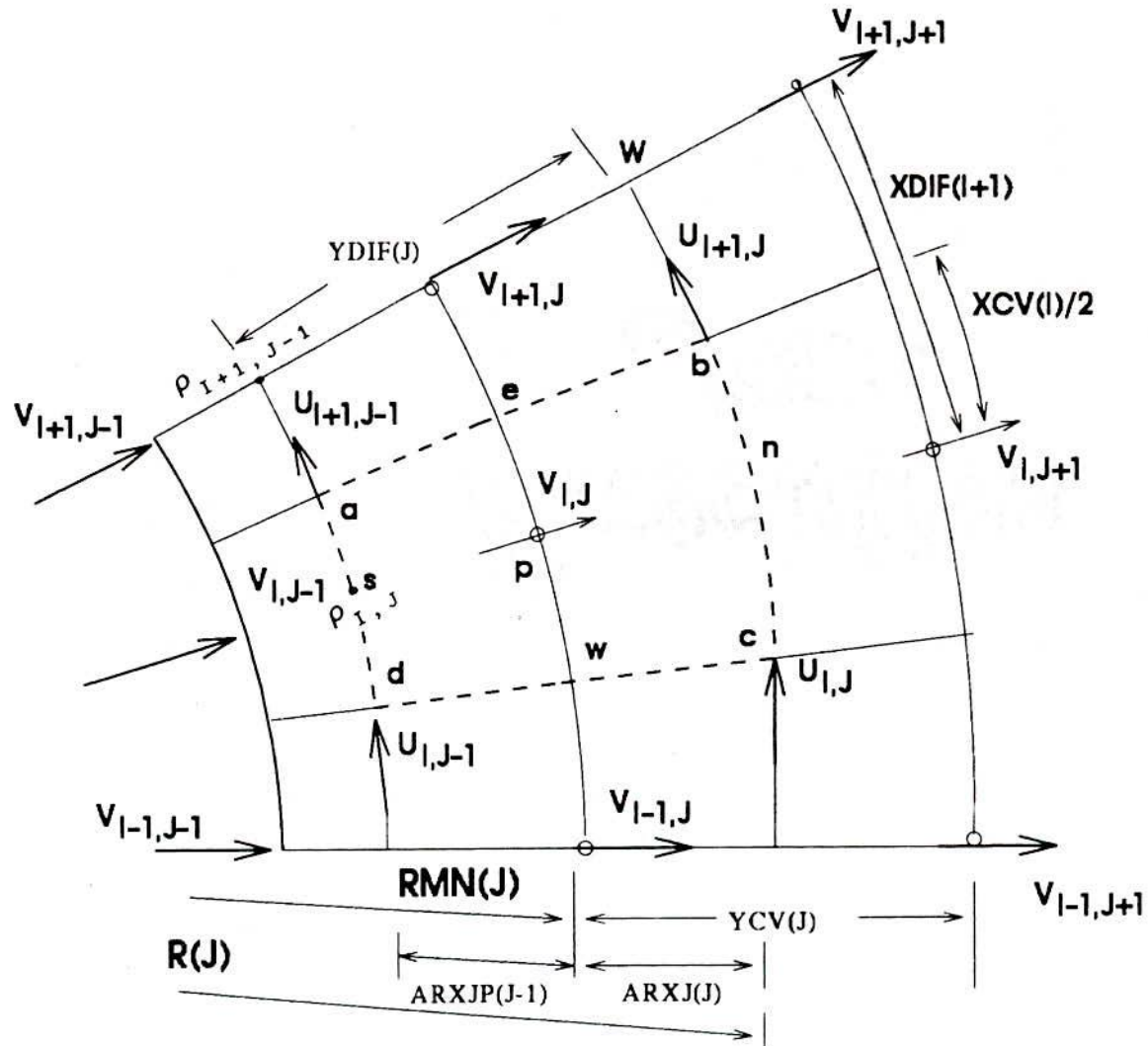


Fig. 3.3.2 : Radial momentum control volume

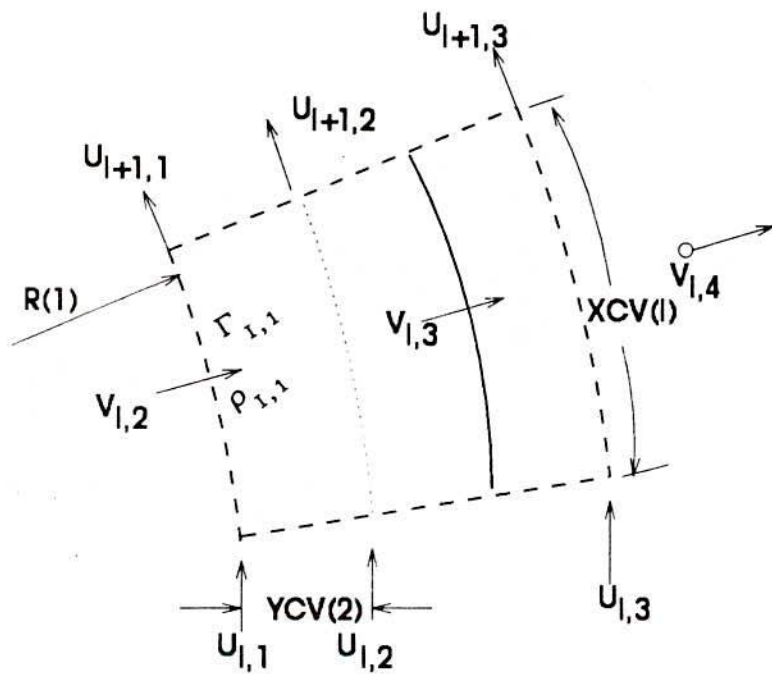


Fig. 3.3.3: First control volume
in radial direction.

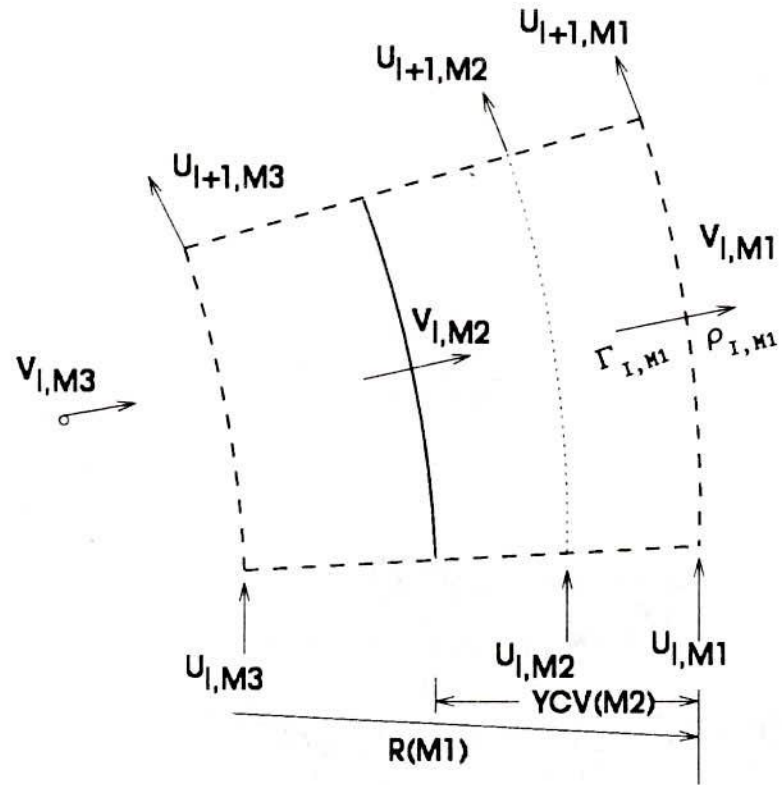


Fig. 3.3.4 : Last control volume.
in radial direction.

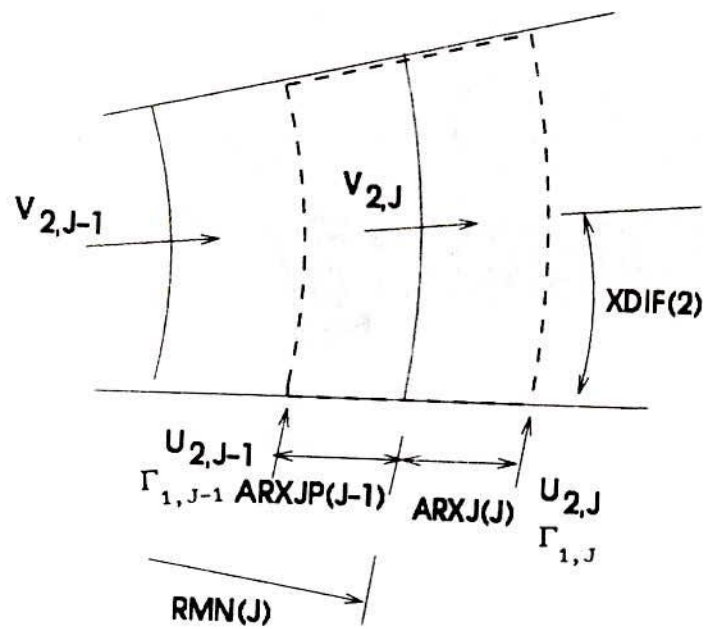


FIG. 3.3.5 : Bottom control volume ($0=0$)

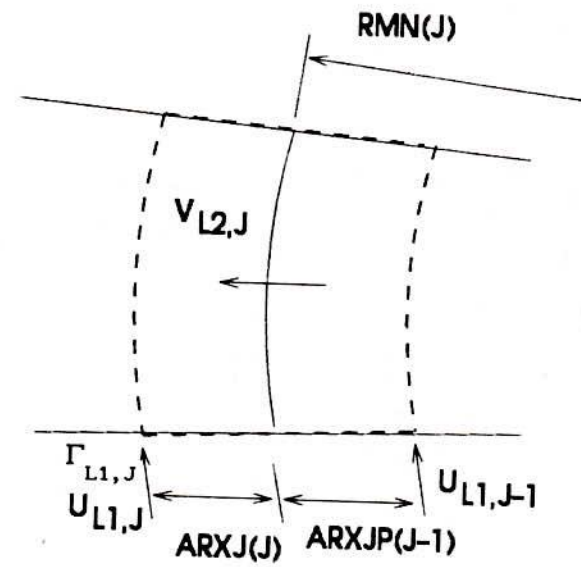


Fig. 3.3.6 : Bottom control volume ($0=$)

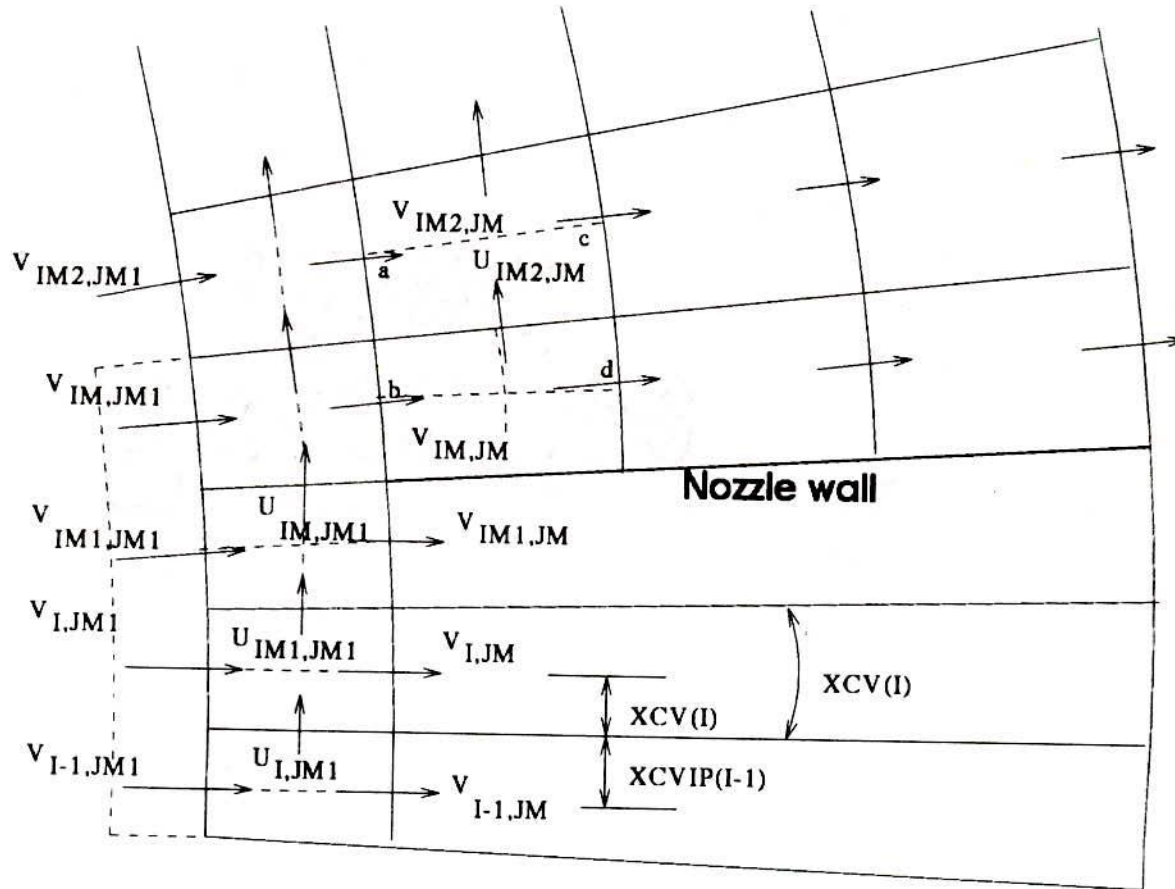


Fig. 3.3.7 : Control volume at nozzle surface.

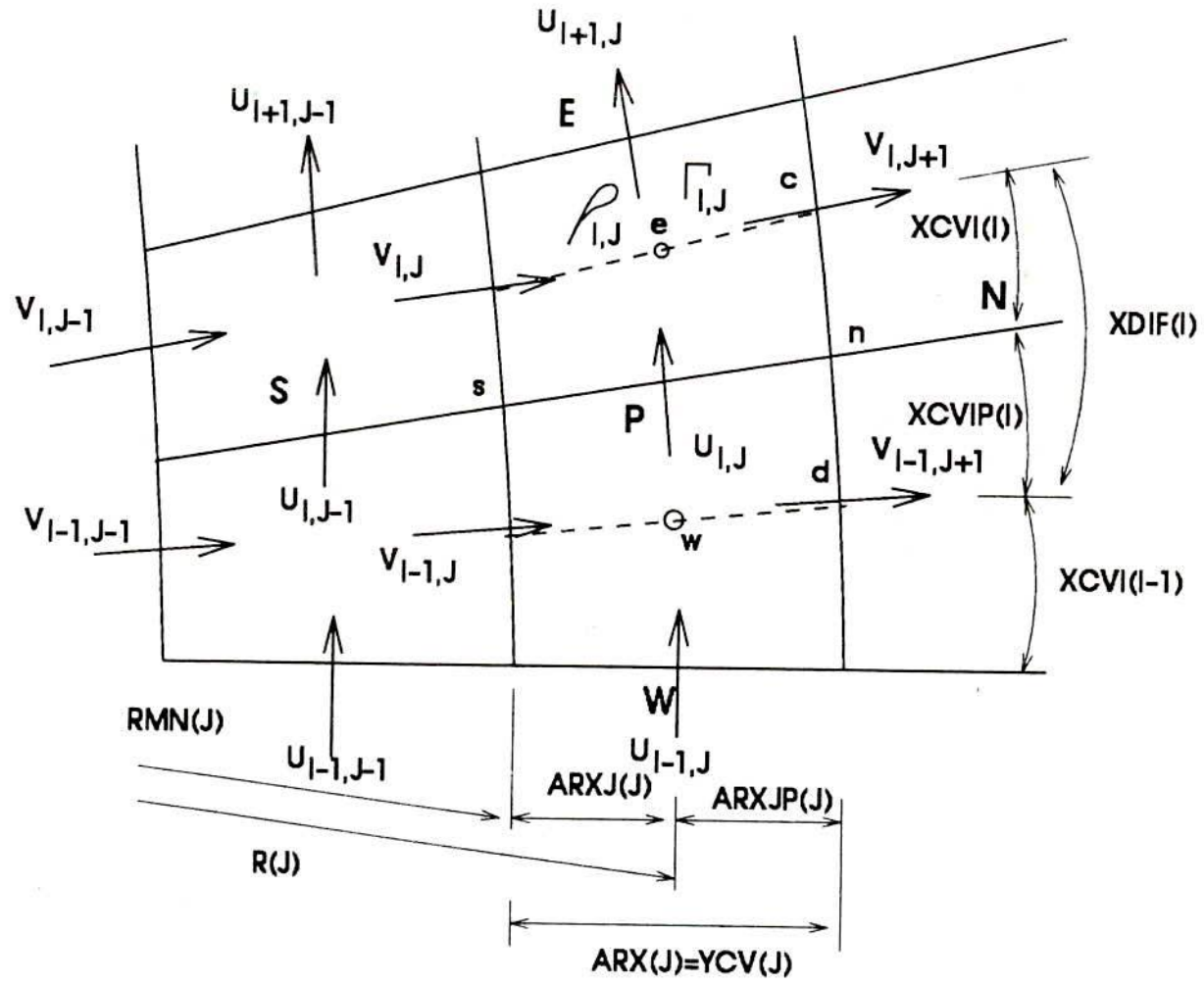


Fig. 3.3.8 : Azimuthal control volume

CHAPTER-IV

RESULTS AND DISCUSSIONS

4.1 FREE SLOT JET

The solutions of the Navier-Stokes equations have been obtained by SIMPLE algorithm for free slot jet. The discretized Equations (3.1.27) along with the boundary conditions (3.1.9a - 3.1.9f) were solved. The domain length, L in axial direction and the height, H were found to be dependent upon each other, since the spread of the free jet increases as the axial length increases. The domain length L= 80 and domain height H= 28 were finally chosen for the numerical solutions. A relaxation factor of 0.5 was used for the two momentum equations and the energy equation. A relaxation factor of 0.8 was used for the pressure correction equation. Normalized residues were calculated for the U and V components of velocity and the temperature. For example, the normalized residue for U component of velocity is defined as follows,

$$\text{Res}(U) = \frac{\sum |a_E U_E + a_W U_W + a_N U_N + a_S U_S + b - a_P U_P|}{\sum |a_P U_P|} \quad (4.1.1)$$

The summation in the above expression extends over all the control volumes. Apart from this, the flow in and out of individual control volumes, was also summed over all the control

volumes to check the overall mass conservation equation. This was done during the pressure correction in the control volumes and this sum is indicated by SSUM.

The velocity profiles were also inspected after a few iterations to check the convergence. It was observed that when the velocity profiles and the temperature profiles at selected points, converge upto sixth place of decimal, the values of residuals were as follows,

$$\begin{aligned}\text{Res}(U) &= 10^{-3} \\ \text{Res}(V) &= 10^{-3} \\ \text{Res}(T) &= 10^{-8} \\ \text{SSUM} &= 10^{-16}\end{aligned}$$

The convergence for the temperature profiles occurred earlier than that for the velocity profiles. Hence, convergence of velocity profiles was taken as the criterion for convergence. The required convergence was obtained within 800 iterations for both the types of jet-exit velocity and temperature profiles. The convergence could not be obtained with a coarse grid. A fine grid is required near the jet exit and near the axis of symmetry to obtain converge solutions. Solutions have been obtained for various grid sizes to illustrate, that the solutions are independent of the grid size. Figure 4.1.1 shows the centreline velocity for four grid sizes, namely, 110x80, 120x88, 130x94 and 145x90, where the first and second digits indicate the number of grid points in x and y directions respectively. It is observed that a grid distribution finer than 120x88 does not change the results significantly, hence this grid distribution has been used in all the calculations. Solutions have obtained for Reynolds

numbers in the range of 60 - 150 and for Prandtl numbers in the range of 0.01 to 10.0 for uniform and parabolic slot-exit velocity and temperature profiles.

Figure 4.1.2 shows the velocity vector plot at $Re=60$ with parabolic velocity profile at the slot-exit. The x-component of velocity becomes zero at a certain distance from the axis of symmetry indicating the jet width. The jet width is observed to increase along the jet axis. The entrainment is observed from the upper boundary. Figure 4.1.3 shows the stream lines for free slot jet at $Re=60$ with parabolic slot-exit velocity profile. The entrainment is observed from large values of Y . The entrained flow is accelerated towards the slot exit at small values of X . The entrainment velocity decreases with increasing axial distance, as evidenced by the increase in spacing between streamlines as X increases.

Figure 4.1.4 shows the velocity profiles at different locations along the jet axis with parabolic slot-exit velocity profile at $Re=60$. The jet velocity decays downstream and the jet width increases. The decay of centre line velocity is observed.

The decay of centreline velocity for both, the uniform and parabolic slot-exit velocity profiles, is shown in Figure 4.1.5. The numerical results of Lai and Simmons [32] and experimental results of Chanaud and Powell [28] are also shown for comparison. The Reynolds number for the uniform slot exit velocity profile is 150 while for the parabolic slot exit velocity profile it is 60. A good agreement is observed with the result of Lai and Simmons away from the origin whereas there is significant deviation at a

few points with the experimental results of Chanaud and Powell [28]. The centreline velocities determined from the similarity solution, as given by Equations (3.1.64 and 3.1.65) are also plotted. It is observed that these are very different from computational results. The same expression when plotted with virtual origin agrees very well with computational results for the uniform jet exit velocity profile. The centreline velocity with virtual origin, for the parabolic jet exit velocity profile, deviates from computational results near the origin and agrees very well far away from the origin.

Figure 4.1.6 shows the effect of Reynolds number on the decay of centre line velocity. The decay of centre line velocity is faster for the parabolic slot-exit velocity profile as compared to that for the uniform slot-exit velocity profile, since the former has smaller exit momentum than the latter and the latter has a potential core while the former does not have it. Actually, at lower values of Reynolds number the jet diffuses at a faster rate as compared to that at higher values of Reynolds number, which cannot be exactly seen in this figure since abscissa is $\bar{X} = X/Re$. This implies that the centreline velocity at $X = 6$ for $Re = 60$ and at $X = 15$ for $Re = 150$ are the same. At a given value of \bar{X} the velocity is larger for larger values of Reynolds numbers except that for the parabolic slot-exit velocity profile and $\bar{X} < 0.07$ where the trend is opposite of this. The curves for $Re = 60, 90$ and $120, 150$ are almost coincident and therefore, independent of Reynolds number as predicted by the boundary layer form of Equations (3.1.48 - 3.1.50). The boundary layer form of equations

is not valid near the jet exit and at smaller values of Reynolds numbers, hence some deviation from coincidence is expected.

The variation of U/U_j , the x-component of velocity with Schlichting's similarity variable $\eta = y/x^{2/3}$ is shown in Figure 4.1.7 at $X = 3.51, 7.09, 18.18$ and 27.19 for $Re = 60$ and uniform slot-exit velocity profile. It is observed that the centreline velocity decreases with X . The increase of jet spread can not be seen since it is absorbed in the variable η . For the parabolic slot-exit velocity profile, the variation of U/U_j , the x-component of velocity with Schlichting's similarity variable η at $Re = 60$ is shown in Figure 4.1.8 at various X locations. The centreline velocity was observed to be smaller than that in Figure 4.1.8 for uniform slot-exit velocity profile. It is observed that the jet spread in terms of η at each location is approximately same as that for the uniform slot exit velocity profile.

Figure 4.1.9 shows the variation of U/U_c with η at $X = 0.5, 3.51, 7.09, 18.18$ and 27.19 for $Re = 90$ for the uniform slot-exit velocity profile. The velocity profiles are nondimensionalized with respect to the local centre line velocity U_c . At $X = 0.5$, the velocity remains uniform over large portion, exhibiting the potential core. The velocity profiles at $X = 18.18$ and 27.19 exhibit a trend towards similarity at large values of X . Figure 4.1.10 shows the same kind of results for the parabolic slot-exit velocity profile at $Re = 90$. In this case the trend toward similarity at larger values of X , is better than that exhibited in Figure 4.1.9. Same results for uniform slot-exit velocity profile at $Re = 90$ are shown in Figure 4.1.11, with jet half width $Y_{0.5U}$ as

the characteristic length which is usually done for turbulent flows. It is observed that the velocity profiles at $X= 18.18$ and 27.19 are similar while those at $X= 0.5, 3.51$ and 7.09 deviate from similarity. The velocity profile at $X= 0.5$ exhibits the potential core and decays at a very fast rate. The trend of similarity is observed to be better for $Y/Y_{0.5U} < 1$ as compared to that for $Y/Y_{0.5U} > 1$.

Figure 4.1.12 shows the velocity variation with $Y/Y_{0.5U}$ for the slot jet with parabolic slot-exit velocity profile at $Re= 90$. The velocity profiles are similar at $X= 18.18$ and 27.19 and trend toward similarity for $Y/Y_{0.5U} < 1$ is better than that for the uniform slot-exit velocity profile. The potential core can not be seen at $X= 0.5$, since slot-exit velocity profile is parabolic. However, a close observation reveals that the velocity profile at $X= 0.5$, is parabolic for small Y , indicating that the core of jet is unaffected by viscosity. Figures 4.1.13 and 4.1.14 show the variation of U/U_c with η and $Y/Y_{0.5U}$ respectively, at $X= 0.5$ and $Re= 60$ for both the types of slot-exit velocity profiles. Potential core is observed in both the figures for uniform slot-exit velocity profiles.

Figures 4.1.15 and 4.1.16 show the variation of axial velocity U/U_c with Schlichting's variable η for uniform and parabolic slot-exit velocity profiles respectively at $X= 0.5$ and for Reynolds numbers of 60, 90, 120 and 150. It is observed that the width of potential core in Figure 4.1.15 is higher for higher values of Reynolds numbers. The velocity decays to zero at a faster rate at lower Reynolds numbers for both the types of

slot-exit velocity profiles. The velocity profiles do not exhibit any trend of similarity at $X= 0.5$, that is near the slot-exit.

Figures 4.1.17 and 4.1.18 show the variation of U/U_c with $Y/Y_{0.5U}$ for the uniform and the parabolic slot-exit velocity profiles respectively, $Y_{0.5U}$ being the velocity half width. It is observed that below the jet half width, that is, $Y/Y_{0.5U} < 1$, the velocity is larger for larger Reynolds numbers whereas the trend is opposite for $Y/Y_{0.5U} > 1$. It appears that the flow may become similar at higher Reynolds numbers, practically for parabolic slot-exit.

The variation of velocity profiles U/U_c with η at various Reynolds numbers and for $X= 27.19$ is shown in Figures 4.1.19 and 4.1.20 for uniform and parabolic slot-exit velocity profiles. It is observed that the profiles are very nearly similar in Schlichting's variable η particularly for parabolic slot-exit profiles. However, the same velocity distributions, when plotted with jet half width as the characteristic length, show similarity in Figures 4.1.21 and 4.1.22 for the uniform and the parabolic slot-exit velocity profiles. At still larger values of X the velocity profiles will become similar in Schlichting's variable η also, as seen from the trends of Figure 4.1.16 at $X= 0.5$ and Figure 4.1.18 at $X= 27.19$. Figure 4.1.23 shows the variation of jet half width with \bar{X} at $Re= 60$ and 90 for both, the uniform and the parabolic slot exit velocity profiles. The jet half width is observed to be independent of Reynolds numbers when plotted with \bar{X} . The jet with parabolic slot exit velocity profile has larger half width than the uniform slot exit velocity profile, since the

former diffuses faster than the latter.

Figure 4.1.24 is a plot of isotherms for $Re = 60$, $Pr = 0.72$ and with parabolic slot-exit velocity and temperature profiles. The outermost isotherm is for $T/T_j = 0.1$, that is, the temperature is 10% of jet exit temperature along this isotherm. This isotherm may be considered to be an indicator of jet spread.

The decay of centre line temperatures at different Reynolds numbers for the uniform and the parabolic slot-exit temperature and velocity profiles are shown in Figure 4.1.25 for $Pr = 0.72$. The decay of centre line temperature is faster for the parabolic slot-exit temperature profile as compared to that for the uniform slot-exit temperature profile. It is observed that the centre line temperatures are coincident for all Reynolds numbers, when plotted against the non-dimensional axial length $\bar{X} = X/Re$. A comparison with Figure 4.1.6 shows that coincidence of centreline temperature is better than that for the centreline velocities at various Reynolds numbers. A superposition of Figure 4.1.25 and 4.1.6 indicates (not shown) that the centreline temperatures at all Reynolds number are very close to the centreline velocities for $Re = 60$ for uniform slot-exit temperature and velocity profiles at $Pr = 0.72$. For the parabolic slot-exit temperature profile, the centreline temperatures are smaller than the centreline velocities at $Pr = 0.72$. The exact coincidence of centreline temperatures with centreline velocities is expected at $Pr = 1.0$, in accordance with Reynolds analogy. The centreline temperature determined from the similarity solution, as given by Equations (3.1.64 and 3.1.65) are also plotted. It is observed that these are very different from

the computational results.

Figure 4.1.26 shows the variation of non-dimensional temperature T^*/T_C^* with Schlichting's similarity variable η at $X=0.55$ and $Re=60, 90, 120$ and 150 for uniform slot-exit velocity and temperature profiles. The temperature remains constant in the potential core, potential core width being larger for larger Reynolds numbers. The temperature drops at a faster rate at lower values of Reynolds numbers, as compared to that at higher values of Reynolds numbers. A comparison with Figure 4.1.15 for the velocities, indicates that the temperature drops at a slower rate than the velocity at all Reynolds numbers since, Prandtl number is less than unity. Figure 4.1.27 shows the similar results for parabolic slot-exit velocity and temperature profiles. There is no visible potential core, since the velocity and the temperature are parabolic at slot-exit. The temperature decays at a faster rate than that for the uniform velocity profiles at slot exit. In both these figures near the slot exit, the temperature profiles do not exhibit similarity. Figure 4.1.28 shows a comparison of the temperature profiles for uniform and parabolic slot-exit profiles at $X=0.55$, $Re=60$ and $Pr=0.72$. It is observed that the temperature decays at a faster rate for parabolic slot-exit temperature profile for reasons mentioned above.

Figures 4.1.29 and 4.1.30 show the variation of T^*/T_C^* with $Y/Y_{0.5T}^*$ for uniform and the parabolic profiles respectively at $X=0.55$, $Y_{0.5T}^*$ being the half width for temperature. It is the location of Y where $T^*/T_C^*=0.5$. The half width for the temperature is greater than that for the velocity, since $Pr < 1.0$. It is

observed that for $Y/Y_{0.5T}^* < 1$, the temperature is larger for larger Reynolds numbers whereas, for $Y/Y_{0.5T}^* > 1$ trend is opposite of this. The coincidence of temperature is observed to be better for the parabolic slot-exit profiles in Figure 4.1.30.

Figure 4.1.31 shows the variation of temperature T^*/T_C^* with similarity variable η for different Reynolds numbers at $X= 27.68$ for uniform slot-exit velocity and temperature profiles. The diffusion of energy like the diffusion of momentum ($Pr=0.72$) is faster at lower values of Reynolds numbers hence, the temperature decays at a faster rate at $Re=60$ as compared to that at $Re=150$, as seen in this figure. A comparison with Figure 4.1.19 indicates that the temperature drops at a slower rate than the velocity at all Reynolds numbers which is expected at $Pr < 1$. The temperature profiles show the trend that Schlichting's similarity solution will be valid far away from the slot exit. Figure 4.1.32 shows the same data with jet temperature half width as the characteristic length. It is observed that the temperature profiles for all the Reynolds numbers are coincident just like the velocity profiles in Figure 4.1.21. Figures 4.1.33 and 4.1.34 show the variation of temperature with η and $Y/Y_{0.5T}^*$ respectively at $X= 27.68$, $Pr= 0.72$ and $Re= 60, 90, 120$ and 150 for the parabolic slot exit profiles. The trends are very similar to Figure 4.1.31 and 4.1.32 respectively except that the temperature profile for $Re= 60$ deviates from the similarity trend. The coincidence of data in Schlichting's similarity variable η is better than that for uniform slot-exit profiles.

Figures 4.1.35 and 4.1.36 show the variation of T^*/T_j^* with η

for $Re= 60$ and $Pr= 0.72$ for uniform and parabolic slot-exit profiles respectively at $X= 3.78, 7.43, 19.27$ and 27.68 . Temperature level is higher near the slot-exit at $X= 3.78$ as compared to that at $X= 27.68$. The potential core has disappeared at $X= 3.78$ in Figure 4.1.35. The centreline temperature is larger for uniform slot-exit profiles and remains larger at all values of η as compared to those for parabolic slot-exit profiles at fixed value of X .

Figure 4.1.37 and 4.1.38 show T^*/T_c^* with η for uniform and the parabolic slot-exit profiles respectively at $X= 0.55, 3.78, 7.43, 19.27$ and 27.68 , $Pr= 0.72$ for $Re=90$. It is observed that at larger distance from the slot-exit, namely $X= 19.27$ and 27.68 , the temperature profiles become almost coincident, whereas velocity profiles did not show such a close similarity. The potential core is seen at $X= 0.55$. Figures 4.1.39 and 4.1.40 show the same temperature distributions T^*/T_c^* with jet temperature half width as the characteristic length. It is observed that temperature profiles tend to be similar except for the temperature very near the jet exit, namely $X= 0.55$. The trend towards similarity is better than that exhibited by the velocity profiles in Figures 4.1.11 and 4.1.12.

Figure 4.1.41 compares the velocity and temperature profiles at $Re= 90$, $X= 19.27$ and $Pr= 1.0$ for both the kinds of velocity and temperature profiles at the slot-exit. It is expected from Reynolds analogy that velocity and temperature profiles will become the same at $Pr= 1.0$. The figure shows that the temperature and velocity profiles are nearly same for both the types of

slot-exit profiles.

Figure 4.1.42 shows the variation of jet temperature half width $Y_{0.5T}^*$, for $Pr = 0.72$ and $Re = 60$ and 90 , and for both the types of slot-exit profiles. The half width increases in the flow direction. A comparison with the jet velocity half width plotted in Figure 4.1.23 indicates that the half width for temperature is larger than that for the velocity, which is expected for $Pr < 1$. The jet temperature half width is independent of Reynolds number.

Figure 4.1.43 shows the temperature variation with η at $Re = 90$, $X = 19.27$ and $Pr = 0.01, 0.1, 1.0$ and 10.0 for both the types of slot-exit velocity and temperature profiles. It is observed that at low value of Prandtl number, namely $Pr = 0.1$, the temperature remains unaffected upto certain distance in η direction and then slowly decreases. The temperature decreases very sharply at higher values of Prandtl numbers. T^*/T_C^* has larger values for parabolic slot-exit profiles as compared to those for the uniform slot-exit profiles at lower Prandtl numbers, while for $Pr = 10$, the trend is opposite of this. The temperature will actually be larger for uniform slot-exit profiles since T_C^* is larger for this slot-exit profiles.

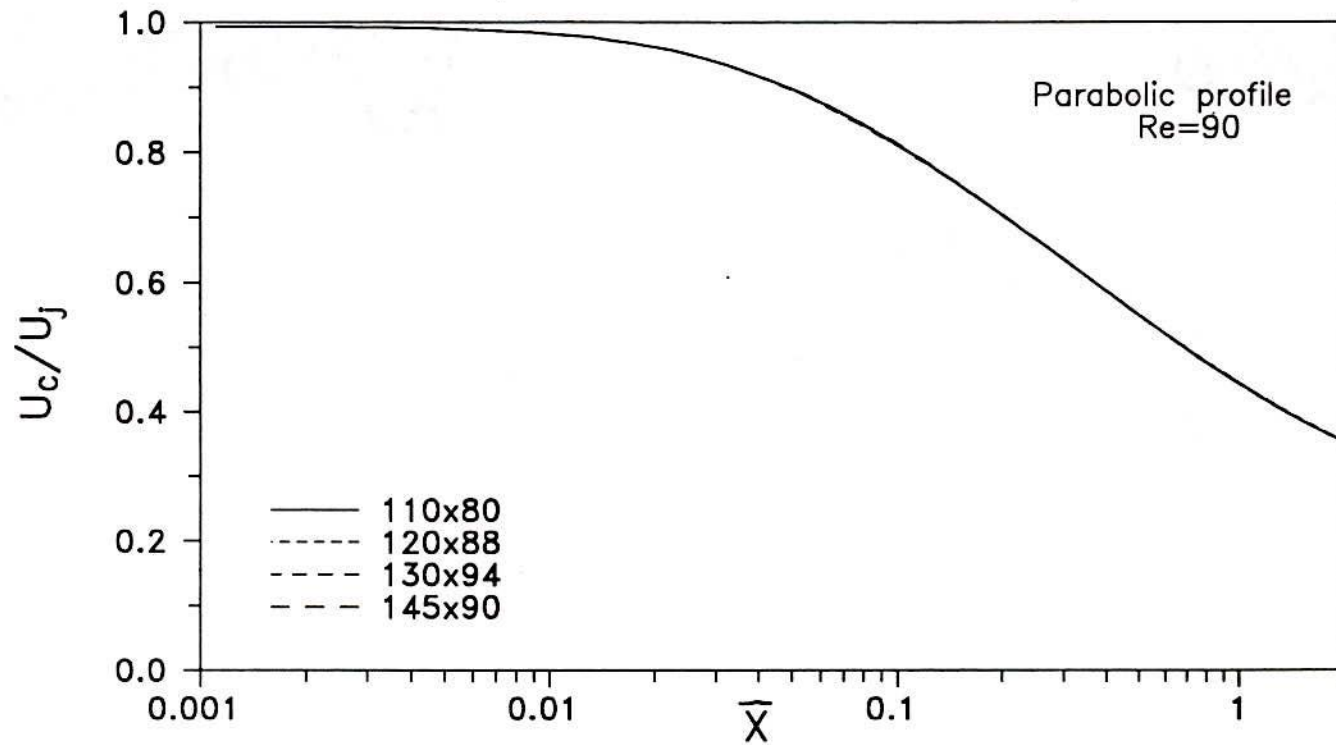


Fig4.1.1: Decay of centre line velocity for slot jet showing the effect of different grid sizes.

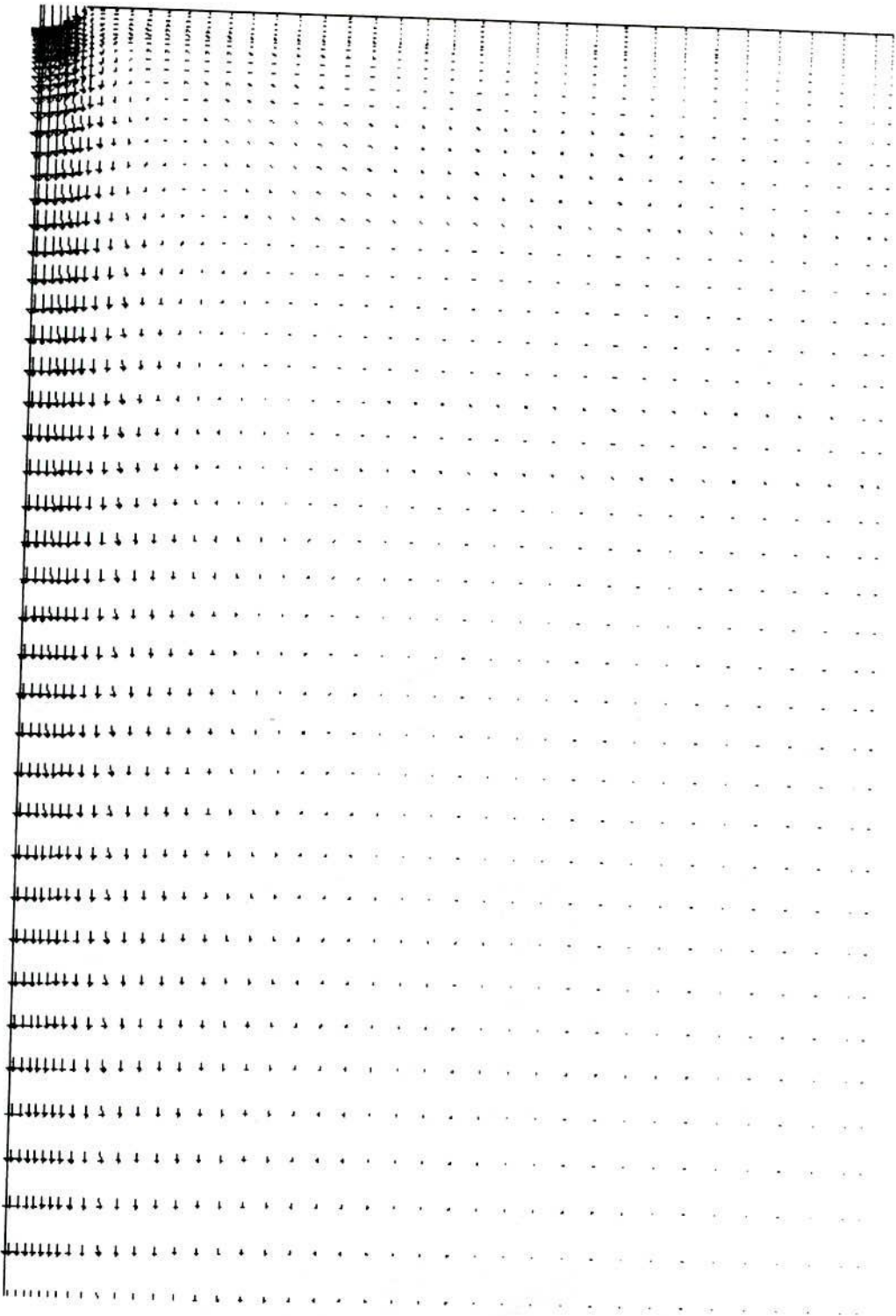


Fig. 4.12 : Velocity vector plot at $Re = 60$

Laminar slot jet with parabolic velocity profile at slot exit

Free slot jet Re=60, Stream lines (Parabolic)

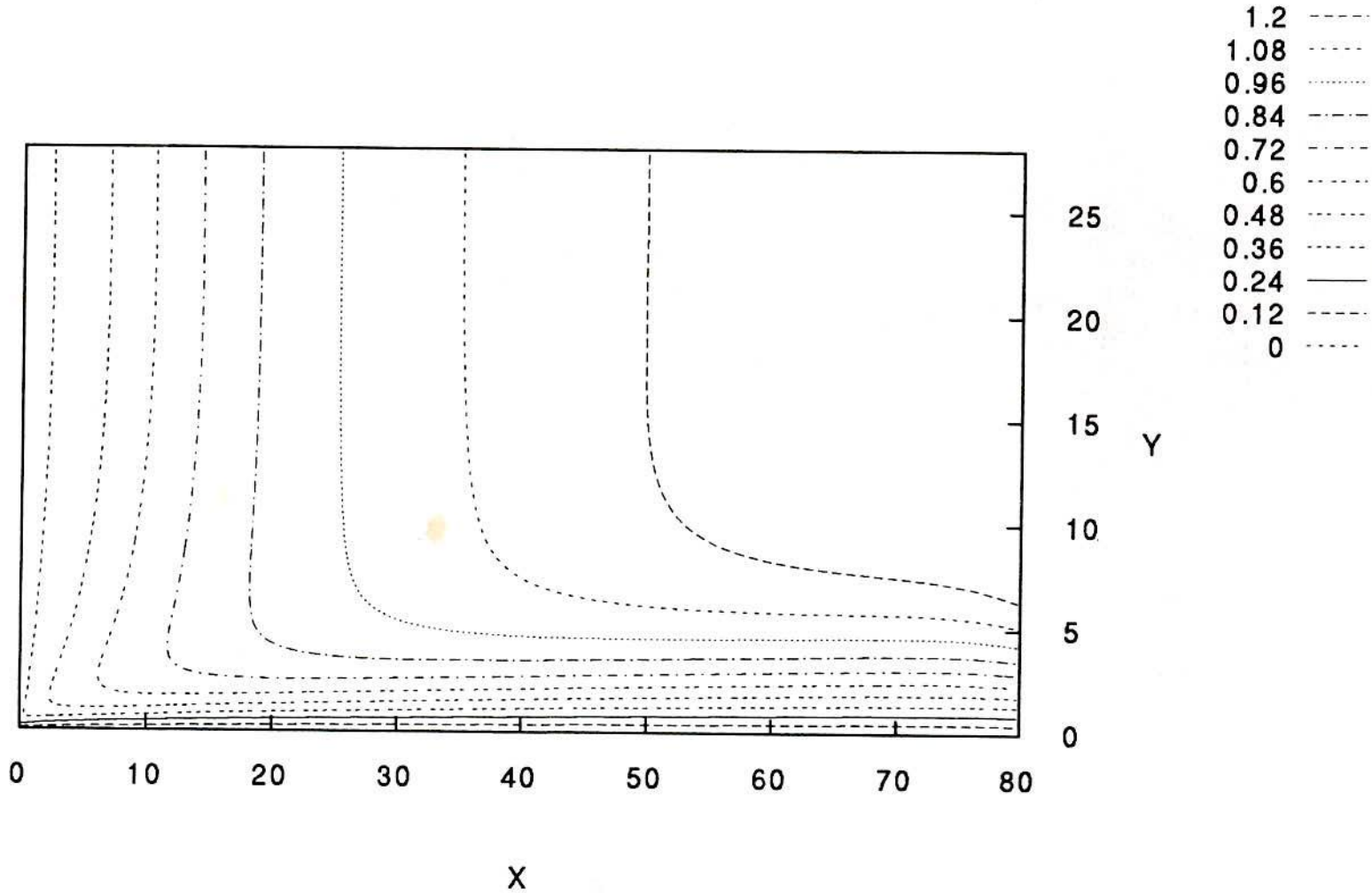


Fig.4.1.3: Streamlines at Re= 60 with parabolic slot exit velocity profile.

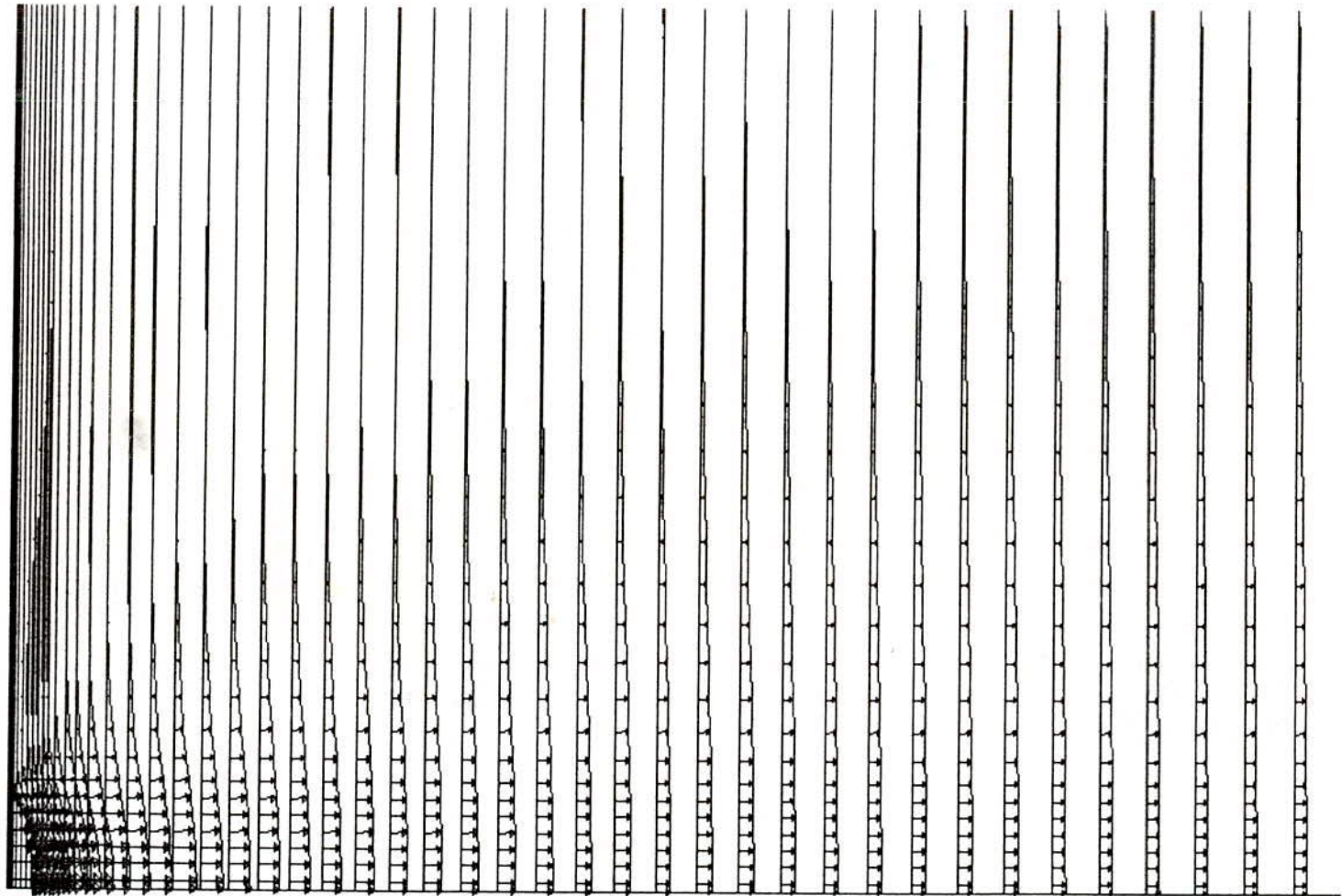


Fig. 4.1.4 : Velocity profiles at different axial locations at $Re = 60$

Laminar slot jet with parabolic jet exit velocity profile.

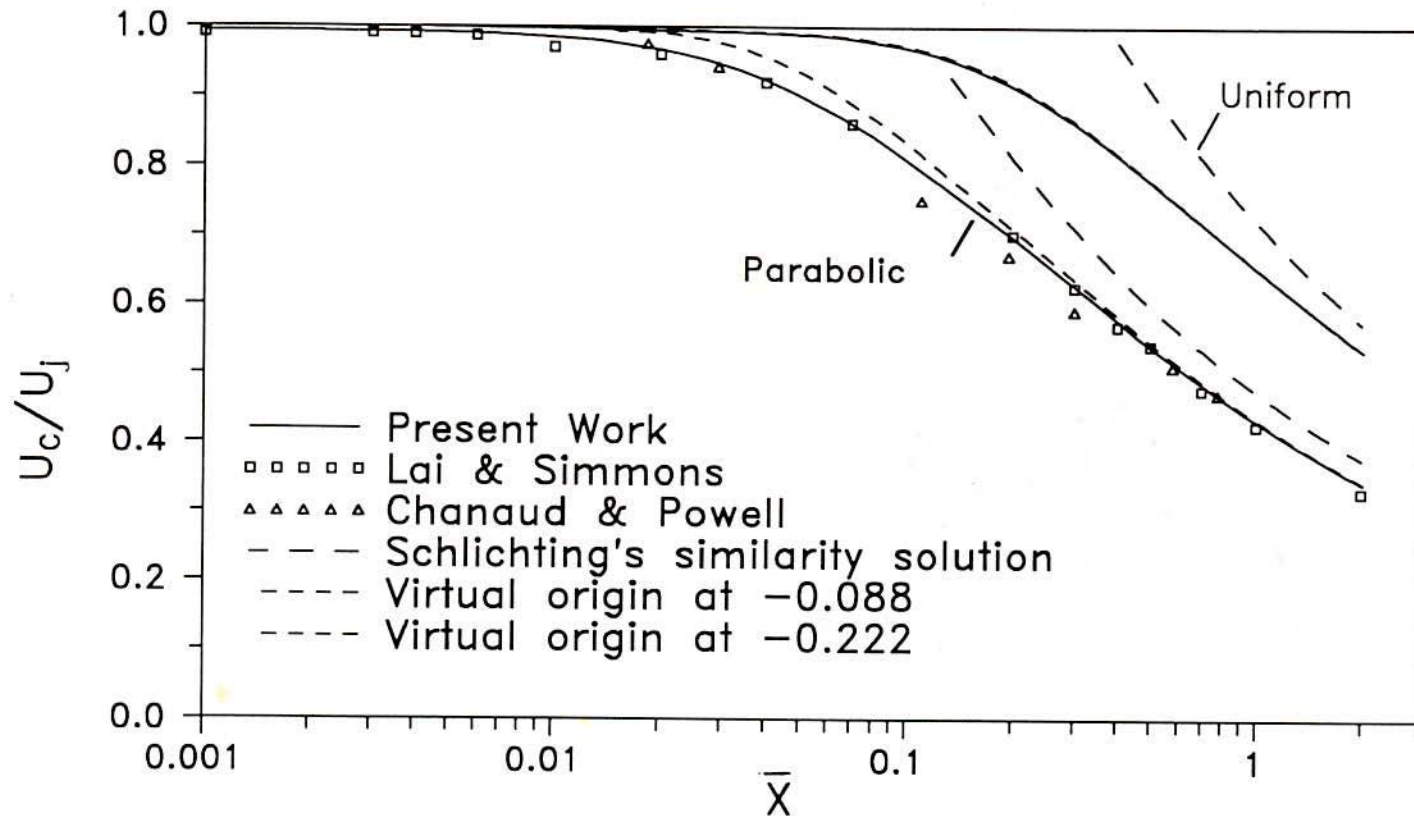


Fig4.1.5: Decay of centre line velocity for slot jet. A comparison with the published results.

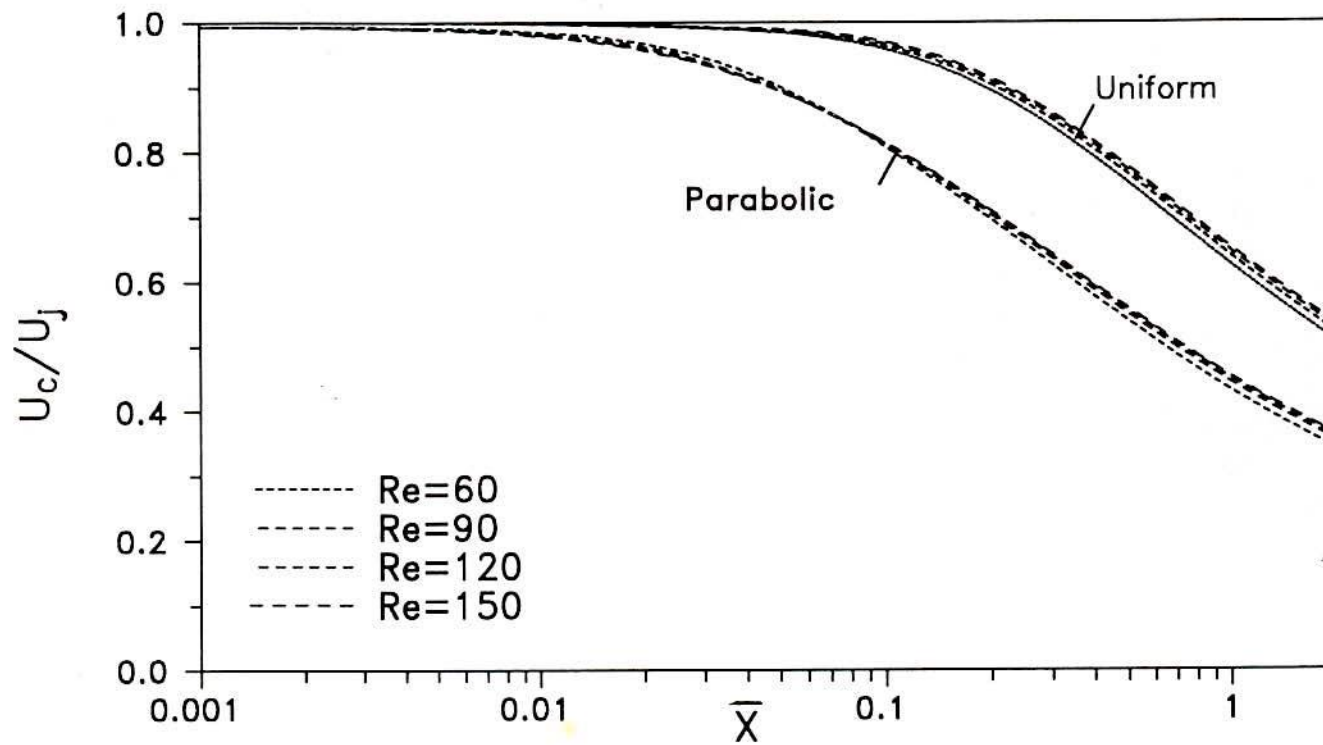


Fig.4.1.6: Decay of centre line velocity for slot jet.

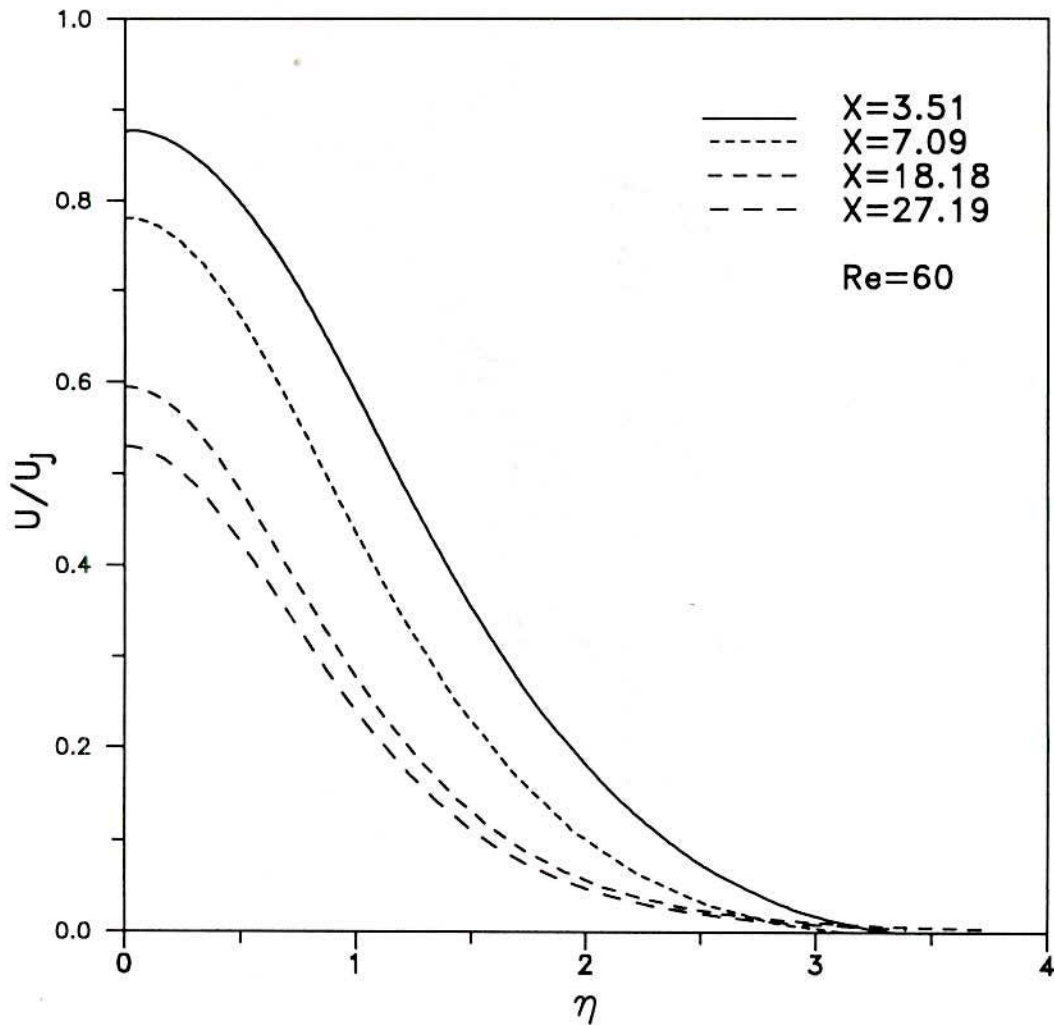


Fig.4.1.7: Axial velocity distribution at different X locations for slot jet with uniform jet exit velocity profile.



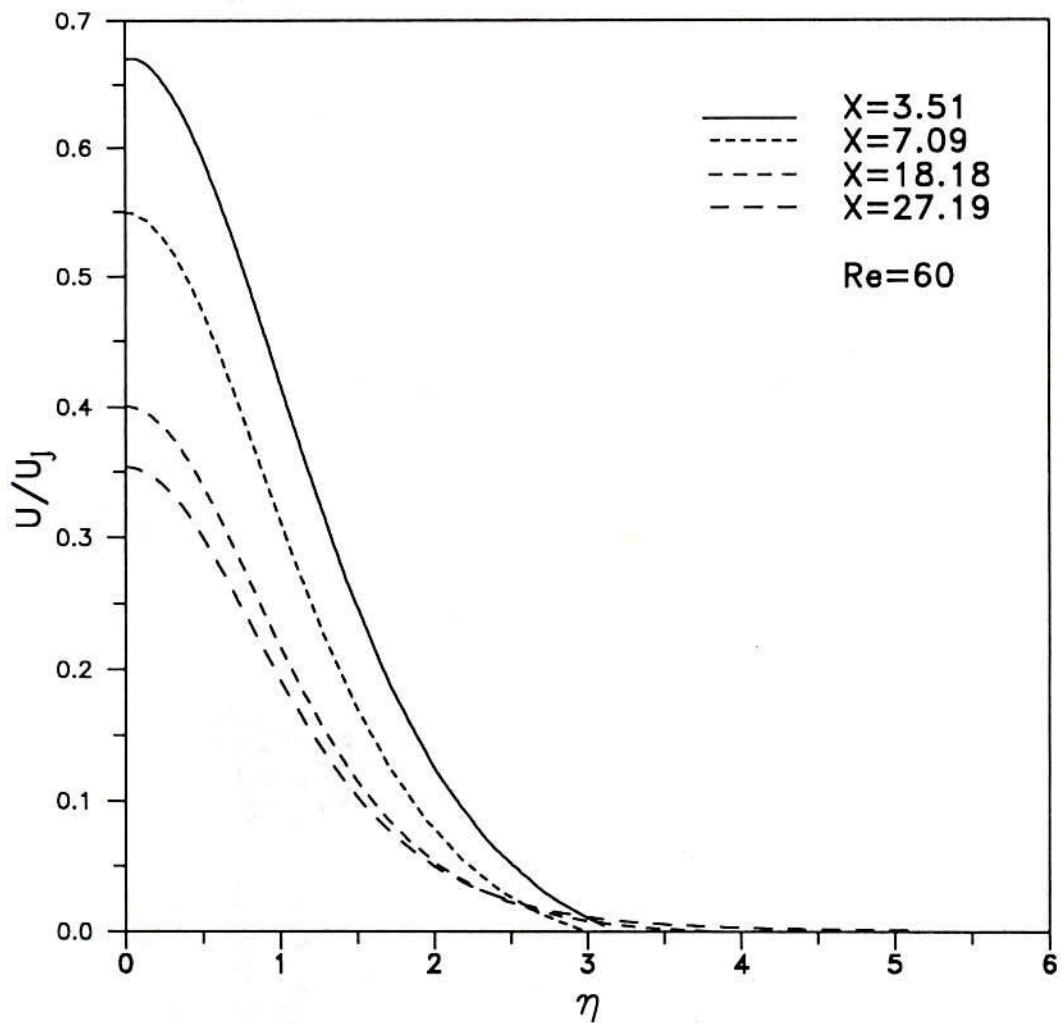


Fig.4.1.8: Axial velocity distribution at different X locations for slot jet with parabolic jet exit velocity profile.

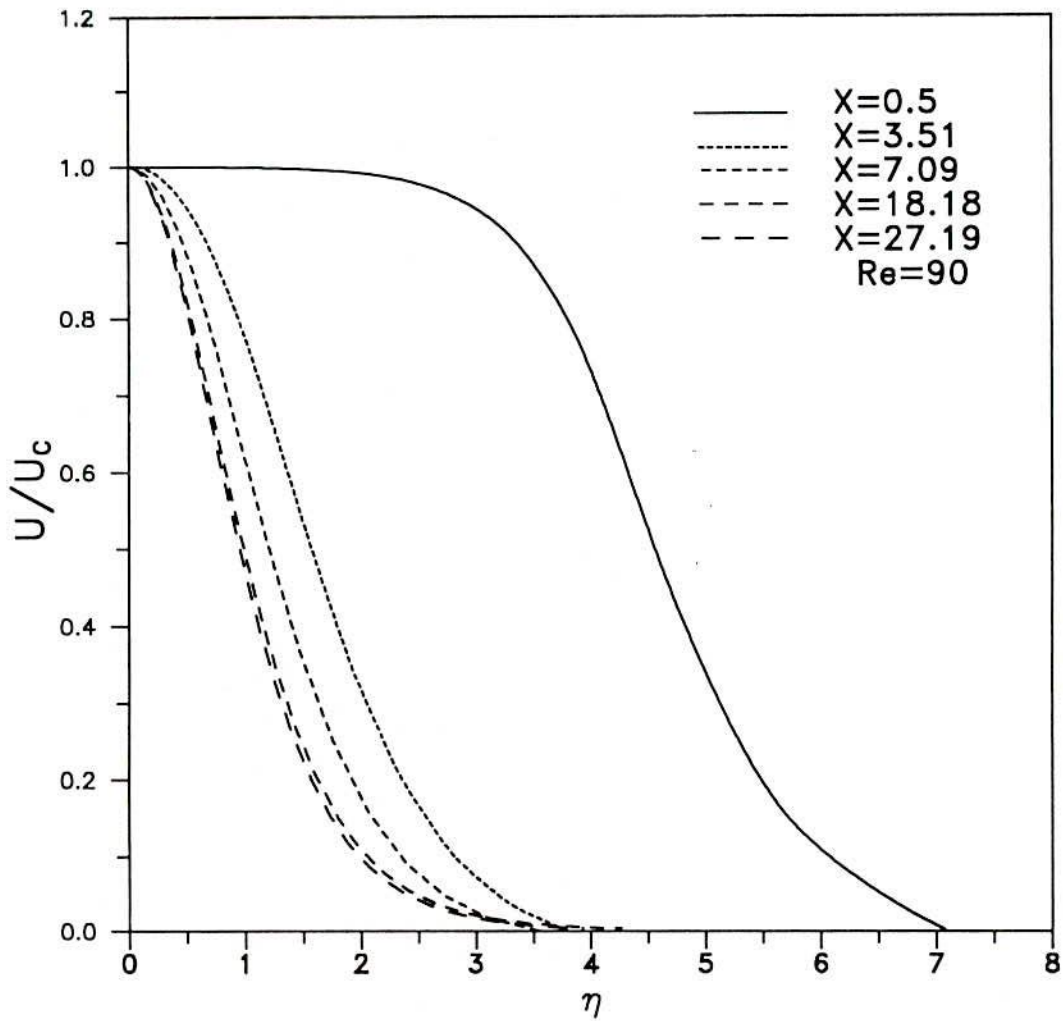


Fig.4.1.9; Axial velocity distribution at different X locations for slot jet with uniform jet exit velocity profile.

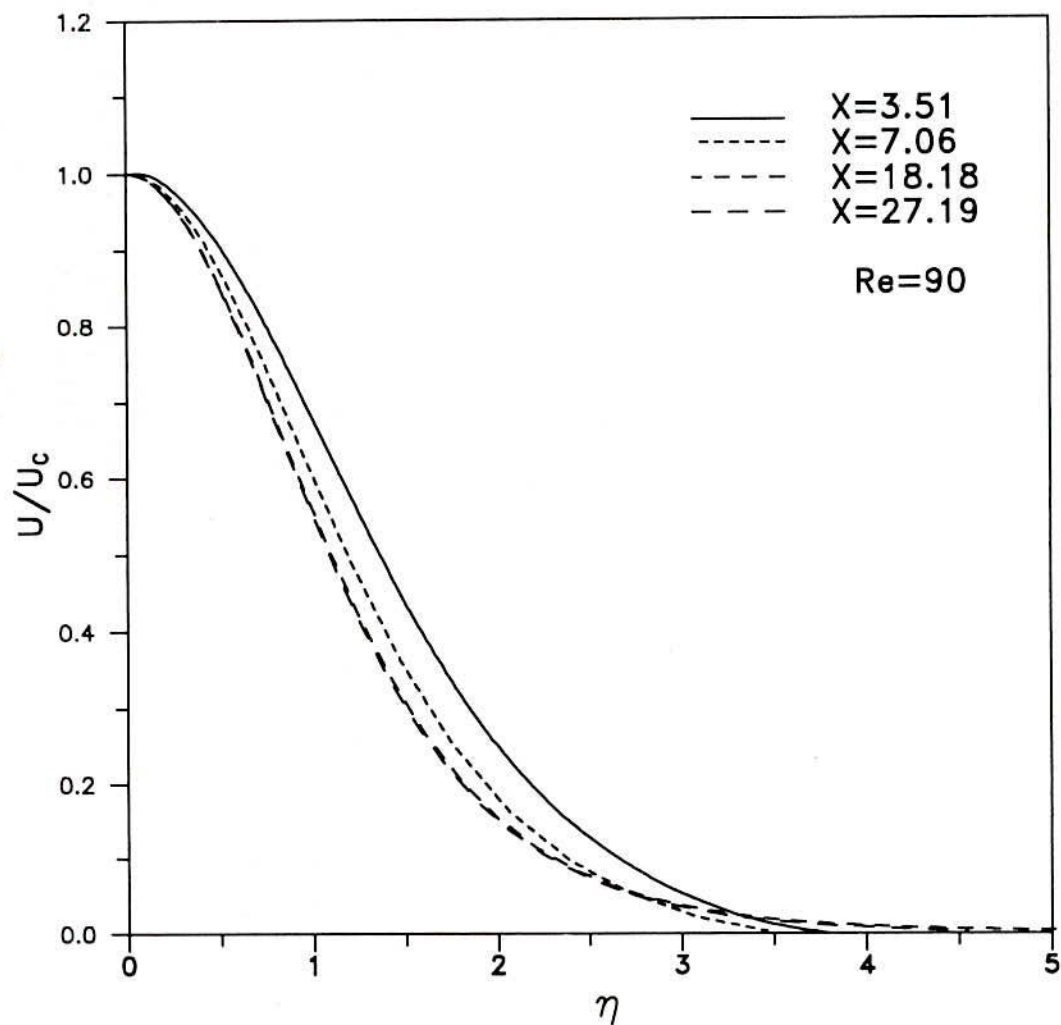


Fig4.1.10 Axial velocity distribution at different X locations for slot jet with parabolic jet exit velocity profile.

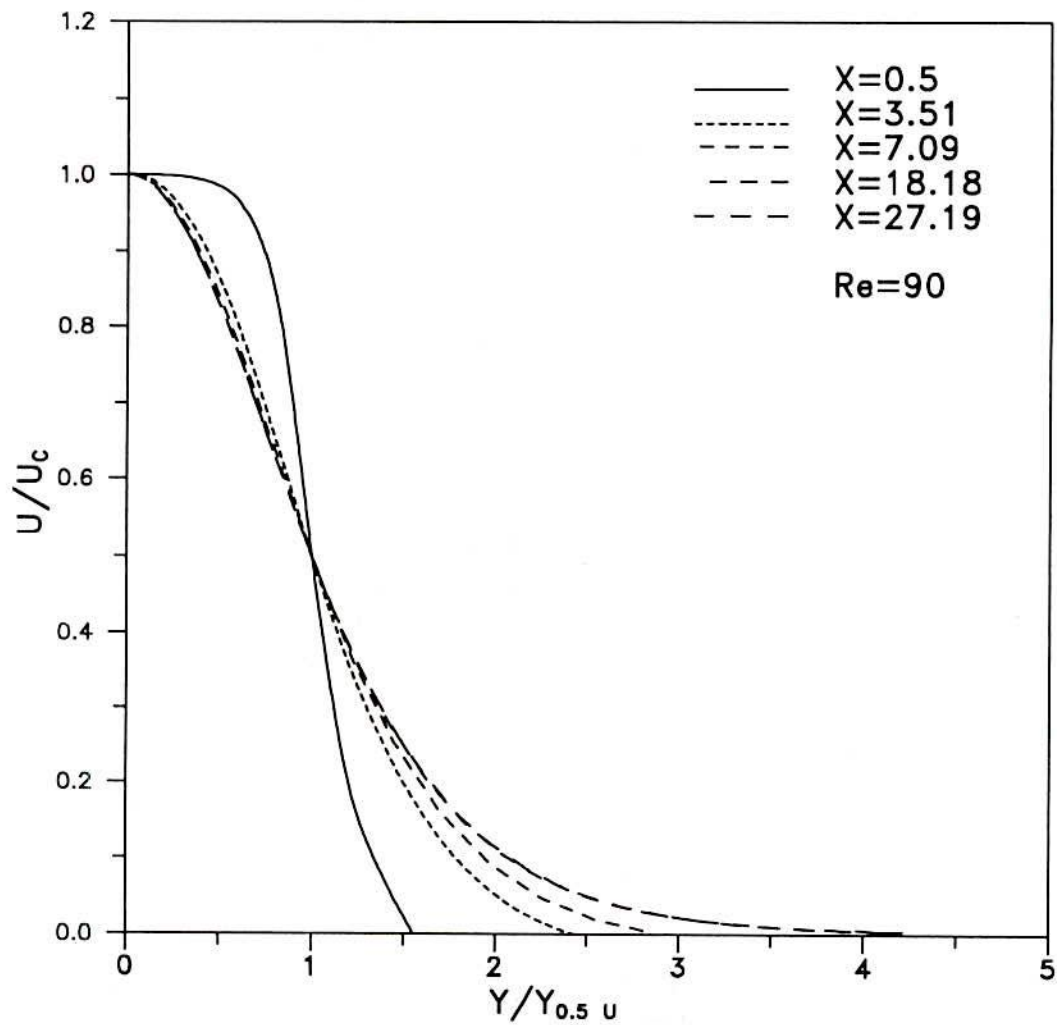


Fig.4.1.11 Axial velocity distribution at different X locations for slot jet with uniform jet exit velocity profile.

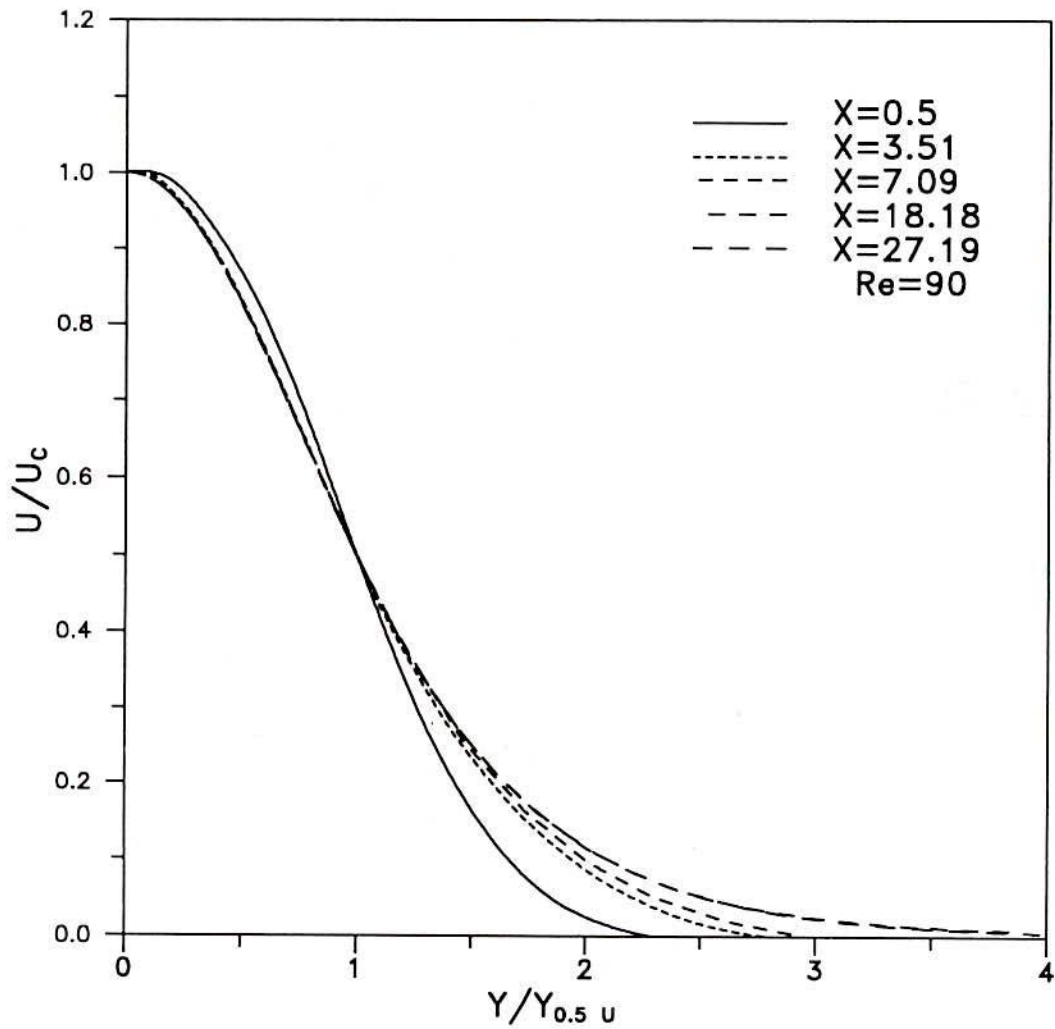


Fig. 4.1.12 Axial velocity distribution at different X locations for slot jet with parabolic jet exit velocity profile.

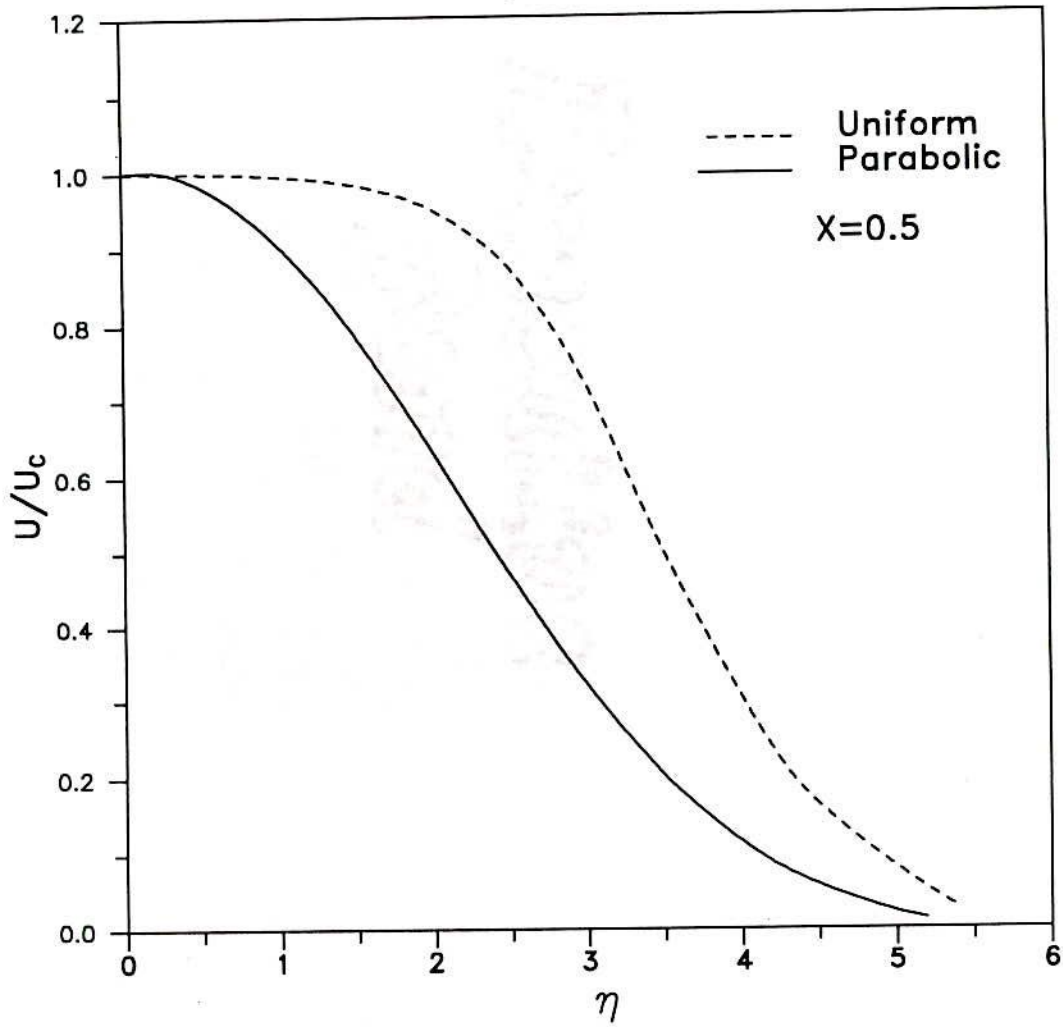


Fig.4.1.13: Axial velocity distribution at $Re=60$ for slot jet with uniform and parabolic velocity profile.

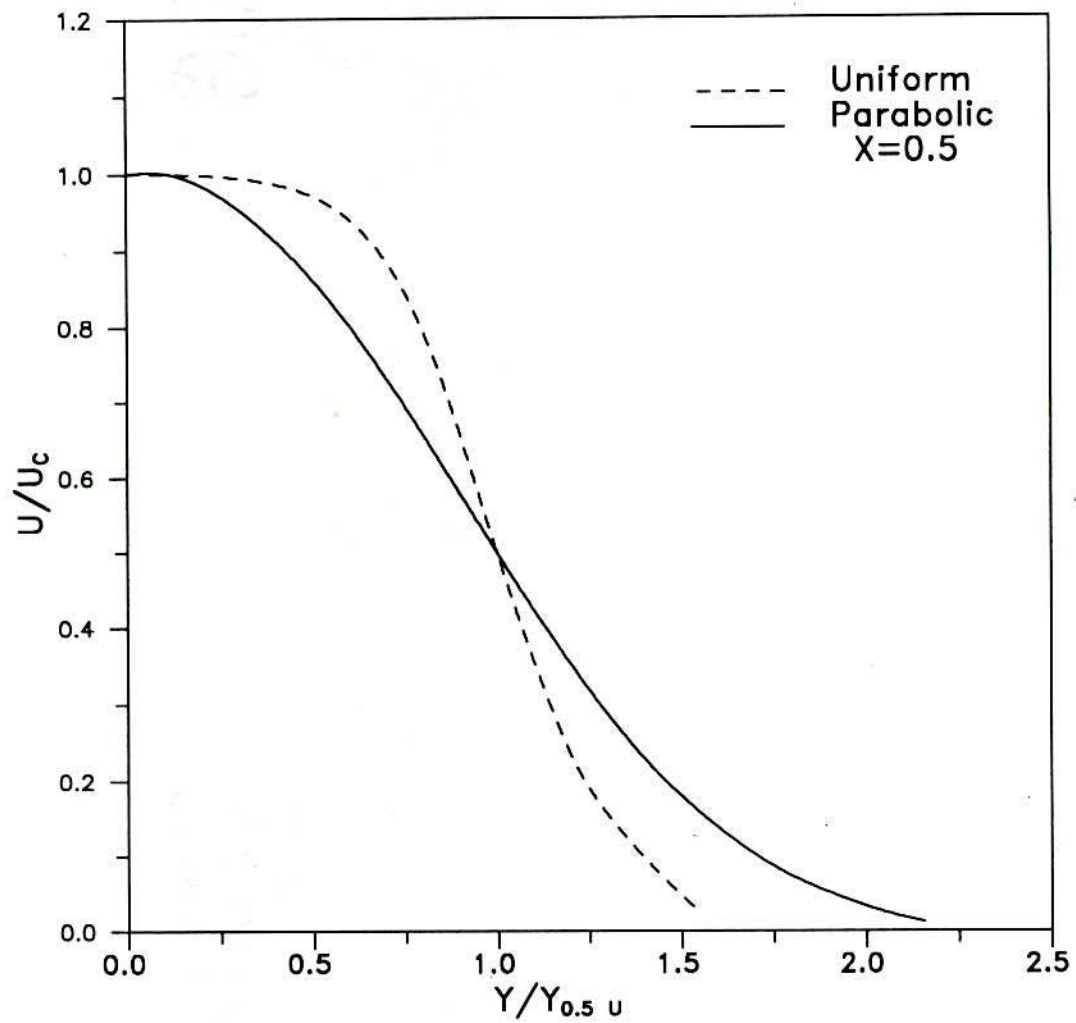


Fig.4.1.14: Axial velocity distribution at $Re=60$ for slot jet with uniform and parabolic velocity profile.

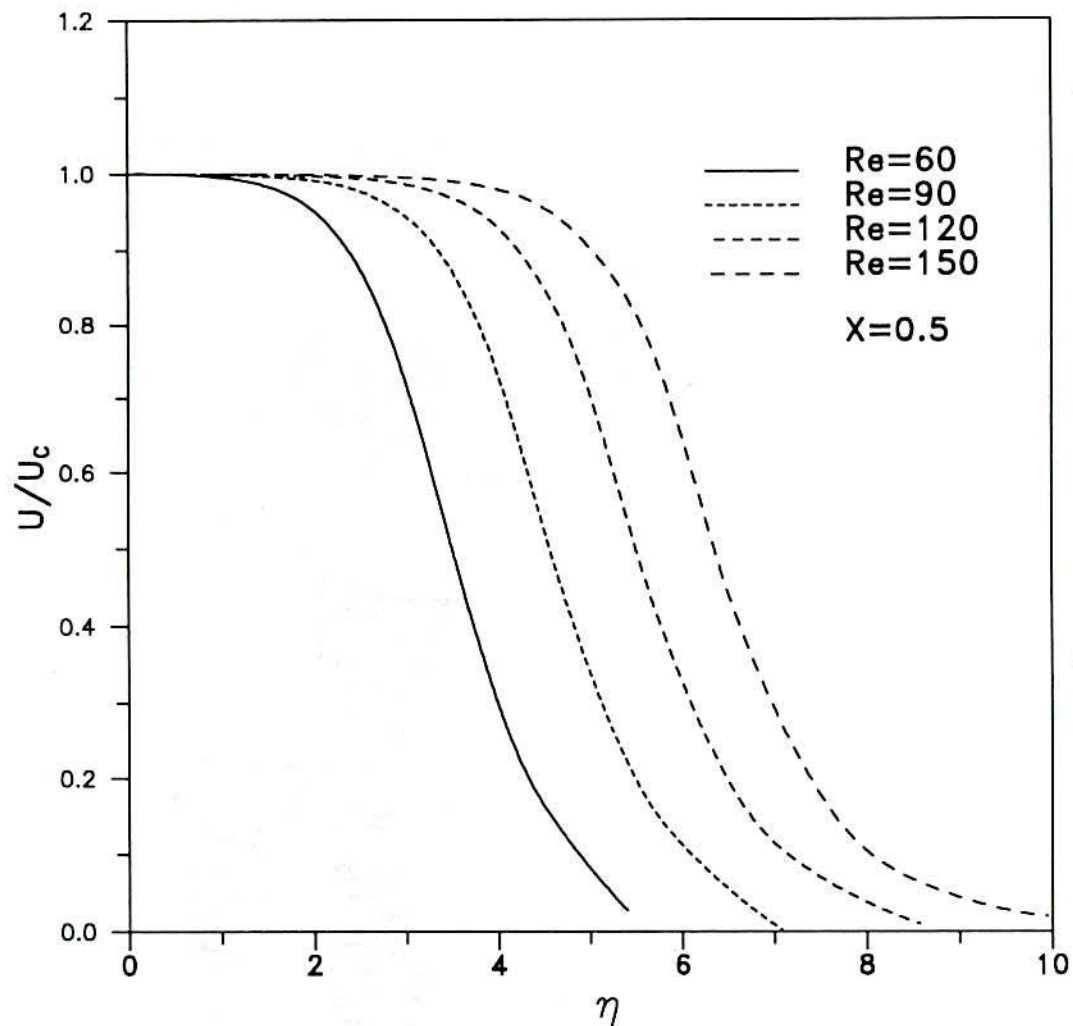


Fig.4.1.15: Axial velocity distribution at different Re for slot jet with uniform jet exit velocity profile.

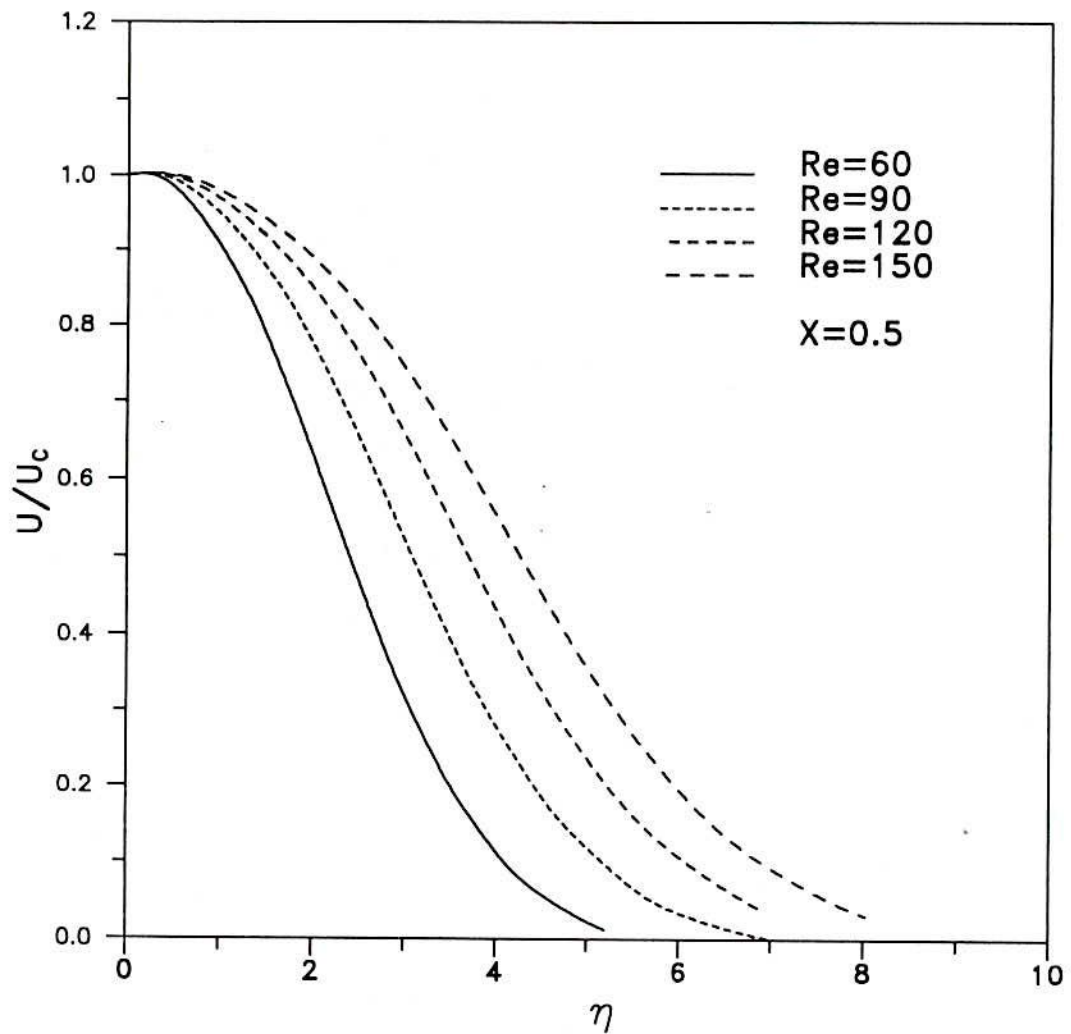


Fig.4.1.16: Axial velocity distribution at different Re for slot jet with parabolic jet exit velocity profile.

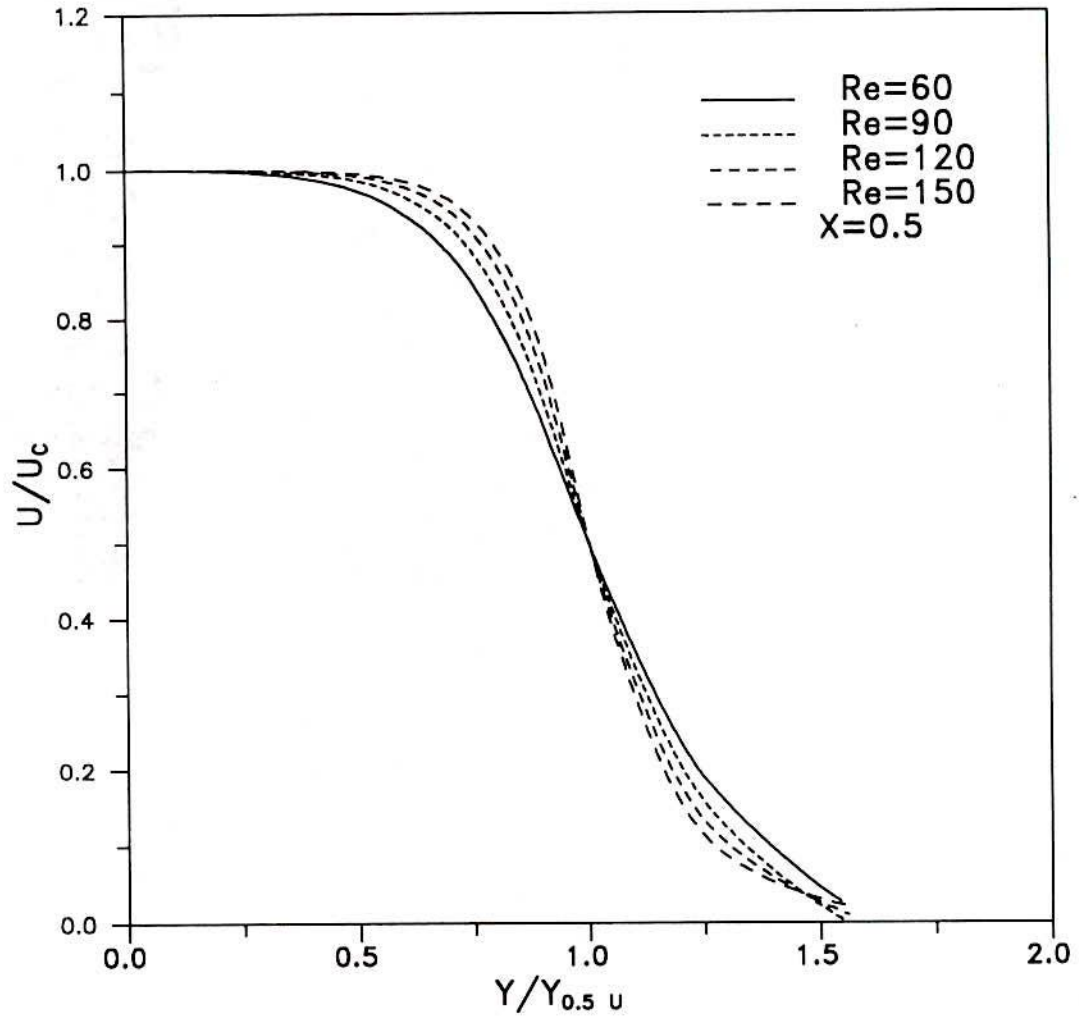


Fig.4.1.17: Axial velocity distribution at different Re for slot jet with uniform velocity profile.

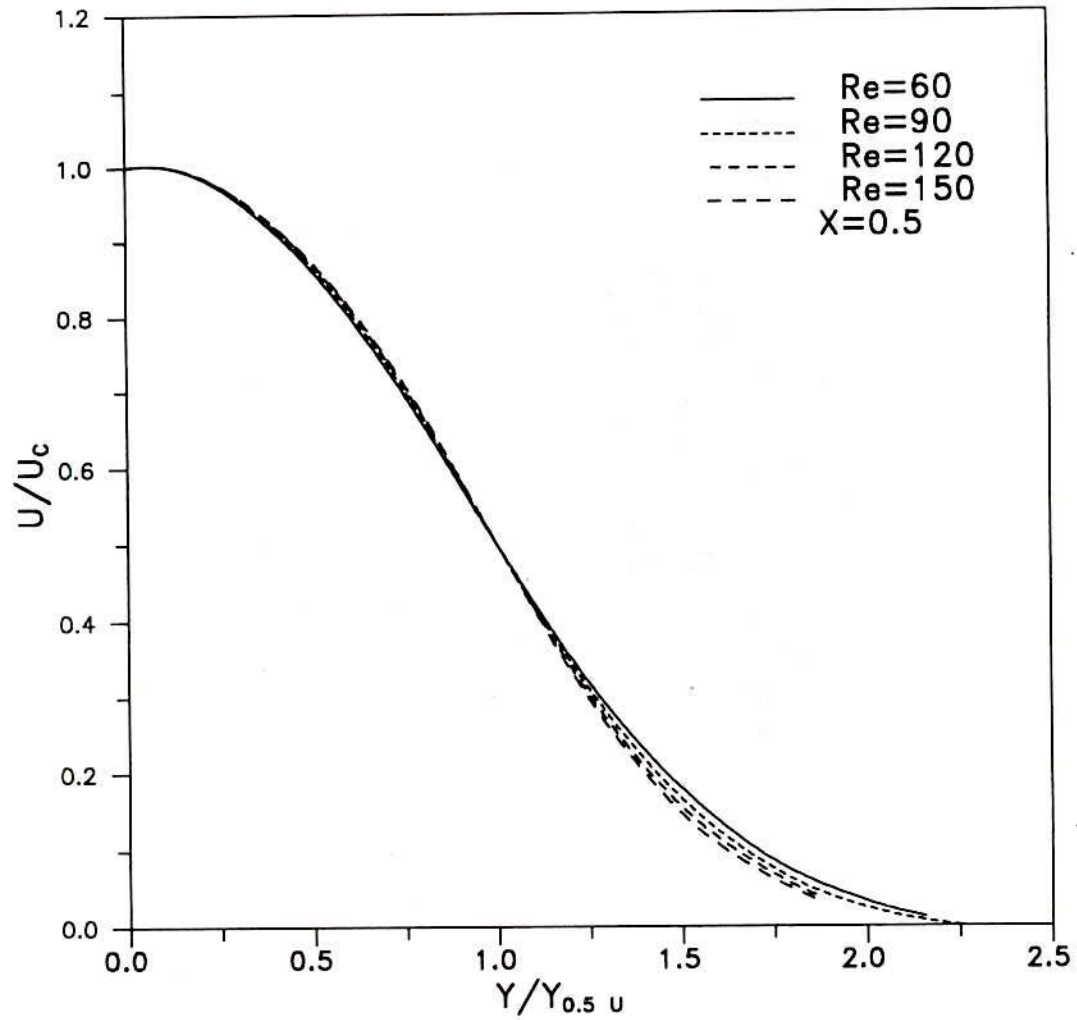


Fig.4.1.18 Axial velocity distribution at different Re for slot jet with parabolic velocity profile.

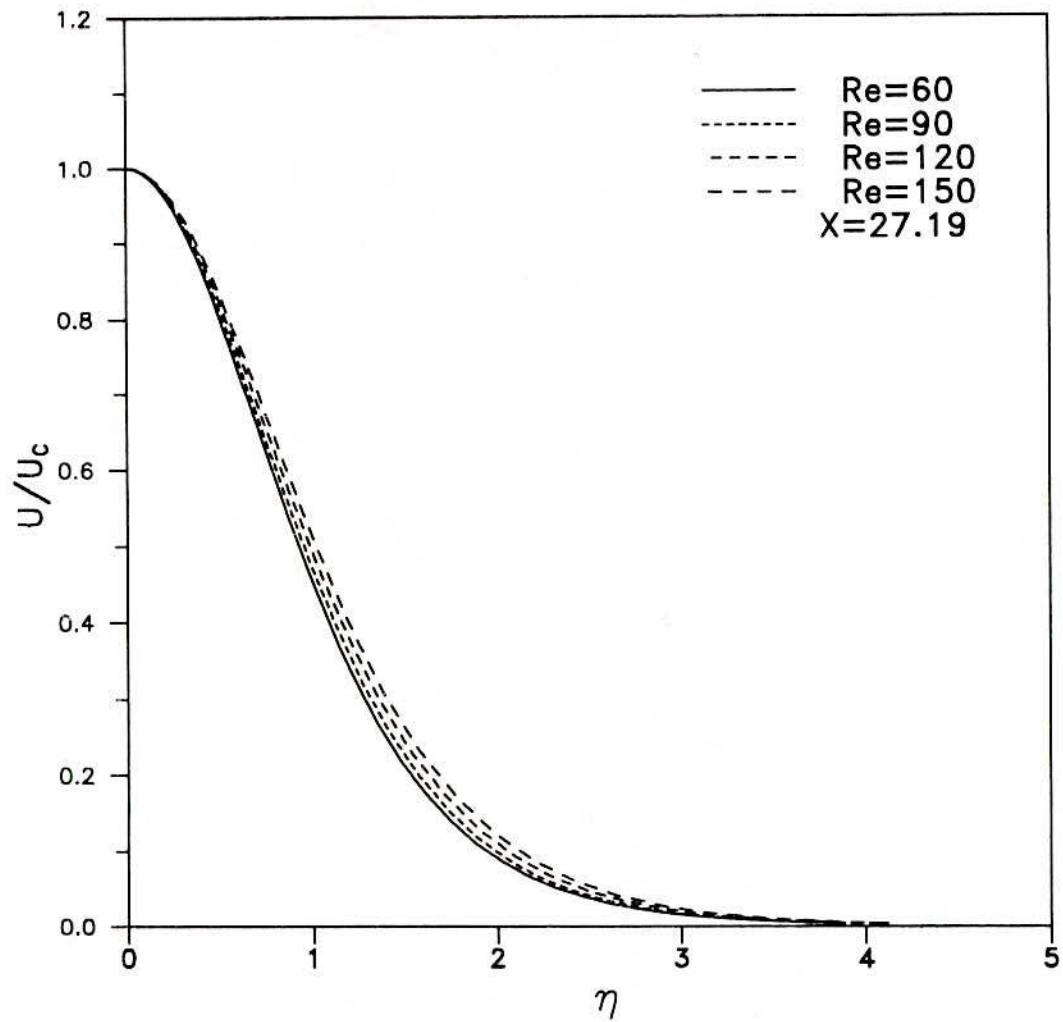


Fig.4.1.19: Axial velocity distribution at different Re for slot jet with uniform velocity profile.

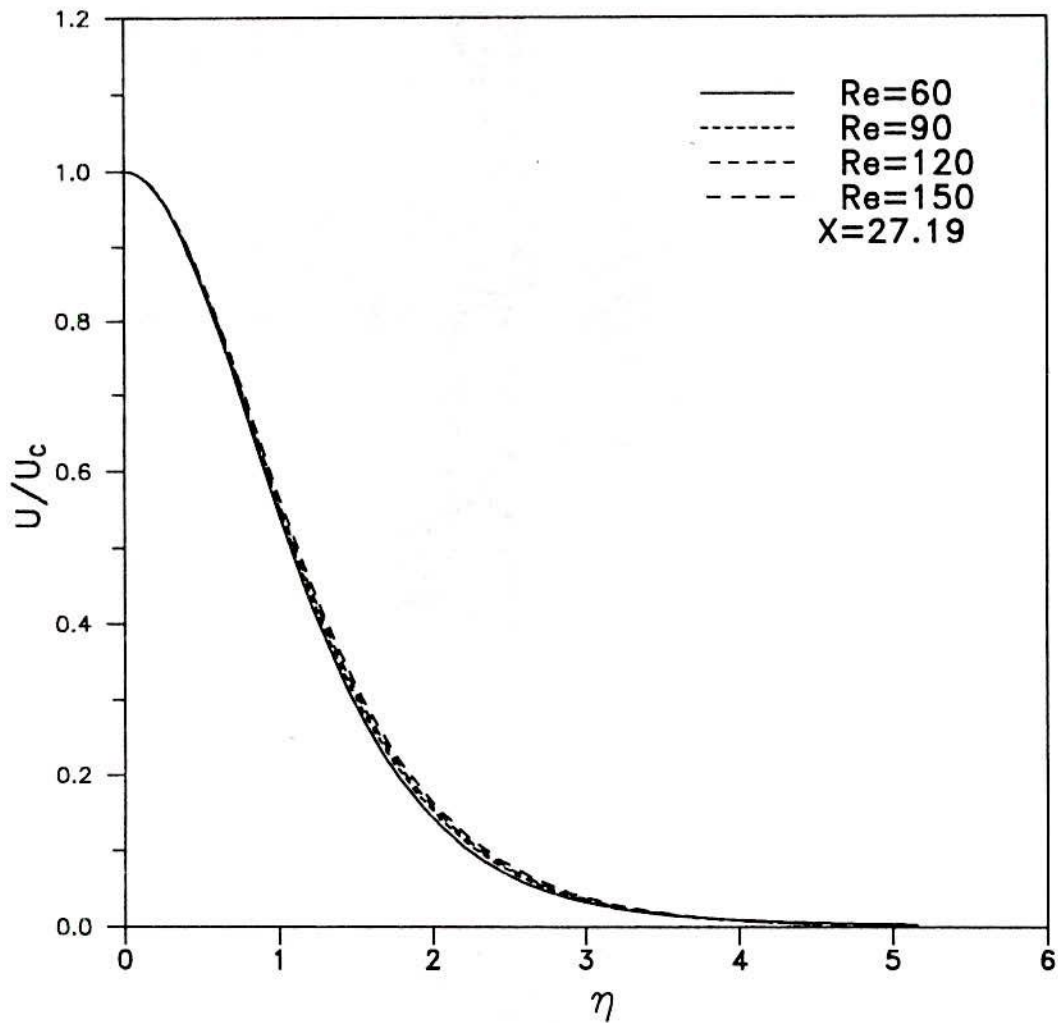


Fig.4.1.20: Axial velocity distribution at different Re for slot jet with parabolic velocity profile.

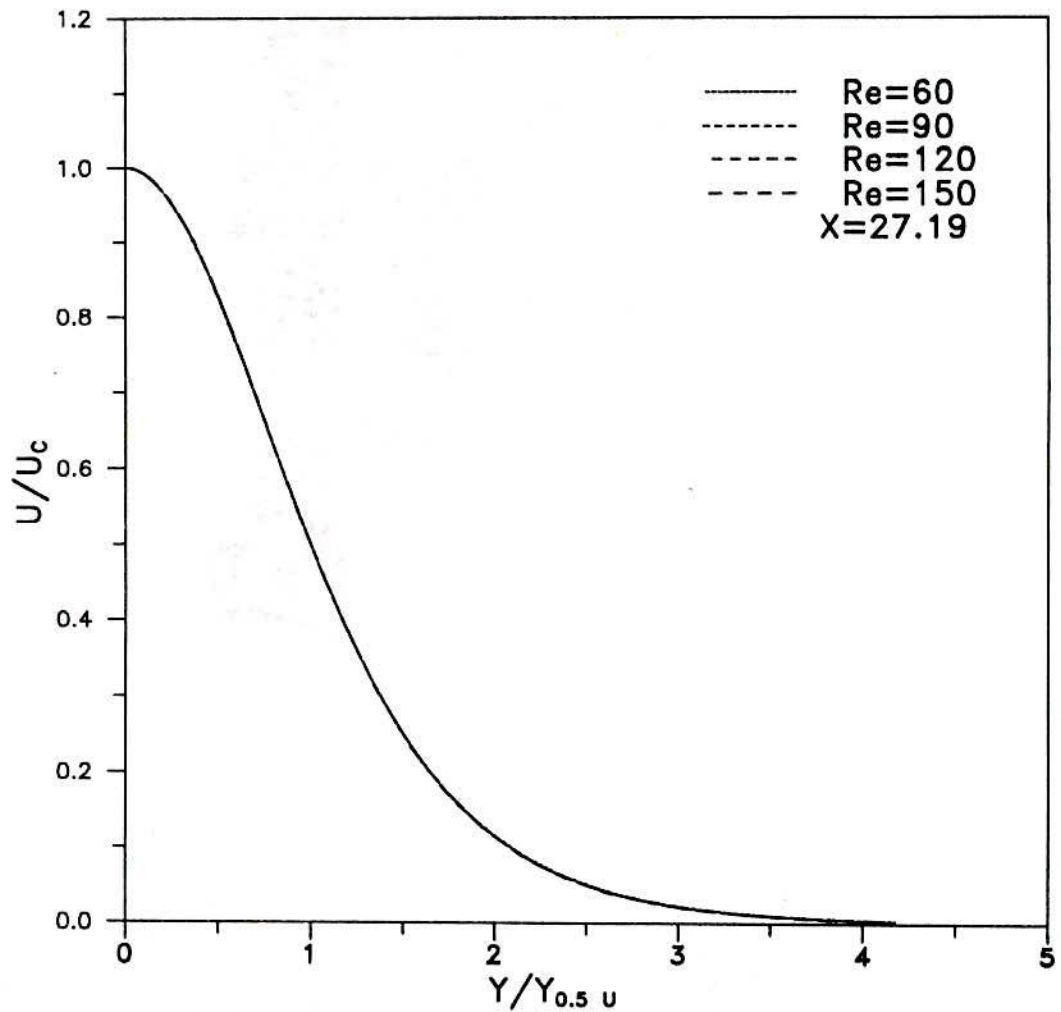


Fig.4.1.21: Axial velocity distribution at different Re for slot jet with uniform velocity profile.

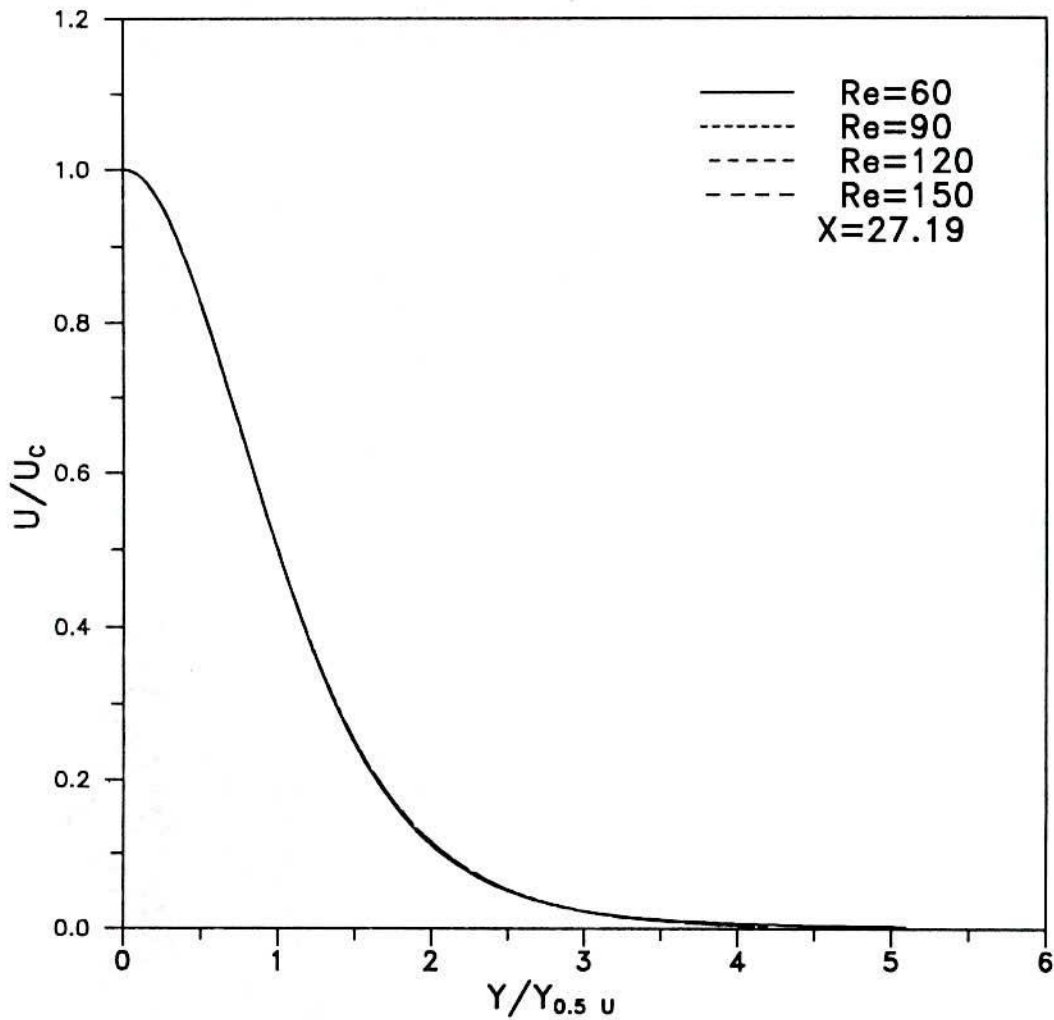


Fig.4.1.22: Axial velocity distribution at different Re for slot jet with parabolic velocity profile.

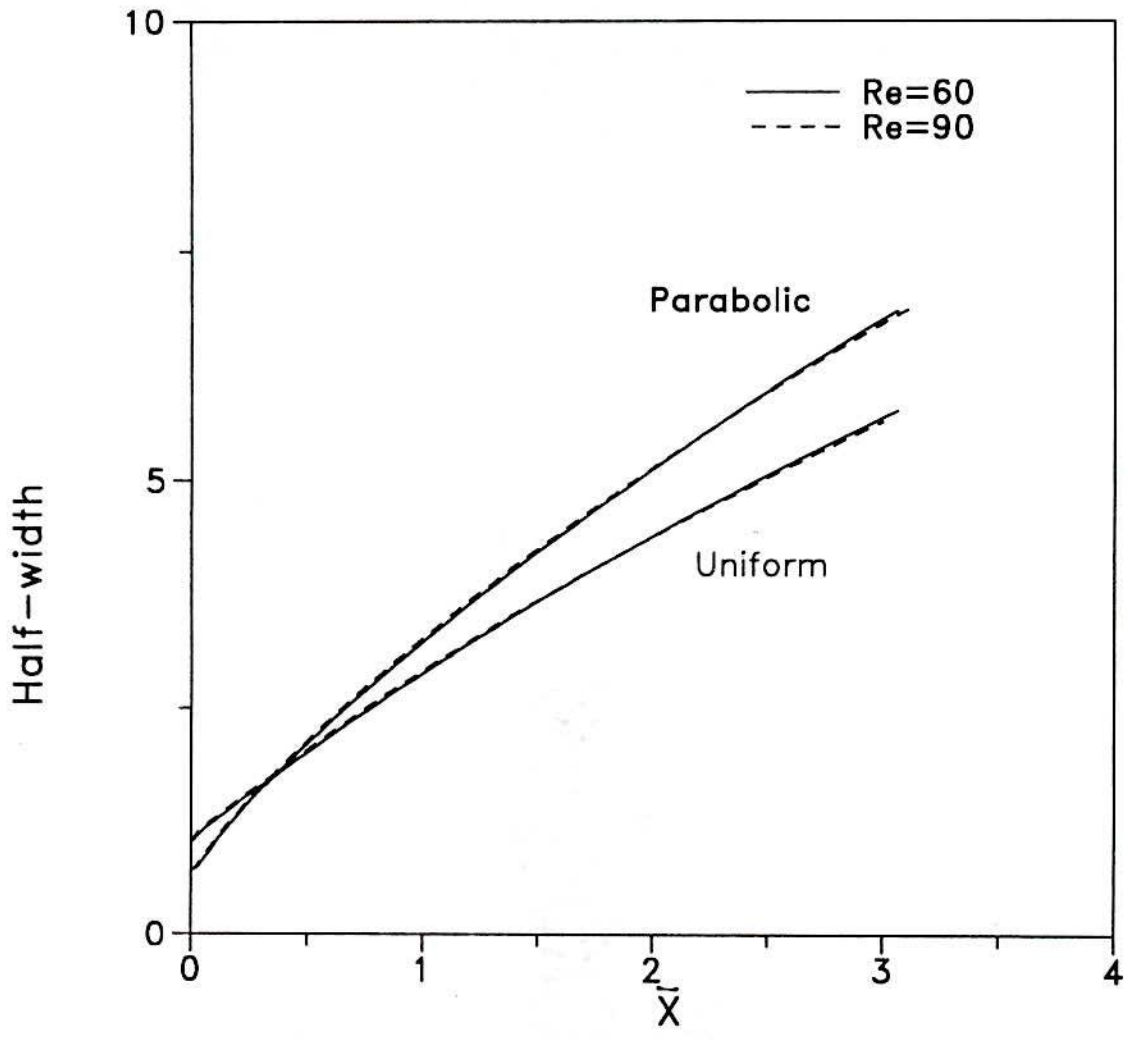
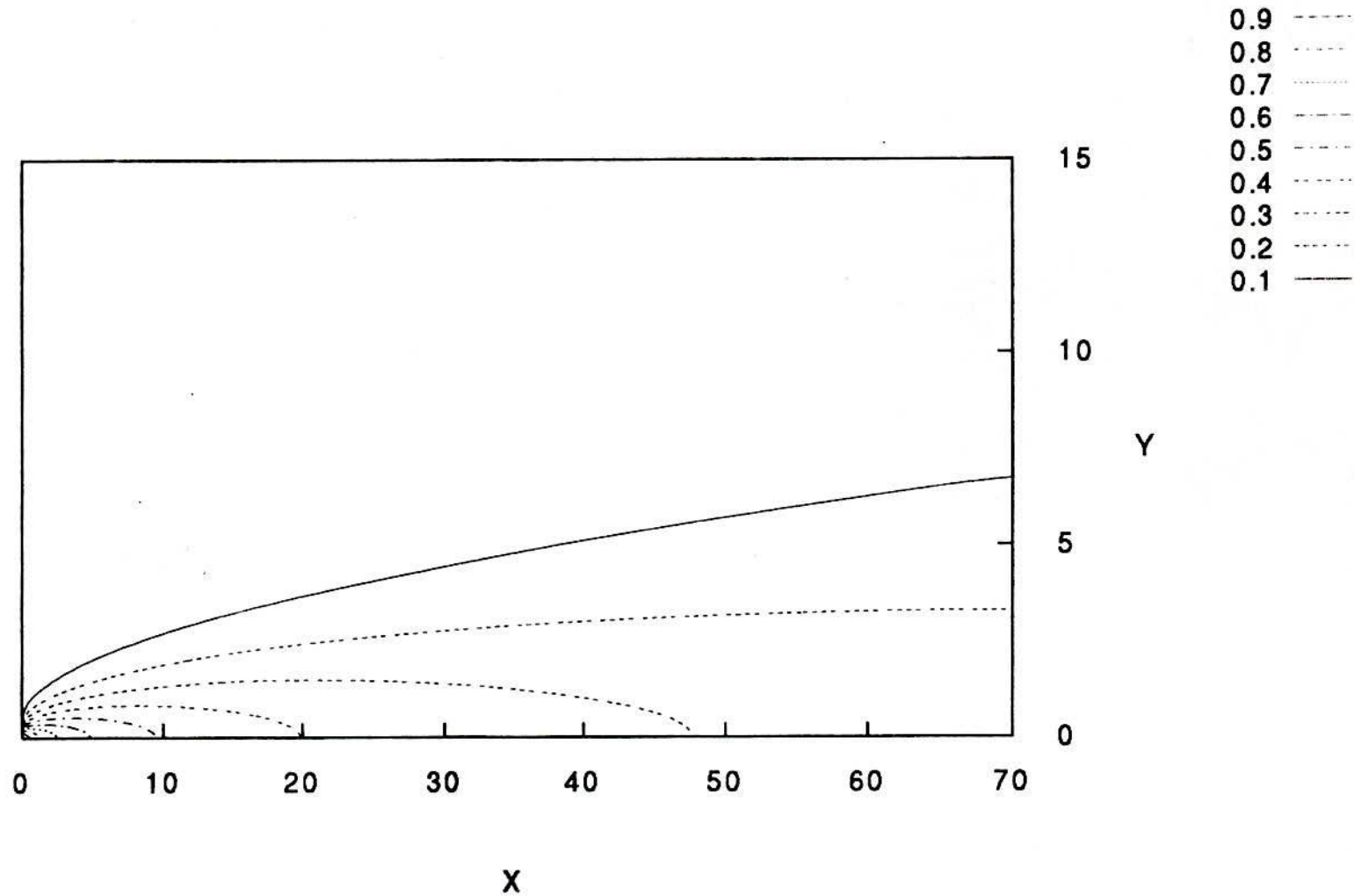


Fig.4.1.23: Spread of jet half width with uniform and Parabolic slot exit velocity profiles.

Free slot jet $Re=60$, Isotherms lines (Parabolic)Fig.4.1.24: Isotherms at $Re= 60$ with parabolic slot exit velocity profile.

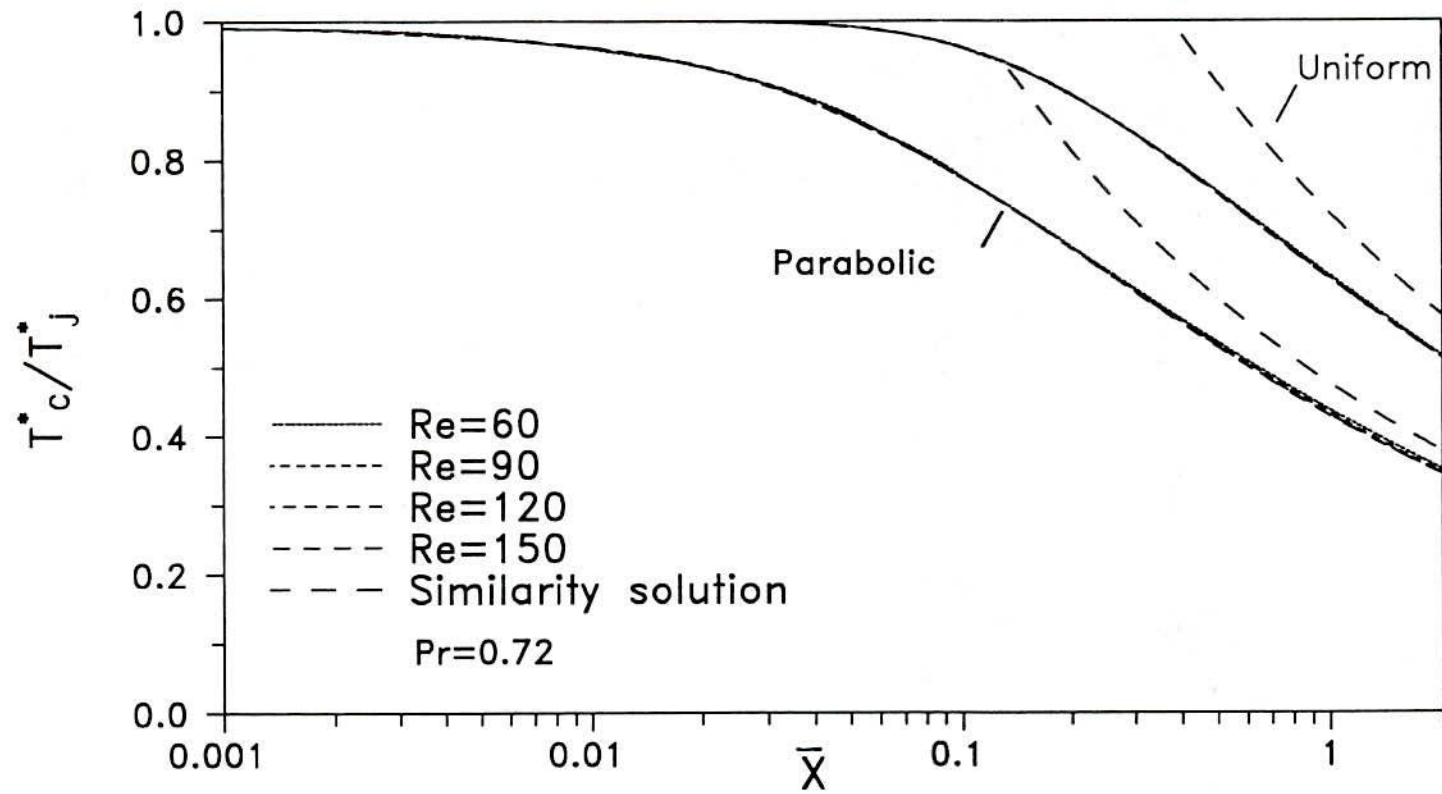


Fig. 4.1.25: Decay of centre line temperature for slot jet.

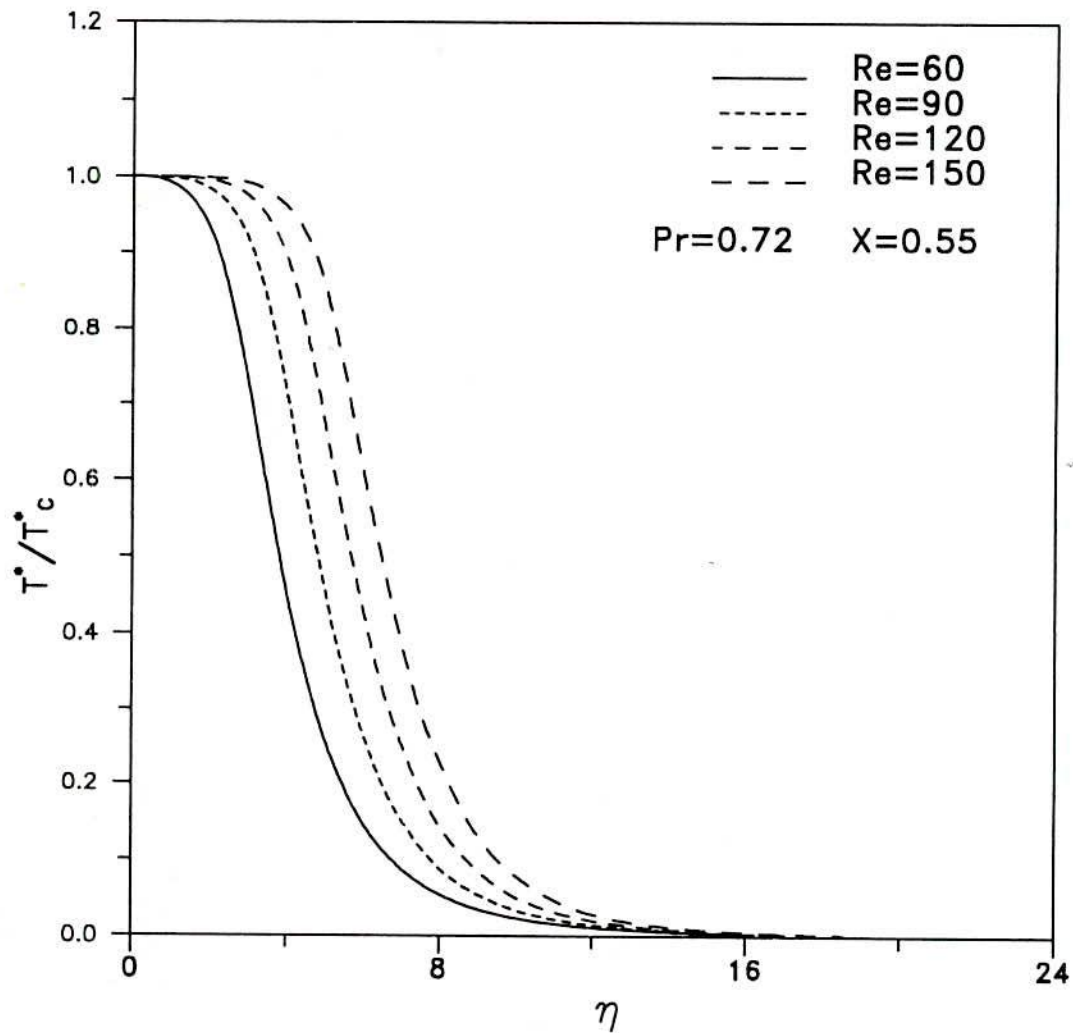


Fig.4.1.26: Temperature distribution at different Re for slot jet with uniform jet exit velocity and temperature profiles.

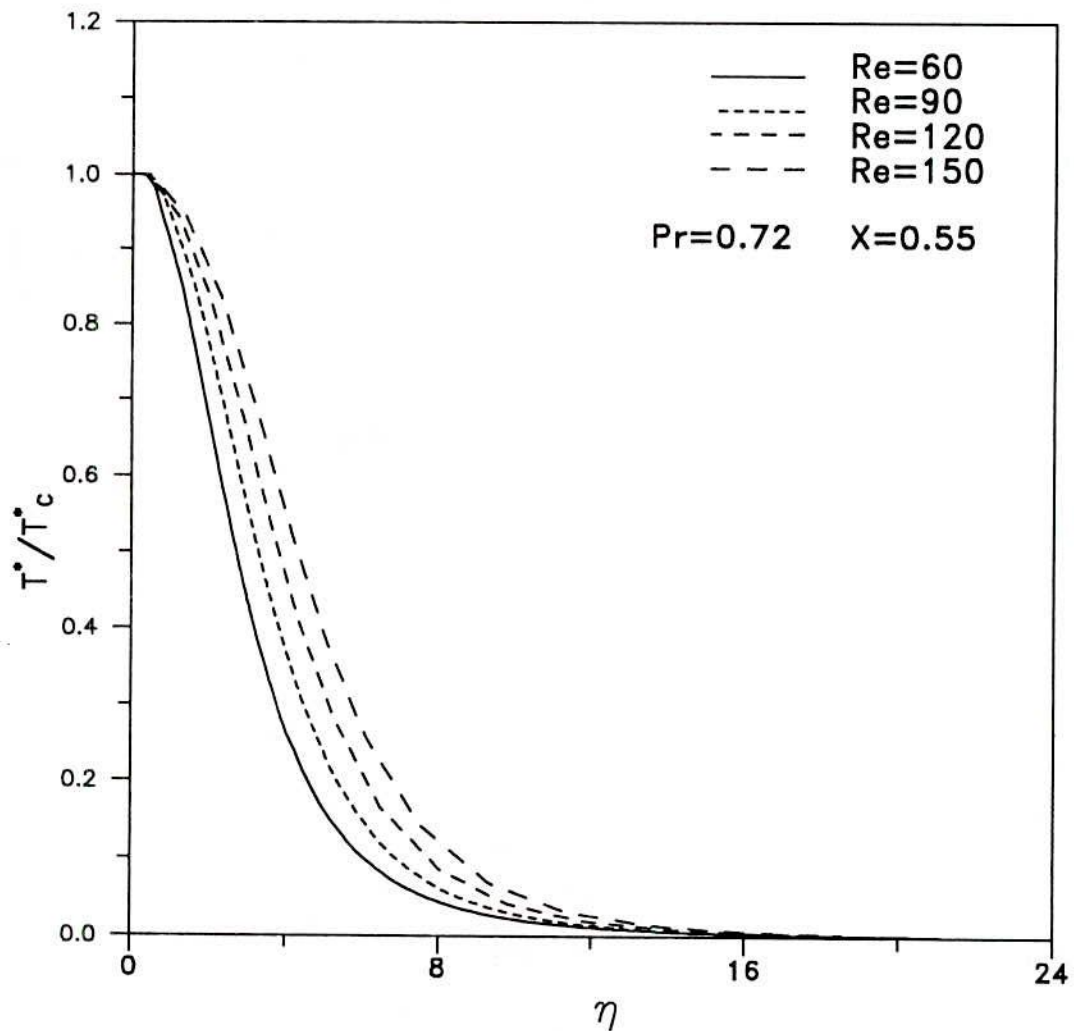


Fig.4.1.27: Temperature distribution at different Re for slot jet with parabolic jet exit velocity and temperature profiles.

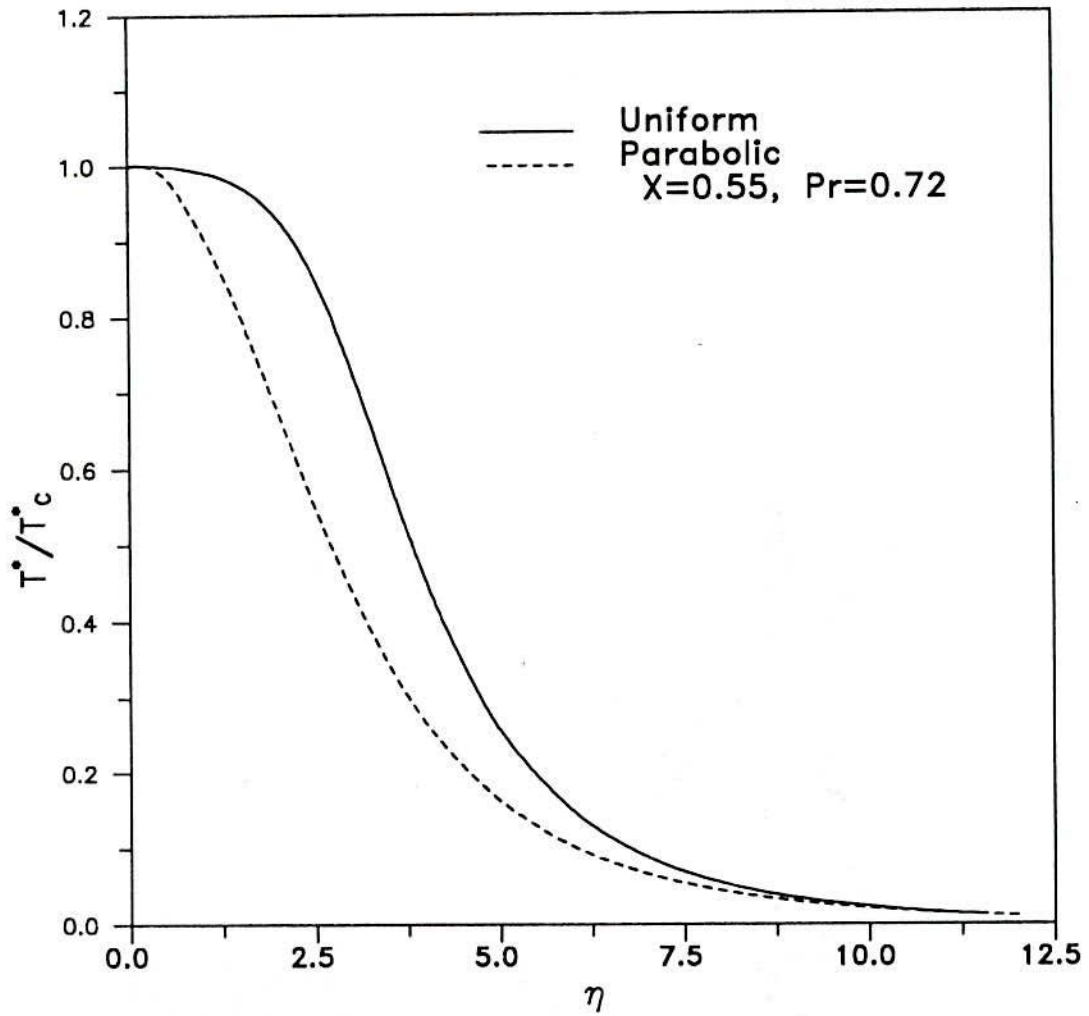


Fig.4.1.28: Temperature distribution at $Re=60$ for slot jet with uniform and parabolic temperature profile.

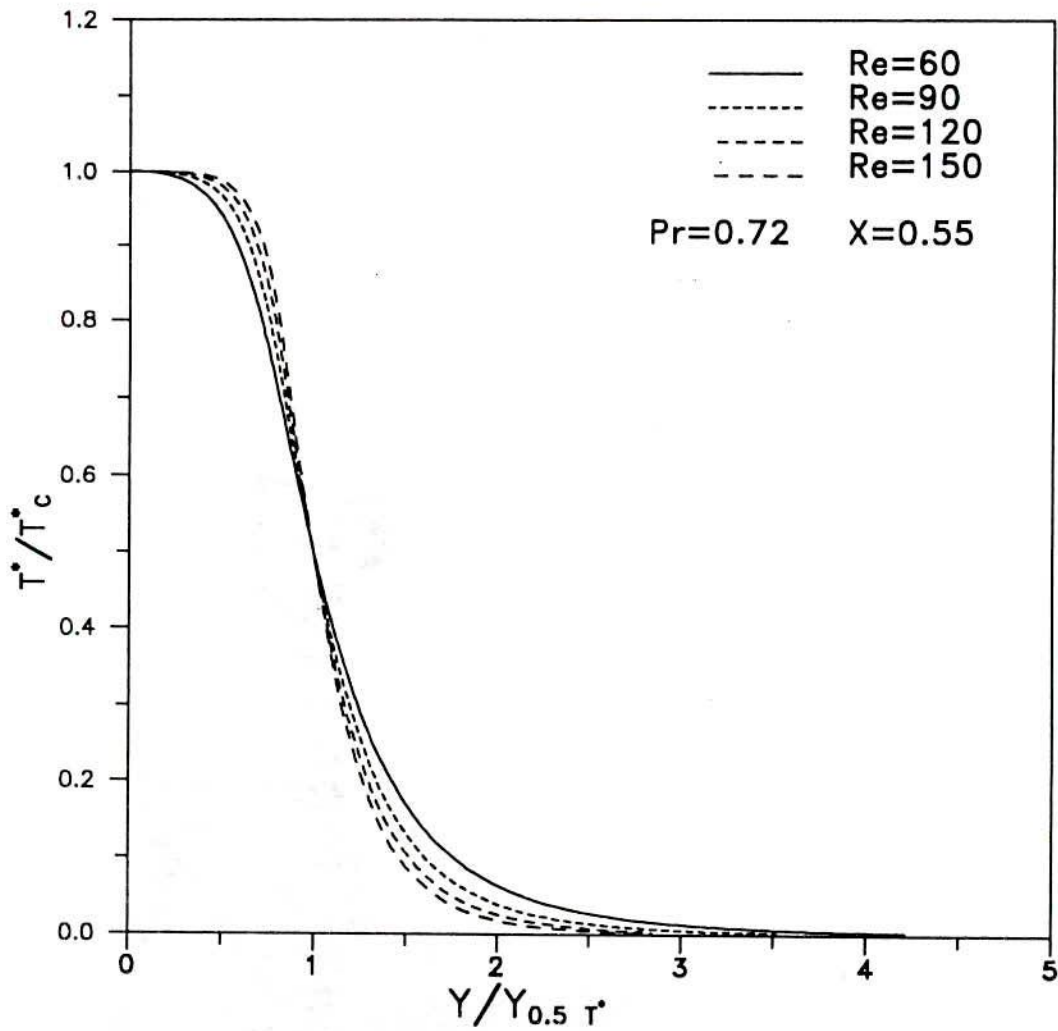


Fig.4.1.29: Temperature distribution at different Re for slot jet with uniform jet exit velocity and temperature profiles.

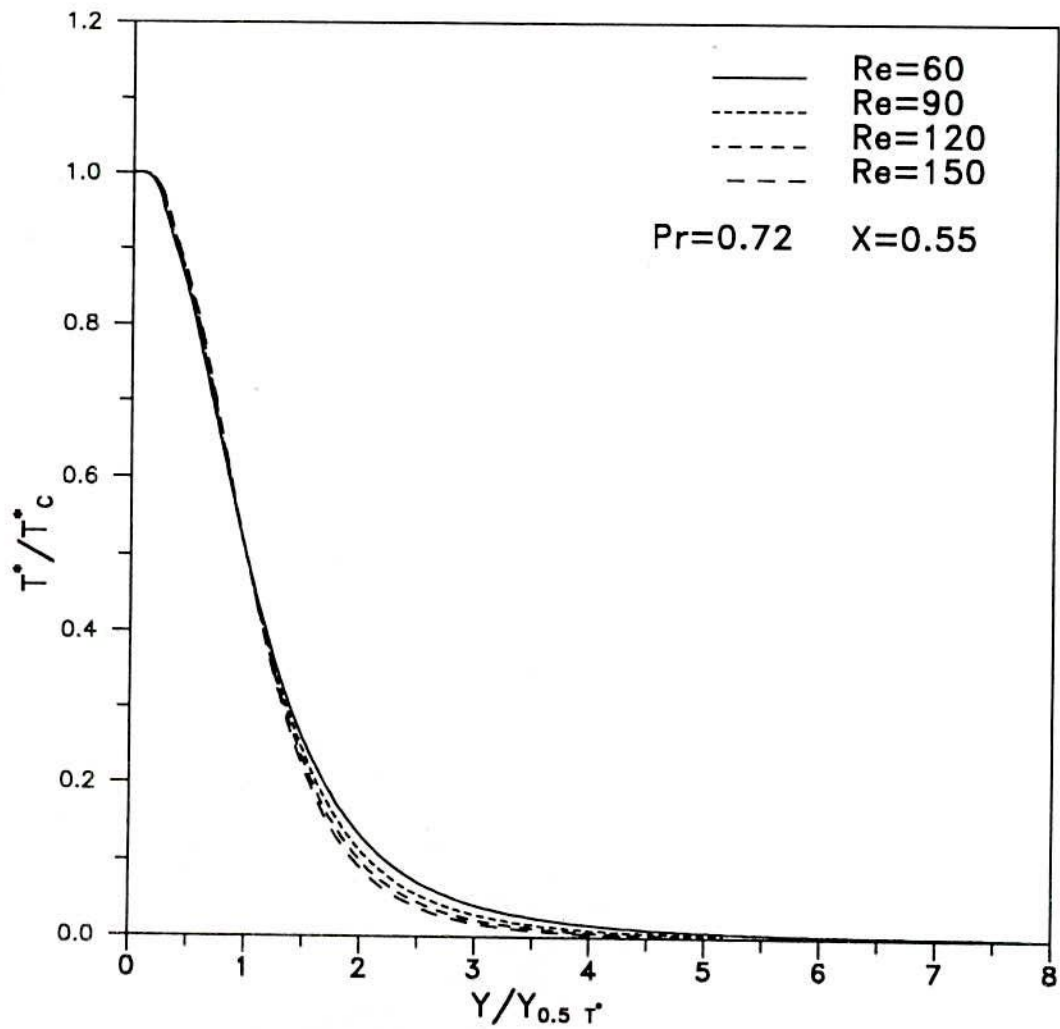


Fig.4.1.30: Temperature distribution at different Re for slot jet with parabolic jet exit velocity and temperature profiles.

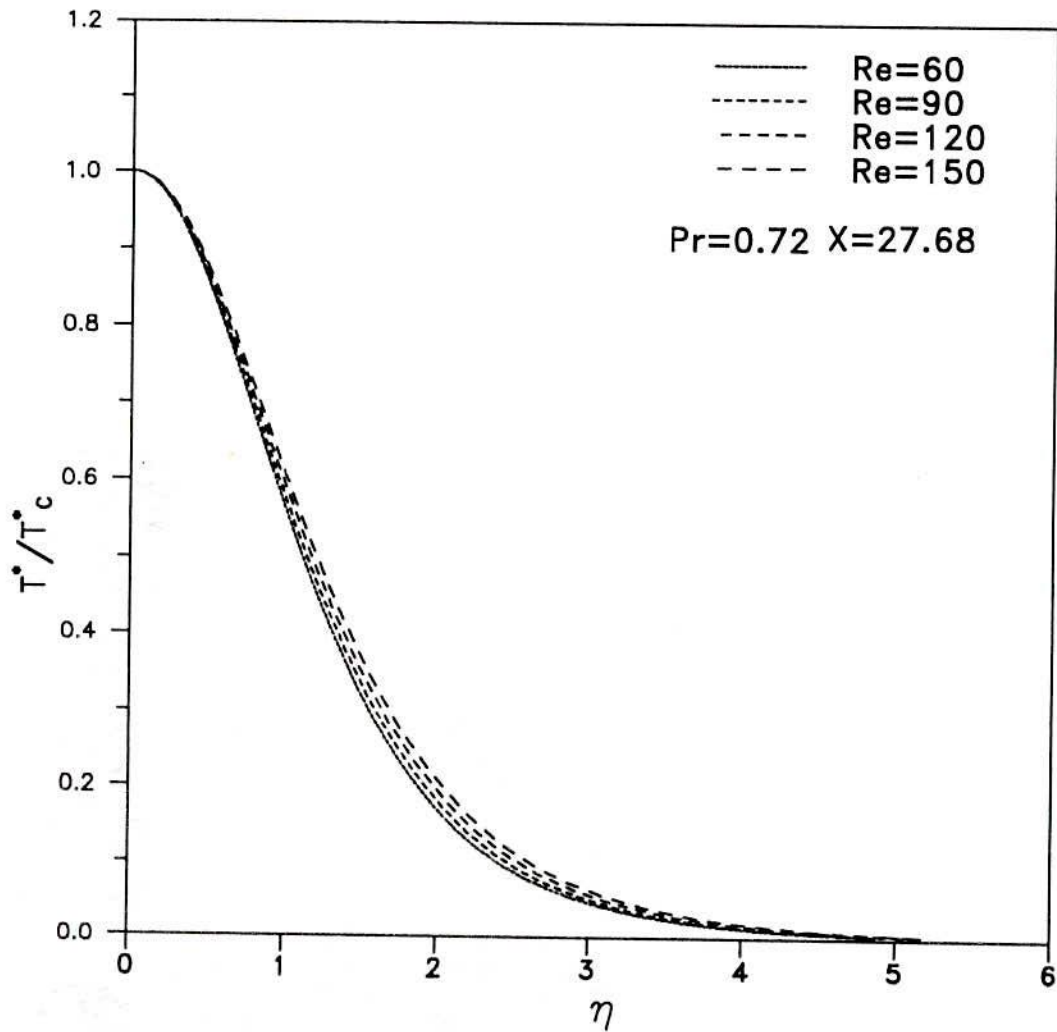


Fig.4.1.31: Temperature distribution at different Re for slot jet with uniform jet exit velocity and temperature profiles.

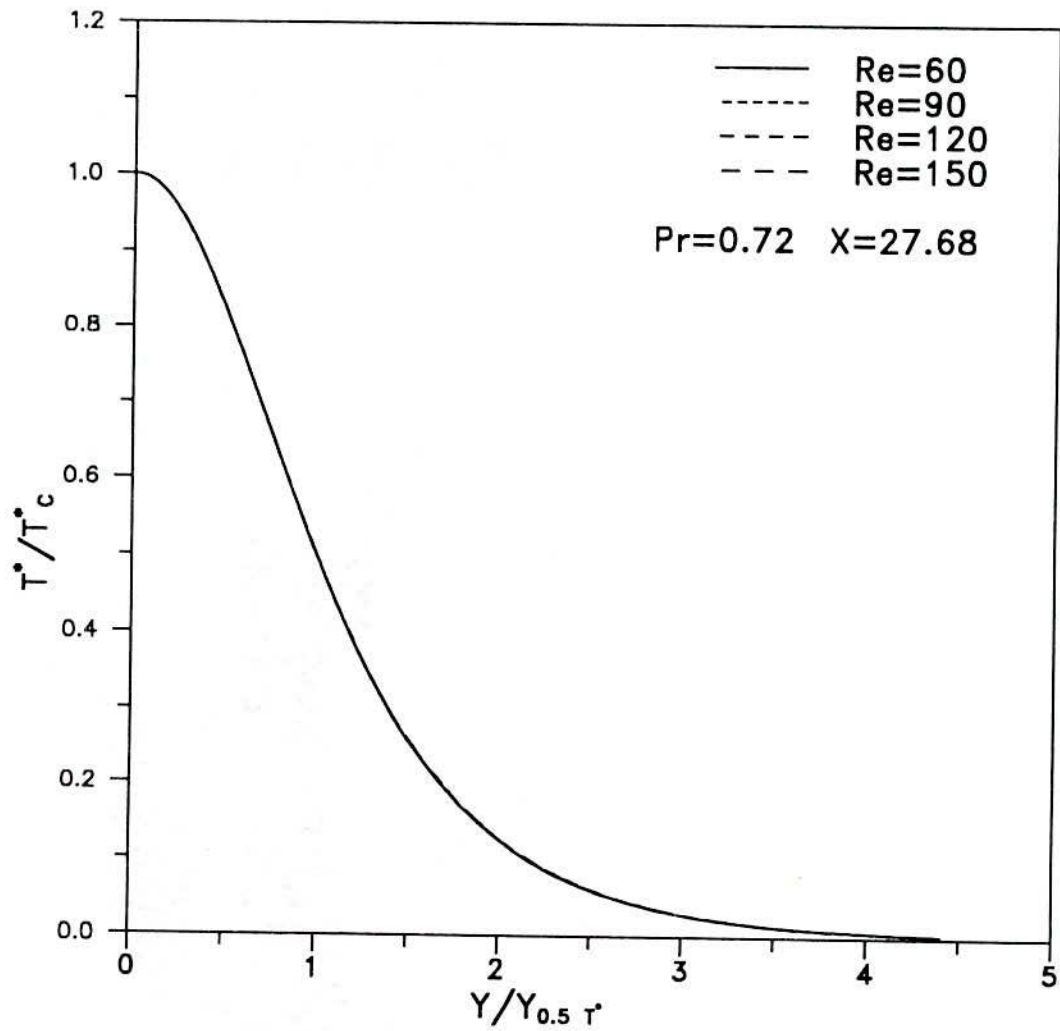


Fig.4.1.32:Temperature distribution at different Re for slot jet with uniform jet exit velocity and temperature profiles.

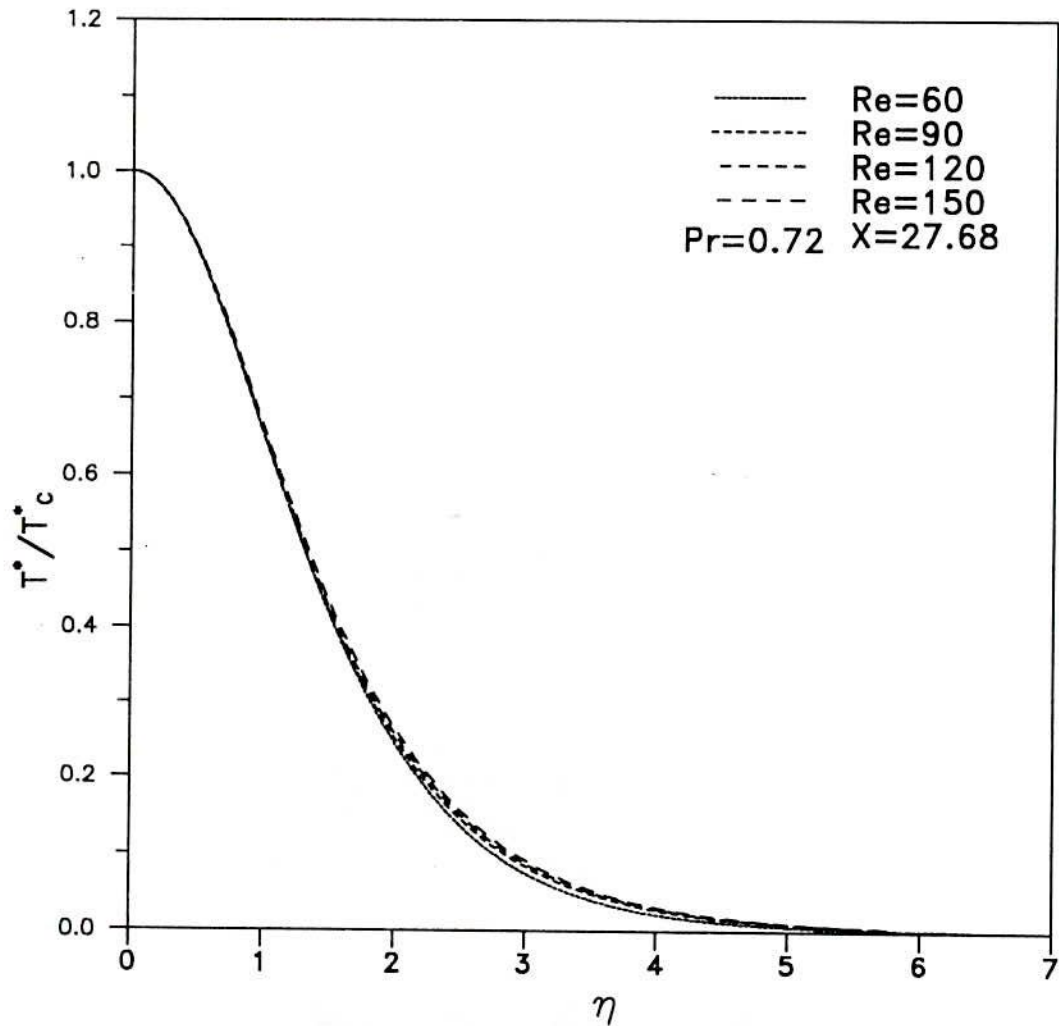


Fig.4.1.33:Temperature distribution at different Re for slot jet with parabolic jet exit velocity and temperature profiles.



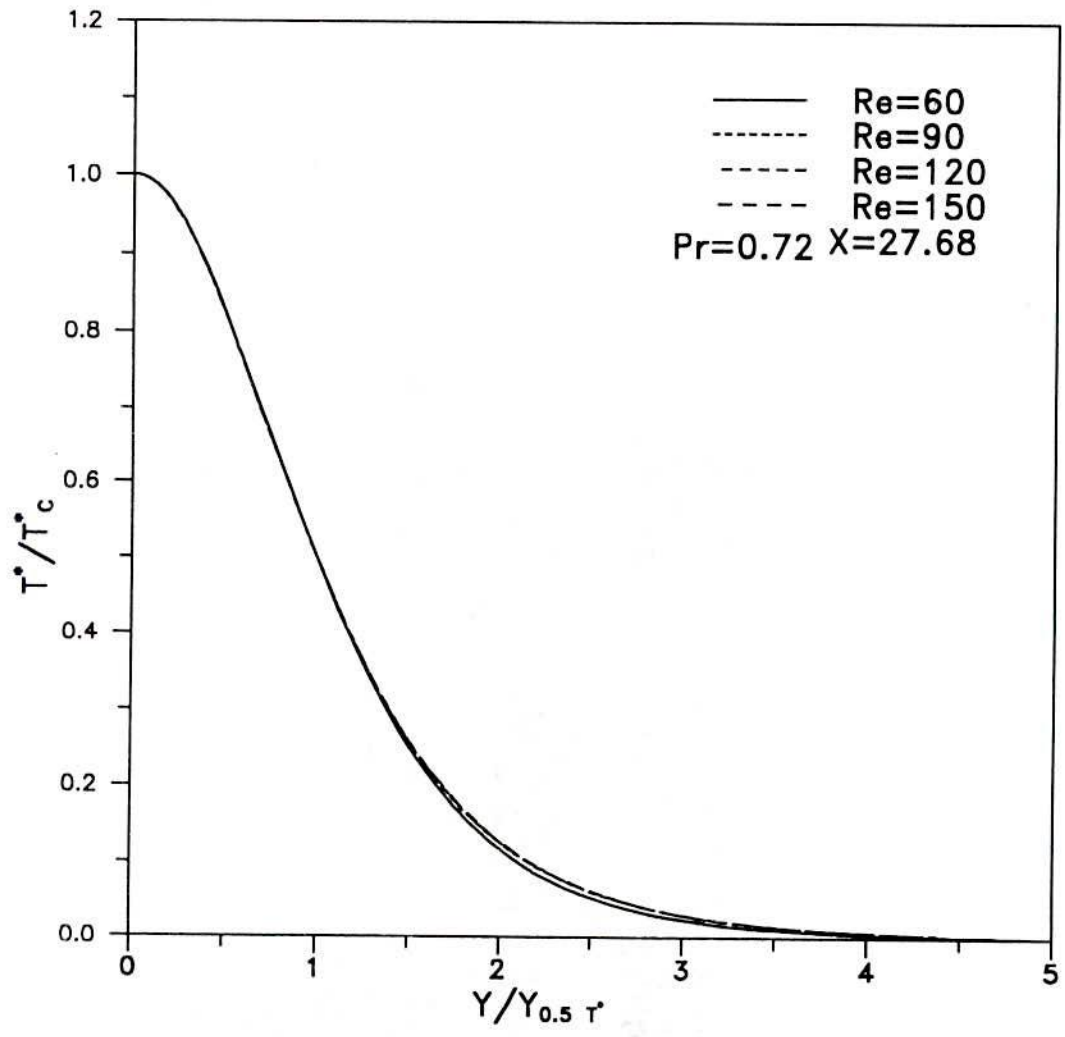


Fig.4.1.34:Temperature distribution at different Re for slot jet with parabolic jet exit velocity and temperature profile.

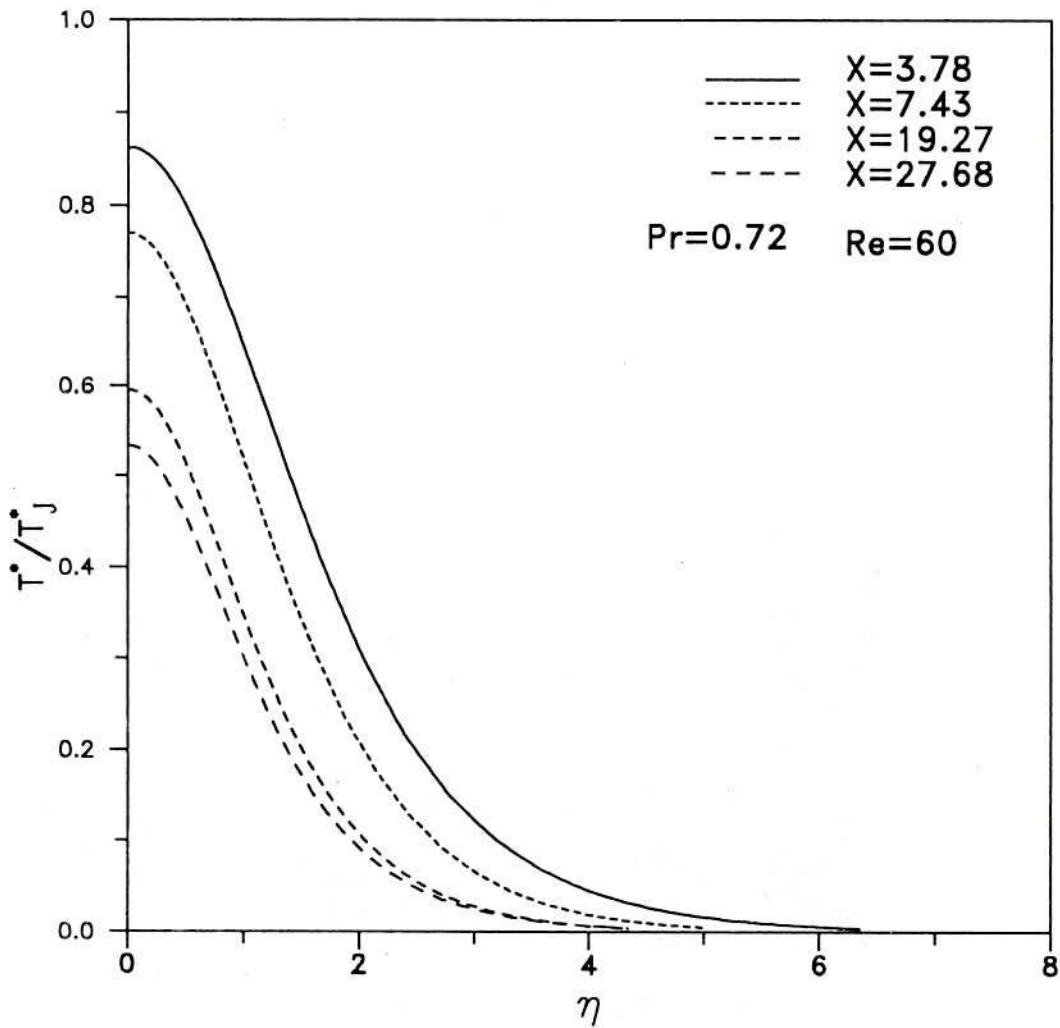


Fig.4.1.35:Temperature distribution at different X locations for slot jet with uniform jet exit velocity and temperature profiles.

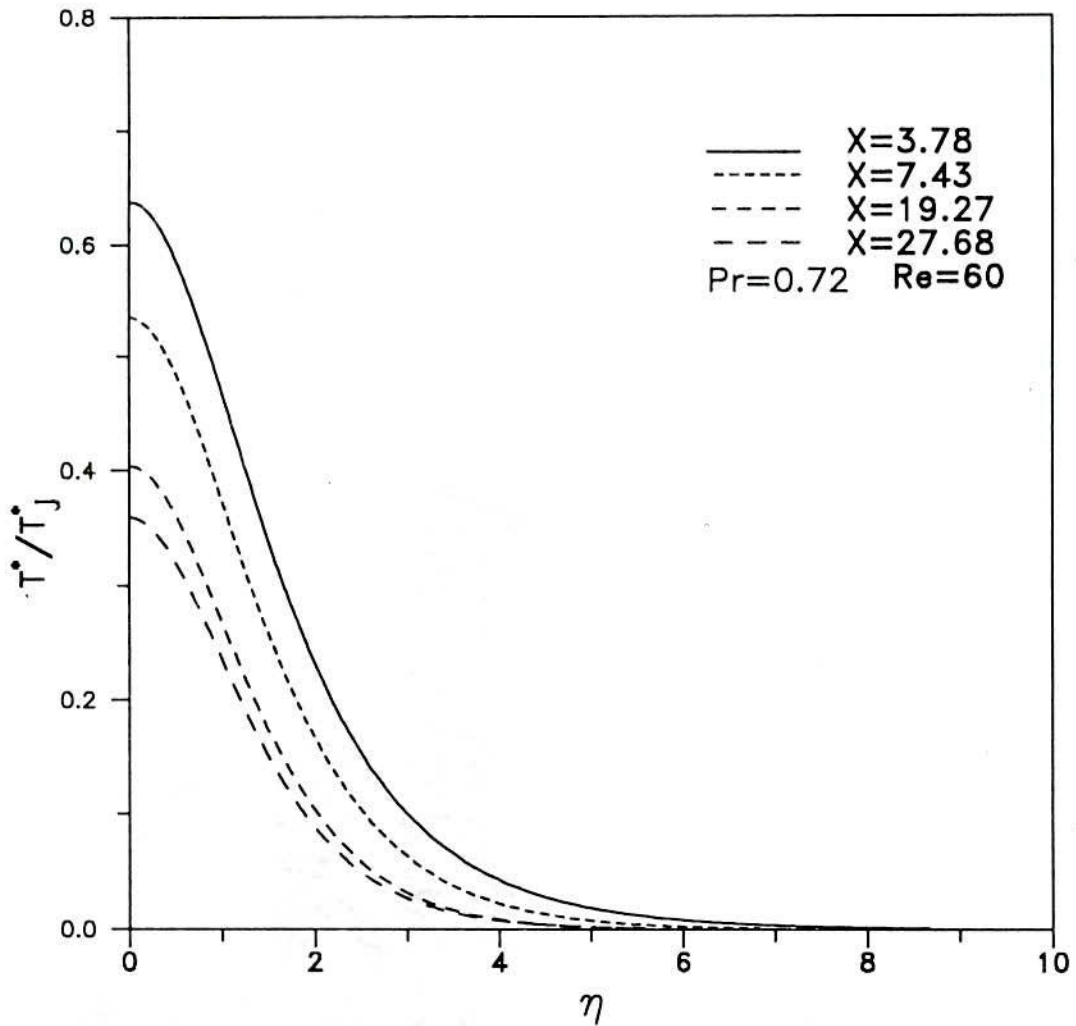


Fig.4.1.36: Temperature distribution at different X locations for slot jet with parabolic jet exit velocity and temperature profile.

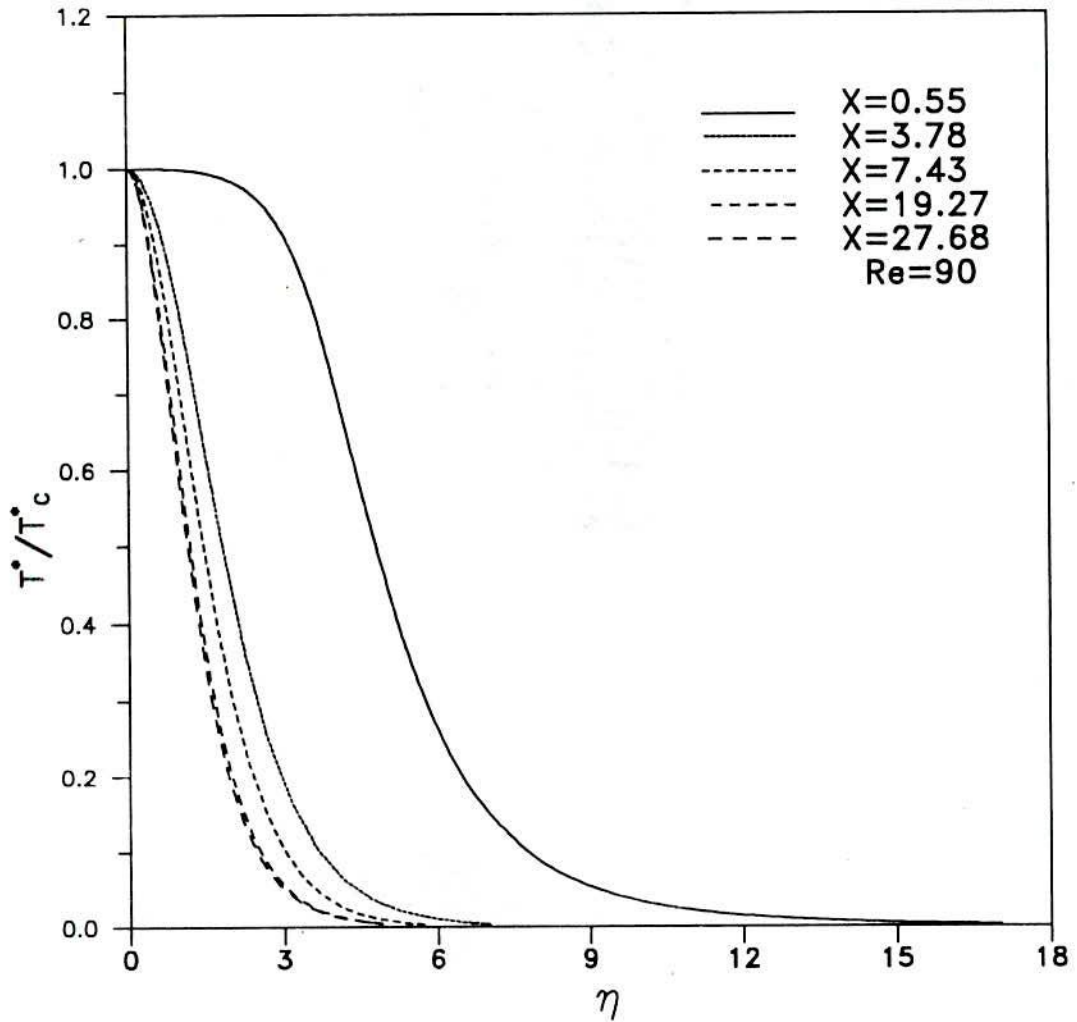


Fig.4.1.37:Temperature distribution at different X location for slot jet with uniform temperature profile.

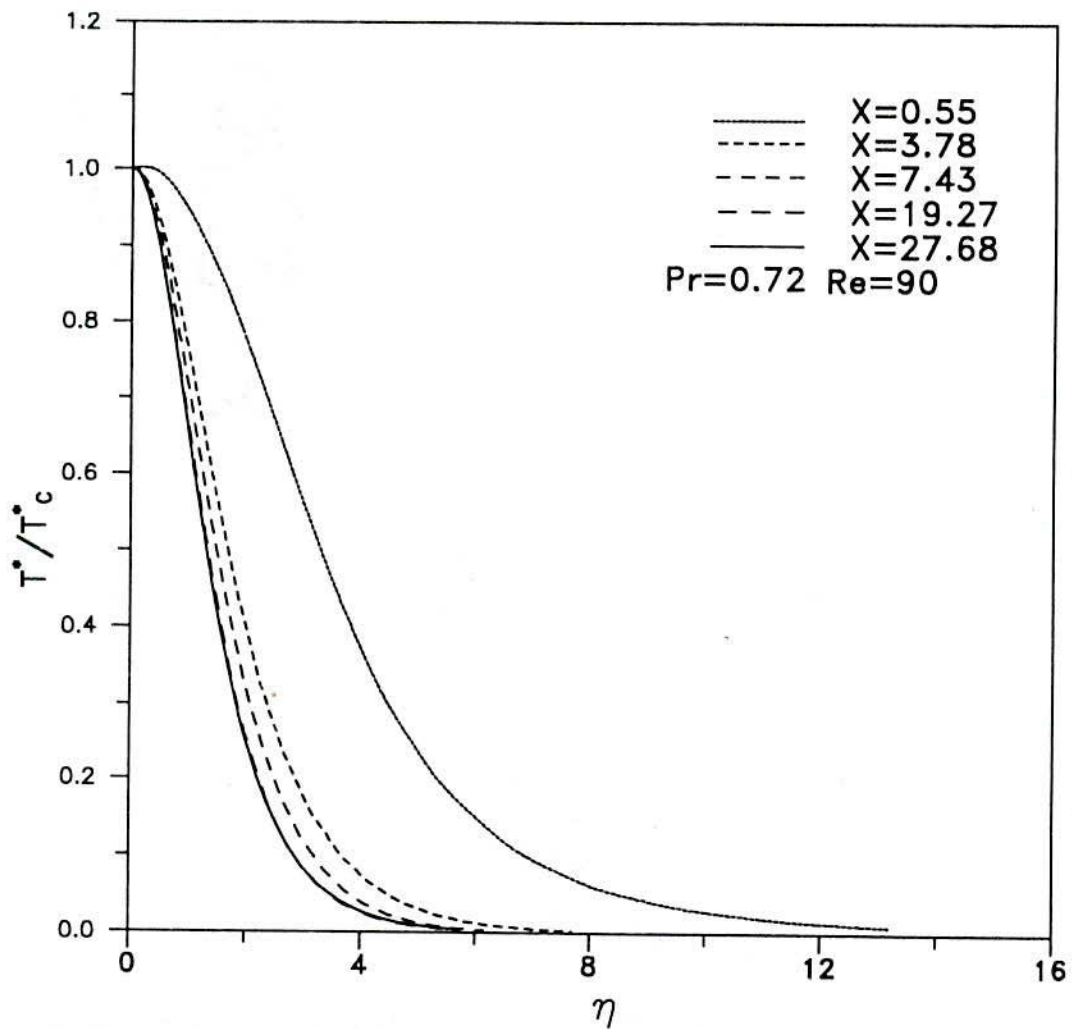


Fig.4.1.38: Temperature distribution at different X locations for slot jet with parabolic jet exit velocity and temperature profiles.

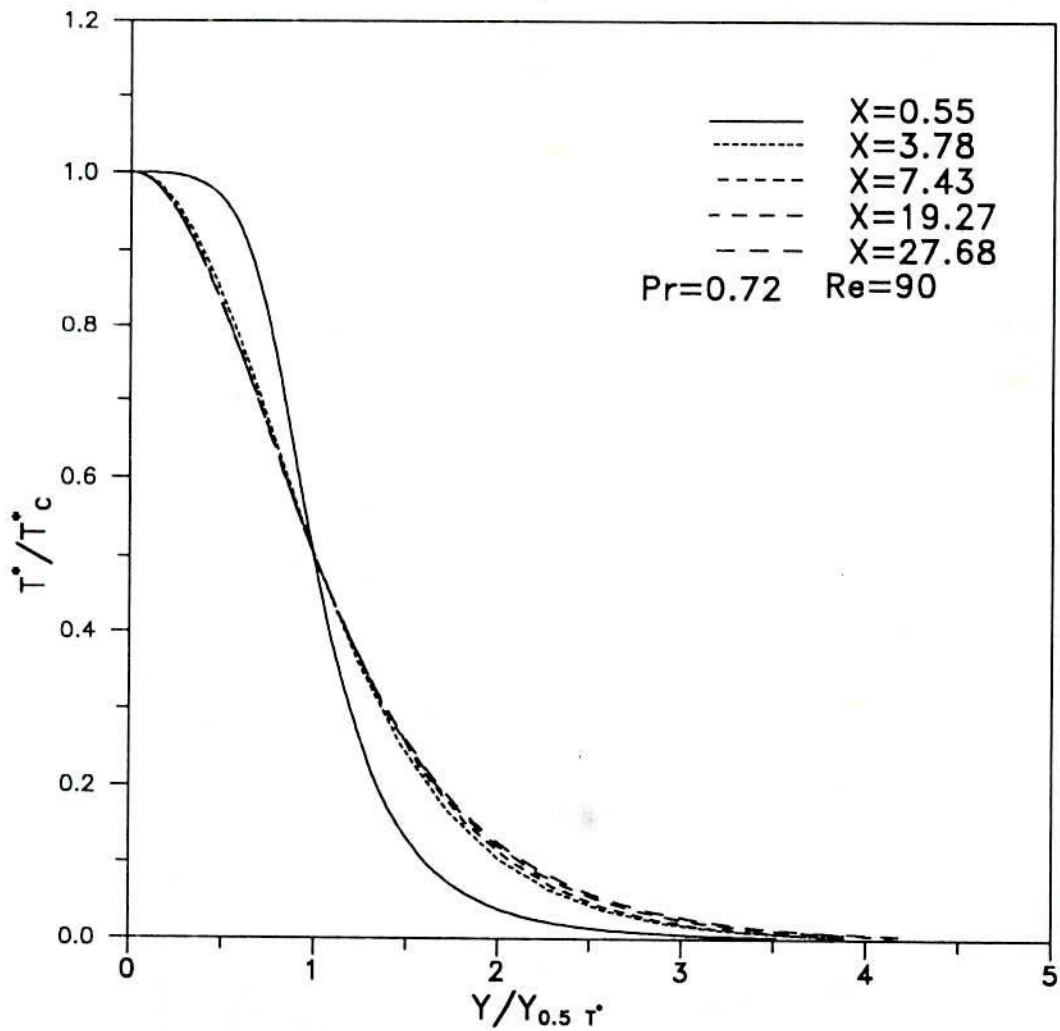


Fig.4.1.39:Temperature distribution at different X locations for slot jet with uniform jet exit velocity and temperature profiles.

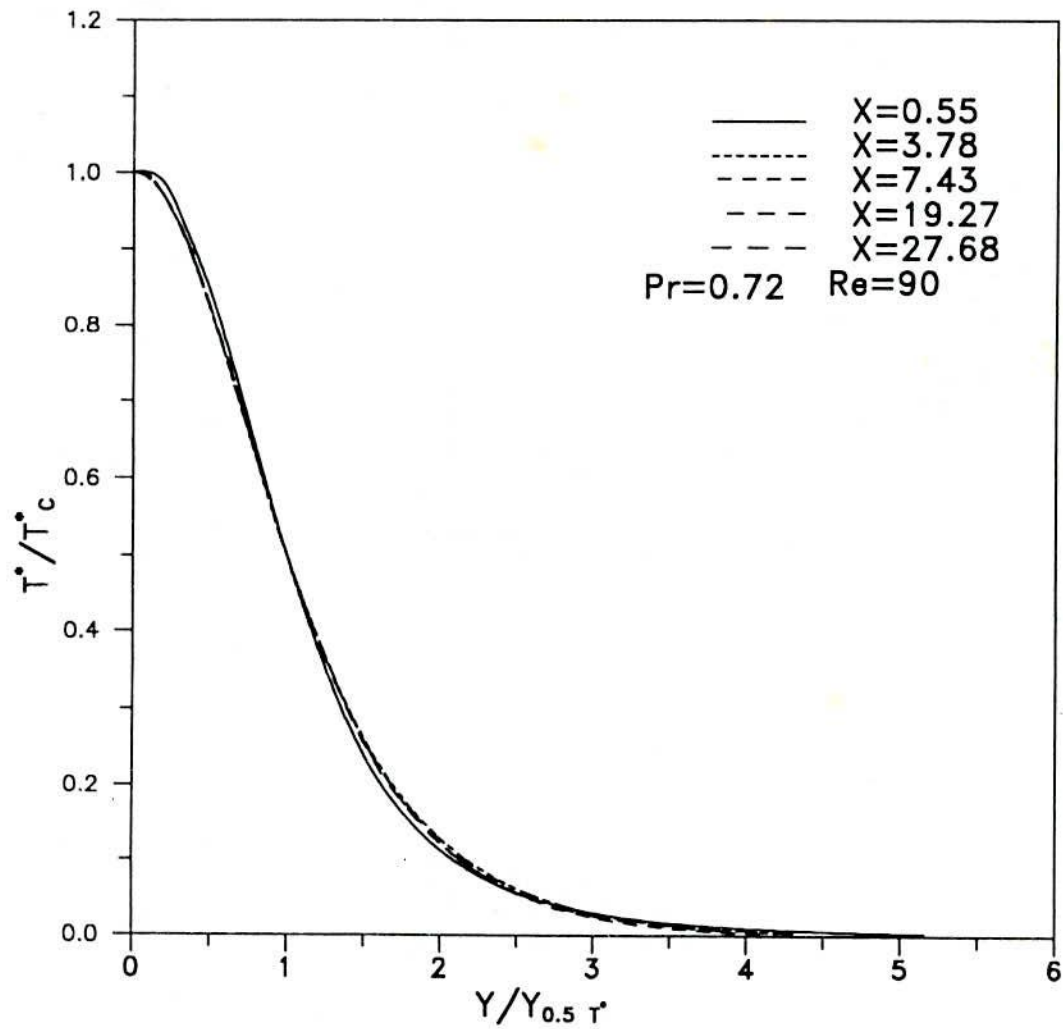


Fig.4.1.40:Temperature distribution at different X locations for slot jet with parabolic jet exit velocity and temperature profiles.

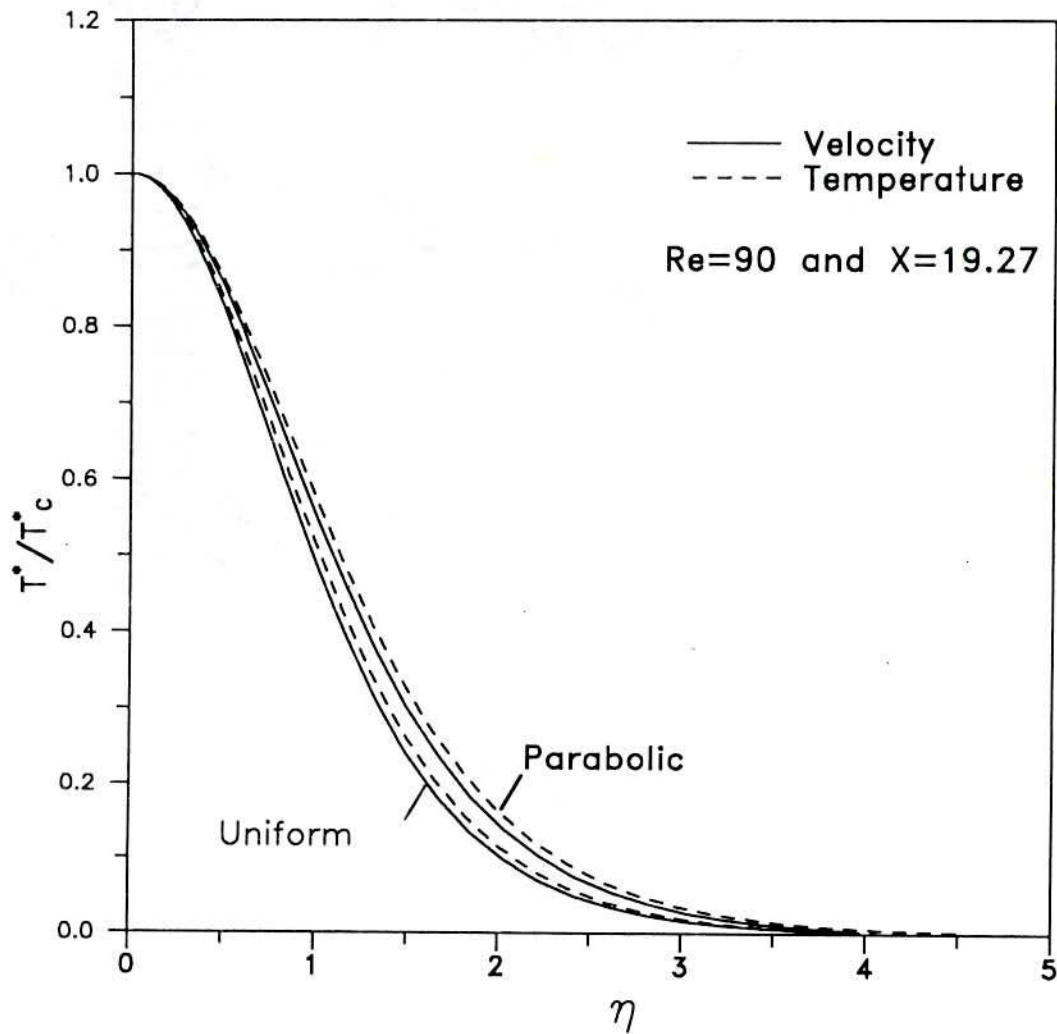


Fig. 4.1.41 Velocity and temperature profiles for $Pr=1$ with parabolic and uniform slot exit velocity and temperature profiles.

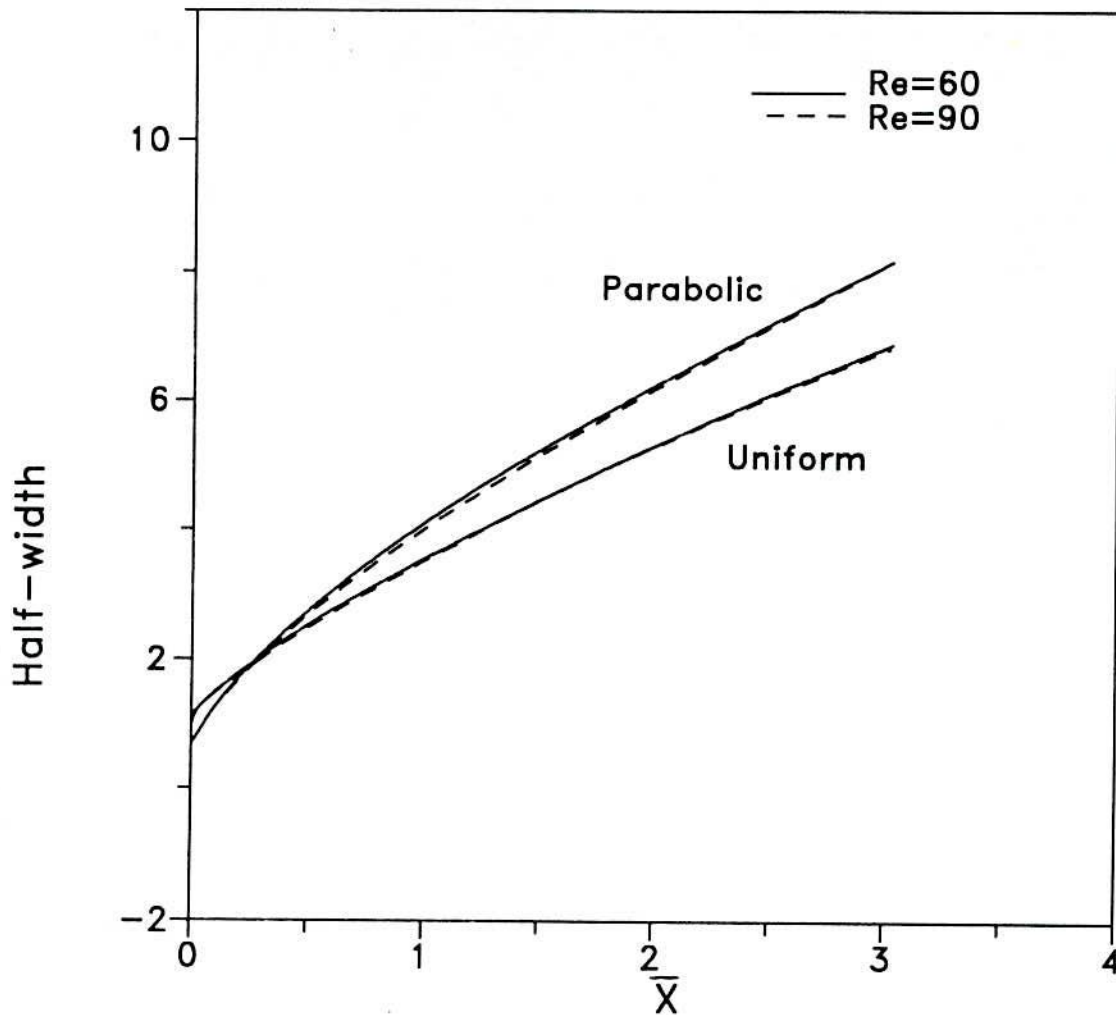


Fig.4.1.42: Spread of jet half width with uniform and Parabolic slot exit temperature profiles.

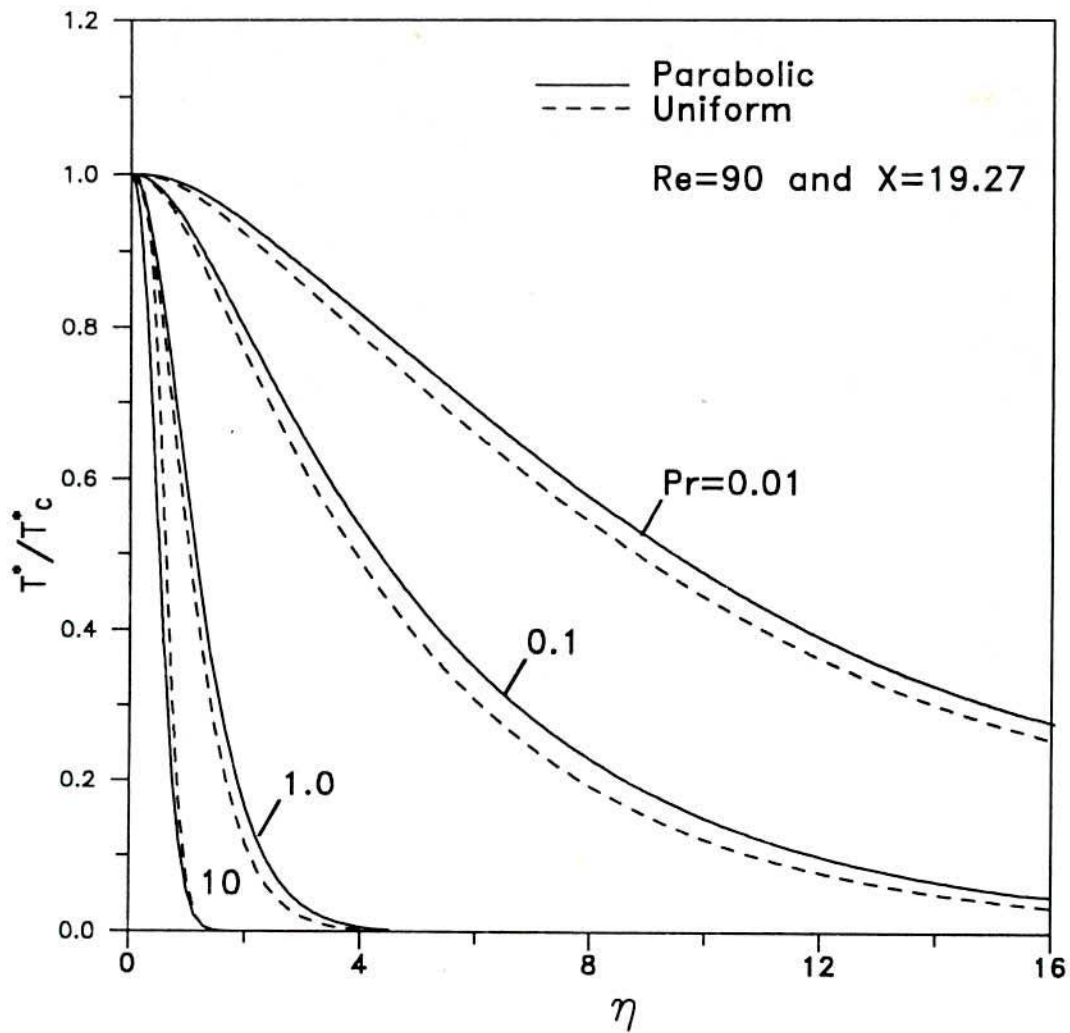


Fig.4.1.43: Temperature profile for various Pr with parabolic and uniform slot exit velocity profile.

4.2 FREE AXISYMMETRIC JET

The solutions of the Navier-Stokes equations for free axisymmetric jet have also been obtained by SIMPLE algorithm. The discretized Equations (3.2.11) along with the boundary conditions (3.2.10a - 3.2.10f) were solved. The domain length, L in axial direction and the radius, R_{\max} were found to be dependent upon each other, since the spread of the free jet increases as the axial length increases. The domain length $L= 23$ and domain radius $R_{\max}= 21$ were finally chosen for the numerical solutions. A relaxation factor of 0.5 was used for the two momentum equations and the energy equation. A relaxation factor of 0.8 was used for the pressure correction equation. Normalized residues for the velocity components and the temperature as defined in Equation (4.1.1), were calculated during every iterations along with SSUM to check the convergence.

The velocity profiles were also inspected after a few iterations to check the convergence. It was observed that when the velocity profiles and temperature profiles converge upto fifth place of decimal the values of residues were as follows,

$$\begin{aligned}\text{Res}(U) &= 10^{-3} \\ \text{Res}(V) &= 10^{-3} \\ \text{Res}(T) &= 10^{-5} \\ \text{SSUM} &= 10^{-16}\end{aligned}$$

In this case also, the solution of energy equation converged earlier than the solution of momentum equations. Hence, the convergence of velocity profiles was taken as the criterion for

convergence. The required convergence was obtained within 500 iterations for both the types of jet-exit velocity and temperature profiles. The solutions were obtained for various grid sizes to observed the effect of grid sizes.

Figure 4.2.1 shows the centreline velocity for four grid sizes, namely, 72x62, 84x72, 94x86 and 104x90 at Reynolds number of 176, $Pr = 0.71$ and for parabolic jet-exit velocity profiles. It is observed that a grid distribution finer than 72x62 does not change the results significantly, hence this grid distribution has been used in all the calculations.

The converged solutions could not be obtained beyond Reynolds number of 300 for uniform jet-exit profiles. The number of iterations required for convergence became very large, hence no attempt was made to obtain solutions for Reynolds numbers greater than 300. On the other hand, converged solutions could be obtained for Reynolds numbers upto 650 for the parabolic jet-exit profiles.

Figure 4.2.2 shows the velocity vector plot inside the computational domain at $Re = 176$ for the parabolic jet exit velocity profile. The jet velocity becomes zero at certain distance above the jet axis and entrainment is observed from the upper boundary. The velocity at each axial location is maximum at jet centreline and decreases away from it. The centreline velocity decreases in x direction and the jet spread increases in x direction.

Figure 4.2.3 shows the streamlines for free axisymmetric jet at $Re = 176$ with parabolic jet-exit velocity profile. The flow entrainment occurs from the top boundary. The entrained flow at

small values of X , turns towards the jet exit and then flows along the jet axis. The pressures were also observed to have small negative values in a region close to jet exit. Also, the entrainment seems to be very large for small values of X as compared to that at large values of X . This is in conformity with the similarity solution of Schlichting which shows that the entrainment velocity decreases as $1/X$ for large values of X .

Figure 4.2.4 shows the velocity profiles at various downstream axial locations for $Re = 176$ with parabolic jet-exit velocity profile. It also shows the velocity profiles in the developing region and the fully developed region. The decrease in centreline velocity and increase in jet width is observed in the downstream direction.

Figure 4.2.5 shows the decay of centreline velocity for different Re with initially parabolic as well as uniform jet-exit velocity profiles. The axial distance is nondimensionalized with respect to Re , which is based on the maximum jet exit velocity and nozzle diameter. These plots indicate that all the data for various values of Re collapse into a single line, which indicates that $\bar{X} = X/Re$ is the proper nondimensional axial distance as shown by Rankin et al. [54]. The centreline velocity decays at a faster rate for the parabolic jet-exit velocity profile as compared to that the uniform jet-exit velocity profile. The collapse of data into a single curve is far better than that observed for the slot-jet. One reason for this is that the Reynolds numbers considered for axisymmetric jet are much larger than those considered for the slot-jet. Hence, collapse of data is better.

Figure 4.2.6 shows the comparison of the velocity variation with half radius at $X= 2.0$ and $X= 6.0$ at $Re= 176$ with the results of Akaike and Nemoto [5] and also with Schlichting's profile [25]. A good agreement is observed with the computational results of Akaike et al. and with Schlichting's results at large values of $R/R_{0.5U}$. Figure 4.2.7 shows the comparison of centreline velocity obtained in this investigation, with the experimental and computational results of Akaike & Nemoto [5] for parabolic jet-exit velocity profile at $Re=176$. It is observed that agreement of our computational results with the experimental results is better than that obtained by Akaike and Nemoto [5].

Figure 4.2.8 shows the variation of axial velocity U/U_j with Schlichting's similarity variable $\eta= R/X$ at $X= 0.55, 2.0, 6.0$ and 9.0 for $Re= 176$ with parabolic jet-exit velocity profile. The centreline velocity decreases with larger values of X , for example at $X= 9.0$, the centreline velocity is 0.61 times the jet-exit velocity. The spread of the jet can not be interpreted from this figure since similarity variable also contains X . Figure 4.2.9 shows the variation of U/U_c with same parameters as in Figure 4.2.8. The velocity profile near the jet exit, that is, $X= 0.55$ is very near parabolic except at larger values of η , where it asymptotically tends to zero. The velocity profiles for larger values of X , decay at fast rate mainly because of the choice of variable η which has X in its denominator. However, the profiles for $X= 6.0$ and 9.0 are very close together. This indicates that, far away from the jet exit, the velocity profiles will become similar in Schlichting's variable η , as was observed for the slot

jet.

Figure 4.2.10 shows the axial velocity variation with η at $X= 6.0$ for $Re= 176$ and 300 with the uniform jet-exit velocity profile. It was observed that jet diffuses at faster rate for lower Reynolds numbers as compared to that at higher Reynolds numbers. In accordance with that the velocity profile for $Re= 300$ is observed to have a larger potential core as compared to that for $Re= 176$. Hrycak [7] has also reported that the potential core length increases as the Reynolds number increases. In this figure $\bar{X}= 0.034$ for $Re= 176$ and $\bar{X}= 0.02$ for $Re= 300$. Akaike and Nemoto [5] have reported that the potential core vanishes at $\bar{X}= 0.04$. It is observed in this figure, that potential core is negligible at $\bar{X}= 0.034$. The jet half radius is also larger for $Re= 300$ as compared to that for $Re= 176$.

Figures 4.2.11 and 4.2.12 show the variation of the axial velocity in radial direction for uniform and parabolic jet-exit profiles, respectively with half radius of the jet taken as characteristic length in radial direction. The velocity profiles are given for $X= 0.0, 0.55, 2.0, 6.0$ and 9.0 and for $Re=176$. It is observed that the axial velocity exhibits a potential core for uniform jet-exit velocity profile. The velocity decreases at a very fast rate for small values of X beyond the potential core. The potential core almost disappears at $X= 9.0$. The potential core for the parabolic jet-exit velocity profile cannot be seen, but the velocity profile is close to the parabolic profile near $R \approx 0$. In this case, the velocity decreases at a faster rate at $X= 2.0$ than at $X= 6.0$ and $X= 9.0$ for $R/R_{0.5U} > 1$ while the trend is

opposite of this for $R/R_{0.5U} < 1$. All the velocity profiles have $U/U_c = 0.5$ at $R/R_{0.5U} = 1$, since $R_{0.5U}$ is half jet radius based on velocity. The velocity profile for $X = 6.0$ or 9.0 are coincident for $R/R_{0.5U} < 1$ and indicate a trend towards collapse into a single profile for $R/R_{0.5U} > 1$. This implies that, velocity profiles will become similar for large values of X .

Figure 4.2.13 shows the variation of axial velocity in radial direction with half radius as characteristic length for different Reynolds number at $X = 6.0$. At higher values of Re , the jet half radius at a given X location is smaller compared to that at smaller Reynolds numbers. Low Reynolds number jet diffuses at a faster rate. Hence, near the centreline, the velocity is smaller for lower Reynolds numbers and far away from the centreline, opposite trend is observed. In fact for $R/R_{0.5U} < 1$, the velocity profiles almost collapse into a single curve, while for $R/R_{0.5U} > 1$ the velocity profiles are spread apart.

Figure 4.2.14 shows the variation of U/U_c with $R/R_{0.5U}$ at $X = 6.0$, $Re = 176$ and 300 for the uniform jet exit velocity profiles. It is observed that velocity remains unchanged along the radius for some distance, that is, there exists a potential core. The length of the potential core is larger for higher Reynolds numbers as compared to that for lower Reynolds numbers at a given location. Figure 4.2.15 shows the comparison of axial velocity profiles for uniform and parabolic jet-exit velocity profiles at $Re = 300$ very near the jet-exit, that is, at $X = 0.55$. It is observed that uniform jet exit velocity profile has a potential core, whereas the parabolic jet-exit velocity profile is almost

like a parabola except at larger radii where it asymptotically tends to zero.

Figure 4.2.16 shows the comparison of axial velocity for the two types of jet-exit velocity profiles for $Re = 300$ at $X = 6.0$. The uniform velocity profile still has a potential core and thereafter decreases at a fast rate. The jet spread radius is observed to be larger for the parabolic jet-exit velocity profile. Figure 4.2.17 shows the variation of jet half radius for velocity with the nondimensional axial distance \bar{X} at $Re = 176$ for the parabolic jet-exit velocity profile. The experimental and computational results of Akaike & Nemoto [5] are also shown for comparison. The agreement is observed to be very good. Akaike & Nemoto [5] have observed that the nondimensional jet half radius (Velocity) for the parabolic jet exit velocity profile is 0.353 at the jet exit plane. But for the parabolic jet exit velocity profile our computation gives half radius (Velocity) is equal to 0.352 at the nozzle exit plane, which is slightly less than the reported value of Akaike & Nemoto [5]. The magnitude of half radius at $X = 0.0$ is independent of Reynolds numbers.

For the uniform jet exit velocity profile, half radius is 0.485 at the nozzle exit plane. The half radius at $X = 0.0$ with initially uniform velocity profile at the jet-exit has not been reported by earlier investigators. The half jet radius for temperature at $X = 0.0$, also has not been reported by any investigator for the parabolic and the uniform jet exit temperature profiles. These are equal to 0.352 and 0.485 respectively and these are also independent of Re .

Figure 4.2.18 shows the isotherms for the axisymmetric warm jet at $Re = 176$ with parabolic jet-exit velocity and temperature profiles. The centreline temperature is observed to decrease along the jet axis. The temperature decreases in the radial direction also. The parabolic temperature profile can be seen at jet-exit along with the spread of thermal boundary layer.

Figure 4.2.19 shows the decay of centreline temperature at different Reynolds numbers for parabolic and uniform jet exit temperature and velocity profiles. The trend of decay is similar to that of the centreline velocity. The proper nondimensional axial distance is observed to be \bar{X} for the collapse of data in case of temperature also.

Figure 4.2.20 shows the temperature variation T^*/T_j^* with similarity variable η at $X = 0.59, 2.18, 6.16$ and 9.19 for $Re = 176$ and $Pr = 0.71$ for parabolic jet-exit velocity and temperature profiles. The trend of temperature profiles is very similar to that for the velocities in Figure 4.2.8. The centreline velocities are however higher than the centreline temperature for parabolic jet-exit profiles. The same trend was observed for the slot jet also. The temperature boundary layer thickness is observed to be greater than velocity boundary layer thickness, which is expected at Prandtl number 0.71.

Figure 4.2.21 shows the variation of T^*/T_c^* with the same parameters as in Figure 4.2.20. The trends of temperature profiles are very similar to those of velocity profiles, as shown in Figure 4.2.9. The temperature profiles at $X = 6.0$ and 9.0 are very close together. This indicates that, far away from jet exit, the

temperature profiles will become similar in Schlichting's similarity variable η , as was observed for the velocities in Figure 4.2.9.

Figure 4.2.22 shows a comparison of temperature profiles T^*/T_C^* for $Re= 176$ and 300 , at $X= 6.0$, $Pr= 0.71$ for the uniform jet-exit profiles. The trend of temperature distribution is very similar to the velocity distribution shown in Figure 4.2.10. The radius of the region of constant temperature (thermal core), is however very small compared to the potential core observed in Figure 4.2.10. A comparison of the two figures further shows that temperature decreases at a slower rate with η than the velocity. The temperature also, diffuses at a faster rate at lower Reynolds numbers as seen in the figure.

Figure 4.2.23, shows the temperature variation with $R/R_{0.5T^*}$ at $X= 0.0, 0.59, 2.18, 6.16$ and 9.19 for $Re= 176$ and $Pr= 0.71$ and for parabolic jet-exit velocity profile. The temperature also decreases rapidly like velocity at lower values of X while at $X =6$ and at $X =9$, the temperature profiles almost collapses into a single curve. This indicates that just like the velocity profiles in Figure 4.2.11, the temperature profiles will also become similar at large values of X .

Figure 4.2.24, shows the temperature variation with $R/R_{0.5T^*}$ at $X =6$, $Pr= 0.71$ and for $Re= 176$ and 300 for uniform jet-exit profiles. The thermal half radius decreases with the increase in Reynolds numbers just like the velocity half radius at given X location. The temperature remains constant upto certain distance in radial direction. This region for velocity is called potential

core and for temperature, it may be called thermal core. The length of thermal core is larger for Reynolds number of 300 than for Reynolds number of 176. Hence, near the centre line, the temperature is lower for lower Reynolds number while far away from the centre line, the trend is opposite to this. The temperature profiles do not exhibit similarity at $Re = 176$ and 300 .

Figure 4.2.25 shows the comparison of temperature profiles for initially uniform and parabolic temperature profiles with $R/R_{0.5T}^*$ at $X = 0.59$, $Re = 300$ and $Pr = 0.71$. Temperature for the uniform jet-exit profiles has a thermal core like the potential core for velocity profile observed in Figure 4.2.16, thereafter it decays at a fast rate. The thermal boundary layer is also more than viscous boundary layer (Jet spread) which is expected at $Pr < 1$.

Figure 4.2.26 shows the comparison for the two types of jet exit profiles at $X = 6.16$, other parameters being same as in Figure 4.2.25. The trend is similar to that for the velocity profiles seen in Figure 4.2.16 except that the thermal boundary layer is more than viscous boundary layer (Jet spread).

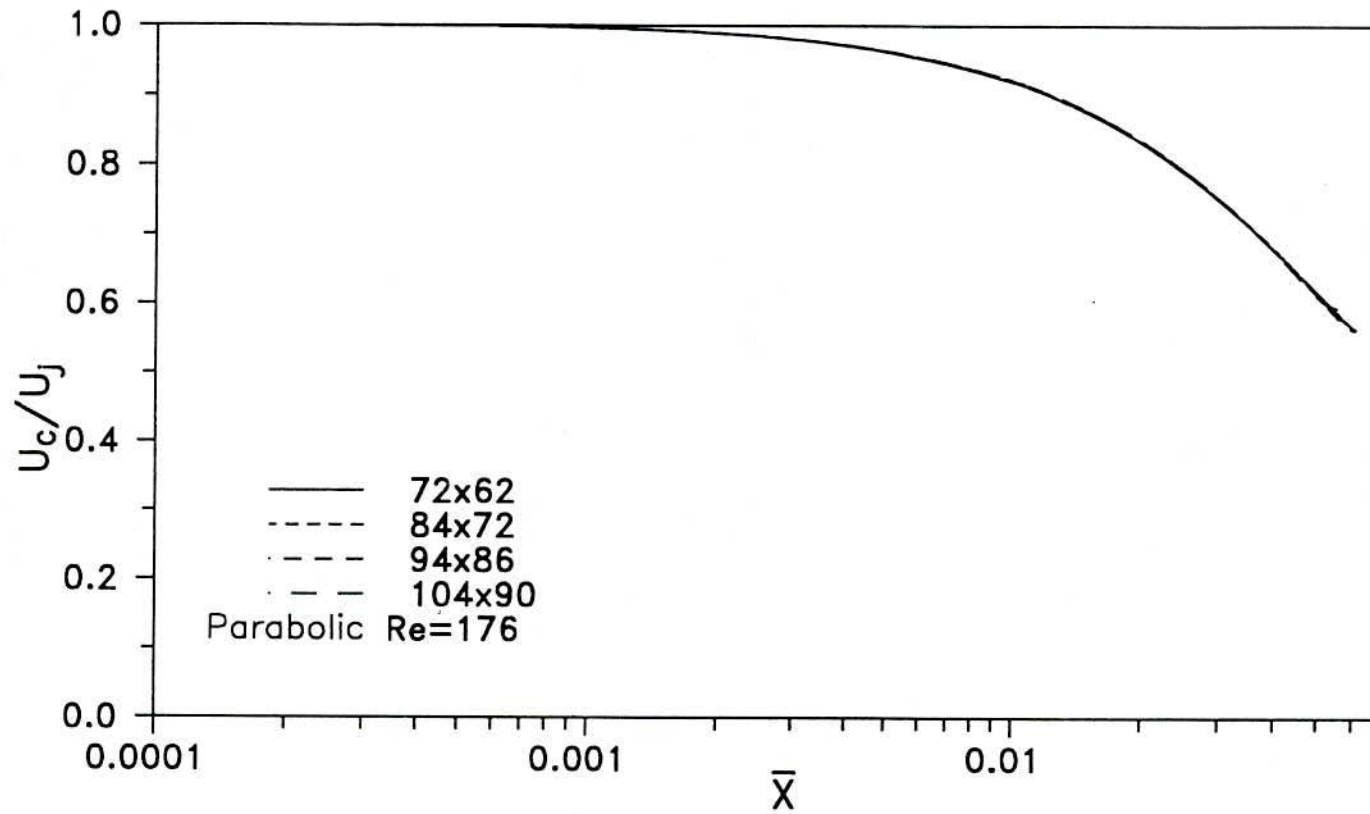


Fig.4.2.1: Decay of centre line velocity for axisymmetric jet
Showing the effect of different grid sizes.

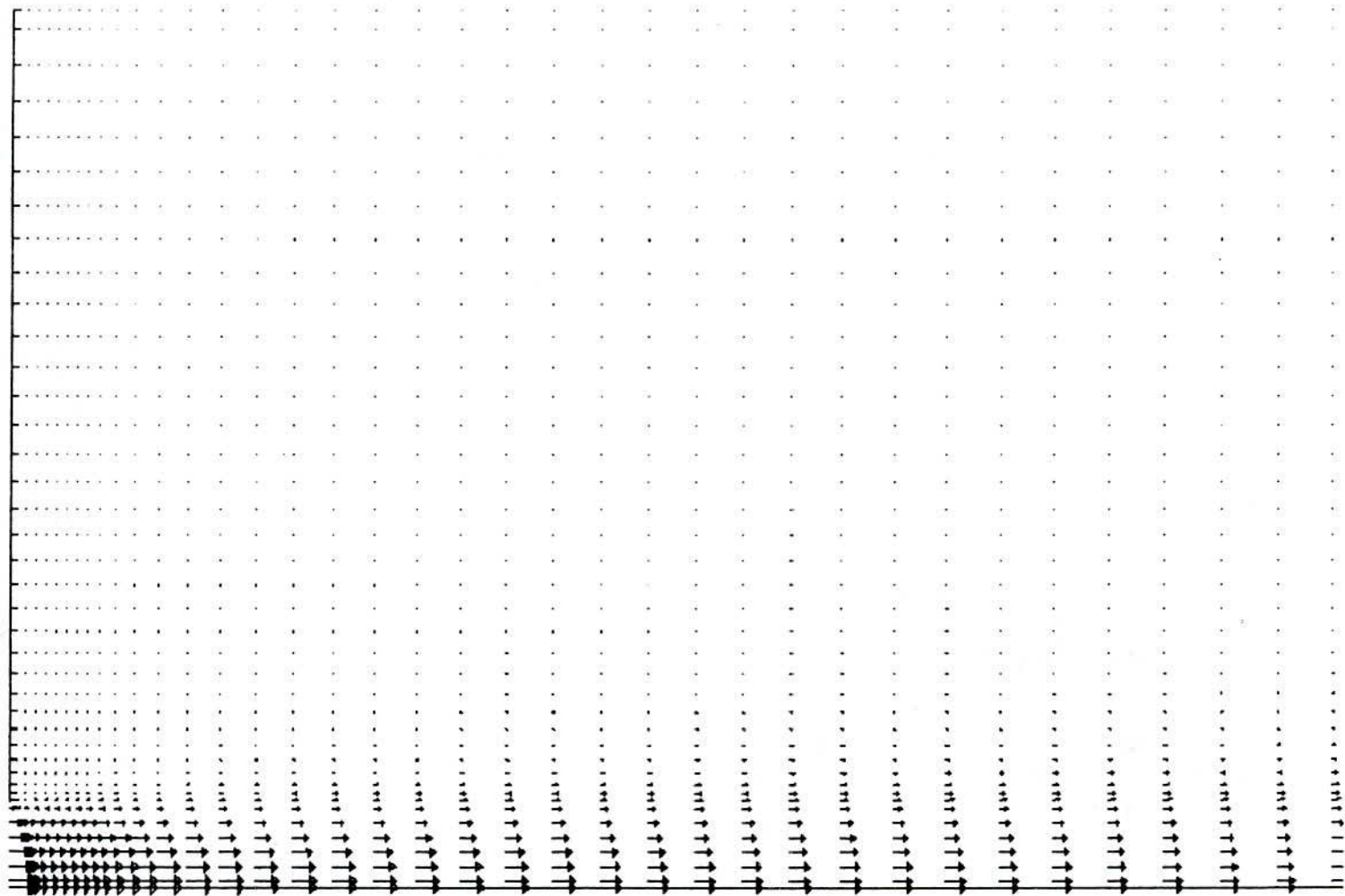


Fig. 4.2.2 : Velocity vector plot, $Re=176$

Axisymmetric free jet with parabolic velocity profile at the nozzle exit.

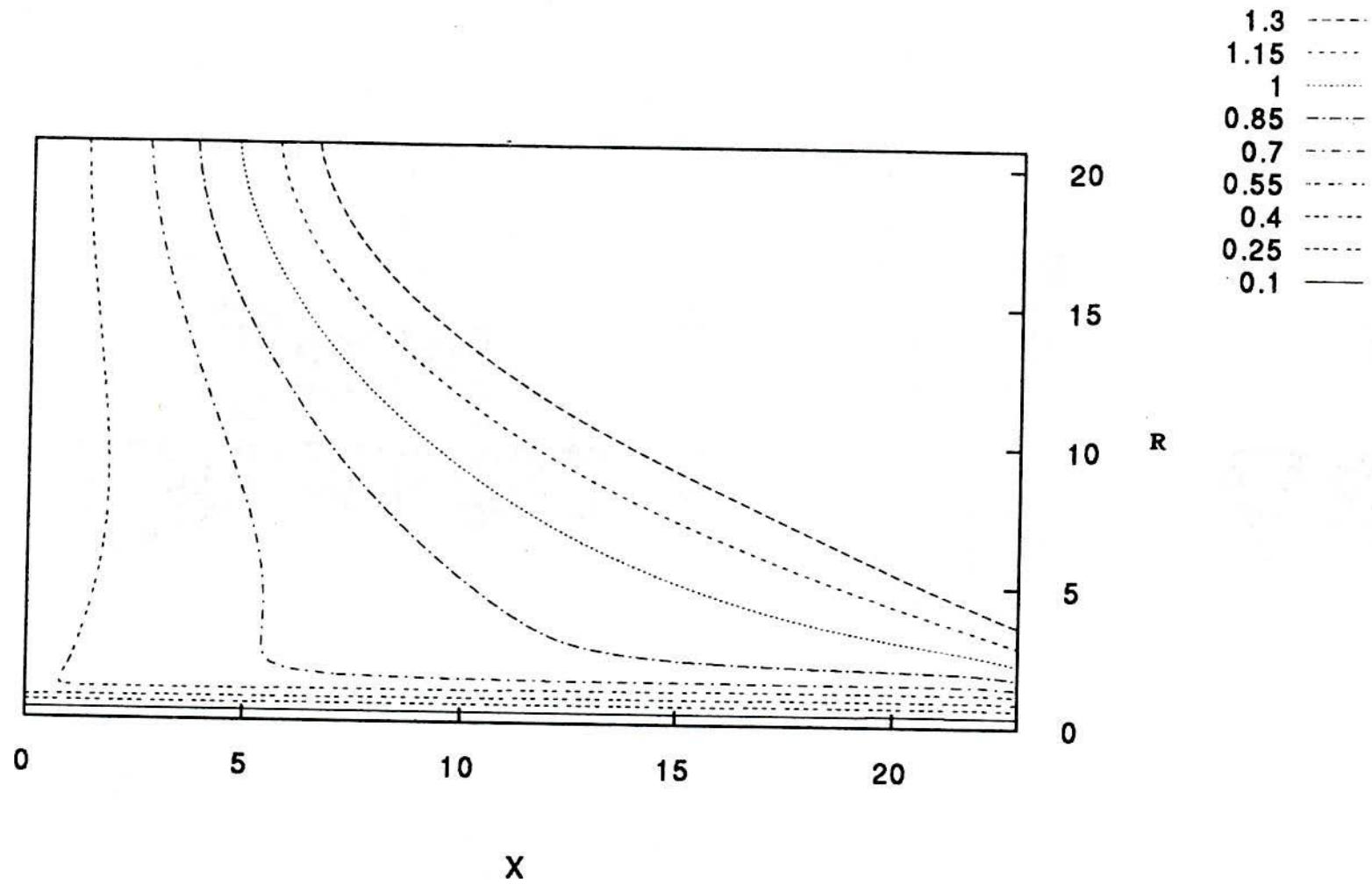


Fig. 4.2.3: Streamlines at $Re = 176$ with parabolic jet exit velocity profile for free axisymmetric jet.

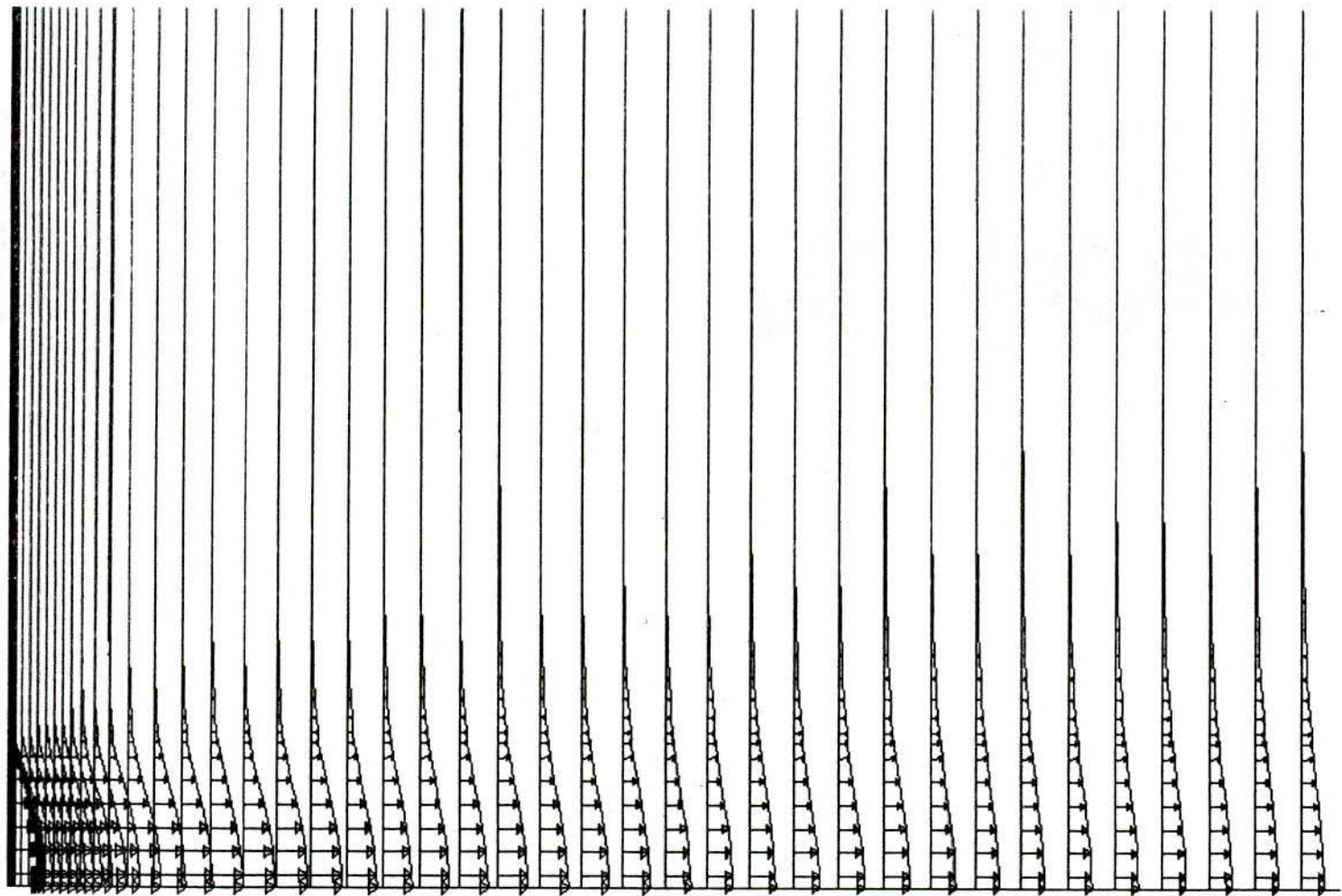


Fig. 4.2.4 : Velocity profile at different axial locations at $Re=176$
Laminar axisymmetric jet with parabolic velocity profile at nozzle exit.

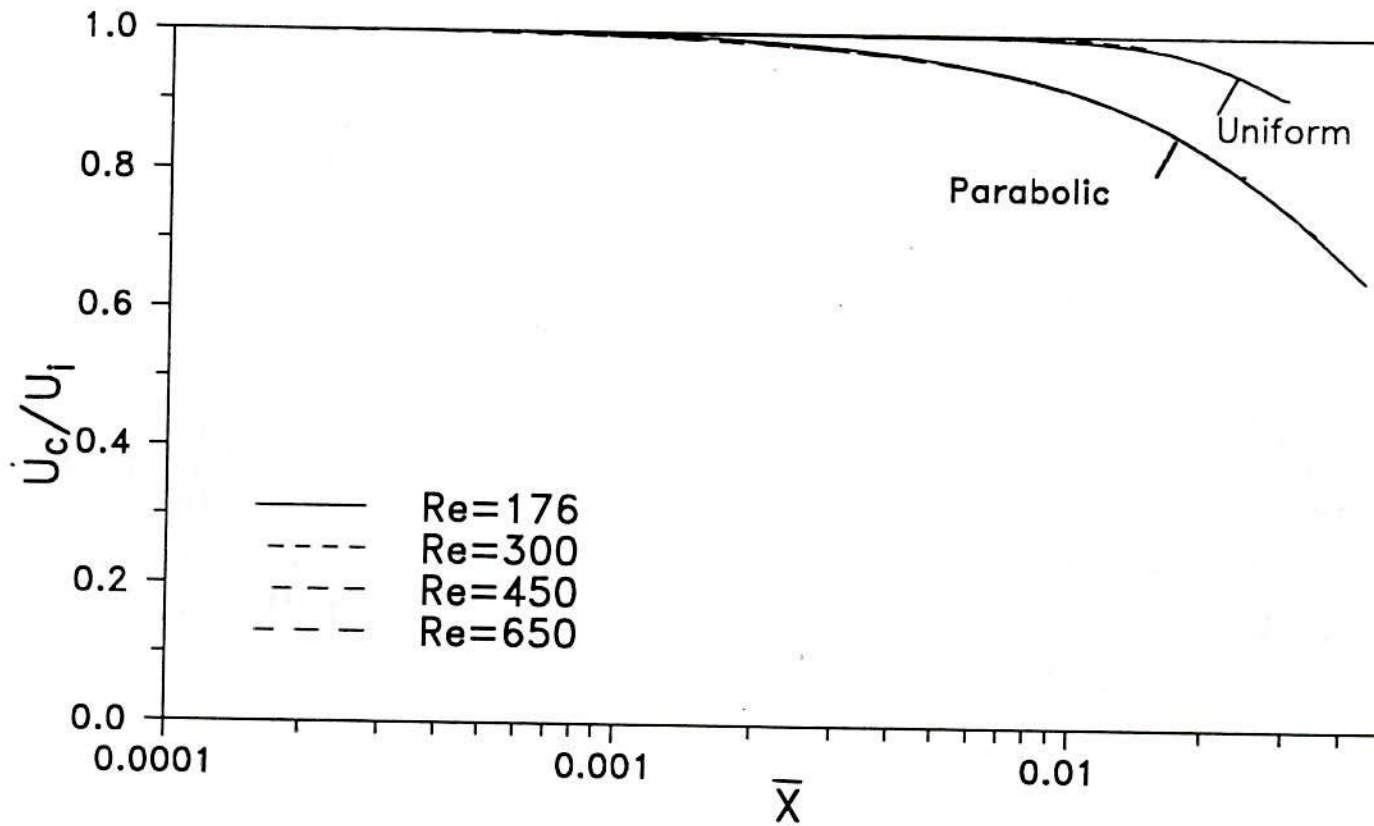


Fig. 4.2.5: Decay of centre line velocity for axisymmetric jet.

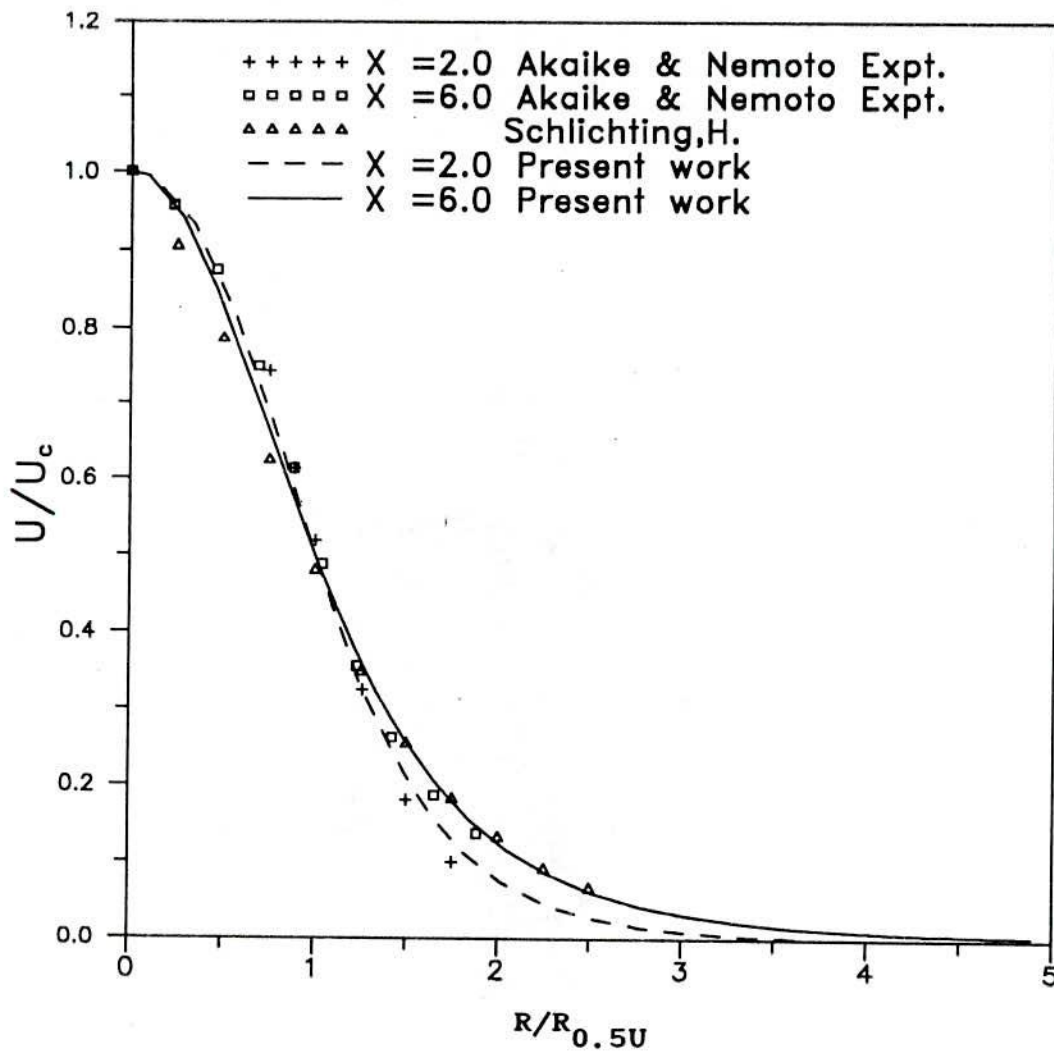


Fig. 4.2.6 : Comparison of velocity profiles at $Re=176$ for axisymmetric jet.

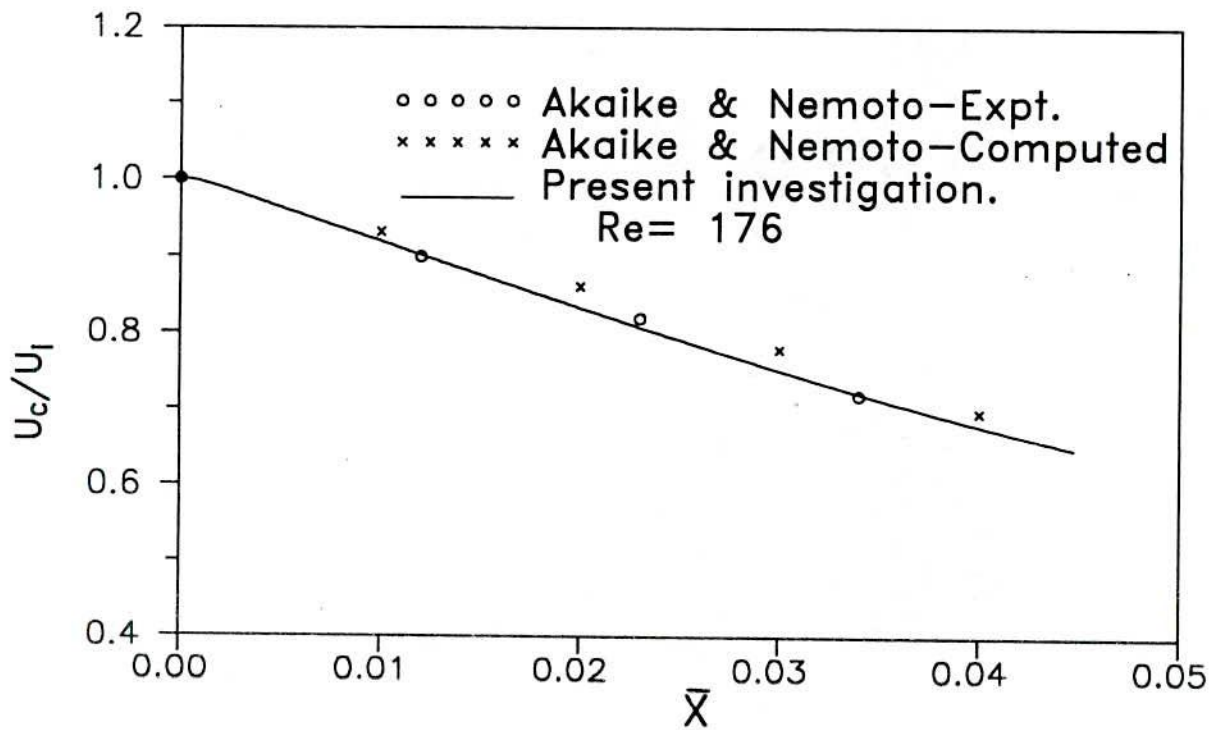


Fig. 4.2.7 : Decay of centre line velocity for axisymmetric jet with parabolic velocity profile.

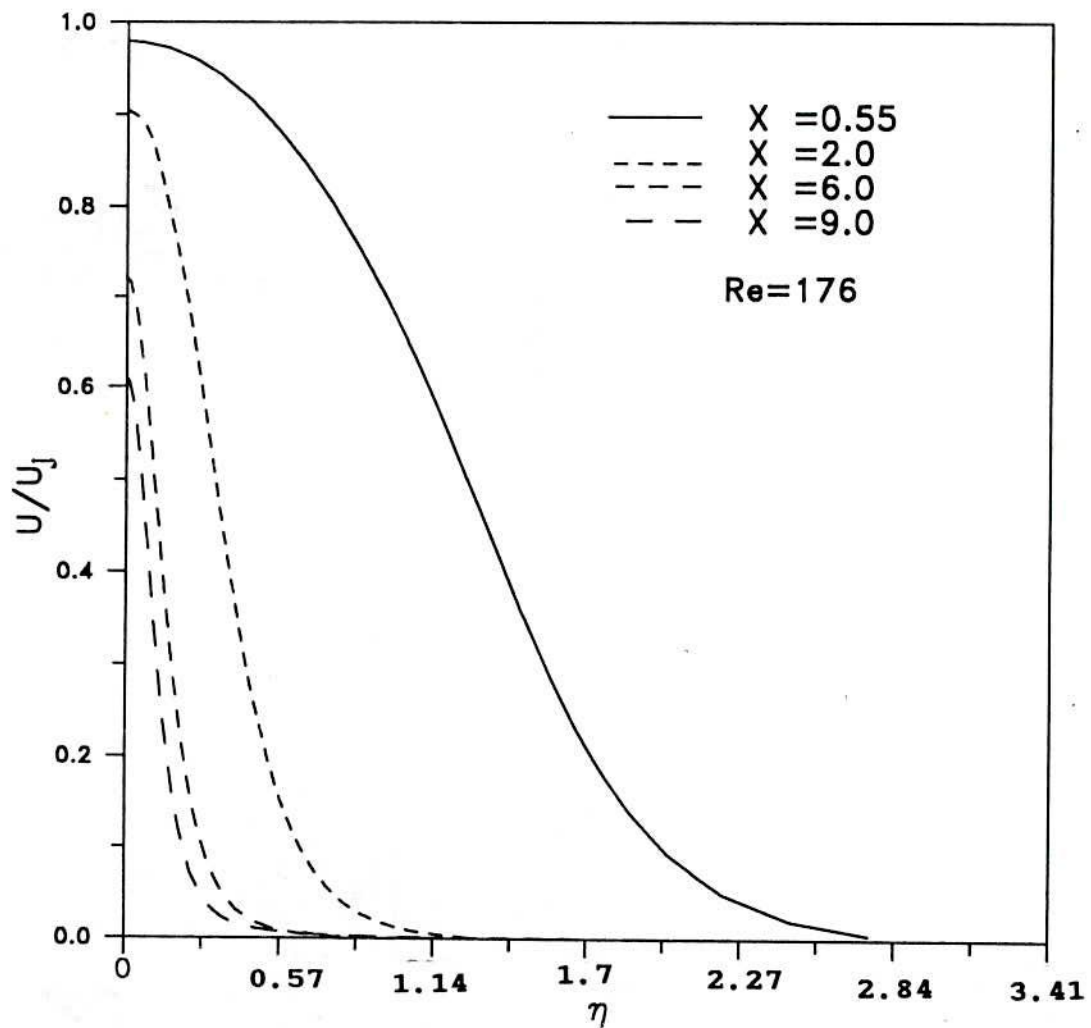


Fig. 4.2.8 : Axial velocity distribution at different X for axisymmetric jet with parabolic velocity profile.

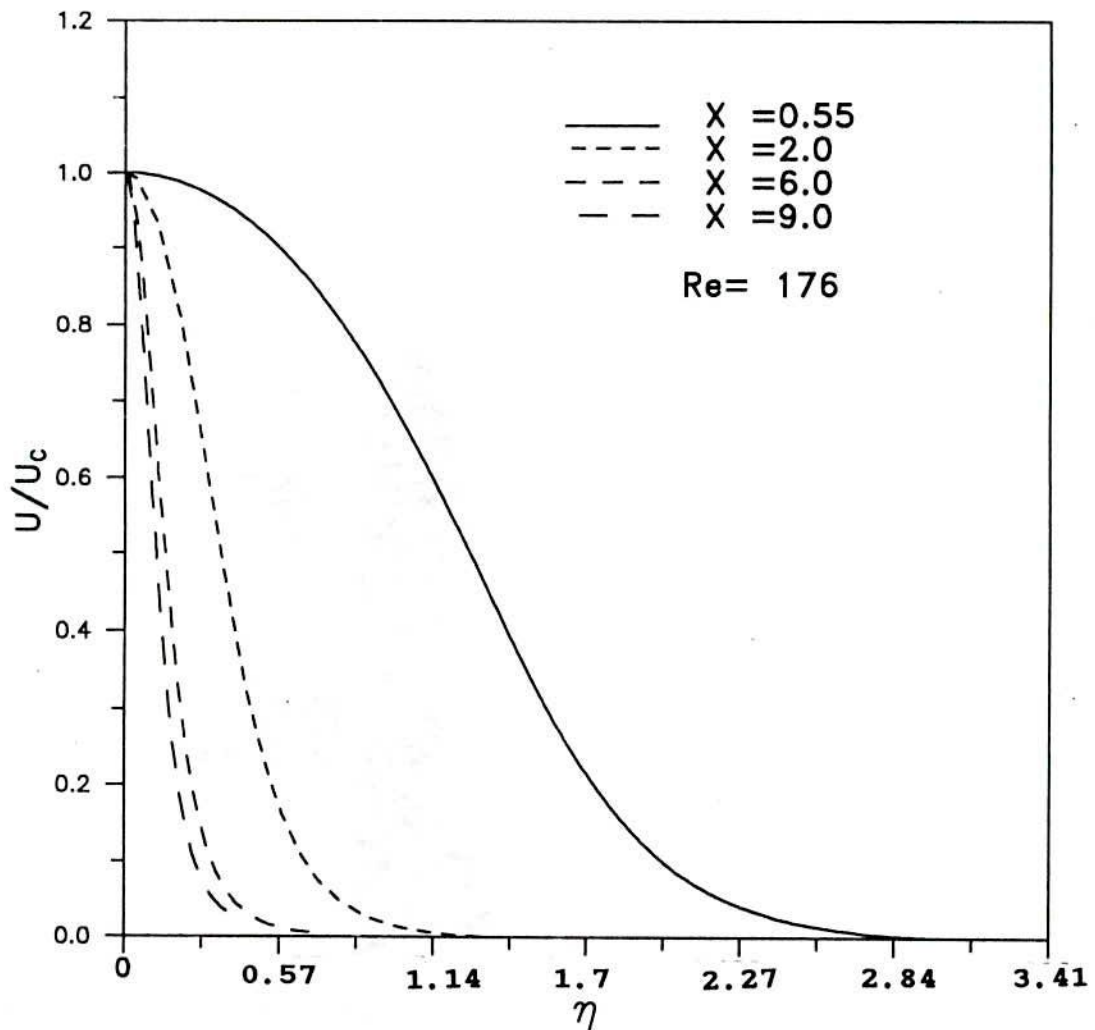


Fig.4.2.9: Velocity distribution at various axial locations for axisymmetric jet with parabolic velocity profiles at exit.



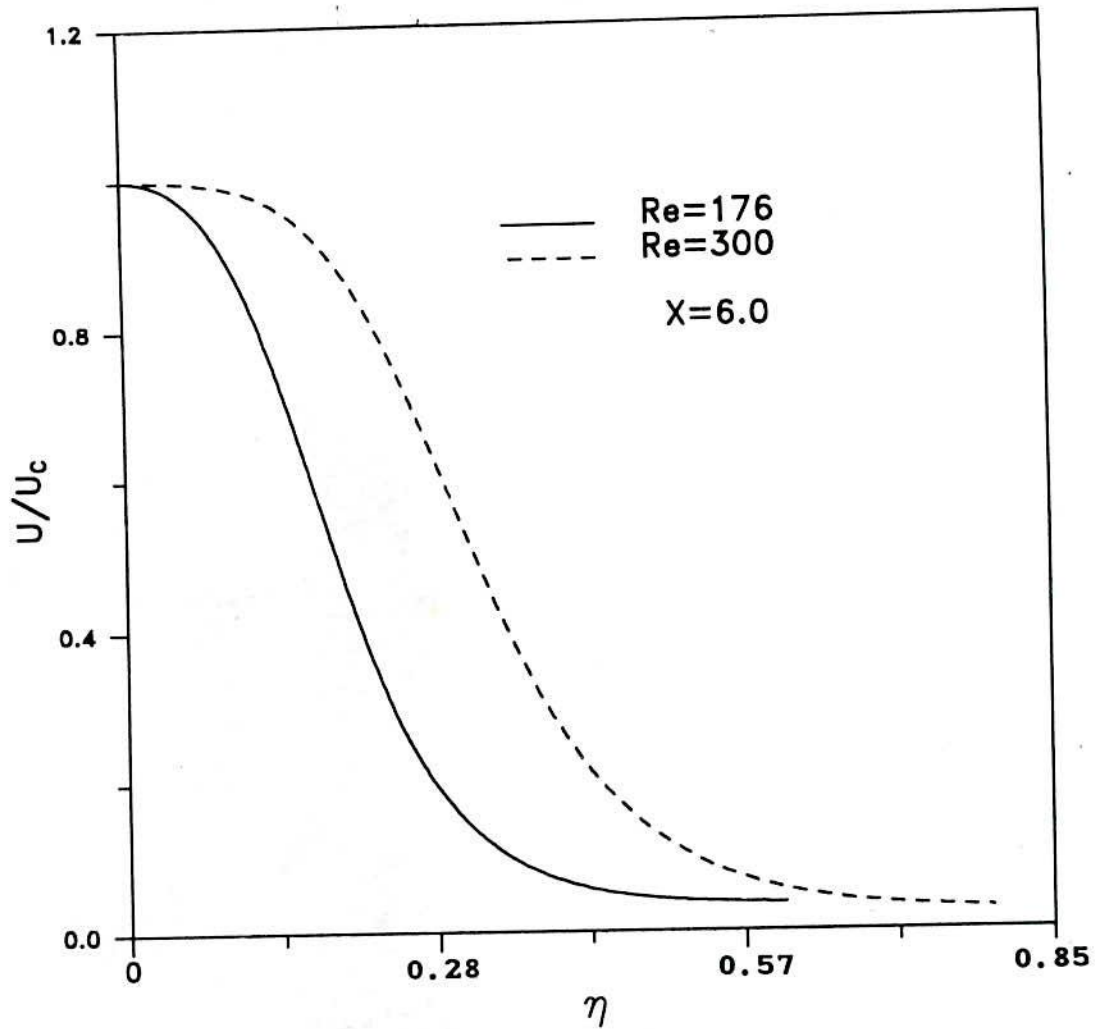


Fig. 4.2.10 : Axial velocity distribution at different Re for axisymmetric jet with uniform velocity profile.

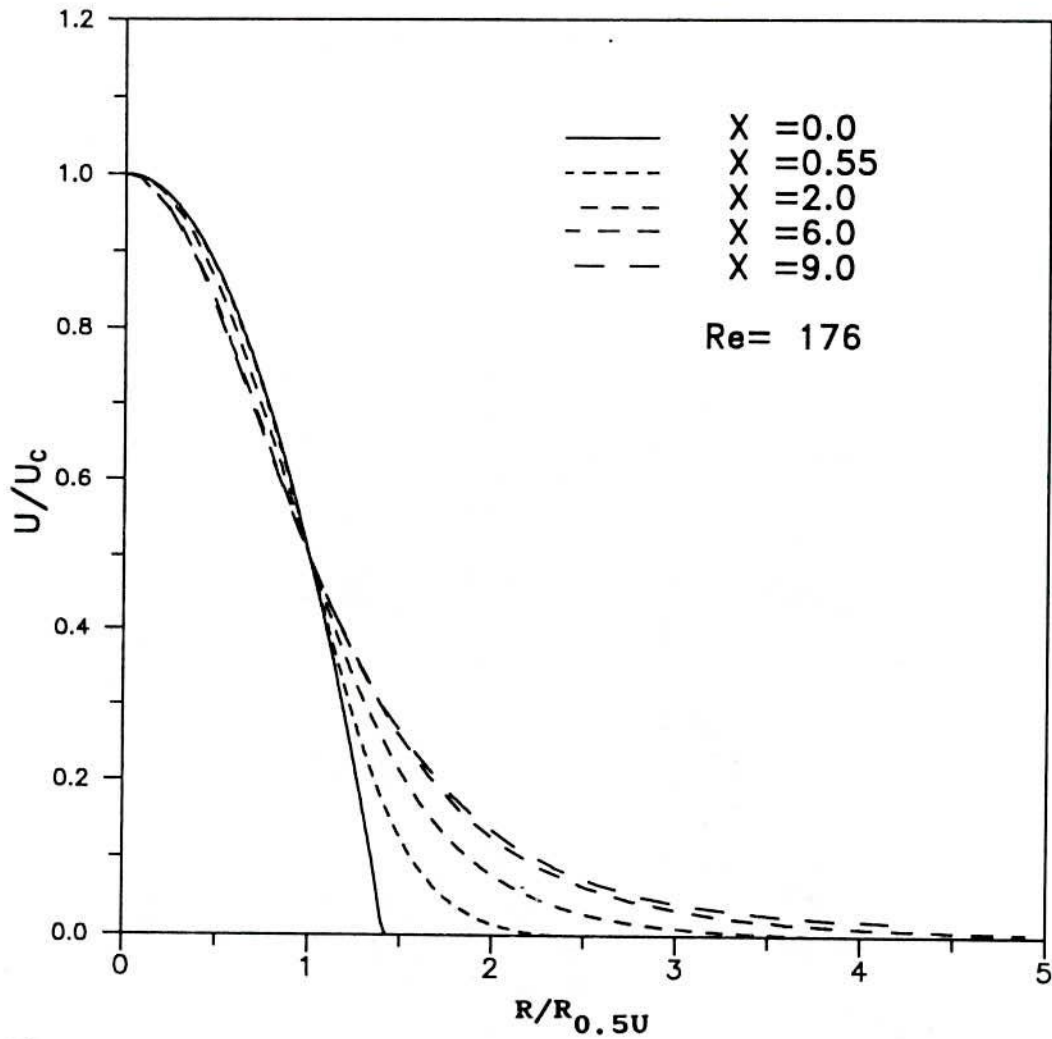


Fig.4.2.11: Axial velocity distribution at different X for axisymmetric jet with parabolic velocity profile.

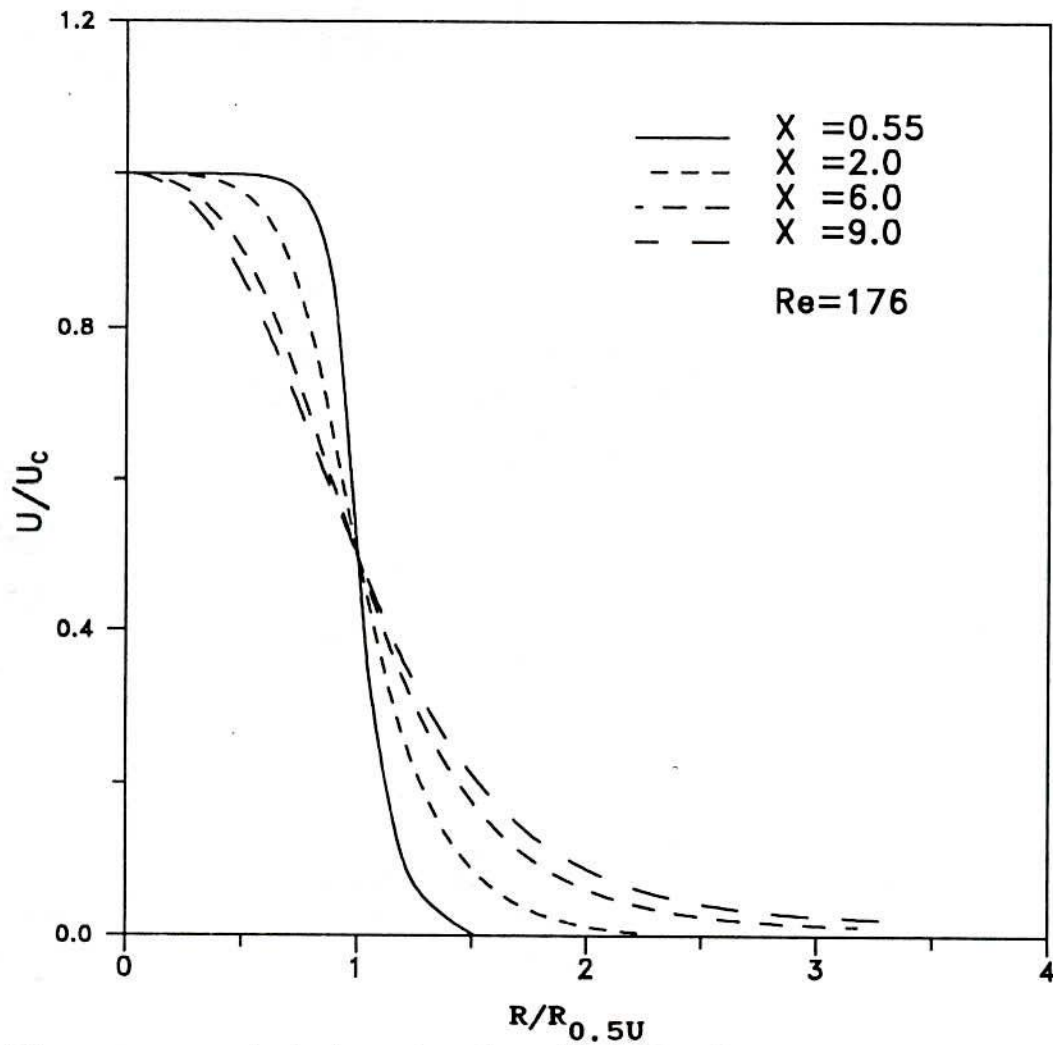


Fig.4.2.12: Axial velocity distribution at different X for axisymmetric jet with uniform velocity profile.

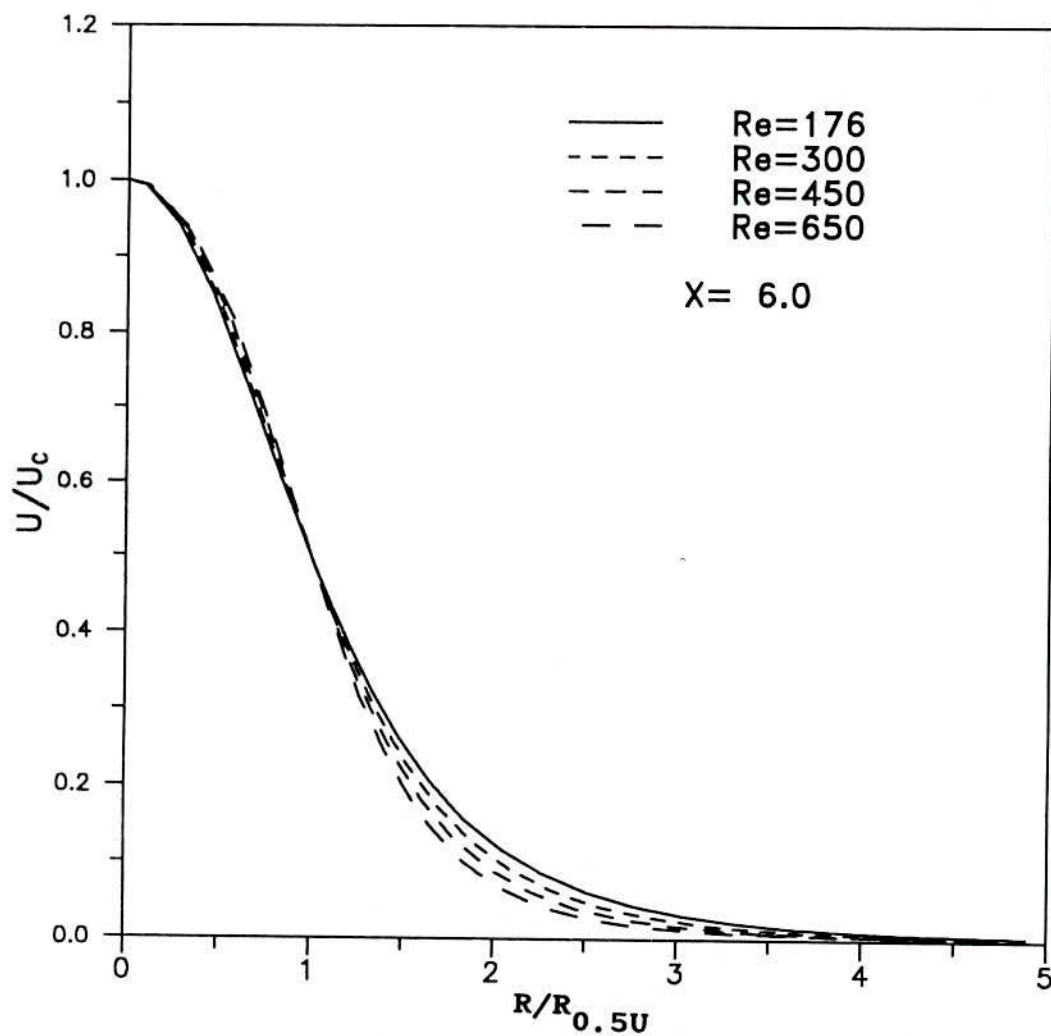


Fig.4.2.13: Axial velocity distribution at different Re for axisymmetric jet with parabolic velocity profile.

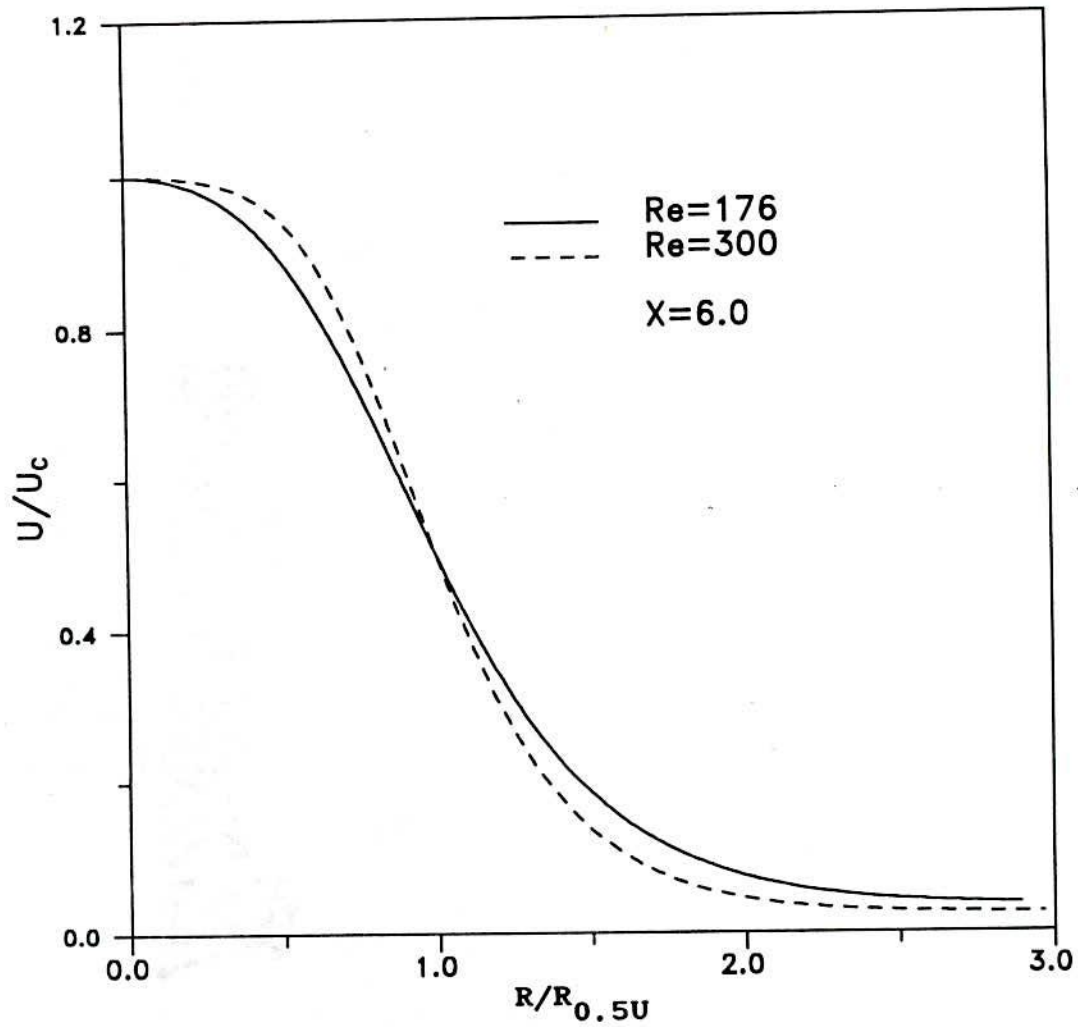


Fig.4.2.14: Axial velocity distribution at different Re for axisymmetric jet with uniform velocity profile.

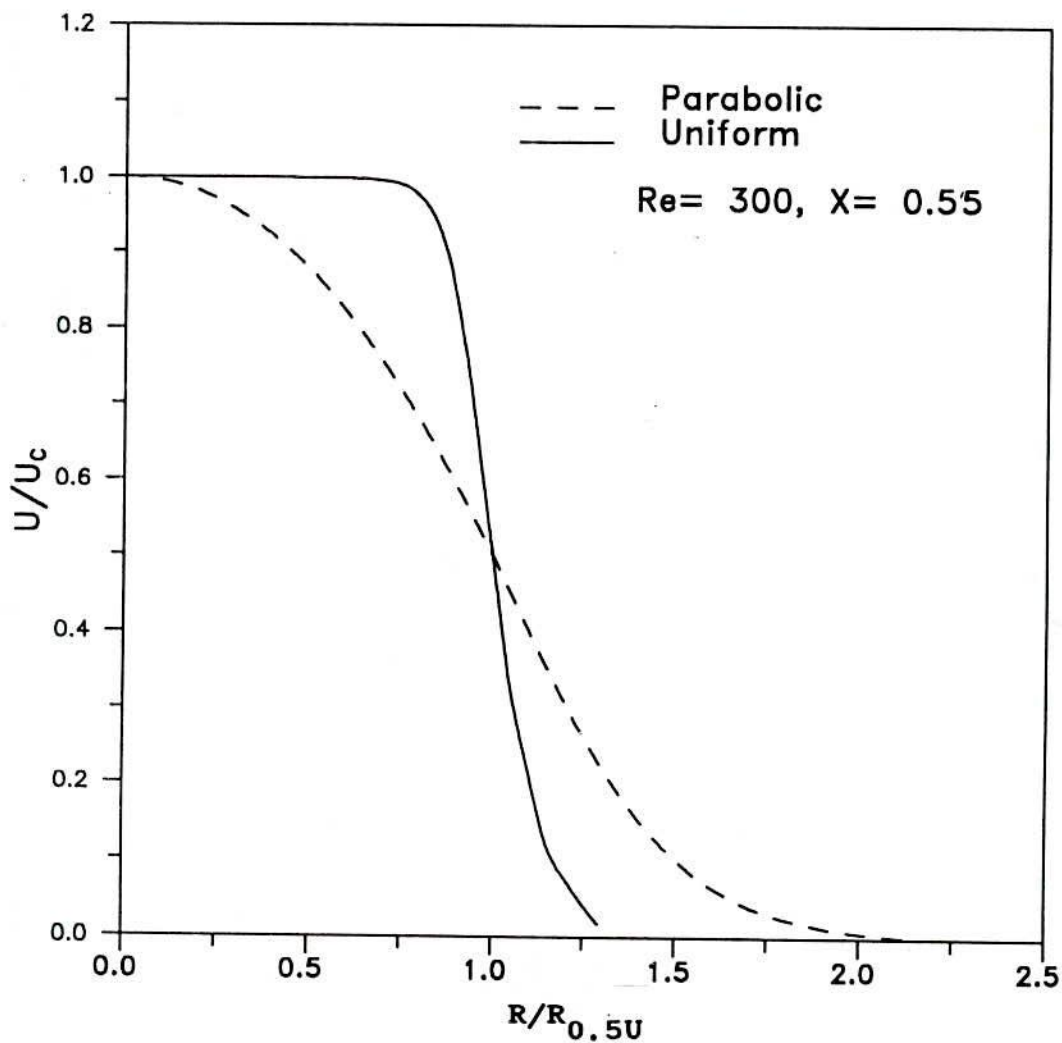


Fig.4.2.15: Comparison of velocity profiles for axisymmetric jet with initially uniform and parabolic velocity profiles.

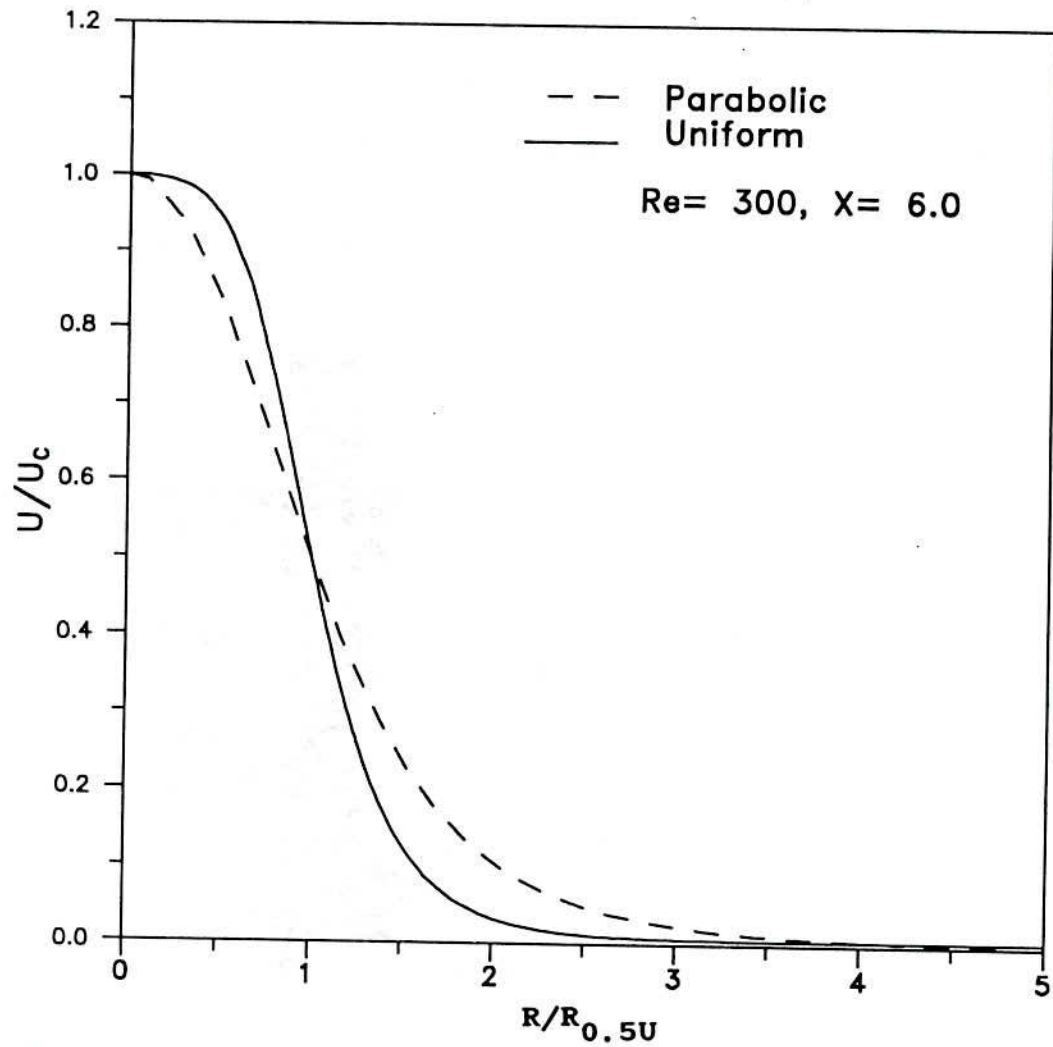


Fig.4.2.16: Comparison of velocity profiles for axisymmetric jet with initially uniform and parabolic velocity profiles.

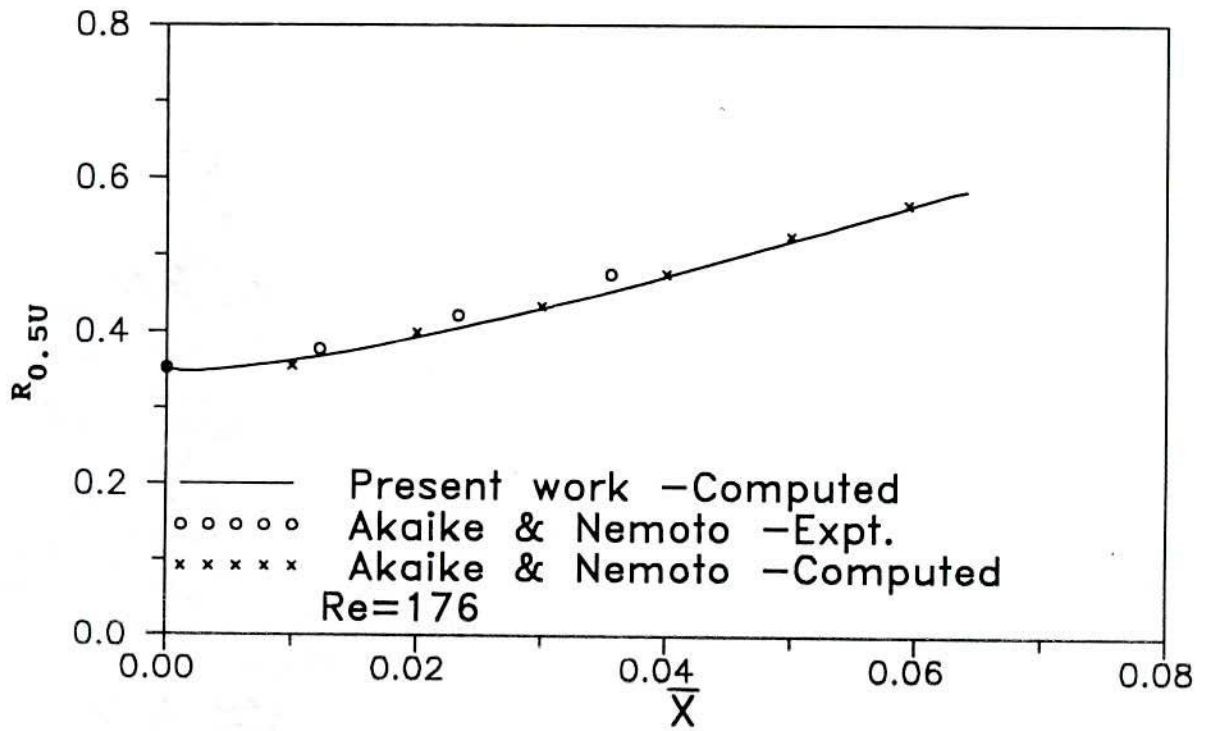


Fig.4.2.17: Variation of half radius $R_{0.5U}$ for axisymmetric jet with parabolic velocity profile.

Isoterhms, Free axisymmetric jet, Re=176 (Parabolic)

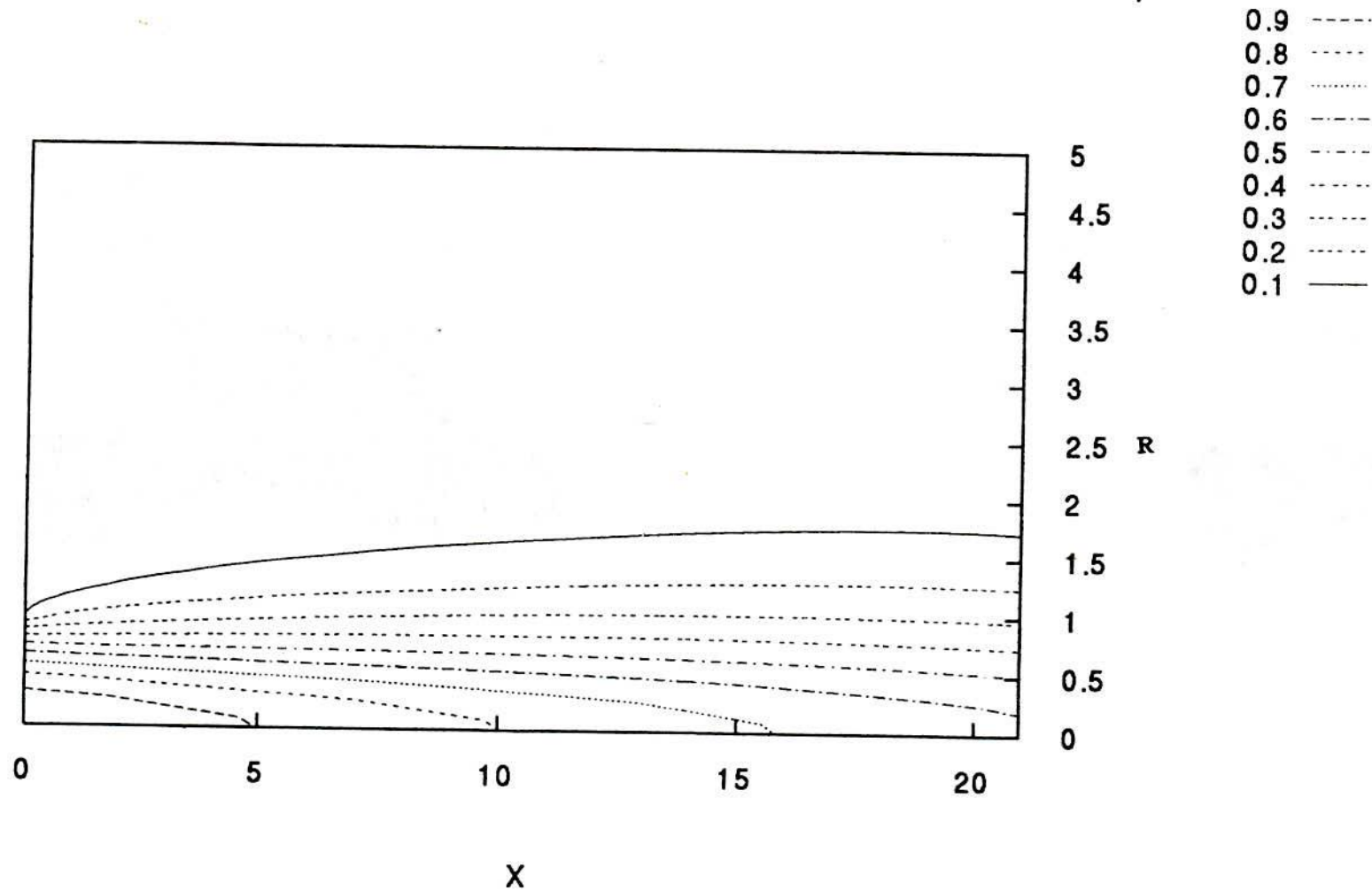


Fig.4.2.18: Isotherms at Re= 176 with parabolic jet exit velocity profile for free axisymmetric jet. Pr= 0.71.

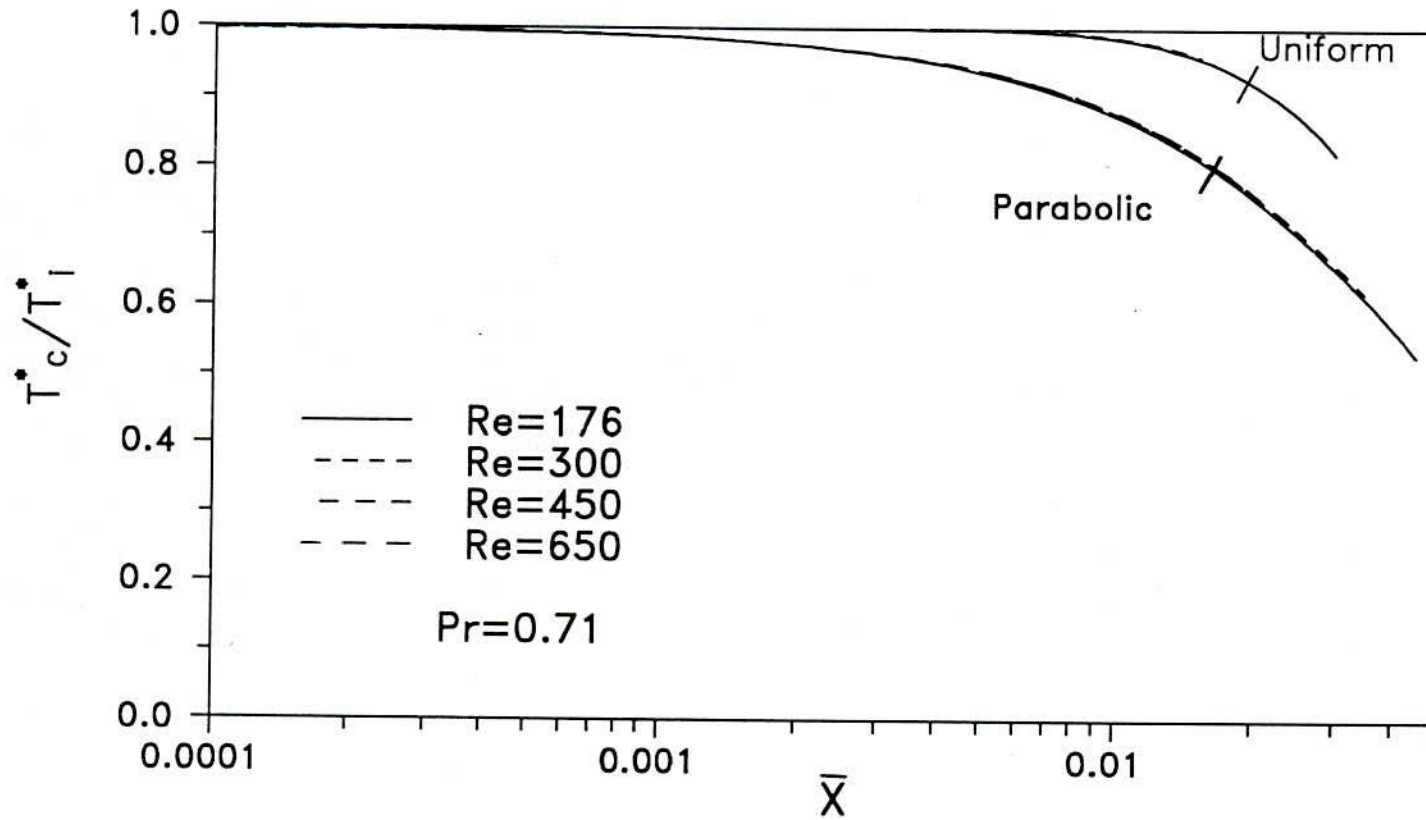


Fig. 4.2.19: Decay of centre line temperature for axisymmetric jet.

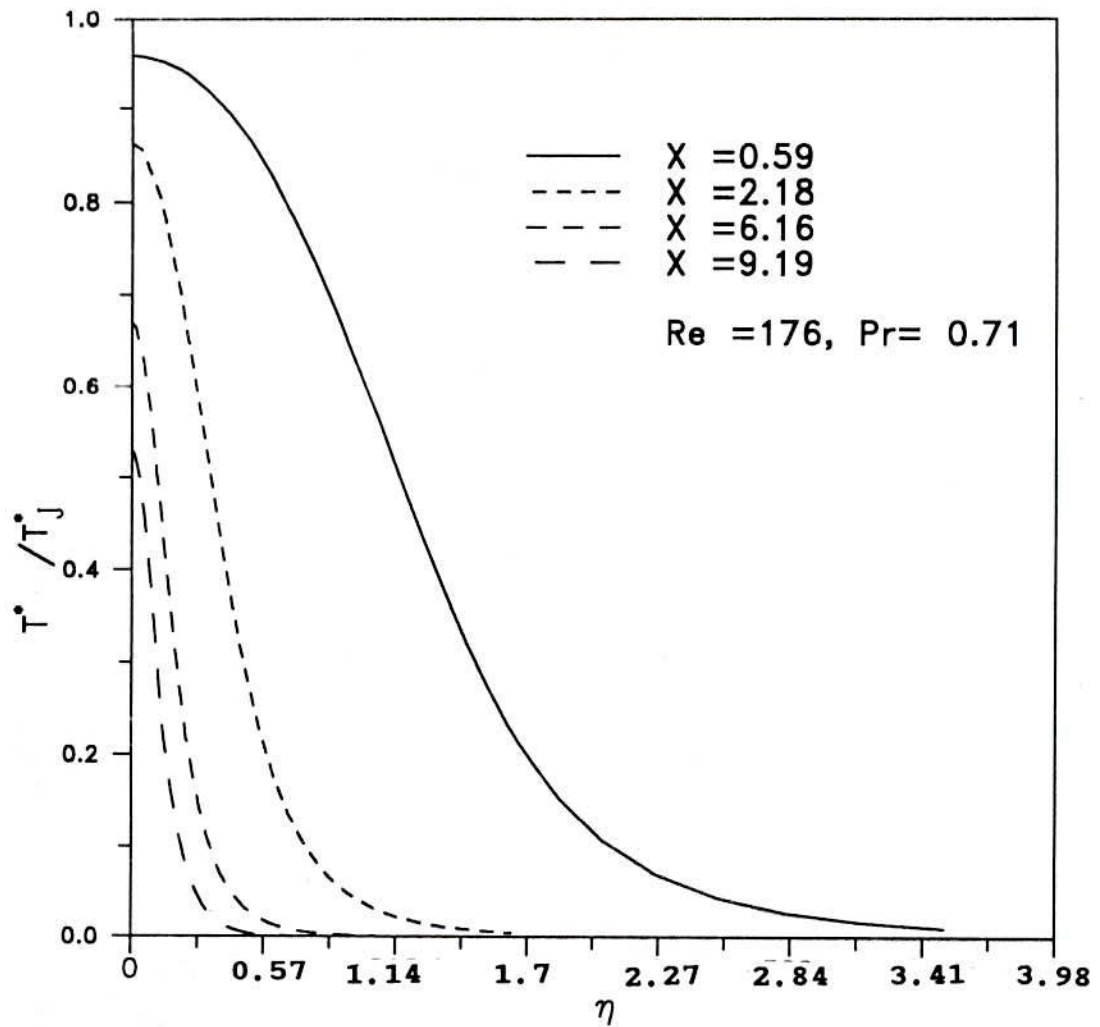


Fig.4.2.20; Temperature distribution at different X for axisymmetric jet with parabolic temperature profile.

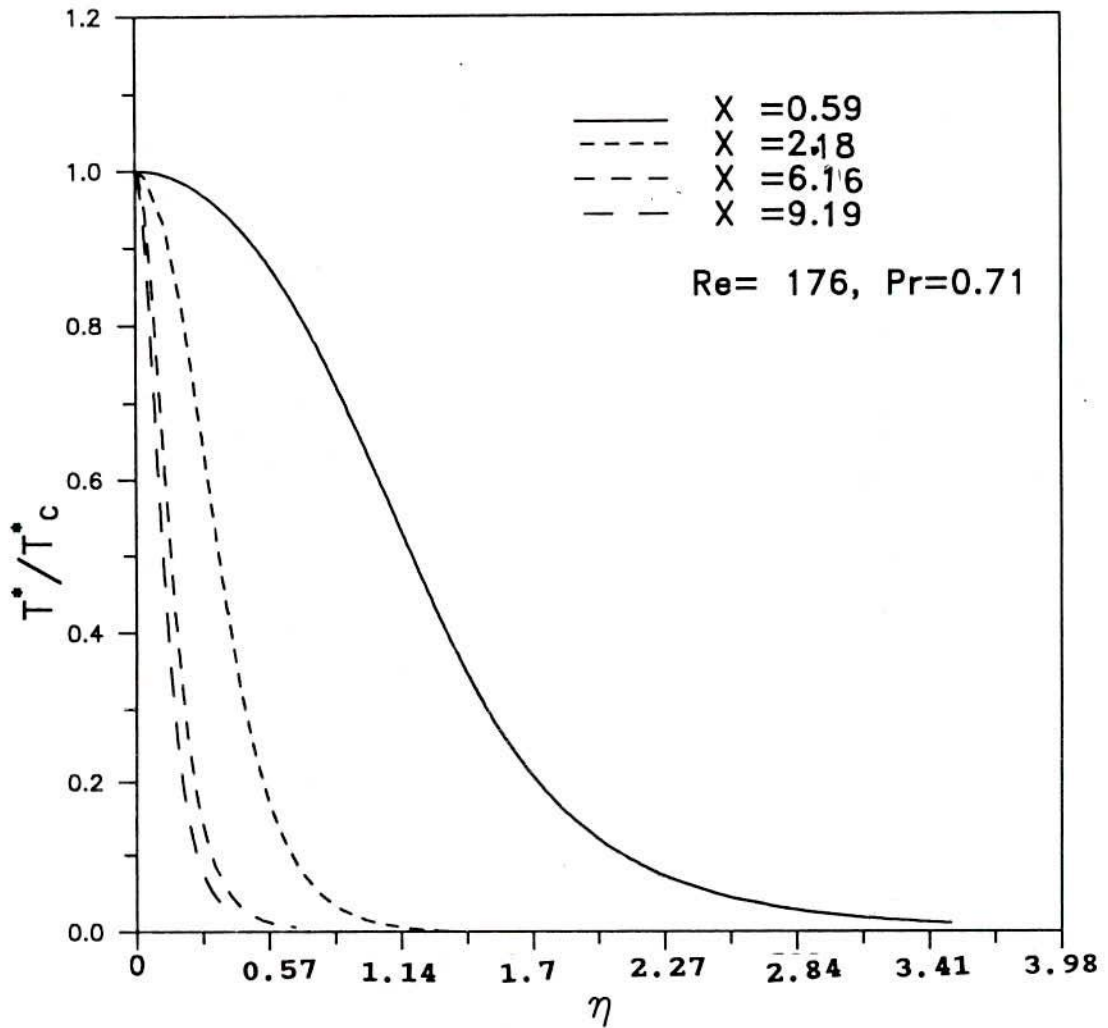


Fig.4.2.21; Temperature distribution at various axial locations for axisymmetric jet with parabolic velocity profiles at slot exit.

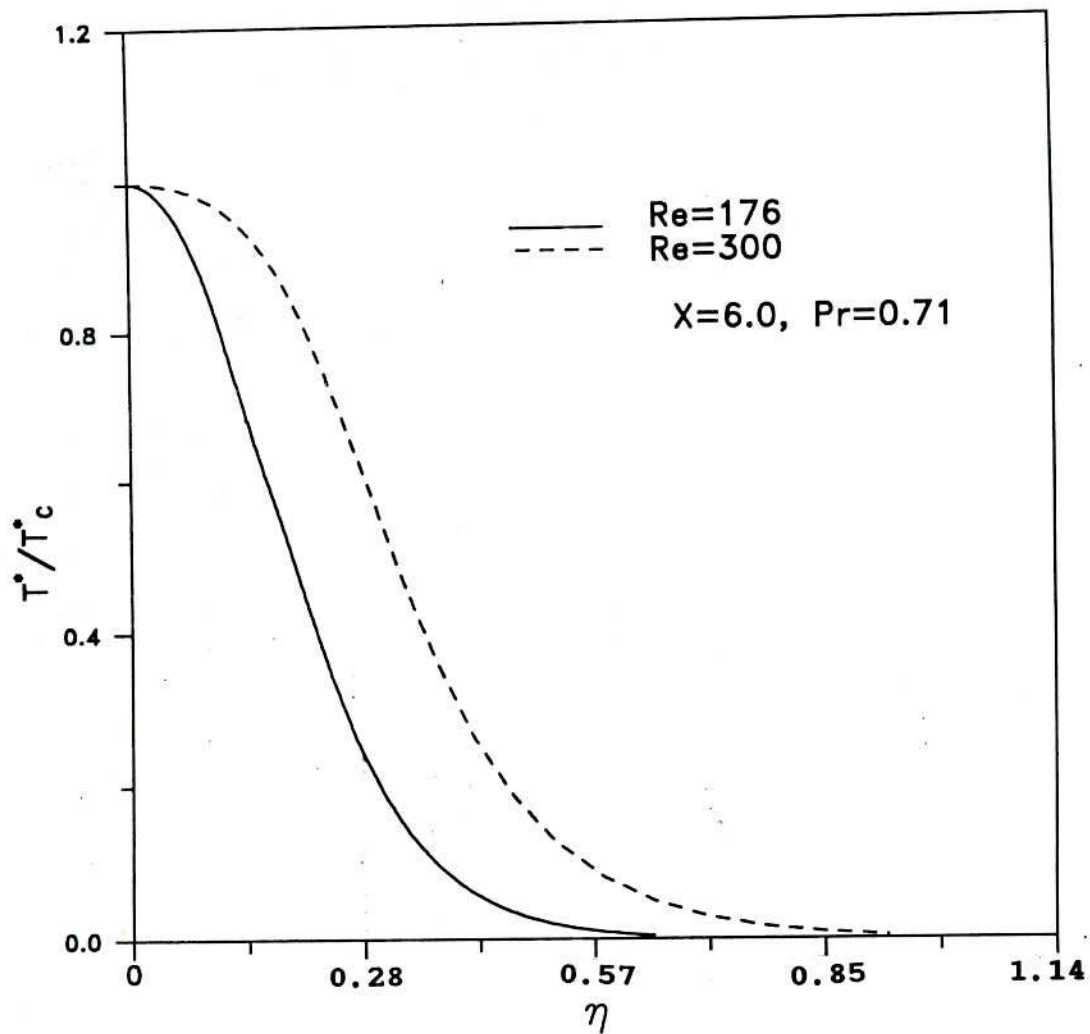


Fig.4.2.22: Temperature distribution at different Re for axisymmetric jet with uniform temperature profile.

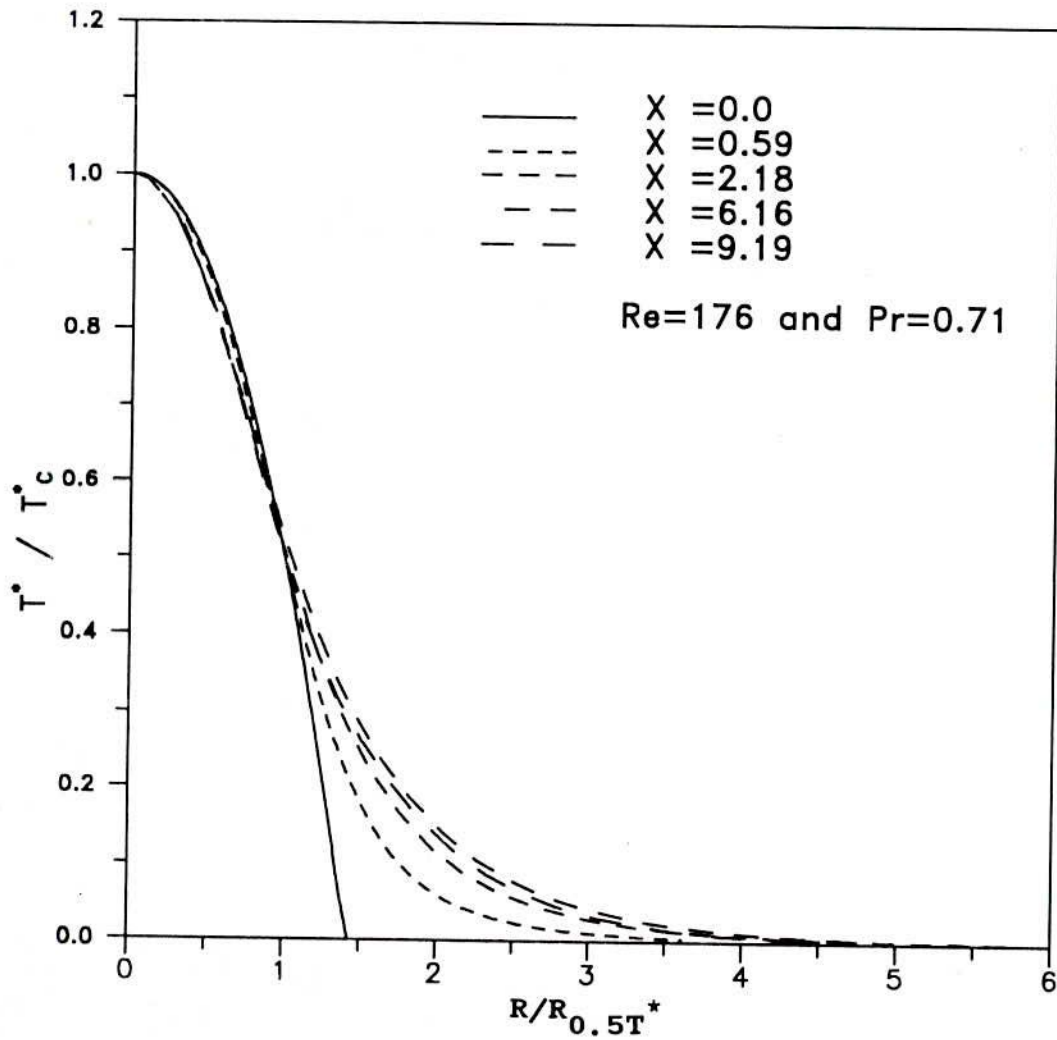


Fig. 4.2.23 : Temperature distribution at different X for axisymmetric jet with parabolic temperature profile.

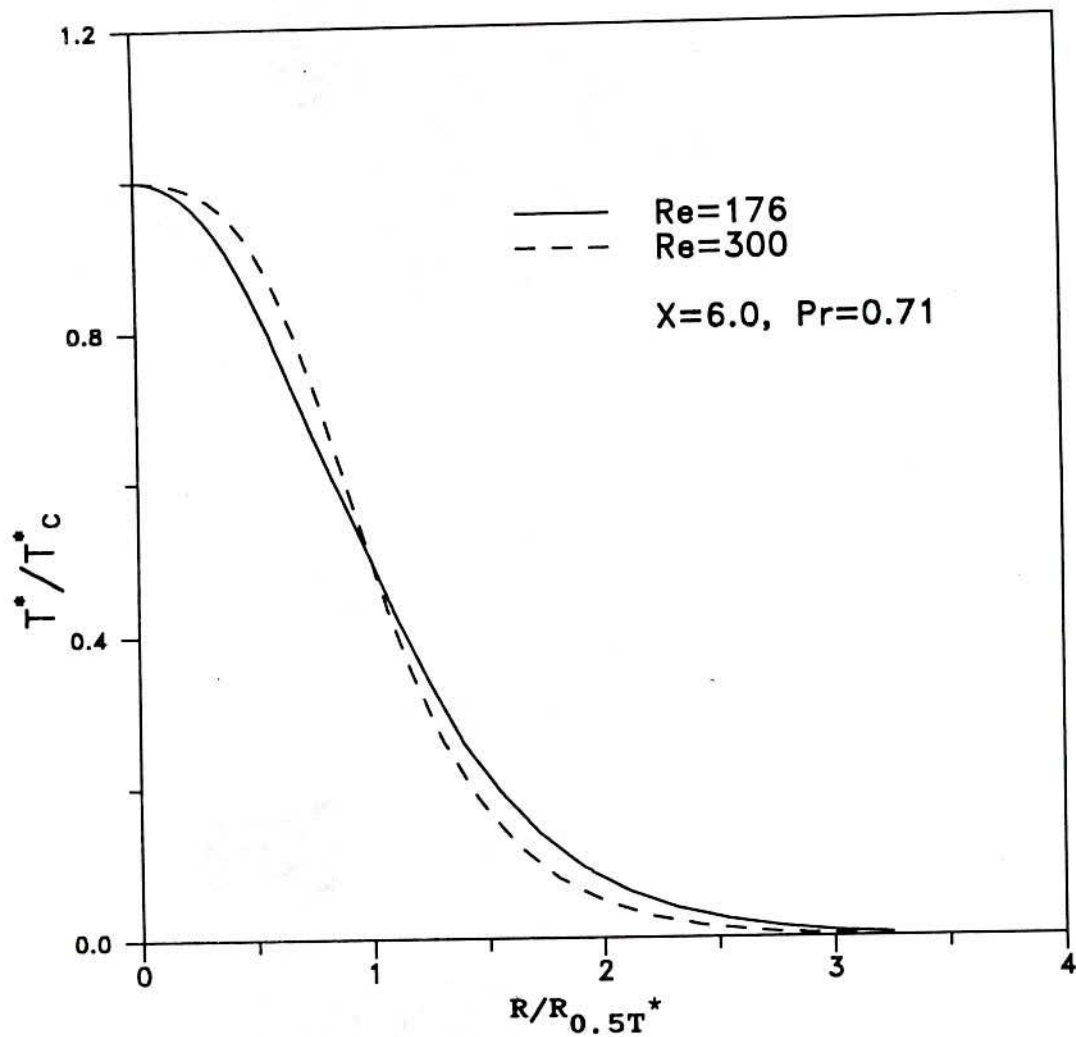


Fig.4.2.24: Temperature distribution at different Re for axisymmetric jet with uniform temperature profile.

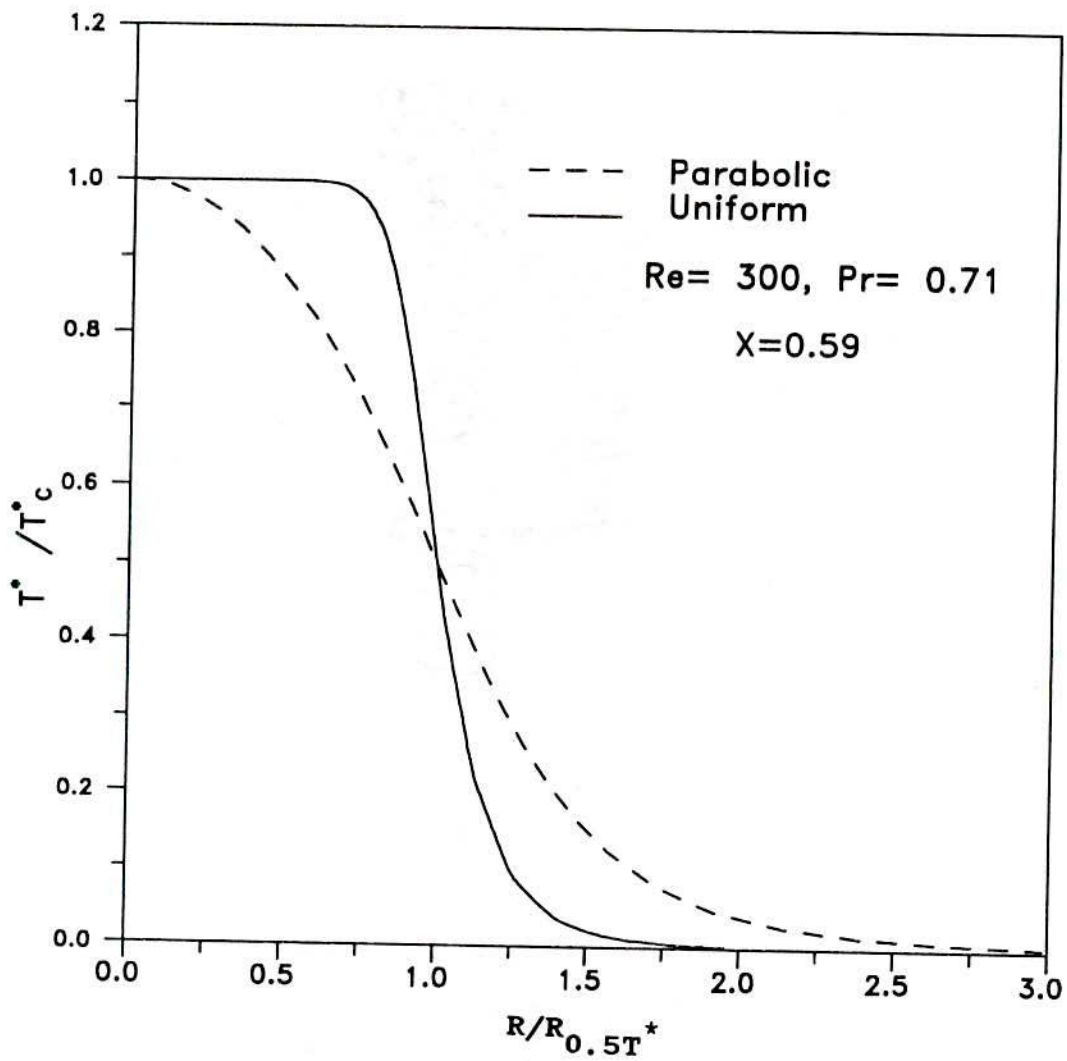


Fig. 4.2.25: Temperature distribution for axisymmetric jet with parabolic & uniform temperature profile

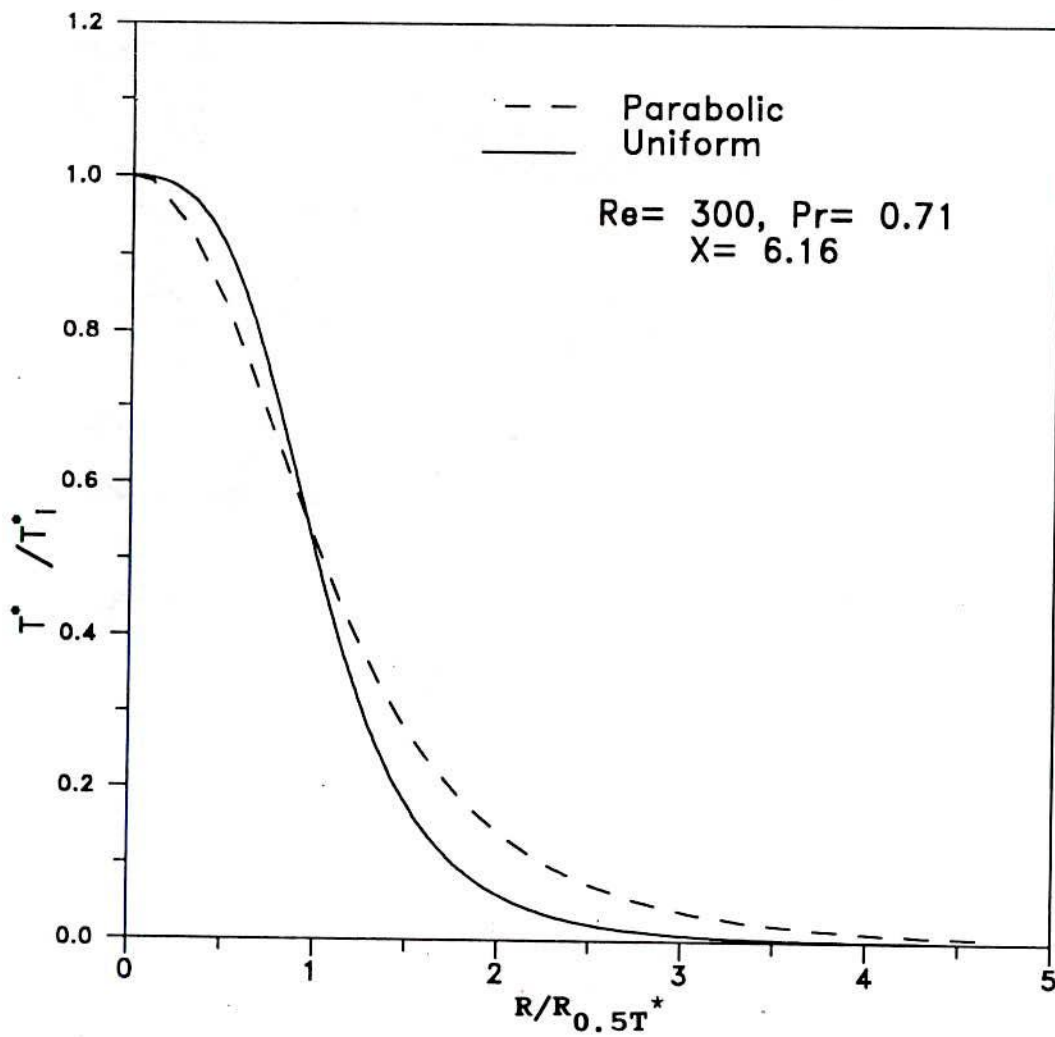


Fig.4.2.26: Temperature distribution for axisymmetric jet with parabolic & uniform temperature profile

4.3 SLOT JET IMPINGEMENT ON A CIRCULAR CYLINDER

The Navier-Stokes equations in this case have been solved by SIMPLEC algorithm with boundary conditions as described in Chapter 3. Unlike the free axisymmetric jets, the jet in this case does not emanate from a nozzle in a vertical wall. The nozzle walls are assumed to be along $\theta = \pm \theta_1 = \text{constant}$. The nozzle exit velocity is assumed to be radial only, with no component in azimuthal direction. This implies that the nozzle exit velocity is directed towards the centre of the cylinder. The flow is symmetric about the jet axis, hence only the upper half of the domain has been considered for computation purpose. The outer boundary of the computation domain is taken to be a circle of radius R_{max} . The entrainment has been assumed to occur radially along this outer boundary. The problem has thus, been considerably idealized.

The modelling of nozzle and application of boundary conditions on the nozzle wall and at nozzle-exit, required special care since boundary control volumes had to be introduced at these locations. All the subroutines of the computer programme had to be modified to include these changes.

The Reynolds number, the nozzle width and the spacing between the jet-exit and cylinder, are the parameters considered for the investigation. Fine grid spacings were taken near the cylinder, nozzle exit and the axis of symmetry, which were gradually expanded to coarse grids in the interior of the domain.

The relaxation factor of 0.5 was used for the two momentum equations and the energy equation. A relaxation factor of 1.0 was

used for the pressure correction equation. Normalized residues for the velocity components and the temperature as defined in Equation (4.1.1), were calculated during every iterations along with SSUM to check the convergence. SSUM is the sum of defect of mass conservation in all the control volumes. The convergence of velocity profiles was taken as the criterion for convergence. The required convergence was achieved in 750 iterations for the uniform slot-exit velocity profile. In this case also, the residues of velocity components, temperature and SSUM are as follows,

$$\begin{aligned}\text{Res}(U) &= 10^{-3} \\ \text{Res}(V) &= 10^{-3} \\ \text{SSUM} &= 10^{-16}\end{aligned}$$

The solutions were obtained for various grid sizes to check the grid independence of the solutions. Figure 4.3.1 shows the local friction factor at $Re=30$, $L/W=8$ and $W=0.4$ and for three grid sizes, namely, 90×90 , 102×110 , and 122×130 . It is observed that a grid finer than 90×90 , does not yield significantly different results, hence, this has been used in all the subsequent calculations.

Figure 4.3.2, shows the variation of friction factor with the azimuthal angle along the cylinder surface for different slot exit Reynolds numbers, $L/W=8$ and $W=0.4$. Friction factor is zero at $\theta=0$ and $\theta=\pi$, where velocity gradient is zero because of symmetry. The flow separation is observed to occur earlier at higher Reynolds numbers. Kang and Greif [64] have made a similar observation regarding the point of flow separation. The sign of friction

factor changes after the point of flow separation, in the recirculating region since the direction of flow reverses in this region. Ultimately, friction factor becomes zero at the rear stagnation point. The rate of change of friction factor and the maximum value, both increase with the increase of Reynolds number. The absolute value of skin friction increases as θ increases from zero value, reaches a maximum negative value and then decreases again. The point of maximum negative value, shifts towards $\theta = 0$ at higher Reynolds numbers. Subsequently, the skin friction becomes zero around $\theta = \pi/2$ indicating flow separation.

Figure 4.3.3, shows the variation of local friction factor with θ at different nozzle-to-cylinder surface spacing ratio L/W , for $Re=60$ and $W=0.4$. The local friction factor decreases with the increase of L/W ratio, since the approach velocity at cylinder surface decreases. The maximum value of friction factor is shifted away from the stagnation point with the increase of nozzle-to-cylinder surface spacing ratio. Flow separation occurs earlier at $L/W=4$ than at $L/W=10$ since the approach velocity is larger at $L/W=4$ than at $L/W=10$. Hence, in all respects the effect of decrease in L/W ratio is equivalent to increase of Reynolds number.

Figure 4.3.4, shows the variation of pressure along the cylinder surface at $W=0.4$, $L/W=8$ and for different Reynolds numbers. The pressure is maximum at the forward stagnation point for all Reynolds numbers. The velocity is zero at the forward stagnation point. The velocity increases and pressure decreases for $\theta > 0$. The pressure continues to decrease upto approximately

$\theta = \pi/4$ and then it starts increasing and finally becoming constant in the recirculation region. The pressure gradient is adverse in the region $\pi/4 < \theta < \pi/2$. The flow separation occurs in this region. The pressure in the recirculation region increases as Reynolds number increases. The pressure is below the atmospheric pressure in the recirculation region. There are two points where the curves for $Re = 90, 120$ and 150 intersect each other. These points indicate that at higher Reynolds numbers, the pressure decreases at relatively faster rate followed by an equally faster recovery.

Figure 4.3.5, shows the pressure variation along the cylinder surface for different L/W ratios at $W = 0.4$ and $Re = 60$. The decrease of pressure is faster at lower L/W ratios than at higher L/W ratios, but recovery is not very fast at higher L/W ratios. All the curves intersect each other around $\theta = 0.3$ radians where pressure seems to be independent of L/W ratios. The pressure in the recirculation region is below atmospheric and increases with the increase of L/W ratio.

Figure 4.3.6 shows the variation of local friction factor for various values of nozzle width, W at $Re = 60$ and $L/W = 8$. The effect of increase in nozzle width W on the friction factor, is the same as that of increasing the Reynolds number. The friction factor is unaffected by the nozzle width for small values of θ . It attains a negative maximum value at $\theta = 0.5$ radians and decreases to zero indicating flow separation. The point of flow separation slightly shifts towards higher values of θ as the nozzle width increases.

Figure 4.3.7 shows the variation of pressure for various

values of nozzle width, W at $Re = 60$ and $L/W = 8$. The effect of increase of nozzle width, W is similar to the increase of Reynolds number. The stagnation pressure increase with the increase in nozzle width. The pressure decreases to a minimum value and then increases slightly, ultimately becoming constant in the recirculating region. The point where the minimum occurs, shifts towards higher values of θ as nozzle width increases. The level of pressure in the recirculating region increases with increase in nozzle width.

Figure 4.3.8 shows azimuthal components of velocity U/U_{\max} in the radial direction with the half jet width as the characteristic length. The results are presented for $W = 0.4$, $L/W = 8$ and $Re = 60$ at $\theta = 30.62^\circ$, 39.47° and 49° . The velocity profiles are typical wall jet profiles. The velocity is zero at the cylinder surface, increases to a maximum value in radial direction and then decreases to a zero value for large values of radius. The half jet width is defined as the radius beyond the maximum of velocity where velocity becomes 50% of maximum velocity. The radius at which the velocity is maximum, increases along θ direction indicating that the boundary layer thickness grows in the θ direction for the values of θ considered. The velocity profiles indicate a trend towards similarity for $R > R_{0.5U_{\max}}$.

Figure 4.3.9 shows the variation of azimuthal component of velocity U/U_{\max} in the radial direction for various Reynolds numbers, for $W = 0.4$, $L/W = 8$ and $\theta = 39.47^\circ$. The jet half width is taken as the characteristic length in this case also. The velocity profiles have the typical trend of wall jet. The location of

maximum velocity shifts very slightly towards smaller radii as the Reynolds number increases.

W=0.4, L/W= 8 and $\theta= 39.47^\circ$	
Re	$R_{0.5U_{max}}$
30	1.254
60	0.849
90	0.685
120	0.594
150	0.538

Table 4.3.1 Variation of Jet Half Width with Reynolds number

Table 4.3.1 gives the values of $R_{0.5U_{max}}$ measured from the cylinder surface, for various Reynolds numbers. It is observed that the half width decreases with increase in Reynolds numbers. The boundary layer becomes thinner and the maximum velocity occurs closer to the cylinder at higher Reynolds numbers. The velocity profiles for $Re= 120$ and 150 are almost coincident for all values of $R/R_{0.5U_{max}}$. The velocity profiles are coincident for all Reynolds number in the range of $R/R_{0.5U_{max}} < 1$ whereas, at lower Reynolds numbers the velocities are smaller for $R/R_{0.5U_{max}} > 1$.

Figure 4.3.10 shows the variation of azimuthal component of velocity in radial direction for various nozzle widths, namely 0.266, 0.4, 0.533 and 0.666 times the cylinder radius, $Re= 60$ and $L/W= 8$. It is observed that the location of maximum velocity shifts towards lower radius as the nozzle width increases.

Re=60 , L/W= 8 and $\theta= 39.47^\circ$	
W	$R_{0.5U_{max}}$
0.266	0.77
0.4	0.8487
0.533	0.951
0.666	1.0

Table 4.3.2 Variation of Jet Half Width with the Nozzle Width

Table 4.3.2 gives the values of jet half width for various nozzle widths. It is observed that the half width increases with the increase of nozzle width. It appears that the location of maximum velocity is independent of the nozzle width if the velocity is plotted in R co-ordinate alone. The cylinder faces a larger volume flow rate as the nozzle width increases, the velocity remaining constant for fixed Reynolds number. In the limit of very large nozzle width ($W \gg 1$), the results should be similar to a cylinder in unconfined flow and wall jet type of velocity distribution will not occur.

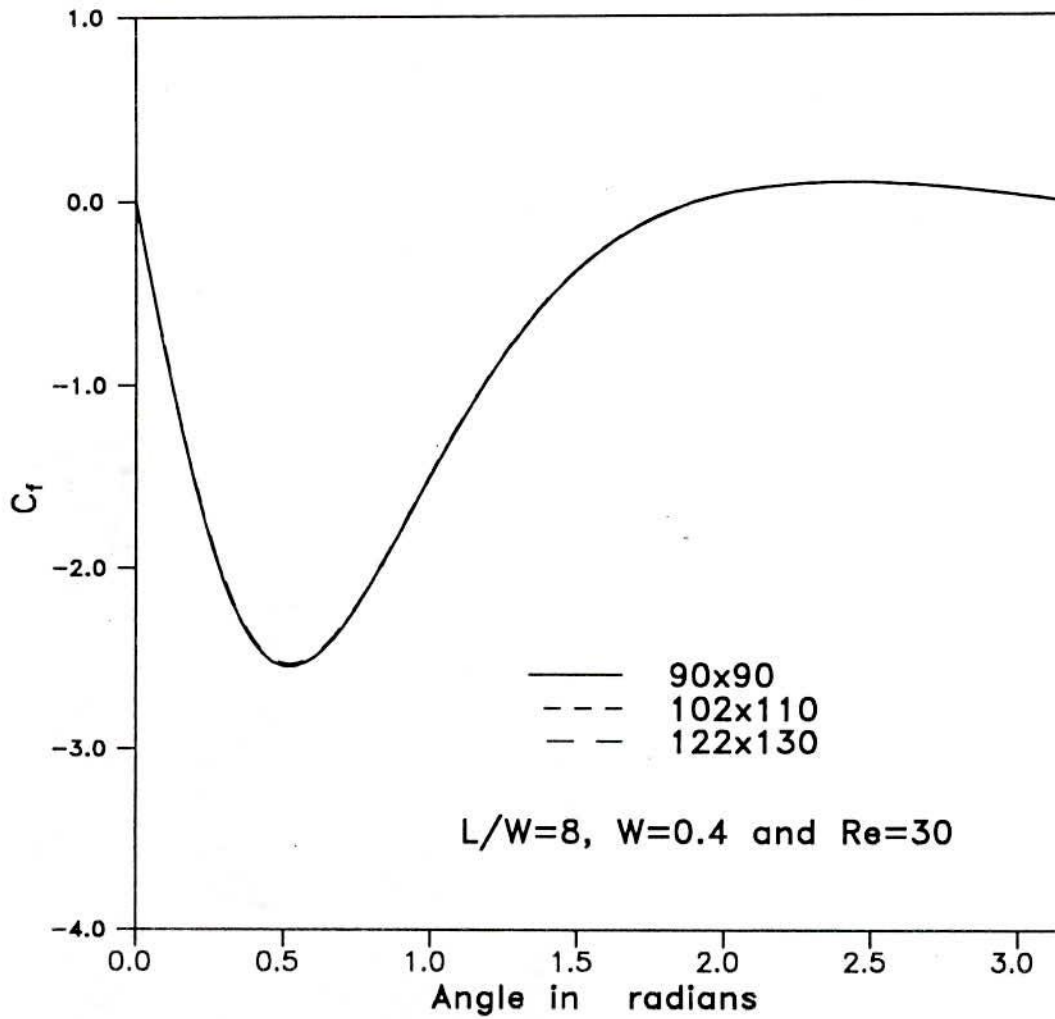


Fig. 4.3.1]: Variation of local friction factor over the cylinder surface with azimuthal angle showing the effect of different grid sizes.

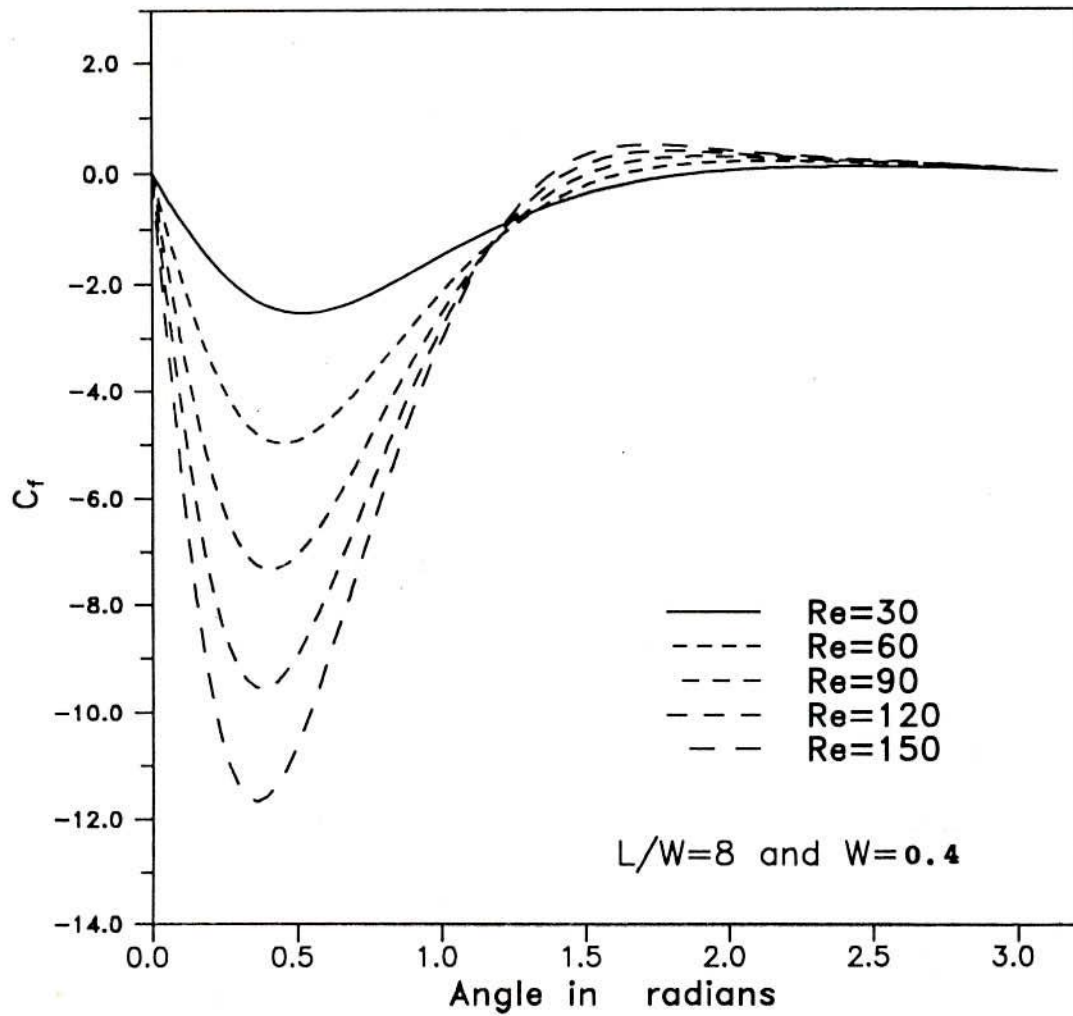


Fig.4.3.2 : Variation of local friction factor over the cylinder surface with azimuthal angle.

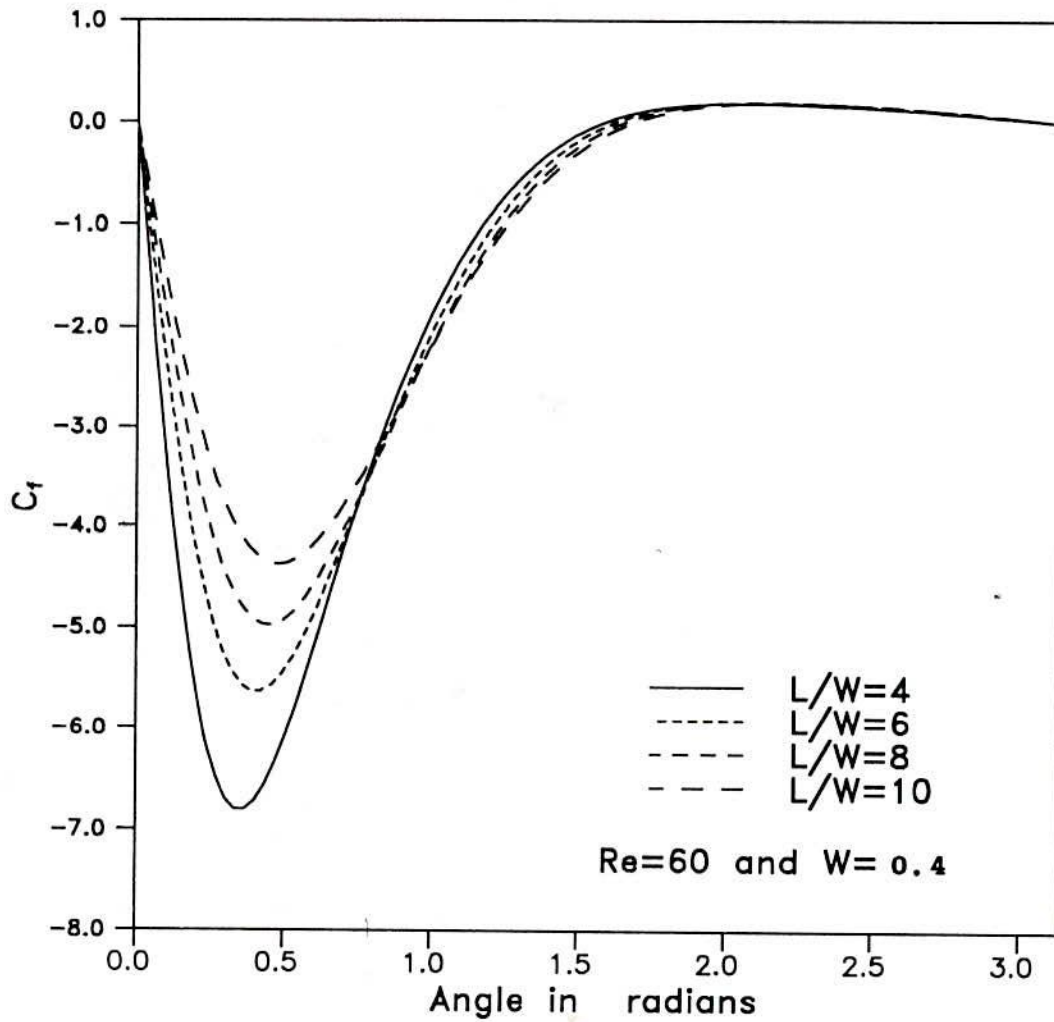


Fig. 4.3.3: Variation of local friction factor over the cylinder surface with azimuthal angle.

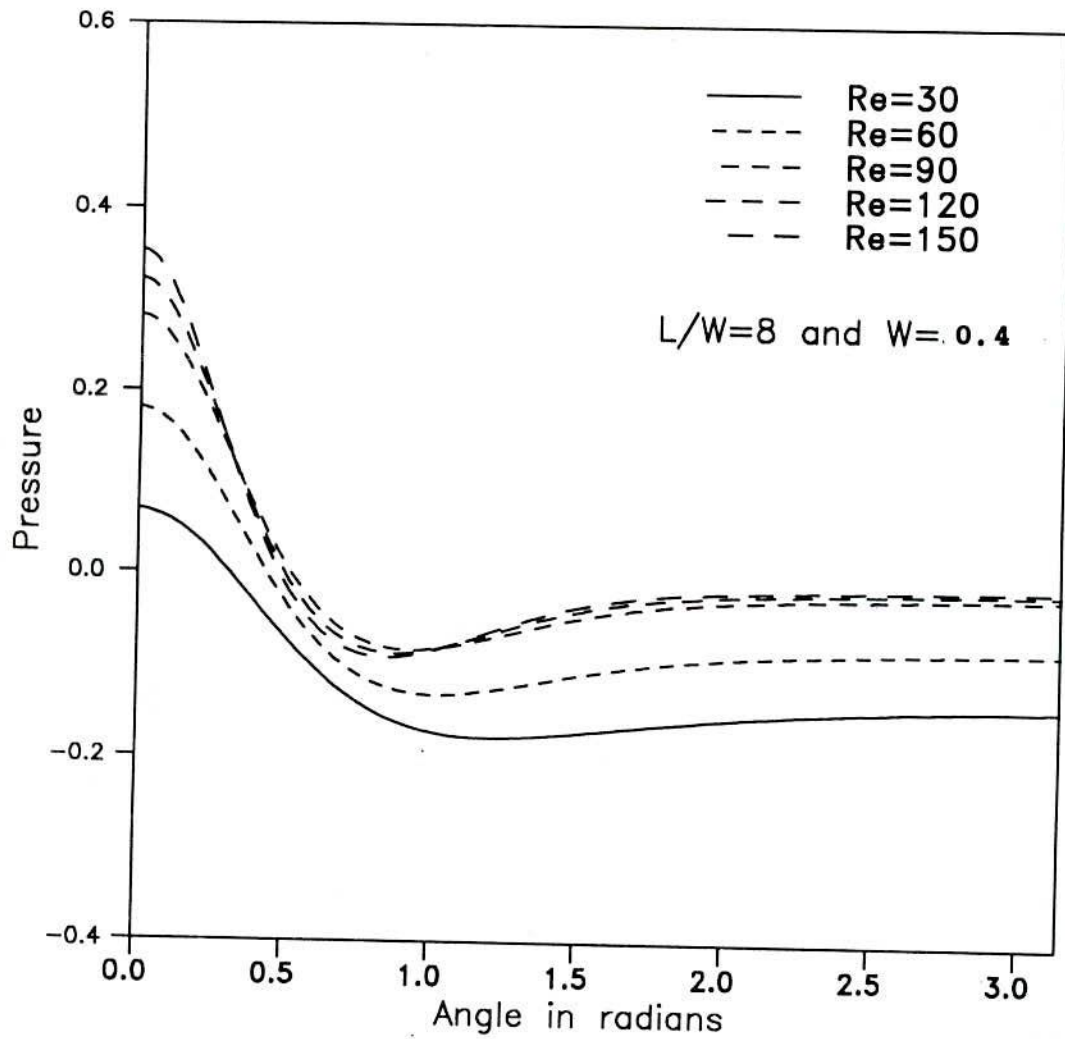


Fig.4.3.4: Variation of pressure over the cylinder surface with azimuthal angle.

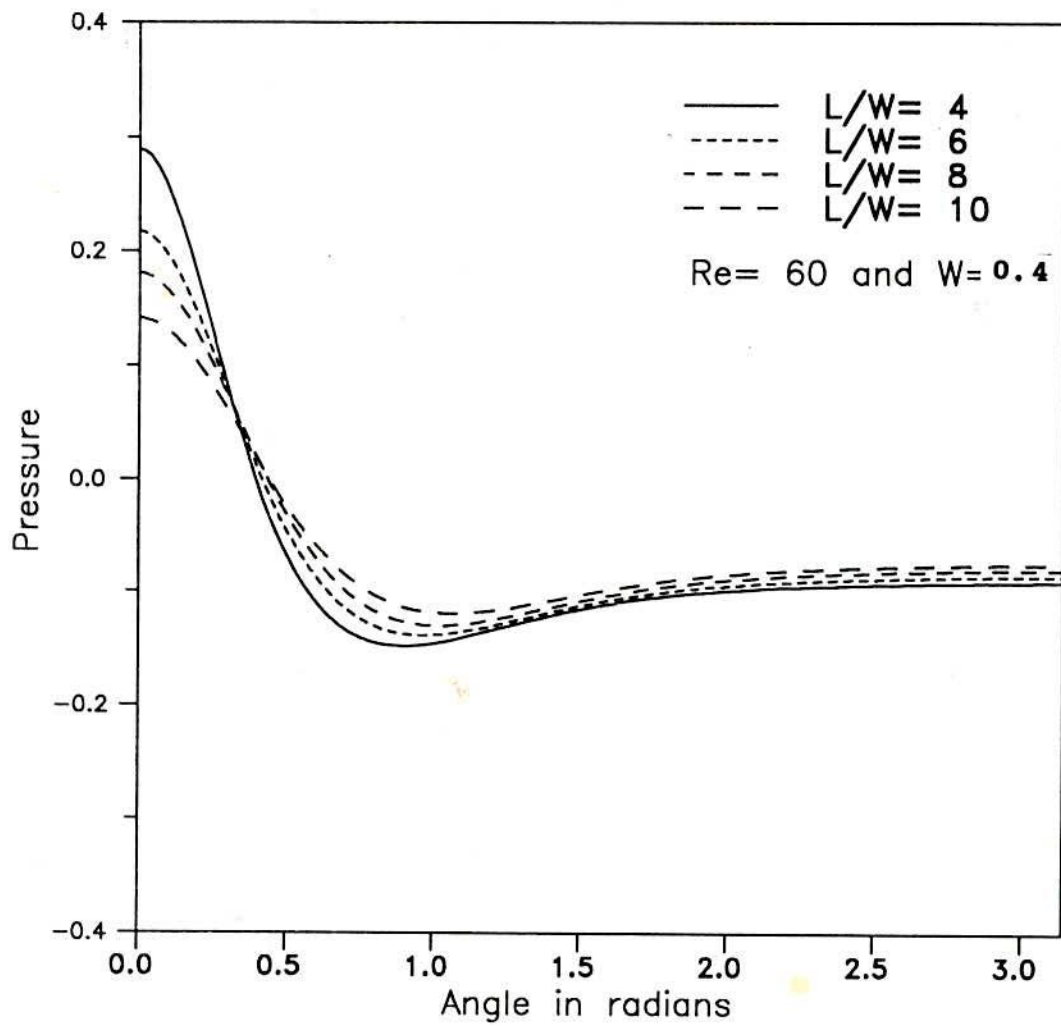


Fig. 4.3.5: Variation of pressure over the cylinder surface with azimuthal angle.

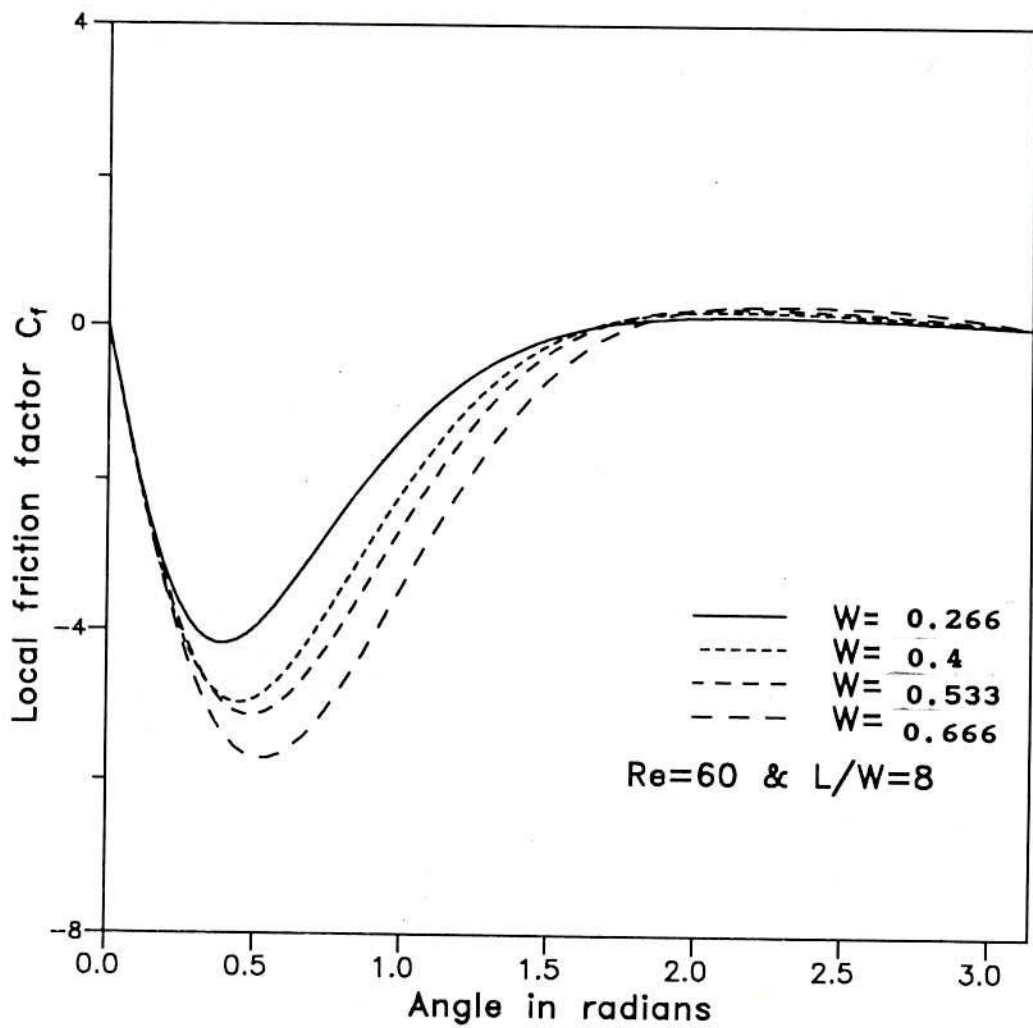


Fig.4.3.6: Variation of local friction factor over the cylinder surface with azimuthal angle.

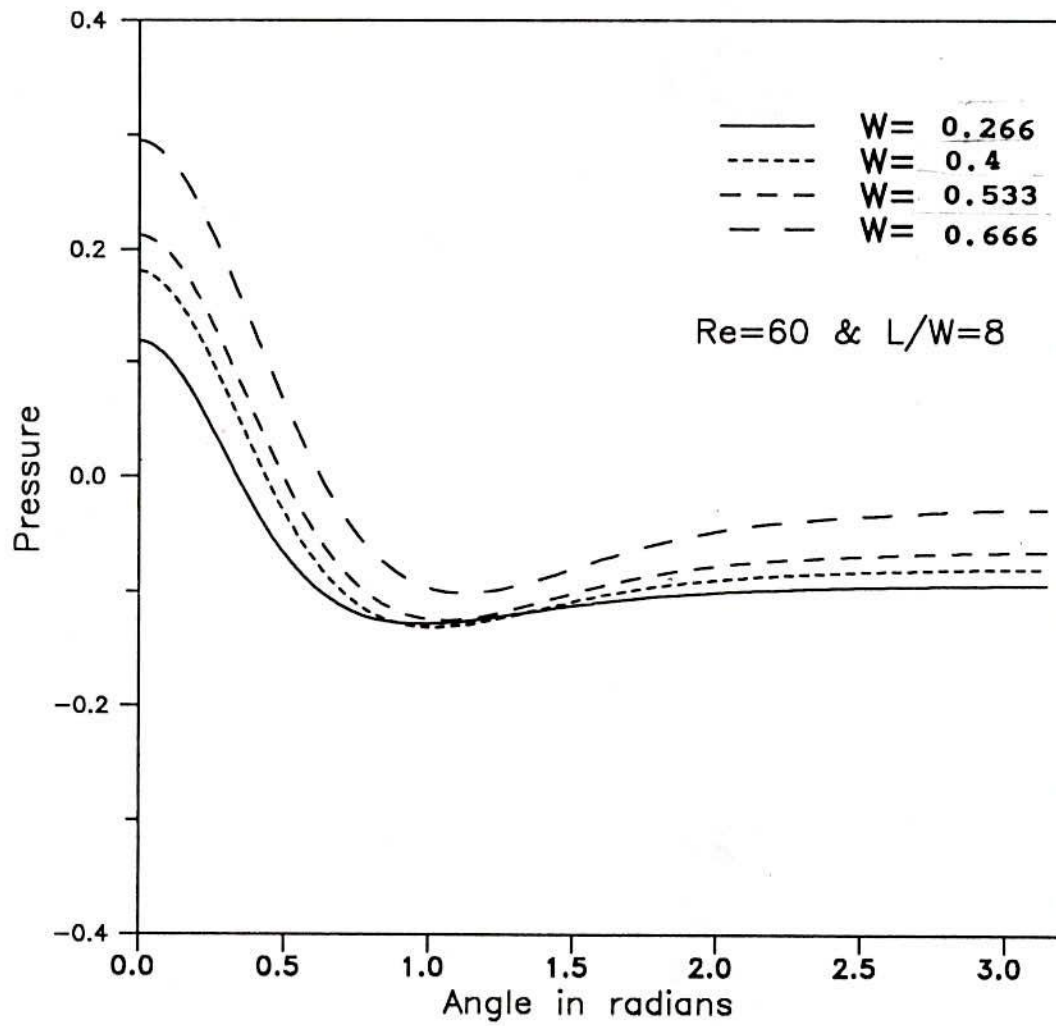


Fig.4.3.7: Variation of pressure over the cylinder surface with azimuthal angle.

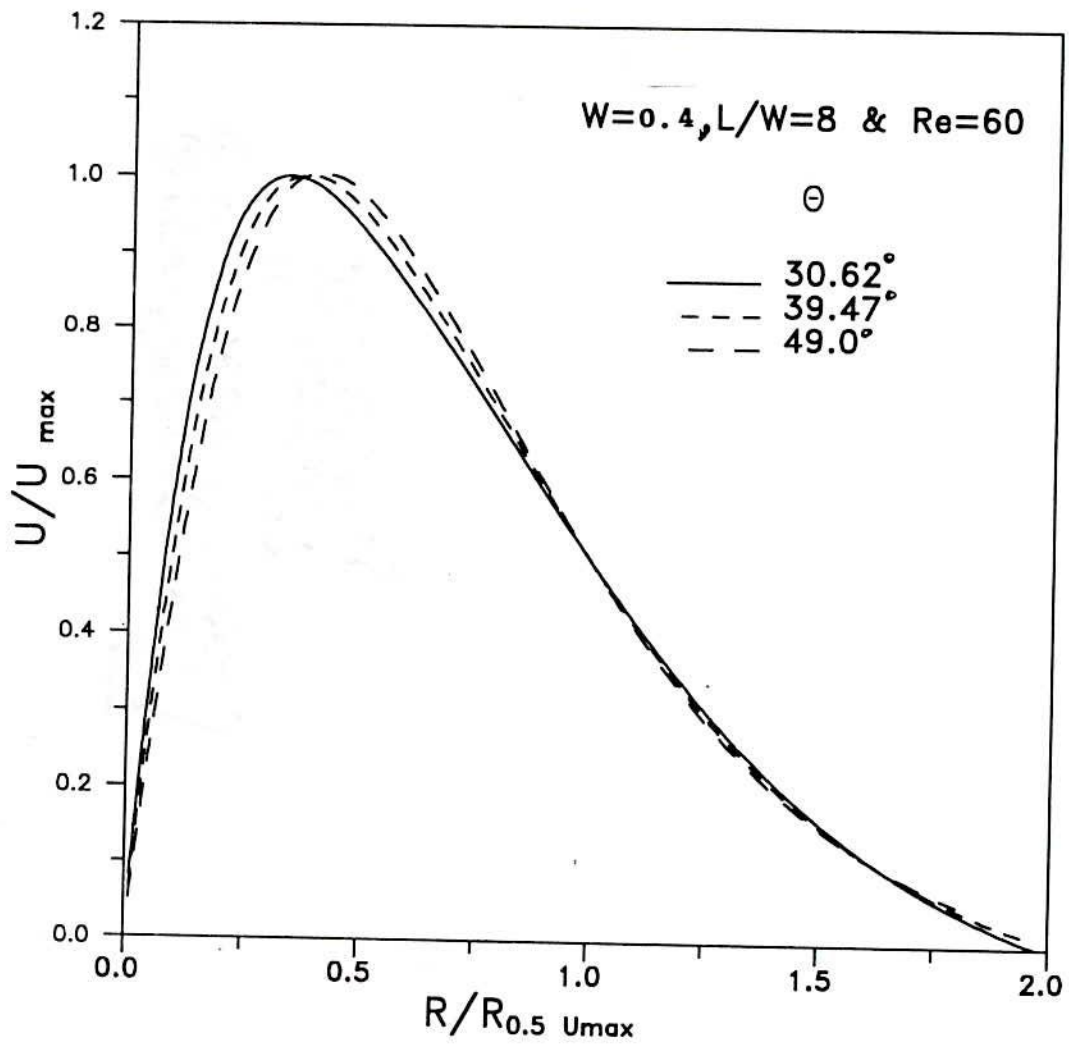


Fig.4.3.8 : Variation of azimuthal velocity along radial direction.

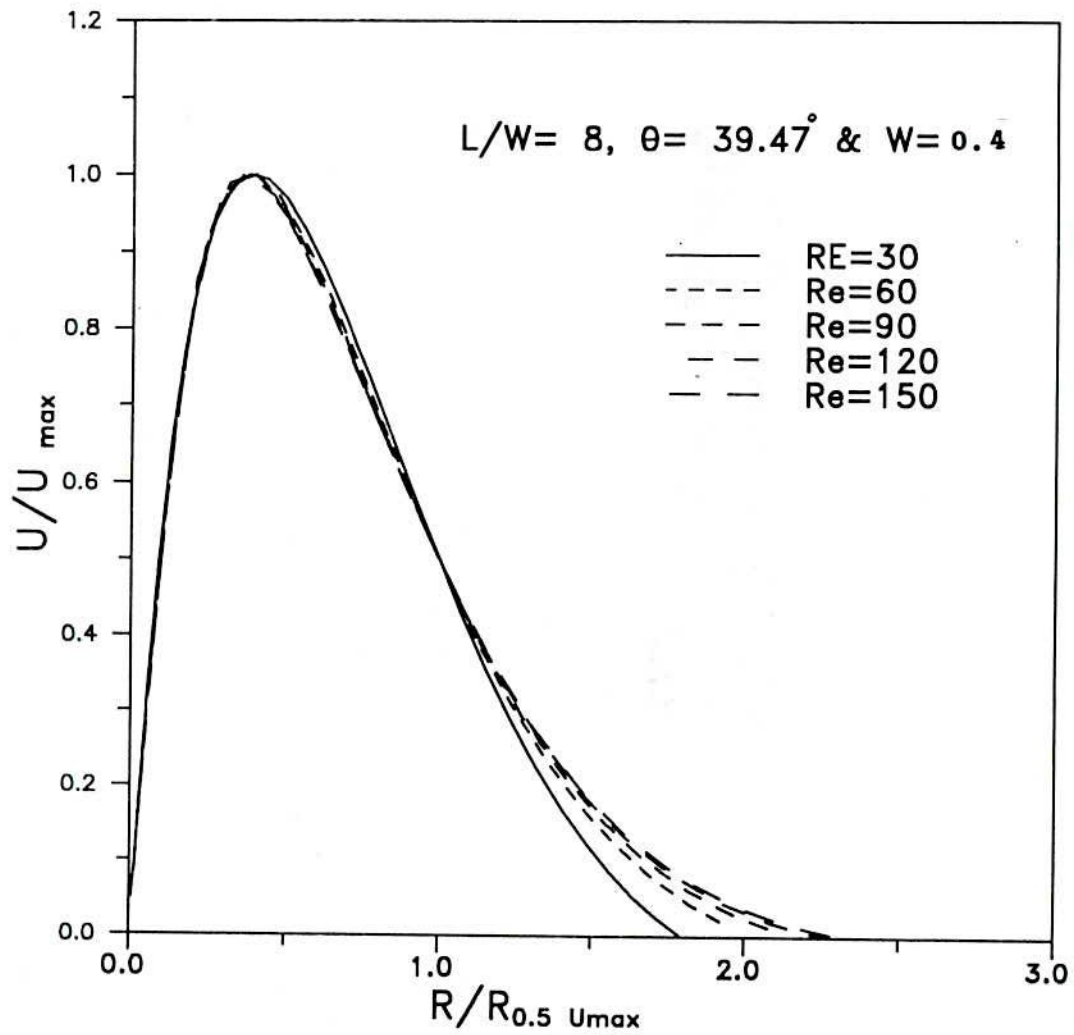


Fig.4.3.9 : Variation of azimuthal velocity along the radial direction.

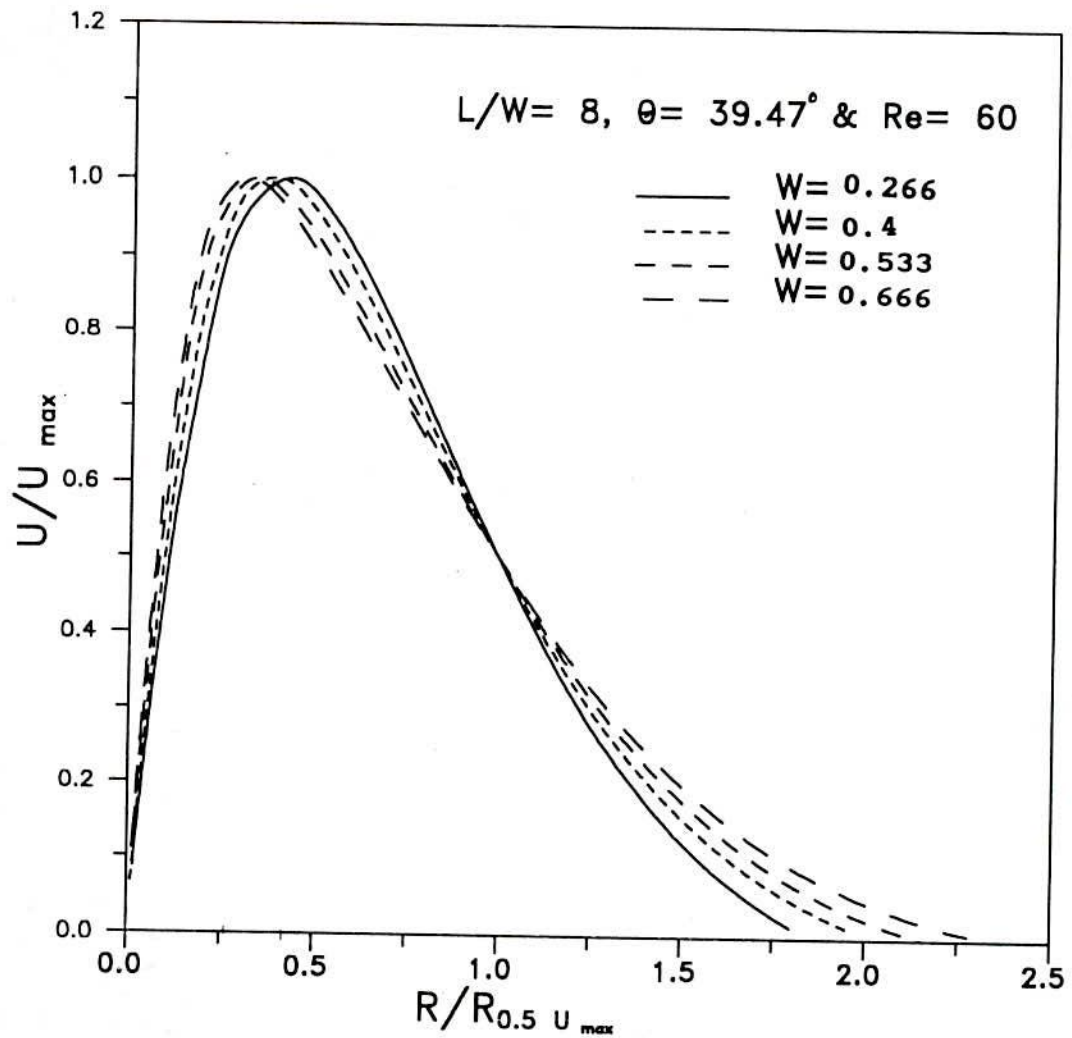


Fig.4.3.10 Variation of azimuthal velocity along radial direction.

4.4 VERTICALLY DOWNWARD SLOT JET IMPINGING UPON A FLAT SURFACE

The Navier-Stokes equations in this case, have been solved by SIMPLEC algorithm with the boundary conditions as described in Chapter 3. The jet in this case also does not emanate from a nozzle located in the wall. The nozzle is located at a height h_1 from the impingement plate. The nozzle walls are in the vertical direction at $X = \pm W/2$. The flow is entrained from large distance in the y direction if the Richardson number is small and the jet turns by 180° and flows along the nozzle wall at high values of Richardson numbers. A boundary at a large distance in y direction is required to consider the entrainment or the reverse flow. Hence, the flow over the nozzle wall has to be considered within the flow domain while the flow inside the nozzle is not a part of the flow domain. This makes the flow domain irregular and boundary control volumes have to be introduced at the nozzle wall and the nozzle exit. The control volumes at the nozzle wall and at the nozzle exit are 1.5 times the usual control volumes, while the control volumes at the corner of right lip of nozzle are usual control volumes. The consistency condition therefore, cannot be satisfied in the control volume at the right lip of the nozzle. All the subroutines of the computer programme had to be modified to include these changes. The upper boundary and right boundary of the domain were chosen far away, after several trials, so that solution is independent of their choice. Finally $L = 48W$ and $H = 24W$ have been used for all the computations. The Reynolds number, Richardson number, Prandtl number and the nozzle-to-plate spacings

are the parameters considered in this investigation.

The results have been presented for Reynolds numbers of 10 to 160 for the uniform slot exit velocity and temperature profiles, and 20 to 210 for the parabolic slot-exit velocity and temperature profiles, Prandtl numbers of 0.05 to 120, Richardson numbers of 0.0 to 1.5 for both, the uniform and the parabolic slot exit velocity and temperature profiles, and nozzle-to-plate spacings of 0.5 to 4.5.

Fine grid spacings were taken near the impingement plate, axis of symmetry, nozzle exit and along the nozzle wall, these were then gradually expanded to coarse grid in the interior of the domain. The relaxation factor of 0.35 was used for the two momentum equations and 0.4 for the energy equation. A relaxation factor of 1.0 was used for the pressure correction equation. Normalized residues of the velocity components and the temperature as defined in Equation (4.1.1), were calculated during every iterations along with SSUM to check the convergence. The convergence was achieved in 900 iterations in most of the cases. It was observed that when the velocity profiles and temperature converge upto sixth place of decimal the values of residual were as follows,

$$\begin{aligned}\text{Res (U)} &= 10^{-3} \\ \text{Res (V)} &= 10^{-3} \\ \text{Res (T)} &= 10^{-6} \\ \text{SSUM} &= 10^{-16}\end{aligned}$$

The solutions were obtained for various grid sizes to check the grid independence of the solutions. Figure 4.4.1 shows the

variation of local Nusselt number along the impingement surface at $Re = 50$, $Ri = 0.0$ and $H_1 = 3$ for four grid sizes namely, 52×42 , 72×56 , 90×62 and 99×80 . It is observed that grids finer than 52×42 do not yield significantly different results, hence this has been used in all the subsequent calculations.

A typical velocity vector plot with uniform slot exit velocity profile is shown in Figure 4.4.2 at Reynolds number, $Re = 50$, nozzle-to-plate spacing, $H_1 = 3$ and Richardson number, $Ri = 0.014$. The velocity profiles at small values of X , are like wall jet with slightly reverse flow near the nozzle exit. The reverse flow is caused by the entrained flow which accelerates towards the nozzle exit. This is probably similar to the jet contraction observed by Van Heiningen et al. [42]. There is an anti-clockwise vortex in the centre of the flow. Deshpande et al. [95] have observed such a vortex in the absence of buoyancy also. It is observed that the flow separates from the impingement surface at a certain distance from the stagnation point and the fluid is entrained from both, the top and the right boundaries. The entrained flow mixes with the main jet flow and rises up. The jet rises like a plume with maximum velocity at its centre. The plume velocity decreases at its periphery. The velocity profiles near the wall change from wall jet behavior to boundary layer behavior as the flow separation occurs and thereafter the velocities are negligibly small near the surface. The jet has been observed to behave almost like a non-buoyant jet for Ri less than 0.014 with uniform slot exit velocity and temperature profiles.

The streamlines for this case are shown in Figure 4.4.3. The

entrainment occur from the left top of the boundary and from the right boundary. The jet turns upwards and rise like a plume. The streamlines $\psi = 1.25$ turns towards the slot exit before following the main jet. The isotherms for this case are shown in Figure 4.4.4 indicating a typical plume behavior. The temperature in the vicinity of the nozzle wall and $X > 25$ is not at all affected by the jet.

The velocity vector plot, streamlines and isotherms with parabolic slot exit velocity profile are shown in Figures 4.4.5, 4.4.6 and 4.4.7, respectively. A comparison of Figures 4.4.2 and 4.4.5 for the velocity vector plots, shows that the velocities in the wall jet region are smaller for the parabolic slot-exit profiles as compared to that for the uniform slot exit profiles. The flow separates and rises up earlier for the former as compared to the latter case. The flow patterns are very similar in these two cases.

A comparison of Figures 4.4.3 and 4.4.6 for the streamlines indicates that the jet with uniform slot exit profiles entrains more flow than the jet with parabolic slot exit profiles. This is essentially due to larger total mass flow rate of the former compared to the latter. The plume in the latter case rises earlier than the former for the same reason.

A comparison of Figures 4.4.4 and 4.4.7 for the isotherms indicates that the plume for the parabolic jet-exit profiles is narrower and rises earlier as compared to that for the uniform slot exit profiles. The temperature within the plume decreases at a faster rate for the former as compared to the latter since,

parabolic slot exit profiles has less thermal energy compared to the uniform slot exit profiles.

The local Nusselt number variation along the impingement surface obtained in the present analysis, the experimental results of Sparrow and Wong [41] and the numerical results of Sami-Al-Sanea [105] are presented in Figure 4.4.8 for comparison purpose at $Re = 225$, $H_1 = 4$ and $Ri = 0$ with parabolic slot-exit profiles. It is observed that the results of the present analysis are in better agreement with the experimental results as compared to the results of Sami-Al-Sanea [105] near the impingement region. Sami-Al-Sanea [105] predicts a higher value of the stagnation point Nusselt number as compared to the experimental results of Sparrow and Wong [41]. The Nusselt number predicted by the present investigation is in between these two results.

The variation of local Nusselt number is shown in Figure 4.4.9 for $Re = 30, 60, 90$ and 120 at $Ri = 0.0$ and $H_1 = 3$ for uniform slot-exit profiles. The local Nusselt number increases with the increase of Reynolds numbers. The maximum Nusselt number does not occur at the stagnation point but it occurs slightly away from the stagnation point. Yuan et al. [8] have also observed this phenomenon. It was observed in this investigation that the location of maximum Nusselt number depends upon nozzle-to-plate spacing. It occurs at $X = 0.375$ for $H_1 > 2.25$ and at or near $X = 0.0$ for $0.5 \leq H_1 \leq 2.0$. Van Heiningen et al. [42] have also observed it, but they have attributed it to numerical inaccuracy. Cartwright and Russell [81] have observed that for turbulent flow, the maximum Nusselt number occurs away from the stagnation point

at high Reynolds numbers. Scholtz and Trass [86] have observed that the maximum Nusselt number occurs one nozzle diameter away from the stagnation point for axisymmetric jet impingement in the Reynolds number range of 700-940 with nozzle-to-plate spacing $H_1 = 0.1$. Miyazaki and Silberman [88] have also observed that the maximum Nusselt number occurs at half a nozzle width away from the stagnation point.

Figure 4.4.10 shows the variation of local Nusselt number at various Reynolds numbers for parabolic jet-exit profiles, other parameters being the same as in Figure 4.4.9. In this case the maximum Nusselt number occurs at the stagnation point. Parabolic jet-exit profiles yield higher stagnation point and local Nusselt number than the uniform slot exit profiles for same Reynolds numbers and the values of other parameters, for example at $Re = 90$, $H_1 = 3$ and $Ri = 0.0$ stagnation point Nusselt number is, 27.35% more for the parabolic profiles than that for the uniform jet-exit profiles. Sami-Al-Sanea [105] has observed that the stagnation point Nusselt number is 45% more for the parabolic profiles than that for the uniform profiles at slot-exit. However, the centre line velocity at slot-exit was 1.5 times the velocity in this investigation. Sparrow and Lee [12] have also observed that stagnation point Nusselt number for parabolic slot-exit profiles is twice than that for the uniform profiles at the slot-exit. In their case also, the centre line velocity at slot-exit was 1.5 times the velocity in this investigation. They have further, given a solution of boundary layer equation also.

Figure 4.4.11 shows the variation of local Nusselt number for

Re= 30, 60, 90 and 120 at $H_1=3$ and Richardson number, $Ri= 0.1$ with uniform slot exit profiles. The Nusselt number increases with the increase of Reynolds numbers starting from stagnation point to $X= 3.25$. The Nusselt number, on the other hand, decreases with increase in Reynolds numbers for $X > 3.25$ and ultimately reduces to zero for all Reynolds numbers at large value of X . Both these phenomenon are due to the detachment of the jet from the surface owing to large buoyancy force at $Ri= 0.1$. Nusselt number remains constant upto a certain distance (around nozzle half width) around the stagnation point for all the Reynolds numbers. A comparison with Figure 4.4.9 for $Ri= 0.0$ shows that the Nusselt number decreases with the increase in Richardson number.

The variation of local Nusselt number for various Reynolds numbers with parabolic slot-exit profiles, is shown in Figure 4.4.12 at $H_1= 3$ and $Ri= 0.1$. A comparison with Figure 4.4.10 indicates that the local Nusselt number decreases with the increase in Richardson number since, the jet has a tendency to rise up and detach from the impingement surface. The stagnation point Nusselt number is approximately 11% lower at $Ri= 0.1$ as compared to that at $Ri= 0.0$ with values of other parameters remaining the same. A comparison with Figure 4.4.11 indicates that the Nusselt number is higher for parabolic slot exit profiles as compared to that for the uniform slot exit profiles for the range of Reynolds numbers investigated, and for values of Ri upto 0.1. The trend of Nusselt number variation with Reynolds numbers changes around $X= 3.25$ in this case also, as was observed for the uniform slot-exit profiles.

Figure 4.4.13 shows the variation of local friction factor along the impingement surface for various Reynolds numbers at $H_1=3$, $Ri= 0.0$ and with uniform slot-exit profiles. The friction factor is zero at the stagnation point and increases along the impingement surface, attaining a maximum value around $X= 1.6$ and subsequently it decreases. It is independent of Reynolds numbers upto $X= 4.0$, beyond which, it is larger for larger Reynolds numbers. It decreases very slowly as X increases beyond $X= 6.0$.

Figure 4.4.14 shows the variation of local friction factor for $Ri= 0.1$, other parameters being the same as in Figure 4.1.13. The friction factor is independent of Reynolds numbers upto $X= 0.5$ only, and the maximum occurs around $X= 1.3$. The friction factor is smaller at larger Reynolds numbers upto $X= 4.5$, beyond which the trend is opposite of this. The friction factor again increases with X for $X > 4.5$ for all Reynolds numbers.

The variation of local friction factor with Reynolds numbers for parabolic slot exit velocity profiles is shown in Figure 4.4.15, at $H_1=3$, and Richardson number, $Ri= 0.1$. In contrast to uniform slot-exit profiles of Figure 4.4.13, the friction factor decreases as the Reynolds number increases and it is not independent of Reynolds numbers around $X= 0.0$. The maximum friction factor occurs around $X= 1.0$ for all Reynolds numbers. The skin friction, in general, is lower for parabolic slot-exit profiles as compared to that for the uniform slot-exit profiles.

Figure 4.4.16 shows the variation of local friction factor with Reynolds numbers for parabolic slot-exit profiles at $H_1=3$ and $Ri= 0.1$. The friction factor increases as the Reynolds numbers

increases near the stagnation point. This trend is opposite to that at $Ri = 0.0$. The maximum friction factor occurs around $X = 1.0$ for all Reynolds numbers. Beyond the peak, the friction factor is smaller at larger Reynolds numbers. The trend reverses again around $X = 4.2$.

Figure 4.4.17 shows the variation of local Nusselt number with Prandtl number at $Re = 100$, $H_1 = 3$ and $Ri = 0.0$ for both the uniform and the parabolic slot-exit profiles. It is observed that the local Nusselt number is, in general, larger for the uniform slot exit profiles than that for the parabolic slot-exit profiles except in the stagnation region. The local Nusselt number increases with Prandtl numbers. The stagnation point Nusselt number is larger for the parabolic slot-exit profiles than that for the uniform slot-exit profiles. The maximum Nusselt number for the uniform slot-exit profiles, occurs slightly away from the stagnation point. The peak of Nusselt number is very pronounced at $Pr = 10$ and tends to become flat at very small and very large values of Prandtl numbers.

The variation of local Nusselt number for various values of Richardson numbers is shown in Figure 4.4.18 for parabolic as well as uniform slot-exit profiles at $Re = 50$ and $H_1 = 3$. The local Nusselt number decreases with the increase in Richardson number, Ri . The local Nusselt number decreases rapidly after the maxima and then the rate of decrease becomes slower with axial distance for both the slot-exit profiles, the rate of decrease being higher for parabolic profile as compared to that for the uniform slot-exit profile. In absence of buoyancy ($Ri = 0.0$) the Nusselt

number decreases very slowly for large values of X , whereas in the presence of buoyancy ($Ri > 0$), the Nusselt number becomes zero at values of X which are smaller for larger Richardson numbers since, the flow detaches from the surface earlier at higher Richardson number. The peak of the Nusselt number becomes flat at higher values of Ri for the uniform slot-exit profiles.

Figure 4.4.19, shows the variation of stagnation point Nusselt numbers with Reynolds numbers for both, the uniform and the parabolic slot-exit profiles. The two slot-exit profiles give the same value of stagnation point Nusselt number approximately at $Re = 38$. The stagnation point Nusselt number increases with the increase in Reynolds number. The parabolic slot-exit profiles give higher Nusselt numbers than uniform slot-exit profiles at Reynolds numbers greater than 38, the percentage increase being higher at higher Reynolds numbers.

The variation of average Nusselt number is shown in the Figure 4.4.20 for both, the uniform and the parabolic slot exit profiles at $Pr = 0.71$, $H_1 = 3$ and $Ri = 0.0$. The average has been taken over a length of 48. The average Nusselt number for both, the uniform and the parabolic slot-exit profiles increases with increase in Reynolds number. The uniform slot-exit profiles have higher average Nusselt number than the parabolic slot exit profiles since the variation of former is more gradual than that of latter as shown in Figure 4.4.18. The mass flow rate and the thermal energy of the jet with parabolic profiles are 66% of those of the jet with uniform profiles at slot-exit, hence lower values are expected for the average Nusselt number.

Figure 4.4.21 shows the variation of maximum Nusselt number with the Prandtl number at $Re = 100$, $H_1 = 3$ and $Ri = 0.0$. The parabolic slot-exit profiles have a higher value of Nusselt number compared to the uniform slot exit velocity profiles for all values of Prandtl numbers. The maximum Nusselt number increases very sharply as the Prandtl number increases from 0 to 20, thereafter the increase is very gradual.

Figure 4.4.22, shows the variation of maximum Nusselt number with Richardson numbers at $Re = 50$ and $H_1 = 3$ for uniform as well as parabolic velocity and temperature profiles at the slot-exit. It is observed that the parabolic slot exit profiles give a higher value of Nusselt number as compared to that for uniform slot-exit velocity and temperature profiles in the Richardson number range of 0.0 - 0.15. For values of Richardson number higher than 0.15, the parabolic slot-exit velocity and temperature profile gives lower values of maximum Nusselt number as compared to that for the uniform velocity and temperature profiles at the slot-exit. The maximum Nusselt number decreases more rapidly with Richardson number for the parabolic velocity and temperature profiles at slot exit as compared to that for the uniform velocity and temperature profiles at the slot exit. The maximum Nusselt number becomes approximately equal to zero at $Ri \geq 1.25$, that is, the jet flow does not contact the impingement surface at this and higher values of Richardson numbers. The jet with parabolic slot-exit profiles detaches from the surface at lower values of Ri as compared to the jet with uniform slot-exit profiles because of, its lower momentum and energy.

Figure 4.4.23 shows the variation of local friction factor with Richardson number, Ri at Reynolds number =50 and $H_1 = 3$, for both, the uniform and the parabolic slot exit velocity and temperature profiles. It is observed that the local friction factor decreases as the Richardson number increases. At $Ri= 1.5$, the local friction factor has negative value throughout the impingement surface since, the jet does not contact the surface at all. The peak of the friction factor shifts towards smaller values of X as the Richardson numbers increases. The friction factor becomes zero along the impingement surface when the jet lifts off from the surface.

Figure 4.4.24 shows the variation of local Nusselt number along the impingement surface with nozzle-to-plate spacing at Reynolds numbers, $Re= 50$ and $Ri= 0.1$, for the uniform as well as the parabolic slot-exit velocity and temperature profiles. It is observed that the local Nusselt number decreases with the increase of nozzle-to-plate spacing since, the approach velocity decreases. The location of maximum Nusselt number has been observed to be at the stagnation point for Ri greater or equal to 0.1 in Figure 4.4.18 for the uniform slot-exit profiles. The Nusselt number is constant near the stagnation region for all values of H_1 except $H_1=0.5$, for uniform slot-exit profiles.

Figure 4.4.25 shows the variation of local friction factor along the impingement surface for different nozzle-to-plate spacings at Reynolds number, $Re= 50$ and $Ri= 0.1$ for the uniform and the parabolic slot exit velocity and temperature profiles. The jet with parabolic slot-exit profiles shows lower value of

friction factor as compared to that for the jet with uniform slot-exit velocity and temperature profiles. The friction factor decreases as the nozzle-to-plate spacing increases.

Figure 4.4.26 shows the variation of pressure coefficient with axial distance along the impingement surface at Reynolds number, $Re = 50$ and $H_1 = 3$ for various values of Ri with the uniform and the parabolic slot exit velocity and temperature profiles. It is observed that the pressure coefficient, near the stagnation point, decreases as the Richardson number increases, whereas it increases in the wall jet region as Ri increases for $Ri > 0$, the rate of increase being higher at higher values of Ri . The pressure coefficient in the wall jet region, attains a constant value for non-buoyant jet.

Figure 4.4.27 shows the variation of pressure coefficient along the impingement surface with nozzle-to-plate spacing at Reynolds number, $Re = 50$ and $Ri = 0.1$, for the uniform and the parabolic slot-exit velocity and temperature profiles. It is observed that the pressure coefficient decreases with nozzle-to-plate spacing.

Correlations

The following correlation has been developed to predict the stagnation point Nusselt number for parabolic slot-exit velocity and temperature profiles.

$$Nu_0 = 0.299 Re^{0.7493} Pr^{0.3794} H_1^{-0.469} \quad (4.4.1)$$

The deviation of the calculated stagnation point Nusselt number from the Equation (4.4.1) and the stagnation point Nusselt number actually obtained by numerical calculations, is shown in Figure 4.4.28. The maximum deviation from the actual values of the stagnation point Nusselt number is $\pm 8.45\%$, whereas the R.M.S. value of the deviation is 0.14.

The average Nusselt number over the non-dimensional surface length of 48, has been correlated in terms of the slot-exit Reynolds number, Prandtl number and nozzle-to-plate-spacing for the parabolic slot-exit velocity and temperature profiles. This correlation is as follows,

$$\text{Nu}_{\text{avg}} = 0.014 \text{ Re}^{0.8157} \text{ Pr}^{0.5462} \text{ H}_1^{-0.0743} \quad (4.4.2)$$

Figure 4.4.29 shows the deviation of calculated average Nusselt number from the Equation (4.4.2) and the numerically obtained average Nusselt number. The maximum deviation of this correlation from the actual data is $\pm 9.2\%$ while the R.M.S. value of the deviation is 0.0012.

The following correlation has been developed to predict the stagnation point Nusselt number for the uniform slot-exit velocity and temperature profiles.

$$\text{Nu}_0 = 0.682 \text{ Re}^{0.523} \text{ Pr}^{0.364} \text{ H}_1^{-0.447} \quad (4.4.3)$$

Figure 4.4.30 shows the deviation of calculated stagnation point Nusselt number from Equation (4.4.3) and the numerically

obtained stagnation point Nusselt number. The maximum deviation from the actual values of the stagnation point Nusselt numbers is $\pm 10.24\%$ whereas the R.M.S. value of the deviation is 0.21.

In case of uniform slot-exit profiles, the maximum Nusselt number occurs slightly away from the stagnation point.

The following correlation has been developed to predict the maximum Nusselt number for the uniform velocity and temperature profiles at slot exit.

$$Nu_{\max} = 0.637 Re^{0.541} Pr^{0.369} H_1^{-0.442} \quad (4.4.4)$$

The deviation of the calculated maximum Nusselt number from the Equation (4.4.4) and the maximum Nusselt number actually obtained from numerical calculations is shown in Figure.4.4.31. The maximum deviation from the actual values of the maximum Nusselt number is $\pm 9.76\%$, whereas the R.M.S. value of the deviation is 0.21.

The correlation for the average Nusselt number over the non-dimensional impingement surface length of 48, in terms of slot exit Reynolds number, Prandtl number and nozzle-to-plate spacing for the uniform velocity and temperature profiles is as follows,

$$Nu_{\text{avg}} = 0.032 Re^{0.74} Pr^{0.5} H_1^{-0.11} \quad (4.4.5)$$

The deviation of the calculated average Nusselt number from the Equation (4.4.5) and the average Nusselt number obtained from numerical calculations is shown in Figure 4.4.32. The maximum

deviation for this correlation is $\pm 9.87\%$ from the actual values and the R.M.S. value of deviation is 0.0038.

Reliable correlations for Nusselt number with Richardson numbers could not be obtained due to abrupt variations.

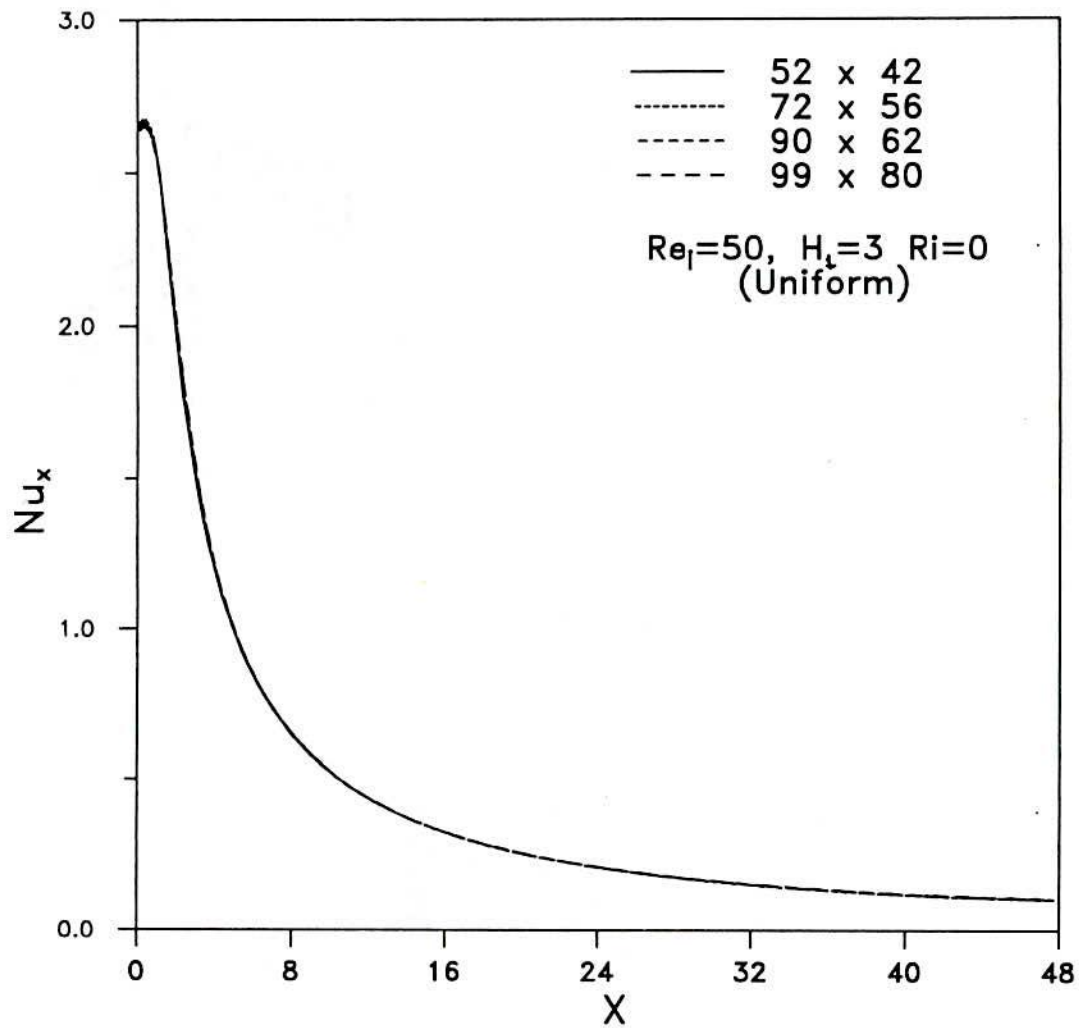


Fig.4.4.1: Local Nusselt number variation along the surface showing the effect of finite difference grid size:

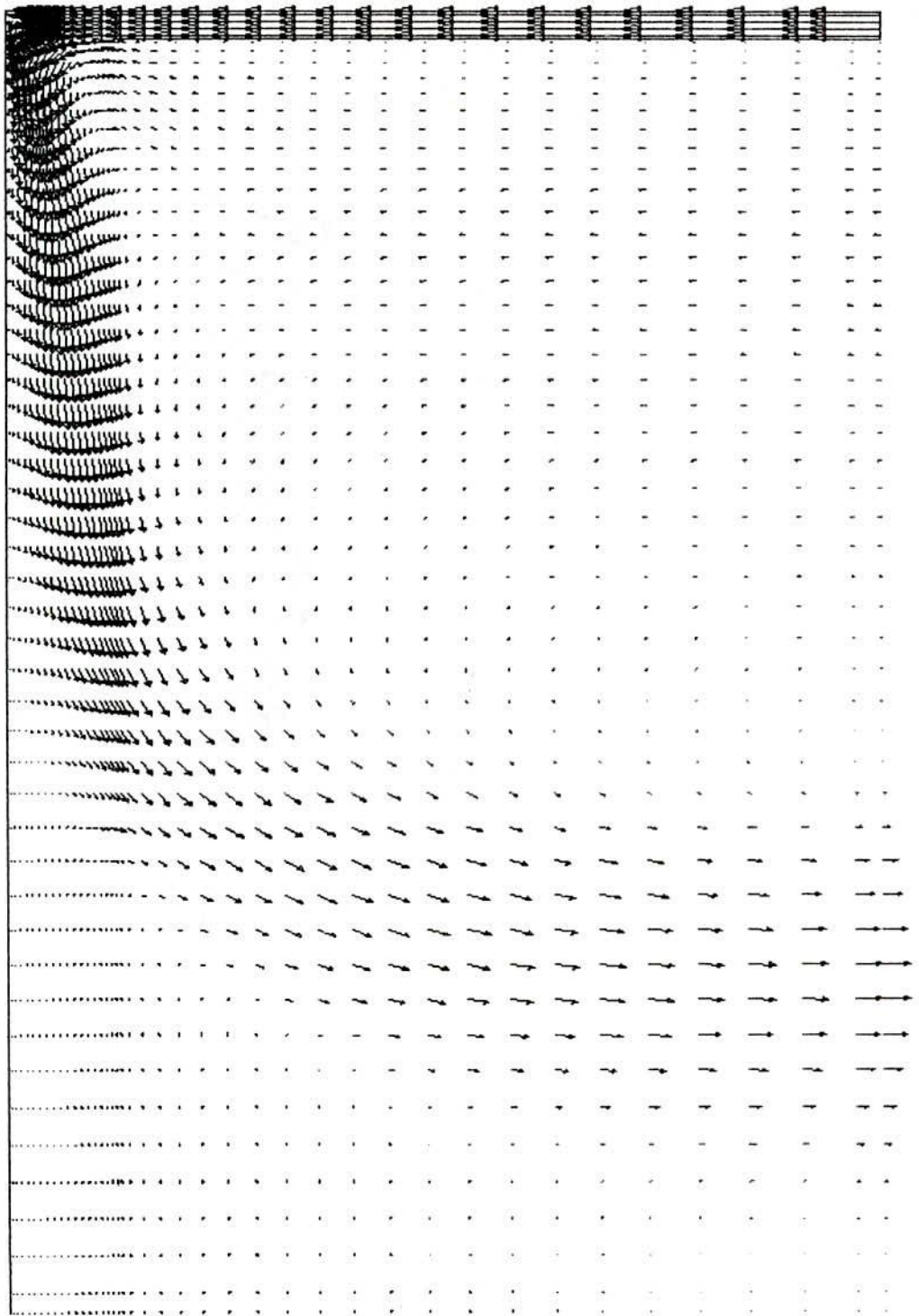


Fig.4.4.2: Velocity vector plot, $Re=50$, $H_f=3$ and $Ri=0.014$
Laminar vertical jet on flat plate with uniform velocity profile at slot exit.

Streamlines, $Re=50$, $Ri=0.014$ and $H_1=3$ (Uniform)

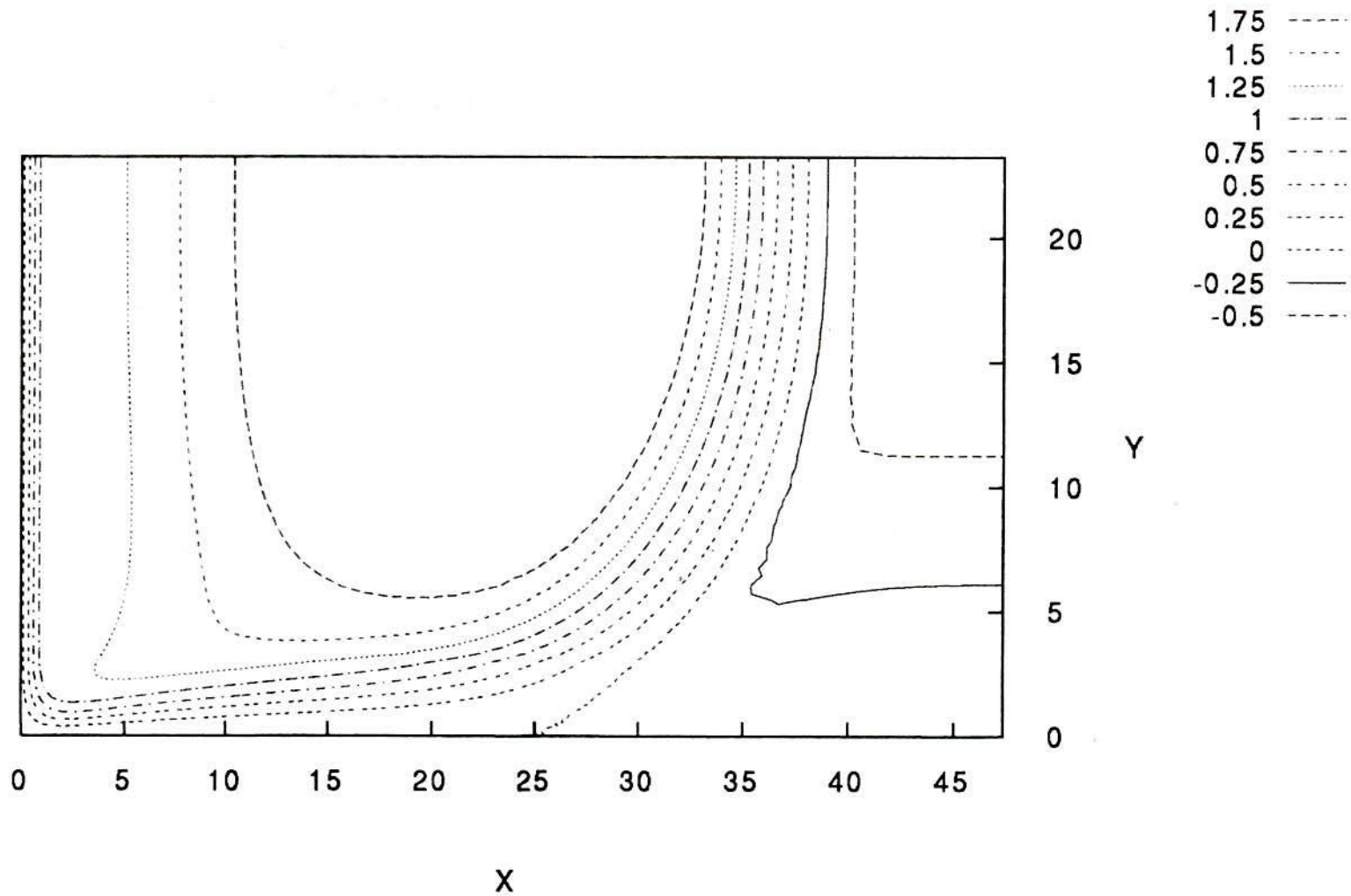


Fig.4.4.3: Streamlines for vertically downward buoyant slot jet impinging upon a flat surface with uniform slot exit velocity profile at $Re= 50$, $H_1=3$ and $Ri= 0.014$

Buoyant slot jet, Isotherms $Re=50$, $Ri=0.014$ and $H_1=3$ (Uniform)

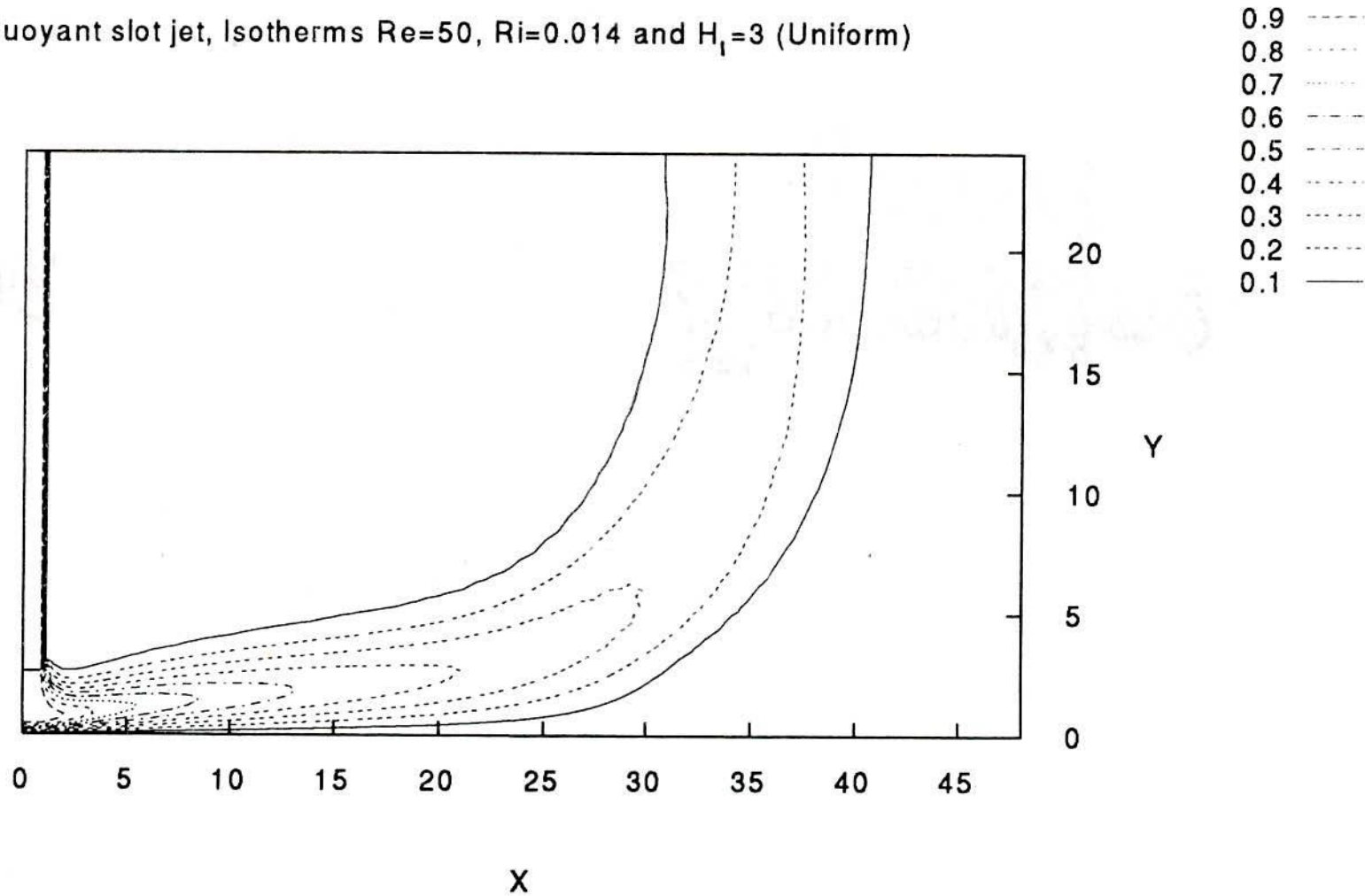


Fig.4.4.4: Isotherms for vertically downward buoyant slot jet impinging upon a flat plate. $Re=50$, $Ri=0.014$, $H_1=3$, $Pr=0.71$.

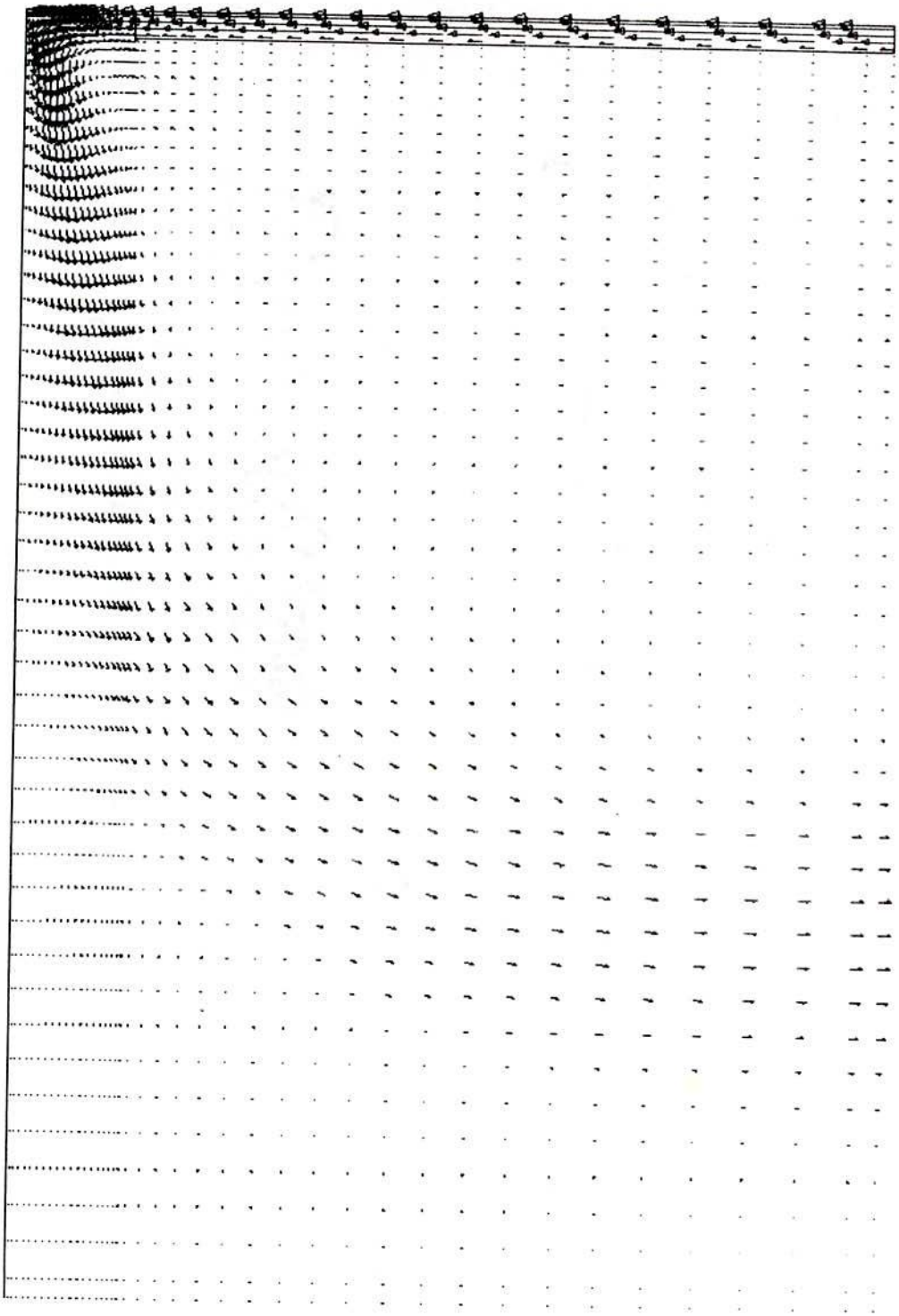


Fig.4.4.5: Velocity vector plot, $Re=50$, $H_1=3$ and $Ri=0.007$
Laminar vertical jet on flat plate with parabolic velocity profile at slot exit.

Streamlines $Re=50$, $Ri=0.007$ and $H_1=3$ (Parabolic)

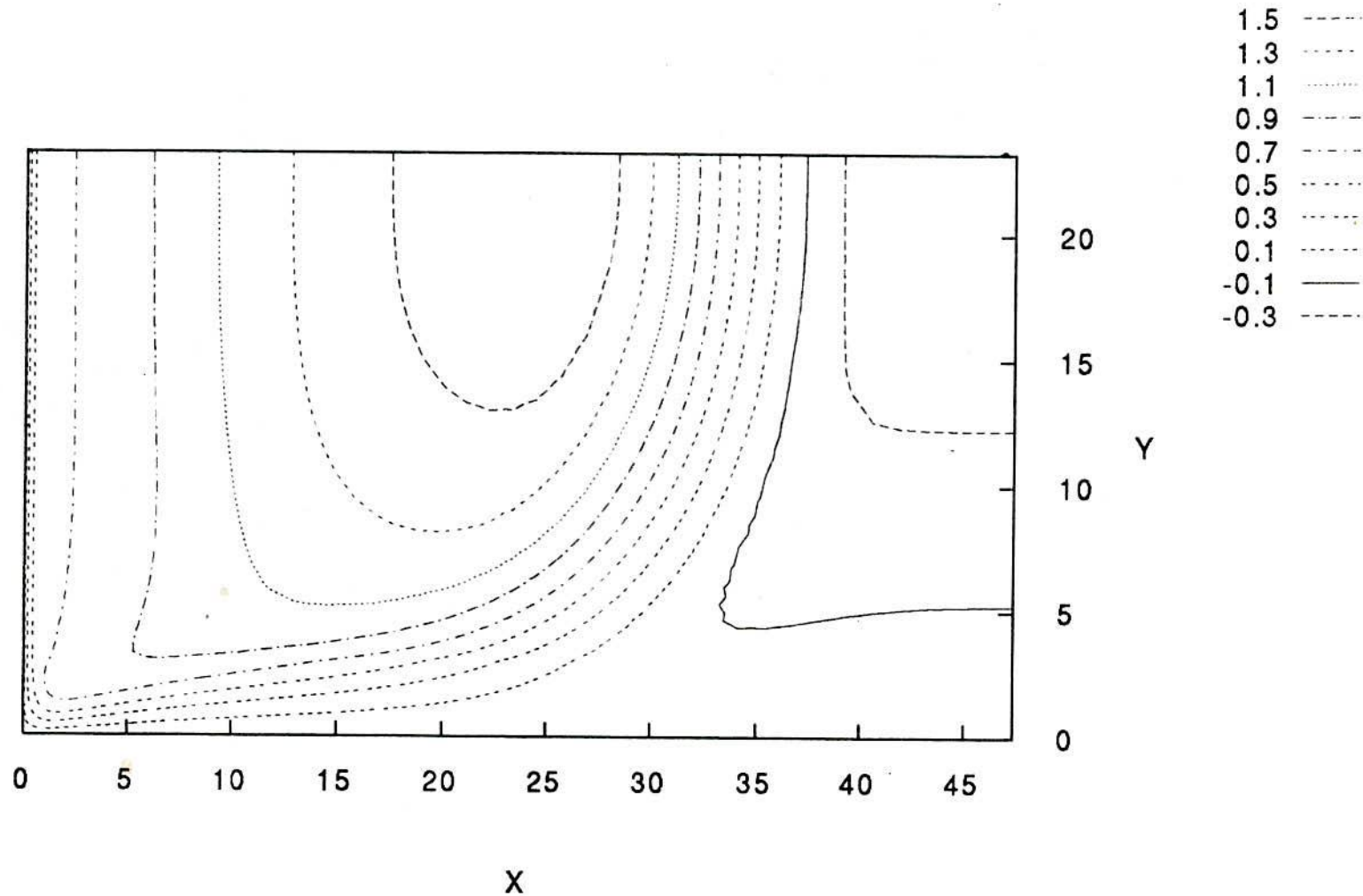


Fig.4.4.6: Streamlines for vertically downward buoyant slot jet impinging upon a flat surface with parabolic slot exit velocity profile at $Re= 50$, $H_1=3$ and $Ri= 0.007$.

Isotherms $Re=50$, $Ri=0.007$ and $H_1=3$ (Parabolic)

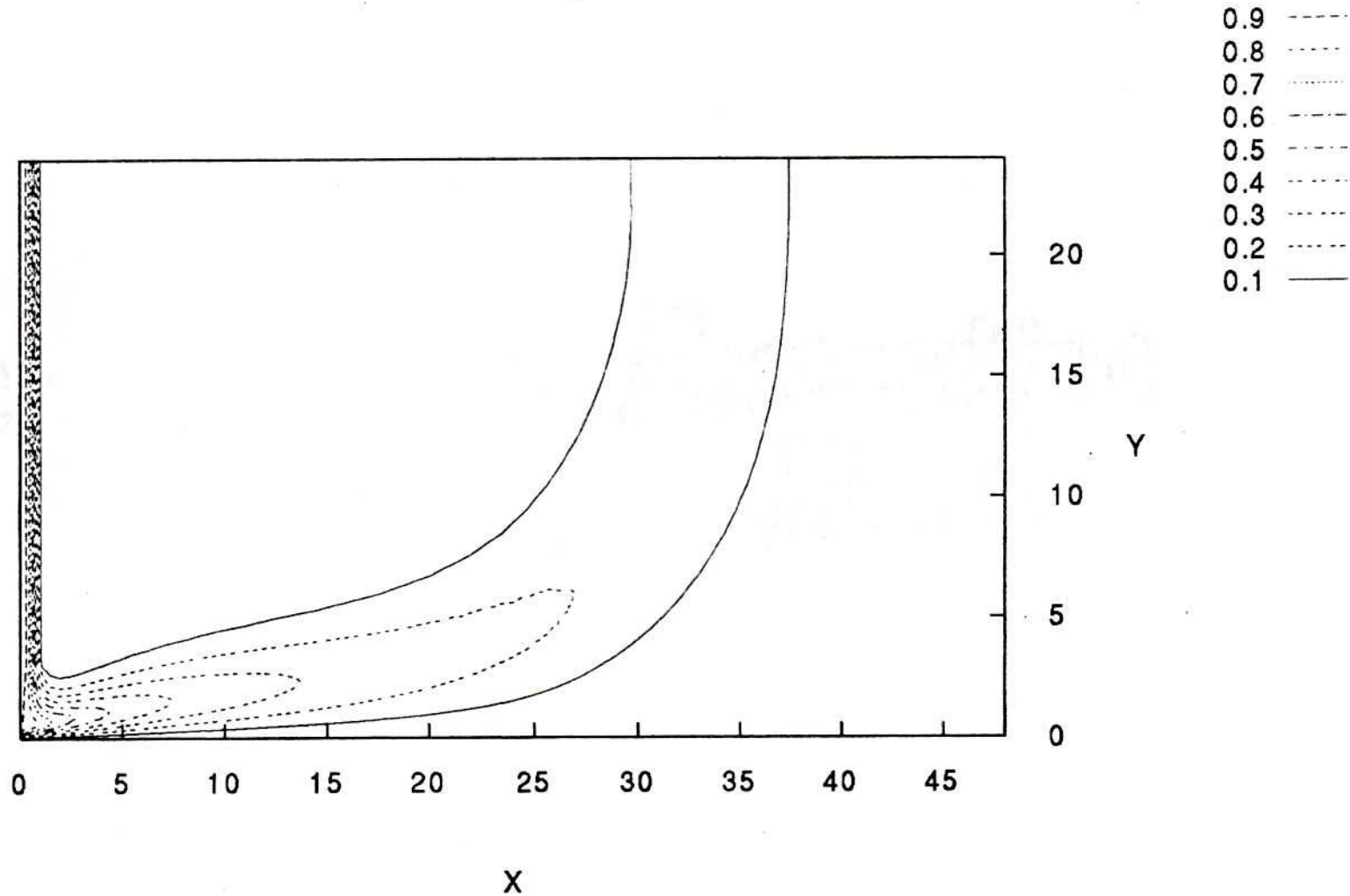


Fig.4.4.7: Isotherms for vertically downward buoyant slot jet impinging upon a flat surface with parabolic slot exit velocity profile at $Re= 50$, $H_1=3$ and $Ri= 0.007$. $Pr= 0.71$.

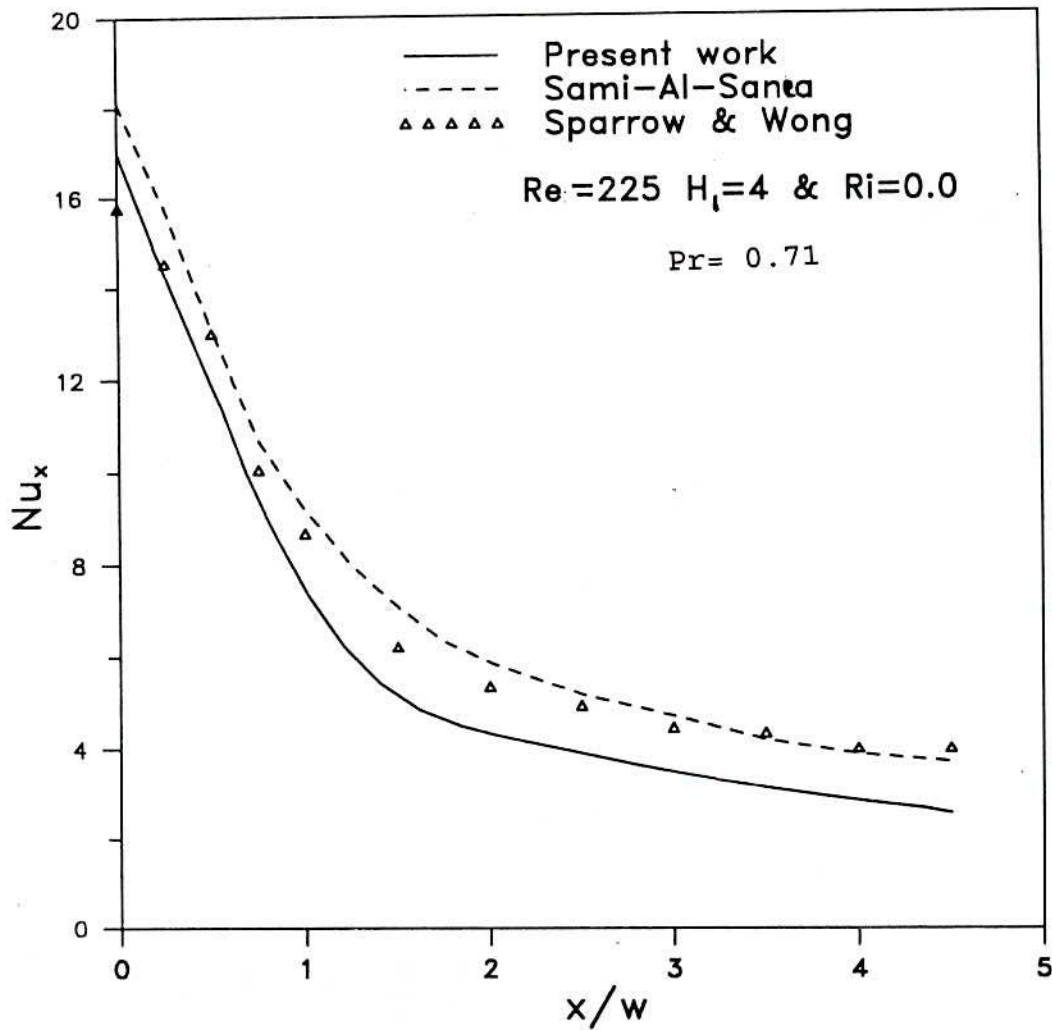


Fig.4.4.8 :Variation of Nusselt no. over the impingement surface with parabolic velocity profile.

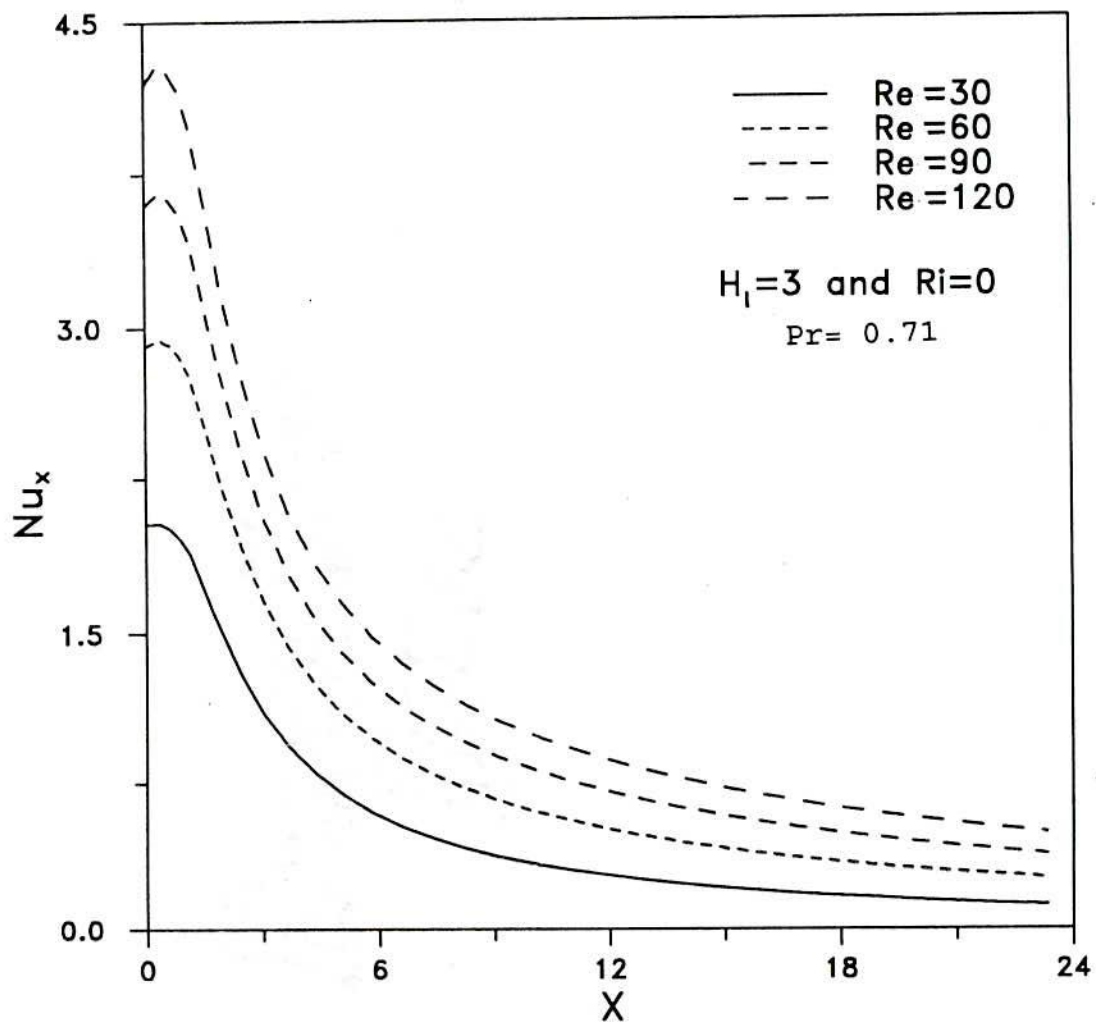


Fig.4.4.9: Variation of local Nusselt number over the impingement surface with uniform velocity profile.

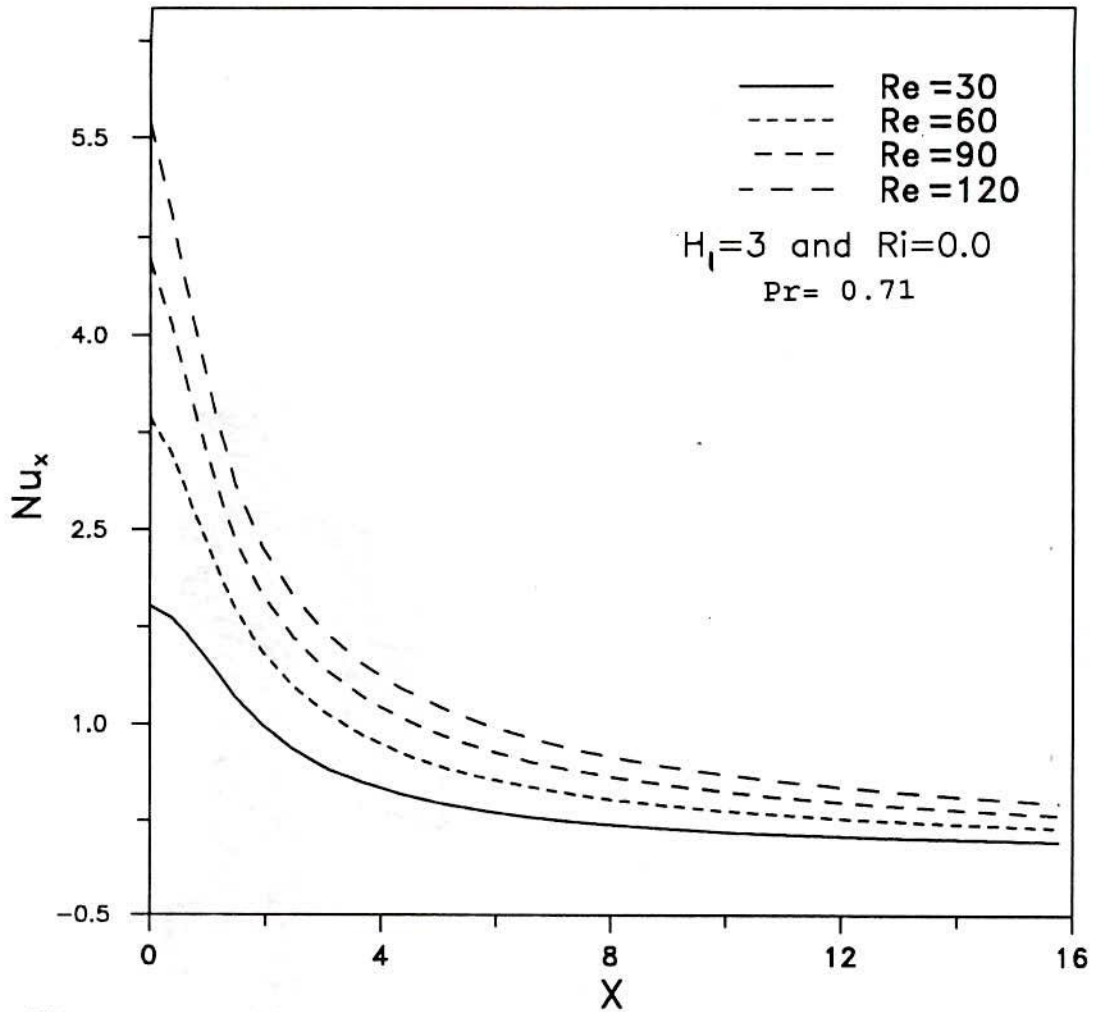


Fig.4.4.10: Variation of Nusselt number over the impingement surface with parabolic velocity profile.

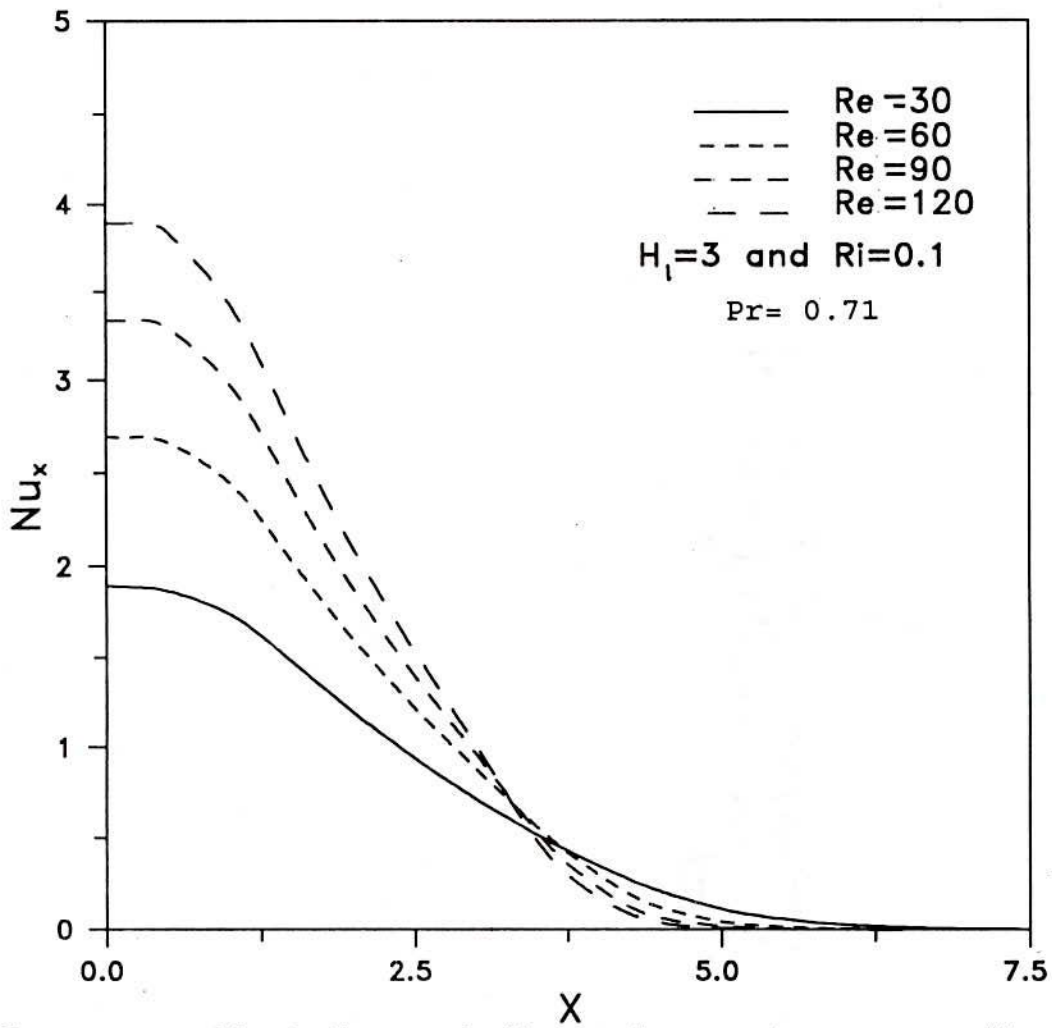


Fig. 4.4.11: Variation of Nusselt number over the impingement surface with uniform velocity profile.

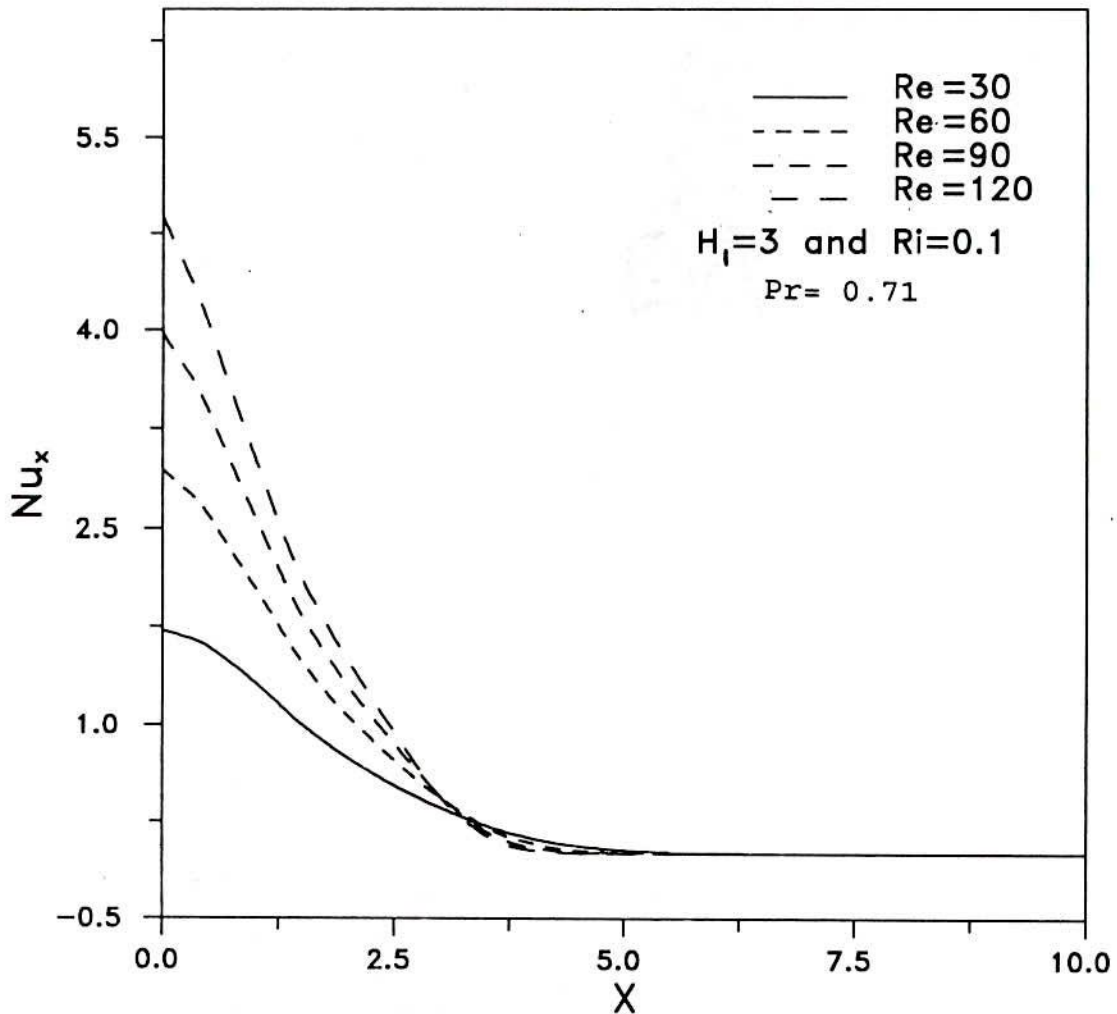


Fig.4.4.12: Variation of Nusselt number over the impingement surface with parabolic velocity profile.

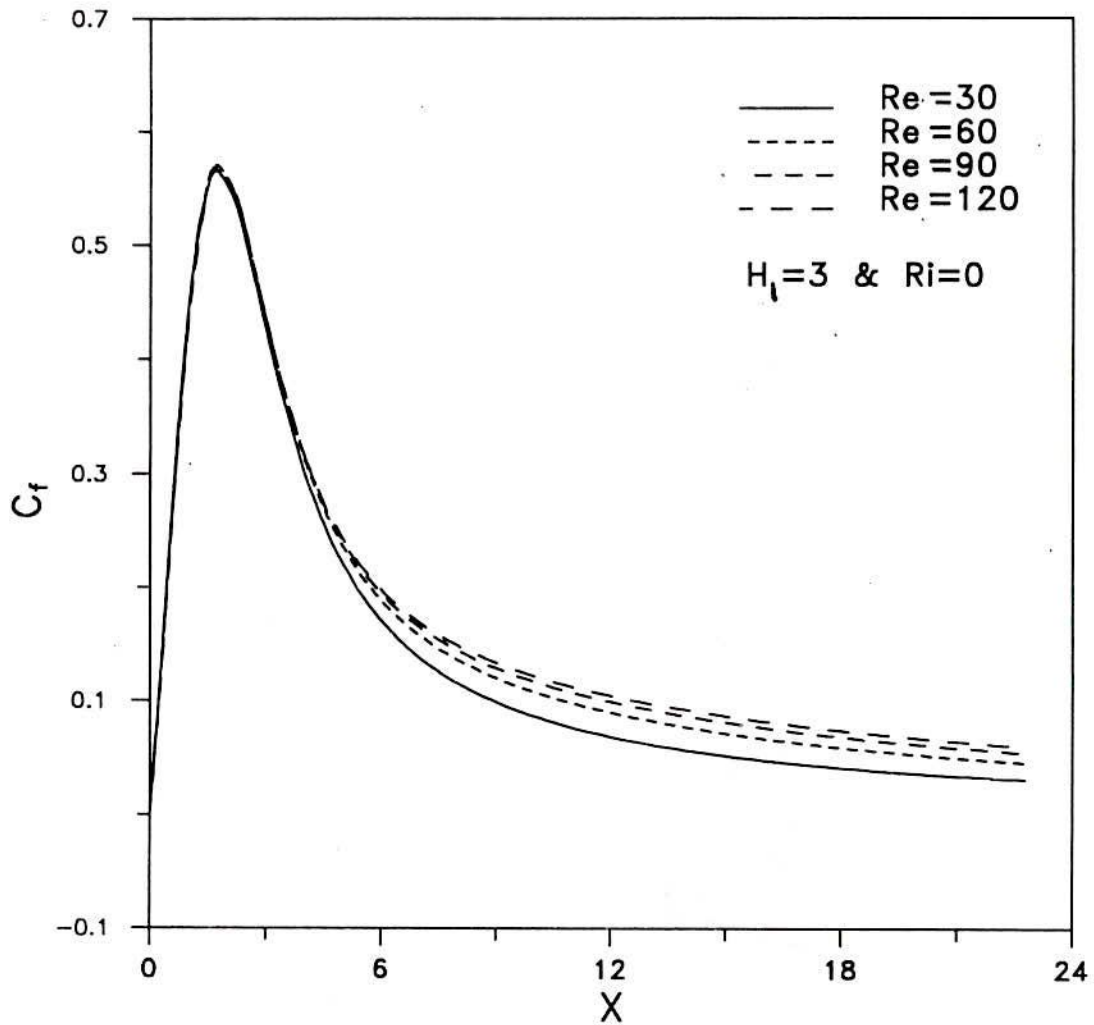


Fig.4.4.13: Variation of local friction factor over the impingement surface with uniform velocity profile.

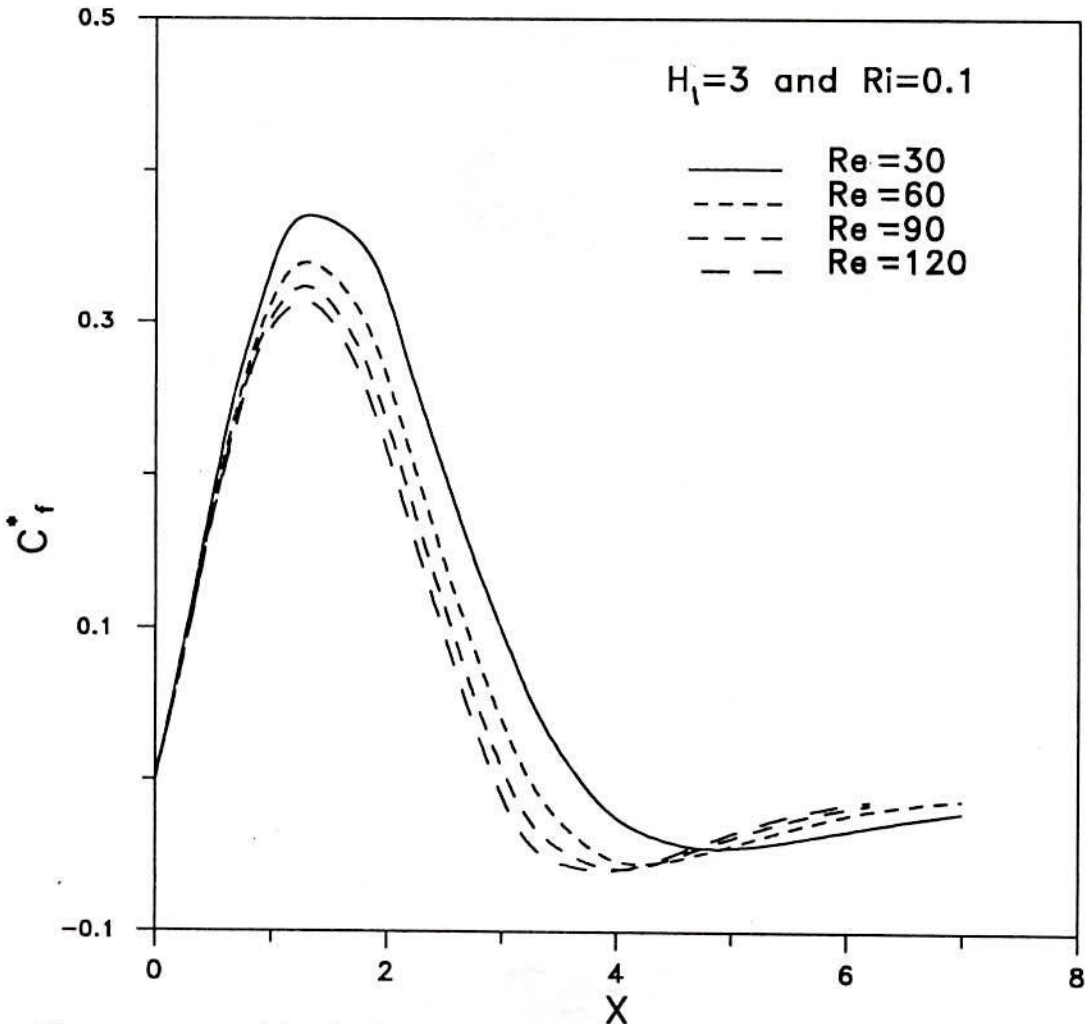


Fig.4.4.14: Variation of local friction factor over the impingement surface with uniform velocity profile.

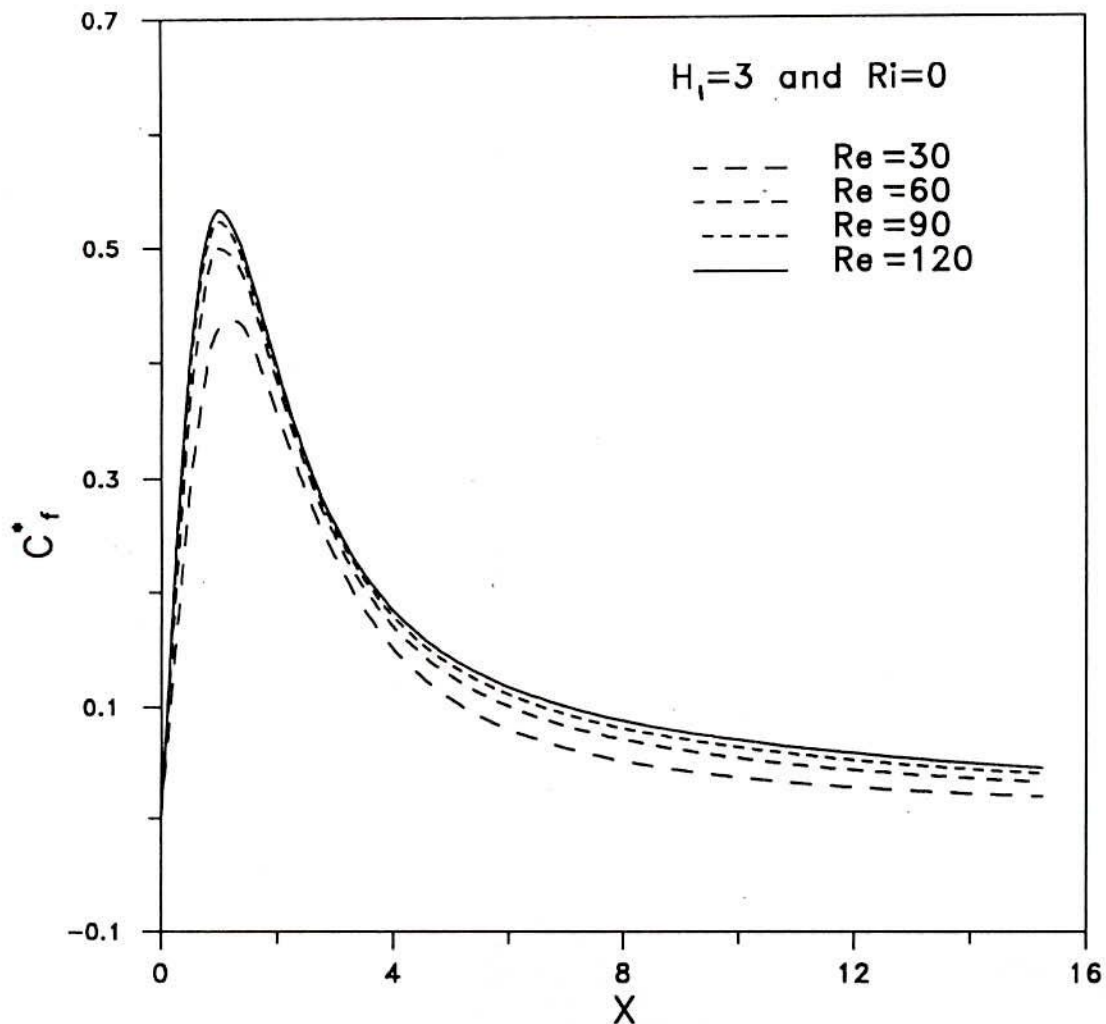


Fig.4.4.15: Variation of local friction factor over the impingement surface with parabolic velocity profile.

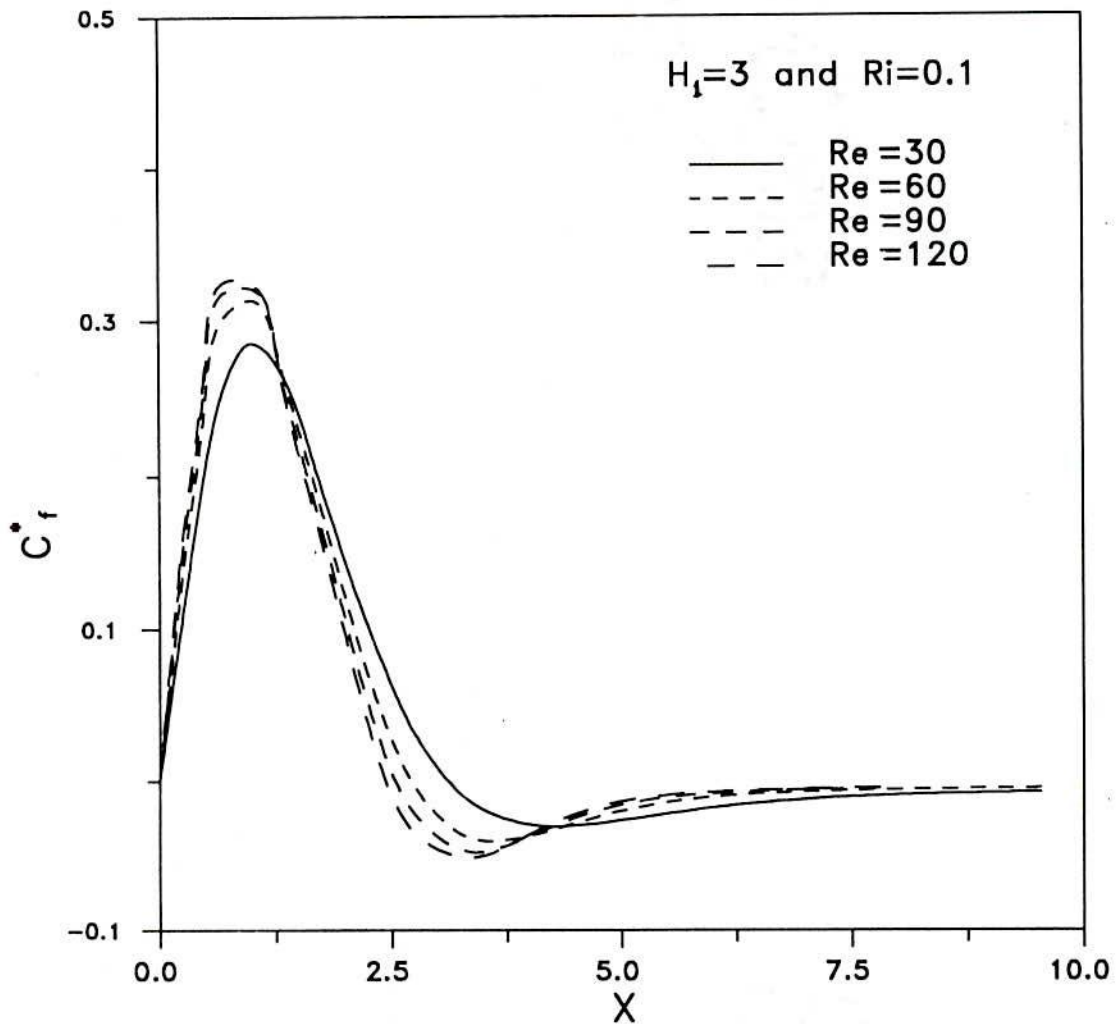


Fig.4.4.16: Variation of local friction factor over the impingement surface with parabolic velocity profile.

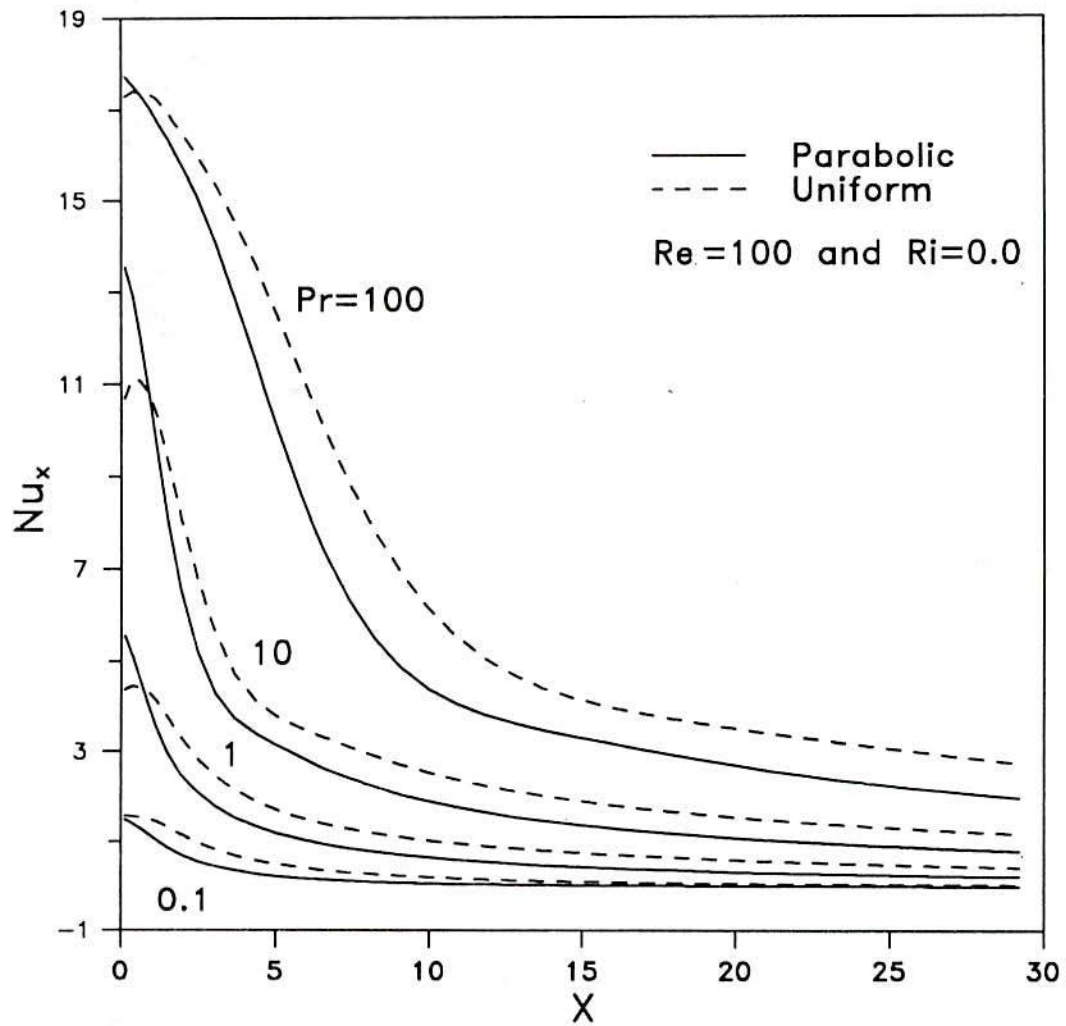


Fig.4.4.17: Variation of local Nusselt number over the impingement surface for different Pr, $h_1 = 3$

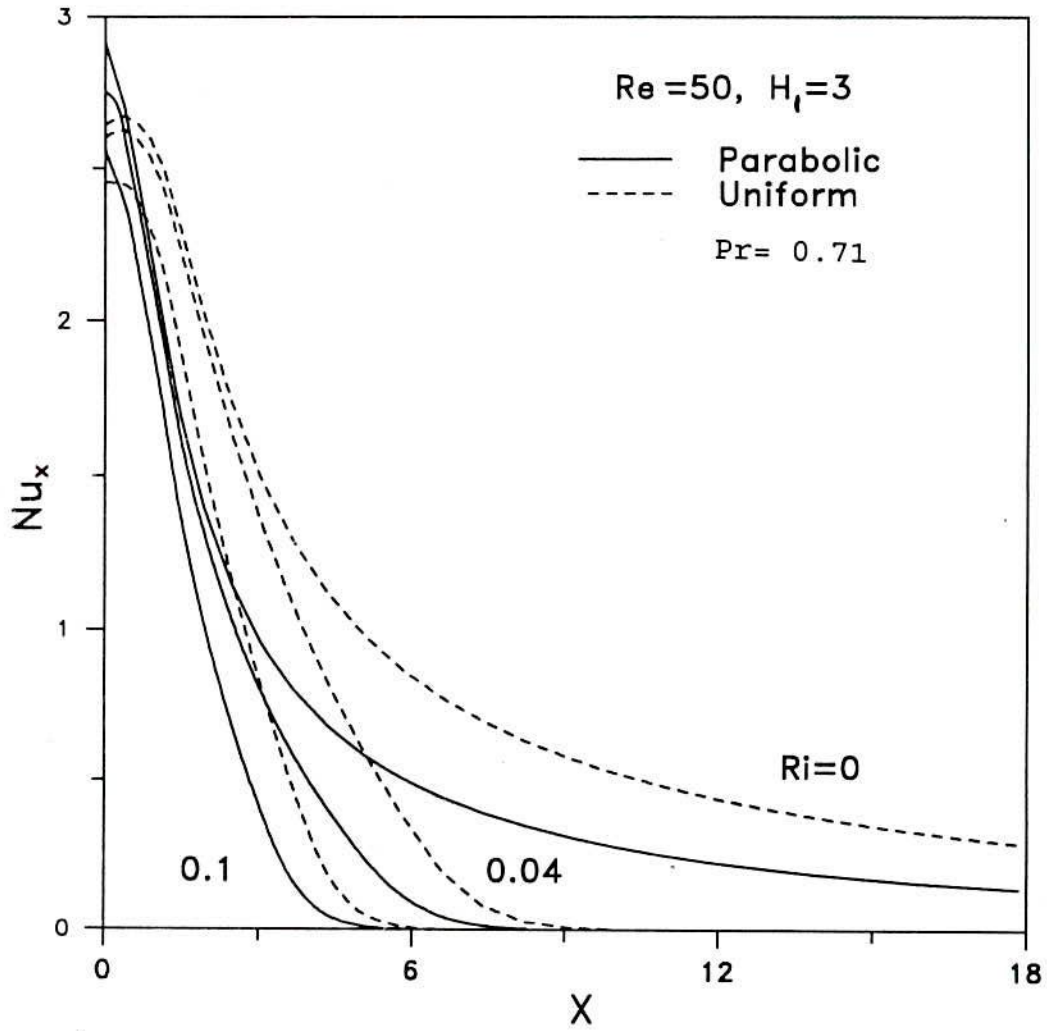


Fig.4.4.18 Local Nusselt number variation along the surface at different Richardson number.

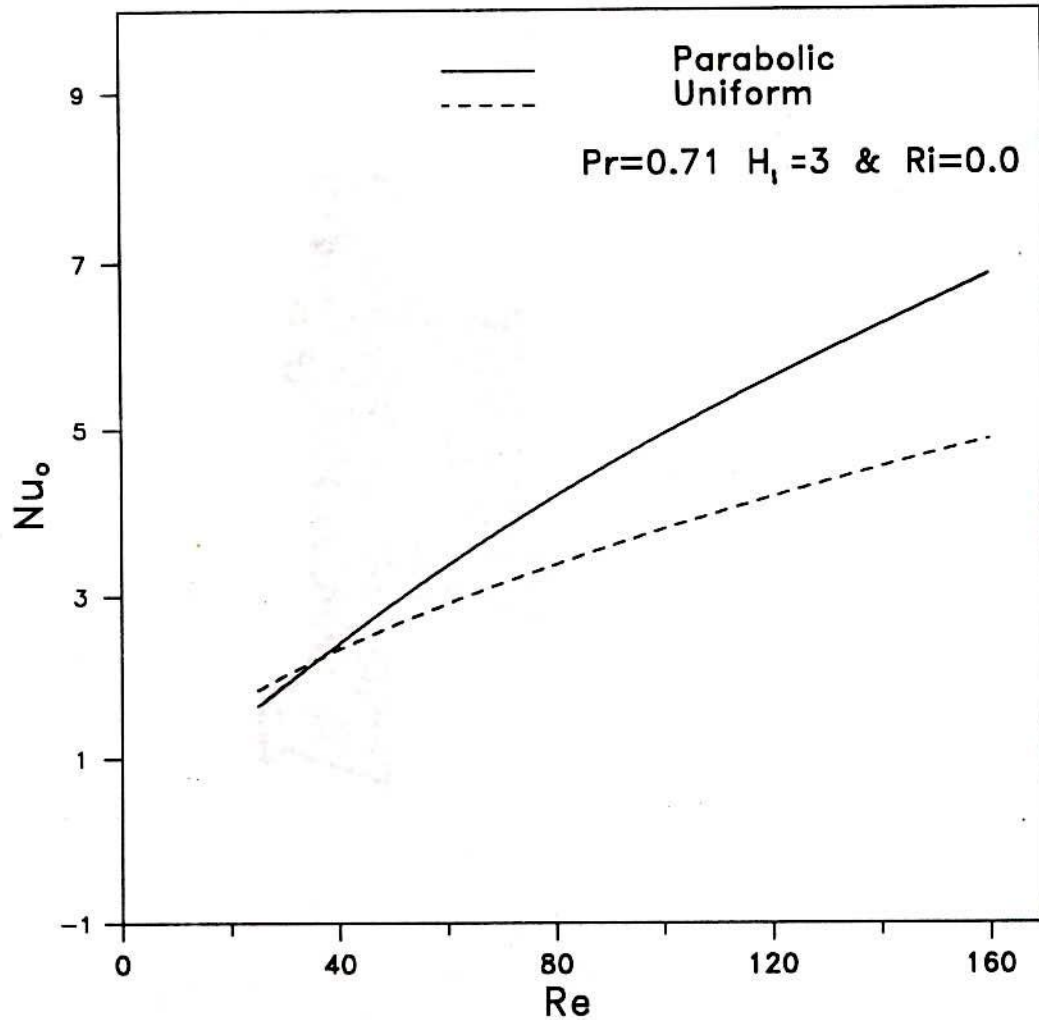


Fig.4.4.19: Variation of Nu_0 over the impingement surface for different Re .

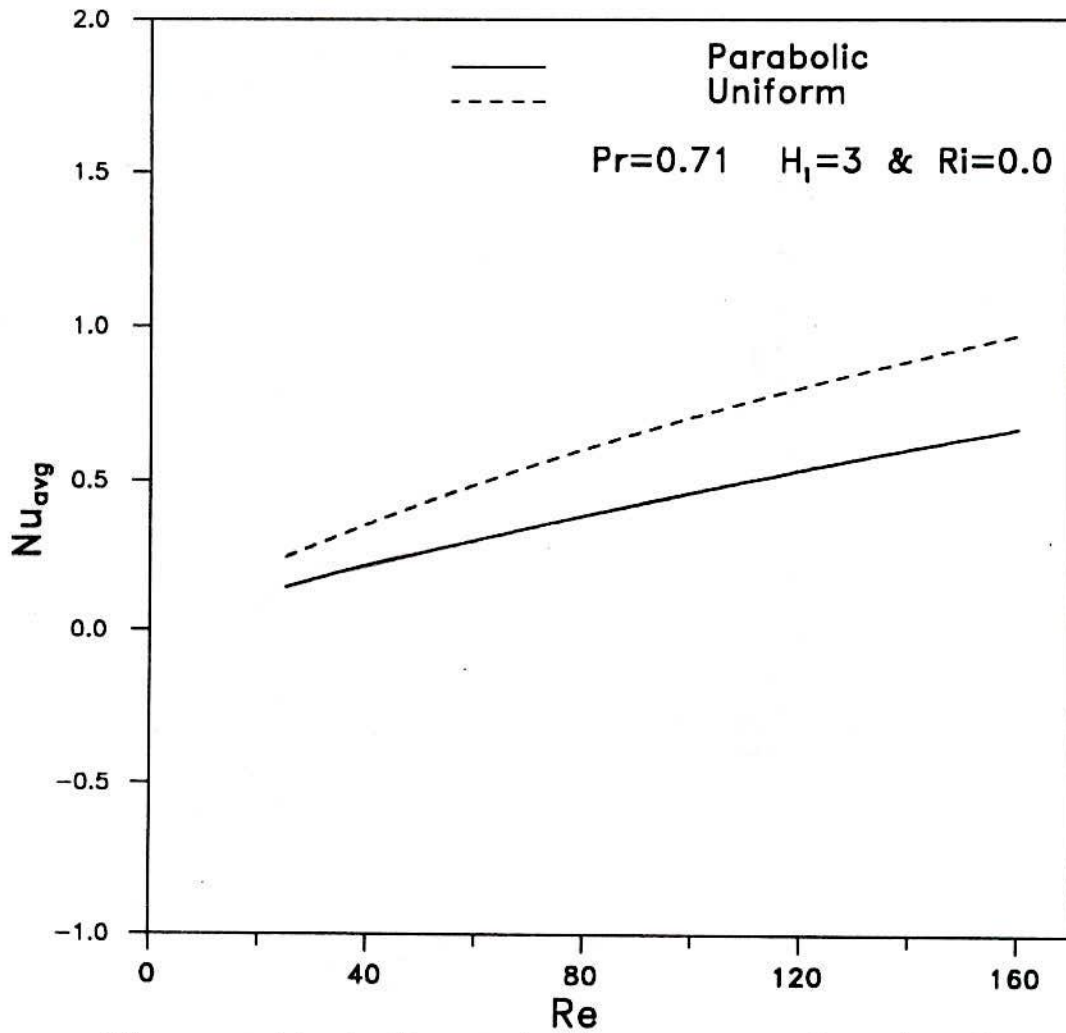


Fig.4.4.20 Variation of Nu_{avg} over the impingement surface for different Re.

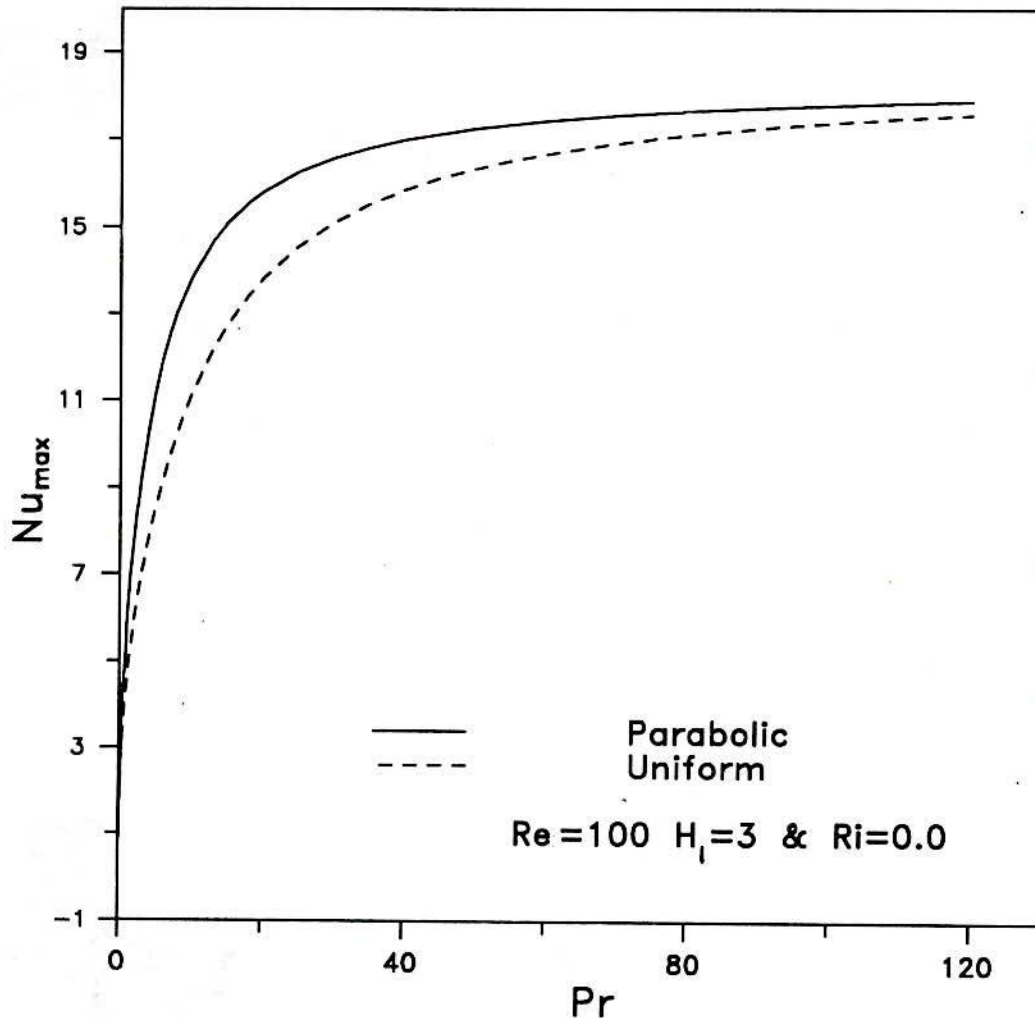


Fig.4.4.21: Variation of Nu_{max} over the surface for different Pr.

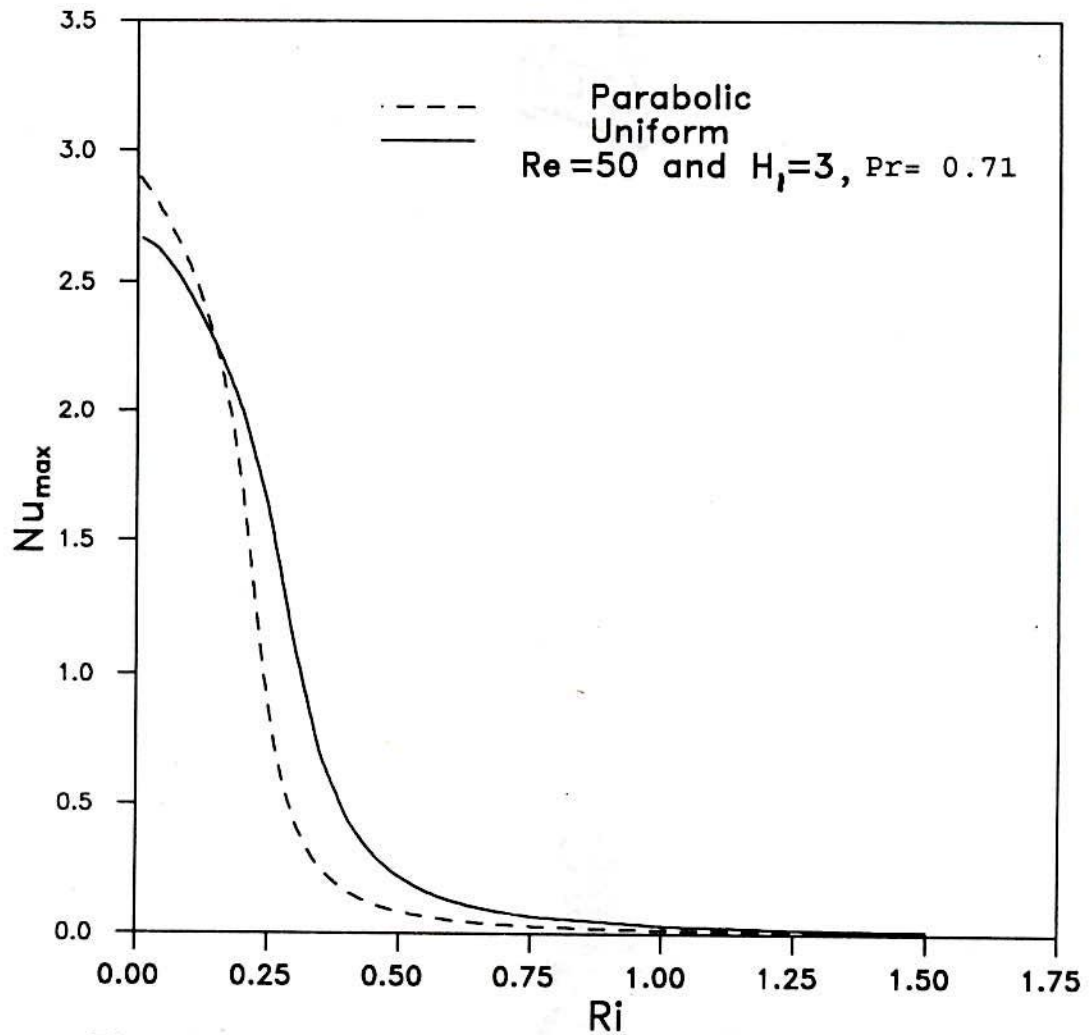


Fig. 4.4.22 : Variation of Nu_{max} over the surface for different Ri.

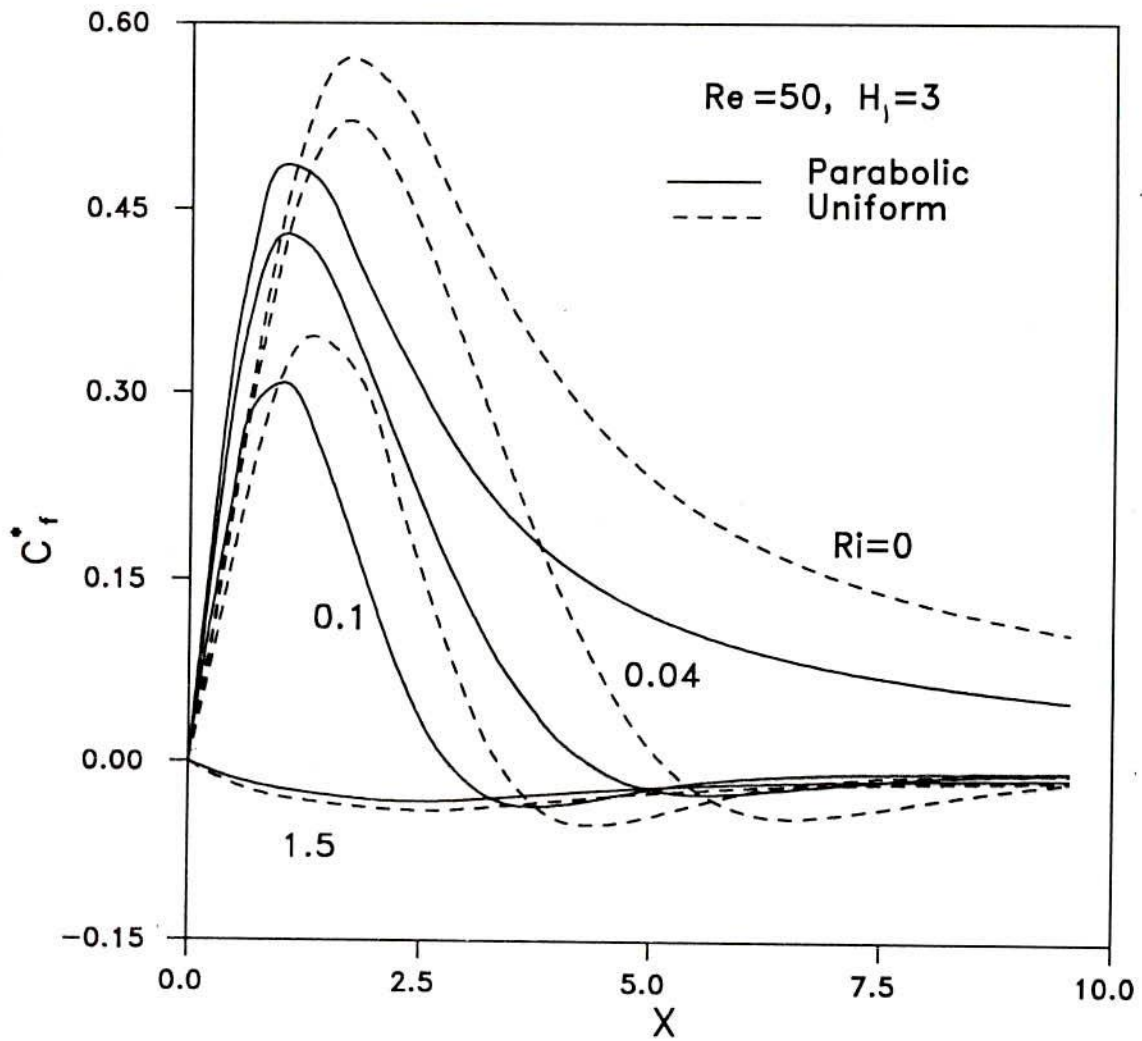


Fig.4.4.23: Local friction factor variation along the surface at different Richardson number.

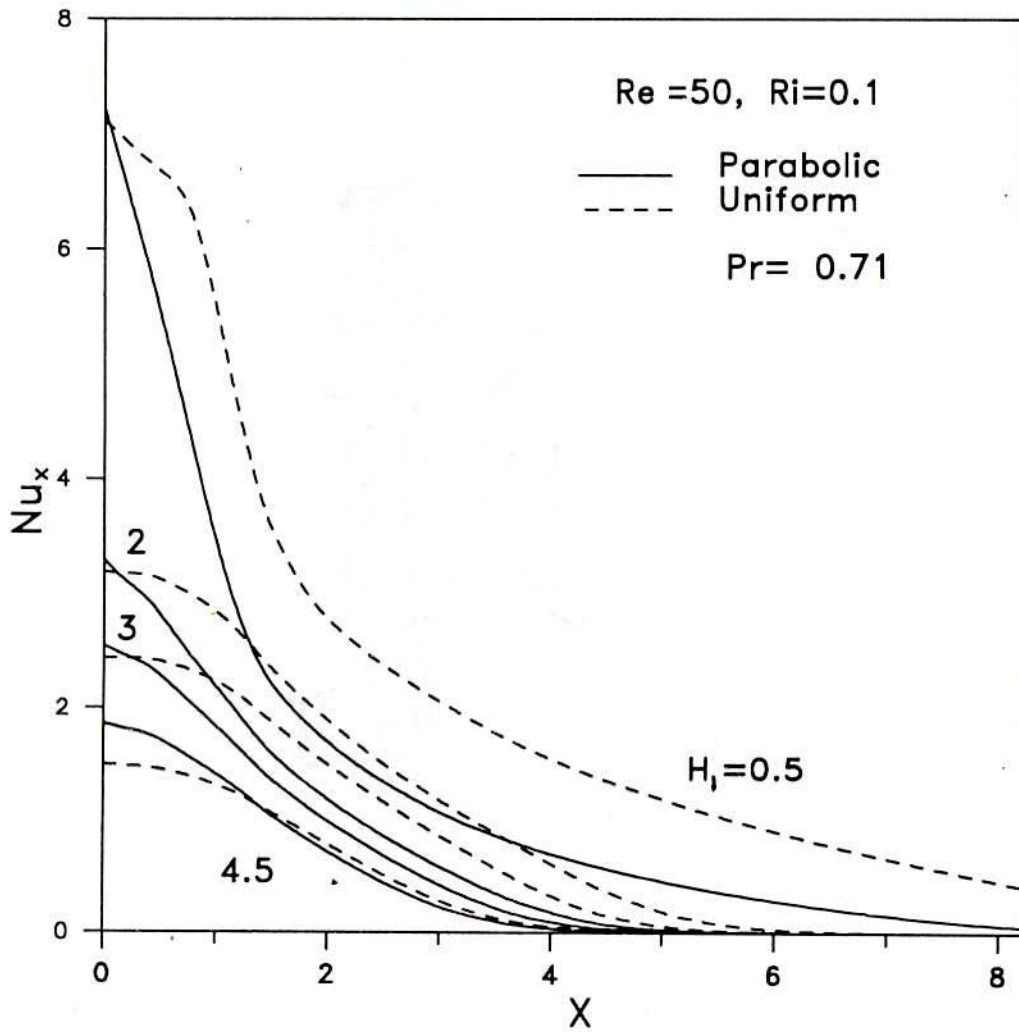


Fig.4.4.24: Local Nusselt number variation along the surface at different nozzle-to-plate spacings.

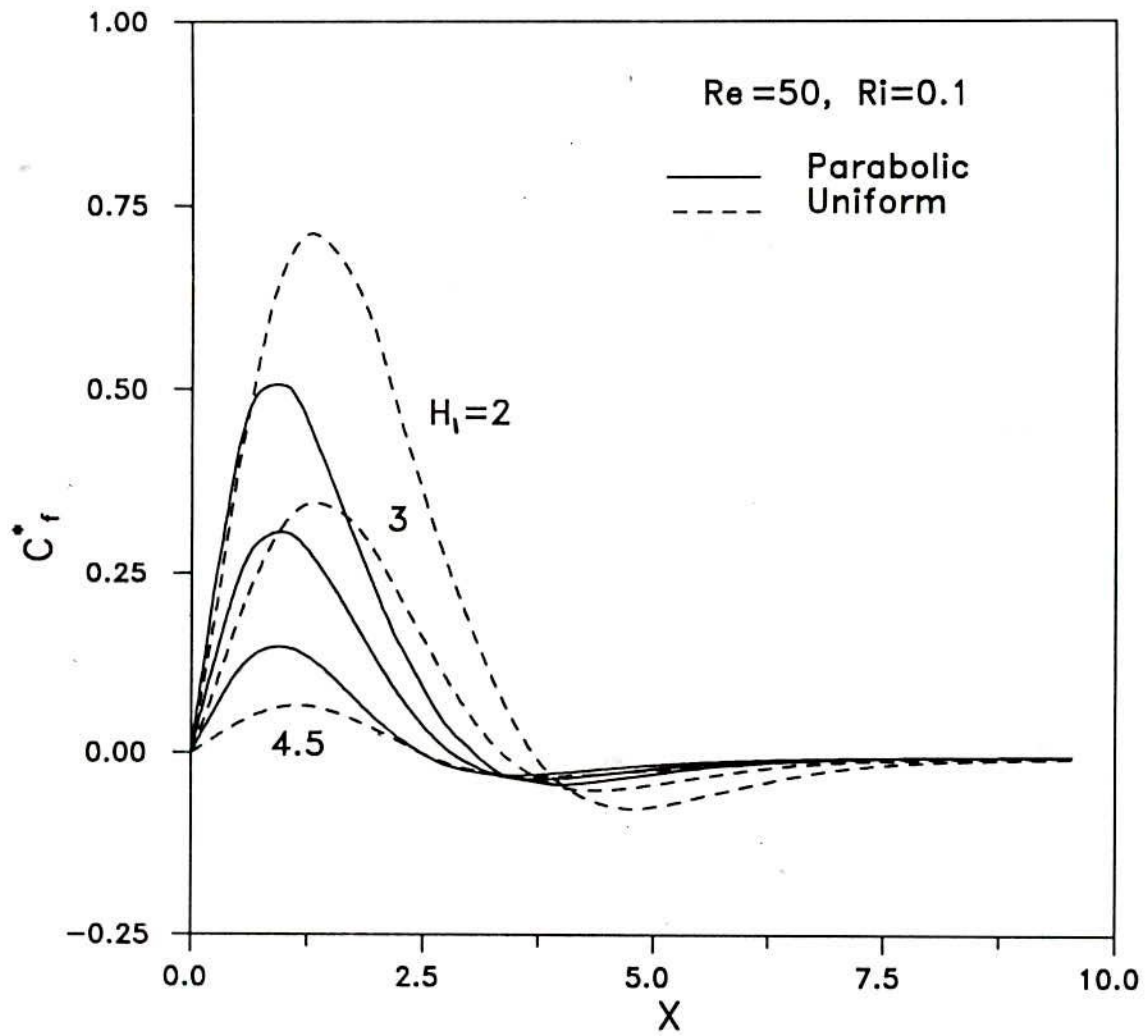


Fig.4.4.25: Local friction factor variation along the surface for various nozzle-to-plate spacings.

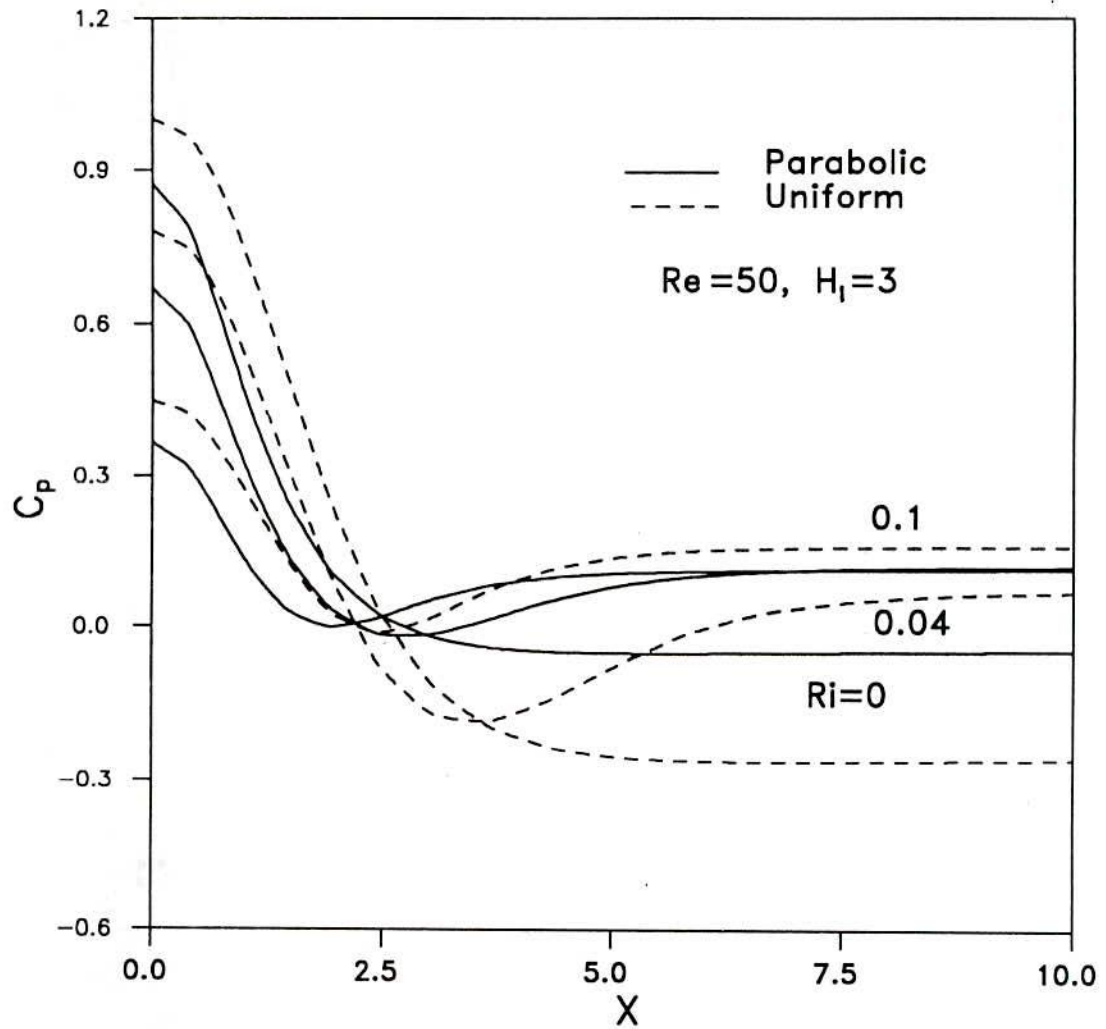


Fig.4.4.26: Variation of pressure coefficient along the surface for various Richardson number.

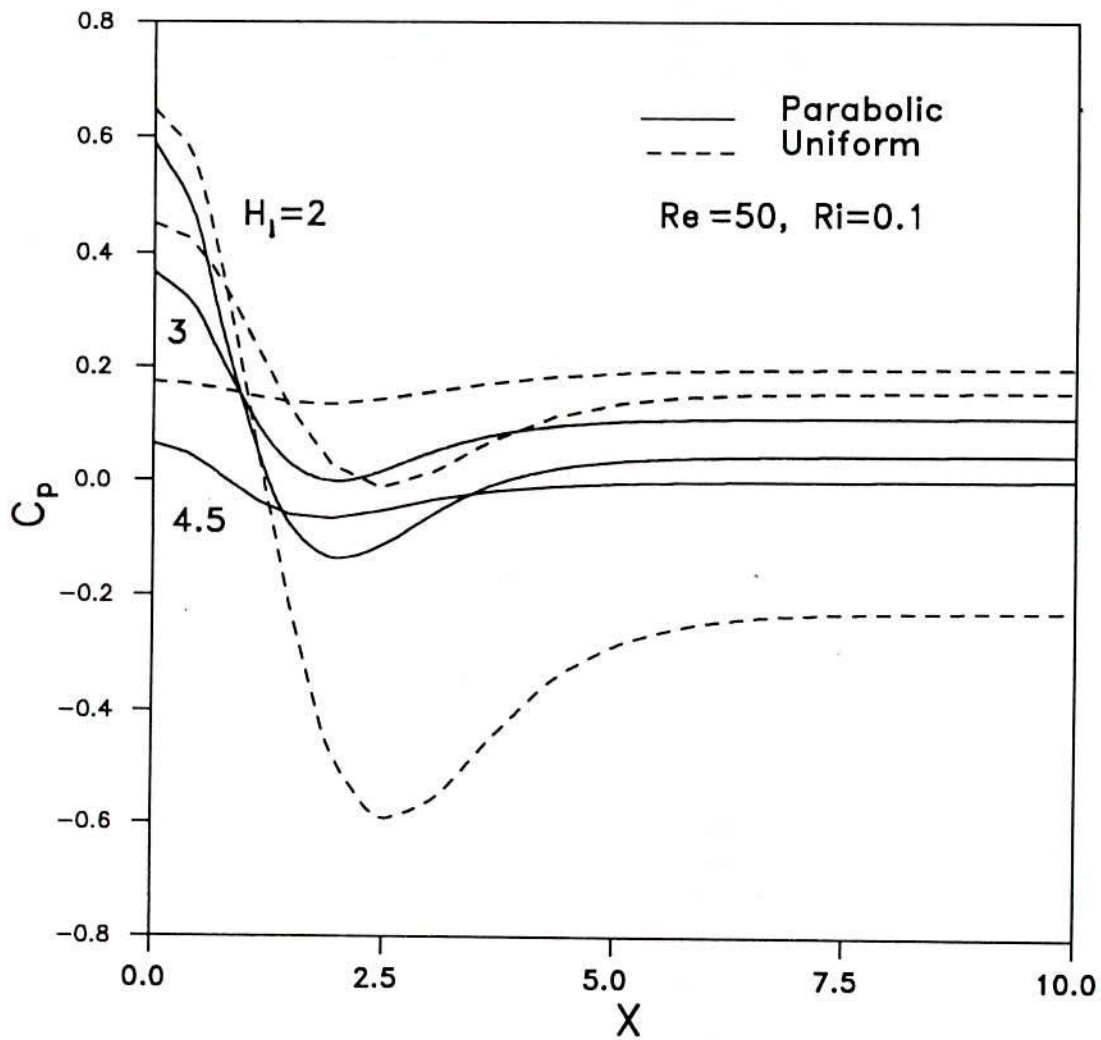


Fig. 4.4.27. Variation of pressure coefficient along the surface for various nozzle-to-plate spacings.

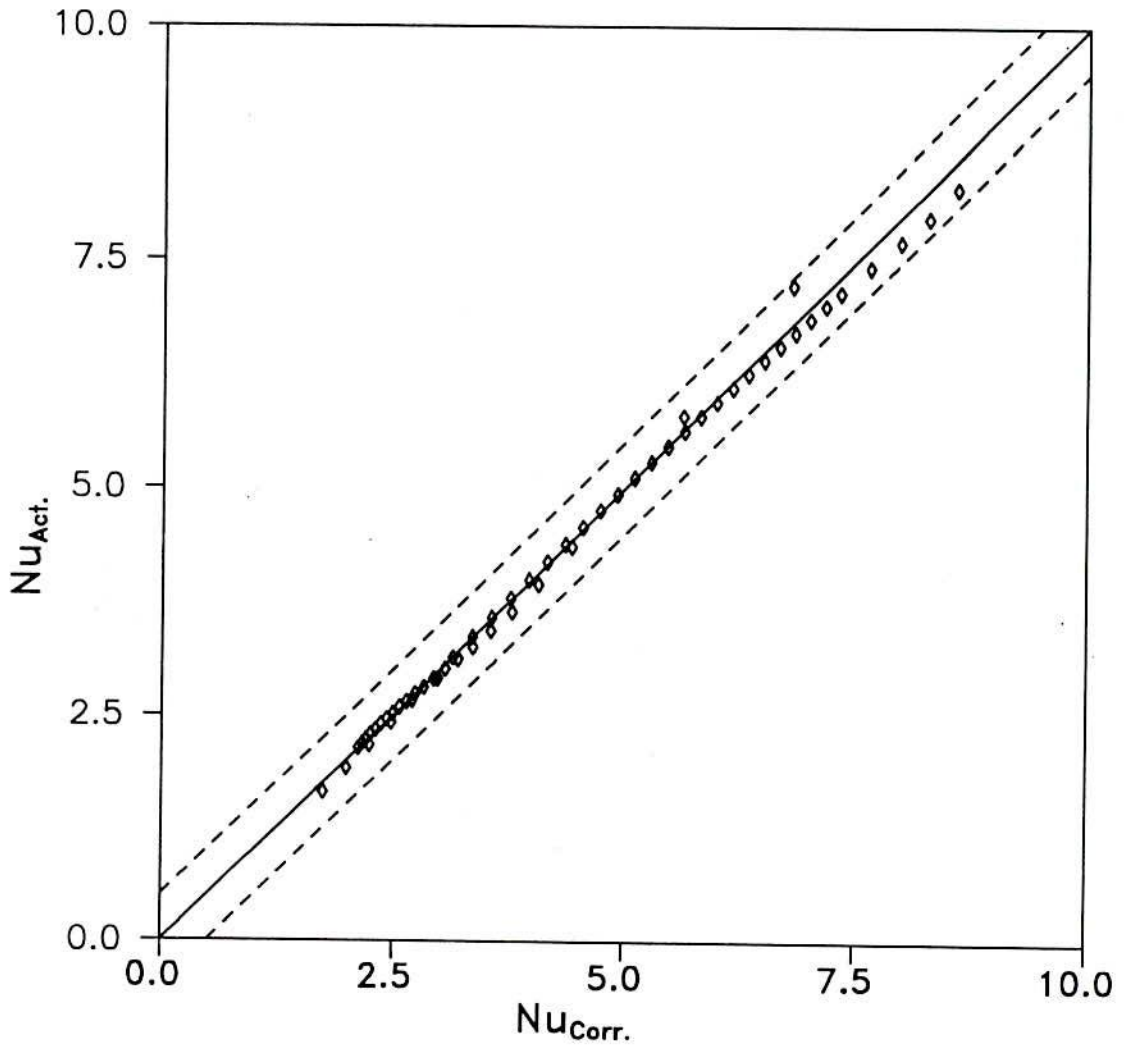


Fig.4.4.28: Correlations for predicting stagnation point Nusselt no. for parabolic velocity profile.

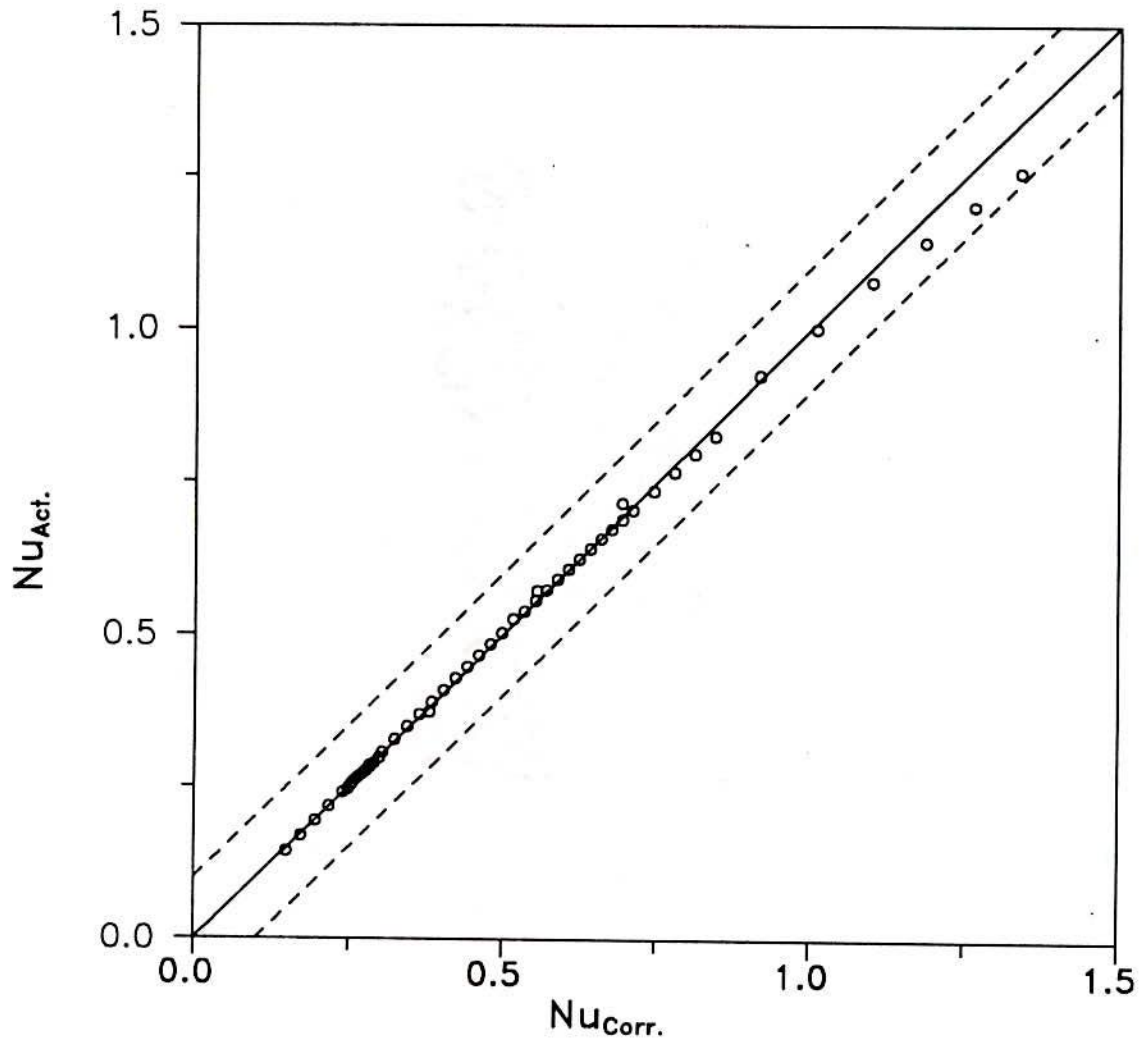


Fig.4.4.29: Correlations for predicting average Nusselt number for parabolic velocity profile.

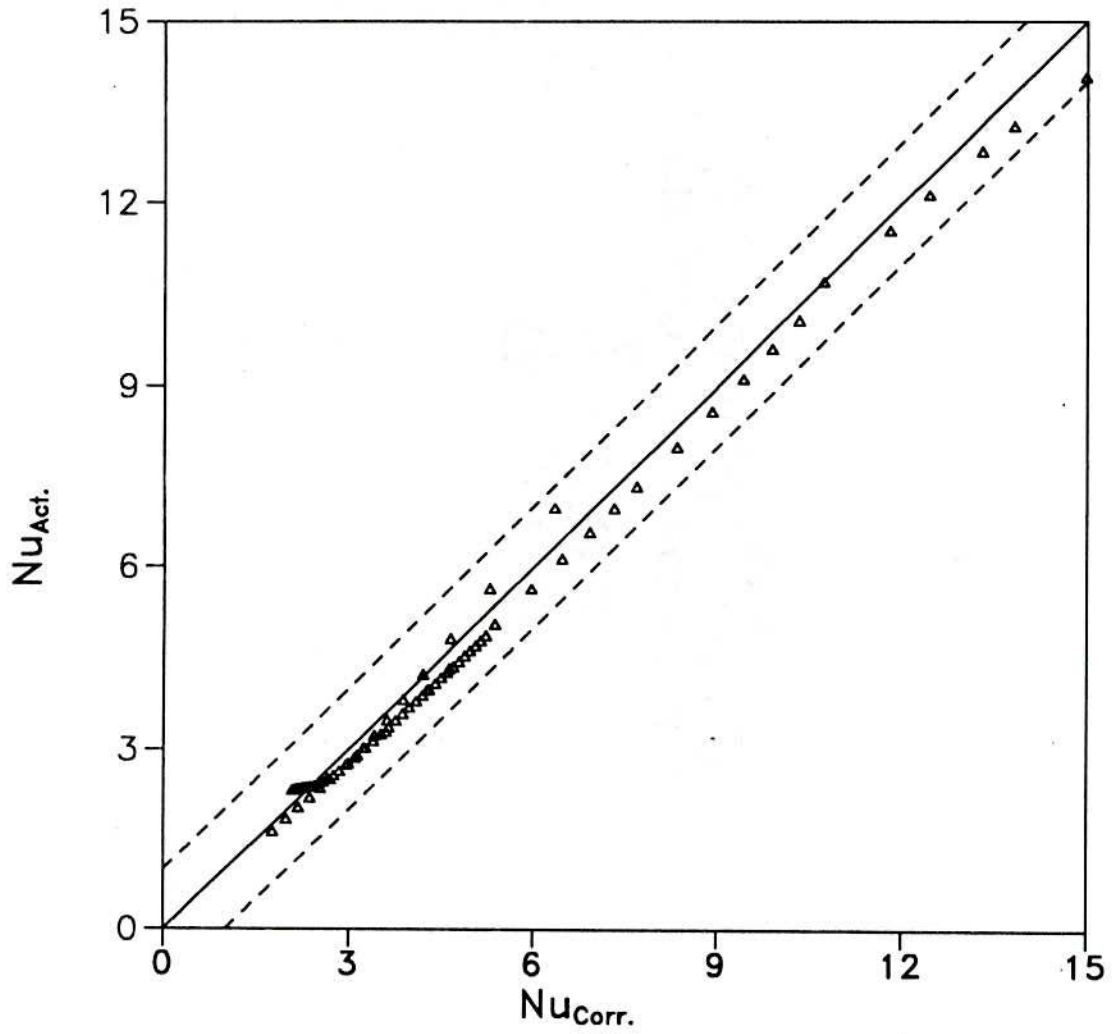


Fig.4.4.30: Correlations for predicting stagnation point Nusselt number for uniform velocity profile.

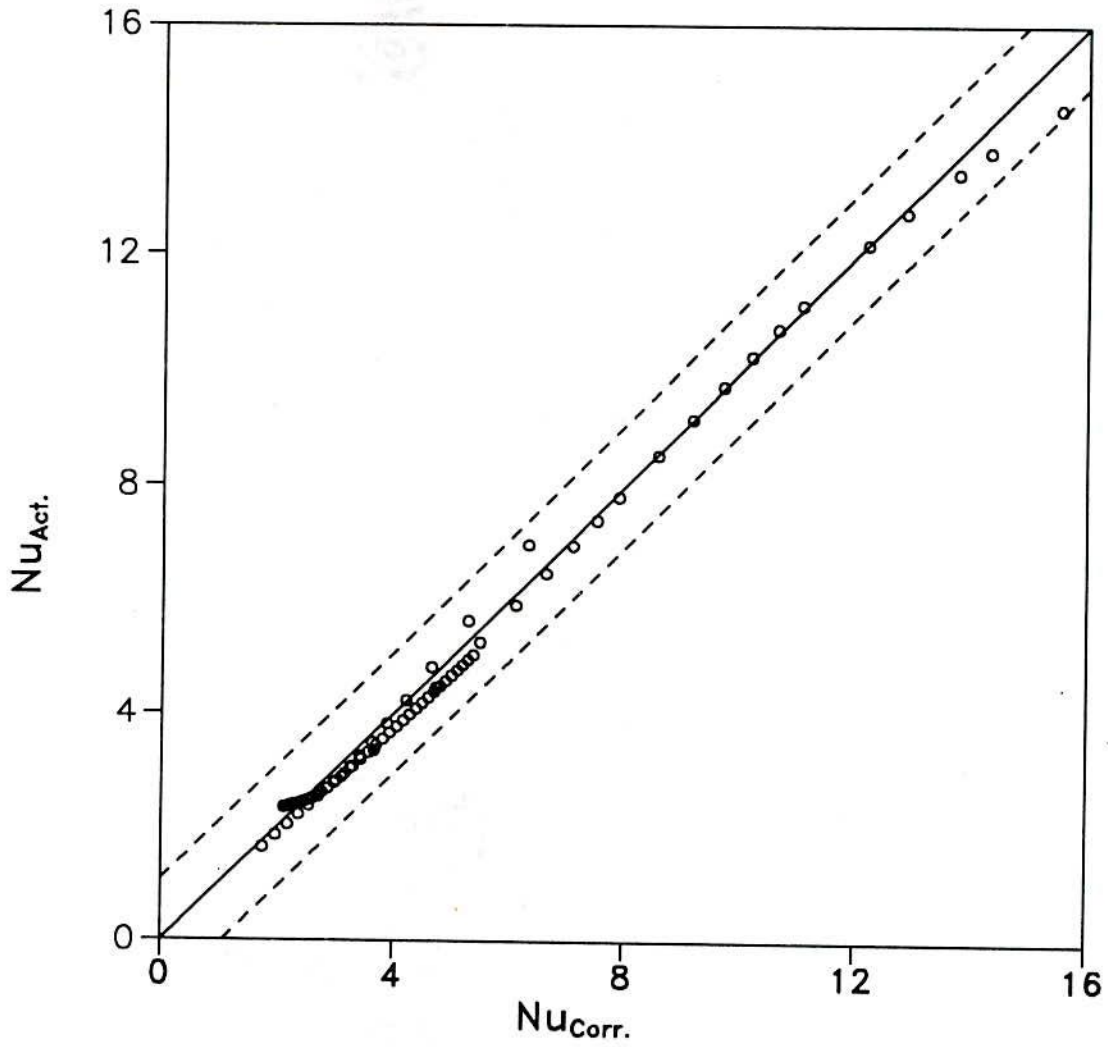


Fig4.4.31: Correlations for predicting maximum Nusselt number for uniform velocity profile.

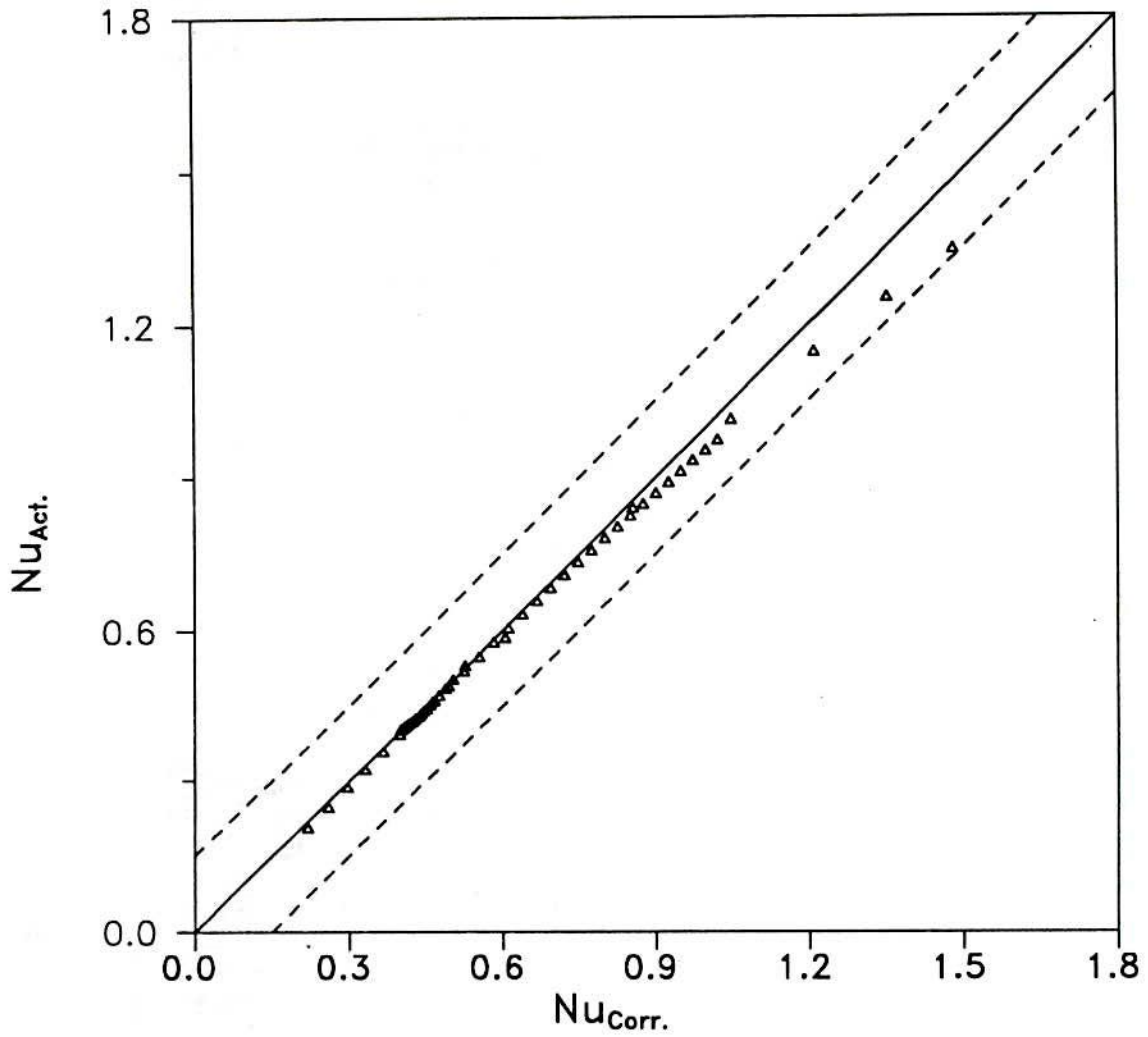


Fig.4.4.32: Correlations for predicting average Nusselt number for uniform velocity profile.

4.5 OFFSET SLOT JET

The solutions of Navier-Stokes equations for the offset slot jet have been obtained by SIMPLEC algorithm with boundary conditions as described in Chapter 3. The nozzle is located on a vertical wall at a height h_1 from the impingement surface. The flow is entrained on the upper side of the jet from a large distance in y direction. The presence of the horizontal surface on the lower side of the jet reduces the entrainment on the lower side of the jet. The jet turns towards the bottom surface due to the reduced entrainment, and attaches to the surface. The fluid entrained by the jet on the bottom side, recirculates between the left wall and the reattachment point.

The upper entrainment boundary and the right outflow boundary were chosen after several trails, so that the solutions are independent of their choice. Finally, $L= 42W$ and $H= 25W$ have been used in all the calculations. Fine grid spacings were taken near the left wall, the bottom wall and the nozzle exit which were gradually expanded to coarse grids in the interior of the domain.

Relaxation factors of 0.5, 0.5, 0.5 and 1.0 were used for x -momentum, y -momentum, energy equations and pressure correction equation respectively. The convergence was achieved after about 1000 iterations in most of the cases. It was observed that when the velocity profiles and temperature converge upto sixth place of decimal, the values of residual were as follows,

$$\text{Res}(U) = 10^{-3}$$

$$\text{Res}(V) = 10^{-3}$$

$$\text{Res}(T) = 10^{-5}$$

$$SSUM = 10^{-12}$$

The Reynolds numbers, Prandtl numbers and the offset ratio are considered as parameters. The solutions have been presented for Reynolds numbers of 30 to 80 for the uniform slot exit profiles, and 50 to 100 for the parabolic slot exit profiles, Prandtl numbers of 0.7 to 10, and offset ratios of 3 to 9.

The solutions were obtained for various grid sizes to check the grid independence of the solutions. Figure 4.5.1 shows the variation of local Nusselt number along the impingement surface at $Re = 65$, offset ratio = 5 and $Pr = 4.34$ for three grid sizes namely, 100×62 , 110×82 and 130×94 . It is observed that the solution does not change significantly for grids finer than 100×62 , hence this has been used in all the subsequent calculations.

Figure 4.5.2 shows the velocity vector plot at an offset ratio, $O.R. = 3$ and $Re = 80$ with uniform slot exit velocity profile. A fine grid has been taken near the reattachment point also, to obtain accurate solutions. The entrainment is observed from the top boundary. The jet attaches to the wall and flows like a wall jet subsequently. There is a recirculation cell in the left lower corner, where the flow entrained by the lower boundary of jet, recirculates.

Figure 4.5.3 shows the stream lines at $Re = 80$ and $O.R. = 5$, with the uniform slot exit velocity profile. The entrained flow is confined to small value of X . The entrainment decreases as the jet velocity decreases and its spread increases along the x -direction. The entrained flow is accelerated towards the slot-exit and then follows the main jet. Recirculation is seen in the left-bottom

corner along with reattachment.

Figure 4.5.4 shows the isotherms for heated offset jet at $O.R.= 3$ and $Re= 80$ with uniform slot-exit velocity and temperature profiles. The temperature in the upper part of recirculation region, does not vary significantly as compared to that in the lower part, particularly near the point of reattachment. The temperature in the core of the jet remains constant upto some distance as indicated by the closed loop isotherms for $T^* = 0.9$. In contrast, Hoch et al. [125] had experimentally observed the temperature to be uniform in the recirculation region of turbulent offset jet.

The velocity vector plot for the offset jet with parabolic slot-exit velocity profile at $O.R.= 3$ and $Re= 80$ is shown in Figure 4.5.5. A comparison with the uniform slot exit velocity profile indicates that less flow is entrained by this jet and reattachment occurs little latter than that for the uniform slot-exit offset jet. The other features are the same as in Figure 4.5.2.

Figure 4.5.6 shows the streamlines for the offset jet with parabolic slot-exit velocity profile at $Re= 80$ and $O.R.= 3$. The total volume flow rate in the case of uniform slot-exit velocity profile is more than that for the parabolic slot-exit velocity profile as indicated by the magnitude of stream function. The characteristics features are same as in Figure 4.5.3 for uniform slot-exit velocity profile. Figure 4.5.7 shows the isotherms for the offset jet with parabolic slot exit velocity and temperature profiles at $Re= 80$ and $O.R.= 3$. The characteristics features are

the same as those in Figure 4.4.4 for uniform slot-exit profiles except that there is no indication of thermal core.

Figure 4.5.8 shows the velocity vector plot, at $O.R.= 7$ and $Re= 80$ for uniform slot-exit velocity profile. The three regions of the flow are observed in this figure, these are, (i) the recirculation region with an clockwise vortex, (ii) the reattachment region and, (iii) the wall jet region. The flow pattern is very similar to that for the offset ratio of 3 in Figure 4.5.3 except that the point of reattachment shifts to the right and a secondary vortex is seen in the left bottom corner. A magnified view of the velocity vector plot of left bottom corner is shown in Figure 4.5.9. The secondary anti-clockwise vortex is clearly seen in this figure. This occurs due to large offset ratio. The streamlines for this case are shown in Figure 4.5.10 which has same characteristic feature as Figure 4.5.3 for $O.R.= 3$ except that the point of reattachment shifts to the right and secondary vortex occurs in the left bottom corner as seen in Figure 4.5.9. Isotherms for this case are shown in Figure 4.5.11. The closed loop for the isotherm $T^* = 0.9$ indicates the possibility of a core in which temperature remains constant upto a certain distance along the jet centreline. A comparison with Figure 4.5.4 for $O.R.= 3$, indicates the existence of two recirculating regions.

The stream lines for the offset jet at $Re=80$, $O.R.= 7$ with parabolic slot-exit velocity profile are, shown in Figure 4.5.12. A comparison with Figure 4.5.10 for the uniform slot-exit velocity profile, indicates that the parabolic slot-exit velocity profile entrains smaller mass flow rate and the secondary vortex is

smaller in size as compared to those for the uniform slot-exit velocity profile. Figure 4.5.13 shows the isotherms for the offset jet at $Re = 80$ and $O.R. = 7$ with parabolic slot-exit velocity profile. The characteristic features are the same as in Figure 4.5.11 for uniform slot-exit profile except that there is no indication of thermal core.

Figure 4.5.14 shows the variation of local Nusselt number with Reynolds numbers at an offset ratio 5 and $Pr = 4.34$ with parabolic velocity and temperature profiles at the slot-exit. It is observed that the local Nusselt number increases with the slot exit Reynolds number. A small hump is observed near $X = 0.0$ at $Re = 100$. The Nusselt number increases in X direction at fast rate near $X = 0.0$. This rate, however reduces slightly away from $X = 0.0$, which is the reason for the hump. The fluid in the secondary recirculation region rotates in counter-clockwise direction and the fluid rotates in clockwise direction in the primary recirculation region. There is interaction between fluids of two recirculation regions travelling in the same direction and some thermal energy is transferred from primary recirculation region to the secondary recirculation region. The hump occurs in this region. The fluid in the secondary recirculation region then comes into contact with the cold slot exit wall and the impingement surface to which it loses some of its thermal energy. It is observed in the Figure 4.5.14 that the local Nusselt number does not vary significantly upto $X = 2.9$ for all Reynolds numbers, which implies that the variation of local Nusselt number in the secondary recirculation region is independent of Reynolds number.

Beyond $X=2.9$, the local Nusselt numbers increases with the increase of Reynolds number. The local Nusselt number decreases monotonically after achieving a maximum value around $X= 8$ which is very close to the point of reattachment. Aung [126] has reported that the maximum Nusselt number occurs downstream of the reattachment point. The location of maximum Nusselt number is independent of Reynolds number for $Re \geq 65$. Actually, it will be shown in Figure 4.5.31 that the location of reattachment point also becomes independent of Reynolds number for $Re > 65$.

Figure 4.5.15 shows the variation of local friction factor with Reynolds number at offset ratio 5 with parabolic velocity and temperature profiles at the slot-exit. There is no flow in the left bottom corner, hence friction factor is also zero at $X= 0.0$. In the primary recirculation region, the velocity is negative at the surface and the friction factor is also negative as seen for $Re= 50$ and 65 . Once the secondary recirculation sets in, the velocity at the surface will be in positive X direction and friction factor will also be positive as seen for $Re= 80$ and 100 near $X=0.0$. Local friction factor increases as the slot-exit Reynolds number increases. The friction factor is zero at the point of reattachment. It is observed from the figure that the reattachment occurs earlier at lower Reynolds numbers and is almost same at $Re= 80$ and 100 . The friction factor increases beyond this point achieving a maximum value and then decreases in the wall jet region.

Figure 4.5.16, shows the local Nusselt number variation with slot-exit Reynolds number at an offset ratio 5 and $Pr= 4.34$ with

uniform slot exit velocity and temperature profiles. The local Nusselt number is almost independent of Reynolds number upto $X=3.1$ except for the hump at $Re=100$. Beyond $X=3.1$, the local Nusselt number increases with increase in slot-exit Reynolds number. The location of the maximum Nusselt number becomes constant at $Re \geq 40$. A comparison with Figure 4.4.14 indicates that the maximum occurs little latter than that for the parabolic slot-exit profiles. It will be shown in Figure 4.5.31 that the reattachment occurs a little latter for uniform velocity profile than that for the parabolic slot-exit profile. Nusselt number has its maxima very close to the reattachment point. The Nusselt number is, in general, larger for uniform slot-exit profiles than that for the parabolic slot-exit profiles.

Figure 4.5.17 shows the variation of local friction factor with slot-exit Reynolds number at $O.R.=5$ and for uniform slot-exit profiles. The friction factor is positive near $X=0.0$ for $Re \geq 65$ which indicates the existence of secondary recirculation region for $Re \geq 65$. A comparison with Figure 4.5.15 indicates that the friction factor is larger, the peaks occur at larger values of X and the reattachment length is more for the uniform slot-exit profiles than those for the parabolic slot-exit profiles.

Figure 4.5.18 shows the variation of local Nusselt number with offset ratios at Reynolds number of 80 and $Pr=4.34$ for the parabolic velocity and temperature profiles at the slot-exit. The local Nusselt number decreases with the increase of offset ratio. Local Nusselt number shows a hump and a flat region near $X=0.0$

for offset ratio 5 and larger due to the secondary recirculation region near the corner and then increases in the primary recirculation region to attain a maximum value near the point of reattachment. The maximum temperature is observed (not shown here) within the recirculation region as reported in Hoch and Jiji [125] and Holland and Liburdy [128]. The local Nusselt number does not change significantly with offset ratio beyond $X = 33$.

Figure 4.5.19 shows the variation of local friction factor with offset ratios at $Re = 80$ for parabolic velocity profile at the slot-exit. Local friction factor, like the Nusselt number decreases with the increase of offset ratio. The friction factor is positive near $X = 0.0$ for offset ratio of 5 and larger. This indicates the presence of secondary recirculation region near $X = 0.0$. The friction factor is zero at the point of reattachment. The figure shows that the point of reattachment shifts towards larger values of X as the offset ratio increases. The location of peaks also shifts towards larger values of X , as the offset ratio increases.

Figure 4.5.20 and 4.5.21 show the variation of local Nusselt number and local friction factor respectively with offset ratio at $Re = 80$ and $Pr = 4.34$ for the uniform velocity and temperature profiles at slot exit. The trends are very similar to those observed in Figures 4.5.18 and 4.5.19 for the parabolic velocity and temperature profiles at slot-exit. A comparison indicates that Nusselt number and friction factor are, in general, larger and peak values occur at slightly larger values of X for uniform profiles as compared to those for parabolic slot-exit profiles.

The extents of primary and secondary recirculation regions are also larger for uniform profiles as compared to those for parabolic profiles at the slot-exit.

Figure 4.5.22 shows the variation of pressure coefficient with Reynolds numbers along the impingement surface at O.R.= 5 with parabolic slot-exit velocity profile. The local pressure coefficient, in general, increases with the increase of Reynolds number. The minimum value of the pressure along the surface occurs at the centre of the primary recirculation region and maximum value of the pressure occurs at the reattachment point as reported in Pelfrey and Liburdy [6]. The reattachment point is identified in this investigation, as the location where the velocity gradient $(\partial U/\partial Y)=0$ along the surface, as suggested by Pelfrey and Liburdy [6]. Pelfrey and Liburdy [6] have obtained a reattachment length of 13 ± 0.05 , at an offset ratio 7 and slot-exit Reynolds number of 15,000 in turbulent flow. But in the present investigation the reattachment length is found to be 12.6, at an offset ratio 7 and slot-exit Reynolds number of 65, and at offset ratio 7 and Reynolds number 80 the reattachment length is 12.65 with the uniform slot exit velocity profile.

Figure 4.5.23 shows the variation of pressure coefficient with Reynolds number at O.R.= 5 for uniform slot exit velocity profile. The pressure levels are in general, higher for the uniform profile as compared to those for the parabolic profile at slot exit. The centre of the primary recirculation region and the reattachment point, both occur at larger values of X as compared to those for parabolic slot-exit profiles.

Figure 4.5.24 and 4.5.25 show the pressure variation with offset ratio for parabolic and uniform velocity profiles respectively at slot-exit and at a Reynolds number of 80. Pressure, in general, decreases as the offset ratio increases. The reattachment points and centres of the primary recirculation region, both shift towards larger values of X with increase of offset ratio. It is observed that the pressure attains a constant value in the wall jet region, the constant being lower at higher offset ratios. The pressure levels, positive and negative, both are, in general, higher for uniform slot exit profiles as compared to those for the parabolic slot-exit profiles. The centre of the primary recirculation region and the reattachment point, both occur at larger values of X for the uniform slot-exit profiles as compared to those for the parabolic slot-exit profiles.

Figure 4.5.26 shows the comparison of Nusselt number at slot exit Reynolds number of 65 and an offset ratio of 5 for uniform and parabolic velocity and temperature profiles at slot-exit. It is observed that the local Nusselt number for the uniform profiles has a higher value than that for the parabolic slot-exit profiles. Figure 4.5.27 & 4.5.28 show the comparison of local friction factor and pressure coefficient respectively for uniform and parabolic velocity profiles at the slot-exit at Reynolds number of 65 and an offset ratio of 5. As discussed earlier, uniform slot-exit velocity profile has higher level of pressure coefficient and friction factor as compared to those for the parabolic slot-exit velocity profile. The location of the centre of primary recirculation region and the reattachment point occur

at higher values of X for the uniform slot-exit profiles as compared to those for the parabolic slot-exit profiles.

Figures 4.5.29 and 4.5.30 show the variation of local Nusselt number with Prandtl number for parabolic and uniform slot-exit velocity and temperature profiles respectively at $Re = 80$ and $O.R. = 5$. It is observed that the local Nusselt number increases with the increase of Prandtl number. As observed earlier, the Nusselt number is, in general, larger for uniform slot exit profiles than that for the parabolic slot exit profiles. This is true at all Prandtl numbers. In both the cases, the location of maximum Nusselt number is independent of Prandtl number. The Nusselt number in the secondary recirculation region, shows a hump at higher Prandtl numbers for the uniform slot-exit profiles.

Figure 4.5.31 shows the variation of reattachment length with Reynolds numbers for uniform and parabolic slot-exit velocity profiles. It is observed that the reattachment length is larger for the uniform slot-exit velocity profile as compared to that for the parabolic slot-exit velocity profile. The reattachment length increases at a faster rate with increase in Reynolds numbers upto $Re = 45$, thereafter the increase with Reynolds numbers is very gradual.

Figure 4.5.32 shows the variation of the maximum Nusselt number with Reynolds number for both, the uniform and parabolic slot-exit velocity and temperature profiles. It is observed that the maximum Nusselt number has a larger values for the uniform slot-exit profile as compared to those for the parabolic slot-exit profiles for all Reynolds numbers.

Figures 4.5.33 and 4.5.34 show the variation of maximum Nusselt number and average Nusselt number respectively with Prandtl number for uniform and parabolic slot exit profiles at $Re = 65$ and $O.R. = 5$. The uniform slot-exit velocity and temperature profiles yields larger values of Nusselt numbers as compared to those for the parabolic slot-exit profiles at all values of Prandtl numbers. Both, the maximum and the average Nusselt numbers increase with increase in Prandtl numbers for both the types of velocity and temperature profiles.

Correlations

A correlation has been developed to determine the maximum Nusselt number with the uniform velocity and temperature profiles at the slot-exit, in terms of slot-exit Reynolds number, Prandtl number and the offset ratio.

$$Nu_m = 0.055 Re^{0.94} Pr^{0.48} (O.R.)^{-0.436} \quad (4.5.1)$$

The deviation of the maximum Nusselt number calculated by the Equation (4.5.1) from the actual Nusselt number is shown in Figure 4.5.35. The maximum deviation for this correlation is $\pm 10.66\%$ and the R.M.S. value of the deviation is 0.231.

The average Nusselt number in the separated region over the reattachment length has been correlated in terms of the slot-exit Reynolds number, Prandtl number and the offset ratio with the uniform slot-exit velocity and temperature profiles.

$$\overline{Nu}_{S,R} = 0.092 Re^{0.76} Pr^{0.44} (O.R.)^{-0.68} \quad (4.5.2)$$

Figure 4.5.36 shows the deviation between the actual average Nusselt number and the average nusselt number calculated from the Equation (4.5.2). The maximum deviation for this correlation from the actual values is $\pm 11.91\%$ and the R.M.S. value of the deviation is 0.108.

The following correlation has been developed to predict the reattachment length in terms of the slot exit Reynolds number and the offset ratio for uniform slot exit velocity and temperature profiles.

$$L_A = 1.04 Re^{0.145} (O.R.)^{0.963} \quad (4.5.3)$$

Figure 4.5.37 shows the deviation of the reattachment length calculated from the Equation (4.5.3) and the actual reattachment length. The maximum deviation for this correlation is $\pm 11.74\%$ and R.M.S. value of the deviation is 0.51.

Similar correlations have been developed for the parabolic velocity and temperature profiles at the slot-exit. The correlation for the maximum Nusselt number is as follows,

$$Nu_m = 0.032 Re^{0.966} Pr^{0.46} (O.R.)^{-0.42} \quad (4.5.4)$$

Figure 4.5.38 shows the deviation between the actual maximum Nusselt number and the maximum Nusselt number calculated from Equation (4.5.4). The maximum deviation is $\pm 8.84\%$ and the R.M.S. value of the deviation is 0.084.

The average Nusselt number in the separated region over the

reattachment length is correlated as follows for the parabolic profiles at slot-exit.

$$\overline{Nu}_{S.R.} = 0.056 Re^{0.757} Pr^{0.43} (O.R.)^{-0.61} \quad (4.5.5)$$

The deviation of the average Nusselt number in the separated region calculated by Equation (4.5.5) from the actual average Nusselt number in the separated region is shown in the Figure 4.5.39. The maximum deviation is $\pm 10.92\%$ and the R.M.S. value of the deviation is 0.068.

The following correlation has been developed for the reattachment length with parabolic slot-exit velocity profiles.

$$L_A = 0.964 Re^{0.155} (O.R.)^{0.957} \quad (4.5.6)$$

Figure 4.5.40 shows the deviation of the reattachment length calculated by Equation (4.5.6) from the actual reattachment length. The maximum deviation is $\pm 9.41\%$ and the R.M.S. value of deviation is 0.136.

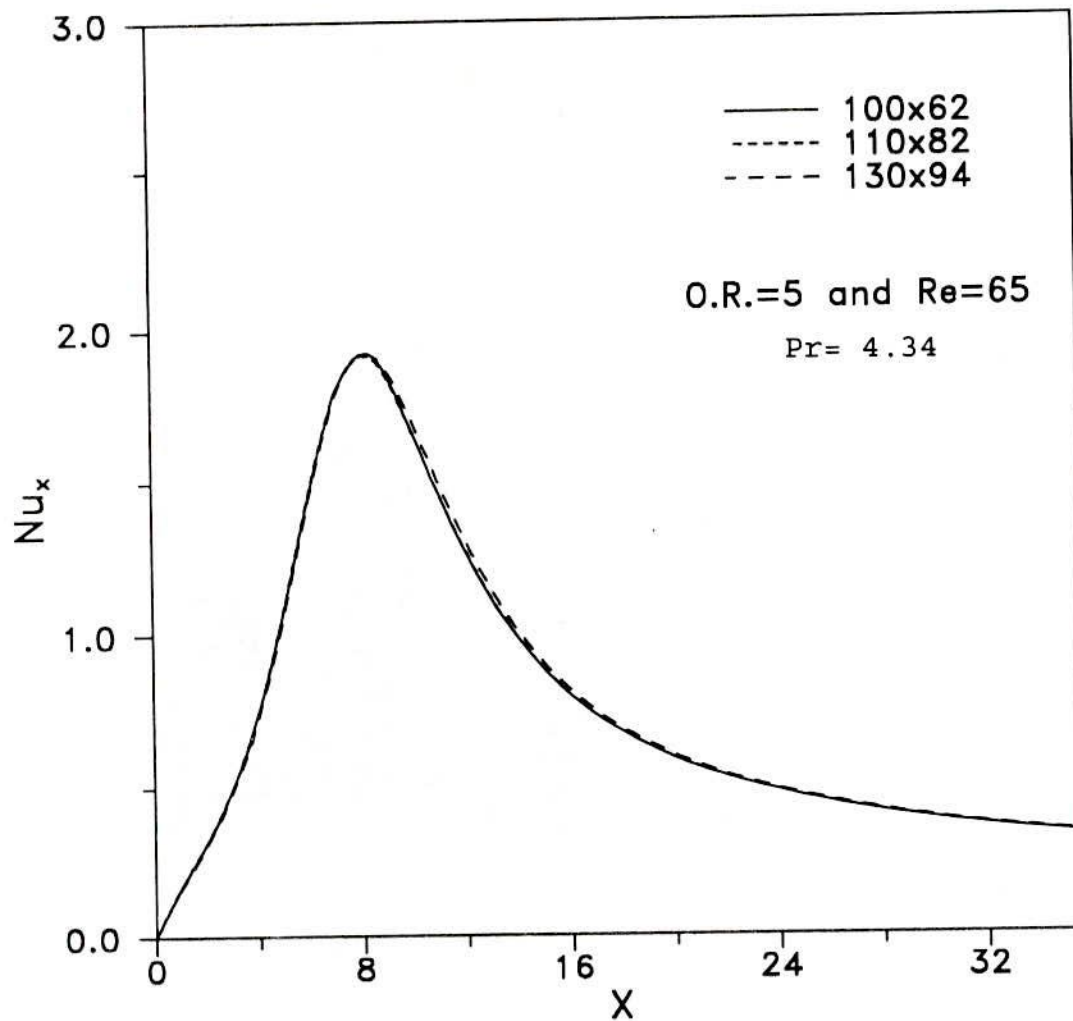


Fig.4.5.1 : Comparison of Local Nusselt number over the offset surface for parabolic velocity profile showing effect of different grid sizes.

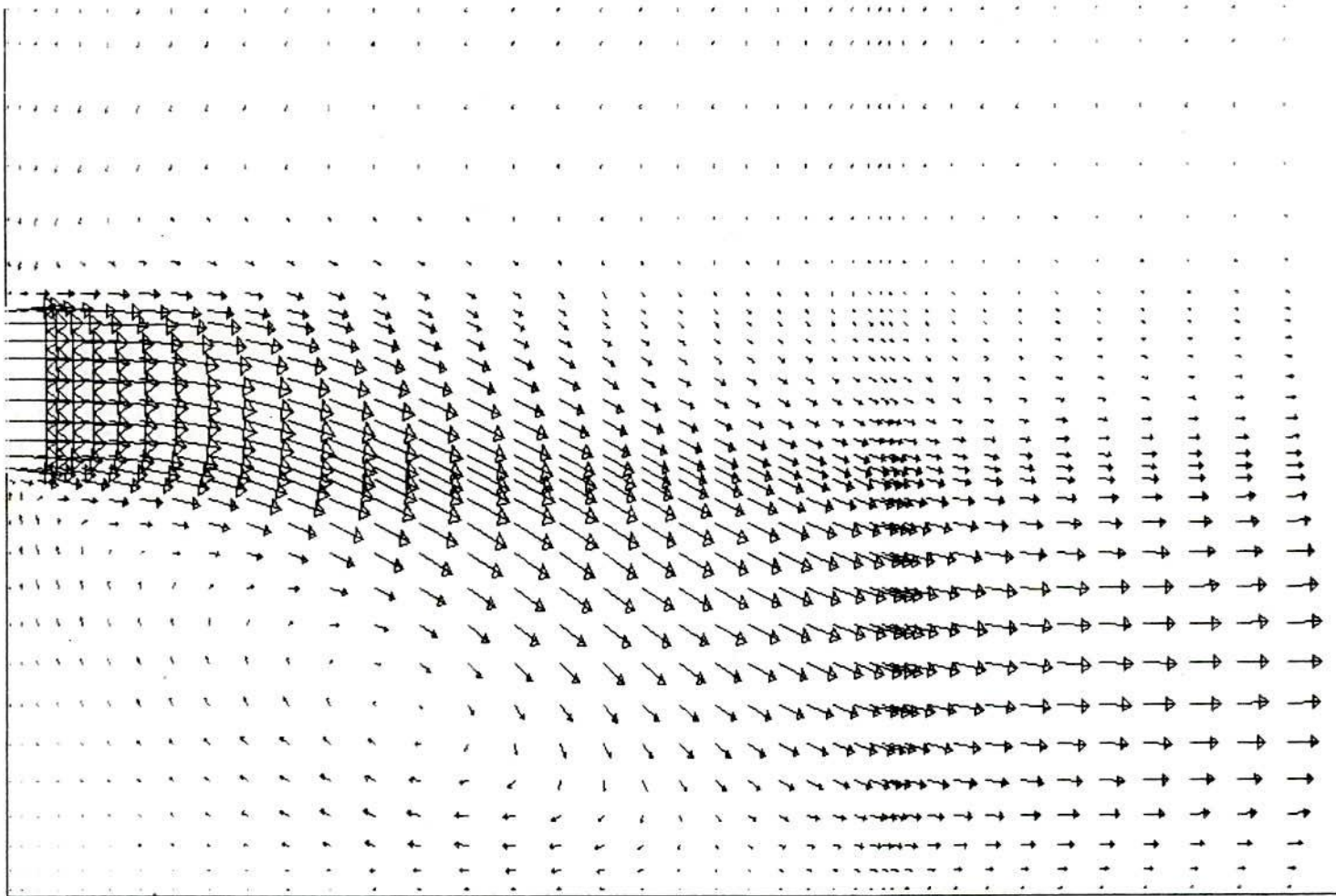


Fig4.5.2: Velocity vector plot, O.R.=3 and Re=80

Offset jet with uniform slot exit velocity profile.

Stream lines, Offset jet, O.R.=3 and Re=80 (Uniform)

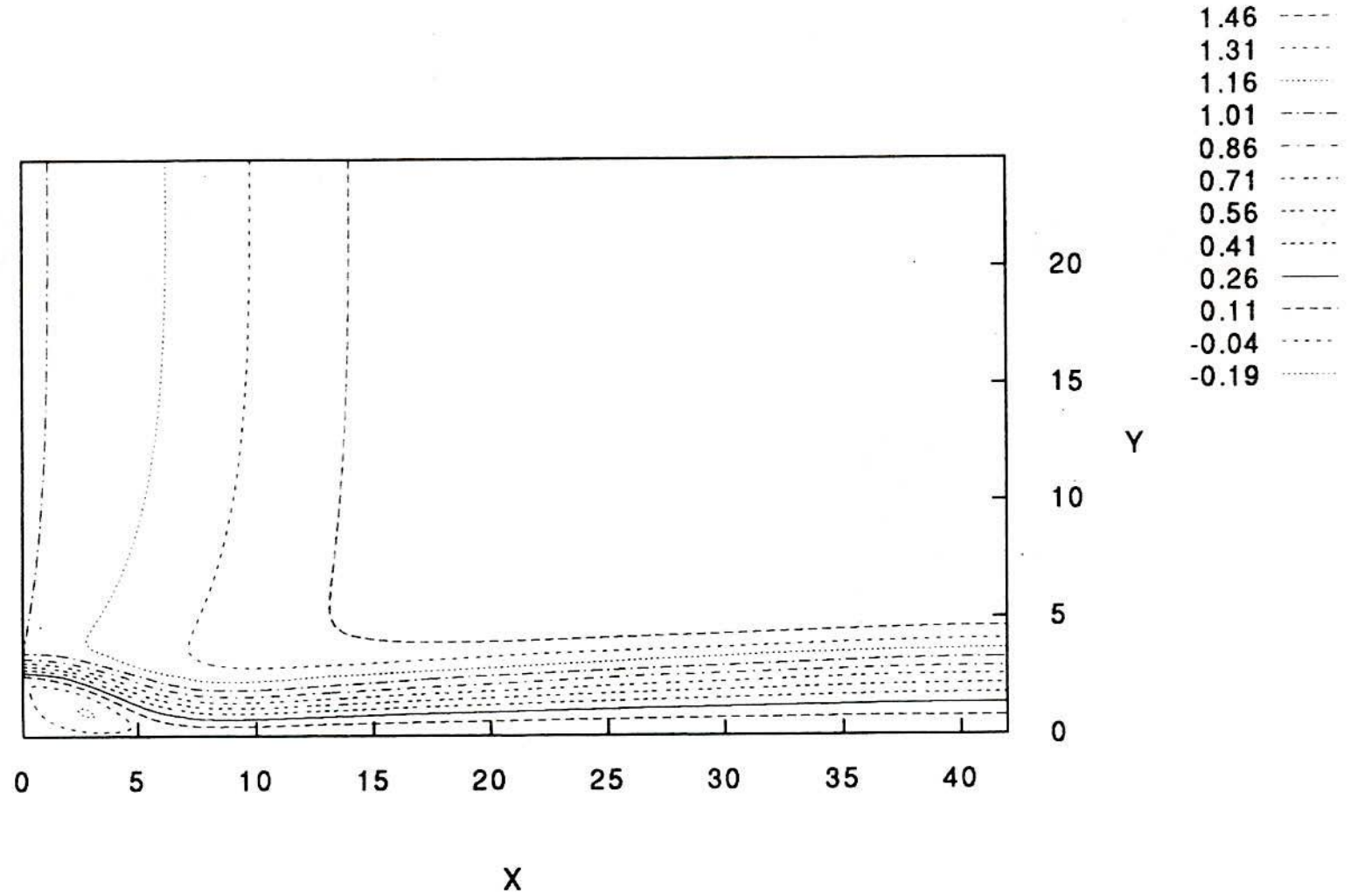


Fig.4.5.3: Streamlines for offset slot jet with uniform slot exit velocity profile at Re= 80, O.R.=3.

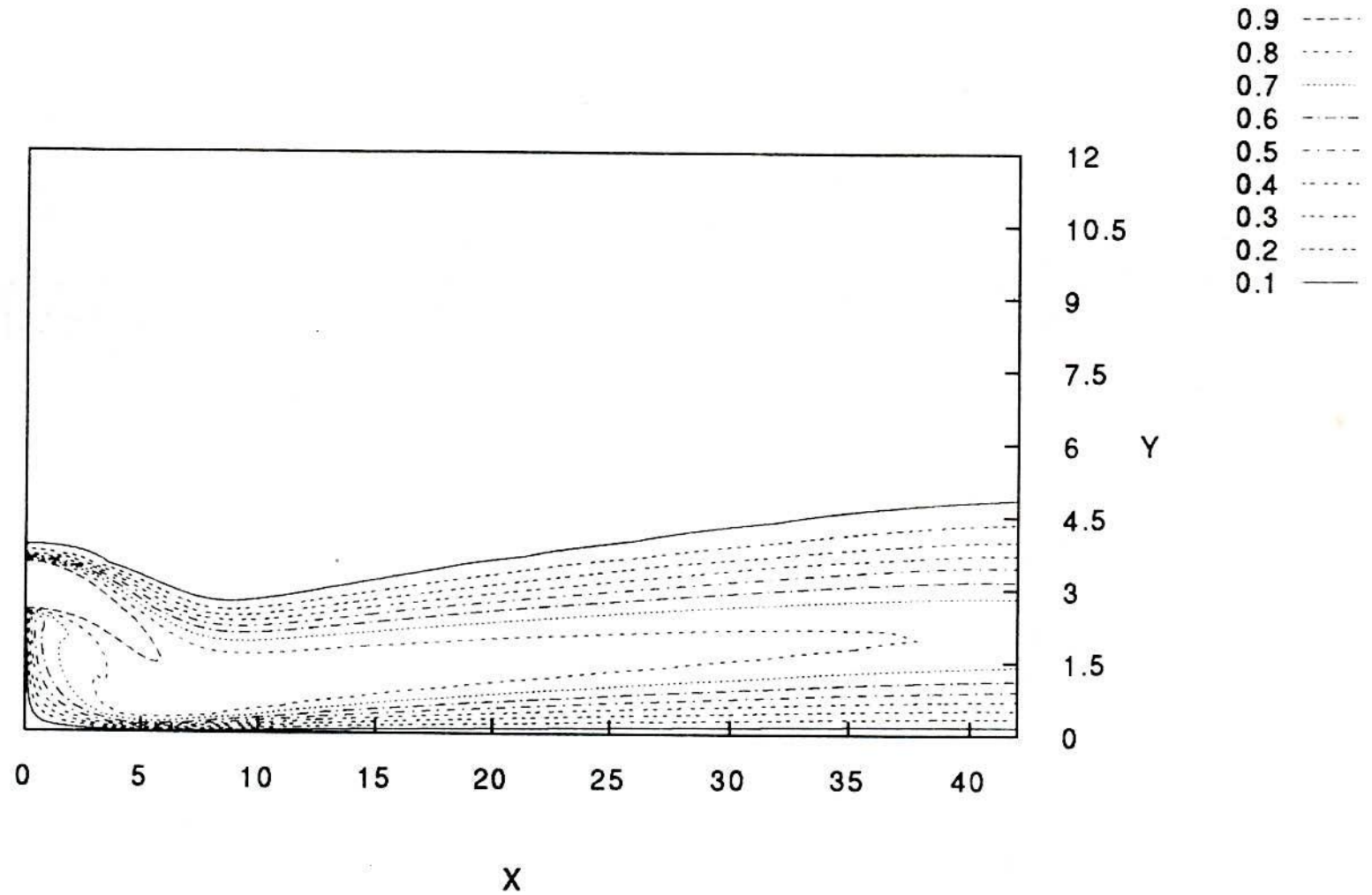
Offset Slot Jet $Re=80$, $O.R.=3$ (Uniform)

Fig.4.5.4: Isotherms for offset slot jet with uniform slot exit velocity profile at $Re=80$, $O.R.=3$, $Pr=4.34$.

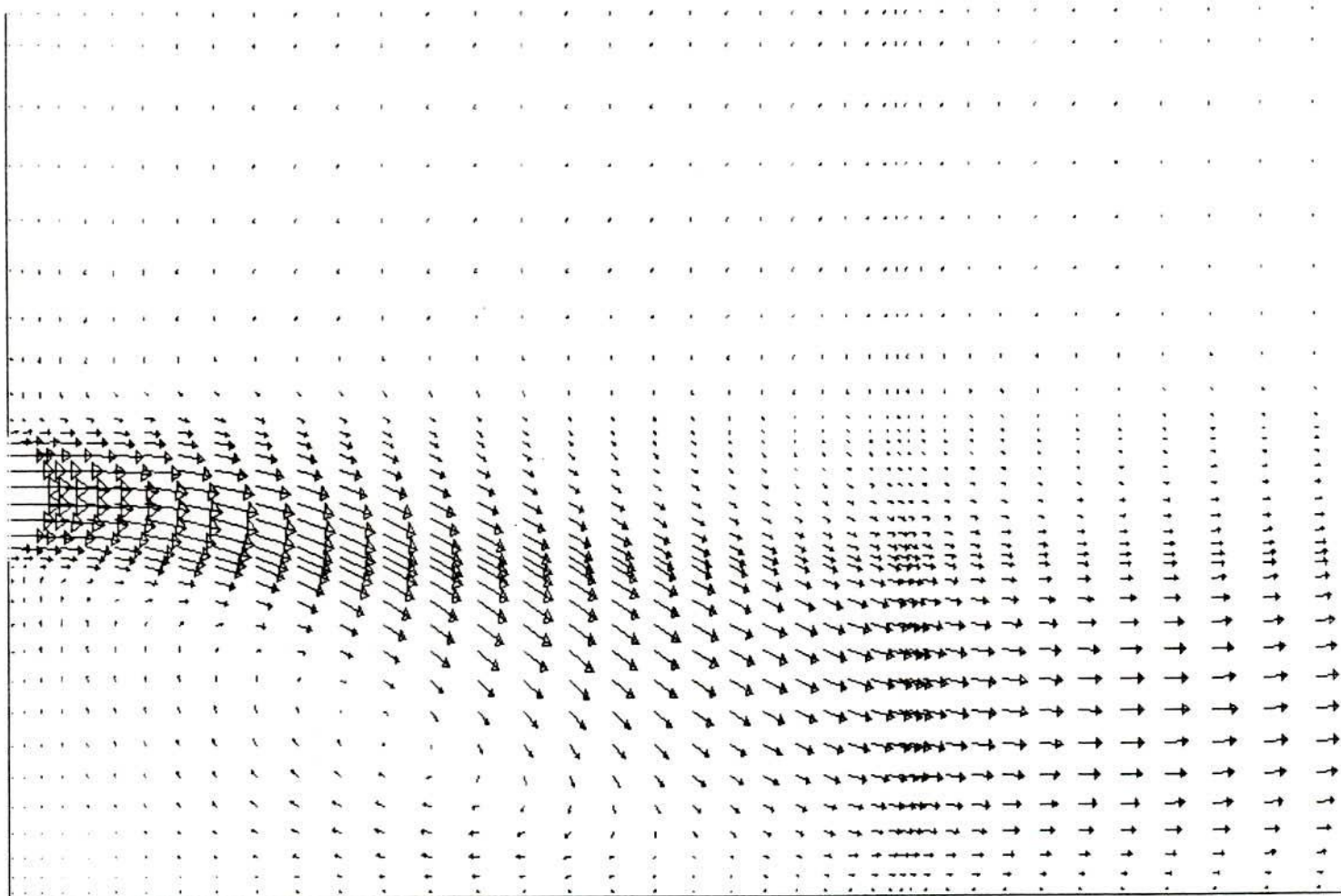


Fig. 4.5.5: Velocity vector plot, O.R.=3 and Re=80

Offset jet with parabolic velocity profile at slot exit.

Stream lines Laminar Offset Jet, O.R.=3 and Re=80 (Parabolic)

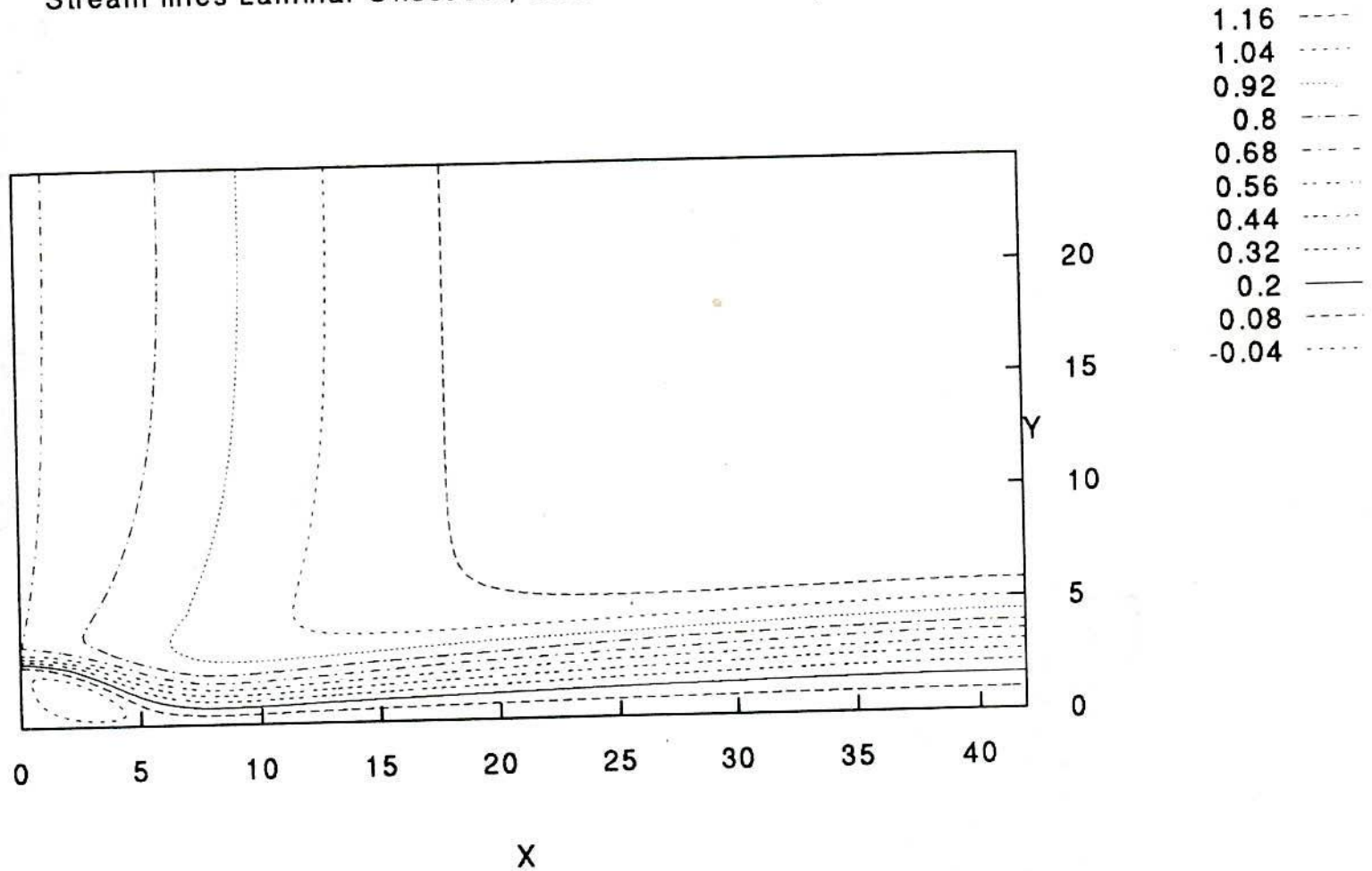


Fig.4.5.6: Streamlines for offset slot jet with parabolic slot exit velocity profile at Re= 80, O.R.=3.



Offset Slot Jet $Re=80$, $O.R.=3$ (Parabolic)

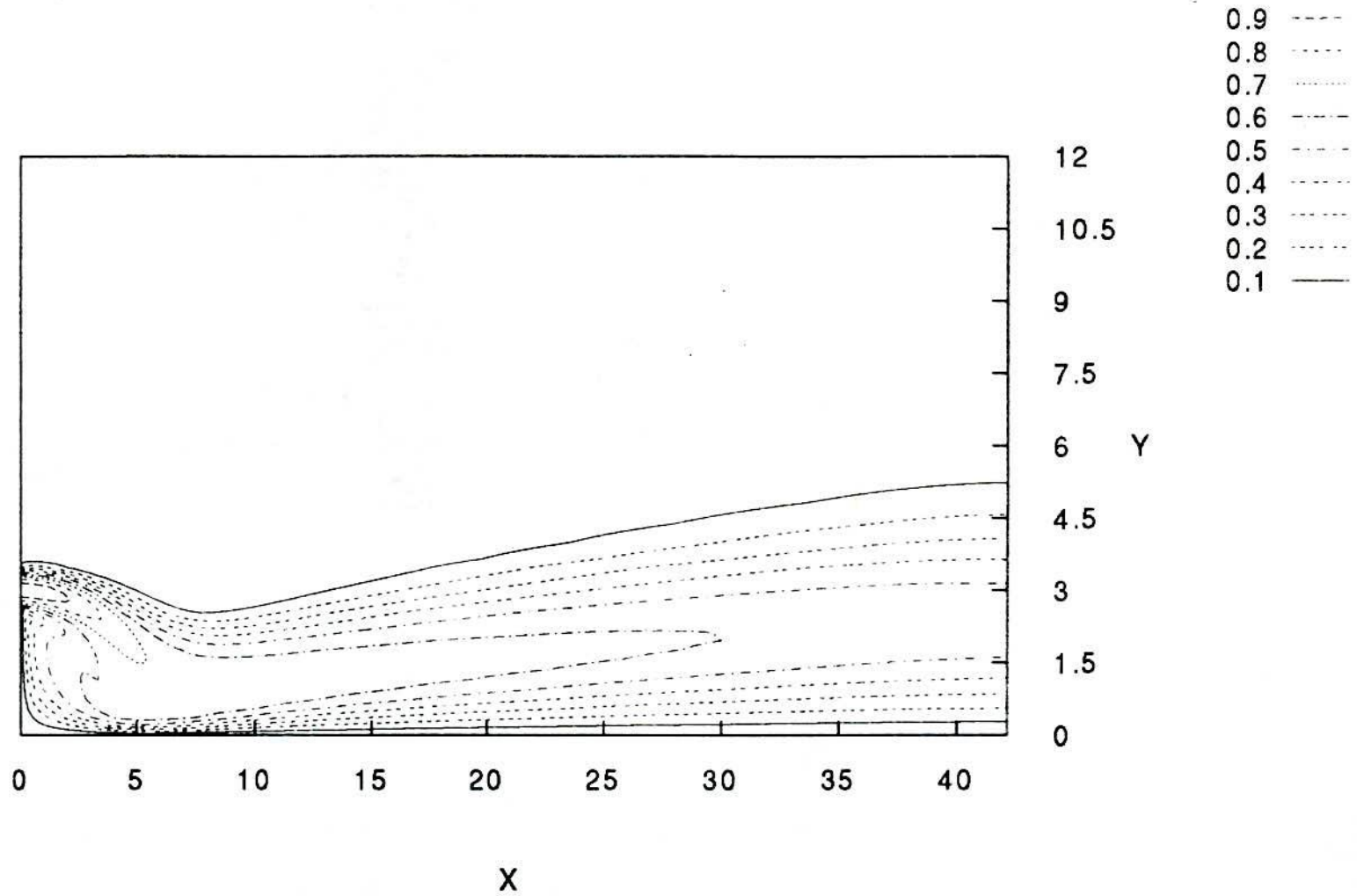


Fig.4.5.7: Isotherms for offset slot jet with parabolic slot exit velocity profile at $Re=80$, $O.R.=3$, $Pr=4.34$.

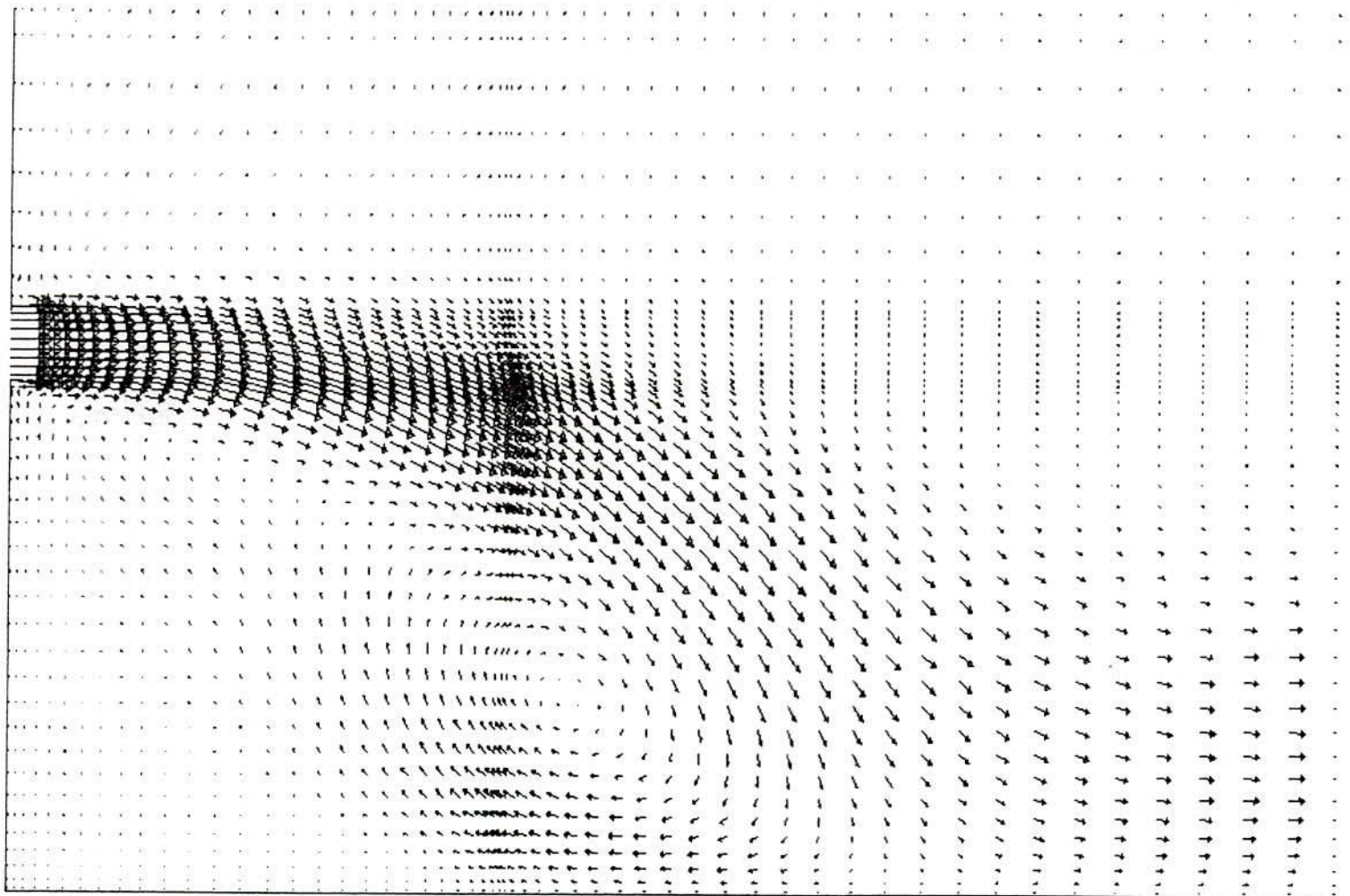


Fig. 4.5.8 : Velocity vector plot, $Re=80$ and Offset Ratio=7
Offset Jet with uniform velocity profile at slot exit.

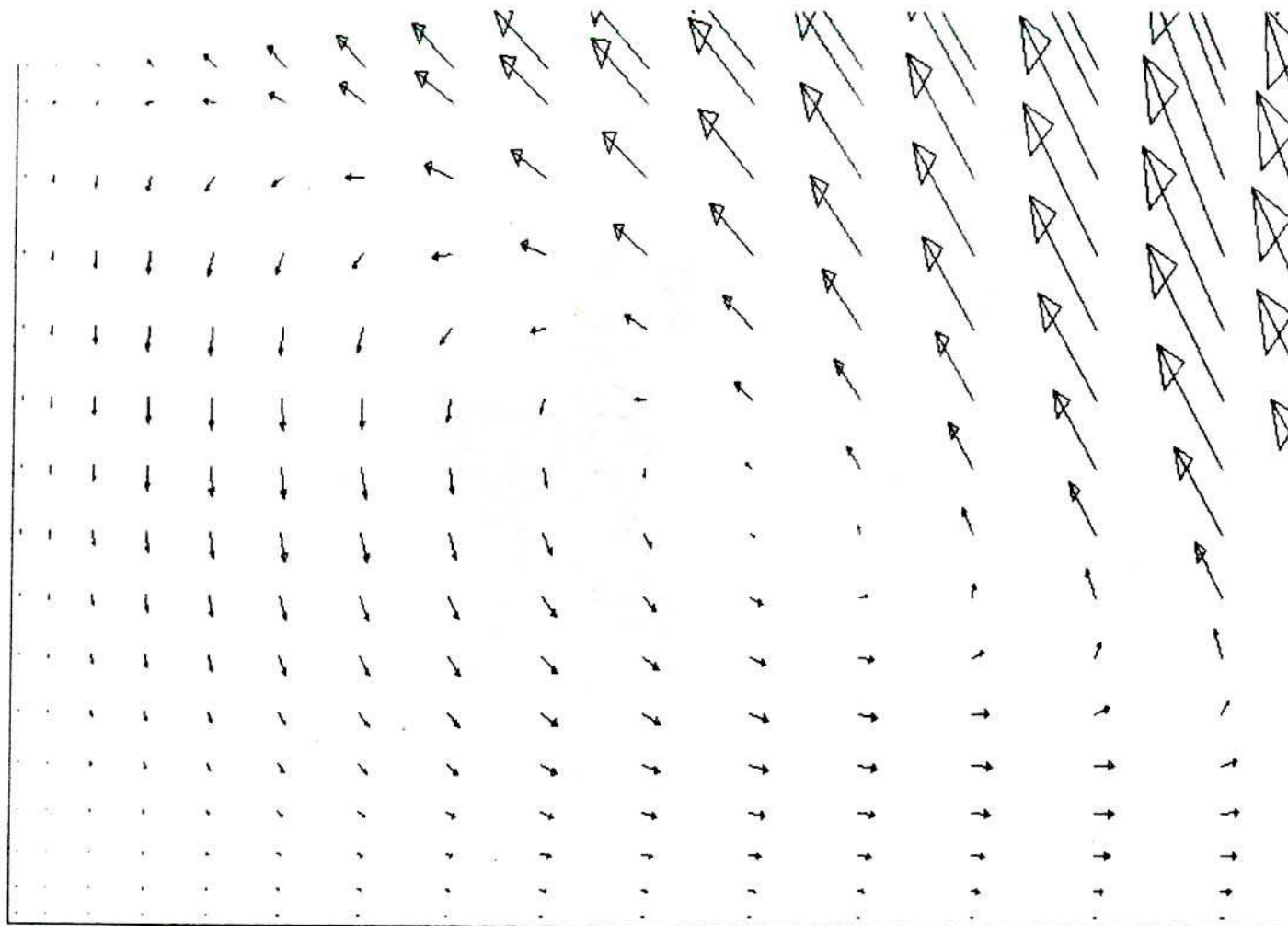
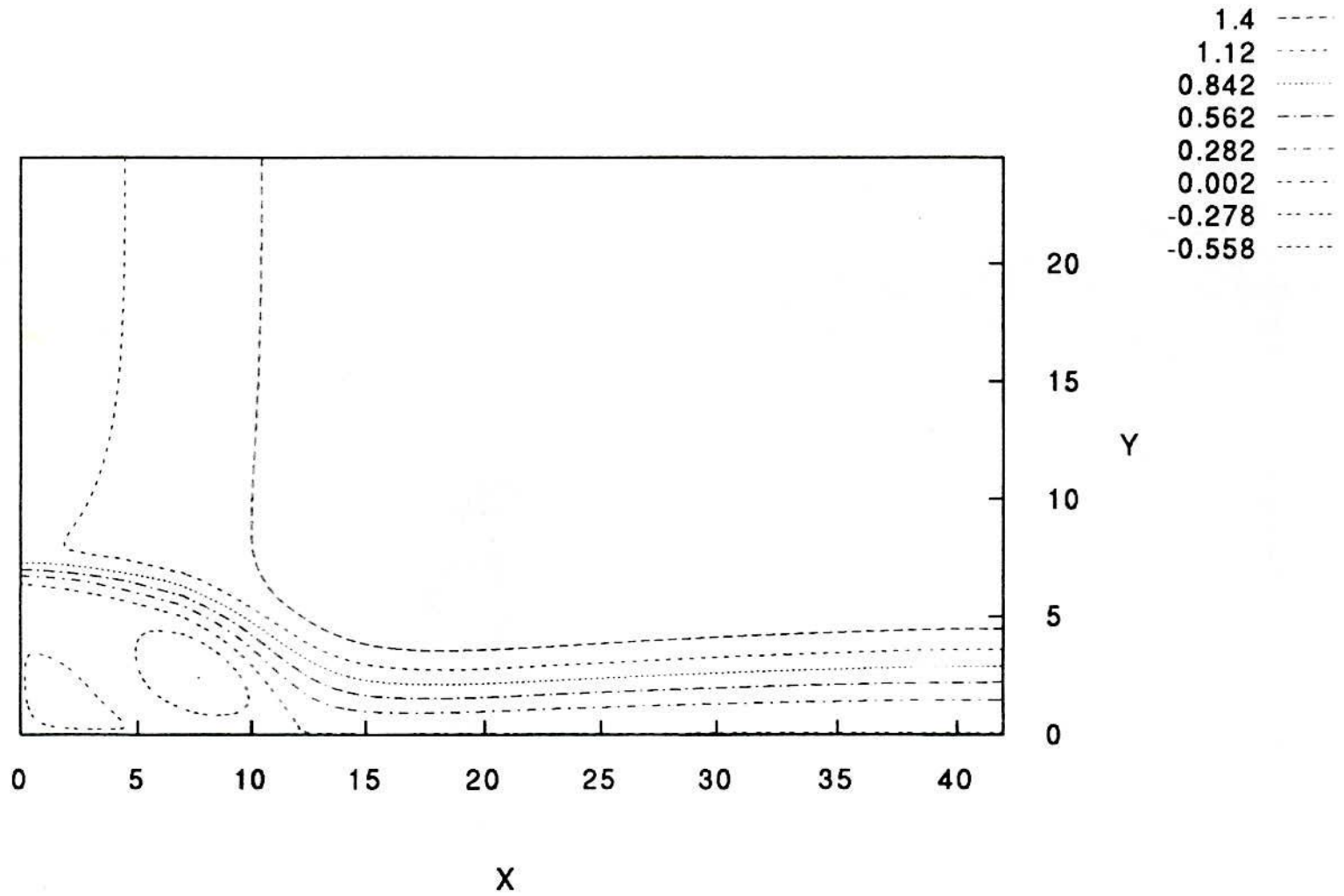


Fig. 4.5.9: Vector plot showing secondary recirculation, $Re=80$ and $O.R.=7$

Offset jet with uniform velocity profile at slot exit.

Stream lines, Offset Jet, O.R.=7 and Re=80 (Uniform)



332

Fig.4.5.10: Streamlines for offset slot jet with uniform slot exit velocity profile at Re= 80, O.R.=7,

Offset Slot Jet $Re=80$, $O.R.=7$ (Uniform)

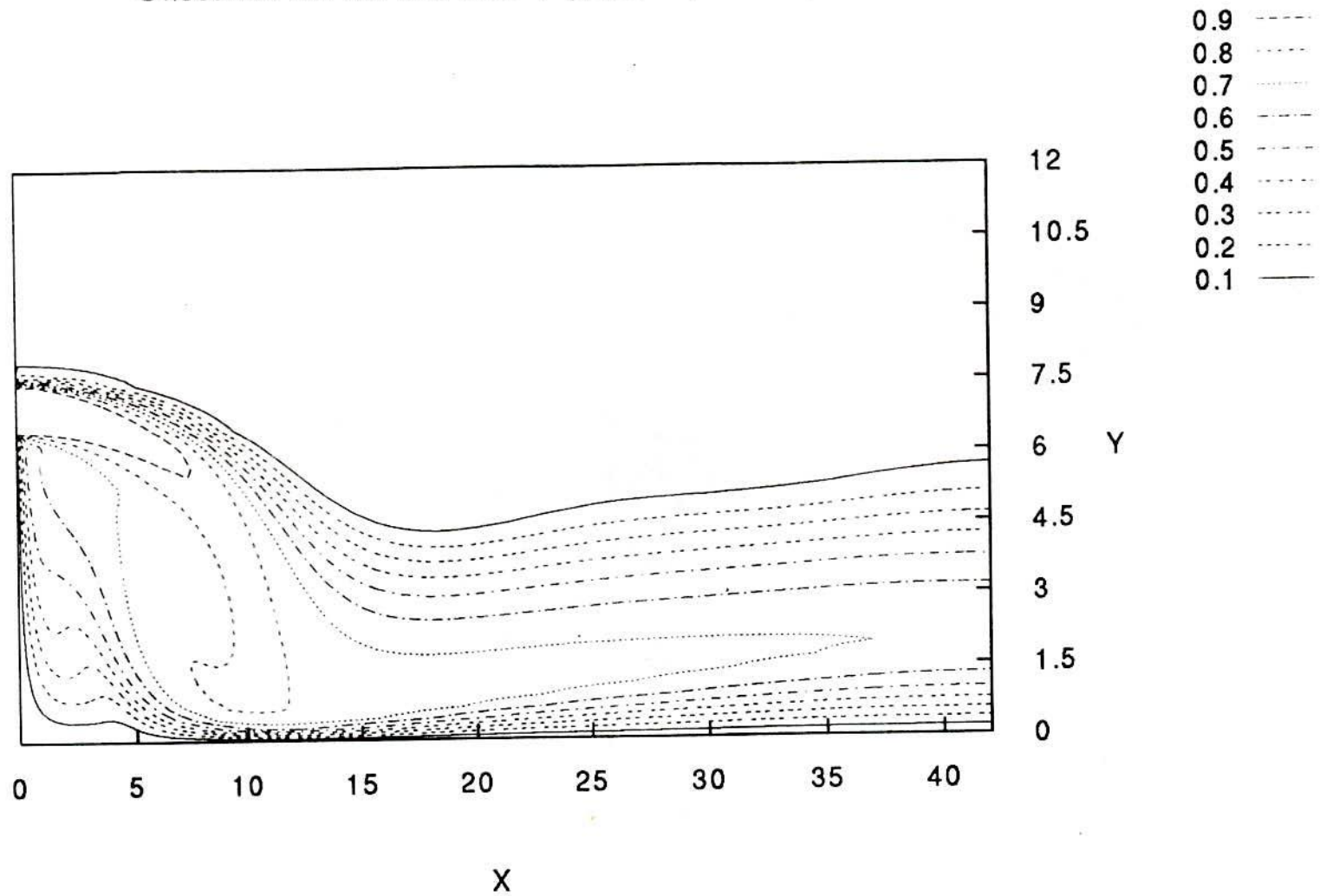


Fig.4.5.11: Isotherms for offset slot jet with uniform slot exit velocity profile at $Re=80$, $O.R.=7$, $Pr=4.34$.

Stream lines, Offset jet, Re= 80 and O.R.= 7 (Parabolic)

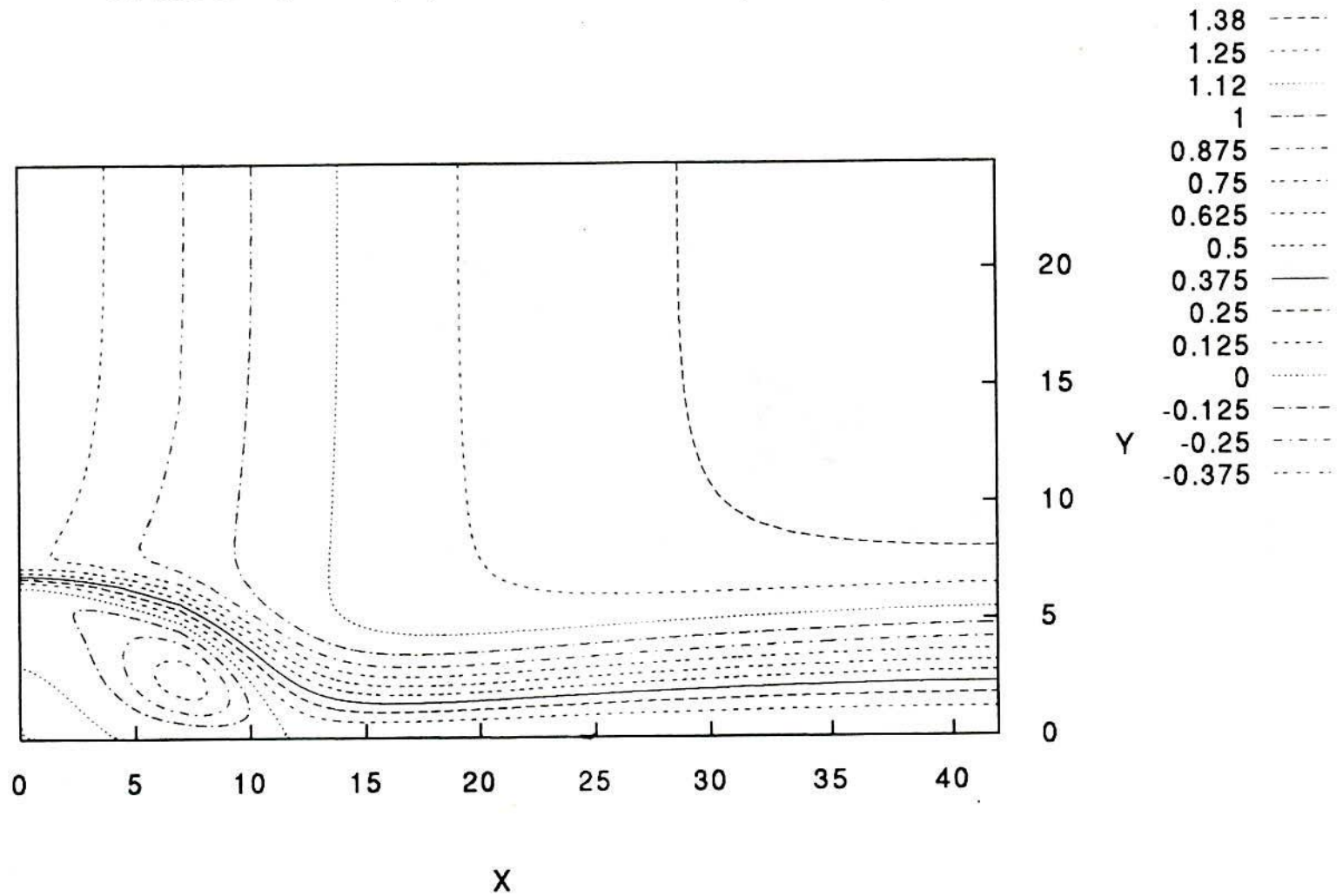
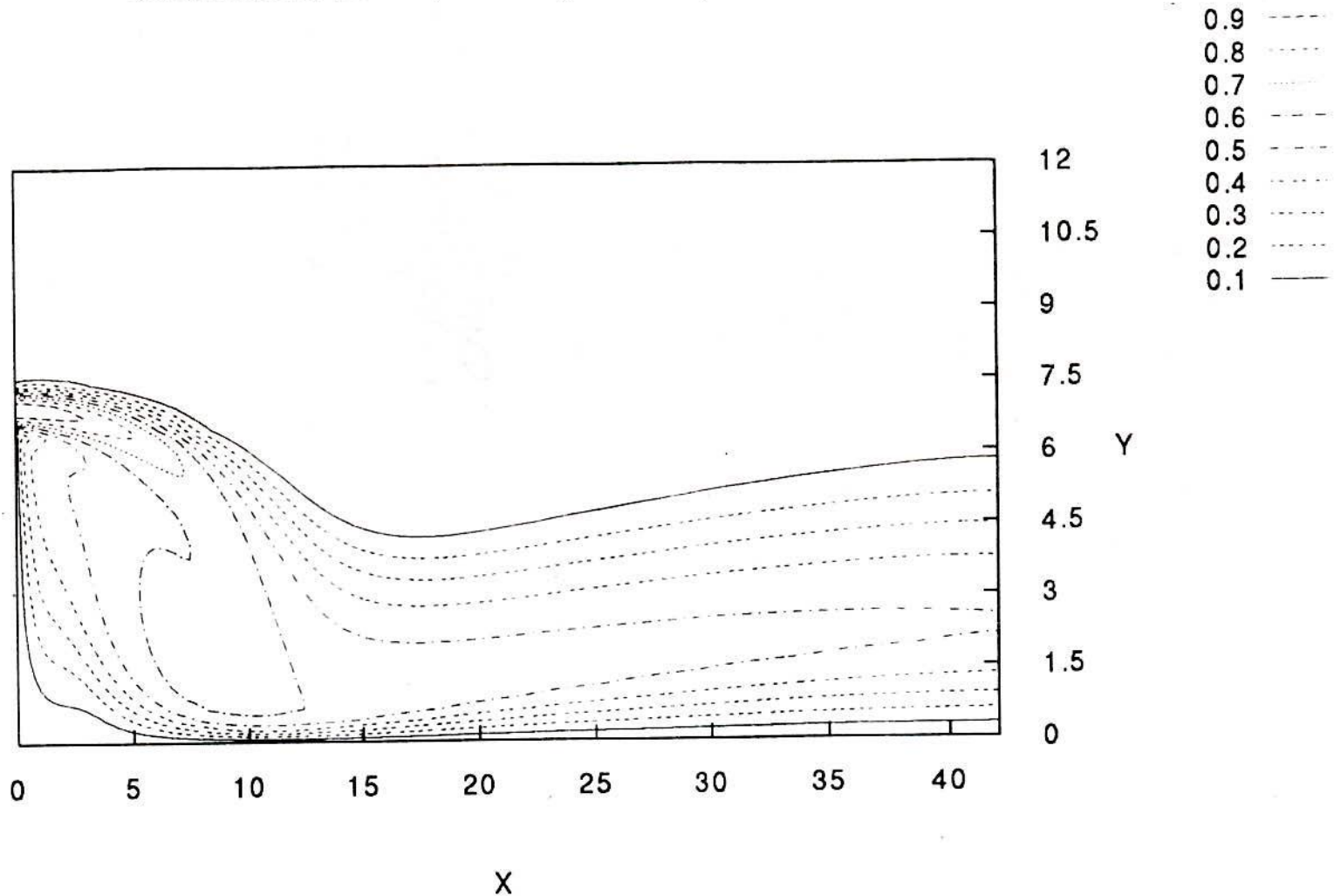


Fig.4.5.12: Streamlines for offset slot jet with parabolic slot exit velocity profile at Re= 80, O.R.=7.

Offset Slot Jet $Re=80$, $O.R.=7$ (Parabolic)



335

Fig.4.5.13: Isotherms for offset slot jet with parabolic slot exit velocity profile at $Re= 80$, $O.R.=7$, $Pr= 4.34$.

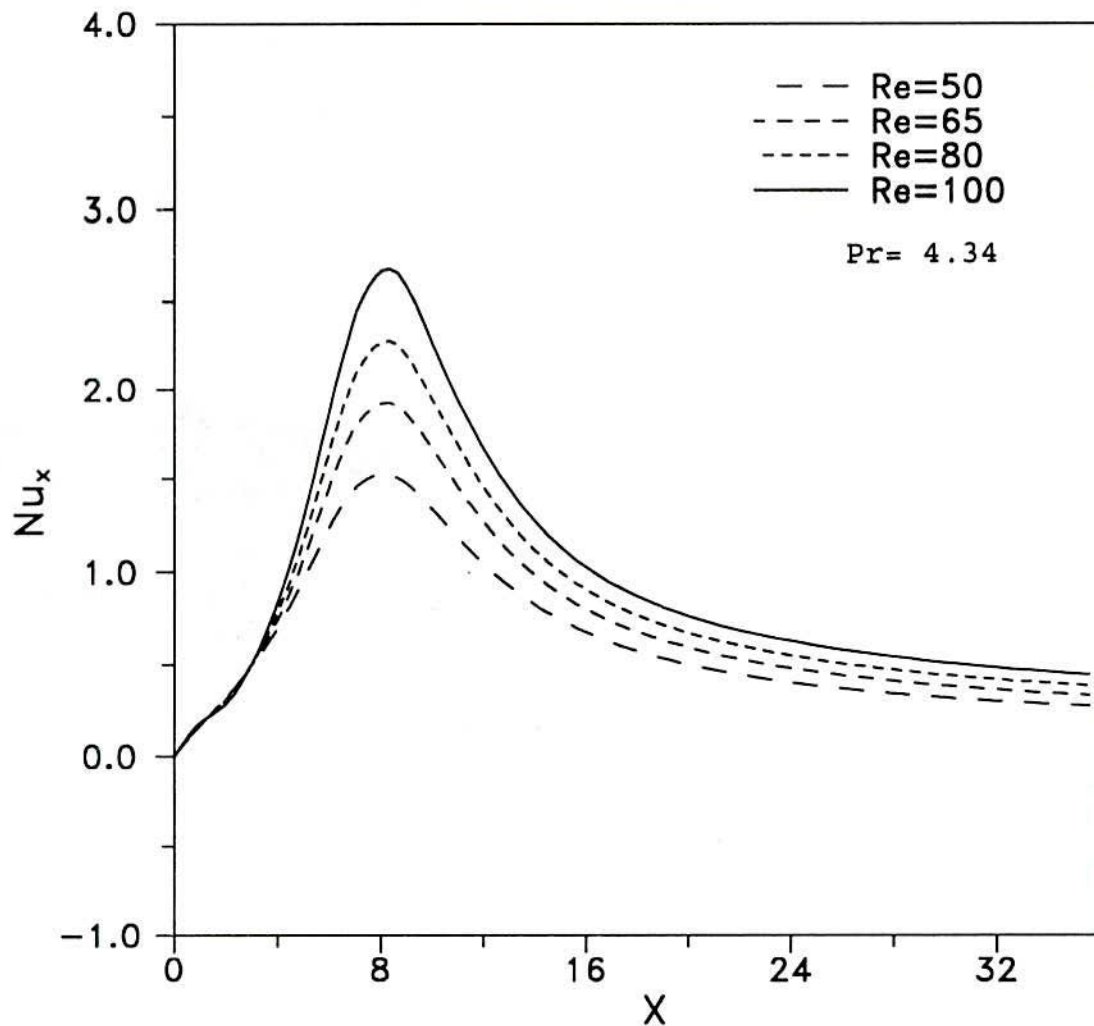


Fig. 4.5.14 : Variation of Local Nusselt number over the offset surface for parabolic velocity profile at offset ratio 5.

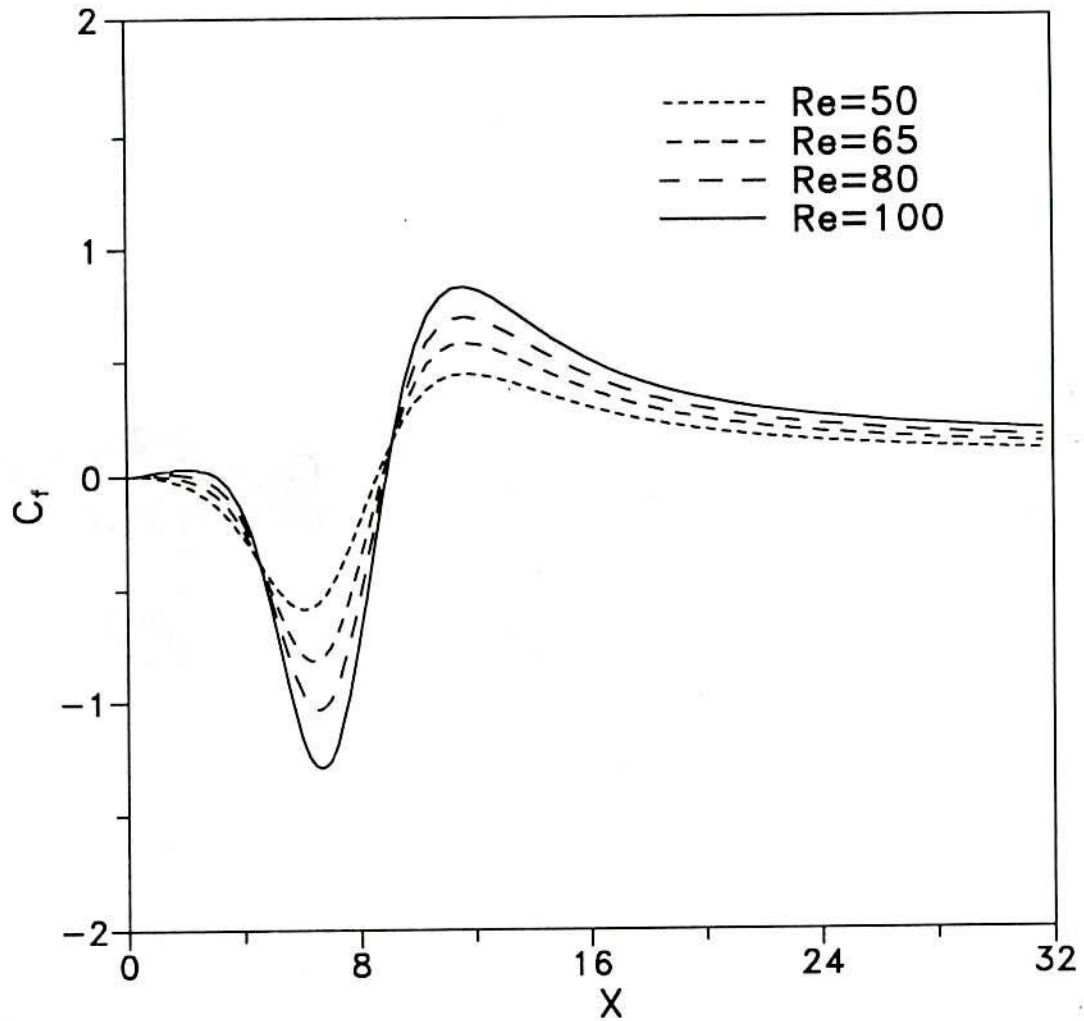


Fig.4.5.15: Variation of local friction factor C_f over the offset surface for parabolic velocity profile at offset ratio=5.

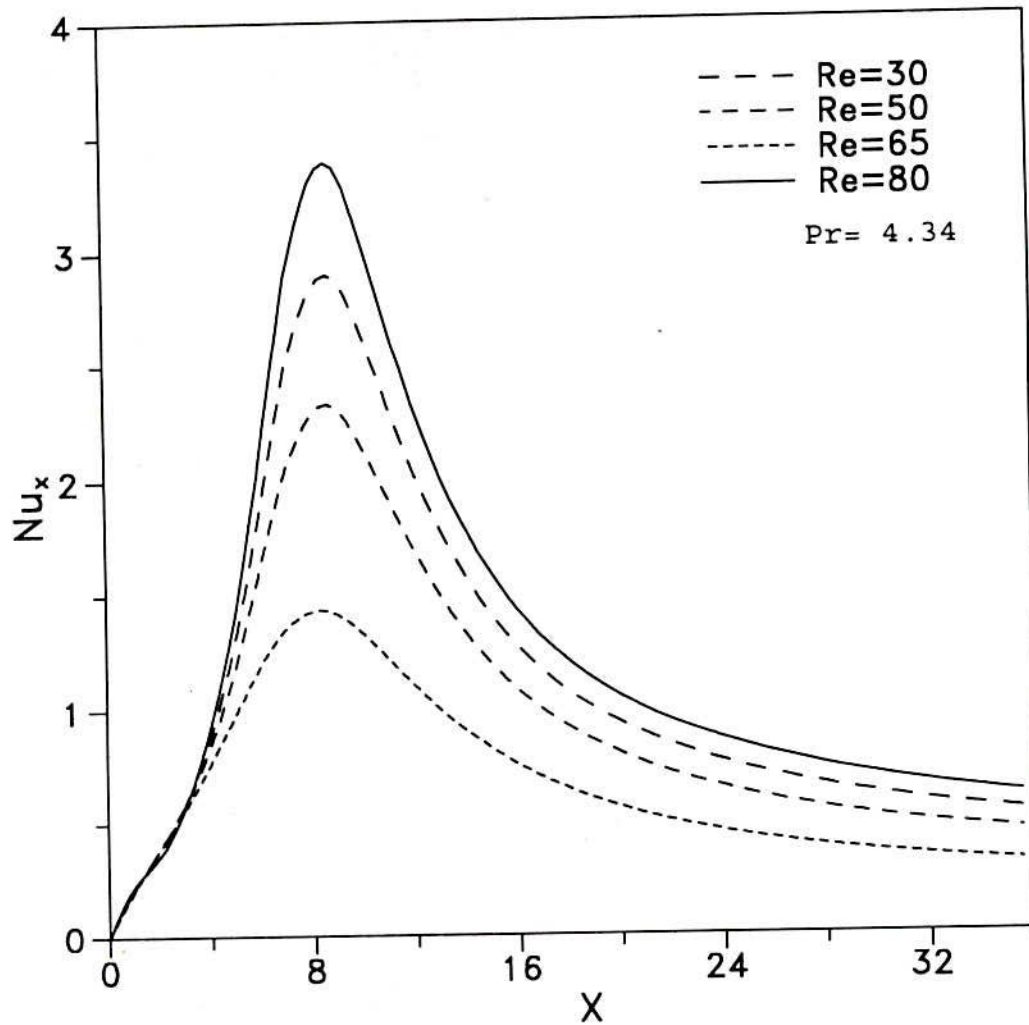


Fig.4.5.16: Variation of local Nusselt number over the offset surface for uniform velocity profile at offset ratio 5.

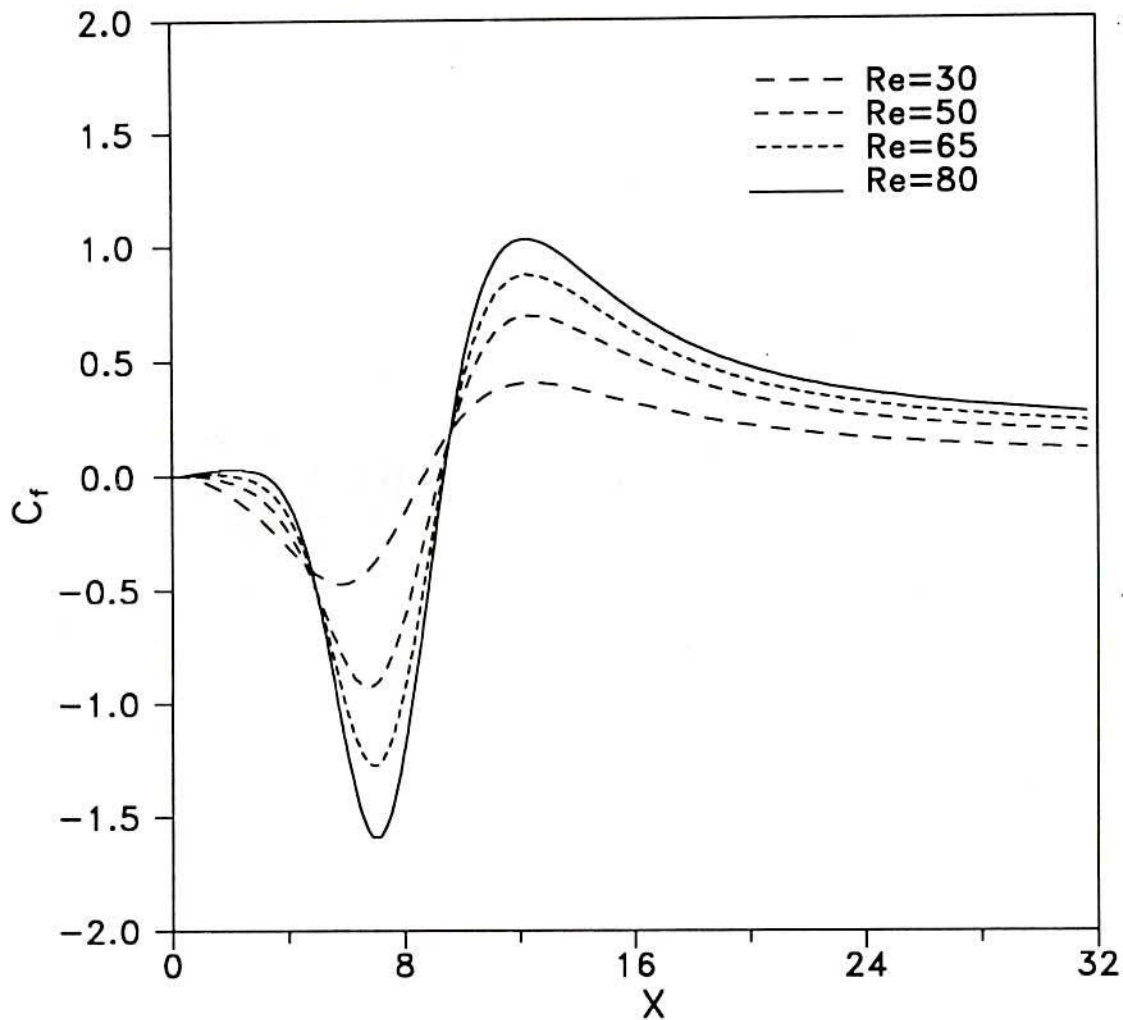


Fig.4.5.17:Variation of local friction factor C_f over the offset surface for uniform velocity profile at offset ratio=5.

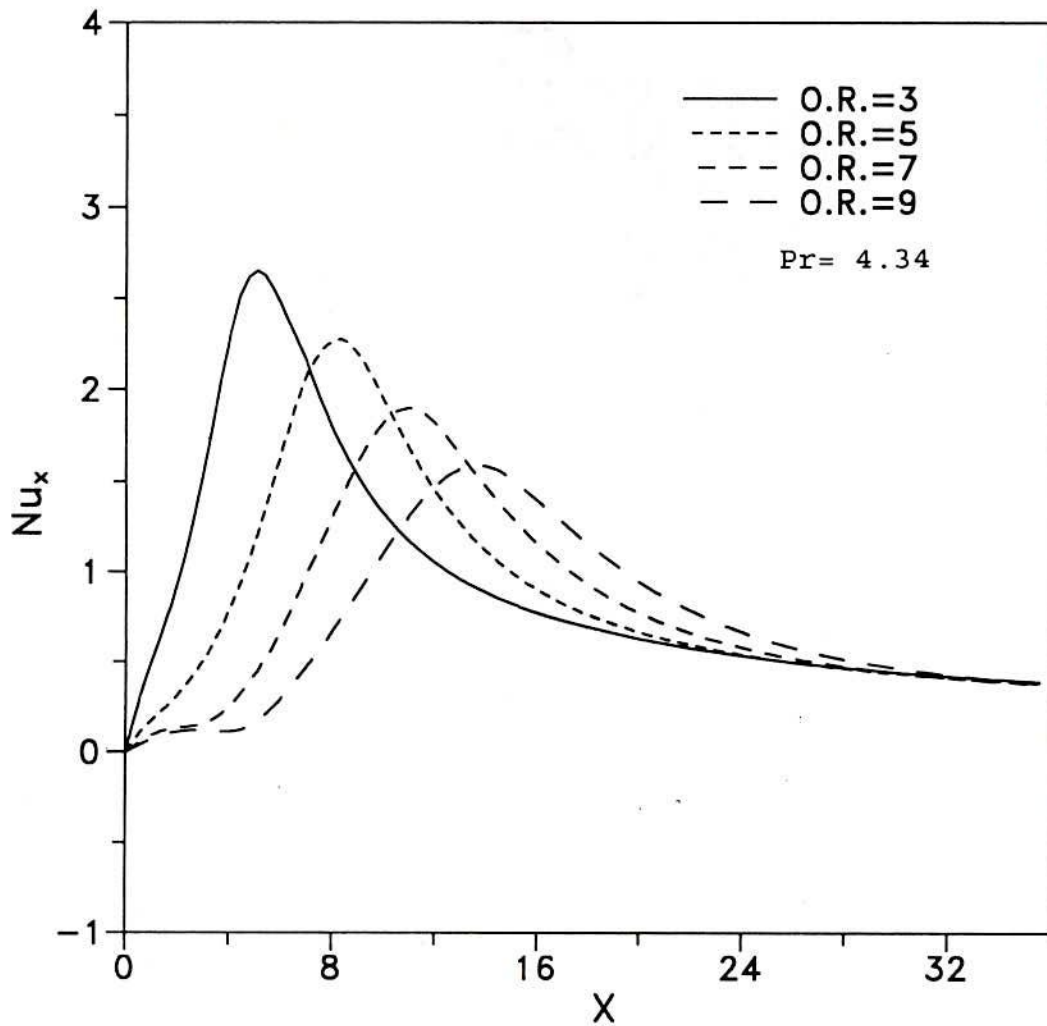


Fig. 4.5.18 : Variation of local Nusselt number over the offset surface for parabolic velocity profile at $Re=80$.

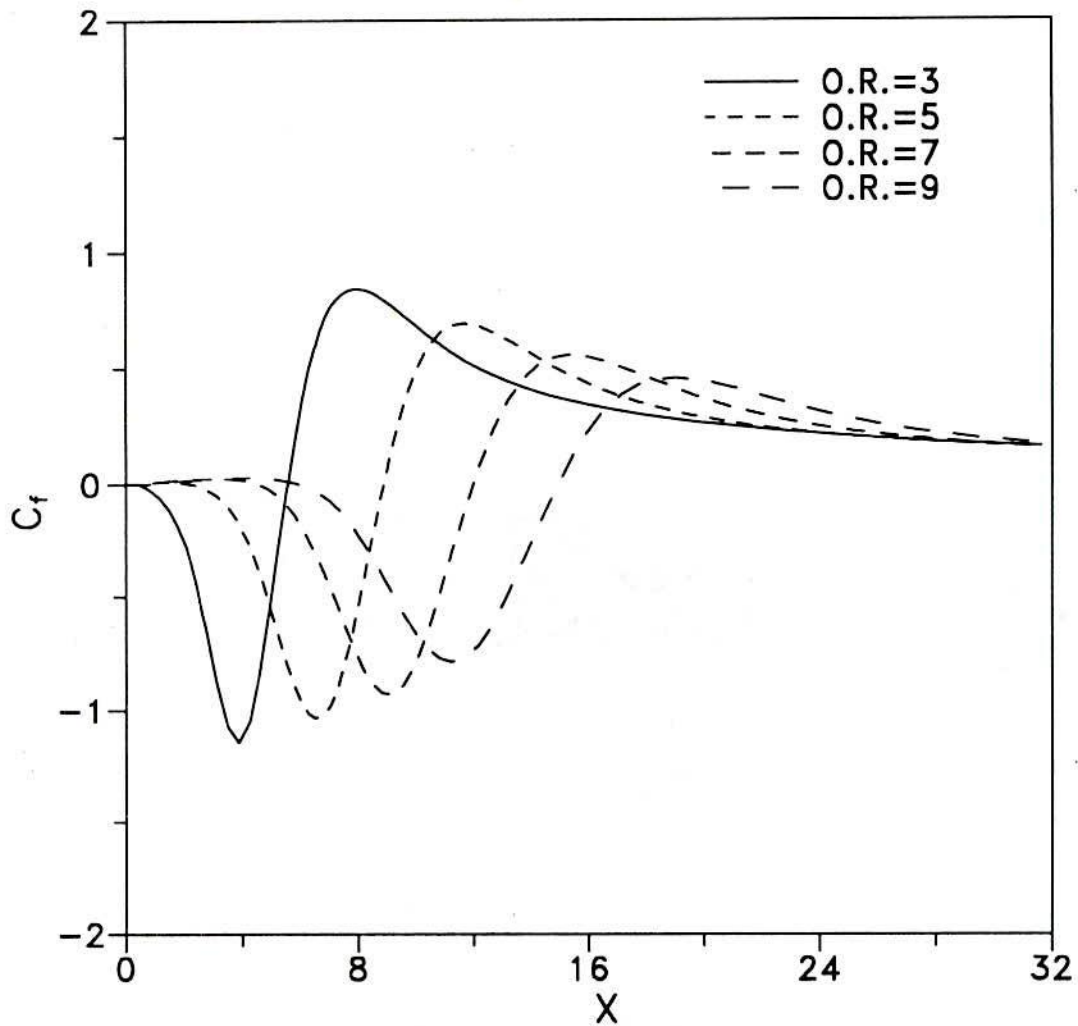


Fig.4.5.19: Variation of local friction factor C_f over the offset surface for parabolic velocity profile at $Re=80$.

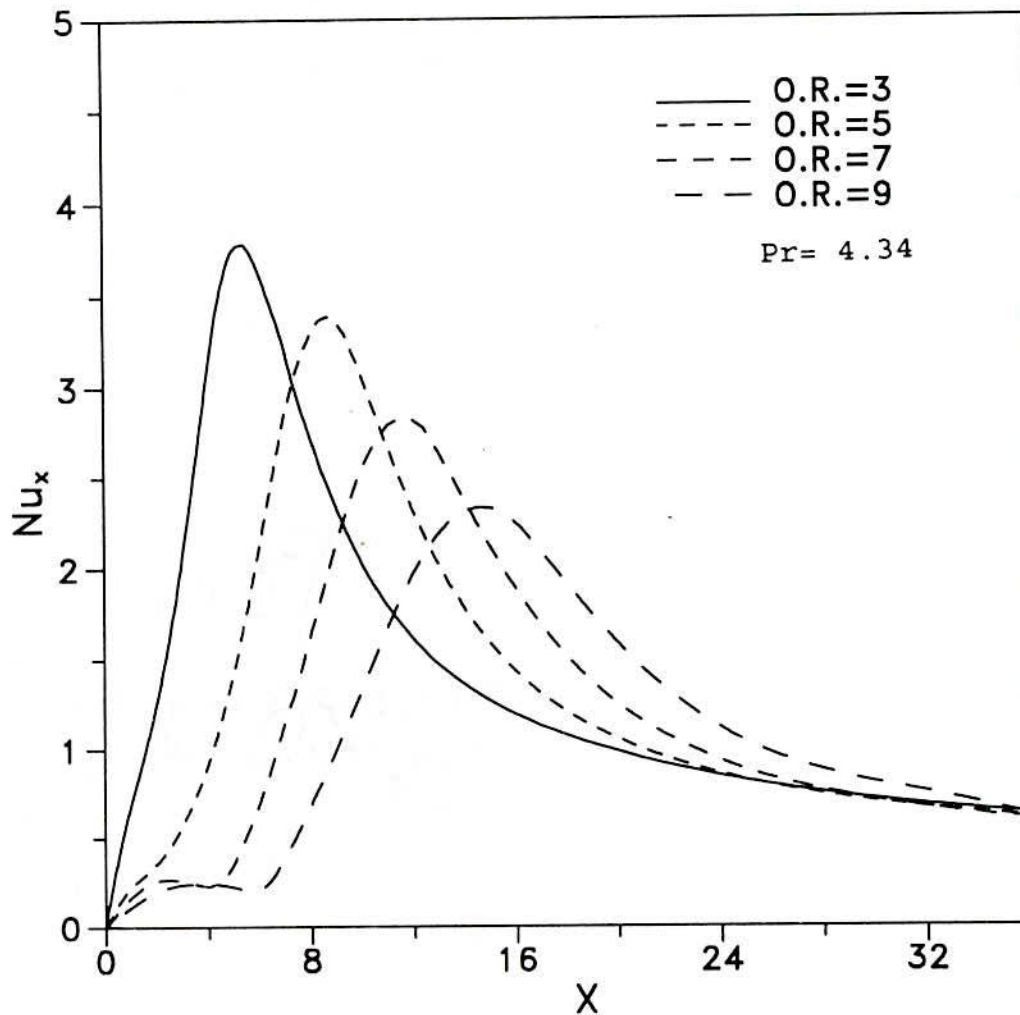


Fig.4.5.20:Variation of local Nusselt number over the offset surface for uniform velocity profile at Re=80.

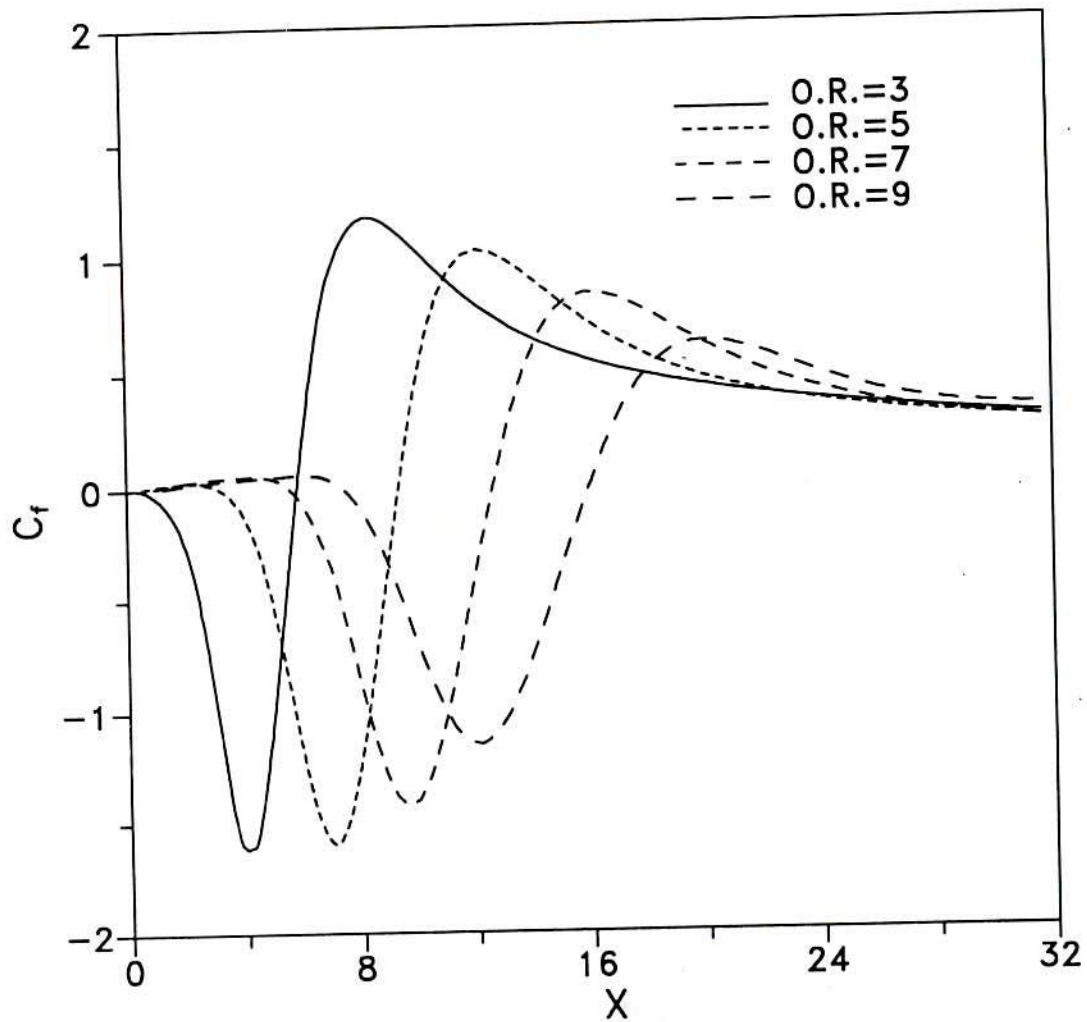


Fig. 4.5.21: Variation of local friction factor C_f over the offset surface for uniform velocity profile at $Re=80$.

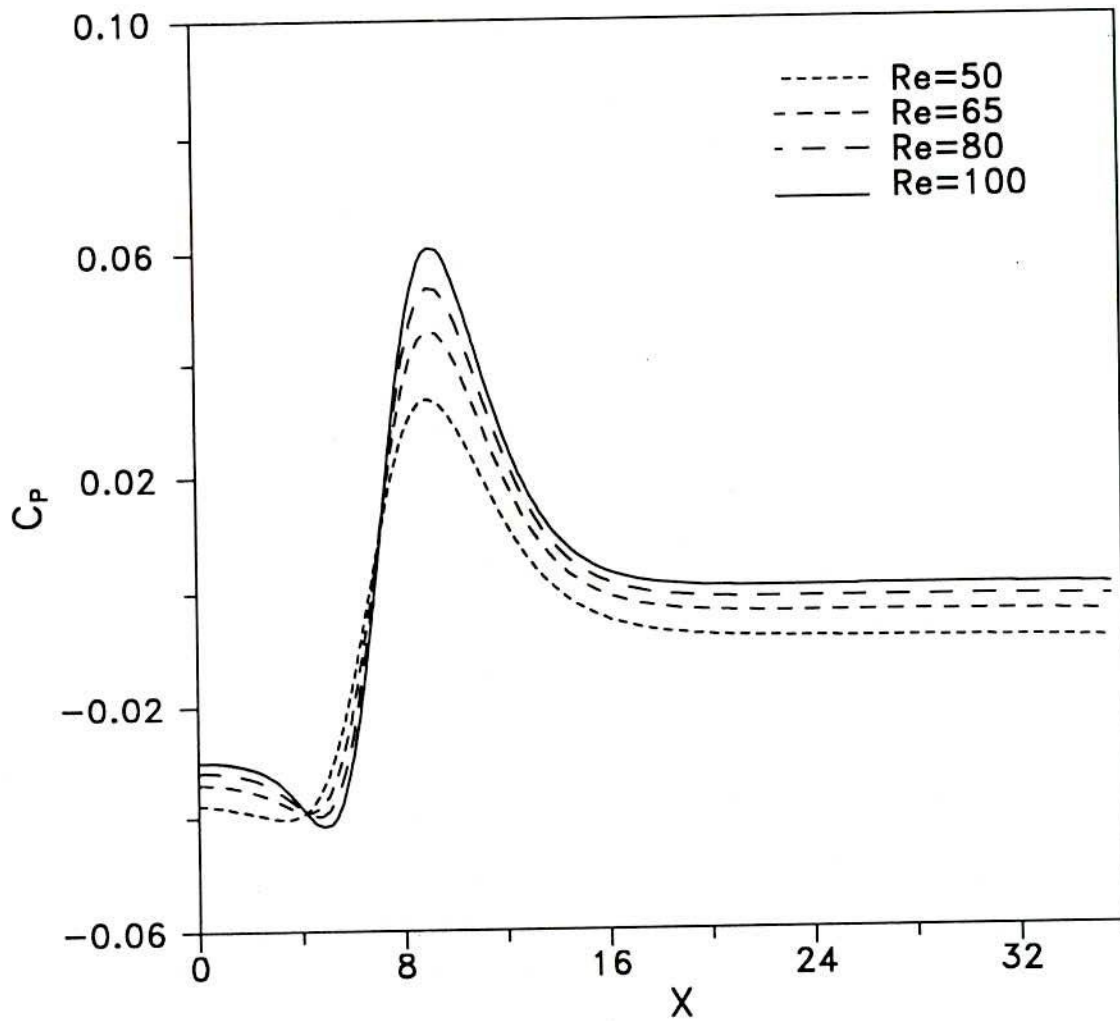


Fig.4.5.22 : Variation of local pressure coefficient over the offset surface for parabolic velocity profile at offset ratio=5.

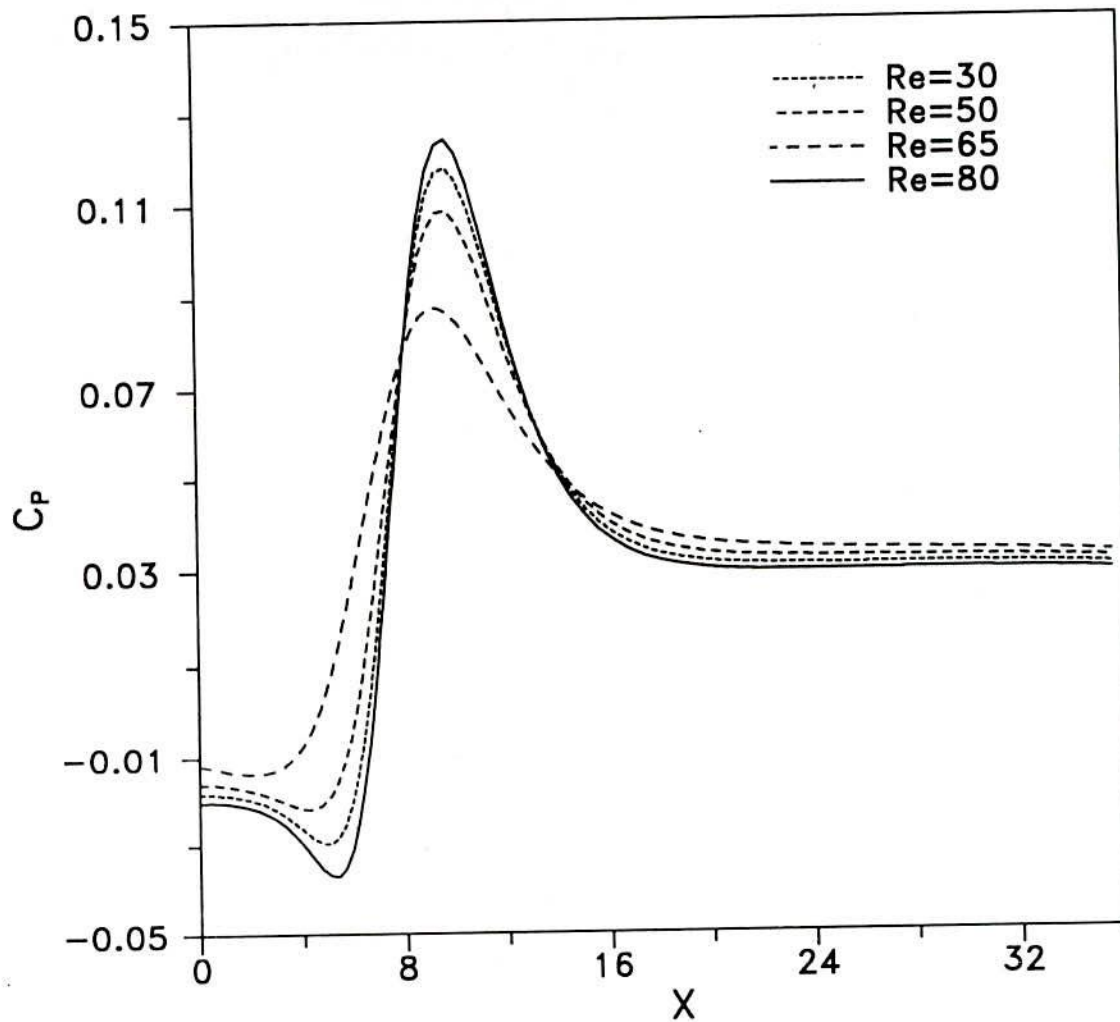


Fig.4.5.23: Variation of local pressure coefficient over the offset surface for uniform velocity profile at offset ratio=5.

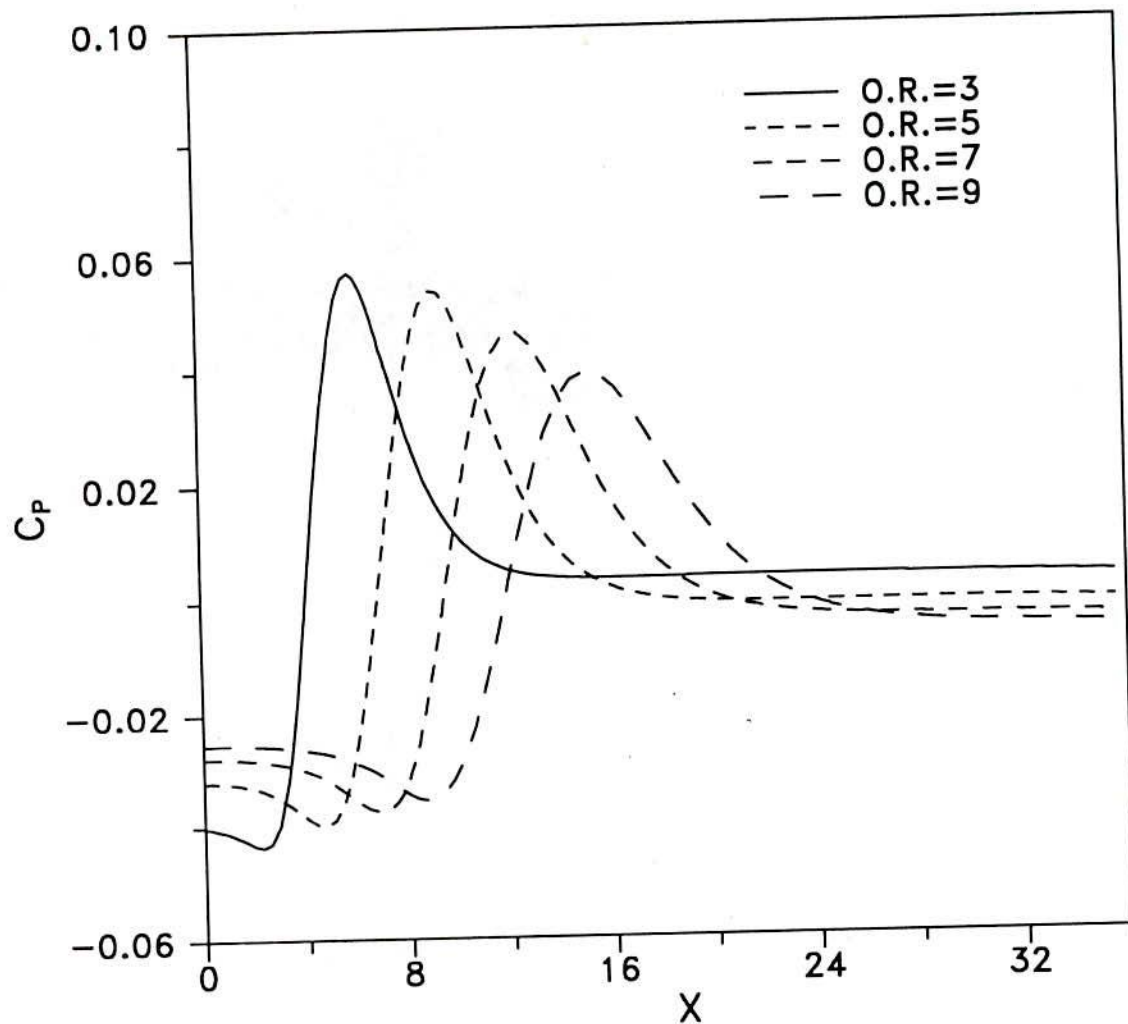


Fig.4.5.24: Variation of local pressure coefficient over the offset surface for parabolic velocity profile at $Re=80$.

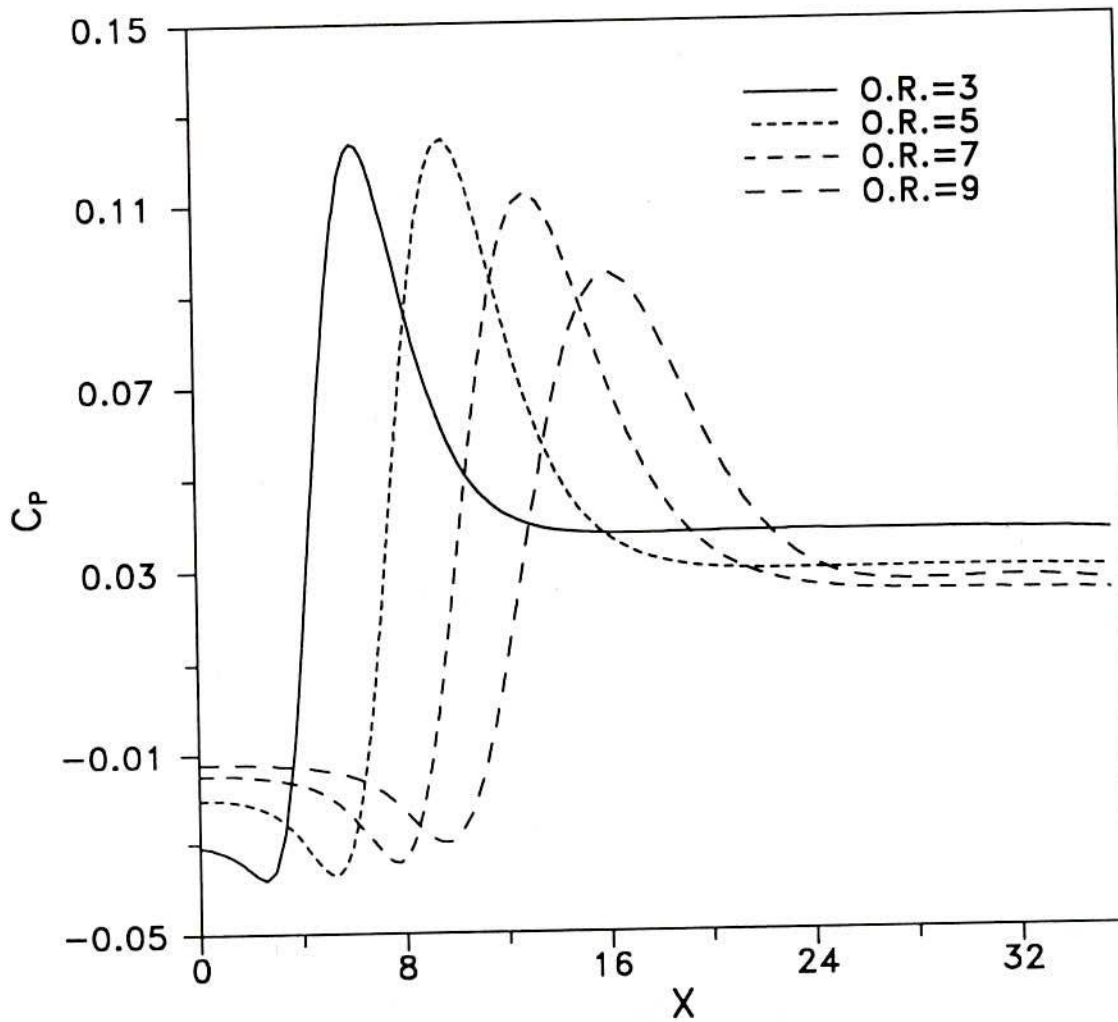


Fig.4.5.25: Variation of local pressure coefficient over the offset surface for uniform velocity profile at $Re=80$.

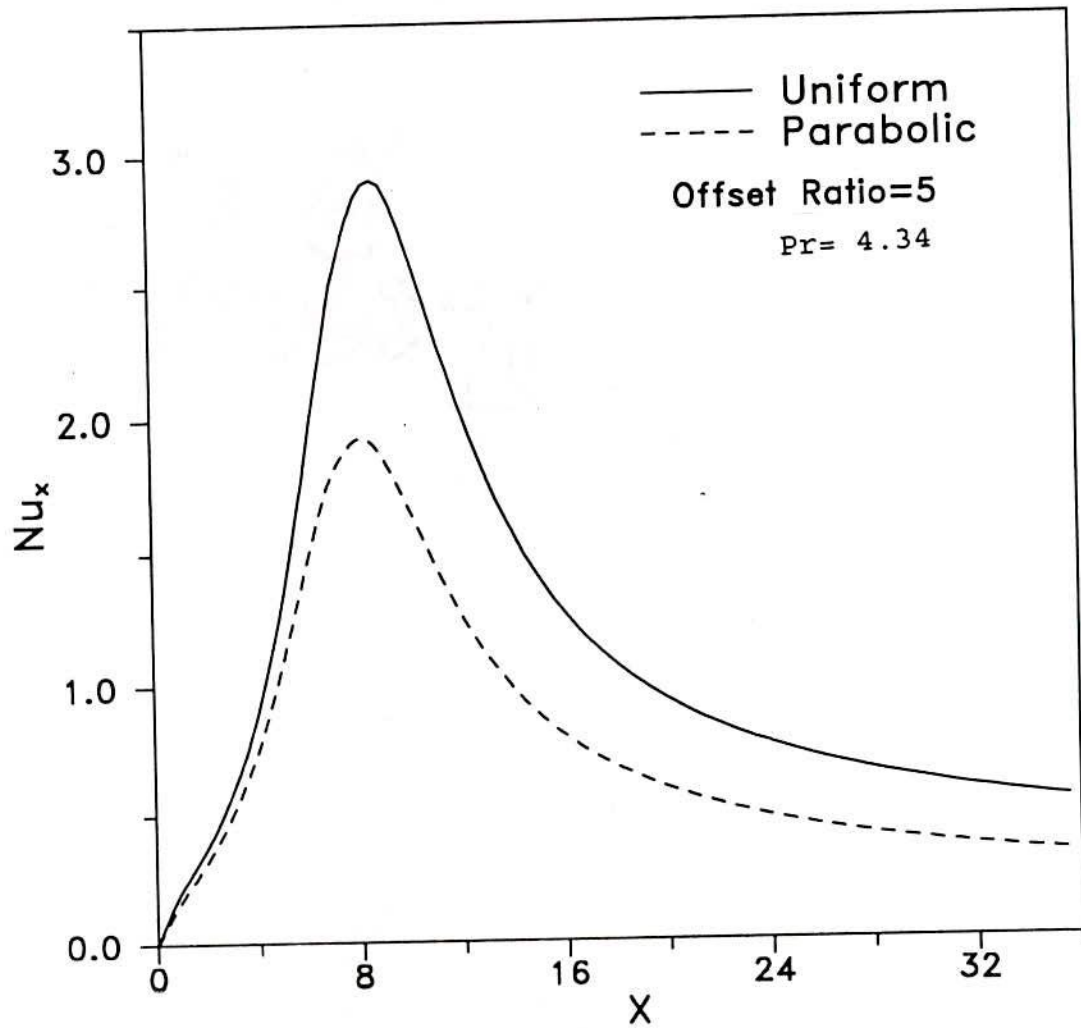


Fig.4.5.26: Variation of local Nusselt number over the offset surface for parabolic and uniform velocity profiles at $Re=65$.

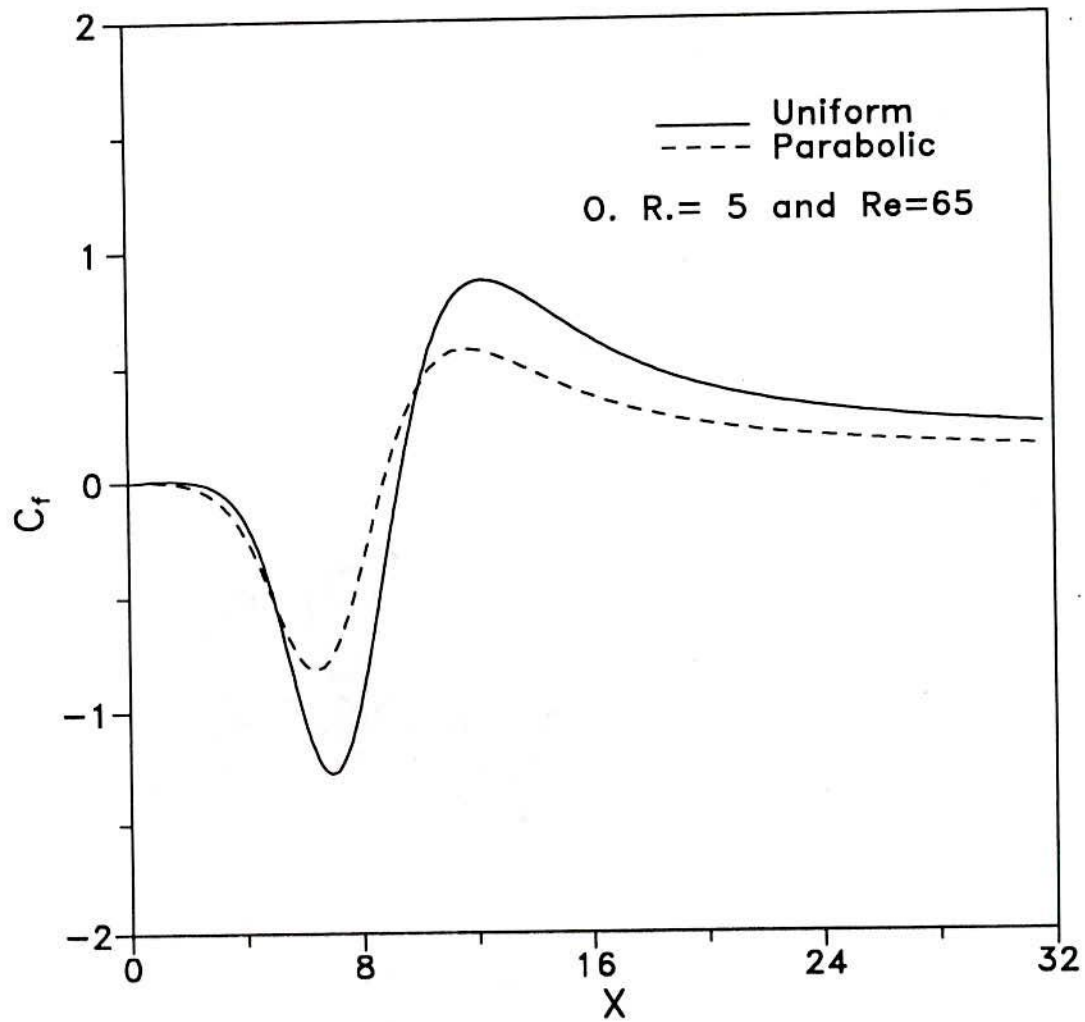


Fig.4.5.27: Variation of local friction factor C_f over the offset surface for parabolic and uniform velocity profiles.

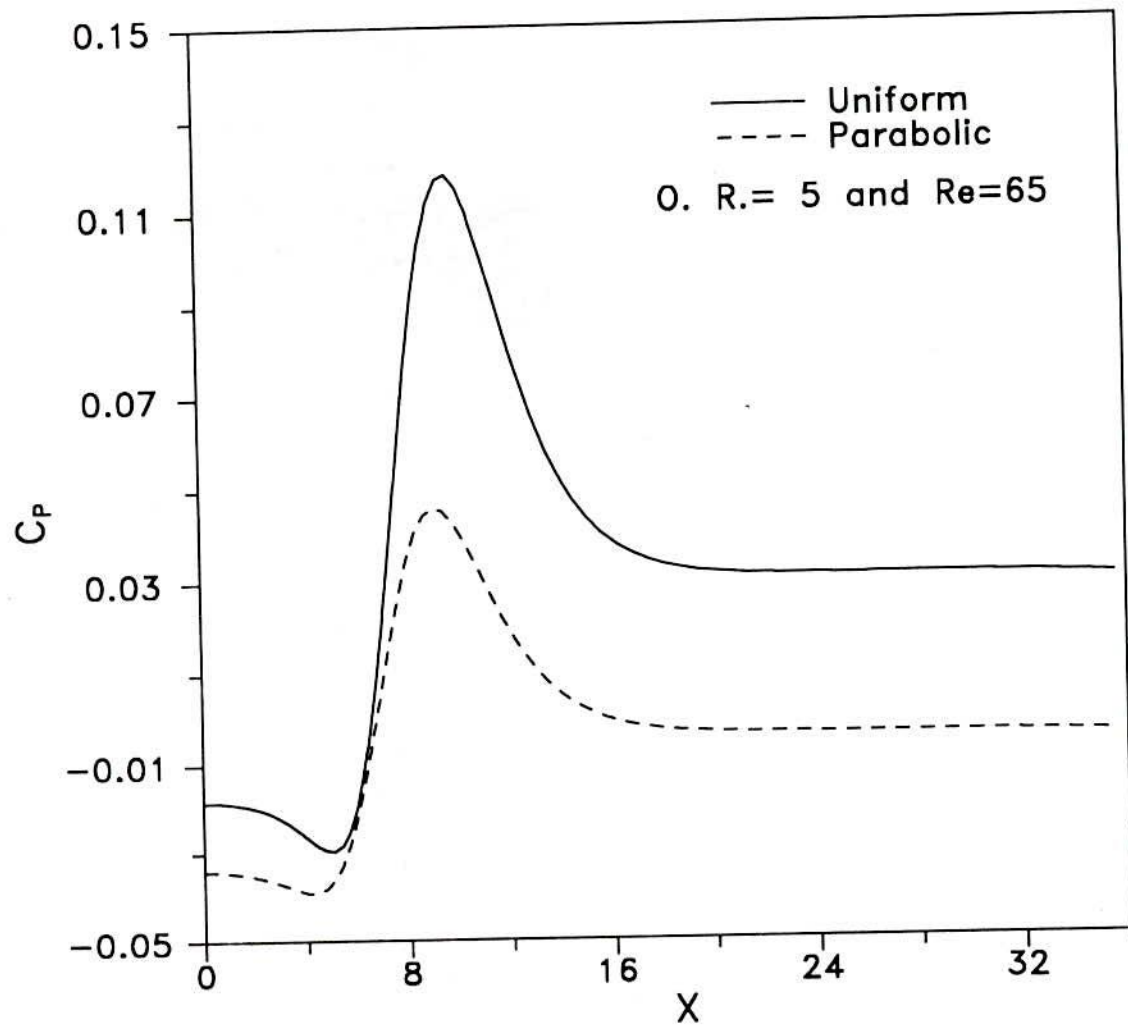


Fig.4.5.28: Variation of pressure coefficient C_p over the offset surface for parabolic and uniform velocity profiles.

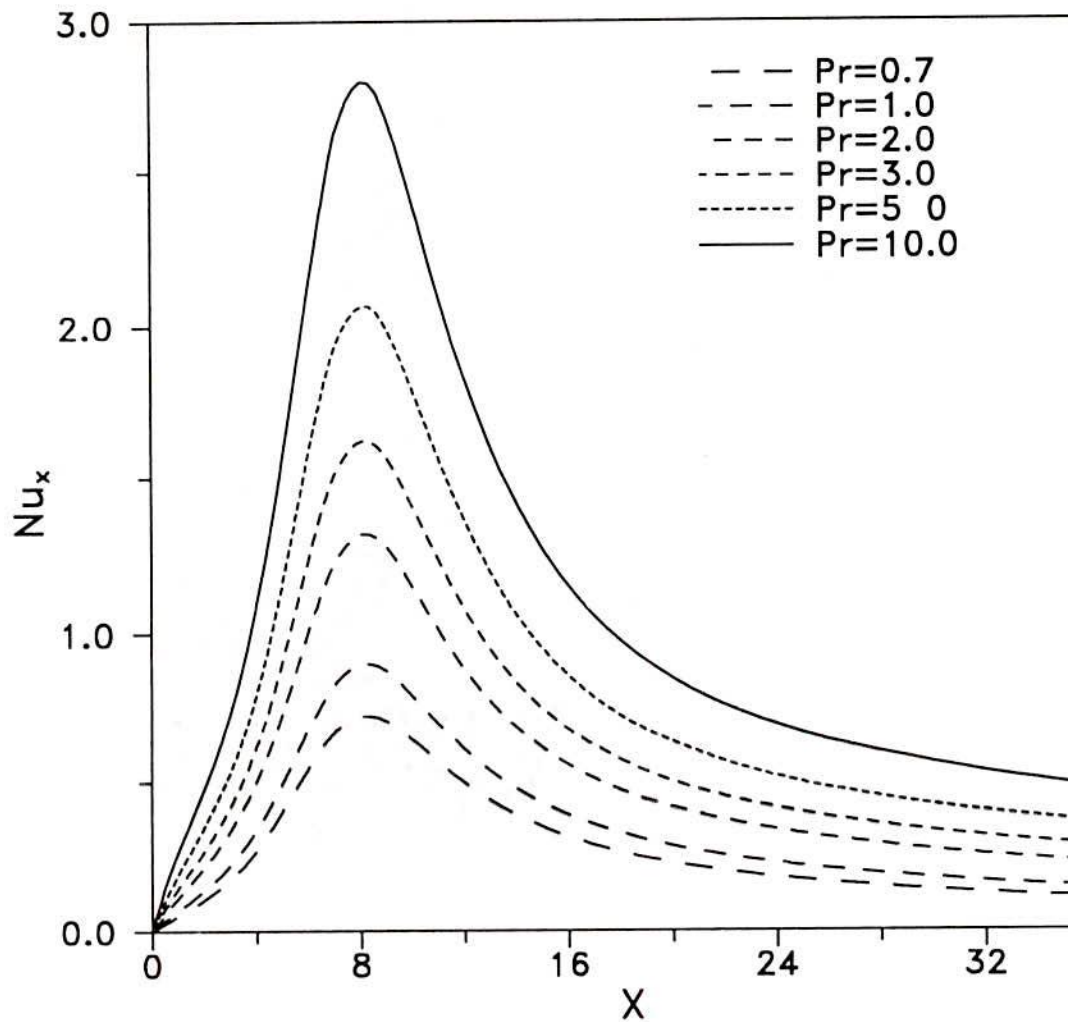


Fig. 4.5.29 : Variation of local Nusselt number over the offset surface for offset ratio=5 and $Re=80$ with parabolic velocity profile.

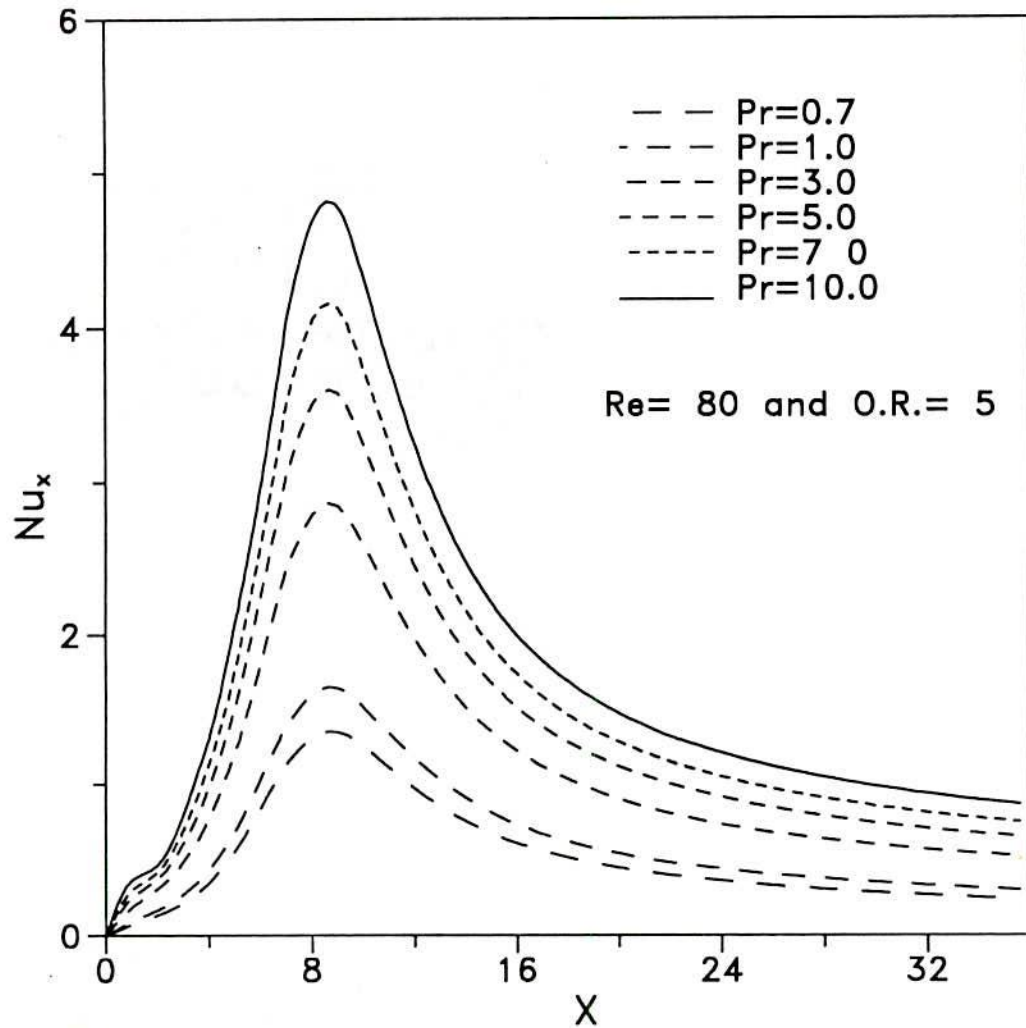


Fig.4.5.30: Variation of local Nusselt number over the offset surface with uniform slot exit velocity.

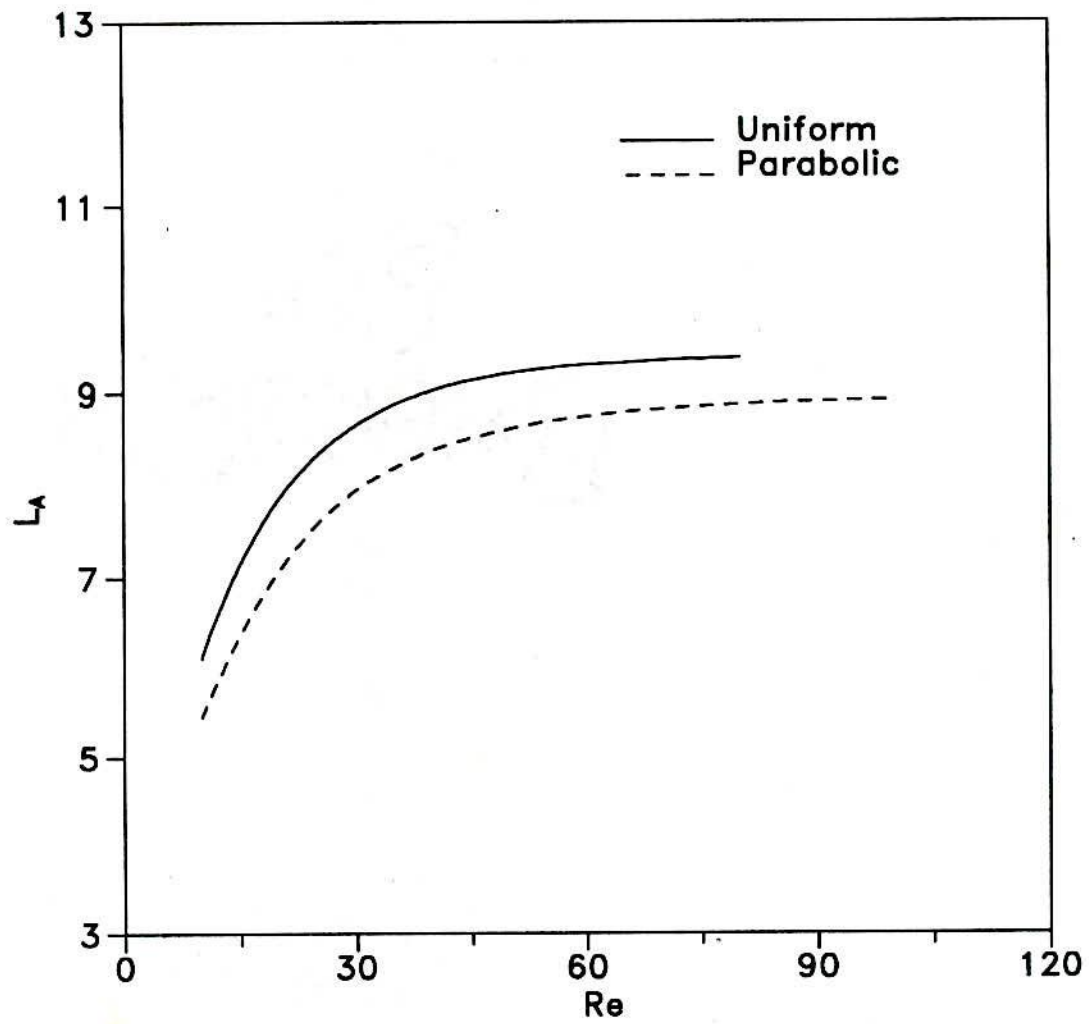


Fig.4.5.31: Variation of reattachment length with Re at offset ratio=5.

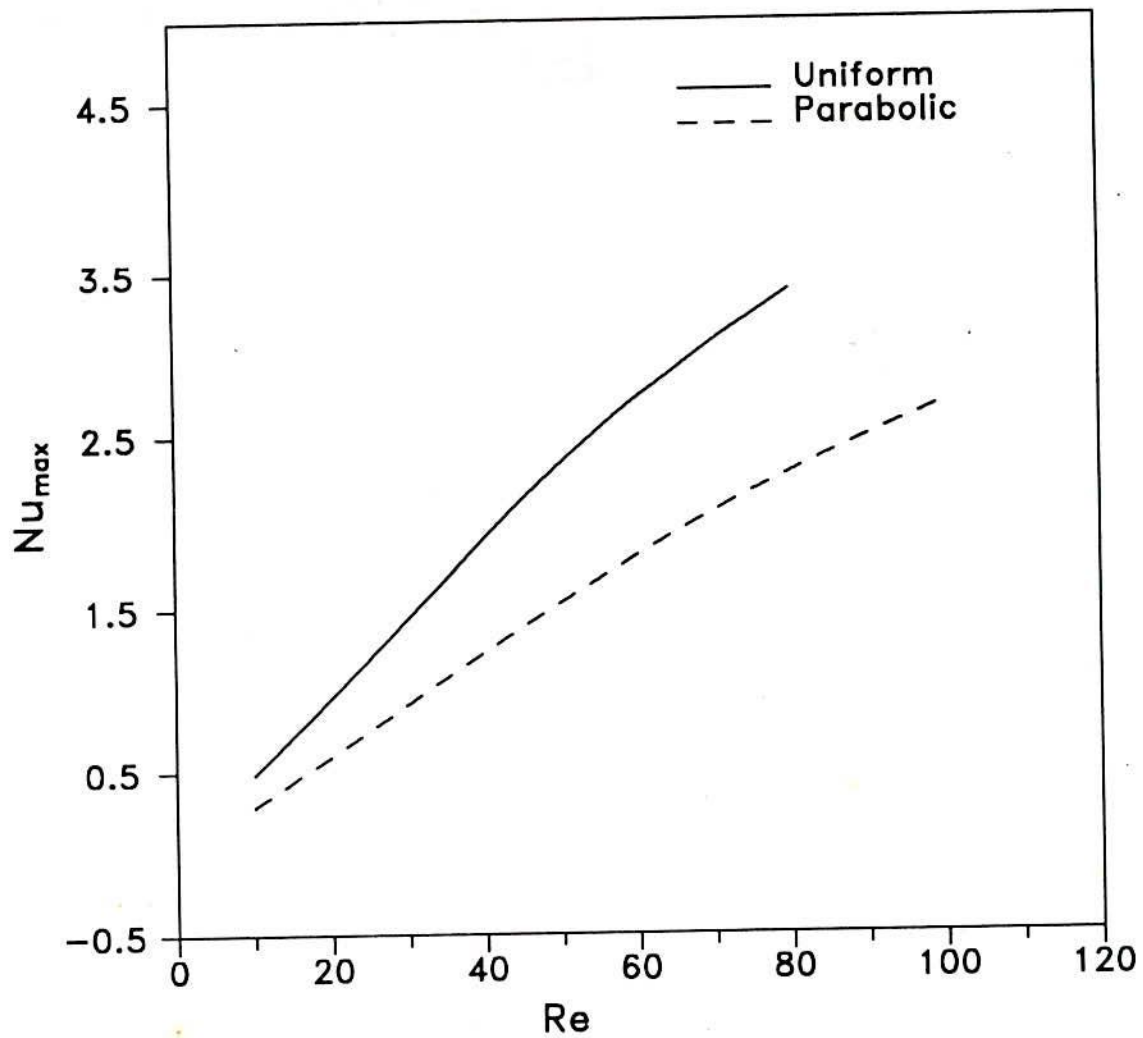


Fig.4.5.32; Variation of maximum Nusselt Number over the offset surface at offset ratio=5 and $Pr=4.34$

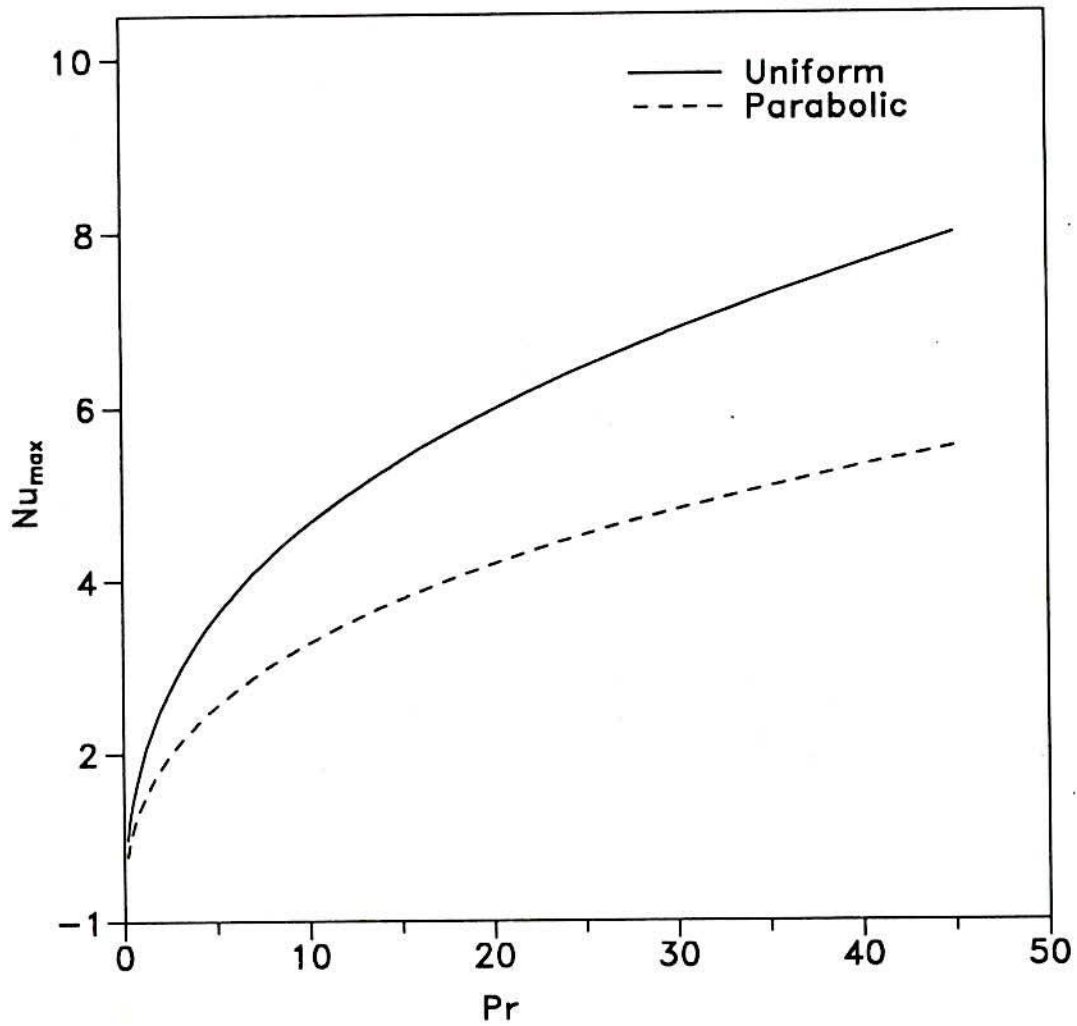


Fig 4.5.33: Variation of maximum Nusselt Number over the offset surface at offset ratio=5 and $Re=65$.

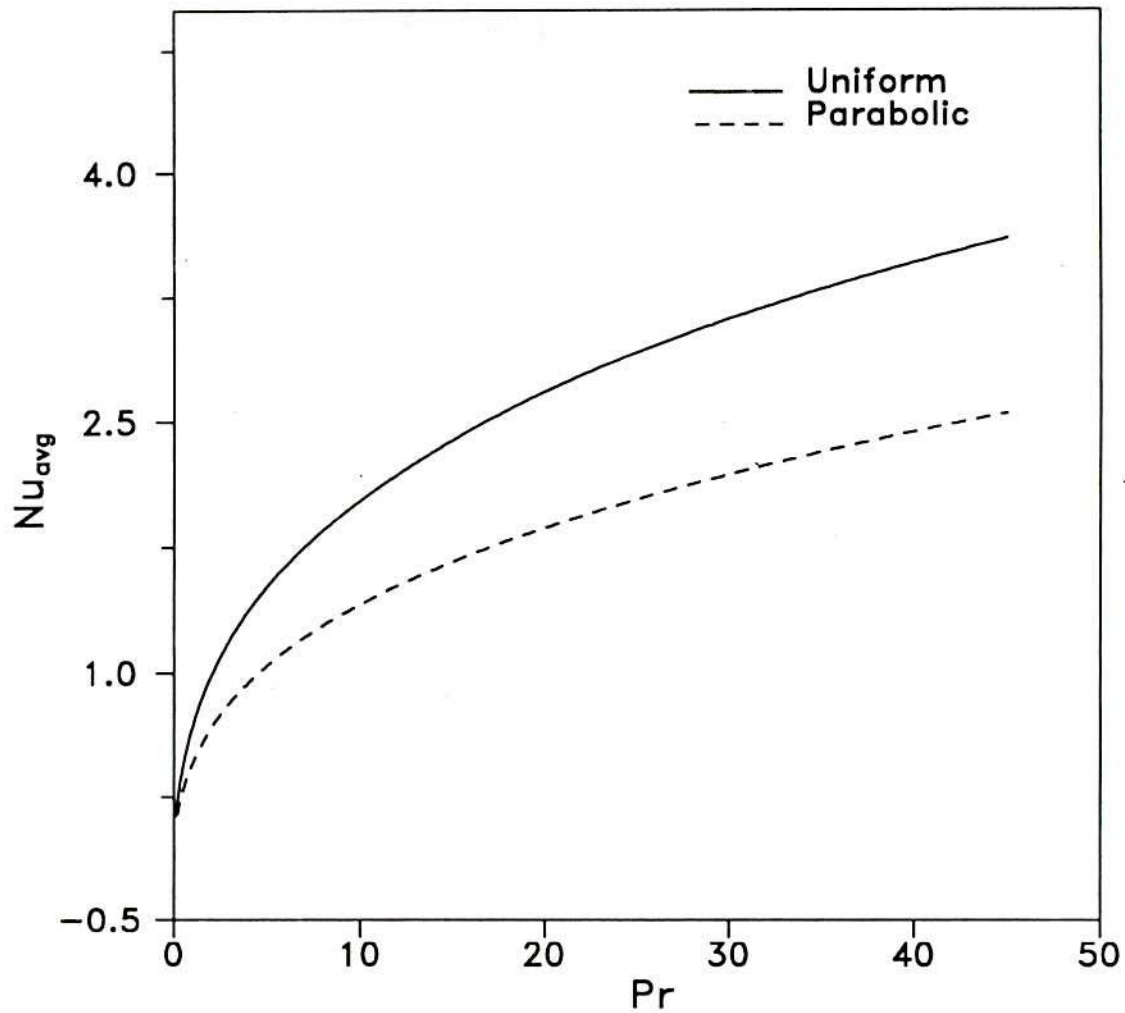


Fig.4.5.34: Variation of average Nu in the separated region for uniform and parabolic velocity profiles at nozzle exit for laminar offset jet.

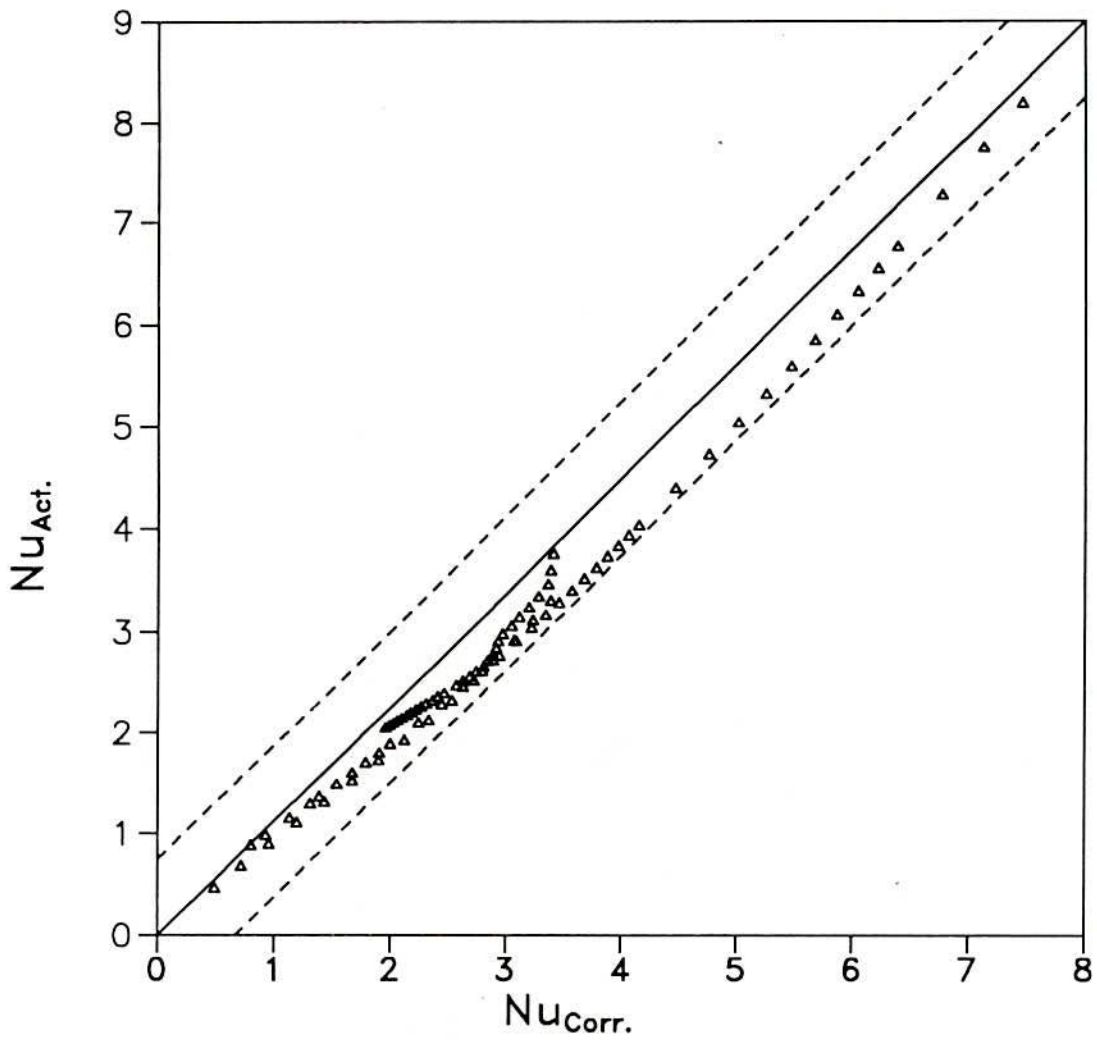


Fig.4.5.35:: Correlation for predicting maximum Nusselt number for laminar offset jet with uniform velocity profile at slot exit.

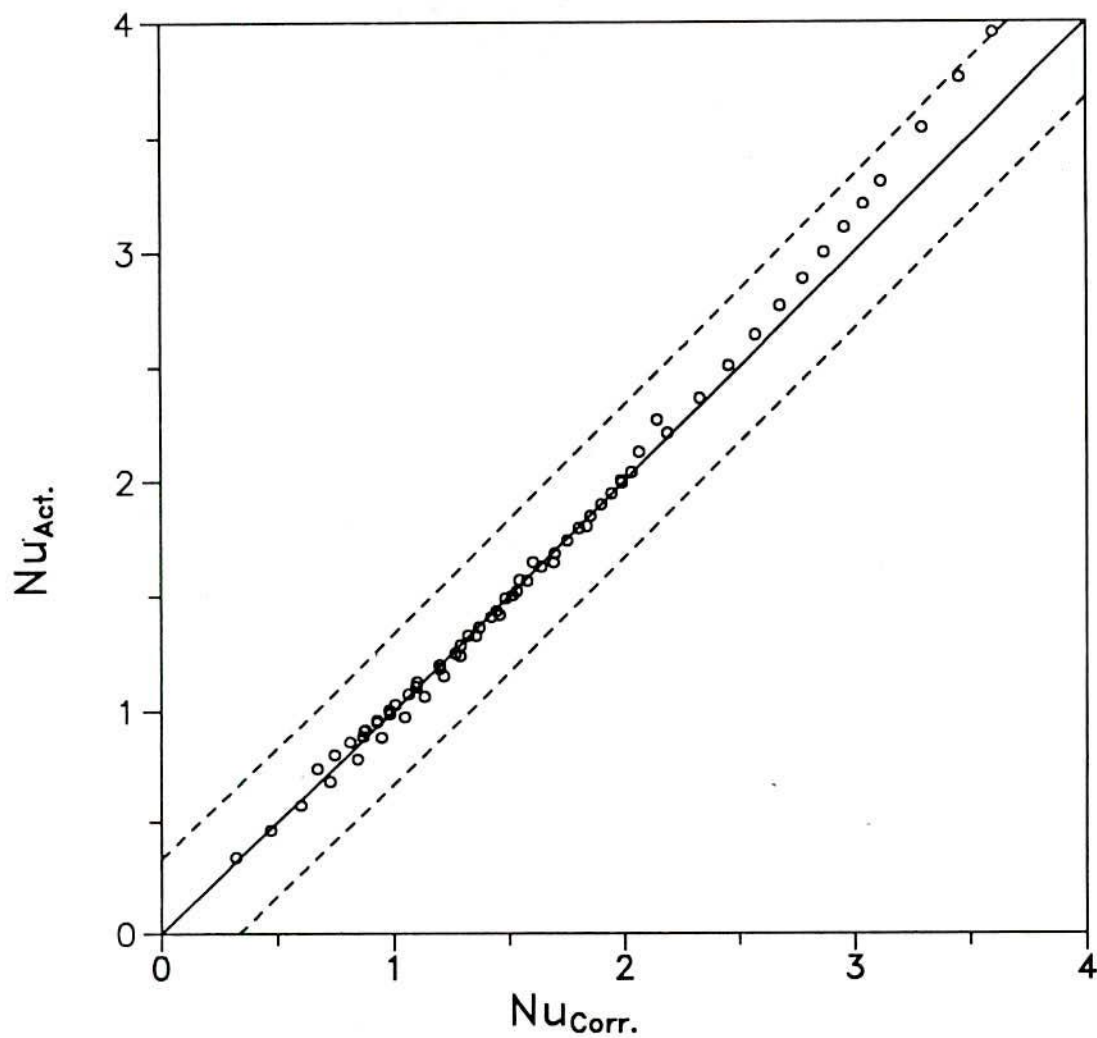


Fig.4.5.36:Correlation for predicting average Nusselt number in the separated region for laminar offset jet with uniform velocity profile at slot exit.

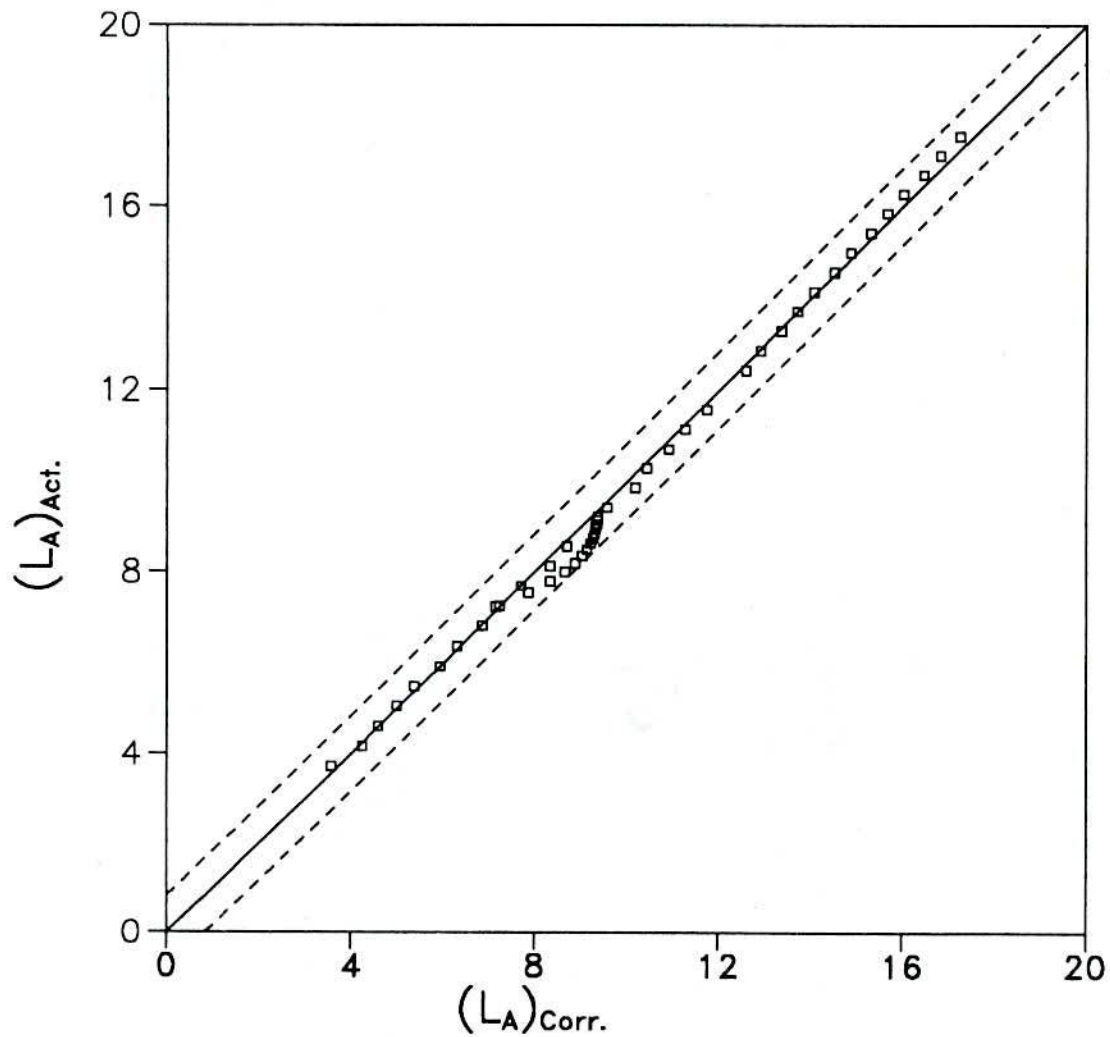


Fig.4.5.37.: Correlation for predicting reattachment length for laminar offset jet with uniform velocity profile at slot exit.

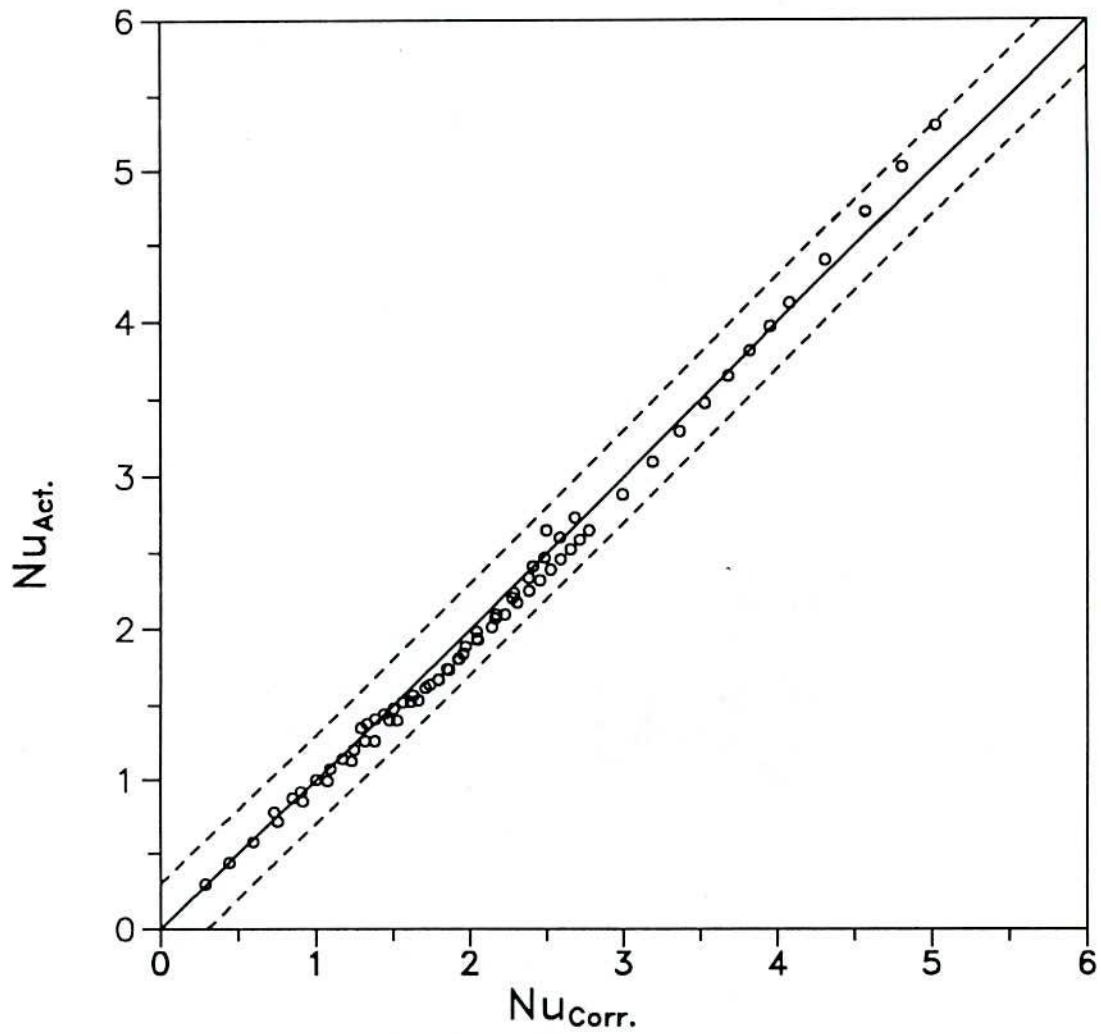


Fig.4.5.38; Correlation for predicting maximum Nusselt number for laminar offset jet with parabolic velocity profile at slot exit.

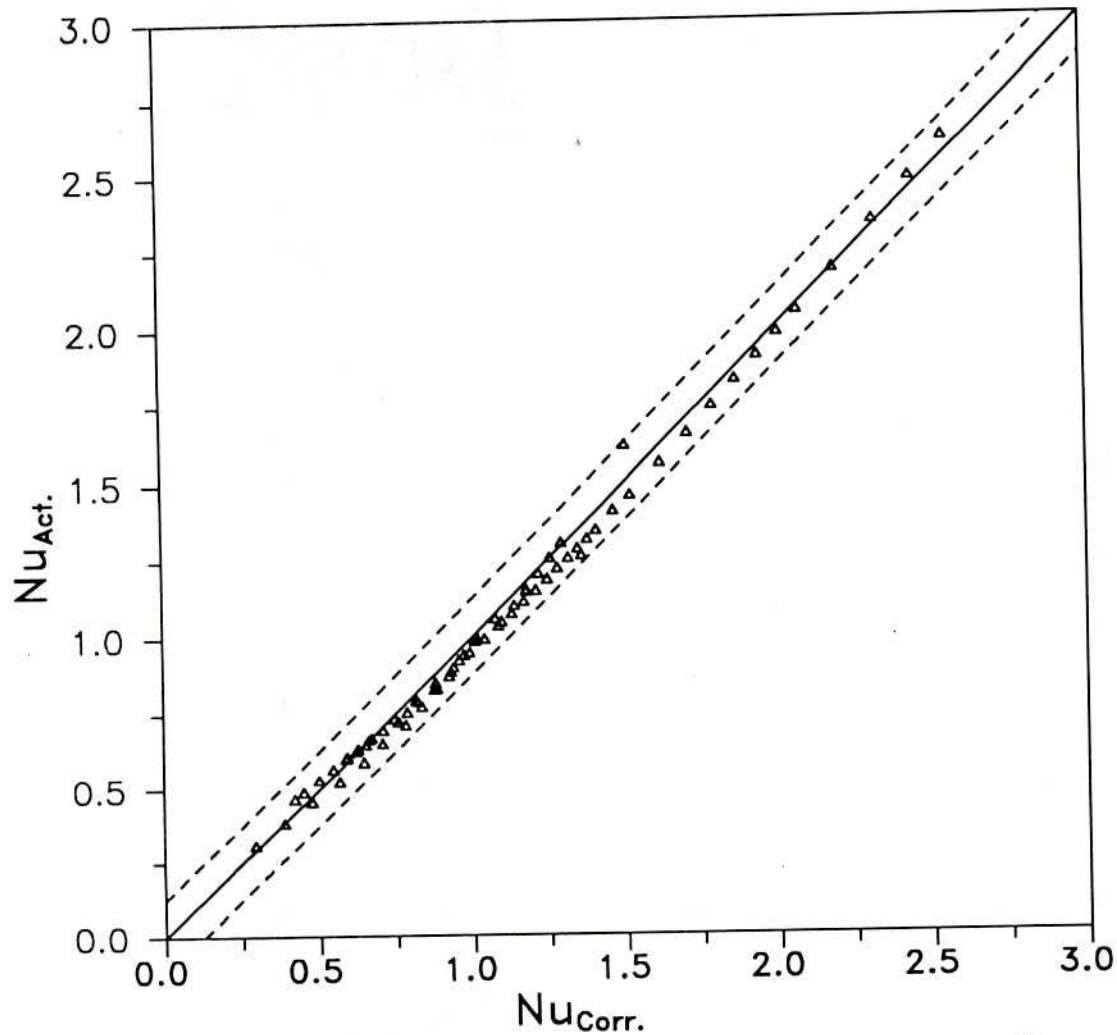


Fig.4.5.39: Correlation for predicting average Nusselt number in the separated region for laminar offset jet with parabolic velocity profile at slot exit.

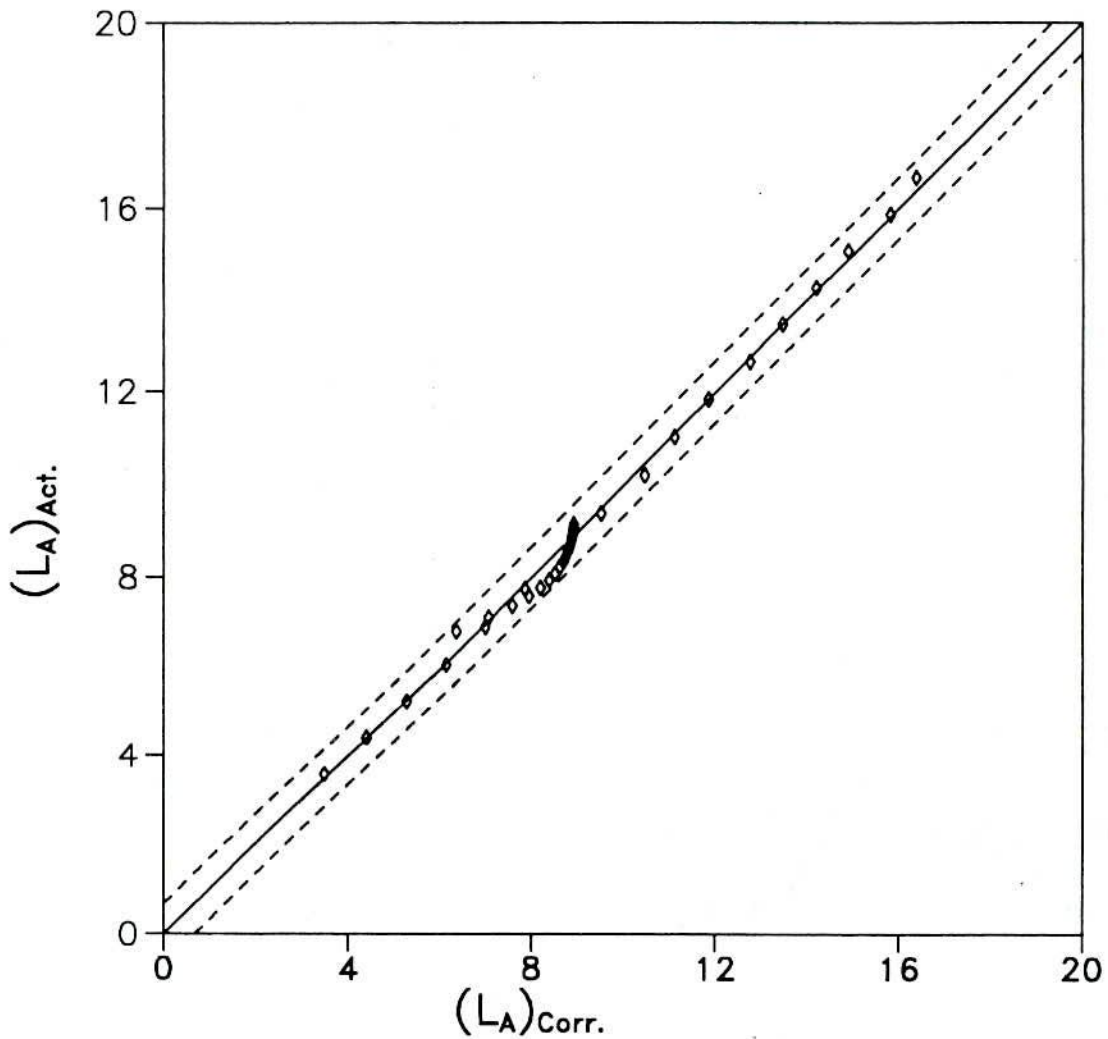


Fig.4.5.40: Correlation for predicting reattachment length for laminar offset jet with parabolic velocity profile at slot exit.

CHAPTER-V

CONCLUSIONS

In this investigation, Navier-Stokes equations and energy equation have been solved by SIMPLE and SIMPLEC algorithms for free jets, jet impingement on a circular cylinder, normal jet impingement on plate with and without buoyancy and an offset jet in the laminar range of Reynolds numbers. The SIMPLE and SIMPLEC algorithms were observed to be quite robust. All the problems treated herein are external flow problems, hence the location of the entrainment and outflow boundaries is very crucial to the convergence of the numerical schemes. Variable grid spacings have been used in all the cases. Convergent solutions could not be obtained at high Reynolds numbers in all the cases. It was observed that number of iterations required for convergence increased as the Reynolds number increased. In some cases, relaxation factors were chosen to be less than 0.5 to obtain converged solutions. Solutions for the parabolic slot-exit profiles, in general, required less number of iterations for convergence than those for the uniform slot-exit profiles. It is felt that solutions for the uniform slot-exit profiles, require very fine grid spacing near the slot lip to achieve convergence. It is felt, that converged solutions could be obtained at still higher Reynolds numbers by choosing smaller relaxation factors and continuing the iterative process over large number of iterations, say a few thousands.

Jet impingement over a circular cylinder has been idealized to a great extent. Even then, the solutions could not be obtained at high Reynolds numbers. The solutions of energy equation had some unexplained features, hence it has not been presented. A large number of changes were introduced in the computer program to apply the boundary conditions at the nozzle wall and nozzle exit. The errors in solution of energy equation may probably be programming error rather than computational error. The extension of nozzle wall has been done so as to consider entrainment at large distance from the nozzle-exit. But, in this process, no-slip and impermeability boundary conditions have to be applied on the nozzle wall. In actual practice, there may not be such long nozzle walls. Some authors have used continuative boundary condition on the nozzle wall. In any case, it is felt that best way to solve the problem is to transform the domain into a rectangular cartesian domain, and solve the transformed equations in rectangular domain as done by Kang and Greif [64]. Even for the free jets, it is felt that an adaptive grid will lead to more accurate solution, since near the jet-exit a smaller domain height is required than further downstream, where the jet spread increases.

For the vertically downward buoyant jet also, major changes were made in the computer program, so as to apply the boundary conditions on the nozzle wall and the nozzle-exit. In this case, the results for skin friction coefficient and Nusselt number in the absence of buoyancy agree with the available results. Solutions did not converge at higher Reynolds numbers,

particularly for uniform slot-exit profiles.

In case of offset jet also, solutions did not converge at higher Reynolds numbers.

In all the cases, it is felt that the solutions obtained at lower Reynolds numbers are representative of the laminar flow solutions.

The following conclusions may be drawn for the five problems, within the range of Reynolds numbers, Prandtl numbers, Richardson numbers and other geometrical parameters considered in this investigation.

5.1 FREE SLOT JET

1. The centreline temperature and velocity, both decay like $\bar{X}^{-1/3}$. $\bar{X} = \frac{x}{W Re}$ is found to be the non-dimensional length for the collapse of data in x direction. In particular, the jet centreline temperature and velocity become coincident for various Reynolds numbers with this choice of \bar{X} . The results agree with the results of Chanaud and Powell [28] Lai and Simmons [32].
2. The velocity variation of the slot jet in y direction becomes independent of Reynolds numbers when plotted against half jet width except at points very close to the slot-exit. Same trend is observed at large distances from the slot-exit if Schlichting's similarity variable η is used.
3. Temperature profiles also exhibit a similar trend when plotted against temperature half width. Temperature variation with Schlichting's similarity variable η also tends to exhibit similarity at large distances from the slot-exit.

4. The centre line velocity and the centreline temperature both decay at faster rate for the parabolic jet exit profiles as compared to that for the uniform jet exit profile.
5. T^*/T_C^* is higher for parabolic slot-exit profiles as compared to that for the uniform slot-exit profiles at $Pr = 0.01, 0.1$ and 1.0 . The temperature distribution shows an opposite trend for $Pr = 10.0$, where it becomes higher for the uniform slot exit profiles as compared to that for the parabolic slot-exit profiles.
6. The half jet width is observed to be almost independent of Reynolds numbers. At the slot-exit, jet velocity half width and jet temperature half width are 0.7 for the parabolic slot-exit velocity and temperature profiles and 1.0 for the uniform slot-exit velocity and temperature profiles.

5.2 FREE AXISYMMETRIC JET

1. The centreline temperature and velocity, both decay like \bar{X}^{-1} . $\bar{X} = \frac{x}{d Re}$ is found to be the non-dimensional length for the collapse of data in x direction. In particular, the jet centreline temperature and velocity become coincident for various Reynolds numbers with this choice of \bar{X} . The results agree with the experimental and numerical results of Akaike and Nemoto [5].
2. The velocity variation of the axisymmetric jet in y direction becomes independent of Reynolds numbers when plotted against half jet radius at a large distances in x direction. The same trend is observed at large distances from the jet-exit if Schlichting's similarity variable η is used.
3. Temperature profiles also exhibit a similar trend when

plotted against temperature half radius at large distances in x direction. The temperature variation with Schlichting's similarity variable η also exhibits similarity at large distances from the jet-exit.

4. The centreline velocity and the centreline temperature, both decay at faster rate for the parabolic jet-exit profiles as compared to those for the uniform jet-exit profiles.
5. The half jet radius is observed to be almost independent of Reynolds numbers. At the nozzle-exit, jet (Velocity) half radius and jet (Temperature) half radius are 0.352 for the parabolic jet-exit velocity and temperature profiles and 0.485 for the uniform jet-exit velocity and temperature profiles.

5.3 SLOT JET IMPINGEMENT ON A CIRCULAR CYLINDER

1. The rate of change of friction factor and the maximum value of friction factor, both increase with the increase of Reynolds numbers and nozzle width W , but decrease with the increase of L/W ratio.
2. The location of the maximum friction factor shifts towards the stagnation point with the increase of Reynolds numbers, but shifts away from the stagnation point with the increase of L/W ratio and nozzle width, W .
3. The point of flow separation moves downstream as the Reynolds number decreases. The conclusion 1, 2 and 3 agree with the observations of Kang and Greif [64].
4. The friction factor is unaffected by the nozzle width for small values of θ and the point of flow separation is

independent of nozzle width.

5. The pressure gradient is adverse in the region $\frac{\pi}{4} \leq \theta \leq \frac{\pi}{2}$.
6. The velocity profiles U/U_{\max} when plotted with jet half width as the characteristics length, have the typical features of wall jet. For small values of $R/R_{0.5U_{\max}}$, particularly below the peak, the velocity profiles are coincident for all Reynolds numbers.

5.4 VERTICALLY DOWNWARDS SLOT JET IMPINGING UPON A FLAT SURFACE

1. Richardson number affects the local Nusselt number, local friction factor and pressure significantly.
2. The maximum value of Nusselt number is same at $Ri = 0.15$ for both the type of profiles and for $Ri \geq 1.25$ it becomes zero since the jet does not contact the impingement surface.
3. The jet behaves like a non-buoyant jet for $Ri \leq 0.007$ with the parabolic slot-exit velocity and temperature profiles and for $Ri \leq 0.014$ with the uniform slot-exit velocity and temperature profile.
4. The stagnation point Nusselt number is larger for the parabolic slot-exit velocity and temperature profiles than that for the uniform slot-exit velocity and temperature profiles for $Re > 38$ and $Ri = 0.0$. In general, stagnation point Nusselt number is larger for parabolic slot-exit profiles than that for the uniform slot-exit profiles.
5. The average Nusselt number is higher for the uniform slot-exit profiles than that for the parabolic slot-exit profiles.

6. The location of maximum Nusselt number is at the stagnation point for nozzle-to-plate spacings of 0.5 to 2.0, and at $X = 0.375$ for nozzle-to-plate spacings greater or equal to 2.25 for uniform slot-exit profiles.
7. The local friction factor is independent of Reynolds numbers upto $X = 4$ with the uniform slot exit velocity and temperature profiles and with parabolic slot exit velocity and temperature profiles, local friction factor is independent of Reynolds numbers at higher values of Re over a narrow region near the stagnation point.
8. The local friction factor and the local Nusselt number decrease with the increase of nozzle-to-plate spacings for the buoyant jet. The maximum Nusselt number occurs at the stagnation point for Richardson number greater or equal to 0.1, for the uniform slot-exit velocity and temperature profiles.
9. Pressure coefficient decreases with the increase of Richardson number and the nozzle-to-plate spacings.
10. Correlations for Nusselt number have been developed to an accuracy of $\pm 10.24\%$ in the absence of buoyancy.

5.5 OFFSET SLOT JET

1. The local Nusselt number and the local friction factor increase with increasing Re but decrease with the increasing offset ratios.
2. The secondary recirculation has been clearly shown at $O.R. = 7$ and $Re = 80$. The friction factor data indicates that it occurs at $O.R. = 5$ also.
3. The local Nusselt number does not vary significantly with



Reynolds number upto $X=2.9$ for the parabolic slot-exit velocity and temperature profiles and upto $X=3.1$ for the uniform slot-exit velocity and temperature profiles.

4. The location of maximum Nusselt number for an offset ratio of 5 becomes constant for $Re \geq 40$ for the uniform slot-exit velocity and temperature profiles, and at $Re \geq 65$ for the parabolic slot-exit velocity and temperature profiles. But the location of maximum Nusselt number increases with an increase in offset ratio. It has been observed that the location of the maximum Nusselt number remains within one nozzle width upstream of the reattachment point in all the cases.
5. The reattachment length at O.R. of 5, is approximately constant for $Re > 65$ with the uniform slot-exit velocity profile, and $Re > 75$ for the parabolic slot-exit velocity profile; but the reattachment length increases with offset ratios.
6. The maximum Nusselt number, for the uniform slot-exit profiles, is approximately double that of the the maximum Nusselt number for the parabolic slot-exit profiles at $Re=65$ and offset ratio, O.R.= 5.
7. The local Nusselt number increases with the Prandtl number for all Reynolds numbers and offset ratios for both the type of profiles.
8. Correlations have been developed to an accuracy of $\pm 12 \%$

5.6 SCOPE OF FUTURE WORK

This investigation has been confined to either uniform or parabolic velocity and temperature profiles at jet-exit. The

effects of uniform temperature profiles with parabolic velocity profiles and vice versa which occur in various physical situations, could be investigated by the methodology used in this investigation. In general, one may extend this investigation to arbitrary velocity and temperature profiles with a core and boundary layer at the nozzle-exit. It was observed that uniform slot-exit velocity profile led to convergence problems because of the sudden change in velocity from maximum value to zero value at the lips of the slot. As a result, converged numerical solutions could not be obtained at higher Reynolds numbers. A further refinement of grid near the slot lips may improve the convergence.

Jet impingement over the cylinder posed a lot of convergence problems and required a large number of iterations for convergence. In fact, the solution of energy equation was observed to have some unexplained behavior, hence it has not been presented. In general, it is felt that solution for the jet impingement over cylinder can be obtained only by coordinate transformation as done by Kang and Greif [64].

Numerical convergence problems were faced particularly for uniform profiles, in case of vertically downwards buoyant slot-jet also, at higher Reynolds numbers. At still higher Reynolds numbers, parabolic slot exit profiles also gave convergence problems. In this case also, solutions may be obtained to investigate the effects of parabolic temperature profiles with uniform velocity profiles and vice versa or arbitrary velocity and temperature profiles at the slot-exit. The problem of vertically upward facing jet with these slot-exit profiles may also be

investigated.

Numerical convergence problems were faced at higher Reynolds numbers and higher offset ratios for the offset jet also, particularly for uniform slot-exit profiles. The effects of slot width may also be investigated in this case.

The jet impingement surface has been considered to be at uniform temperature. Actual jet impingement problems are conjugate problems, where the finite impingement surface is cooled by the jet. The analysis may be extended to such problems. The impingement surface may have arbitrary temperature or specified heat flux also, which may be investigated by the methodology.

The effect of variable properties may also be investigated. Finally, the analysis may be extended to an array of jets.

REFERENCES

1. Adcock, J.N., " The laminar jet system for cooling hot steel strip.", J. of the Iron and Steel Institute, Vol. 200, pp 909-913, 1962
2. Morgan, E.R., Dancy, T.E. and Korchynsky, M., " Improved steels through hot strip mill controlled cooling.", J. Metals, Vol. 17, pp 829-831. 1965.
3. Kohring, F.C., " Waterwall water-cooling systems.", Iron and Steel Engineer, pp 30-36, June, 1985.
4. Hollworth, B.R. and Durbin, M. " Impingement Cooling of Electronics", ASME J. Heat Transfer, Vol. 114, pp 607-613, August, 1992.
5. Akaike, S. and Nemoto, M., " Potential core of a submerged laminar jet.", Trans. ASME, J. Fluids Engg., Vol. 110, pp 392-398, 1988.
6. Pelfrey, J.R.R. and Liburdy, J.A., "Mean Flow Characteristics of a Turbulent Offset Jet", ASME J. Fluids Engineering, Vol 108, pp 82-88 March 1986.
7. Hrycak, P., Lee, D.T., Gauntner, J.W. and Livingood, J.N.B., "Experimental flow characteristics of a single turbulent jet impinging on a flat plate.", NASA TN D-5690, March, 1970.
8. Yuan, T.D., Liburdy, J.A. and Wang, T., " Buoyancy effects on laminar impinging jets.", Int. J. Heat and Mass transfer, Vol. 31, No. 10, pp 2137-2144, 1988.
9. Cebeci, T. & Bradshaw, P., "Physical and Computational Aspects of Convective Heat Transfer", Springer-Verlag, New York

- Inc., chap. 8, pp 239-246, 1984.
10. Patankar, S.V., "Numerical Heat Transfer and Fluid Flow.", Hemisphere, Washington, D.C., 1980.
 11. Fumizawa, M., Hishida, M. and Kunugi, T., "Numerical study on a laminar round jet of a high-density gas discharging into stagnant air", Int. J. Chem. Engg., Vol. 32, No. 2, pp 302-312, 1992.
 12. Sparrow, E.M. and Lee, L., "Analysis of flow field and impingement heat/mass transfer due to nonuniform slot jet.", Trans. ASME, J. Heat Transfer, Vol. 97, pp 191-197, 1975.
 13. Doormaal, van J.P. and Raithby, G.D., "Enhancements of the *SIMPLE* method for predicting incompressible fluid flows", Numerical heat transfer, vol 7, pp 147-163, 1984.
 14. Tetervin, N., "Laminar flow of a slightly viscous incompressible fluid that issues from a slit and passes over a flat plate.", NACA TN 1644, 1948.
 15. Glauert, M.B. "The wall jet", J. Fluid Mechanics, 1956, vol 1, pp 625-643, 1956
 16. Schwarz, W.H. and Cosart, W.P., "The two-dimensional turbulent wall-jet.", J. Fluid Mechanics, vol 10, Part 4, pp 481-495, 1961
 17. Myers, G.E., Schauer, J.J. and Eustis, R.H., "Heat Transfer to Plane Turbulent Wall Jets.", J. Heat Transfer, Vol. 85, pp 209-214, August, 1963.
 18. Bajura, R.A. and Szweczyk, A.A., "Experimental Investigation of a Laminar Two-Dimensional Plane Wall Jet.", J. Phys. Fluid, Vol. 13, No. 7, pp 1653-1664, July, 1970.

19. Bajura, R.A. and Catalano, M.R., "Transition in a Two-dimensional plane wall jet.", J. Fluid Mechanics, Vol. 70, pp 773-799, 1975.
20. Rajaratnam, N., "Turbulent jet", Elsevier, Amsterdam, 1976.
21. Hammond, G.P., "Complete Velocity Profile and 'Optimum' Skin Friction Formulas for the Plane Wall-Jet", J. Fluid Engg., Vol. 104, pp 59-66, 1982.
22. Tsuji, Y., Morikawa, Y., Nagatani, T. and Sakao, M., "The stability of a two-dimensional wall jet .", Aero. Quart., Vol. 28, pp 235-246, 1977.
23. Hsiao, F.B. and Sheu, S.S., "Flow transition and wall boundary layer properties in the near field region of a plane wall jet." Conf. of Boundary layer Transition and Control, Vol. 1, 38.1-38.10, Cambridge U.K., 1991.
24. Hsiao, F.B. and Sheu, S.S., "Double Row Vortical Structures in the Near field Region of a Plane Wall Jet.", J. Expt. in Fluids, 17, pp 291-301, 1994.
25. Schlichting, H., Boundary Layer Theory, 6th. edition, McGraw-Hill, New York, pp. 179-183, 1979.
26. Bickley, W., "The Plane Jet," Philosophical Magazine, series 7, vol. 23, pp. 727-731, 1939.
27. Andrade, E.N. de C., "The Velocity Distribution in a Liquid-into-Liquid Jet. Part-2: The Plane Jet", J. Fluid Mechanics, Vol. 51, pp 784-793, 1939.
28. Chanaud, R.C. & Powell, A., "Experiments Concerning the sound-Sensitive Jet," J. Acoustical Society of America, vol. 34, pp. 907-915, 1962.

29. Sato, H. and Sakao, F., "An experimental investigation of the instability of a two-dimensional jet at low Reynolds numbers.", J. Fluid Mechanics, Vol. 20, Part 2, pp 337-352, 1964.
30. Pai, S.I. & Hsieh, T., "Numerical Solution of Laminar Jet Mixing with and without Free Stream," Applied Scientific Research, vol. 27, pp. 39-62, 1972.
31. Peyret, R. "Unsteady evolution of a horizontal jet in a stratified fluid.", J. Fluid Mechanics, Vol. 78, pp 49-63, 1976
32. Lai, J.C.S. and Simmons, J.M., " Numerical solution of periodically pulsed laminar free jets.", AIAA J., Vol. 19, No. 6, pp 813-815, 1981.
33. Curle, N., "On hydrodynamic stability in unlimited fields of viscous flow", Proc. Royal Soc. Ser. A, Vol. 238, pp 489-501, 1957
34. Tatsumi, T. and Kakutani, T., "The stability of a two-dimensional laminar jet", J. Fluid Mechanics Vol 4, pp 261-275, 1958.
35. Howard, L.N., "Hydrodynamic stability of a jet", J. Math. Phys. Vol. 37, pp 283-298, 1959.
36. Clenshaw, C.W. and Elliott, D. "A numerical treatment of the Orr-Sommerfeld equation in the case of a laminar jet", Q. J. Mech., Vol. 13, pp 300-313, 1960.
37. Kaplan, R.E., "Ph.D. Thesis, M.I.T. Cambridge Mass.
38. Fox, J. and Lessen, M. "The stability of boundary layer type flows with infinite boundary conditions", 50 Jahre

- Grenzschichtforschung (Editors : Görtler, H. and Tollmein, W.), Vieweg Braunschweig. 122-126, 1955.
39. Rosenhead, L., Laminar Boundary Layers, p 561, Oxford University Press, 1966.
 40. Gardon, R. and Akfirat, J.C., " Heat transfer Characteristics of impinging two-dimensional air jets.", Trans ASME, J. Heat Transfer, Vol. 88, pp 101-108, 1966.
 41. Sparrow, E.M. and Wong, T.C., " Impingement transfer coefficients due to initially laminar slot jets.", Int. J. Heat and Mass transfer, Vol. 18, pp 597-605, 1975.
 42. Van Heiningen, A.R.P., Mujumdar, A.S. and Douglas, W.J.M., "Numerical prediction of the flow field and impingement heat transfer caused by a laminar slot jet.", Trans. ASME, J. Heat Transfer, Vol. 98, pp 654-658, 1976.
 43. Gauntner, J.W., Livingood, J.N.B. and Hrycak, P., " Survey of literature on flow characteristics of a single turbulent jet impinging on a flat plate", NASA TN-5652, 1970.
 44. Andrade E.N. da C. and Tsien, J.M., " The Velocity Distribution in a Liquid-into-Liquid Jet", Proc. of Phys. Society of London, Vol. 49, Part-4, No. 7, pp 381-391, 1937.
 45. Landau, L.D., "A new exact solution of the Navier-Stokes equations", C.R. Acad. Sci. URSS, Vol 43, pp 286-289, 1944.
 46. Squire, H.B., "The Round Laminar Jet", Quart. J. Mech. and Applied Math., Vol. 4, Part 3, pp 321-329, 1951.
 47. Reynolds, A.J., "Observations of a liquid-into-liquid jet", J. Fluid Mechanics, Vol 14, pp 552-556, 1962.

48. McNaughton, K.J. and Sinclair, C.G., " Submerged jets in short cylindrical vessels. *Fluids Mechanics* Vol 2 2 367-375, 1966.
49. Morton, B.R., " Entrainment models for laminar jets, plumes and wakes.", *Phys. Fluids*, Vol 10, pp 2120-2127, 1967.
50. Kent, J.C., " Unsteady viscous jet flow into stationary surroundings", *Computers & Fluids*, Vol. 1 pp 101-117, 1973.
51. Hatta, K. and Nozaki, T., " Two-dimensional and axisymmetric jet flows with finite initial cross section.", *Bulletin of JSME*, Vol. 18, No. 118, pp 349-357, 1975.
52. Rankin, G.W. and Sridhar, K., " Developing region of laminar jets with uniform exit velocity profiles.", *ASME, J. Fluids Engg.*, Vol. 100, No. 1, pp 55-59, 1978.
53. Rankin, G.W., Sridhar, K., Arulraja, M. and Kumer, K.R., " An experimental investigation of laminar axisymmetric submerged jets.", *J Fluid Mechanics*, Vol. 133, pp 217-231, 1983.
54. Arulraja, M., "Analysis of developing region of a submerged laminar free jet", M.A.Sc. Thesis, 1982.
55. Tucker, H.J. and Islam, S.M.N., "Development of Axisymmetric Laminar to Turbulent Free Jets from Initially Parabolic Profiles." *J. Fluid Engg.*, Vol. 108, pp 321-324, 1986.
56. Hrycak, P., Jachna, S. and Lee, D.T., "A Study of Characteristics of Developing, Incompressible, Axi-Symmetric Jets", *Int. Heat Transfer Conf.*, Vol. 1, No. 1, pp 63-72, 1974.
57. Martin, H., " Heat and mass transfer between impinging gas jets and solid surfaces, *Advances in Heat Transfer*, Vol. 13, pp 1-60, Academic Press, New York, 1977.

58. Schuh, H and Persson, B., "Heat transfer on circular cylinders exposed to freejet flow", Int. J. Heat Mass Transfer, vol. 7, pp 1257-1271, 1964
59. Kumada, M., Mabuchi, I. and Kawashima, Y., " Mass transfer on a cylinder in the potential core region of two-dimensional jet.", Heat Transfer-Japanese Research, 2(3), pp 53-66, 1973.
60. Sparrow, E.M., Altemani, C.A.C. and Chaboki, A., " Jet impingement heat transfer for a circular jet impinging in crossflow on a cylinder.", Trans. ASME, J. Heat Transfer, Vol. 106, pp 570-577, 1984.
61. Sparrow, E.M. and Alhomoud, A., " Impingement heat transfer at a circular cylinder due to an offset or non-offset slot jet.", Int. J. Heat and Mass transfer, Vol. 27, No.12, pp 2297-2306, 1984.
62. Faruque, O., Arora, R.C., and Brahma, R.K., " Experimental investigation of jet impingement on a cylinder.", Preprint of 9th. Eurotherm Seminar on Heat Transfer in Single Phase flow, Rhur-Universitat, Bockhum, FRG, July, 1989.
63. Arora, R.C., Brahma, R.K. and Pk. Md. Omar Faruque, " Heat Transfer by Slot Jet Impingement on a Cylinder", J. of Energy, Heat and Mass Transfer, vol. 15, pp 253-259, 1993.
64. Kang, S.H. and Greif, R., "Flow and Heat Transfer to a Circular Cylinder with a Hot Impinging Air Jet.", Int. J. Heat and Mass Transfer, Vol. 35, No.9, pp 2173-2183, 1992.
65. Freidman, S.J. and Mueller, A.C., "Heat transfer to flat surface", Proc. General discussion on heat transfer, Inst. Mech. Engrs., London, pp 138-142, 1951.
66. Perry, K.P., "Heat Transfer by Convection from a Hot Gas Jet to

- a Plane Surface", Proc. Inst. Mech. Engrs., Vol 168, pp 775-784, 1954.
67. Ehrich, F.F., "Some hydrodynamic aspects of valves.", ASME paper 55-A-114, 1955.
68. Vickers, J.M.F., "Heat transfer coefficients between fluid jets and normal surfaces", Industrial and Engineering Chemistry, Vol 51, pp 967-972, 1959.
69. Daane, R.A. and Han, S.T., "An analysis of air-impingement drying", Inst. of paper chemistry, Tappi, Vol 44, No. 1, pp 73-80, 1961.
70. Schrader, H., "Trocknung Feuchter Oberflächen Mittels Warmloftstrahlen; Strömungsvorgänge und Stoffübertragung", Forschungsheft no 484, VDI, 1961.
71. Metzger, D.E., "Spot cooling and heating of surfaces with high velocity impinging air jets. Part-1: Slot jets on plane surfaces.", TR No. 52, Stanford University, 1962.
72. Gardon, R. and Cobonpue, J., "Heat Transfer Between a Flat Plate and Jets of Air Impinging on It", Int. Developments in Heat Transfer. Proceedings, 2nd. Int. Heat Transfer Conference, ASME, New York, N.Y., pp 454-460, 1962.
73. Gardon, R. "A transducer for the measurement of heat flow rate", Trans ASME, J. Heat Transfer, Vol 82, pp 396-398, 1960.
74. Huang, G.C., "Investigations of Heat-Transfer Coefficients for Air Flow Through Round Jets Impinging Normal to a Heat-Transfer Surface", J. Heat Transfer, Vol. 85, pp 237-245, August, 1963.
75. Watson, E.J., "The radial spread of a liquid jet over a

- horizontal plane.", J. Fluid Mechanics, Vol. 20, pp 481-499, 1964.
76. Chaudhury, Z.H., " Heat transfer in a radial liquid jet.", J. Fluid Mechanics, Vol. 20, pp 501-511, 1964.
77. Gardon, R. and Akfirat, J.C., "The Role of Turbulence in Determining the Heat Transfer Characteristics of Impinging Jets", Int. J. Heat and Mass Transfer, Vol. 8 pp 1261-1272, 1965.
78. Korger, M. and Krizek, F., " Mass transfer coefficient in impinging flow from slotted nozzle.", Int. J. Heat and Mass transfer, Vol. 9, pp 337-344, 1966.
79. Schuh, H. and Pettersson, R., " Heat transfer by arrays of Two-dimensional jets directed normal to surfaces including the effects of a superposed wall parallel to flow.", Proc. of the 3rd. International Heat Transfer Conference, AIChE, Vol. 2, pp 280-291, 1966.
80. Cadek, F.F., " A fundamental investigation of jet impingement heat transfer", Ph. D. Thesis, University of Cincinnati, 1968.
81. Cartwright, W.G. and Russell, P.J., " Characteristics of a turbulent slot jet impinging on a plane surface.", Proc. Inst. Mech. Engrs., 3H 182, pp 309, 1967-1968.
82. Runchal, A.K., Spalding, D.B. and Wolfshtein, M., " The numerical solution of elliptic equations for transport of vorticity, heat and matter in two-dimensional flows.", Imperial college, Mech. Engg. Deptt., Rep. SF/TN/14, 1968.
83. Kumada, M. and Mabuchi, I., " Studies on the heat transfer of impinging jet (1st. report, mass transfer for two-dimensional

jet of air impinging normally on a flat plate) Bull. JSME, Vol. 13, pp 77-85, 1970.

84. Wolfshtein, M., "Some solutions of the plane turbulent impinging jet.", Trans. ASME, J. Basic Engg., Vol. 92, pp 915-922, 1970.
85. Gosman, A.D., Pun, W.M., Runchal, A.K., Spalding, D.B., and Wolfshtein, M., "Heat and mass transfer in recirculating flows", Academic Press, New York, 1969.
86. Scholtz, M.T. and Trass, O., "Mass transfer in a nonuniform impinging jet.", AIChE J., Vol. 16, pp 82-96, 1970.
87. Andreyev, A.A., Dakhno, V.N., Savin, V.K. and Yadayev, B.N., "Investigation of heat transfer in a gradient flow region for plane turbulent jet impinging on a plate situated normal to the flow.", NASA TT F-14195, 1972.
88. Miyazaki, H. and Silberman, E., "Flow and heat transfer on a flat plate normal to a two-dimensional laminar jet issues from a nozzle to finite height.", Int. J. Heat and Mass transfer, Vol. 15, pp 2097-2107, 1972.
89. Livingood, J.N.B. and Hrycak, P., "Impingement heat transfer from turbulent air jets to flat plates — A literature survey", NASA TM X-2778, May, 1973.
90. Ero, M.I.O. "Heat and mass transfer in close proximity impinging two-dimensional laminar jets.", AIAA J., Vol. 16, pp 611-613, 1978.
91. Masliyah, J.M. and Nguyen, T.T., "Mass transfer due to an impinging slot jet.", Int. J. Heat and Mass transfer, Vol. 15, pp 237-244, 1979.

92. Obot, N.T., Mujumder, A.S., and Douglas, W.J.M., "The effect of nozzle geometry on impingement heat transfer under a round turbulent jet.", Winter Annual Meeting, NY, pp 1-12, 1979.
93. Obot, N.T., Mujumder, A.S., and Douglas, W.J.M., "Design correlations for heat and mass transfer under various turbulent impinging jet configurations." Developments in Drying, New Jersey, pp 388-402, 1979.
94. Inada, S., Miyasaka, Y. and Izumi, R., "A study of the laminar flow heat transfer between a two-dimensional water jet and a flat with constant heat flux.", Bull. JSME, Vol. 24, pp 1803-1810, 1981.
95. Deshpande, M.D. and Vaishnav, R.N., "Submerged laminar jet impingement on a plate.", J. Fluid Mechanics, Vol. 114, pp 213-236, 1982.
96. Hin-Sum Law and Masliyah, J.H., "Mass Transfer due to Confined Laminar Impinging Two-Dimensional Jet", Int. J. Heat and Mass Transfer, Vol 27, No. 4, pp 529-539, 1984.
97. Striegl, S.A. and Diller, T.E., "The effect of entrainment temperature on jet impingement heat transfer.", Trans. ASME, J. Heat Transfer, Vol. 106, pp 27-33, 1984.
98. Downs, S.J. and James, E.H., "Jet impingement heat transfer- a literature survey.", ASME paper 87-HT-35, 1987.
99. Elbanna, H. and Sabbagh, J.A., "Flow Visualization and Measurements in a Two-Dimensional Two-Impinging-Jet Flow", AIAA, Journal, Vol.27, pp 420-426, 1989.
100. Wnag, X.S., Dagan, Z. and Jiji, L.M., "Heat transfer between a circular free jet and a solid surface with non-uniform wall temperature or wall heat flux-1. Solution for the stagnation

- region." Int. J. Heat and mass Transfer vol.32, pp 1351-1360, 1989.
101. Zumbrunnen,D.A., Incropera,F.P. and Viskanta,R., "Convective Heat Transfer Distributions on a Plate Cooled by Planar Water Jets.", J Heat Transfer, Vol. 111, pp 889-896, 1989.
 102. Goldstein,R.J., Sobolik,K.A. and Seol,W.S., "Effect of Entrainment on the Heat Transfer to a Heated Circular Air Jet Impinging on a Flat Surface.", Trans. ASME Vol.112, pp 608-611,1990
 103. Wolf,D.H., Viskanta,R. and Incropera,F.P., "Local convective heat transfer from a heated surface to a planar jet of water with a nonuniform velocity profile.", Trans ASME, J. Heat Transfer, Vol.112, pp 899-905, 1990.
 104. Goldstein, R.J. and Seol, W.S., "Heat Transfer to a row of impinging circular air jet including the effect of entrainment.", Int. J. Heat and Mass Transfer, Vol.34, pp 2133-2147, 1991.
 105. Sami-Al-Sanea, "A numerical study of the flow and heat transfer characteristics of an impinging laminar slot-jet including crossflow effects", Int. J. Heat and Mass Transfer, vol 35, No 10, pp 2501-2513, 1992.
 106. Pun,W.M. and Spalding,D.B., " A general computer program for two-dimensional elliptic flows", Report No. HTS 76/2, Dept. of Mech. Engg., Imperial college, London, 1976.
 107. Brahma,R.K., "Prediction of stagnation point heat transfer for a slot jet impinging on a flat surface", Wärme-und Stoffübertragung, Vol 27, pp 61-66, 1992.
 108. Womac,D.J., Ramadhyani,S. and Incropera,F.P., "Correlating

Equations for Impingement Cooling of Small Heat Sources with Single Circular Liquid Jets.", J. Heat Transfer, Vol. 115, pp 106-115, February, 1993.

109. Stevens, J. and Webb, B.W., "Measurements of flow structure in the stagnation zone of impinging free-surface liquid jets." Int. J. Heat and Mass Transfer, Vol. 36, No. 17, pp 4283-4286, 1993.
110. Stevens, J. and Webb, B.W., "Measurements of flow structure in the radial layer of impinging free-surface liquid jets", Int. J. Heat and Mass Transfer, Vol. 36, No. 15, pp 3751-3758, 1993.
111. Elison, B. and Webb, B.W., "Local heat transfer to impinging liquid jets in the initially laminar, transitional, and turbulent regimes", Int. J. Heat and Mass Transfer, Vol. 37, No. 8, pp 1207-1216, 1994.
112. Lytle, D. and Webb, B.W. "Air jet impingement heat transfer at low nozzle-plate spacings", HMT-94-034, Proceeding ISHMT-ASME heat and mass transfer conference and twelfth national heat and mass transfer conference, January 5-7, 1994, Bhabha atomic research centre, Bombay, India, pp 271-276.
113. Huang, L. and El-Genk, M.S., "Heat Transfer of an Impinging Jet on a Flat Surface.", Int. J. Heat and Mass transfer, Vol. 37, No. 13 pp 1915-1923, 1994.
114. Mollendorf, J.C. and Gebhart, B., "Thermal Buoyancy in Round Laminar Vertical Jets", Int. J. Heat and Mass Transfer, Vol. 16, pp 735-745, 1973.
115. Seban, R.A., Behnia, M.M. and Abreu, K.E., "Temperatures in a Heated Air Jet Discharged Downward", Int. J. Heat and Mass Transfer, Vol. 21, pp 1453-1458, 1978.

- Bonndary Interaction", ASME J. Fluid Engineering, Vol 103, pp 154-161 March 1981.
- 125.Hoch,J. and Jiji,L.M., "Theoretical and Experimental Temperature Distribution in Two-Dimensional Turbulent Jet-Boundary Interaction", ASME J. Heat Transfer, Vol 103, pp 331-336 May 1981.
- 126.Aung,W., "An Experimental Study of Laminar Heat Transfer Downstream of Back steps", ASME J. Heat Transfer, Vol 105, pp 823-829 November 1983.
- 127.Aung,W.,Baron,A. and Tsou,F., "Wall independency and effect of initial shear-layer thickness in separated flow and heat transfer", Int. J. Heat and Mass Transfer, Vol 28, No:9 pp 1757-1771, 1985.
- 128.Holland,J.T. and Liburdy,J.A., "Measurements of the thermal Characteristics of heated offset jets", Int. J. Heat and Mass Transfer, Vol 33, No.1, pp 69-78, 1990.